

Lecture Notes in Mechanical Engineering

Gullapalli Sivaramakrishna
S. Kishore Kumar
B. N. Raghunandan *Editors*


Proceedings of the National Aerospace Propulsion Conference

Select Proceedings of NAPC 2020

 Springer

Lecture Notes in Mechanical Engineering

Editorial Board

Francisco Cavas-Martínez , Departamento de Estructuras, Construcción y Expresión Gráfica Universidad Politécnica de Cartagena, Cartagena, Murcia, Spain

Francesca di Mare, Institute of Energy Technology, Ruhr-Universität Bochum, Bochum, Nordrhein-Westfalen, Germany


Mohamed Haddar, National School of Engineers of Sfax (ENIS), Sfax, Tunisia

Young W. Kwon, Department of Manufacturing Engineering and Aerospace Engineering, Graduate School of Engineering and Applied Science, Monterey, CA, USA

Justyna Trojanowska, Poznan University of Technology, Poznan, Poland

Series Editors

Fakher Chaari, National School of Engineers, University of Sfax, Sfax, Tunisia

Francesco Gherardini , Dipartimento di Ingegneria “Enzo Ferrari”, Università di Modena e Reggio Emilia, Modena, Italy

Vitalii Ivanov, Department of Manufacturing Engineering, Machines and Tools, Sumy State University, Sumy, Ukraine

Lecture Notes in Mechanical Engineering (LNME) publishes the latest developments in Mechanical Engineering—quickly, informally and with high quality. Original research reported in proceedings and post-proceedings represents the core of LNME. Volumes published in LNME embrace all aspects, subfields and new challenges of mechanical engineering. Topics in the series include:

- Engineering Design
- Machinery and Machine Elements
- Mechanical Structures and Stress Analysis
- Automotive Engineering
- Engine Technology
- Aerospace Technology and Astronautics
- Nanotechnology and Microengineering
- Control, Robotics, Mechatronics
- MEMS
- Theoretical and Applied Mechanics
- Dynamical Systems, Control
- Fluid Mechanics
- Engineering Thermodynamics, Heat and Mass Transfer
- Manufacturing
- Precision Engineering, Instrumentation, Measurement
- Materials Engineering
- Tribology and Surface Technology

To submit a proposal or request further information, please contact the Springer Editor of your location:

China: Ms. Ella Zhang at ella.zhang@springer.com

India: Priya Vyas at priya.vyas@springer.com

Rest of Asia, Australia, New Zealand: Swati Meherishi at swati.meherishi@springer.com

All other countries: Dr. Leontina Di Cecco at Leontina.dicecco@springer.com

To submit a proposal for a monograph, please check our Springer Tracts in Mechanical Engineering at <https://link.springer.com/bookseries/11693> or contact Leontina.dicecco@springer.com

Indexed by SCOPUS. All books published in the series are submitted for consideration in Web of Science.

Gullapalli Sivaramakrishna · S. Kishore Kumar ·
B. N. Raghunandan
Editors

Proceedings of the National Aerospace Propulsion Conference

Select Proceedings of NAPC 2020

 Springer

Editors

Gullapalli Sivaramakrishna
Combustion Group, Gas Turbine Research
Establishment
Defence Research and Development
Organisation
Bengaluru, Karnataka, India

S. Kishore Kumar
Gas Turbine Research Establishment
Defence Research and Development
Organisation
Bengaluru, Karnataka, India

B. N. Raghunandan
Department of Aerospace Engineering
Indian Institute of Science
Bengaluru, Karnataka, India

ISSN 2195-4356

ISSN 2195-4364 (electronic)

Lecture Notes in Mechanical Engineering

ISBN 978-981-19-2377-7

ISBN 978-981-19-2378-4 (eBook)

<https://doi.org/10.1007/978-981-19-2378-4>

© The Editor(s) (if applicable) and The Author(s), under exclusive license to Springer Nature Singapore Pte Ltd. 2023

This work is subject to copyright. All rights are solely and exclusively licensed by the Publisher, whether the whole or part of the material is concerned, specifically the rights of translation, reprinting, reuse of illustrations, recitation, broadcasting, reproduction on microfilms or in any other physical way, and transmission or information storage and retrieval, electronic adaptation, computer software, or by similar or dissimilar methodology now known or hereafter developed.

The use of general descriptive names, registered names, trademarks, service marks, etc. in this publication does not imply, even in the absence of a specific statement, that such names are exempt from the relevant protective laws and regulations and therefore free for general use.

The publisher, the authors, and the editors are safe to assume that the advice and information in this book are believed to be true and accurate at the date of publication. Neither the publisher nor the authors or the editors give a warranty, expressed or implied, with respect to the material contained herein or for any errors or omissions that may have been made. The publisher remains neutral with regard to jurisdictional claims in published maps and institutional affiliations.

This Springer imprint is published by the registered company Springer Nature Singapore Pte Ltd. The registered company address is: 152 Beach Road, #21-01/04 Gateway East, Singapore 189721, Singapore

Preface

The third National Aerospace Propulsion Conference (NAPC-2020) is a biennial event being held since 2017. This conference is an amalgamation of the erstwhile National Propulsion Conference (NPC) and National Conference on Air-Breathing Engines (NCABE) conferences. NAPC-2020 was organized jointly by Gas Turbine Research Establishment (GTRE), DRDO, Bengaluru, and BMS College of Engineering, Bengaluru (BMSCE), and hosted by BMSCE on a digital platform during December 17–19, 2020.

The proceedings constitutes about 65% of the research articles presented at the conference. All published papers were subjected to a rigorous refereeing process, which resulted in uniformly high quality. The papers cover the state-of-the-art design, analysis and developmental testing of gas turbine engine modules and sub-systems like compressor, combustor, turbine and alternator, advances in spray injection and atomization, aspects of combustion pertinent to all types of propulsion systems and nuances of space, missile and alternative propulsion systems.

We owe our sincere gratitude and appreciation to all the members of the technical committee and reviewers. DRDO, Ansys, TSI, Numeca, Liberty International (Scannivalve) and TEQIP-3 have supported as major contributors to the conference by providing necessary finances, and we duly acknowledge their support. We thank Mr. M. Z. Siddique, Director, GTRE, and Dr. B. V. Ravishankar, Principal, BMSCE, for their support and encouragement.

We also owe our profound gratitude to Dr. L. Ravikumar, Department of Mechanical Engineering, BMSCE, for playing the pivotal role as Secretary in organizing the NAPC-2020. With his team of dedicated colleagues and students, Prof. Ravikumar enabled the conduct of the conference on digital platform without any glitch and earned the appreciation of all the participants.

There are many others who have contributed to the publication of these proceedings whom we are unable to mention individually. We thank all of them.

Bengaluru, India

Gullapalli Sivaramakrishna
S. Kishore Kumar
B. N. Raghunandan

Contents

Gas Turbine Propulsion—Fans and Compressors	
Sensitivity Study of Stagger Angle on the Aerodynamic Performance of Transonic Axial Flow Compressors	3
Manjunath S. Dalbanjan and Niranjan Sarangi	
Numerical Simulations on Performance of a Hybrid and a Tandem Rotor	15
Shubhali More, Amit Kumar, and A. M. Pradeep	
Flow-Field Investigation of an Inter-compressor Duct Under Different Inflows and Their Influence on the Performance of a Low-Pressure Compressor	35
Jerry T. John, C. Dileep Kumar, Sourav Pramanick, Lenin Loitongbam, A. M. Pradeep, N. Vidhyashankar, and Reza Abbas	
Effects of Radial Distortion on Low-Speed Tandem Stage Axial Compressor	55
Hitesh T. Chhugani, Amit Kumar, and A. M. Pradeep	
Design and Analysis of Outlet Air Collector Duct for Axial Compressor Test Rig	79
Kirubakaran Purushothaman, N. R. Naveen Kumar, P. K. A. Geetha, C. Kishore Kumar, and Ajay Pratap	
Gas Turbine Propulsion—Turbines	
Aerodynamic Design of Axial Flow Turbine for a Small Gas Turbine Engine	99
D. Harish, R. D. Bharathan, Sharad Kapil, S. V. Ramana Murthy, and D. Kishore Prasad	

Effect of Hub Clearance on Performance of Radial Turbine	113
R. D. Bharathan, P. Manigandan, Sharad Kapil, S. V. Ramana Murthy, and D. Kishore Prasad	
Effect of Various Periodic Surface Concepts for Numerical Investigation of Flow Field Through Variable Area LP Turbine Nozzle	125
Hardikkumar Bhavsar and Chetankumar Mistry	
Numerical Investigation of Aerodynamic Performance Parameters in Linear Blade Cascade for High-pressure Turbine	145
Nitish Kulkarni, D. Harish, R. D. Bharathan, Sharad Kapil, S. V. Ramana Murthy, R. Senthil Kumaran, and D. Kishore Prasad	
Aerodynamic Design of a Axial Turbine Stage for a Small Gas Turbine Engine	157
S. N. Agnimitra Sunkara, Prathapanayaka Rajeevalochanam, and N. Vinod Kumar	
Gas Turbines—Systems, Components and Structures	
Development of Test Bench for Micro Gas Turbine Engine	177
Prathapanayaka Rajeevalochanam, N. Vinod Kumar, S. N. Agnimitra Sunkara, Narendra Sharma, Swaroop Shashidhar, and R. Jai Maruthi	
Development Strategy for Evaluating Gas Turbine Driven High-speed Alternator	191
Poonam Kumari, V. Prabakar, and A. N. Vishwanatha Rao	
Independent Verification and Validation of Aero Engine Propulsion System Software	199
Sonal Shekhawat, Arshad Iqbal, Usha Srinivasan, and Sreelal Sreedhar	
Influence of Chiral Lattice on Modal Characteristics of Structures	209
Rukmangad S. Barad, B. K. Nagesh, Sanjay Barad, and T. N. Suresh	
Micromechanics Approach to Determine Fatigue Life of Ceramic Matrix Composite	231
Kumar Rajesh and Rajeev Jain	
Space and Missile Propulsion	
Design and Analysis of KIIT Nanosatellite’s Micro-Pulsed Plasma Thruster	253
Dibyesh Satpathy, Shalika Singh, Subham Mahanty, Sidhant Patra, and Isham Panigrahi	
Use of N₂O–O₂ as the Oxidizer for the Hybrid Rocket Application	273
Rajiv Kumar and K. Thamizarasan	

Effect of Protrusion Configuration on Combustion Stability of Hybrid Rocket Motor 291
 Mengu Dinesh and Rajiv Kumar

Prediction of Wake Structure Transition for a Linear Plug Nozzle Using Detached Eddy Simulation (DES) 307
 M. Manu Mohan, N. Balakrishnan, and N. Munikrishna

Computational Study of Aero-acoustic Feedback in Supersonic Cavity Flow 319
 Priyansh Jain, Tarun Chavan, Mayukhmali Chakraborty, and Aravind Vaidyanathan

Numerical Investigation of Blockage of Scramjet Strut Injector Model in a Supersonic Wind Tunnel 345
 Anbarasan Sekar, Mayukhmali Chakraborty, and Aravind Vaidyanathan

Performance Investigation of a Rectangular Ramjet Intake with Throat Flush Slot Bleed System 357
 Subrat Partha Sarathi Pattnaik and N. K. S. Rajan

Alternative Propulsion Systems

JP-10 Propellant Powered Rotating Detonation Waves for Enhancing the Performance of Hypersonic and Supersonic Missiles 387
 Kiran Ivin and Ajay V. Singh

Design and Analysis of Rotating Detonation Wave Engine 415
 V. Ramanujachari, Rahul Dutta Roy, and P. Amrutha Preethi

Design and Performance Evaluation of Plug Nozzle for Rotating Detonation Wave Engine 431
 V. Ramanujachari, Rahul Dutta Roy, and P. Amrutha Preethi

Feasibility Study of Hybrid Propulsion for Light Aircraft 451
 G. Muthuselvan, B. R. Pai, M. Janaki Rami Reddy, Sadanand S. Kulkarni, M. E. Mohana Sundaram, Umesh Kumar Sinha, and S. Santhosh Kumar

Combustion and Combustors

Combustion Synthesis of Functional Nanoparticles 467
 Ajay V. Singh

Using Ozone and Hydrogen Peroxide for Manipulating the Velocity Deficits, Detonability, and Flammability Limits of Gaseous Detonations 493
 D. Santosh Kumar and Ajay V. Singh

Thermal Design of Cooling Configurations for an Afterburner V-Gutter of Advanced Aeroengine	509
Hanumanthu Gari Poornasree, Batchu Suresh, V. Kesavan, and D. Kishore Prasad	
A Numerical Investigation on the Effect of Lip Geometry with Tangential Film Cooling on an Annular Combustor	527
Ananda Prasanna Revulagadda, Buchi Raju Adapa, Sangamesh C. Godi, Arvind Pattamatta, and C. Balaji	
Nanoboron Slurry Fuel Droplet Combustion for High-Particle Loading Ratio	543
Sunil Kumar Kumawat, Apurv Dilip Ghugare, Abhijeet Kumar, Srikrishna Sahu, and Ravikrishnan Vinu	
Effect of Surface Temperature on Fuel Drop Splashing on Solid Surfaces	555
Akshay Sreenivasan and Sivakumar Deivandren	
Transition Dynamics Between Luminous and Blue Whirling Flames	569
Sagar Singhal, Manish Sharma, Herambraj Nalawade, and Pratikash P. Panda	
Spray Injection and Atomization	
Flow Dynamics in a Triple Swirl Burner	583
Neha Vishnoi, Agustin Valera-Medina, Aditya Saurabh, and Lipika Kabiraj	
Sheet Atomization of Gel Propellant Simulant	601
K. Vivek, Aditya Saurabh, Devendra Deshmukh, Deepak Agarwal, and Lipika Kabiraj	
A Parametric Study on Rotary Slinger Spray Characteristics Using Laser Diagnostics	615
Arnab Chakraborty, Mithun Das, Srikrishna Sahu, and Dalton Maurya	
CFD Analysis of Primary Air Flow Field of a Swirl Injector Using Embedded LES-Based Hybrid Model	629
Rampada Rana, N. Muthuveerappan, and Saptarshi Basu	

About the Editors

Gullapalli Sivaramakrishna is a Scientist ‘G’ in Gas Turbine Research Establishment (GTRE), Defence Research and Development Organisation (DRDO), Ministry of Defence, Government of India. After graduating from Osmania University in Mechanical Engineering, he did Post Graduation in Design and Development of I. C. Engines and Gas Turbines from NIT Warangal. He has 27 years of experience in CFD based Design and Development of Gas Turbine Combustion Systems. He has been recently designated as the Technical Director of Combustion Group in GTRE. He was Deputy Programme Director of a National Initiative of GTRE, DRDO titled “Multi Centric Gas Turbine Enabling Technology (GATET)” from its inception in 2009 till 2014; became Programme Director of the same in the year 2014 and held the post up to its full term (till 2017). Through this initiative, he has pursued several technology development projects in various areas of relevance to bridge the technology gaps as well as to initiate research in emerging technology areas pertinent to gas turbines, in collaboration with academia and R&D institutions in India. He has authored about 35 technical publications in National & International Conferences. He was one of the editors of the proceedings of a couple of National Conferences and International Seminars. Being a part of the technical committee, he has conducted a few National Conferences and International Seminars relevant to aerospace propulsion. He is the General Secretary of National Council for Air Breathing Engines (NCABE) Trust established to provide a forum and stimulus to the R&D activities in the field of aerospace propulsion in the country. He is the recipient of National Science Day Award of DRDO.

S. Kishore Kumar has been working as a DRDO Fellow in Gas Turbine Research Establishment, DRDO since 2016. He was an AICTE-INAE Distinguished Visiting Professor from 2014–2016 and was formerly Scientist G & Associate Director heading CFD, Compressor, Turbine, Combustor, Afterburner, Heat Transfer and Secondary Air System Groups in GTRE. He was Programme Director of Gas Turbine Enabling Technology (GATET)—A National Initiative of GTRE, DRDO from its inception in 2009 to 2014. He has published over 100 papers in journals and conferences and edited seven proceedings related to Aerospace Technologies. He has guided twelve doctoral students. He is presently a member of the Board of Governors, IIT Madras, ICFAI University-Dehradun, ICFAI University—Tripura and Member of Board of Management, IFHE, Hyderabad. He is Associate Editor of *Journal of Aerospace Sciences and Technologies*, founder member of editorial committee, e-news, AeSI and was the founder Honorary Secretary of CFD Division of AeSI and currently Vice Chairman of National Council for Air Breathing Engines. He is a Fellow of AeSI and Life Member of Combustion Institute, FMFP and CSI.

B. N. Raghunandan is a specialist in the area of Aerospace Propulsion and Combustion. During his long tenure at the Indian Institute of Science, he held many senior positions such as Dean, Faculty of Engineering and Chairman, Department of Aerospace Engineering. He has been active in promoting the area of Aerospace Propulsion and is currently serving as the Chairman, National Council for Air Breathing Engines.

Gas Turbine Propulsion—Fans and Compressors

Sensitivity Study of Stagger Angle on the Aerodynamic Performance of Transonic Axial Flow Compressors



Manjunath S. Dalbanjan and Niranjan Sarangi

Abstract Gas turbine engines are widely used in the aviation industries because of high power to weight ratio. The gas turbine engine consists of the three main components: compressor, combustion chamber, and turbine. The design of the axial flow compressor depends on various design parameters such as blade stagger angle, blade height, blade chord, rotor tip clearance, and stator tip clearance. Blade stagger angle is a critical parameter which plays vital role in performance of the gas turbine engines. In this study, a steady state analysis has been carried out to understand the effect of rotor and stator blade stagger angle on the aerodynamic performance of single stage axial flow transonic compressor through three dimensional viscous analysis using ANSYS CFX 19.2 software. The analysis was carried out for various stagger angle configuration varying from 24° to 36° for rotor and 06° to 18° for stator. The study concluded that as the rotor stagger angle is increased from 24° to 36° , the mass flow is reduced by 16.5%, peak pressure ratio by 2.8%, and increase peak efficiency by 6.8%. The effect of change of stator stagger angle from 06° to 18° is insignificant.

Keywords Axial flow compressor · Stagger angle · Tip clearance · Surge margin · Computational Fluid Dynamics (CFD) · Pressure ratio · Efficiency

1 Introduction

The majority of the gas turbine power plants and particularly in aircraft applications use axial flow compressor. It is a difficult task to achieve high efficiency and a wide operating envelop of compressor without compromising the performance of the compressor. The axial flow compressor performs efficiently and meets the design

M. S. Dalbanjan (✉) · N. Sarangi
DRDO-Gas Turbine Research Establishment, Bengaluru, India and affiliated to Visvesvaraya Technological University, Belagavi, Karnataka, India
e-mail: manjunathsdal.gtre@gov.in

N. Sarangi
e-mail: niranjansarangi@gtre.drdo.in

© The Author(s), under exclusive license to Springer Nature Singapore Pte Ltd. 2023
G. Sivaramakrishna et al. (eds.), *Proceedings of the National Aerospace Propulsion Conference*, Lecture Notes in Mechanical Engineering,
https://doi.org/10.1007/978-981-19-2378-4_1

requirement with in the compressor operating envelope. Aerodynamic instability occurs due to adverse pressure gradient in the compressor which will significantly affect the performance of the compressor. Various studies are carried out to understand the effect of blade stagger angle. Schobeiri [1] showed improvement in gas turbine efficiency at off design condition by adjusting the compressor and turbine blade stagger angles. A Gaussian probabilistic density function simulation approach used by Zheng et al. [2] to study the impact of random stagger angle variability on the compressor performance showed that the blades with variation of the stagger angle cause more uneven pressure distribution across span of the blade. Chun et al. [3] considered a low hub to tip ratio transonic compressor to understand the effect of stagger angle on aerodynamic performance. Schnoes et al. [4] studied various stagger angle configuration to design a multi-stage axial flow compressor using optimization technique. The study concluded that the stagger angle effect on the efficiency of the compressor is dominant. Cao et al. [5] have carried out experimental studies on contra-rotating axial flow pump to understand the pressure distribution across span of the blade by adjusting the stagger angle. Myoren et al. [6] concluded that for an axial compressor rotor in transonic stage by variation of stagger angle, the stalling margin can be enhanced using the multi-objective optimization technique. Cho et al. [7] concluded by decreasing the stagger angle at the mean radius and increasing at hub and tip, resulting in improvement of efficiency and optimum pressure. Li et al. [8] describes that the decrease in the stagger angle will reduce the turbulence at suction side of the rotor blade. Oyama et al. [9] developed an optimization technic to obtain the desired stagger angle for the given design parameters to achieve the required aerodynamic performance. Yoon et al. [10] studied the influence of design parameters on tip vortex in a four stage axial flow compressor by considering stagger angle, tip clearance, and flow coefficient. Most of the studies are limited to stagger angle of rotor at design point. Available literature in public domain indicates that substantial work has not been done on the sensitivity of the stagger angle on rotor and stator and its combined effect on aerodynamic performance.

The emphasis of this study is to evaluate the sensitivity of the stagger angle on rotor and stator blades and to investigate its effect on the aerodynamic performance of a single stage axial flow transonic compressor are discussed in detail in this paper.

2 Methodology

The aerodynamic analysis is carried out to study the sensitivity of blade stagger angle on the aerodynamic performance parameters by using commercially available 3D Computational Fluid Dynamics (CFD) software package. The computational methodology followed for the analysis process is explained below.

2.1 CFD Code Benchmarking Study

Computational fluid dynamics (CFD) has emerged as a most powerful tool for determining the flow physics inside the casing for turbomachinery applications. Before adopting any CFD software, a careful validation should be done by considering a standard test case. A standard transonic compressor test cases NASA stage 37 by Reid and Moore [11] is considered for the assessment of CFD tool. A detailed analysis is done and the predicted performance parameters are compared with the experimental test results of NASA stage 37. The detail CFD code benchmarking analysis is done in previous study by Dalbanjan and Sarangi [12]. The outcome of the validation study showed that the efficiency is slightly higher predicted by CFD tool compare to the published test data. Whereas pressure ratio and mass flow are showing good match within 1%. The validation of predicted and measured performance plots are shown in Figs. 1 and 2.

Fig. 1 Mass flow rate versus pressure ratio for NASA stage 37

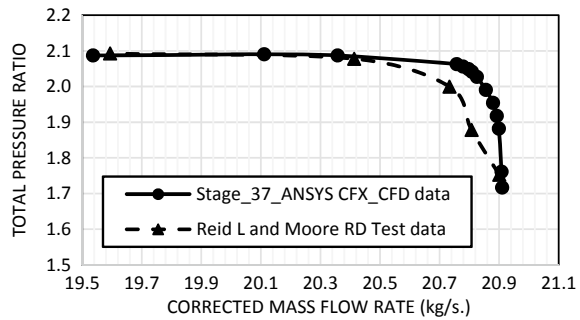


Fig. 2 Mass flow rate versus efficiency for NASA stage 37

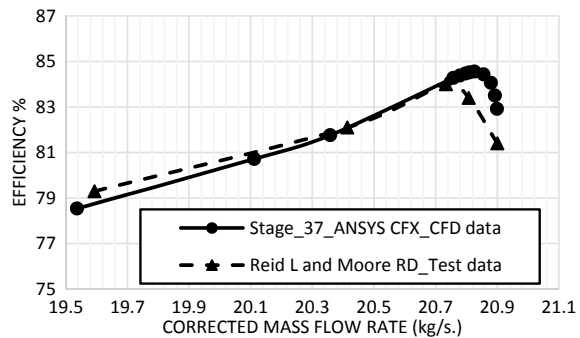
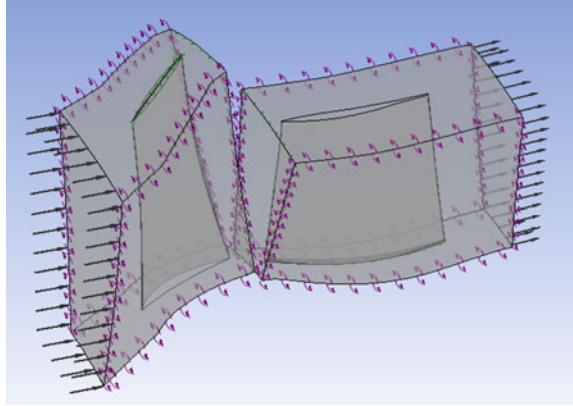


Fig. 3 Geometric model of rotor and stator domain



2.2 Solid Modeling of Blade Geometry in Flow Domain

The geometry is modeled using 3D modeling software. The geometric model consists of extended inlet domain, rotor blade, stator blade, and extended outlet domain so that the output flow parameters are measured after the flow settles down. Single passage with rotor and stator domain extended up to 1 chord of downstream blade was considered for analysis to reduce the computational time. Figure 3 shows the rotor and stator geometric model.

2.3 Grid Generation and Grid Convergence Study

A grid independence study was carried out to ensure that the results obtained are independent of the grid size or elements. The mesh topology used for flow domain is H-type and O-type near the rotor and stator blade surface to capture the boundary layer. In the tip region, 10 elements were created and nonmatching grid topology was used with appropriate alignment of interface. Mesh distribution was varied in spanwise, streamwise, and circumferential direction for rotor and stator domains, near the blade surface and casing wall more dense grid was selected to maintain the y^+ value of less than 1. The grid quality requirement was met with minimum and maximum angle being greater than 20° and less than 165° , respectively. The advection scheme and high resolution turbulence numeric were selected along with the $k-\omega$ shear stress transport (SST) turbulence viscosity model. The $k-\omega$ SST model accounts for the transport of turbulent shear stress and gives highly accurate predictions of the onset and the amount of flow separation under adverse pressure gradients. Mesh for both rotor and stator stage domain were generated as shown in Fig. 4. Four different cases by varying number of grids in rotor and stator blades were considered. Figures 5 and 6 show the plots of performance parameters like corrected mass flow and pressure ratio with respect to grid size. It is observed from Figs. 5 and 6 that the grid-2 onwards

Fig. 4 Mesh domain for rotor and stator

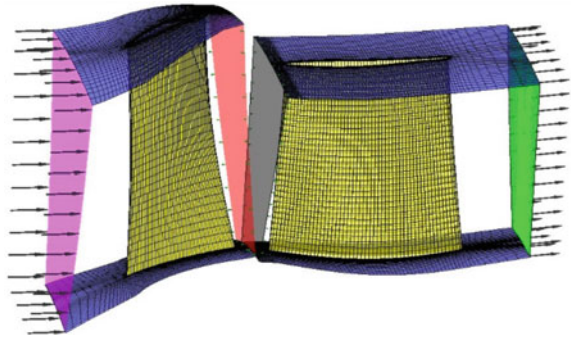


Fig. 5 Comparison of corrected mass flow rate for various grid configuration

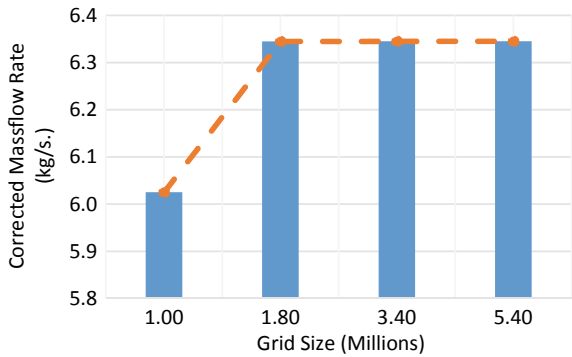
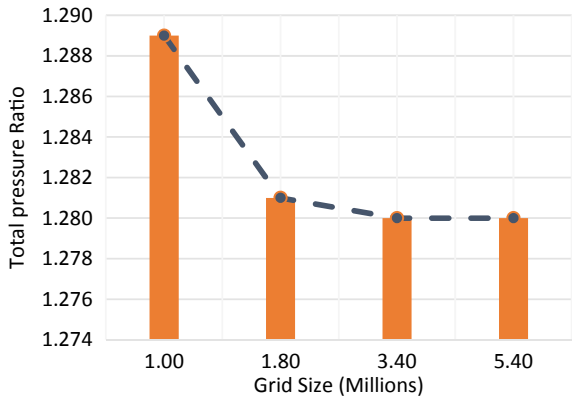


Fig. 6 Comparison of total pressure ratio for various grid configuration



the variation in parameters are insignificant. Thus, for further analysis grid-3 was selected with grid size of 3.40 million elements. Table 1 shows the performance parameters for different grid sizes.

Table 1 Comparison of all four grid cases at 100% speed

Cases	Grid Size (Millions)	Corrected mass flow (kg/s.)	Total pressure ratio
Grid-1	1.00	6.0251	1.289
Grid-2	1.80	6.3451	1.281
Grid-3	3.40	6.3453	1.280
Grid-4	5.40	6.3454	1.280

2.4 Boundary Condition

The appropriate boundary conditions were applied for the flow domain, at inlet of rotor stagnation pressure and stagnation temperature. Stage mixing model as an interface between rotor and stator was selected. Mixing plane calculates the circumferentially averaged flow parameters from the rotor and passes to the inlet of the stator. Static back pressure was applied at the exit of stator. For blade, hub and casing adiabatic and no-slip wall boundary condition was specified. The numerical simulation was performed using multi-block grid with pressure-based implicit solver ANSYS CFX 19.2 software. Constant speed characteristics at design speed were generated by gradually increasing the Static back pressure at the stator outlet. After reaching the peak efficiency point, the static back pressure was increased in the smaller steps of 1 kPa to capture the near stall point and to obtain a converged solution. The residual convergence level for all the parameters is specified as 1×10^{-6} to get more accurate solution.

2.5 Solution Methodology

The study involves variation of stagger angle for rotor. In the first phase, the analysis is performed by keeping the stator stagger angle at 12° which is obtained from the design and varying the rotor stagger angle from 24° to 36° with the increment of 1° at the design speed. The optimum rotor stagger angle is selected as 30° obtained from the analysis which is meeting the design mass flow requirement. The second phase involves variation of stator stagger angle from 06° to 18° at the increment of 1° by keeping the rotor stagger angle constant. Figures 7 and 8 show the rotor and stator stagger angle with respect to axis of the compressor. Figure 9 shows the variation of rotor stagger angle at the mid span of the blade for 24° , 30° , and 36° , and Fig. 10 shows the variation of stator stagger angle at the mid span of the blade for 06° , 12° , and 18° .

Fig. 7 Rotor stagger angle with respect to axis of the compressor

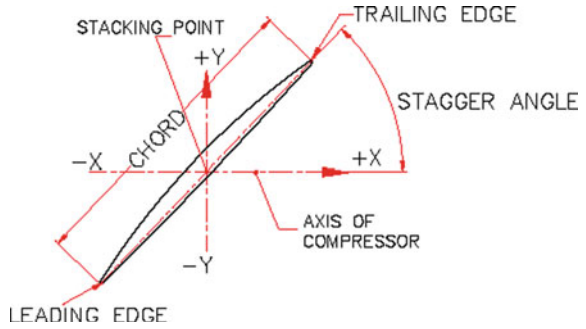


Fig. 8 Stator stagger angle with respect to axis of the compressor

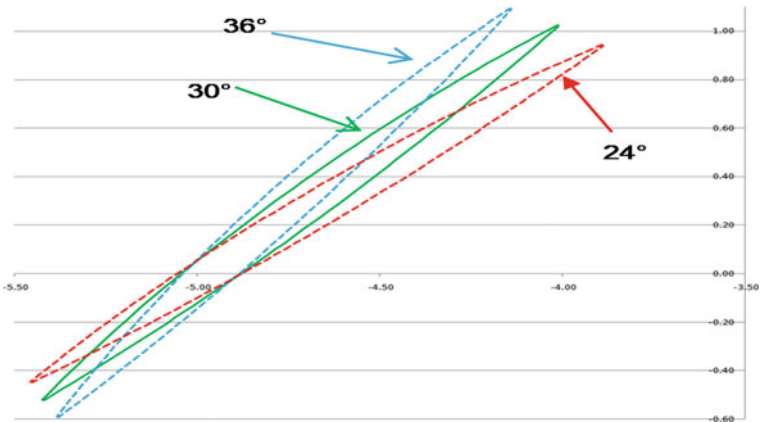
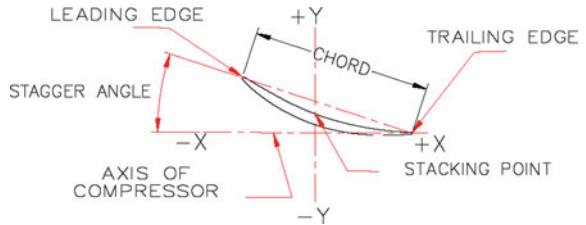


Fig. 9 Variation of rotor stagger angle

3 Results and Discussion

The simulation was carried out at design speed, and the constant speed characteristics were generated for various stagger angle configuration for rotor and stator.

Figure 11 shows the corrected mass flow rate versus total pressure ratio for various combination of stagger angle configuration ranging from 24° to 36° for rotor blade. It can be observed that the increase in stagger angle from 24° to 36° the mass flow

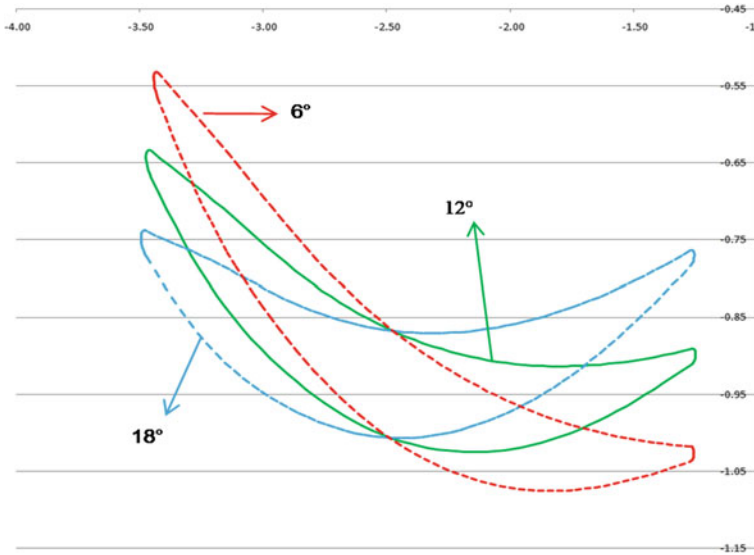


Fig. 10 Variation of stator stagger angle

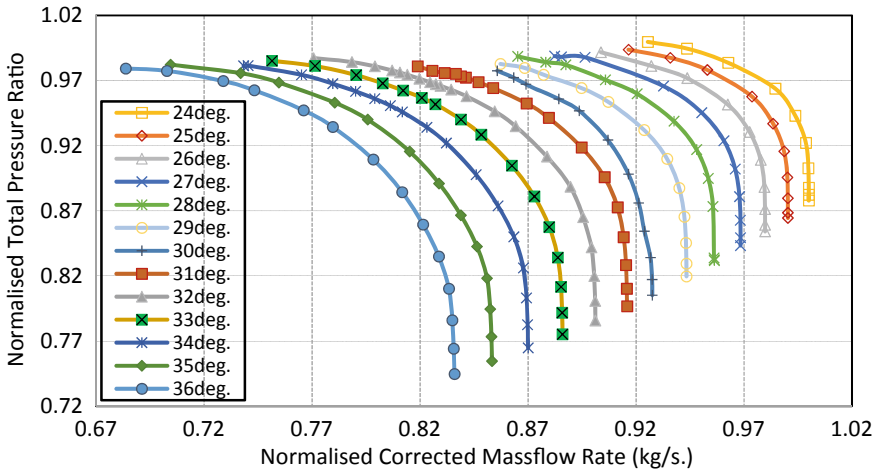


Fig. 11 Normalized corrected mass flow rate versus total pressure ratio for rotor

swallowing capacity is reduced with slight drop in pressure ratio. The mass flow is reduced by 16.5% and peak pressure ratio is reduced by 2.8% when stagger angle is increased from 24° to 36°. This shows that the mass flow is more sensitive to rotor stagger angle. The plot also shows the zone of maximum and minimum mass flow for the configuration under consideration. It provides the ready reference for selection of rotor stagger angle to achieve the design mass flow.

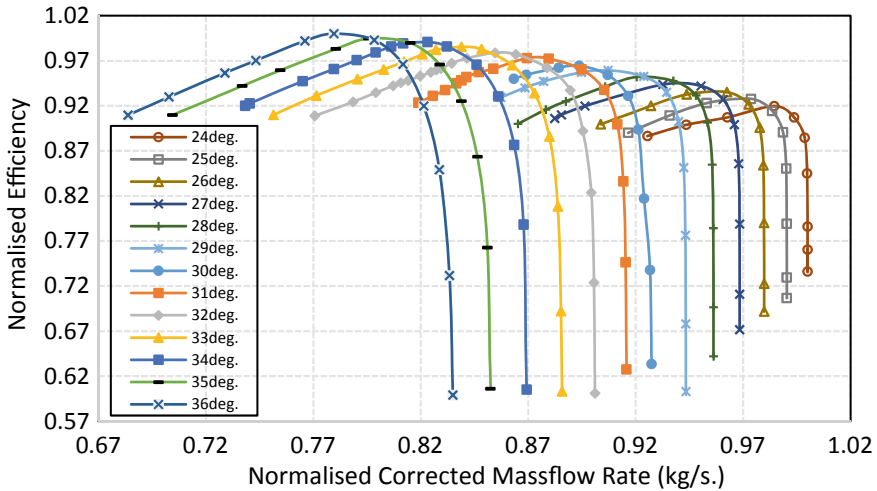


Fig. 12 Normalized corrected mass flow rate versus efficiency for rotor

Figure 12 shows the corrected mass flow rate versus efficiency for various combination of stagger angle configuration ranging from 24° to 36° for rotor blade. It is observed that as the stagger angle is increased from 24° to 36° the efficiency is increased with drop in mass flow. The mass flow is reduced by 16.5% and peak efficiency is increased by 6.8 points when stagger angle is increased from 24 to 36° . The lower mass flow is due to the reduction in blade passage area as the stagger angle is increased and the increase in efficiency is due to the absence of separation zone at the rotor outlet. This shows that the rotor efficiency is sensitive to the stagger angle. The plot also shows the zone of maximum and minimum peak efficiency for the configuration under consideration. It provides the ready reference for selection of rotor stagger angle to achieve the design efficiency.

Figure 13 shows the corrected mass flow rate versus total pressure ratio for various combination of stagger angle configuration ranging from 06° to 18° for stator blade. It is observed that there is no significant variation of mass flow and pressure ratio due to variation in stagger angle of stator blades from 06° to 18° and the loss in the performance parameter is negligible.

Figure 14 shows the corrected mass flow rate versus efficiency for various combination of stagger angle configuration ranging from 06° to 18° for stator blade. As the stagger angle is increased from 06° to 18° , the efficiency is decreased with minimal variation in mass flow. The peak efficiency is decreased by 3.5 points when stagger angle is increased from 06° to 18° . As the stator stagger angle is increased, the losses are higher due to flow separation at the pressure side near the trailing edge of stator which results in lower efficiency.

Figure 15 shows the blade loading plot for rotor at mid span for various stagger angle configuration. It is observed that increasing stagger angle improves the static pressure at the expense of degradation in blade performance. Rotor is performing

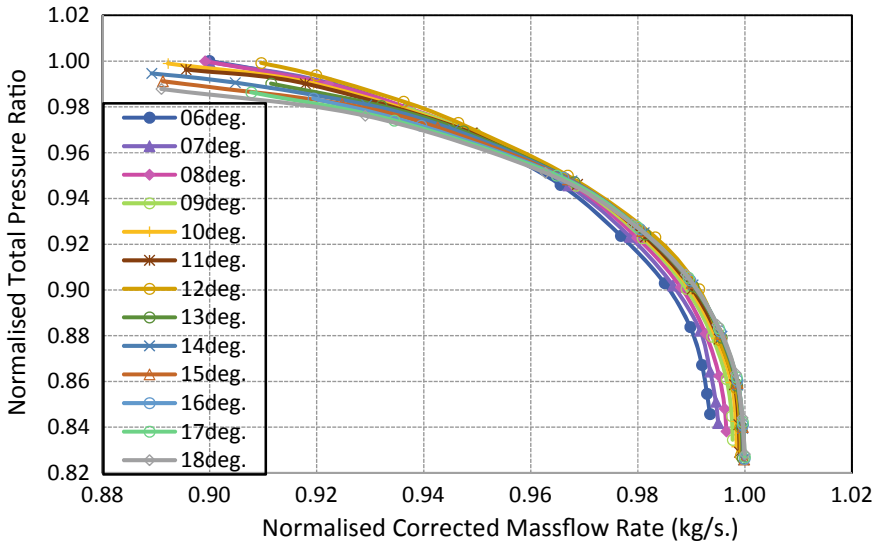


Fig. 13 Normalized corrected mass flow rate versus total pressure ratio for stator

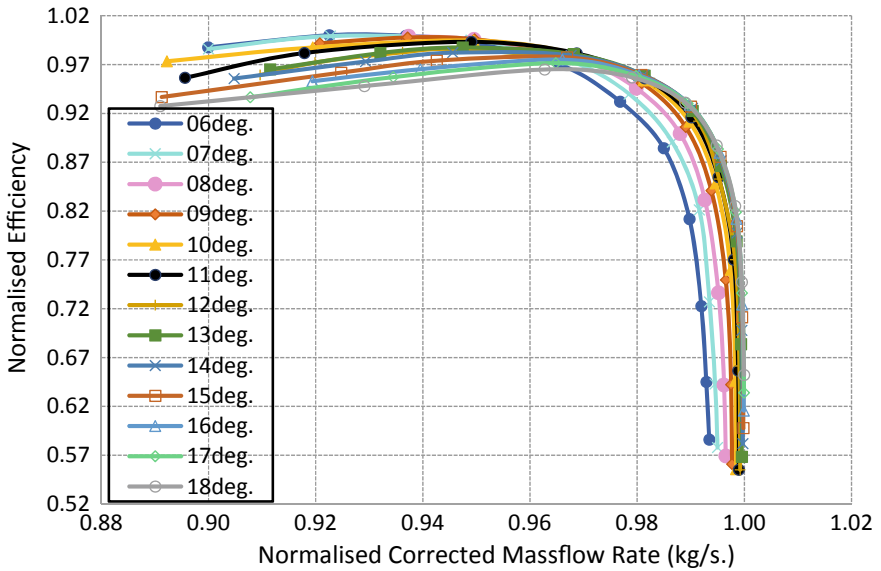


Fig. 14 Normalized corrected mass flow rate versus efficiency for stator

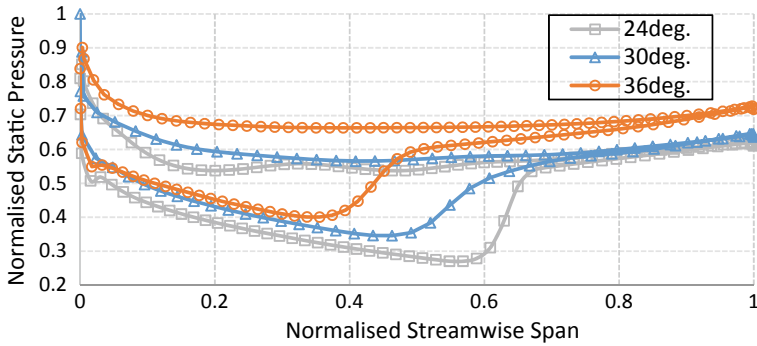


Fig. 15 Blade loading for rotor

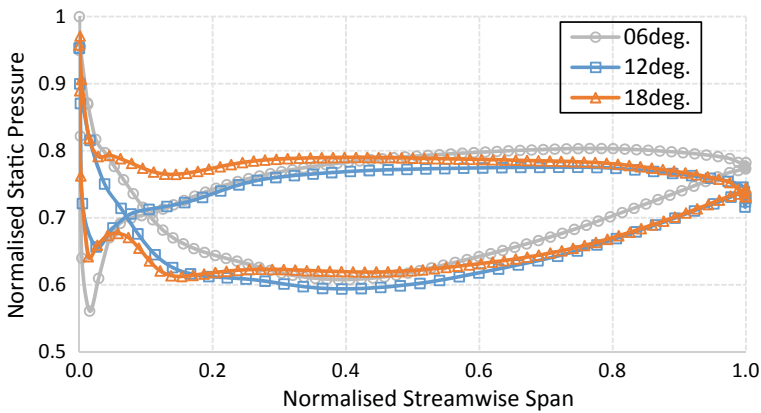


Fig. 16 Blade loading for stator

better up to 60% of span when stagger angle is 24° but as stagger angle is increased to 36° there is a gain of 15% in static pressure at the expense of spanwise degradation in blade loading.

Figure 16 shows the blade loading plot for stator at mid span for various stagger angle configuration. It is observed that the effect of stagger angle is not sensitive on the blade loading parameters of stator. The stator is performing as per design requirement.

4 Conclusions

A 3D steady state viscous CFD analysis is carried out to investigate the sensitivity of stagger angle on the aerodynamic performance of a transonic single stage axial

flow compressor using commercial code ANSYS CFX 19.2 software. The analysis is carried out for various stagger angle configuration varying from 24° to 36° for rotor and 06° to 18° for stator. It is observed that as the rotor stagger angle is increased from 24° to 36° , the mass flow is reduced by 16.5%, peak pressure ratio is reduced by 2.8% and peak efficiency is increased by 6.8 points. It is interesting to see that the stator is not sensitive to the stagger angle and the effect is insignificant when the stator stagger angle is varied from 06° to 18° . The study concludes that the rotor stagger angle is highly sensitive for controlling the mass flow and efficiency compare to stator stagger angle. The data generated in this study provides the ready reference for selection of rotor and stator stagger angle for meeting the requirements of aerodynamic design parameters such as mass flow and efficiency.

References

1. Schobeiri MT (2018) Improving the efficiency of gas turbines during off-design operation by adjusting the turbine and compressor blade stagger angles. *J Appl Mech Eng* 7(1):673–682
2. Zheng S, Teng J, Fan L, Qiang X (2017) The impact of uncertain stagger angle variation on high pressure compressor rotor performance. In: *Proceedings of Shanghai Global Power and Propulsion Forum*. GPPS-0045
3. Chun ZS, Qin MS, Long WZ (1981) Effect of blade stagger angle on performance of a transonic compressor with low hub-tip ratio. In: *ASME, gas turbine conference & products show*
4. Schnoes M, Voß C, Nicke E (2018) Design optimization of a multi-stage axial compressor using throughflow and a database of optimal airfoils. *J Glob Power Propulsion Soc* 2:516–528
5. Cao L, Watanabe S, Honda H, Yoshimura H, Furukawa A (2014) Experimental investigation of blade-to-blade pressure distribution in contra-rotating axial flow pump. *Int J Fluid Mach Syst* 7(4):632–640
6. Myoren C, Takahashi Y, Kato Y (2013) Multi-objective optimization of three-dimensional blade shape for an axial compressor rotor in transonic stage. *Int J Gas Turbine Propulsion Power Syst* 5(1):545–554
7. Cho CH, Cho SY, Ahn KY, Kim YC (2009) Study of an axial-type fan design technique using an optimization method. *J Process Mech Eng* 223(4):726–732
8. Li MX, Zhang CH, Liu Y, Zheng SY (2013) Parametric modeling and stagger angle optimization of an axial flow fan. In: *6th international conference on pumps and fans with compressors and wind turbines*
9. Oyama A, Liou MS, Obayashi S (1988) High-fidelity swept and leaned rotor blade design optimization using evolutionary algorithm. In: *NASA Glenn Research Center*
10. Yoon YS, Song SJ, Shin HW (2006) Influence of flow coefficient, stagger angle, and tip clearance on tip vortex in axial compressors. *J Fluids Eng* 128(3):736–742
11. Reid L, Moore RD (1978) Design and overall performance of four highly loaded high speed inlet stages for an advanced high pressure ratio core compressor. In: *NASA TP 1337*
12. Dalbanjan MS, Sarangi N (2019) An effect of tip clearance on aero performance in axial flow compressors for aero gas turbine engines. *Int J Mech Prod Eng Res Dev* 9(4):769–776

Numerical Simulations on Performance of a Hybrid and a Tandem Rotor



Shubhali More, Amit Kumar, and A. M. Pradeep

Abstract In the quest of maximizing the pressure ratio and the efficiency of the gas turbine engine, designing a compressor that can generate the required pressure ratio with a minimum number of stages is one of the challenges. A single blade, if designed with a higher diffusion factor, has an inherent problem of flow separation. Tandem or slotted blades with the help of nozzle-gap phenomenon have shown promising results in terms of higher pressure ratio and efficiency, but it has mechanical complexity and lower stall margin. The hybrid rotor called part-span tandem has been designed to get the benefits of both a single rotor as well as tandem rotor blades. Design methodology as well as parallel comparison of results of a low speed hybrid rotor, tandem rotor, and a single rotor is included in the paper. CFD results such as pressure distribution at different span locations, total pressure rise, static pressure rise, contours of Mach number, entropy, the behavior of the tip leakage flow, and performance curve are included in this paper. Full span tandem rotor has higher pressure rise, and the hybrid rotor has a better stall characteristic.

Nomenclatures

C_p	Static pressure coefficient = $P - P_{in}/0.5\rho U_{tip}^2$
\dot{m}	Mass flow rate (kg/s)
P	Static pressure (Pa)
P_0	Total pressure (Pa)
t/s	Tandem percentage pitch
U	Tangential speed of rotor (m/s)
$\Delta X1/\Delta X2$	Tandem overlap in the axial direction
Z/H	Span percentage

S. More (✉) · A. Kumar · A. M. Pradeep
Indian Institute of Technology Bombay, Mumbai, Maharashtra 400076, India
e-mail: shubhalimore182@gmail.com

A. M. Pradeep
e-mail: ampradeep@aero.iitb.ac.in

© The Author(s), under exclusive license to Springer Nature Singapore Pte Ltd. 2023
G. Sivaramakrishna et al. (eds.), *Proceedings of the National Aerospace Propulsion Conference*, Lecture Notes in Mechanical Engineering,
https://doi.org/10.1007/978-981-19-2378-4_2

Greek Symbols

φ	Flow coefficient = C_a/U_m
$k-\varepsilon$	K-Epsilon turbulence model
ρ	Density (kg/m^3)
ω	Total pressure loss coefficient = $\frac{(P_{0_rel_LE} - P_{0_rel_TE})}{0.5 * \rho * U_{tip}^2}$
ψ	Stagnation total pressure rise coefficient = $(P_0 - P_{0in})/0.5\rho U_m^2$

Subscript

ex	Exit location
in	Inlet location
m	Mean section
rel	Relative frame of reference
x	Variable location
tip	Tip section

Abbreviations

AB	Aft blade
AO	Axial overlap
CDA	Control diffusion airfoil
DCA	Double circular airfoil
DF	Diffusion factor
DR	Degree of reaction
FB	Forward blade
LE	Leading edge
PP	Percentage pitch
PS	Pressure side
SS	Suction side
SST	Shear stress turbulence model
TE	Trailing edge
TLV	Tip leakage vortex

1 Introduction

A gas turbine designer’s aim is for higher specific thrust and lower fuel consumption. Compressors occupy a larger section in the gas turbine engine. A compressor blade with higher diffusion capability can significantly contribute to lowering the engine weight and therefore making it more compact. However, the maximum diffusion factor and flow turning angle has a limit because of the adverse pressure gradient and flow separation.

Due to the high turning angle of a single blade, flow near to the trailing edge (TE) on the suction side (SS) of the blade leads to separation. In the tandem blade, a single blade airfoil is divided into two airfoils to form a separate forward blade (FB) and aft blade (AB) as shown in Fig. 1. A nozzle like a gap is formed between these two tandem blades. Due to the pressure difference near the gap nozzle, the flow from the pressure side (PS) of FB passes through the gap nozzle and provides an extra source of energy to the sluggish flow over the suction surface of the aft blade. Due to extra momentum transfer, flow separation can be effectively delayed. As the diffusion factor (DF) limit increases, pressure rises per stage, and blade loading capacity increases and hence improvement in overall performance characteristics.

But Saha and Roy [1] have noted down tandem is less effective as compared to baseline in a low diffusion region (camber angle less than 40° region), as the nozzle gap is less efficient due to available low momentum of the fluid and also flow complexities at the tip region which increases because of tip leakage vortex (TLV) phenomenon. In the tandem rotor, the numbers of blades are more compared to a single rotor blade which increases the total tolerance requirement. The hybrid rotor is designed to get the benefit of higher pressure rise along with the efficiency of the

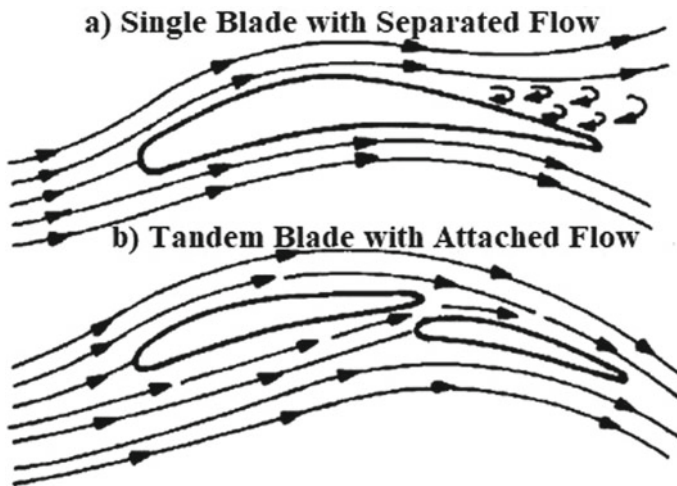


Fig. 1 Fundamental of tandem blade

tandem rotor as well as the better stall margin and design simplicity of the single rotor. The part-span tandem rotor is a mixed combination of tandem airfoils in high diffusion region and single airfoils in low diffusion regions and both are stacked together to form a hybrid rotor blade.

Saha and Roy [1] experimentally analyzed that tandem airfoil blade CDA (Control Diffusion Airfoil) 32–21 which has extra 5° camber results in more turning of flow without separation than tandem airfoil CDA 21–21 and single airfoil blade CDA 43. Kumar and Pradeep [2] have noted from the numerical investigation that tandem shows a 3.6% increase in a total pressure rise and a 2.3% increase in efficiency than a single rotor stage at the design point. Also, it is found that at off-design condition, tip leakage losses are lower at the tip of AB than the tip of FB at the design condition. McGlumphy [3] and McGlumphy et al. [4] done numerical investigation using RANS and Baldwin–Lomax turbulence model on tandem airfoil NACA-65 in the low speed region and analyzed results with the varying AO (Axial Overlap) and PP (percentage pitch) parameter. Noted that optimum choice for the design of tandem considering aerodynamic parameters and mechanical limitations into account was tandem with 0% AO and 85% PP. Kumar and Pradeep [5] performed high fidelity optimization numerical study and concluded that if there is significant variation in stagger and camber, then the optimized value of AO and PP at one section may or may not be optimum at other sections. Guochuan et al. [6] tested experimentally the different Double Circular Arc (DCA) profile type tandem airfoil with camber, stagger, AO, and PP as a design variable and reported for optimum results. The values of AO and PP combination differ based on the application of the blade. It is also noted that the blade chord ratio in the range of 0.6–1.0 will give optimized results. Falla's [7] computational study using RANS and $k-\omega$ turbulence model on a NACA-65 tandem airfoil reported that low AO and high PP gave suitable results for tandem configuration. McGlumphy [3], McGlumphy et al. [4], Roy, and Saha [8], Bammert, and Beelte [9] and Roy et al. [10] had primarily focused their investigations on the tandem stator or tandem cascade and have found that compared to a single blade, the tandem blade has a higher diffusion capability. In some limited literature, Hasegawa [11], Bammert, and Beelte [9] investigated the tandem rotor for a stage.

Roy et al. [10] has noted down the limitation of the tandem blade and presented the concept of a hybrid blade. It is also noted that the performance of the tandem blade depends more on the tangential gap than the axial gap. Results are superior to single airfoil if the gap is optimized. Yoon et al. [12] used RANS with SST $k-\omega$ turbulence model and demonstrated that for a given flow rate but with the slot, a minor change in the efficiency and total pressure ratio can be achieved. It also concluded that to enhance the stall margin slot is a better option than increasing tip clearance.

2 Experimental Setup

Experiments are carried out on the compressor test rig schematic of which is shown in Fig. 2, in the turbo-machinery laboratory of the IIT, Bombay. The hub and a tip

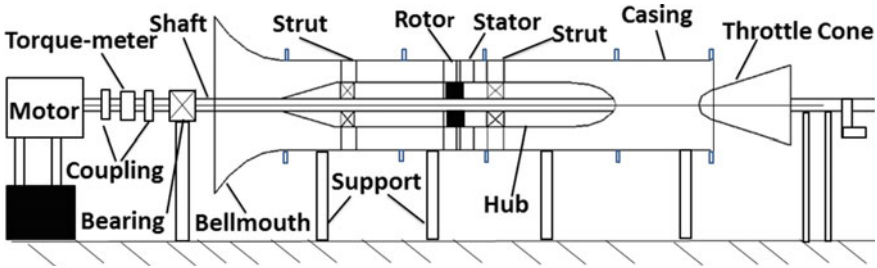


Fig. 2 Schematic of a single-stage compressor test rig

diameter of the test rig are 250 mm and 500 mm, respectively. It is specially designed for low speed applications. Mass flow variation at the outlet is achieved with the help of an automated throttle mechanism. The positions of total pressure and Kiel probes are depicted in Fig. 3. Pitot static rakes have been placed at $1.5C$ ahead of the leading edge (LE) of the rotor, while 4 Kiel pressure rakes are circumferentially placed at $0.5C$ downstream of TE of the stator. Based on experimental data, a performance map can be plotted.

The baseline stage comprised 19 rotor blades and 21 stator blades. A constant tip clearance of 1 mm is maintained for rotor blades. Owing to the low speed application, the C4 type of airfoil is used for both rotor and stator blades. The design RPM of the rotor blade is 2700, whereas the design mass flow rate is 6 kg/s. The aspect ratio of the designed blade is 1.5. The design parameters of the baseline stage are listed in Tables 1 and 2.

Fig. 3 Schematic of probe position

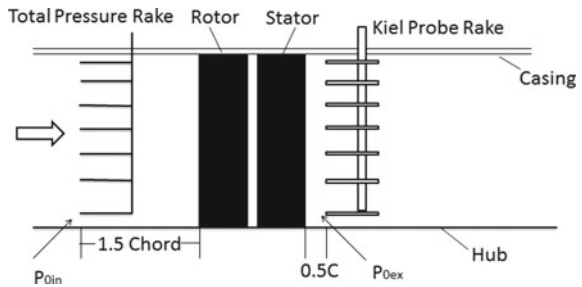


Table 1 Single rotor design specification

Rotor	Tip	Mean	Hub
DF	0.5	0.54	0.47
DR	0.78	0.70	0.50
Camber	23°	35°	60°

Table 2 Single stator design specification

Rotor	Tip	Mean	Hub
DF	0.53	0.48	0.45
Camber	50.0°	50.0°	52.0°

3 CFD Validation

For the validation purpose, the experimental data are compared with the CFD results of the baseline stage. A steady RANS simulation is carried out with two different turbulence models, namely Shear Stress Turbulence (SST) and K-Epsilon ($k-\epsilon$). The total pressure coefficient (Ψ) is plotted with the flow coefficient (ϕ) and depicted in Fig. 4. SST model demonstrates better matching with the experimental data than the $k-\epsilon$ model. At the design point, the maximum deviation in the prediction of the SST model from experimental data is 1.3%. $k-\epsilon$ model largely under predict the total pressure value at a higher mass flow rate. At a lower mass flow rate, a slight over-prediction is observed for the $k-\epsilon$ model. At the design point, the deviation between the $k-\epsilon$ model than the experimental value is 7.5%. Hence, further CFD analysis is carried out with the SST turbulence model.

The paper compares the performance of the single rotor, tandem rotor, and hybrid rotor. All three rotors are designed for equal pressure rise. The total pressure distribution along the blade span is kept the same for all three blades. Design specifications of the single rotor given in Table 3. Works of the literature suggest a higher PP and lower AO tandem configuration as an optimum design configuration. Kumar and

Fig. 4 Performance map of baseline stage

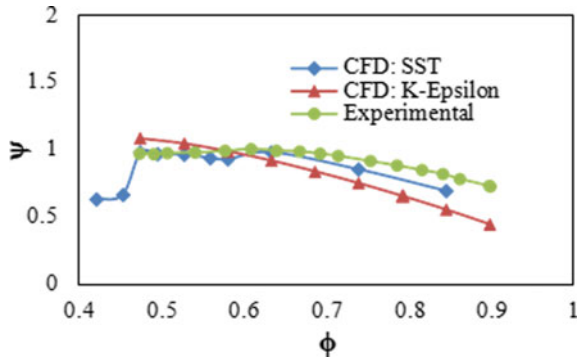


Table 3 Design details of the single rotor

Rotor	Tip	Mean	Hub
DF	0.63	0.62	0.48
Camber	33.0°	48.0°	66.0°
Stagger	49.0°	33.0°	10.0°

Table 4 Design specifications of the forward and aft blade of tandem

Rotor	Forward blade			Aft blade		
	Tip	Mean	Hub	Tip	Mean	Hub
DF	0.44	0.46	0.44	0.52	0.49	0.31
Camber	16.5°	20.6°	30.9°	26.1°	35.3°	42.6°
Stagger	57.5°	46.4°	28.1°	45.1°	26.6°	0.6°

Pradeep [5] selected a tandem rotor, with 5% AO and 85% PP, for their CFD analysis. The same tandem rotor is taken as a reference for the design of a hybrid rotor. The design details of the tandem forward and the aft rotor are listed in Table 4.

The single rotor blade serves as a baseline for CAD model of the hybrid rotor blade. At mid-span, a nozzle type of slot is made till a mid-section of the blade. While doing so, a single airfoil is split into two airfoils. A constant nozzle shape is maintained till mid-section airfoil. To facilitate the smooth flow in this region, the LE portion of AB has been slightly modified. From hub to mid-span, the blade has two airfoils, while from mid-span to tip, the blade has a single airfoil. Figure 5 shows two airfoils and the gap nozzle of the hybrid blade. Because of stagger angle, AO changes from hub to tip but gap shape and length of the nozzle are constants till mid-span. Table 5 contains design parameters used for the hybrid blade. The reader should understand the difference between a tandem rotor blade and a hybrid rotor. In the tandem rotor, both forward and aft rotor blade have designed separately but they are arranged in a manner that a nozzle type shape is formed in between. The exit angle of the FB serves as an inlet angle for the AB. On the contrary, the geometry of the hybrid blade is obtained by making a nozzle type slot in a single rotor design. Unlike the tandem rotor, the radius of the trailing edge of the forward airfoil and the leading edge of the aft airfoil are not pre-defined.

In-build Design Modular and Mesh of ANSYS WORKBENCH used to prepare unstructured mesh. A steady RANS (Reynolds-Averaged Navier–Stokes) equation with the SST turbulence model is used for analysis, and the numerical investigation

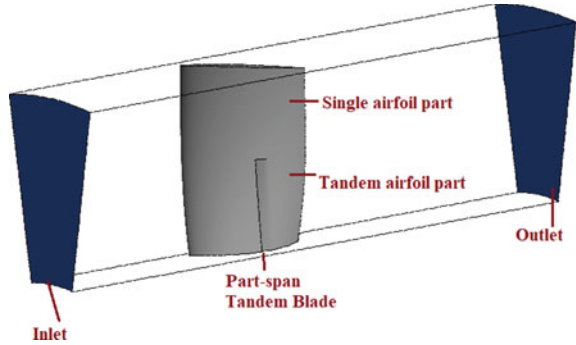
Fig. 5 Nozzle gap of hybrid blade



Table 5 Geometric parameters of hybrid blade

Aspect ratio	1.5
Axial overlap at mid (%)	2.80
Axial overlap at hub (%)	4.37

Fig. 6 Computational domain of hybrid rotor



is done with the help of ANSYS CFX solver. Figure 6 shows the CFD domain used for the numerical study. Inlet is at upstream of rotor LE by 1.5 times of airfoil chord, and outlet is at downstream of rotor TE by a distance of 2.5 times of chord. Ambient pressure at inlet and mass flow rate at the outlet are implemented as a boundary condition of the domain. After grid independence study, 2.2 million, 1.8 million, and 2.1 million mesh elements were selected for performance analysis of single, tandem, and hybrid blades, respectively, with considering wall y^+ and quality of the mesh.

4 Results and Discussion

CFD results were extracted and analyzed at the design point $\phi = 0.64$, and off-design/near stall condition, $\phi = 0.61$. Contours of Mach number with streamlines are extracted at the three different span locations (Z/H) (10, 50, and 90%) for the single rotor, tandem rotor, and the hybrid rotor. Figures 7 and 8 shows the Mach number contours of the single rotor under design and off-design condition. Near the design point, the low velocity zone is visible near the trailing edge portion of the single rotor. However, at a 50% span, streamlines indicate reverse flow near the trailing edge of the rotor suction surface. At other span locations, flow is attached to the blade surface and flow reversal is not seen. Under the off-design condition, the

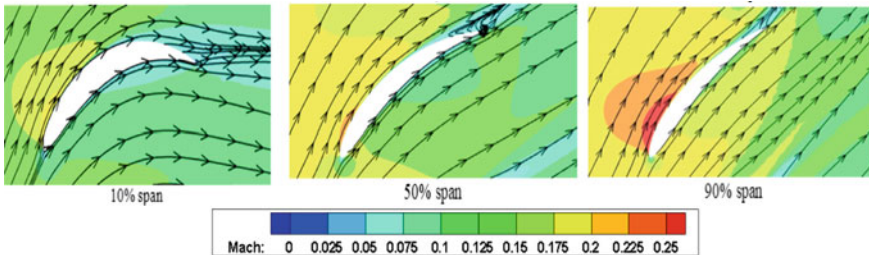


Fig. 7 Mach contours of single rotor at $\phi = 0.64$

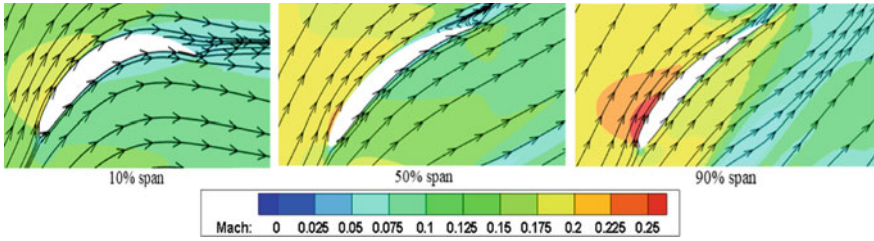


Fig. 8 Mach contours of single rotor at $\phi = 0.61$

performance of the single rotor further deteriorates and a low velocity zone enlarges further. On the contrary, the tandem rotor exhibits improved performance under design and off-design conditions (Figs. 9 and 10). Nozzle gap plays an important role in the performance of the tandem rotor. Momentum transfer through the gap is less effective near to the hub region as compared to the tip region. The lower momentum toward the hub region is mainly attributed to two factors. Firstly, the tandem rotor is designed with a low hub to tip ratio, and less energy available toward the lower span adversely affects the performance of the tandem rotor. Secondly, the pressure difference in the vicinity of the gap nozzle acts as a driving force the momentum transfer through the gap nozzle. As the pressure gradient is significantly higher toward the tip region, improved performance of the tandem rotor is observed under design and off-design condition. With less flow velocity and higher incidence,

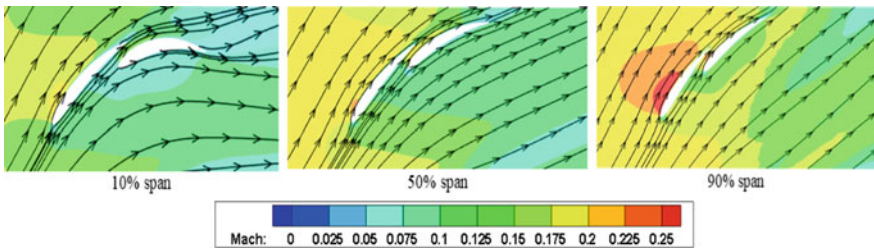


Fig. 9 Mach contours of tandem rotor at $\phi = 0.64$

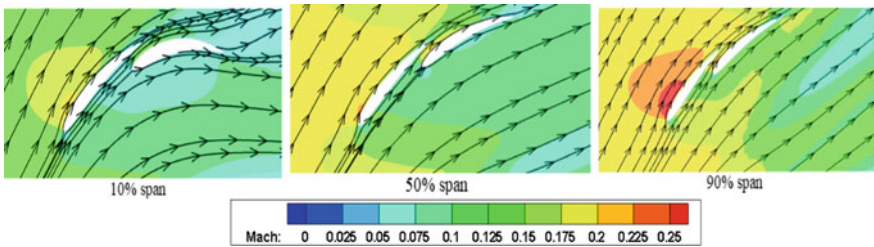


Fig. 10 Mach contours of tandem rotor at $\phi = 0.61$

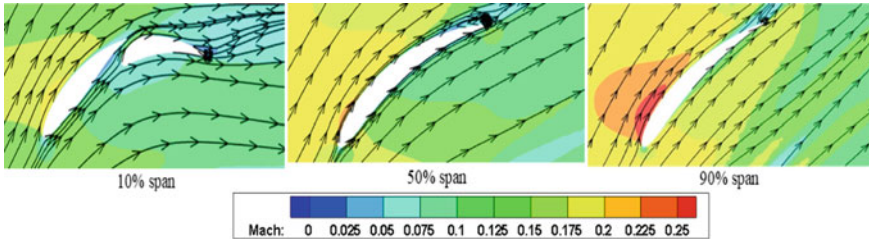


Fig. 11 Mach contours of hybrid rotor at $\phi = 0.64$

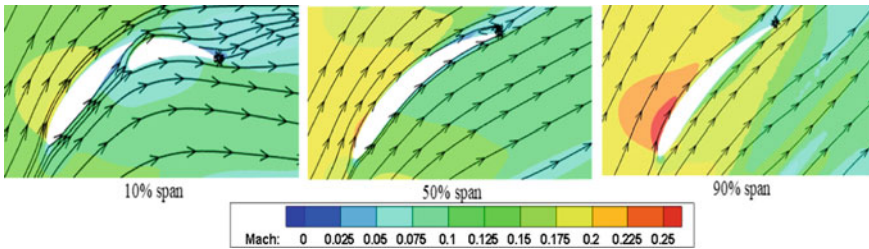


Fig. 12 Mach contours of hybrid rotor at $\phi = 0.61$

the effectiveness of the gap decreases under the off-design condition. At all spans, due to effective and optimum nozzle effect, tandem shows a lesser low velocity zone on SS of blade surface near to TE as compared to a single rotor (Figs. 11 and 12). The flow separation, which was visible in the case of a single rotor, is effectively mitigated with the help of higher momentum fluid. Mach number contours of the hybrid rotor are shown by Figs. 11 and 12. Similar to the tandem rotor case, a nozzle type shape forms in case of hybrid rotor at a lower span. The shape and size of the nozzle of hybrid rotor is different from that of the tandem rotor. At 10% span location, streamlines are attached to the AB surface under design and off-design condition. Similar to earlier cases, low velocity zones are visible near the trailing edge of the rotor blade. In the case of the hybrid rotor, aft section airfoil is too close to the pressure surface of the forward airfoil, which alters the pressure distribution pattern in that vicinity. At 50% span location, hybrid rotor shows a relatively enlarged portion of low velocity fluid. At mid-span, a transformation from tandem airfoil to a single airfoil takes place. Therefore, additional losses occur at the interface for the hybrid rotor. At the off-design conditions, the low velocity region on the blade surface has slightly moved further upstream and enlarged. The effect of TLV can be seen at a 90% span location, where a large low velocity zone is visible in the blade passage. In the case of a hybrid rotor, redesigning the nozzle gap for optimum AO can enhance the momentum transfer.

The static pressure coefficient (C_p) at various spanwise locations of the blade is shown in Figs. 13 and 14 for design and off-design condition, respectively. Blade loading increases from the hub toward the tip, and it is as per the design of single

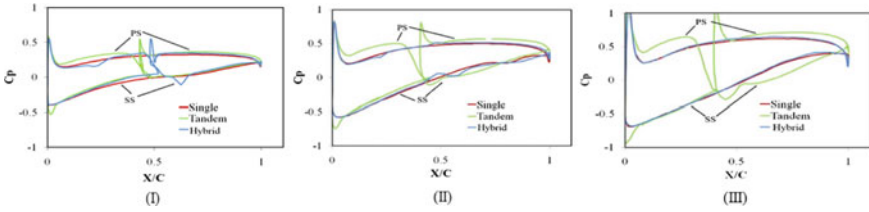


Fig. 13 Pressure coefficient (C_p) distribution at design condition (I) 10% span (II) 50% span (III) 90% span

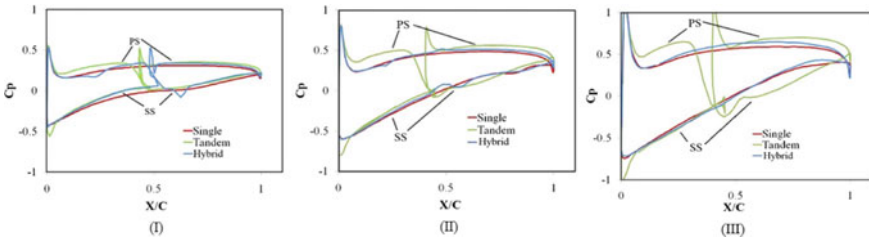


Fig. 14 Pressure coefficient (C_p) distribution at off-design condition (I) 10% span (II) 50% span (III) 90% span

and tandem rotors. Blade loading is nearly the same for all the cases at 10% span location. As the hybrid rotor is a modification of a single rotor, thus both hybrid rotor and single rotor demonstrates approximately equal blade loading, except at lower spans, where a small difference in C_p can be seen due to LE curvature of AB. Quick acceleration over aft airfoil results in a drop in C_p on SS at ~ 0.62 X/C. In the case of the tandem rotor, momentum transferred through gap nozzle increases the acceleration over SS of AB, which is reflected as higher negative C_p and improved blade loading. Accelerated flow over AB is due to the shape of AB and momentum transfer from the gap nozzle. The effect of gap nozzle in the tandem case is seen more clearly at 50 and 90% of the span.

As per the design, the tip section is designed for higher pressure rise. However, with the help of the nozzle-gap effect, a continuous diffusion is achieved near the tip section in the case of the tandem rotor. Clearly, the blade section is designed with a higher diffusion factor, the tandem rotor demonstrates its superiority over the single rotor. The position of AB increases the loading on the PS of FB. As TE of FB comes under the stagnation portion of AB, it increases pressure over PS of FB. The single rotor has a flatter distribution of C_p on SS, which shows less diffusivity of the blade. As a design and off-design points are close enough, there is no much variation in the nature of plots. Relatively, the tandem has higher diffusion at 50 and 90% span up to TE of the rotor. Due to the nozzle gap, higher turning capability developed in tandem, and hence, higher static pressure rise achieved.

A significant portion of losses occurs in the turbo-machinery are associated with TLV. Hence, it is important to analyze the behavior of TLV of new designs. The

formation and propagation of TLV inside the blade passage are shown with the help of entropy contours, which are drawn at different chordwise planes. Figures 15, 16, and 17 illustrate TLV of the single rotor (Fig. 15), tandem rotor (Fig. 16), and hybrid

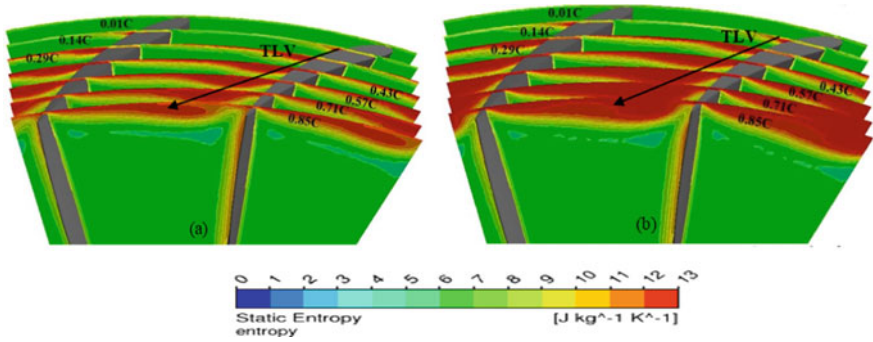


Fig. 15 Entropy contours of single rotor **a** design, **b** off-design condition

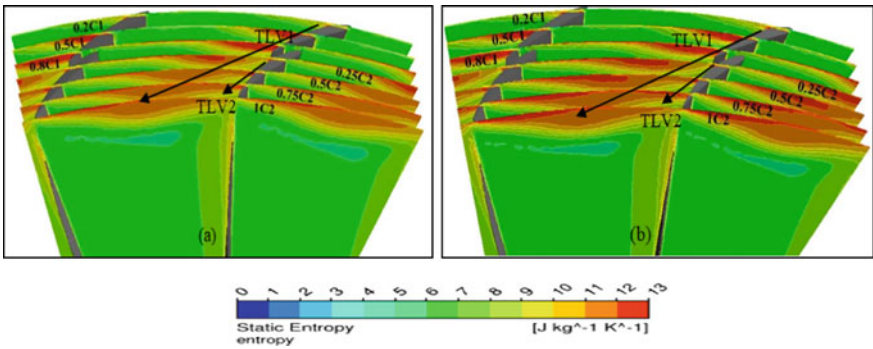


Fig. 16 Entropy contours of tandem rotor **a** design, **b** off-design condition

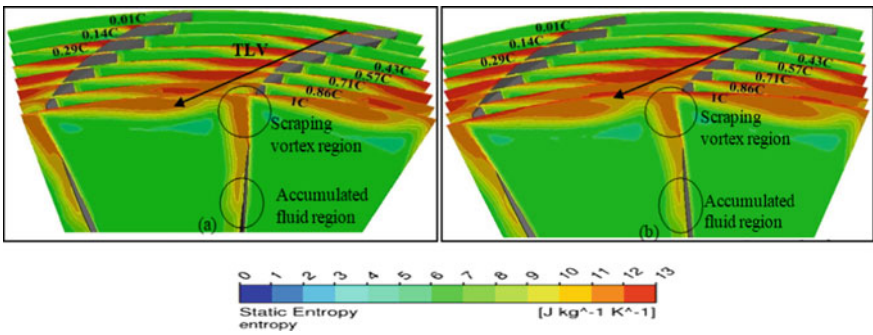


Fig. 17 Entropy contours of hybrid rotor **a** design, **b** off-design condition

rotor (Fig. 17) rotors, respectively, under design and off-design condition. Leakage flow, due to pressure difference between PS and SS, interacts with the main flow and form TLV. Strength of vortex increases as vortex moving toward the mid chord. This vortex migrates toward the PS side of the adjacent blade. Near to TE, TLV stretches and spreads across the passage. For a single rotor, the core of TLV is visible at 14%C. In the case of tandem rotor, two separate TLV can be observed, each associated with FB and AB. The strength of AB TLV is substantially lower than the strength of FB TLV. In tandem, the second TLV starts from AB and interacts with the wakes of FB as well as with the TLV of FB. TLV1 and TLV2 have a different orientation. It appears that TLV2 is more aligned in an axial direction than TLV1. The intensity of TLV1 and TLV2 is lower than the TLV of the single rotor. In the case of the tandem rotor, blade loading is split; hence, two relatively smaller vortices can be seen.

Interestingly, the strength of TLV of the hybrid blade is lower than the strength of single rotor TLV. The entropy region of TLV increases under the off-design condition for all cases except TLV2, which shows a decrement due to reduced tip loading. Stall initiates in the tip region in all rotor cases is due to the TLV effect. Under the off-design condition, entropy generation is highest for the single rotor. In the case of a single rotor and hybrid rotor, scraping vortex of intensity is visible. The boundary layer of casing rolled up because of the rotating tip and forms scraping vortex which creates high entropy region near to blade SS. For the hybrid rotor, another noticeable entropy zone is visible at or around mid-span blade. However, its strength is substantially lower than the TLV. Further, the strength of TLV and scraping vortex is more at off-design compared to the design point due to higher loading at the tip.

Figures 18, 19, and 20 show contours of Mach number at 98% span of the single rotor, tandem, and hybrid rotor at design and off-design conditions. Low Mach number region indicates blockage created due to TLV. The blockage for the single rotor is considerably higher than the blockage created in other cases. At 98% span, 60% of the blade passage is covered with low velocity fluid. As the strength of TLV increases under off-design condition, blockages region enlarges further and 90% of the blade passage is blocked due to TLV. In the tandem configuration, blockage due to TLV1 and TLV2 merge and form a larger blockage region. It is noteworthy that

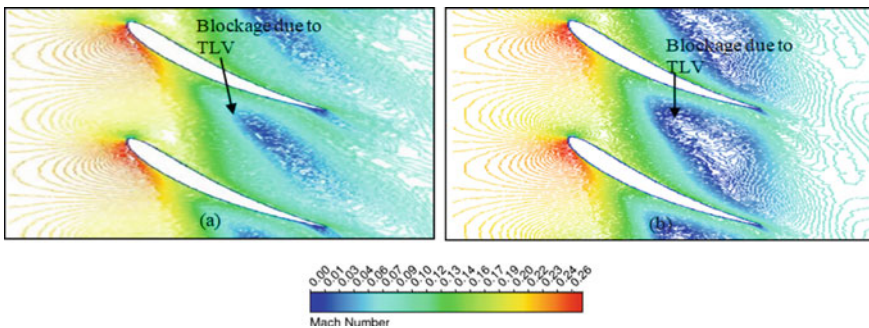


Fig. 18 Mach number contour at 98% span location of single rotor at **a** design, **b** off-design point

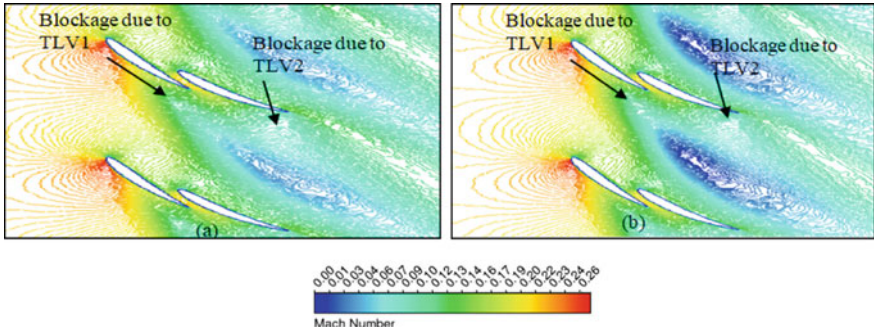


Fig. 19 Mach number contour at 98% span location of tandem rotor at a design, b off-design point

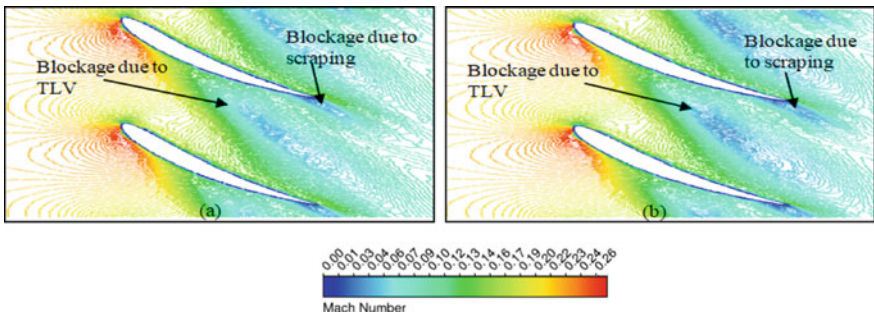


Fig. 20 Mach number contour at 98% span location of part-span tandem rotor at a design, b off-design point

the flow through gap nozzle reduces the blockage region in the case of the tandem rotor. Scrapping vortex also acts as a source of blockage for the single and hybrid rotor; however, its effect is confined near the trailing edge only.

Static pressure variation from inlet to an outlet under design and off-design condition is plotted in Fig. 21. At LE of the blade due to curvature of the blade, flow accelerates so there is a drop in static pressure at nearly 0.31 streamwise location. Along the blade surface of the rotor, there is a smooth increase in pressure. At 0.34 locations, there is small crust in the tandem case because of LE of AB. There is no large drop in static pressure at LE of AB because of the overlapping region. Under both design and off-design conditions, the tandem rotor shows a higher static pressure rise than the single rotor and hybrid rotor case. The static pressure rise increases at a lower mass flow rate. It is true for all cases. As mass flow rate decreases, blade loading increases due to the higher incidence. The hybrid tandem blade does not show any crust like a tandem rotor. The static pressure rise for hybrid rotor is higher than the single rotor.

Figure 22 shows the surface streamlines over SS of the blades under design condition. Near the hub region, 60% of the blade surface is occupied by radial lines for

Fig. 21 Comparison of static pressure variation between tandem and hybrid blade

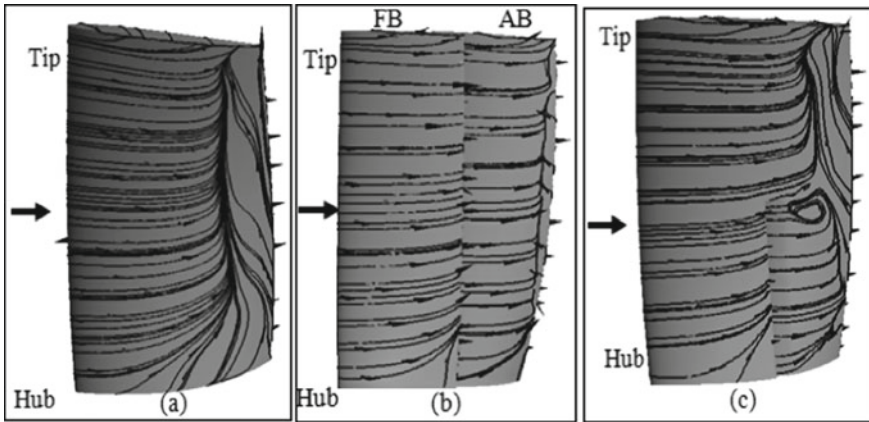
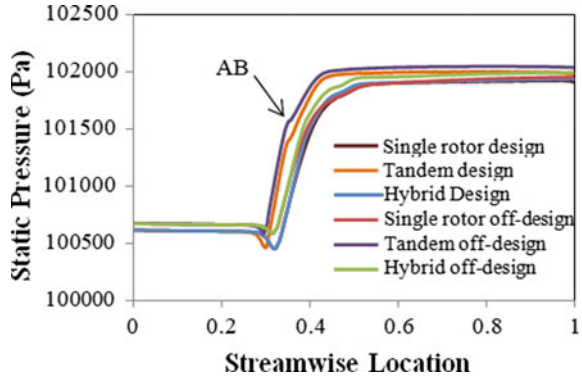


Fig. 22 Skin friction lines at design point over SS **a** single rotor, **b** tandem, **c** hybrid rotor

the single rotor case. At a higher span, flow on SS of single rotor adheres up to 75% of the chord; thereafter, strong radial flow is visible. There are no major changes in surface streamlines at off-design condition (Fig. 23) as these two conditions are close to each other and stall start downstream of the rotor causes no major effect on surface streamlines. In the tandem rotor case, FB’s SS is free from any flow reversal. However, small flow separation is visible near the trailing edge portion of AB’s SS under design and off-design condition. In case of hybrid rotor, surface streamlines over AB’s SS can be interpreted in two distinct regions. The behavior of the surface streamlines up to 50% span can be closely related to the tandem rotor case. Near the mid-span, surface streamlines indicate a formation of strong separation vortex in the case of a hybrid rotor. As explained in the earlier section, near the mid-section, the transformation from two airfoils to single airfoil takes place. At this critical junction, due to the additional boundary layer and inadequate momentum flow, the flow separates from the blade surface at 0.7 chord.

The strength of this vortex increases under the off-design condition.

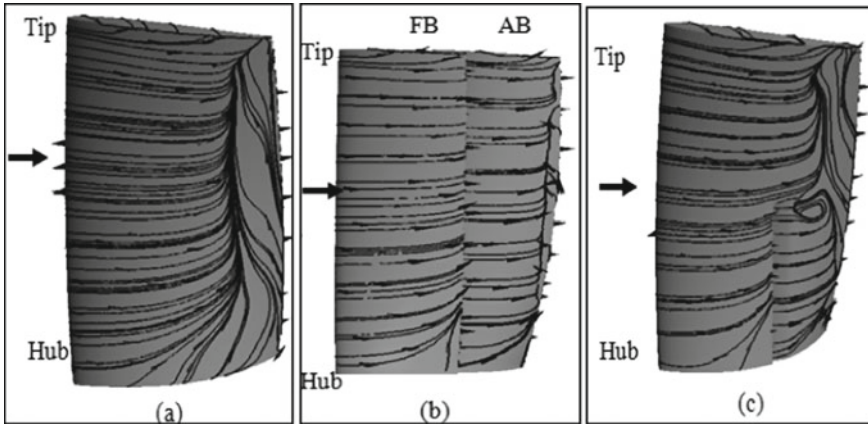


Fig. 23 Skin friction lines at off-design point over SS a single rotor, b tandem, c hybrid

Figure 24 shows the spanwise variation of the total pressure loss coefficient (ω). Due to strong TLV, all cases show higher losses in the tip region (Fig. 24). Moving toward the off-design condition from a design point, losses occur due to TLV further increase. As expected from the earlier discussion, the single rotor experiences a higher loss due to TLV than the tandem rotor and hybrid rotor. After 85% blade span, there is a sharp jump in the loss coefficient for the single rotor. It is important to note that despite having two separate TLV, losses occur due to TLV is much lower in the case of tandem rotor than other cases. It appears that the momentum through gap nozzle promotes the better mixing of TLV with the main flow and subsequently a lower tip leakage loss. The losses of the hybrid blade are higher than the tandem rotor but lower than the single rotor. At a 5% blade span, the tandem rotor and hybrid rotor see a small jump in loss coefficient presumably due to hub corner separation.

Fig. 24 Total pressure loss coefficient across rotor blade along span

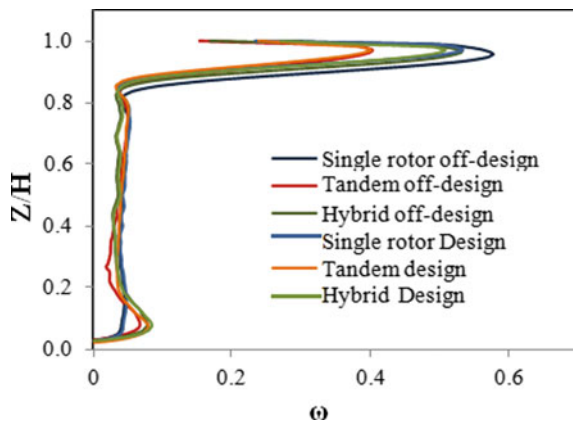


Fig. 25 Stagnation pressure rise coefficient versus flow coefficient

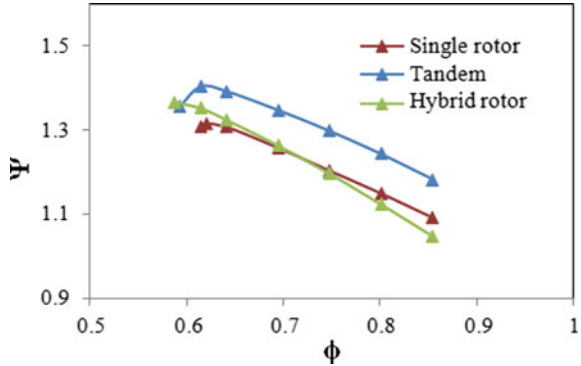
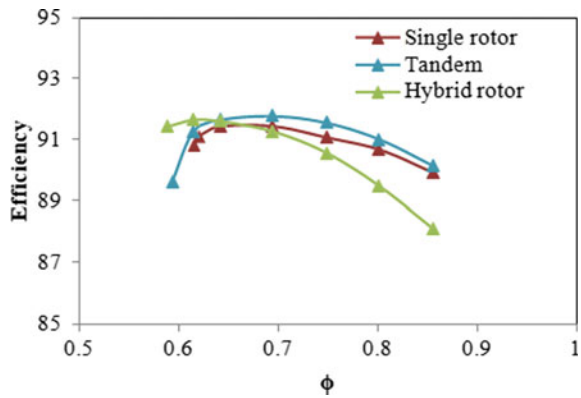


Fig. 26 Isentropic efficiency versus flow coefficient



From a 10% span to an 85% blade span, the loss coefficient is fairly constant and approximately equal for all cases.

Figures 25 and 26 show the performance characteristics of a single rotor, tandem, and hybrid blades. The total pressure rise increases gradually from a higher mass flow rate toward a lower mass flow rate. Near the stall point, the stagnation pressure coefficient drops for the tandem rotor, whereas for other cases experience an abrupt stall. The tandem rotor shows a higher pressure rise as compared to other two cases for the entire range of operation. Under design condition, the tandem rotor has a 5.1% higher total pressure rise than hybrid and a 6.5% higher pressure rise than the single rotor case. This trend is fairly maintained for the entire range of operation. The stall margin for the hybrid rotor is 8.3% while the stall margin for a single rotor and tandem rotor is 4% and 7.5%, respectively. At higher mass, flow rate tandem and single rotors have higher efficiency than hybrid configuration. However, near the stall point, tandem shows a large drop in efficiency. The tandem rotor is able to achieve a higher pressure rise without having any efficiency penalty.

5 Conclusions

The paper discusses the CFD analysis of the single rotor, tandem rotor, and part-span tandem (hybrid) rotor blade. A parallel comparison has been drawn to highlight the benefit and drawbacks of each case. Various parameters like TLV, static pressure variation, Mach number contours, streamlines, and losses have been studied to understand the flow physics with proper reasoning. The error range of the predictions made in the study is in an acceptable range and supported by proper validation and strong theory. The conclusions drawn from the results of low speed analysis are as follows:

- The tandem rotor demonstrates a higher pressure rise as compared to other both cases for the entire range of operation. Under design condition, the tandem rotor has a 5.1% higher total pressure rise than hybrid rotor and a 6.5% higher pressure rise than the single rotor case.
- The stall margin for the hybrid rotor is 8.3% while the stall margin for a single rotor and tandem rotor is 4% and 7.5%, respectively.
- The losses associated with TLV are substantially higher for the single rotor case. The entropy region increases under the off-design condition.
- Despite having two separate TLV, losses occur due to TLV is much lower in case of the tandem rotor than other cases
- In the tandem rotor, the gap nozzle imparts energy to flow on SS of AB. However, near to the hub, the gap nozzle is not working efficiently due to the low momentum of flow and boundary layer effect. The effectiveness of the gap nozzle increases toward the higher span.
- In the case of the hybrid rotor, the nozzle gap is less efficient at the interface zone as compared to the lower spans nozzle gap.
- Blade loading increases from hub to tip. The tandem rotor demonstrates a higher diffusion capability than the other rotors, particularly at a higher span.

References

1. Saha UK, Roy B (1997) Experimental investigations on tandem compressor cascade performance at low speeds. *Thermal Fluid Sci* 14:263–276
2. Kumar A, Pradeep AM (2018) Optimization of the Gap-nozzle n Tandem Configuration. In: *Proceedings of the Asian congress on gas turbines, ACGT2018-TS08*
3. McGlumphy J (2008) Numerical investigation of subsonic axial-flow tandem airfoils for a core compressor rotor. PhD diss., Virginia Tech
4. McGlumphy J, Ng W, Wellborn SR, Kempf S (2009) Numerical investigation of tandem airfoils for subsonic axial-flow compressor blades. *J Turbomach* 131(2):021018
5. Kumar A, Pradeep AM (2018) Performance evaluation of a tandem rotor under design and off-design operation. In: *Proceedings of ASME turbo expo: turbomachinery technical conference and exposition, GT2018-75478*

6. Guochuan W, Biaonan Z, Guo B (1985) Experimental investigation of tandem blade cascades with double-circular arc profiles. In: Beijing international gas turbine symposium and exposition, ASME, pp V001T02A036–V001T02A036
7. Falla GAC (2004) Numerical investigation of the flow in tandem compressor cascades, Master's thesis, Institute of Thermal Power Plants, Vienna University of Technology, Austria
8. Roy B, Saha UK (1995) High diffusion cascades for axial flow compressor applications. In: Proceedings of 15th Canadian congress of applied mechanics, pp 356–363
9. Bammert K, Beelte H (1980) Investigations of an axial flow compressor with tandem cascades. *J Eng Power* 102(4):971–977
10. Roy B, Srivastava VP, Mulmule A (2009) Aerodynamic design of Part-Span tandem bladed rotor for low speed axial compressor/fan. In: AIAA applied aerodynamics conference, AIAA 2009–3964
11. Hasegawa H, Akinori M, Shinya S (2003) Development of highly loaded fan with tandem cascade. 41st Aerospace Sci Meet Exh
12. Yoon S, Ajay R, Chaluvadi V, Michelassi V, Mallina R (2019) A passive flow control to mitigate the corner separation in an axial compressor by a slotted rotor blade. In: Proceedings of ASME turbo expo, turbomachinery technical conference and exposition, GT2019

Flow-Field Investigation of an Inter-compressor Duct Under Different Inflows and Their Influence on the Performance of a Low-Pressure Compressor



Jerry T. John, C. Dileep Kumar, Sourav Pramanick, Lenin Loitongbam, A. M. Pradeep, N. Vidhyashankar, and Reza Abbas

Abstract The present computational study focusses on the flow physics analysis of an aero-derivative inter-compressor duct with struts along with the low-pressure (LP) compressor for a generic small turbofan engine. The transition duct connects the transonic fan to LP compressor. For numerical analysis, four inflows under consideration are Inflow-A (uniform inflow), Inflow-B (fan exit condition with uniform flow at fan inlet), Inflow-C (fan exit condition with radial hub distortion at fan inlet) and Inflow-D (fan exit condition with circumferential distortion at fan inlet). A pair of streamwise counter-rotating pair of vortices forms at the duct-struts-hub corner region for Inflow-A. But, for all other inflows, the vortex formation is deflected on the leeward side of the strut owing to the tangential component generated by the upstream stage. Besides, the exit conditions of the duct are imposed on the LP compressor to estimate its performance and the phenomena that lead to stall. For each inflow, the flow separation at the tip side of the stator leads to compressor stall. In general, the paper briefly elucidates how different inflows ingested by the transonic fan affect the duct and subsequently the LP compressor in a gas-turbine engine.

Keywords S-duct · Compressor · Streamwise counter-rotating vortices · Distortion · Stall

J. T. John (✉) · C. Dileep Kumar · S. Pramanick · L. Loitongbam · A. M. Pradeep
Indian Institute of Technology Bombay, Mumbai, Maharashtra 400076, India

A. M. Pradeep
e-mail: ampradeep@aero.iitb.ac.in

N. Vidhyashankar · R. Abbas
Gas Turbine Research Establishment, Bengaluru, Karnataka 560093, India
e-mail: vidhyashankar@gtre.drdo.in

R. Abbas
e-mail: rezaabbas@gtre.drdo.in

Nomenclature

A	Cross-sectional area (m^2)
C_p	Static pressure rise coefficient (–)
C_{ax}	Strut axial chord length (m)
h_{in}	Duct inlet height (m)
L	Length of the duct (m)
LE	Leading edge
M_{rel}	Relative Mach number (–)
P	Static pressure (Pa)
P_0	Total pressure (Pa)
R	Radius (m)
RANS	Reynolds averaged Navier Stokes
TE	Trailing edge
U_{tip}	Rotor peripheral speed at tip (m/s)
V_z	Axial velocity (m/s)
Y_s	Total pressure loss coefficient (–)
Ψ	Loading coefficient (–)
ϕ	Flow coefficient (–)

Duct and Compressor Stations

T_I	Duct inlet plane
T_E	Duct exit plane
RLE	Rotor LE plane
RTE	Rotor TE plane
SLE	Stator LE plane
STE	Stator TE plane

1 Introduction

The current era of gas-turbine technology aims in developing and implementing turbofan engines for commercial aircraft, with a focus on the improvement in efficiency, the reduction in the fuel burnt, and the emission the engine emits. In view of the radii difference that exists between the transonic fan and core compressor, the inter-compressor duct which connects them takes the form of an S-shape since the flow at the fan outlet which is axial has to undergo a radius change and subsequently has to be directed to the core compressor which has an axial inlet.

Despite having a simple shape, the aerodynamic perspective of the duct is entirely complex on account of the pressure gradient it generates at the two bends as described

in the findings of Duenas et al. [2]. At the first bend, the casing endwall faces a strong adverse pressure gradient followed by a favourable pressure gradient and then an adverse pressure gradient. The converse trend is observed for the hub endwall.

Often non-turning struts are employed in an inter-compressor duct to provide structural stability and to allow coolant oils to pass. The strut-hub corner region is of the utmost importance when designing a compressor transition duct. Under the combined action of both streamwise and radial pressure gradient, a pair of streamwise counter-rotating vortices form at the strut-hub corner region which has a significant impact on the drop in total pressure as observed by Karakasis et al. [5]. Moreover, this reduced total pressure flow when ingested by the core compressor has a negative impact on their performance in terms of pressure rise and efficiency. A two-decade back study by Sonoda et al. [9, 10] carried out both experimental and numerical investigation on the influence of downstream passage on the development of flow in an inter-compressor duct. After that, the authors further investigated the impact of boundary layer thickness on the duct flow field. They observed that a curved passage resulted in a significant drop in total pressure compared to a straight passage, with the drop being amplified in the case of a thickened boundary layer.

Further, such regions of enhanced total pressure loss act as inlet distortion to the downstream core compressor components and affect their performance. Bandyopadhyay and Ahmed [1] investigated the effects of curvatures on boundary layer stability experimentally. Their study led to the conclusion that a concave surface destabilizes the boundary layer; whereas, a convex surface stabilizes the boundary layer. In the case of an inter-compressor duct, the concave surface is at the first bend of the casing layer and the second bend of the hub layer. A recent work by Verma et al. [13] carried out an extensive study on the performance of an inter-compressor duct under the influence of different inflows, namely uniform, radial tip distortion and radial hub distortion for a low-bypass ratio turbofan engine. They observed that in the presence of distortion, the fan as well as the inter-compressor duct are significantly affected, with the duct being drastically affected in the presence of radial hub distortion. A similar finding is identified from the work of Walker et al. [14]. Hence, the primary aim of an inter-compressor duct is to transit the flow from one component to other with the minimum drop in total pressure. The duct under consideration for the present study consists of two thick and two thin non-turning struts followed by a low-pressure core compressor geometry which operates in the transonic regime.

In general, the paper addresses the following questions:

1. How does the inter-compressor duct behave under the influence of uniform and upstream stage representative condition?
2. What is the response of an LP compressor to different inflow generated by the duct and the phenomena that lead to the onset of stall?

2 Geometric Description

The geometry under consideration consists of an inter-compressor duct and an LP compressor borrowed from an existing industry relevant small turbofan engine. The compressor transition duct includes two thick struts and two thin struts with a t/c ratio of 0.234 and 0.0516, respectively. Other non-dimensional geometrical value of the duct is $\Delta R/L = 0.563$, $h_{in}/L = 0.265$, $R_{in}/L = 1.294$ and $A_{out}/A_{in} = 0.319$. Moreover, the LP compressor consists of 21 blades for the rotor domain and 24 blades for the stator domain and operates in the transonic regime with a design loading coefficient (ψ) of 1.27 and flow coefficient (ϕ) of 1.08. Therefore, owing to the periodicity, to carry out the numerical investigation, a 180° passage is taken for the duct-struts domain, and a single passage for the LP compressor domain comprising one rotor blade and one stator blade.

2.1 Solver Description and Grid Details

The simulations for the current study are carried out using the commercial CFD code NUMECA FINE/Turbo v12.1[7, 8]. For the entire work, steady RANS simulations are employed which make use of the mixing plane approach at the interface of the rotor–stator domain whereby, the flow parameters are averaged in the circumferential direction and are passed to the successive domain. A drawback of this method is that the pitchwise non-uniformities are mixed out. Further, the turbulence closure is achieved using the two-equation $k-\omega$ SST turbulence model. This model is used on account of its ability to capture flow at regions of adverse pressure gradient and from validation. The solver EURANUS is based on a cell centred-finite volume approach. Second-order central differencing scheme is used to discretize the spatial flux, and the temporal flux is discretized using the fourth-order Range-Kutta method. To speed up the convergence, multi-grid approach is utilized with 800 number of iterations specified for the coarse and medium grid, so that the fluctuations in the residuals are nullified. Consecutively, for the fine grid, the simulations are run for a more number of iterations until a converged solution is obtained. Besides, the numerical stall is determined to be the case beyond which a converged solution is no longer possible.

The hybrid O4H topology is used to mesh the duct as well as the LP compressor which employs a combination of H-topology on the upstream, downstream and pitchwise passage direction and an O-topology around the blade boundary. Following the grid independence study, the inter-compressor duct consists of $133 \times 195 \times 97$ grid points in the streamwise, pitchwise and radial direction. Moreover, 37 grid points are placed around the strut boundary to capture the strut-hub corner separation accurately. On the other hand, the rotor of the LP compressor consists of $85 \times 75 \times 57$ grid points in the streamwise, pitchwise and radial direction with 17 grid points in the rotor tip clearance. The stator of the LP compressor consists of $81 \times 75 \times 49$ grid points in the streamwise, pitchwise and streamwise direction. Care is taken to

ensure that the y^+ along the endwalls is below 1. Further details of the software can be found in the Numeca FINE/Turbo user manual and theoretical manual (2016).

2.2 Solver Validation

The solver EURANUS of Numeca FINE/Turbo is validated with the standard test case of Rotor-67, a transonic fan rotor. The low-aspect-ratio rotor delivers a pressure ratio of 1.63 at a corrected mass flow of 33.25 kg/s. Further, the rotor rotates at a design speed of 16,043 rpm yielding a relative Mach number of 1.38 at the tip. The rotor consists of 22 blades with a hub to tip ratio of 0.43. For the present validation, only the rotor of the stage-67 is taken, and the data for validation is obtained from the technical report published by NASA authored by Strazisar et al. [11]. The radial profiles of the total pressure ratio and total temperature ratio at peak efficiency point are compared with the experimental result. From the plots, both SA (Spalart Allmaras) and SST (Shear Stress Transport) turbulence model match well with the experimental results with a variation of less than 5%. Moreover, the SST turbulence model is taken for further analysis on account of the ability of the turbulence model to capture flows in regions of an adverse pressure gradient.

2.3 Method of Data Imposition

2.3.1 Method of Data Imposition for Duct-Struts Domain

For Inflow-A, a uniform flow value of total pressure, total temperature and normalized axial velocity vector perpendicular to the inlet domain are specified at domain inlet marked in Fig. 1. The domain inlet is the extended portion of the duct (1.25 times the strut C_{ax}) to allow the flow to develop which is a common practice followed in CFD and is described in detail by Vahdati et al. [12]. On the other hand, all other inflows are specified at location T_1 . In the case of Inflow-B and Inflow-C, 1D mass averaged

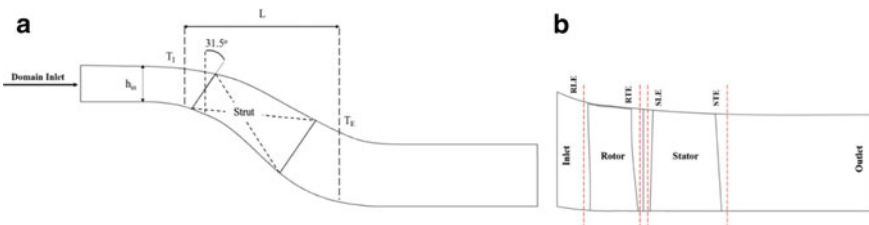


Fig. 1 Schematic representation of **a** duct meridional section and **b** LP compressor meridional section with the stations labelled

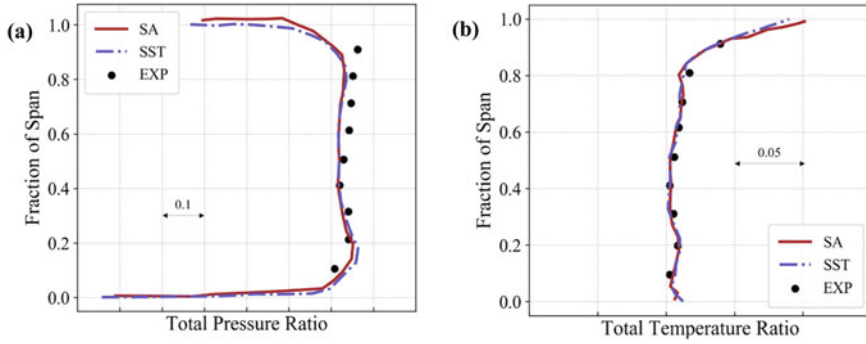


Fig. 2 Radial profiles validation of Rotor67 at peak efficiency point. **a** Total pressure ratio and **b** total temperature ratio

profiles of total pressure, total temperature and normalized velocity vectors having spanwise non-uniformity are extracted from the exit of the upstream stage. Further, the extracted quantities are imposed at the duct inlet (location T_1). A slight difference exists in the case of Inflow-D, whereby surface data having flow non-uniformity in both spanwise and pitchwise direction is used, and the method of imposition is same as in the case of Inflow-B and Inflow-C. For this case, a 360° duct-struts domain is used with twice the grid count (Fig. 2).

2.3.2 Method of Data Imposition for LP Compressor Domain

In the case of LP compressor, 1D mass averaged profiles of total pressure, total temperature and normalized velocity vectors having spanwise non-uniformity are extracted at location T_E of the inter-compressor duct and are imposed at the inlet of the LP compressor. For the case of Inflow-D, surface data is not used due to the requirement of high grid count for the LP compressor as the full 360° annulus is to be used for steady RANS simulation to generate the performance map. Hence to overcome this, 1D mass averaged radial profiles are used.

3 Results and Discussions

Two primary quantities to describe the performance are static pressure rise coefficient (C_p) and total pressure loss coefficient (Y_s) and are mathematically expressed as:

$$C_p = \frac{P_{TI} - P_{TE}}{P_{0,TI} - P_{TI}} \quad (1)$$

$$Y_s = \frac{P_{0,TI} - P_{0,TE}}{P_{0,TI} - P_{TI}} \tag{2}$$

3.1 Inter-compressor Duct Response Under Uniform Flow and Upstream Stage Representative Condition

The flow physics happening in the duct-struts case with uniform flow condition is briefly elucidated. Along with the duct domain, four total pressure isolines sections are shown in Fig. 3 with the respective location of each section mentioned. At the mid chord of the strut near the hub, a pair of counter-rotating vortices starts to develop (two vortices are formed on account of angular momentum conservation) under the combined action of the streamwise and radial pressure gradient. Strut mid chord is located at the second bend of the S-duct where adverse pressure gradient acts along with the hub. Further downstream, at the trailing edge of the struts, the vortices near completion and the complete counter-rotating vortices can be observed at the duct exit section. The core of a vortex is a low-pressure region.

Moreover, vortex moves from a region of low pressure to high pressure and pump boundary layer fluid into the free stream, thus raising the mixing loss. Also, as the vortices migrate downstream, their intensity decreases which are evident from the last two cut sections. Furthermore, after the second bend, adverse pressure gradient acts along the casing end wall and results in the growth of the casing boundary layer.

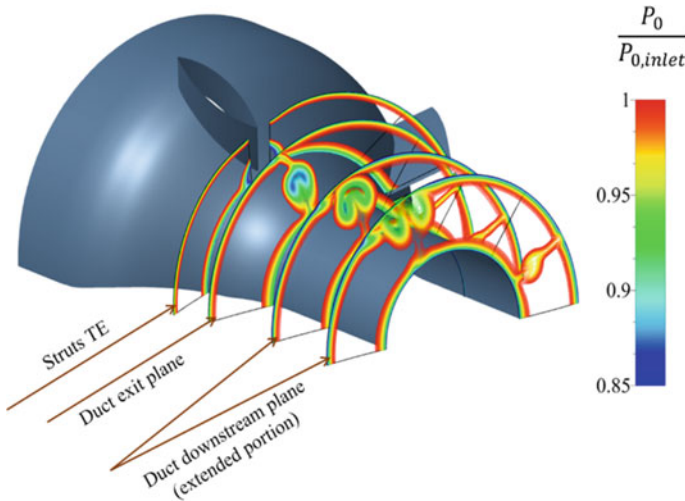


Fig. 3 Normalized total pressure isolines along duct streamwise direction with the location of the sectional plane taken from struts T_E to the exit of extended portion for Inflow-A representing the formation of counter-rotating pair of vortices and their radial migration

Since, due to the effect of the radial pressure gradient (acting from the casing endwall to hub end wall), the fluid streamlines attached to the casing layer tend to separate. But the casing boundary layer separation is suppressed due to the radial migration of contra-rotating streamwise vortices. A similar observation is found in work by Karakasis et al. [5]. For rest of the inflows, the hub corner vortex is deflected on the leeward side of the strut given the role played by the tangential component of velocity generated by the upstream stage and the flow-field development is the same.

Total pressure loss coefficient at location T_E depicted in Fig. 4 for Inflow-A, and Inflow-C clearly shows the difference in the predicted loss for the two inflows. Inflow-C is predicted to deliver a higher loss compared to Inflow-A. Moreover, the vortex formation is not symmetric for Inflow-C and is deflected on the leeward side of the strut owing to the tangential component generated by the upstream fan. On the other hand, the vortex formation for Inflow-A is symmetric. As stated earlier, Inflow-A is with uniform flow at duct inlet, and Inflow-C is with radial hub distortion at transonic fan inlet. Distortion in any form is undesirable to the gas-turbine engine, and it significantly affects the performance of the inter-compressor duct on account of the shed blade wakes and thick boundary layer pooling into the duct, which is per the findings of Sonoda et al. [9, 10] Hu et al. [4] and Verma et al. [13]. Moreover, the structure of the secondary flow vortices depends on the intensity of the upstream wakes, as observed by Norris and Dominy [6]. In the case of Inflow-A, a pair of streamwise counter-rotating pair of vortices develop on both the thick and thin struts, respectively. In contrast for all other inflows, the vortex formation is deflected on the leeward side of the struts. Notably, for all other inflows, the vortex formation is more pronounced for the thin strut, which is because of the inability of the strut to guide the flow incident on the LE at an angle.

Figure 5 depicts the variation in static pressure along the duct endwalls. Along the hub end wall at the first bend, the flow experiences a favourable pressure gradient, and as a result, the magnitude of C_p becomes negative and drops to a minimum value of -0.325 . After that, the C_p is observed to increase and reaches a maximum of 0.344 due to the presence of long adverse pressure gradient after the first bend.

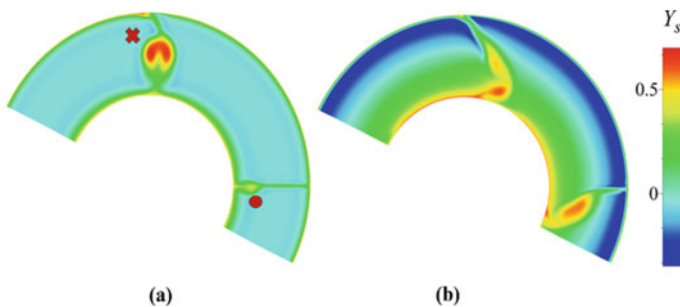


Fig. 4 Total pressure loss coefficient contour for **a** Inflow-A and **b** Inflow-C at location T_E . Symbol 'x' represents the vortex formation on the thick struts, and symbol 'o' represents the vortex formation on the thin struts

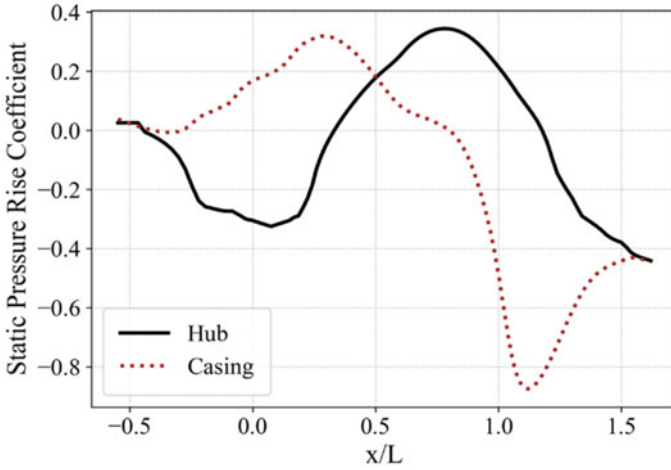


Fig. 5 Static pressure distribution along duct end walls

Further, the C_p decreases along the aft part of the duct and reaches a stable value. The reverse trend is observed in the case of the casing end wall where the value of C_p peak at 0.318. Thereafter, under the role of long favourable pressure gradient, C_p is observed to decrease to a minimum value of -0.875 and later reaches a constant value.

In the case of compressor-transition duct, the concave surface is at the first bend of casing endwall and second bend of hub endwall. Furthermore, from the C_p distribution along endwalls, a positive value of C_p denotes adverse pressure gradient; whereas, a negative value of C_p denotes favourable pressure gradient. Notably, at the aft portion of the duct, the C_p of both hub and casing endwall coincide which elucidates that static pressure distribution is constant along a straight channel and a drop in C_p denotes that flow is expanding at the aft portion of the duct to conserve the mass flow. Gao et al. [3] made a similar conclusion from their work.

Mass averaged radial profiles of total pressure loss coefficient at the exit of the inter-compressor duct (Fig. 6) depict a tremendous increase for Inflow-C. Inflow-C is the case with radial hub distortion at the upstream stage inlet. A flow with distortion reduces the momentum and consecutively thickens the boundary layer. The same happens here as well for Inflow-C, the thicker boundary layer flow along with the wakes shed by upstream stage further undergoes a reduction in momentum owing to the diffusion process at the struts-hub corner region. This momentum reduction leads to more pronounced vortex formation, which causes a drastic drop in total pressure, and hence an increase in the total pressure loss coefficient.

On the other hand, for Inflow-D, the effects of distortion are present on the tip region of the upstream stage, and hence, the penalty of distortion is taken by the bypass duct. Because of this, the loss profile for Inflow-D falls between Inflow-B

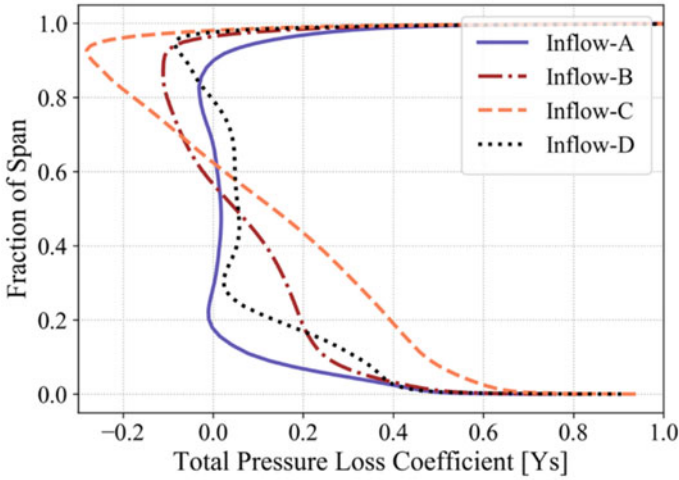


Fig. 6 Total pressure loss coefficient variation for different inflows (sectional plane taken at location T_E)

Table 1 Mass averaged total pressure loss coefficient for different inflows

Inflow-type	Y_s
Inflow-A	0.0351
Inflow-B	0.0356
Inflow-C	0.0436
Inflow-D	0.0512

and Inflow-C. Notably, the total pressure loss coefficient is the minimum for Inflow-A due to the uniformity in the flow imposed at the inflow boundary of the duct.

Table 1 represents the mass averaged Y_s calculated at the exit of the inter-compressor duct. Here Inflow-D corresponds to a higher value of Y_s , which contradicts with the explanation stated above. The point to be noted here is that, for Inflow-D, surface data having flow non-uniformity both in the spanwise and pitchwise direction is imposed. On the other hand, for Inflow-B and Inflow-C, 1D mass averaged radial profiles are imposed. Through using 1D mass averaged profiles, the losses are under-predicted as described by Karakasis et al. [5]. Despite the disadvantage the profiles offer, it can be used in a single passage domain, thereby saving the computational time. However, for surface data imposition a full passage is to be employed, which increases the grid requirement and the computational cost per simulation. Further, how different inflows affect the downstream LP compressor is briefly explained in the following subsection.

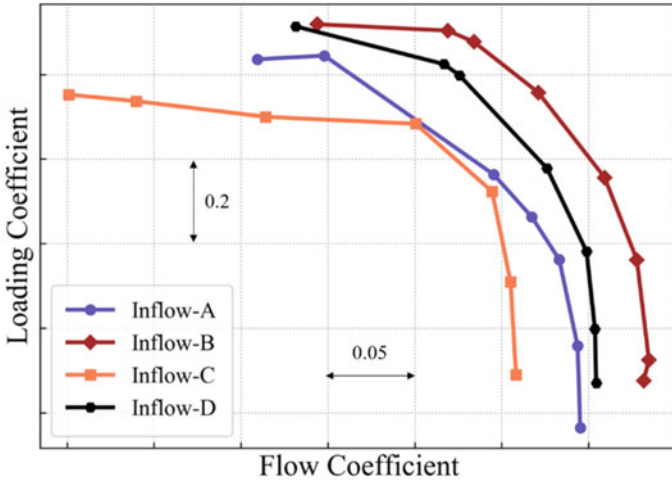


Fig. 7 Performance map of the LP compressor

3.2 Response of LP Compressor Under the Influence of Inter-compressor Duct

The two parameters of interest describing the LP compressor are loading coefficient (ψ) and flow coefficient (ϕ) and are mathematically represented as:

$$\psi = \frac{P_{0,RLE} - P_{0,RTE}}{\rho U_{tip}^2} \tag{3}$$

$$\phi = \frac{V_z}{U_{tip}} \tag{4}$$

Figure 7 represents the performance map of the LP compressor. A significant drop in the performance of the LP compressor is observed under Inflow-C in terms of acquired pressure rise, isentropic efficiency and inducted mass flow. From the performance map, it is evident how a momentum deficit flow is deleterious to the compressor performance. The root flow from the transonic fan in a turbofan engine is of utmost importance as the presence of distortion can downgrade the performance of core compressor components as observed by Walker et al. [14]. The response of compressor under different inflows is explained in detail and the nature of imposed total pressure profile is represented in Fig. 8.

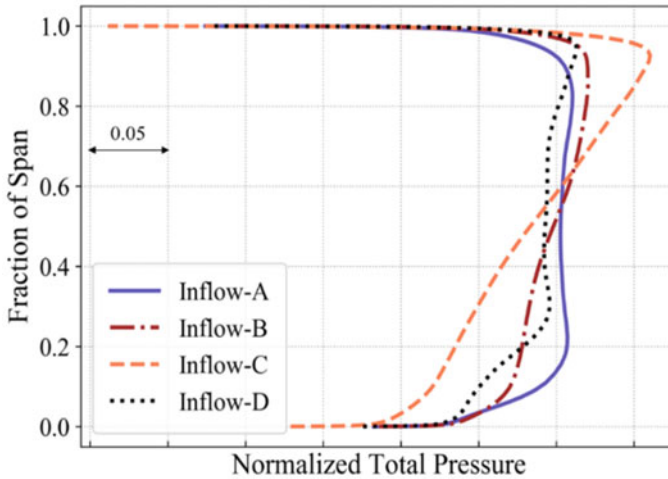


Fig. 8 Normalized total pressure radial profile imposed at the inlet of the LP compressor for different inflows

3.2.1 Inflow-A

Choke and peak efficiency point: The flow at 5% span is accompanied by the formation of wakes for both the rotor and stator domain. At the stator domain on account of the shock impinging the stator blades, the momentum of the flow after the shock is immediately reduced. This reduction in the flow momentum along with the diffusion process leads to pronounced wake formation. The wake formation at the TE of the rotor and stator blades continues to higher span, and at higher span due to the sudden increase in flow angle, a region of flow reversal is encountered by the stator. However, the separation is not as significant as observed in the near stall point. On the other hand, at peak efficiency, the flow field is similar to Inflow-B.

Near stall point: For Inflow-A, the input total pressure profile to the LP compressor is smooth on account of the uniform flow at the duct inlet. At 10% span, at the diffusive part of the rotor and stator blades, the flow is incapable of overcoming the streamwise pressure gradient. As a result, a small separation bubble formation takes place at TE of rotor and stator domain. But as the flow advances towards higher span, there is an increase in the low-momentum region, but the flow is completely attached. Notably, at 55% span, a small separation region starts to form at the diffusive part of the stator blade due to the streamwise pressure gradient. With the advancement of flow to a higher span, the flow impinges the blade at a high angle of incidence, and thus, the entire flow separates along the stator chord.

3.2.2 Inflow-B

Choke and peak efficiency point: The presence of strong shock causes a considerable reduction in the momentum of flow for both the rotor and stator domain, as seen in Fig. 13. This reduction in the momentum of the flow due to the presence of shock is the key reason for the wake generation process in addition to the streamwise pressure gradient. At 95% span, the wake formation on the rotor domain dwindles followed by a trailing edge separation on the stator blades. An important point to follow is that in the choke regime at every span location, there is shock-induced separation on the suction surface of the stator blade. But the flow is completely attached in the rotor domain despite the presence of shock.

On the other hand, at the peak efficiency point, the flow is similar to the choke condition. Besides the absence of shock in the stator domain is a massive benefit to the pressure rise and improvement in the efficiency of the stator domain. There is wake formation on both the rotor and stator blades but is not as significant when compared to the choke operating point. Figure 10 depicts the normalized axial velocity contour at station STE. It is evident from the figure that the flow is completely attached at the peak efficiency point, and at this operating point, the flow angle incident on the rotor blade is nearly constant (figure not shown). But, as the flow approaches the stator domain, we see a considerable change in the flow angle. Due to this substantial change of flow angle, the flow in the suction surface of the stator blades is prone to a region of flow reversal. At peak efficiency point, the LP compressor is prone to stator suction surface separation (Fig. 9) under Inflow-A and Inflow-B, and the key culprit is the increase in absolute flow angle, shown in Fig. 12.

Near stall point: The scenario is entirely different for the near stall operating point. Even for this operating point, the flow angle incident on the rotor blade almost follows

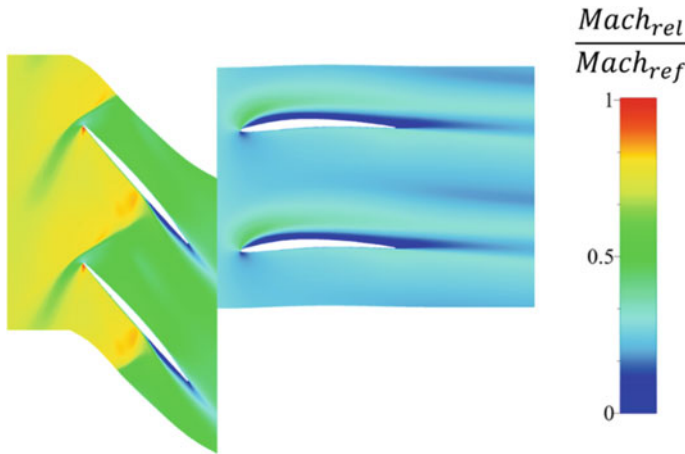


Fig. 9 Blade to blade relative Mach number contour at 95% span depicting the separation region along the suction surface of the stator blades at peak efficiency point for Inflow-B

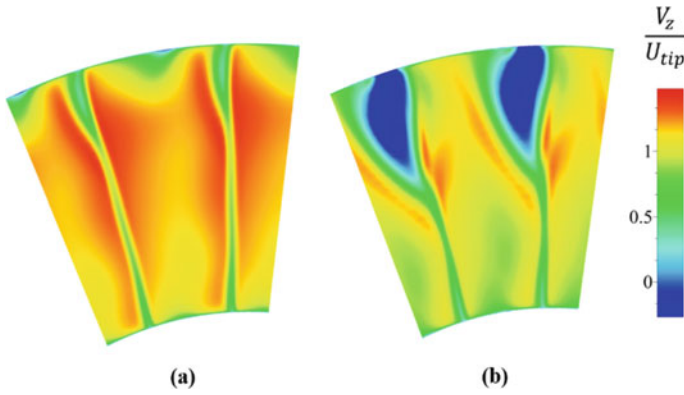


Fig. 10 Normalized axial velocity contour at section STE for **a** peak efficiency point and **b** near stall operating point (comparison made for Inflow-B)

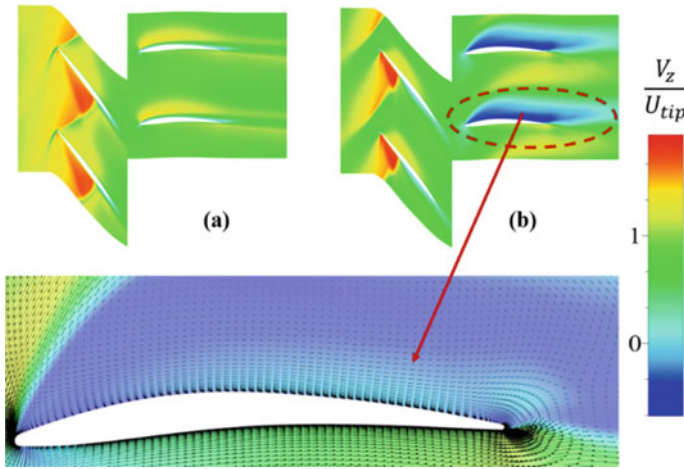


Fig. 11 Normalized axial velocity contour at 95% span for **a** peak efficiency point and **b** near stall point representing the separated velocity vectors along the stator suction surface (the comparison is made for Inflow-C)

a constant trend with a minor deviation observed near the hub (figure not shown). Although, under this uniformity of flow angle, at the exit of the rotor, the flow angle changes considerably (Fig. 12). Since at near stall regime, the streamwise pressure gradient is significant and in addition, due to the diffusion process the flow undergoes, a more pronounced wake formation occurs on both the rotor and stator blades. As observed for Inflow-A, a region of flow reversal starts to develop at 55% span owing to the significant adverse pressure gradient acting in the streamwise direction. This region of flow reversal is followed by flow at a high incidence towards higher span. At high-flow incidence, the stator blades are unable to guide the flow properly, and

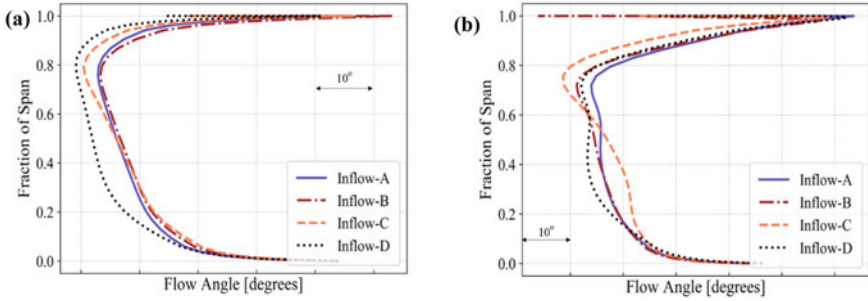


Fig. 12 Absolute flow angle variation at location SLE at **a** peak efficiency point and **b** near stall point

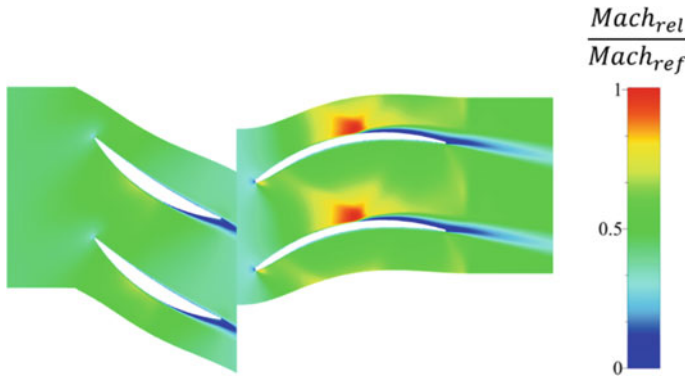


Fig. 13 Blade to blade relative Mach number contour at 5% span depicting the wake formation on the suction surface of both the rotor and stator blades at choke operating point (observed for all inflows)

due to the lack of guidance, the flow eventually separates along the entire stator suction surface region. Figure 10 shows the normalized axial velocity contour at peak efficiency point and the near stall point showing the region of flow reversal at near stall point. The region of flow reversal is significant, and it covers the entire stator tip region. Further, the maximum gain in total pressure is for Inflow-B as depicted in Fig. 15.

3.2.3 Inflow-C

Choke and peak efficiency point: The choke and peak efficiency point is accompanied by the formation of low-momentum region on the aft portion of the rotor suction surface owing to the process of diffusion at 5%. Following that, due to the formation of shock on the stator domain at the choke point, there is a considerable build-up of a

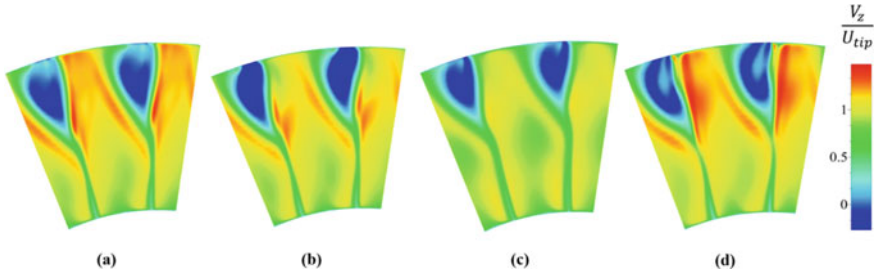


Fig. 14 Normalized axial velocity contour at section STE for **a** Inflow-A, **b** Inflow-B, **c** Inflow-C and **d** Inflow-D representing the secondary flow region at the tip region of the stator. The comparison is made at near stall operating point

low-momentum region. But the presence of shock is absent for the stator domain at peak efficiency point. Moreover, at 50% span for choke regime, there is a separation bubble formation on the suction surface of the rotor blade and extends up to the tip. Further, a low-momentum region develops on the pressure surface of the stator blade. On the other hand, the low-momentum region is absent in the case of peak efficiency point as the flow advances to a higher span.

Near stall point: Same as in the case of choke and peak efficiency point, there is a low-momentum region development on the suction surface of the rotor blade at 5%. This low-momentum region increases in size as the flow progresses towards higher span. Eventually, it leads to the formation of a recirculation region along the rotor blade suction surface, and a fully evident separation bubble is observed on the aft portion of the rotor suction surface at 50% span. Despite having separated flow on the rotor blades, up to 50% span the flow along the stator blades is completely attached. After 50% span, the separation region along the rotor blades starts to dwindle, but at the same time, along the aft portion of the stator blade, an area of separation begins to form around 70% span. The reason for separation is attributed to the considerable streamwise pressure at the near stall point. This flow separation is followed by high flow incidence from 80% span. At the tip, due to the combined contribution of high flow incidence and streamwise pressure gradient, the flow along the stator suction surface is completely separated, as shown in Fig. 11. Moreover, from Fig. 14, it is evident that the region of extension of separated flow is minimum for Inflow-C compared to all other inflows (Fig. 13).

3.2.4 Inflow-D

Choke and peak efficiency point: Under influence of Inflow-D, the flow field is the same as other inflows with the presence of shock reducing the momentum of the flow, and thereby, leading to more pronounced wake formation. The flow field at peak efficiency point is similar to the choke operating point with the absence of shock benefitting the pressure rise across the stator domain.

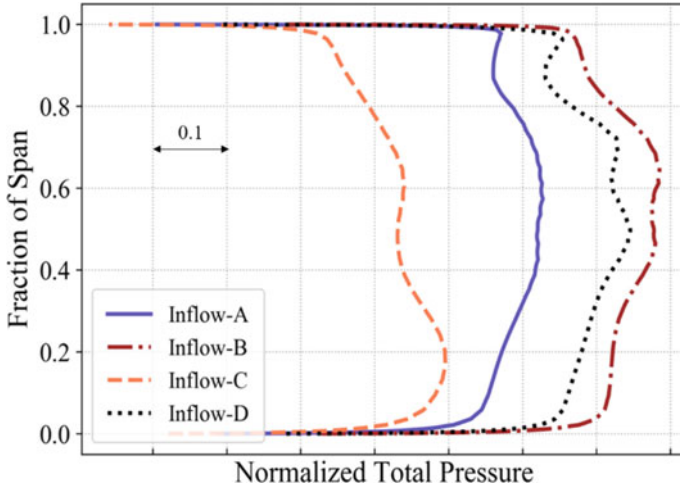


Fig. 15 Mass averaged radial profiles of normalized total pressure taken at location STE at near stall operating point

Near stall point: The near stall point operation of the LP compressor under Inflow-D is similar to other inflows. But as seen in Fig. 14, the separation region starts to develop at 55% span same as in the case of Inflow-A and Inflow-B with the circumferential extent being on the higher side compared to Inflow-A and Inflow-B.

In general, the flow field exhibited by the compressor for Inflow-A, Inflow-B and Inflow-D shows a similar trend. But a difference in flow field is observed for Inflow-C. As noted from the performance map, the presence of distortion reduces the performance of the compressor stage deliberately and in turn, affects the gas-turbine engine as a whole. Besides, if the distortion is present at the tip region of the fan, then the penalty of distortion is encountered by the by-pass duct. The compressor and duct perform significantly better in the tip distortion case compared to hub distortion. The highest performance exhibited by the compressor is for Inflow-B and the worst performance under the influence of Inflow-C.

Thus, to conclude, the presence of uniformity in the flow is beneficial to the core compressor components. In contrast, the presence of distortion in the root flow of the fan is deleterious and Fig. 15, representing the normalized total pressure radial profiles validates the above statements (Fig. 16).

4 Conclusions

The effects of clean and distorted inflows on the flow field of an inter-compressor duct followed by an LP compressor are investigated numerically. Present work summarizes the following conclusions:

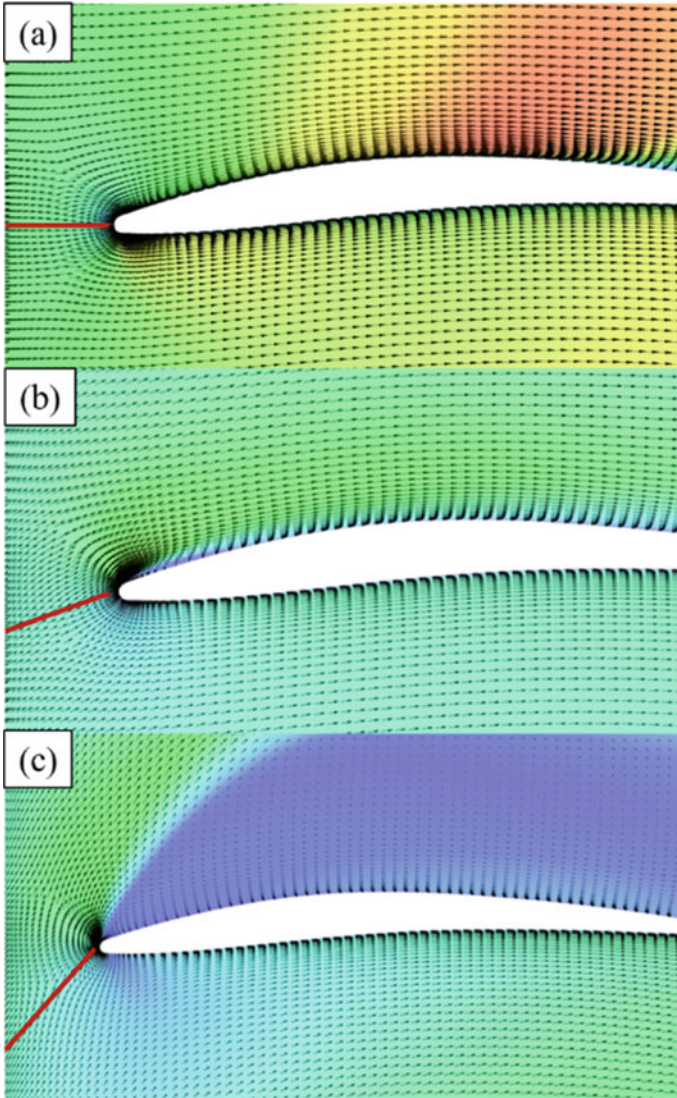


Fig. 16 Mach number contours and velocity vectors at 95% span representing the stagnation streamlines in red colour for **a** choke point, **b** peak efficiency point and **c** near stall operating point

- In the absence of swirl, a pair of streamwise counter-rotating pair of vortices develop on the strut-hub corner region. The pair of vortices migrate radially upwards and thicken the casing boundary layer and further, preventing the boundary layer from separating.

- Under upstream stage influence, the vortices are deflected on the leeward side of the strut on account of swirl. Moreover, the structure of vortices depends on the intensity of wakes emanating from the upstream stage.
- Inflow-C deteriorates the duct performance causing an increase in total pressure drop and a decrease in static pressure recovery.
- Despite the presence of distortion, the duct performs considerably better in the case of Inflow-D compared with Inflow-C, since the penalty of distortion is taken the bypass duct.
- For the LP compressor as well, Inflow-C deleteriously affects the compressor performance in terms of pressure rise and efficiency since the distortion from the duct is convected to the compressor stage.
- The compressor operates tremendously better for Inflow-B. On the other hand, the highest efficiency achieved by the compressor is in for the case of Inflow-A owing to the uniformity in the flow.
- The onset of stall is accompanied by the formation of large flow separation on the suction surface of the stator blade at the tip owing to the combined action of high flow incidence and streamwise adverse pressure gradient for each inflow.
- In general, the presence of distortion on the fan root flow harms the performance of core compressor components compared to distortion present at the tip section of the fan.

Acknowledgements The authors would like to express sincere gratitude to Centre of Propulsion Technology (CoPT) for funding the project.

References

1. Bandyopadhyay P, Ahmed A (1993) Turbulent boundary layers subjected to multiple curvatures and pressure gradients. *J Fluid Mech* 191:137–176
2. Duenas CO, Miller RJ, Hodson HP et al (2007) Effect of length on compressor inter-stage duct performance. In: *Proceedings of ASME turbo expo*, Montreal
3. Gao L, Deng X, Feng X et al (2014) Effect of inlet conditions on compressor intermediate duct. *Proc IMechE Part G J Aerosp Eng* 229(6):1154–1168
4. Hu S, Zhang Y, Zhang X et al (2011) Influences of inlet swirl distributions on an inter-turbine duct: part I—casing swirl variation. In: *Proceedings of ASME turbo expo*, Vancouver
5. Karakasis MK, Naylor EMJ, Miller RJ et al (2010) The effect of an upstream compressor on a non-axisymmetric S-duct. In: *Proceedings of ASME turbo expo*, Glasgow
6. Norris G, Dominy RG (1997) Diffusion rate influences on inter-turbine diffusers. *Proc IMechE Part A J Power Energy* 211(3):235–242
7. Numeca International (2016) FINE/turbo v12.1 user manual. Numeca International, Brussels, Belgium
8. Numeca International (2016) FINE/turbo v12.1 theoretical manual. Numeca International, Brussels, Belgium
9. Sonoda T, Arima T, Oana M (1998) The influence of downstream passage on the flow within an annular S-shaped duct. *ASME J Turbomach* 120(4):714–722
10. Sonoda T, Arima T, Oana M (1999) The effect of inlet boundary layer thickness on the flow within an annular S-shaped duct. *ASME J Turbomach* 121(3):626–634

11. Strazisar AJ, Wood JR, Hathaway MD (1989) Laser anemometer measurements in a transonic axial-flow fan rotor. NASA technical paper 2879
12. Vahdati M, Sayma AI, Freeman C et al (2005) On the use of atmospheric boundary conditions for axial flow compressor stall simulations. *ASME J Turbomach* 127(2):349–351
13. Verma V, Singh G, Pradeep AM (2020) The effect of inlet distortion on low bypass ratio turbofan engines. *Proc IMechE Part G J Aerosp Eng* 234(8):1395–1413
14. Walker AD, Mariah I, Tsakmakidou D et al (2019) The influence of fan root flow on the aerodynamics of a low-pressure compressor transition duct. *ASME J Turbomach* 142(1):1–11

Effects of Radial Distortion on Low-Speed Tandem Stage Axial Compressor



Hitesh T. Chhugani, Amit Kumar, and A. M. Pradeep

Abstract Aero-engine compressor designers have a challenging task of developing compressors that have a higher-pressure ratio and better efficiency with a lower number of stages. Such designs would require blades with high diffusion factor and hence the inherent risk of flow separation. Tandem blade is an interesting concept, which possibly addresses this problem. In tandem blading, the forward blade and the aft blades are arranged in such a manner that a converging nozzle flow path is created between the two blades. The flow accelerates through this nozzle, energizes the suction surface flow, and thereby prevents the early onset of flow separation. This paper presents the steady computational analysis of a tandem rotor stage and baseline stage in low-speed axial flow compressor at design and off-design condition using ANSYS CFX. The study is further extended to analyze the effect of radial distortion on the performance of tandem rotor and the single rotor.

Nomenclature

AA	Aft airfoil
AB	Aft blade
AO	Axial overlap
C_a	Axial velocity
C_{FA}	Chord of the forward airfoil
C_{FB}	Chord of the forward blade
DR	Degree of reaction
DF	Diffusion factor
FA	Forward airfoil
FB	Forward blade

H. T. Chhugani (✉) · A. Kumar · A. M. Pradeep
Indian Institute of Technology Bombay, Mumbai 400076, Maharashtra, India
e-mail: hiteshchhugani@gmail.com

A. M. Pradeep
e-mail: ampradeep@aero.iitb.ac.in

D	Lieblein diffusion factor
PP	Percentage pitch
PS	Pressure surface [Pa]
P_{ST}	Static pressure [Pa]
SS	Suction surface
TLV	Tip leakage vortex
U_{mid}	Tangential speed at rotor mean section
P_0	Total pressure [Pa]
R/H	Span percentage
Q	Q-Criterion
S	Shear strain rate
C_p	Static Pressure rise Coefficient = $\frac{P_{ST} - P_{ST_inlet}}{P_{O_INLET} - P_{ST_INLET}}$

Greek Symbols

α_2	Absolute air angle at the exit of conventional rotor
Θ_{AA}	Aft airfoil Camber
K	Airfoil blade angle relative to axial coordinate
Θ	Camber angle
ρ	Density
ϕ	Flow coefficient = $\frac{Ca}{U_{mid}}$
Θ_{FA}	Forward airfoil Camber
η	Isentropic Efficiency
Θ_{OV}	Overall Camber
Ψ	Stagnation Pressure Loss coefficient = $\frac{P_{O_LE} - P_{O_TE}}{\frac{1}{2} * \rho * U_{mid}^2}$
ω	Total pressure loss coefficient = $\frac{P_{O_LE} - P_{O_TE}}{P_{O_INLET} - P_{ST_INLET}}$

Subscripts

11	Forward airfoil/blade at inlet
12	Forward airfoil/blade at exit
21	Aft airfoil/blade at inlet
22	Aft airfoil/blade at exit

1 Introduction

The compressor is a major part of an aeroengine, which acquire large portion, and it largely affects the performance of an aero engine. Future demands of smaller,

lighter, and more efficient aeroengines can be achieved by evolving compressors design. This can be done by designing a stage that can achieve a higher-pressure rise without affecting the overall efficiency. In the compressor, flow separation restricts the upper limit of pressure rise per stage. Several studies in the past were focused on controlling the boundary layer to achieve a higher total pressure ratio per stage. Such studies include slotted blades, boundary layer suction, and boundary layer blowing and tandem blading. However, very few of those have been implemented by industries in the compressor rotor owing to the nature of the operation and mechanical difficulties involved.

Such studies include slotted blades, boundary layer suction, and boundary layer blowing and tandem blading. However, very few of those have been implemented by industries in the compressor rotor owing to the nature of the operation and mechanical difficulties involved. In recent years, researchers have drawn lot of interest in Tandem blading. Tandem blade is a set of two blades, one is forward blade and second is an aft blade. Figure 1 shows the schematic configuration of Tandem Blade.

There are two important defined parameters, which fix the position of the aft blade with respect to the forward blade. Firstly, axial overlap (AO) determines the axial position of the aft blade, with positive overlap; aft blade will come closer to the forward blade. While the tangential position of the aft blade can be altered by varying the percentage pitch (PP), the axial overlap and the percentage pitch are defined as follows:

$$AO = \frac{\Delta L}{L} \tag{1}$$

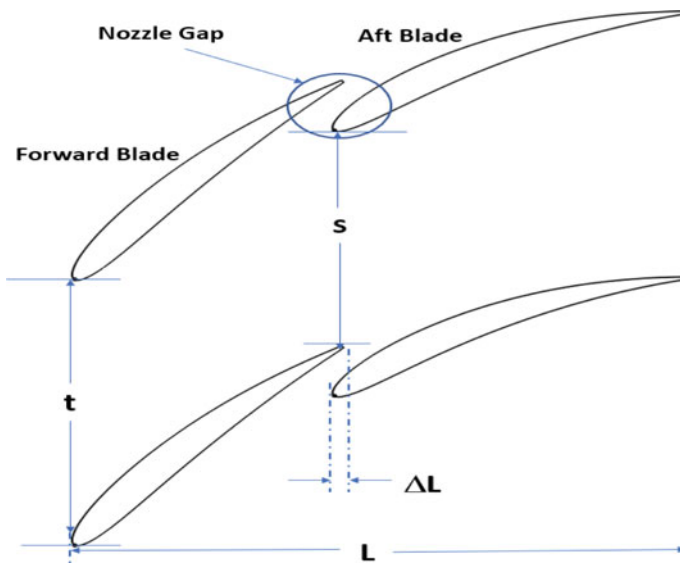


Fig. 1 Schematic of tandem blade

$$PP = \frac{s}{t} \quad (2)$$

This forward blade and aft blade are positioned in such a way that it forms a gap between them, which act as a nozzle for the flow coming from pressure surface of the forward blade. This region between FB and AB is termed as a gap nozzle. As flow passes through this region, it gets accelerated and thus it provides additional momentum to flow that prevents flow separation over the suction surface of the aft blade. Hence, this mechanism allows the compressor designer to design a compressor blade with higher flow turning angle, thus achieving higher-pressure rise per stage is possible by using tandem balding configuration. The exit angle of the forward blade is considered as inlet angle for the aft blade while designing the tandem rotor. FB is supposed to operate as a conventional rotor; however, flow over AB is well controlled by FB in design and off-design condition. Many researchers have conducted their experimental and computational investigation in past also.

Roy and Saha [1] carried out low-speed studies to find the diffusion capability of the tandem cascade (CDA 21–21) and compared it deflection capability with CDA 43 (single airfoil) with CDA 21–21 (tandem). Experimental studies over CDA 43 and CDA 21–21 (single and tandem cascade) showed that CDA 21–21 (tandem cascade) can have higher deflection capability but their operating range is very less. Falla [2] computational study on a tandem airfoil with NACA-65, reported that a tandem configuration with low AO and high PP is suitable for tandem configuration. Various key points were emerged out of the work conducted on 2D-Tandem Airfoils. PP and AO play have a first order effect on the performance of tandem airfoil. Higher PP and lower AO were able to achieve the best performance. Loading distribution between forward and aft blade affect the performance of tandem airfoil. McGlumphy et al. [3, 4] did a computational analysis in a subsonic region of NASA 65 tandem airfoil. Performance analysis was done for different combination, i.e., by changing Axial Overlap and Percentage Pitch. Along with that, the effect of blade loading split between AB and FB on overall performance was studied, for different PP and AO. Based on aerodynamic parameters and the mechanical limitations, the optimum design of Tandem blade was chosen with 85% PP and 0 AO. Hasegawa et al. [5] carried out a test on single stage transonic compressor in which tandem rotor and single blade stator were used along with outlet guide vanes, effectively making stator as the tandem blade. Linnemann [6] conducted a series of test at low speed on blower which has both tandem stator and rotor. To determine optimum configuration, the position of the tandem blade was varied. The conclusion from various test came out as tandem airfoil with 0 AO and 80% PP can give maximum pressure rise and maximum efficiency for both rotor and stator. Brent and Clemmons [7] carried out experiments over two different tandem rotors and single blade rotor. The two tandem rotors used were having different load split of 50–50 and 20–80 on forward and aft blade. In the case of 20–80 load split, more losses were observed in comparison with 50–50 load split. Bammert and Staude [8] carried out experimentation and tested tandem rotor in a 5-stage compressor. Out of 5 stages, middle 3 stages consist of a tandem rotor. Similarly, the low operating range was observed and also was able to achieve

higher loading because of tandem rotors. GE J-79 compressor and an advanced single stage LP compressor built by Honeywell (2005) are some examples of commercial turbomachinery where tandem blades are employed as stators. Weber and Steinert [9] carried out CFD and experimental investigation on a transonic tandem compressor cascade which was designed for high flow turning. The total pressure loss coefficient reported was 0.15.

The compressor is designed with the assumption of clean inlet flow. The inlet flow condition can severely affect the performance of the aircraft compressor. In actual scenario, the flow at engine inlet is generally distorted. The extent of distortion depends on engines application and its size. Engine encounters non-uniformity in the inlet flow during maneuvers, ingestion of foreign objects, and crosswinds. Similar to the tandem case, results of the lower operating range are observed in aero engine with the non-uniform flow at inlet. There are various experimental and computational work which have analyzed flow physics in the conventional compressor under distorted inflow conditions. Lee et al. [10, 11] observes considerable loss in overall performance and stability of the engine together along with that increase Specific Fuel Consumption and drop in engine thrust was observed. Numerical investigation of inlet distortion due to crosswind effects for high bypass ratio turbofan engine was done by Liu et al. [12]. In experimental and computational studies, special screens are used to replicate the different inflow distortion conditions. These screens are mounted upstream of the compressor. In the future's engine concept like BLI engines (2014), the boundary layer developed over fuselage is ingested into the intake of engines. Therefore, from a future perspective, it is important to understand the effect of distorted inlet flow on the overall performance of a compressor with highly loaded tandem blades. This knowledge can be helpful in designing a compressor with tandem blades. Researches carried out were more related to tandem stator and cascade which concluded higher diffusion factor for tandem cases. Kumar and Pradeep [13] study the performance and feasibility of the tandem rotor when used with a single rotor. The better performance was observed in comparison with a conventional rotor at the design point. The present computational study compares the performance of a stage with the conventional rotor and with the tandem rotor under clean and radially distorted inflow condition. The effect of the tandem rotor and conventional rotor on the single stator is also analyzed. The paper also analyzes the effect of the tandem blade on tip leakage flow and how the tip leakage is affected under radially distorted inflow condition. The main goal of this study is to understand the effect of the radial hub and tip distortion on tandem blade rotor stage. The study can be useful in the future to for the optimization of the tandem blade rotor stage. If the tandem blades are used in commercial turbomachinery, we will have a comparatively smaller size engine as it will bring down the number of compressor stages.

2 CFD Validation

The validation of computational results is done with experimental results of baseline stage. Experimental results on baseline stage are referred from Kumar and Pradeep [13]. Table 1 show blade design parameters of the baseline stage. ANSYS CFX is used for steady RANS computational analysis. The domain length of the inlet is 1.5 chord upstream of rotor trailing edge while the domain length of outlet is 2.5 chord downstream of stator trailing edge. The structured mesh is generated using ANSYS Turbogrid through Automatic Topology and Meshing (ATM) method. Mesh generated around the rotor and stator blade is O-Grid while the mesh generated in the passage is H-Grid with the width factor of 0.5. For Near wall, design specification in case of both baseline rotor and stator y^+ method is used. In the case of the rotor, the constant tip gap of 1 mm is maintained. Before validating the results with experimental data, the grid-independent study is performed to determine grid-independent mesh. The parameters used to see grid independency is isentropic efficiency. The solution is called grid-independent when a change in isentropic efficiency is ± 0.5 to 1%.

Figure 2a shows the grid independence study of baseline stage with the help of isentropic efficiency. In the case of baseline rotor stage, grid independency solution is obtained for the number of elements equal to 1.5 million. ANSYS-CFX Pre is used to apply boundary conditions and turbulence model and set the convergence criteria. The turbulence model used for computational analysis is SST $K-\omega$. This model is preferred for analysis, as its results match well with experimental results. Turbulence intensity selected for simulation is 5%. The total pressure of 101325 Pa and total temperature of 300 K are defined as the inlet boundary condition. The mass flow rate is used as an outlet boundary condition. The RPM of the rotor is set to 2700. Convergence criteria is set to be achieved when RMS residual is below 10^{-6} . Isentropic efficiency and mass imbalance are two other monitors to check the convergence of the solution.

Figure 2b shows the comparison of experimental results and computational results of the baseline stage. CFD results show good agreement with the experimental data.

Table 1 a Design parameters of the single rotor (2019) **b** design parameters of the stator of the baseline stage (2019)

a			
Baseline rotor	Tip	Mean	Hub
DF	0.50	0.54	0.47
DR	0.78	0.70	0.50
Camber angle (°)	23.0	35.0	60.0
b			
Baseline stator	Tip	Mean	Hub
DF	0.53	0.48	0.45
Camber angle (°)	50.0	50.0	52.0

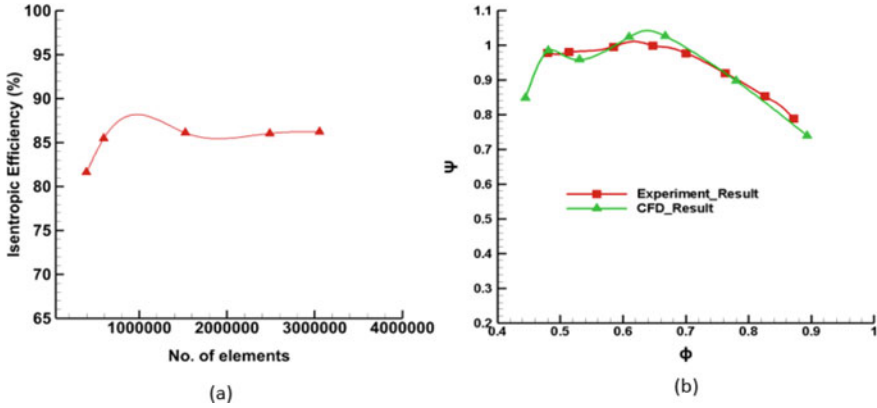


Fig. 2 a Grid independence of baseline stage b experimental validation of CFD result of baseline stage

With CFD validation, further computational analysis of the tandem stage is carried out under different inflow conditions.

3 Design of Tandem Rotor Stage

The combination of tandem rotor and the single stator is referred as a tandem stage in this paper (Table 2), whereas the baseline stage is consisting of a single rotor and single stator (Table 1). In the design of a tandem rotor, a higher-pressure rise is attempted by increasing the flow turning angle. Both the tandem rotor and the single rotor are designed with 2700 RPM. The designed mass flow rate for both the stages, i.e., baseline stage (single rotor and single stator) and tandem stage is 6 kg/s. Based

Table 2 a Design specifications of the tandem rotor (2019) b design parameters of the stator of the baseline stage (2019)

a						
Tandem rotor	Forward blade			Aft blade		
	Tip	Mean	Hub	Tip	Mean	Hub
DF	0.44	0.46	0.44	0.52	0.49	0.31
Camber angle	16.5°	20.6°	30.9°	26.1°	35.3°	42.6°
Stagger	57.5°	46.4°	28.1°	45.1°	26.6°	0.86°

b			
Baseline Stator	Tip	Mean	Hub
DF	0.53	0.48	0.45
Camber Angle	50.0°	50.0°	52.0°

on the past literatures, a higher PP and low AO (5AO and 85PP) is selected for the computational analysis. The blade loading is equally split between the forward and the aft rotor. Owing to the low-speed application, C4 blade profile is used for the designing of rotor and stator in both stages. The chord length of the baseline stage rotor is equal to sum of chord length of AB and FB. A total number of 19 forward rotor blades and 19 aft rotor blades are used in tandem stage design, whereas 19 single rotor blades are used in the baseline stage. In both stages, 21 numbers of single stator blades are used.

ANSYS CFX is used for steady RANS computational analysis. The domain length of inlet is 1.5 chord upstream of rotor trailing edge, while the outlet is positioned at 2.5 chord downstream of stator trailing edge. As ATM failed to generate good quality of mesh in case of the tandem rotor, traditional control point method is used to generate the mesh in the tandem rotor domain. The overall skewness of 18° achieved in tandem rotor domain. H-Grid is formed in Inlet and outlet domain, while O-grid is formed around blade surface. The width factor in case of a stator with the tandem rotor is set to 0.5. For Near wall, design specification in case of both tandem rotor and stator y^+ method is used.

Figure 3 shows the grid independence of the tandem rotor stage. The isentropic efficiency is almost constant after 2.82 million nodes; therefore, 2.82 million nodes are finalized for the computational analysis. The boundary condition, turbulence model, turbulence intensity, and convergence criteria in tandem rotor stage are similar as of baseline stage. In the case of the tandem rotor, constant tip gap of 1 mm is maintained.

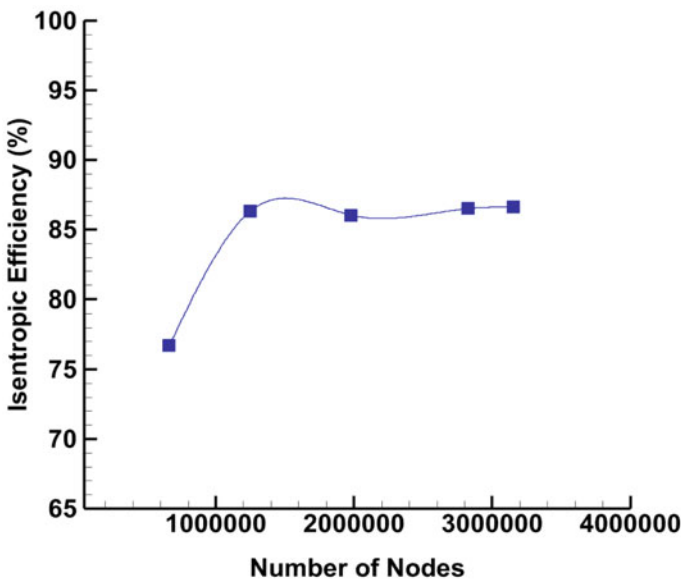


Fig. 3 Grid independence of tandem rotor stage

4 Results and Discussion

The computational results for tandem rotor stage and baseline stage are analyzed at design and off-design condition for different inflow condition. Figure 4 shows the total pressure profile of clean flow, radially hub distorted and radially tip distorted flow at inlet. The radial distortion flow is created using the distortion screen, which is positioned 400 mm upstream of the rotor leading edge. The boundary layer profile of radial hub distortion and radial tip distortion are extracted with the help of the 7-hole probe, which is traversed at 1.5 chord upstream of rotor LE.

4.1 Clean Flow

- (1) Mach contour, embedded with streamline, are plotted at a different percentage of blade span, i.e., 10, 50, and 90% for tandem rotor stage and baseline stage at. Figures 5a and 6a show the Mach contours for tandem rotor stage at design mass flow rate, i.e., $\varphi = 0.64$ and off-design condition, i.e., $\varphi = 0.534$. Similarly, Fig. 5a, b show the Mach contours at the different percent of blade span for baseline stage under design ($\varphi = 0.64$) and off-design condition ($\varphi = 0.534$). In Fig. 6a, at 10% span, small flow reversal is observed near the trailing edge of the aft blade at design mass flow rate.

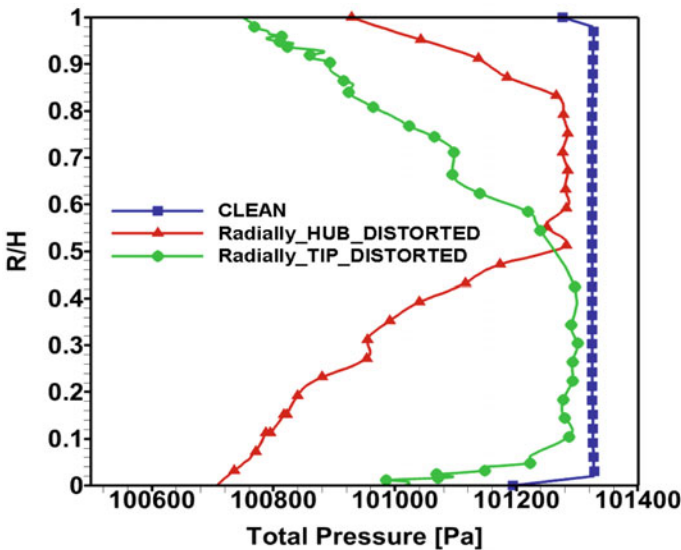


Fig. 4 Total pressure profile at inlet

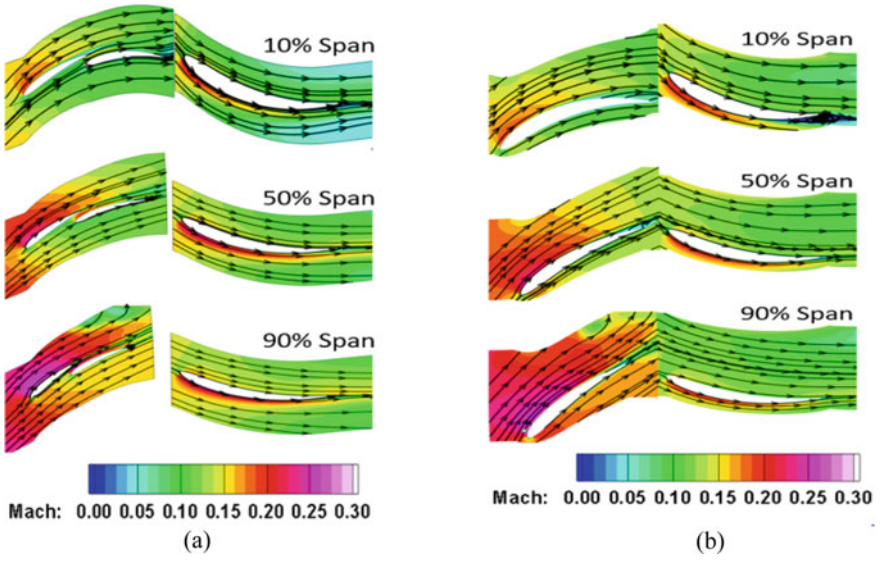


Fig. 5 a Mach contour of tandem rotor stage at $\phi = 0.64$ under clean inlet flow condition b Mach contour of baseline stage at $\phi = 0.64$ under clean inlet flow condition

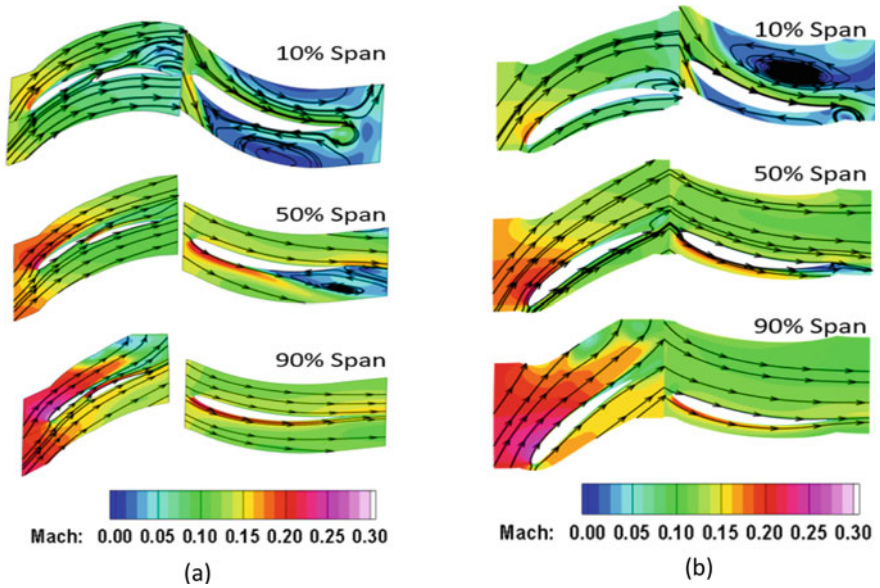


Fig. 6 a Mach contour of tandem rotor stage at $\phi = 0.534$ under clean inlet flow condition b Mach contour of baseline stage at $\phi = 0.534$ under clean inlet flow condition

At higher span, as the effectiveness of the tandem blading increases, flow separation gets attenuated and both tandem rotor blades operate more efficiently (50 and 90% span in Fig. 5a). The Mach number increases from hub to tip region in both baseline and Tandem stage. At 10% span of tandem stage, flow separation region over aft blade SS enlarges further (Fig. 5b). In the comparison of the tandem rotor, baseline rotor is free from flow reversal under design point; however, lower blade Sect. (10 and 50% span in Fig. 6b) shows a significant deviation in streamlines under off-design condition. The stator of the tandem stage is designed with higher flow turning angle, lower energy with higher incidence lead to huge flow reversal over stator blade suction surface at lower span (Fig. 6a). Similar nature of flow is also visible over the stator of the baseline stage, where 90% of the blade portion is covered with the reverse flow (Fig. 6b).

Losses occur in the tip region accounts for the one-third of overall losses in turbomachinery. Therefore, it is imperative to analyze the new design for tip leakage losses. The tip leakage behavior is compared under the design and the off-design condition. When the tip leakage flow meet with the mainstream flow in a passage between the rotor blades, it rolls up into Tip leakage vortex (TLV) near the suction side of the blade. TLV is presented with the help of Q-Criterion, which represents the local balance between the magnitude of vorticity (Ω) and shear strain rate (S) in Fig. 7a, b. In case of a tandem rotor (Fig. 7a), two strong TLV are observed one from FB and another from AB. The trajectory of TLV depends upon the axial momentum of the mainstream flow and tangential momentum of Tip leakage flow. In case of the tandem blade, the loading is divided among the FB and AB; therefore, the strength of each TLV is weaker than TLV from baseline rotor blade. Strength of the TLV of the forward blade is significantly higher than TLV of the aft blade. Further, The TLV from AB interacts with the flow coming from the nozzle gap. Tip leakage vortex of the aft blade is appeared to be more aligned axially after the interaction with

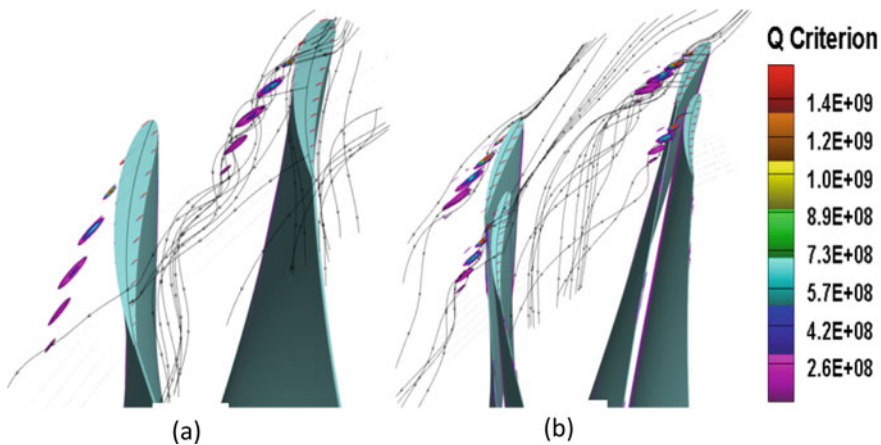


Fig. 7 Q-Criterion plot for **a** baseline rotor **b** tandem rotor at $\varphi = 0.64$ under clean inlet flow condition

gap-nozzle flow. Under design condition, the streamlines from FB-TLV are directed toward the LE of adjacent AB. While in case of baseline rotor blade, it is directed toward TE of the adjacent blade. As the PP of the tandem blade is higher, i.e., 85%, therefore, wake from FB interacts with the AB-TLV and decelerate the AB-TLV in that region.

To further signify the blockage created due to TLV, Mach number contours are drawn at 95 and 98% blade span and shown in Fig. 8a, b. Blockage at 98% span is substantially higher than the blockage at 95% span, as strength of TLV is higher near the tip. In case of the tandem rotor, owing to stronger tip leakage vortex, significantly higher flow blockage is observed near 98% span. FB-TLV and AB-TLV merges downstream and forms a large flow blockage in this region. The blockage region in the single rotor is lower than the tandem rotor blockage. However, other than TLV, a scrapping vortex is visible near the trailing edge of the single blade; however, the strength of the scrapping vortex is considerably lower than TLV. Unlike the tandem rotor, TLV and scrapping vortex moves separately without any evidence of immediate mixing.

Under the off-design condition, Q-Criterion is plotted near tip region at near stall condition for baseline and tandem rotor in Fig. 9a, b, respectively. At near stall condition, the tip leakage vortex enlarges in comparison with TLV at the design condition. Near the stall condition, the momentum of mainstream flow is lower. Therefore, the tangential momentum dominates over the axial momentum of the flow. For the baseline rotor, TLV is directed toward the mid-chord of the baseline rotor blade. On the contrary, TLV was directed toward trailing edge under design condition. Similarly, in case of a tandem rotor blade, FB-TLV is affecting the TE of the FB of the adjacent tandem blade near stall condition. The AB-TLV makes a higher angle with the axial flow direction. The strength of AB-TLV decreases due to reduced tip loading near the stall point.

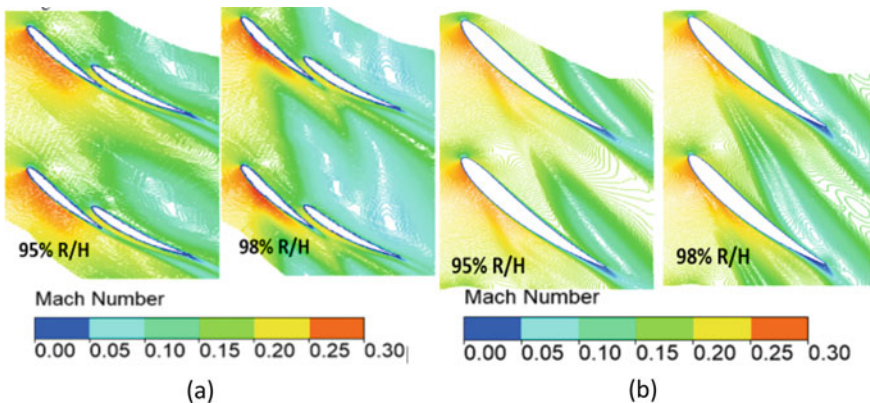


Fig. 8 Mach contour at 95 and 98% span of **a** tandem rotor blade span **b** baseline rotor blade at $\varphi = 0.64$

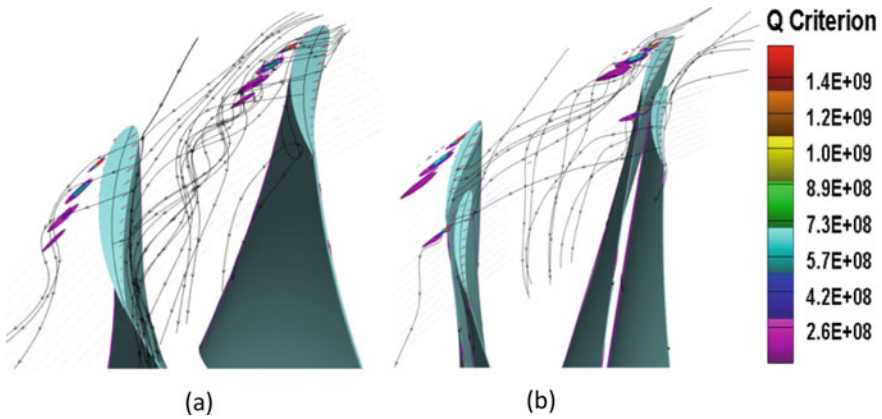


Fig. 9 Q-Criterion plot for **a** baseline rotor **b** tandem rotor at $\varphi = 0.534$ under clean inlet flow condition

Figure 10a, b show the Mach contour plot at 98 and 95% of baseline and tandem rotor blade span, respectively, at near stall condition. For both rotors, the blockage region increases significantly near the stall point. Further, for the baseline rotor, the trajectory of TLV changes and it is directed toward the mid-chord section of the blade, which is different from what was observed under design point. The flow blockage due to scrapping vortex is increased near stall condition. Near stall condition, the scrapping vortex is observed at lower chord length in comparison with what is observed at the design condition. Due to higher tangential momentum of scrapping vortex, TLV and scrapping vortex interacts and forms a bigger blockage region.

Similarly, in case of a tandem rotor blade, the flow blockage due to TLV increases at near stall condition (Fig. 10a) in comparison with design condition. Even at 95% of blade span, significant blockage region is observed. At near stall condition, a small

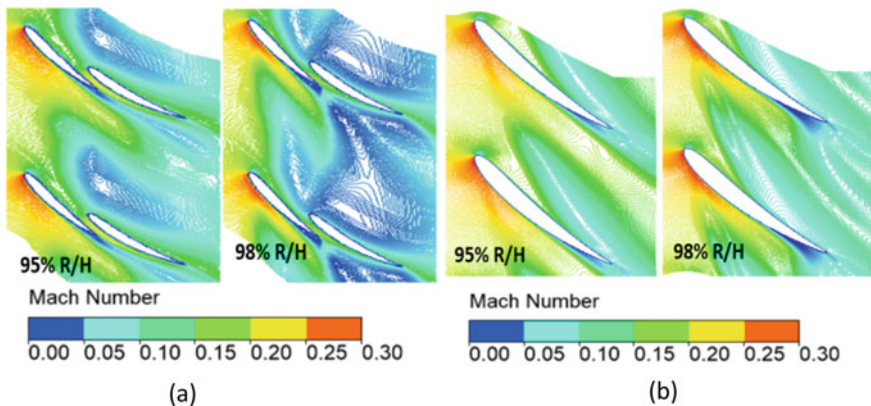


Fig. 10 Mach contour at 95 and 98% of **a** tandem rotor **b** baseline rotor blade span at $\varphi = 0.534$

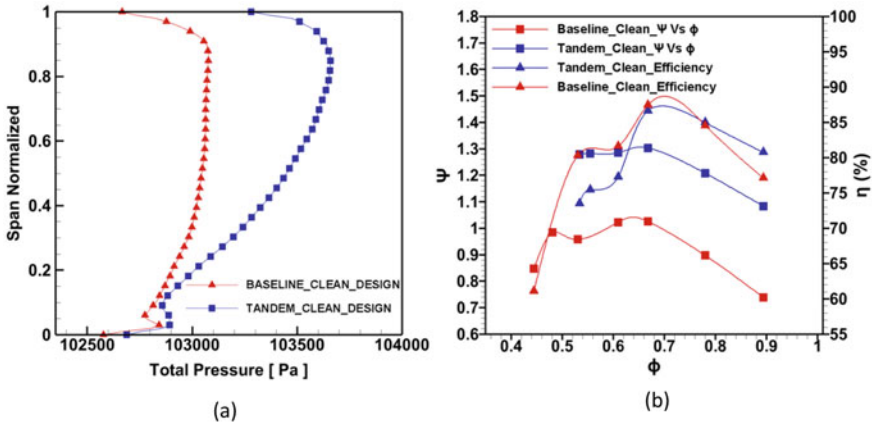


Fig. 11 **a** Total pressure across the blade span at $\phi = 0.64$ **b** isentropic efficiency and total pressure rise coefficient versus flow coefficient (ϕ) under clean inlet flow condition

amount of flow blockage is also observed near trailing edge of FB, which is due to FB wake. At 98% span, blockage region further enlarges. Other than FB-TLV and AB-TLV, wake emanating from FB and AB also contributes to the blockage region. All vortices combine and make a larger flow blockage region near tip in comparison with baseline rotor.

Figure 11a shows the spanwise profile of total pressure at the exit of a stator for the tandem rotor stage and baseline stage under design condition. It is observed that throughout the blade span pressure rise is higher in case of tandem rotor stage. Design of tandem rotor is such that the pressure rise is higher near tip compare to the hub region.

Figure 11b shows the comparison of isentropic efficiency for tandem rotor stage and baseline stage. At a higher mass flow rate, the adiabatic efficiency of the tandem stage is marginally higher than the baseline stage. However, at the lower mass flow rate, a significant drop in adiabatic efficiency of the tandem rotor is observed. The large drop in efficiency for the tandem stage is largely attributed to huge flow separation over the stator suction surface. Other than this, losses associated with TLV are significantly increased near the stall point, which results in a further drop in adiabatic efficiency. Figure 19 compares the performance map of the baseline stage and a tandem stage. At the design mass flow rate, the tandem stage demonstrates an increment of around 26.58% in total pressure than the baseline stage. The drop in a stall range is observed for the tandem rotor stage. The tandem rotor stage has a stall margin of 20%, which is 13% lower than the stall margin of the baseline stage.

4.2 Radial Hub Distortion

The performance of the tandem stage and the single stage under radial hub distortion is compared in this section of the paper. Mach contour is plotted at 10, 50, and 90% of blade span for baseline and tandem rotor stage at design condition, i.e., $\varphi = 0.64$. At 10% of blade span, the flow coming from nozzle gap detached from around mid-chord of the SS of AB. This is mainly because of distorted flow near the hub region and lower effectiveness of the nozzle gap. The flow looks like what was observed under clean flow inlet condition at near stall condition. Due to cumulative effect of higher flow turning angle, higher incidence, a low hub to tip ratio, and considerable boundary layer growth at lower span, huge flow separation is observed over stator suction surface even at design mass flow rate.

In the case of the baseline rotor (Fig. 12b), flow shows a significant deviation of around 75% of the blade chord. Like the previous case of the tandem stage, 90% stator suction surface is covered with the reverse flow. However, the vortex core is shifted toward the trailing edge of the stator in the baseline stage. At higher span, tandem stage exhibits the improved performance. Improved performance at higher span is mainly attributed to a reduction in inlet distortion level, increase in nozzle gap effectiveness, and lower camber angle of the blade. At 50% span, small flow separation is visible at the trailing edge of the stator suction surface of the tandem stage (Fig. 12a). On the contrary, at higher span, flow adhere to the blade profile in the case of the baseline stage.

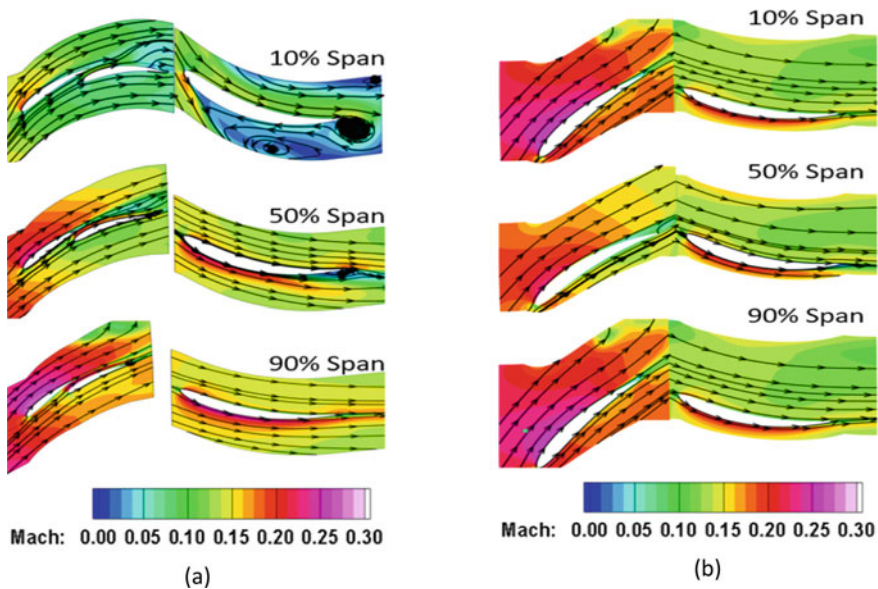


Fig. 12 Mach contour of **a** tandem rotor stage **b** baseline rotor stage at $\varphi = 0.64$ under radial hub distorted inlet flow condition

Figure 13a, b shows the Q-Criterion plot near tip region of baseline rotor and tandem rotor, respectively, at design condition, i.e., at $\varphi = 0.64$. In the case of hub distortion, the mass flow rate near the tip region is higher in comparison with clean inlet flow condition. The AB seems so more loaded near the tip region under hub distortion case. Therefore, the intensity of AB-TLV is slightly higher in hub distortion case. Interestingly, FB in the tandem rotor and baseline rotor appears to be slightly less loaded in hub distortion case.

Thus, TLV from FB in the tandem rotor and baseline rotor is slightly weaker in hub distortion case. Due to the higher mass flow rate near the tip region, TLV is slightly more oriented in the axial direction in comparison with what is seen in clean flow. AB-TLV is also more directed in a streamwise direction in comparison with what is observed in clean flow. The blockage region due to TLV is further signified with the help of Mach number contours at 95 and 98% span is shown in Fig. 14a, b. Due to higher mass flow toward the tip region, the flow blockage is observed somewhat lower in case of hub distortion case in comparison with clean inlet flow condition.

Figure 15a shows the total pressure along the blade span of baseline stage and tandem rotor stage at $\varphi = 0.64$. The total pressure rise for the tandem stage is highly distorted. Interestingly, at blade section lower than the mid-span, the baseline stage demonstrates marginally higher total pressure rise than the tandem rotor. Thereafter, the tandem stage has a significantly higher total pressure rise than the baseline stage.

Figure 15b shows the comparison of isentropic efficiency for tandem rotor stage and baseline stage. At the design point, the baseline stage has around 4% higher isentropic than the tandem rotor stage. Figure 15b shows the performance map of the baseline stage and a tandem stage. At the design mass flow rate, the tandem stage demonstrates an increment of around 31.89% in total pressure than the baseline stage. In comparison with a clean flow drop of around 6.5% is observed in the tandem rotor stage under radial hub distortion condition. Both stages experience a drop in stall

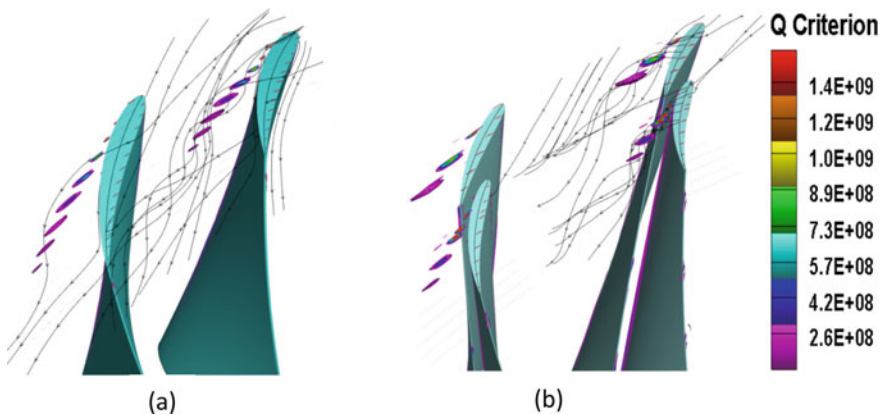


Fig. 13 Q-Criterion plot for **a** baseline rotor **b** tandem rotor at $\varphi = 0.64$ under radial hub distorted inlet flow condition

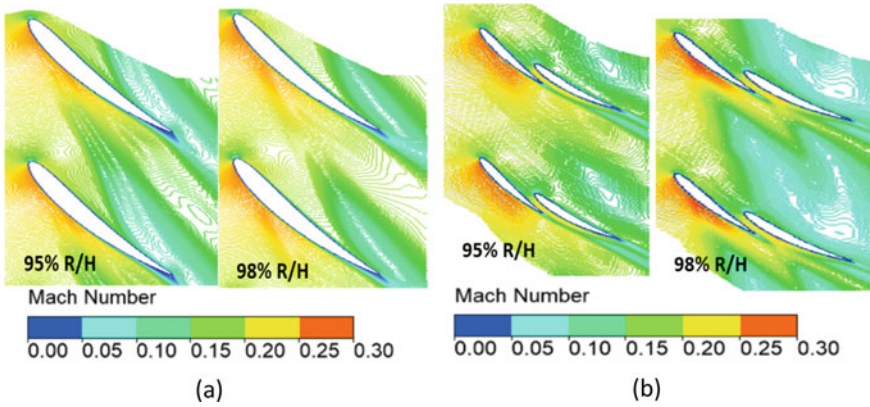


Fig. 14 Mach contour at 98 and 95% of blade span for **a** baseline rotor **b** tandem rotor at $\varphi = 0.64$ under radial hub distorted inlet flow condition

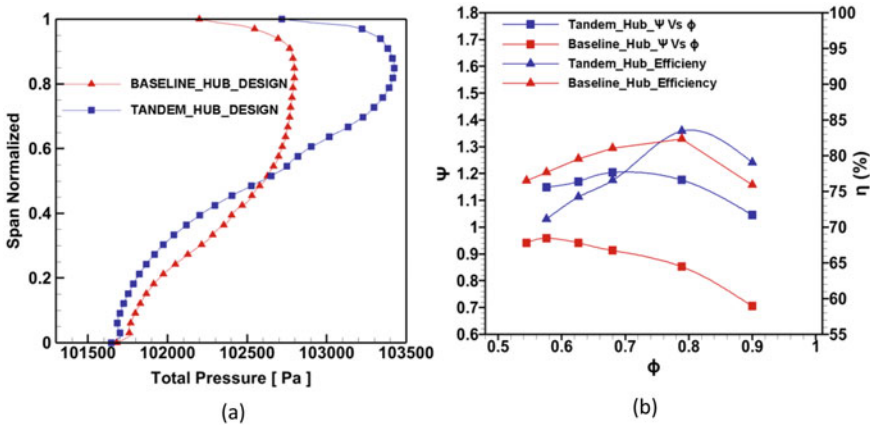


Fig. 15 **a** Spanwise total pressure profile at stator exit of baseline and tandem rotor stage at $\varphi = 0.64$ under radial hub distorted inlet flow condition **b** isentropic efficiency and total pressure rise coefficient versus flow coefficient (φ) under radial hub distortion inlet flow condition

margin under hub distorted flow. In comparison with the baseline stage, the tandem stage has 4% lower stall margin under hub distorted flow.

4.3 Radial Tip Distortion

The tip distorted profile used at the inlet of the computational domain is shown in Fig. 5. Mach contour is plotted at 10, 50, and 90% of blade span for baseline and tandem rotor stage at design condition in Fig. 16a, b. In case of a tip distortion, Mach

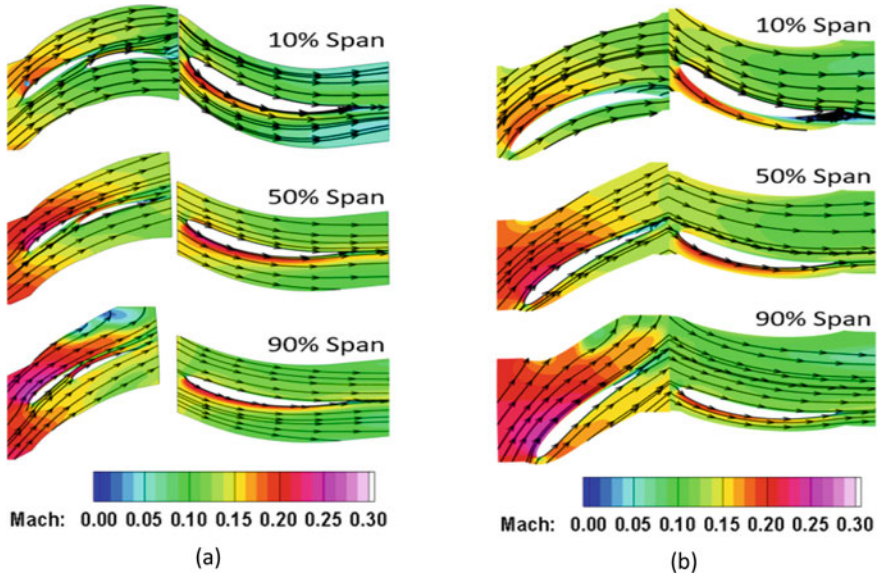


Fig. 16 Mach contour of **a** tandem stage **b** baseline stage at $\varphi = 0.64$ under radial tip distortion inlet flow condition

number at 10% of blade span is slightly higher than what is observed in case of clean flow. In Tandem rotor (Fig. 16a), low Mach number region is observed at 90% of span, mainly due to the reduced axial velocity near the tip region. In both baseline and Tandem rotor stage, the flow streamlines at 10, 50, and 90% of blade span look similar to what is observed in case of clean of flow.

Like previous cases, TLV under tip distortion is illustrated using Q-Criterion plot and streamlines in Fig. 17. As the flow is distorted near the tip region, a higher incidence results in a higher tip loading and consequently a stronger the tip leakage vortex. Due to the lower axial momentum of flow near the tip region, TLV has higher tangential momentum and TLV makes a higher angle to the axial flow direction. The flow physics near the tip region in both baseline and tandem rotor appear similar to what was observed under clean inlet flow condition near stall point. The streamlines show that in case of the baseline rotor, the TLV is directed toward the mid-chord of the adjacent blade. In case of the tandem rotor, the TLV from FB is directed toward the LE of AB of an adjacent tandem rotor blade. Similarly, as it is observed before, AB-TLV is weaker in comparison with the FB-TLV. In comparison with the baseline rotor, both TLV combines and results in a higher loss near the tip region.

Figure 18 show the Mach contour near the tip region at the design condition. At 98% of baseline rotor blade span, the TLV and scrapping vortex interact and create a large flow blockage region. This effect reduces at 95% of span. For the tandem rotor, a large area of flow blockage observed under tip distortion, even at design mass flow rate. There is an interaction of FB-TLV, AB-TLV, and wake from the FB lead to large flow blockage in comparison with what is observed in the case of baseline

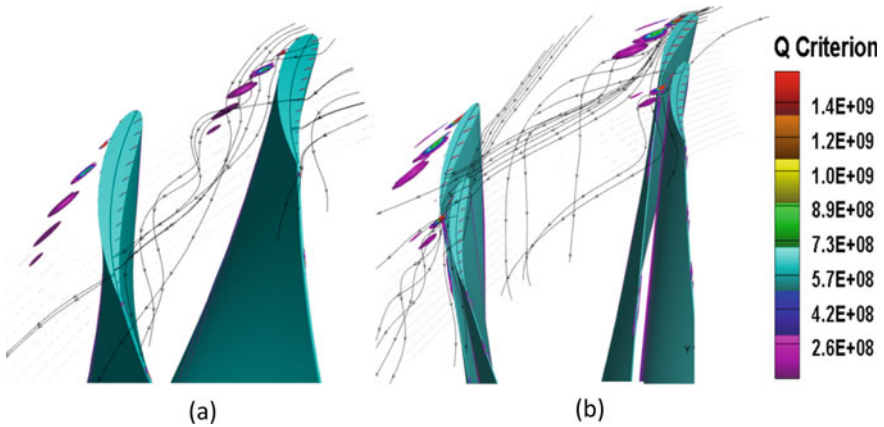


Fig. 17 Q-Criterion plot for **a** baseline rotor **b** tandem rotor at $\varphi = 0.64$ under radial tip distortion inlet flow condition

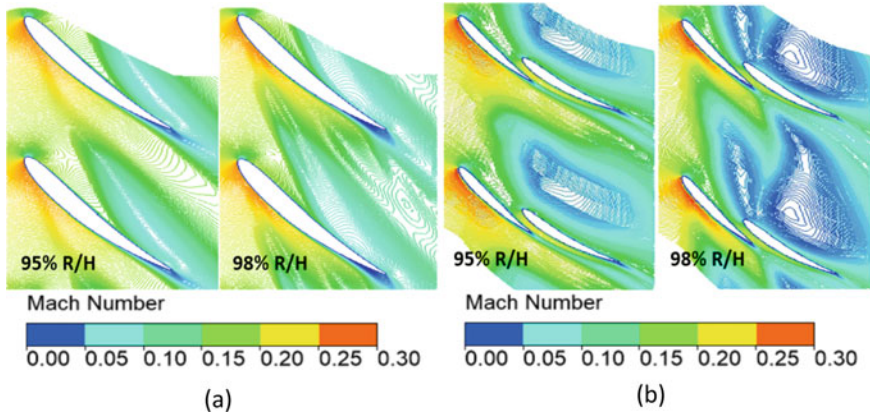


Fig. 18 Mach contour at 98 and 95% of **a** baseline rotor **b** tandem rotor at $\varphi = 0.64$ under radial tip distortion inlet flow condition

rotor. This large area of flow blockage near the tip region leads to the sudden stall of the tandem rotor stage. A significant blockage can be even seen at 95% of the blade span.

Due to the lower axial momentum of flow near the tip region, TLV has higher tangential momentum and TLV makes a higher angle to the axial flow direction. The flow physics near the tip region in both baseline and tandem rotor appear like what was observed under clean inlet flow condition near stall point. The streamlines show that in case of the baseline rotor, the TLV is directed toward the mid-chord of the adjacent blade. In case of the tandem rotor, the TLV from FB is directed toward the LE of AB of an adjacent tandem rotor blade. Similarly, as it is observed before,

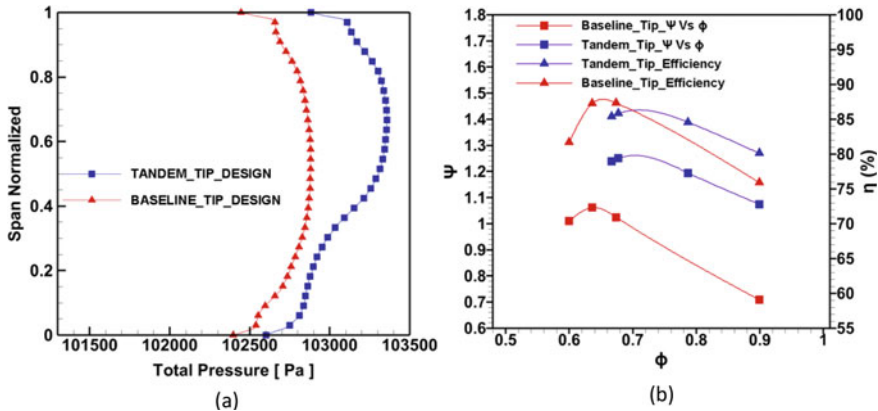


Fig. 19 a Spanwise total pressure profile at stator TE of tandem rotor stage and baseline stage at $\phi = 0.64$ under radial tip distortion inlet flow condition b isentropic efficiency and total pressure rise coefficient (Ψ) versus flow coefficient (ϕ) under radial tip distortion inlet flow condition

AB-TLV is weaker in comparison with the FB-TLV. In comparison with the baseline rotor, both TLV combines and results in a higher loss near the tip region.

Figure 19a shows the total pressure profile at the exit of stator near the design point. Tandem rotor demonstrates higher-pressure rise throughout the span the baseline stage. Effect of the distorted tip region can be seen in the total pressure profile. After 75% of the blade span, the total pressure drops gradually toward the tip region. The difference in total pressure seems to be more significant at higher span.

Fig. 19b shows the comparison of isentropic efficiency for tandem rotor stage and baseline stage. At the design point, the baseline stage seems to have around 1.5% higher isentropic efficiency than tandem rotor stage. Figure 19b shows the performance map of the baseline stage and a tandem stage. At design condition, tandem rotor yields 22.12% higher-pressure rise in comparison with the baseline case under tip distortion. Tandem stage stall even before it reaches its design mass flow rate. The early stall under the tip distortion is attributed to higher incidence near the tip region and highly loaded tip design. A relax tip design could improve the stall margin of the tandem stage. The baseline stage has 10% higher stall margin in comparison of the tandem stage.

4.4 Tandem Rotor Stage

Figure 20a shows the spanwise variation of total pressure for the tandem stage under different inflow condition. The total pressure rise under clean flow is higher than the other cases. Pressure rise appears to be more affected under the hub distortion, where the highly distorted profile can be seen realized. The drop in total pressure can be noticed after 75% span under the tip distorted case.

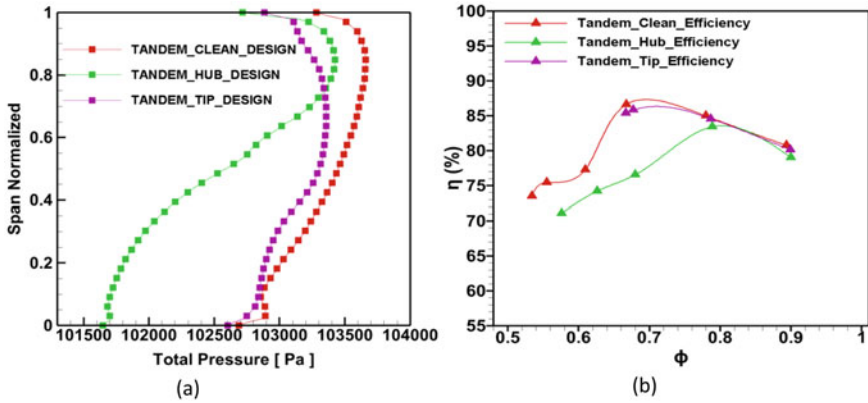
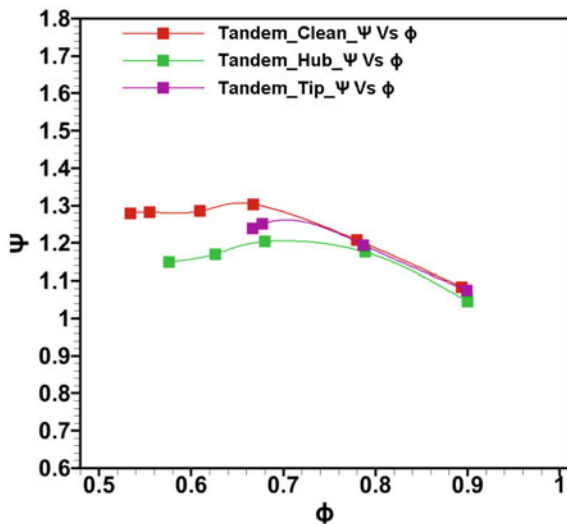


Fig. 20 a Spanwise total pressure profile at stator TE of tandem rotor stage at $\phi = 0.64$ b isentropic efficiency for tandem rotor stage

Figure 20b compares the isentropic efficiency of Tandem rotor stage under clean, radially hub distorted and radially tip distorted inflow conditions. After $\phi = 0.67$, efficiency drops significantly under the hub distortion case. Around 10% of the drop in isentropic efficiency is observed in the case of radially hub distortion in comparison with clean inlet flow condition at $\phi = 0.64$.

Figure 21 shows the performance map of Tandem rotor stage under clean flow, radially hub distorted flow and radially tip distorted flow. Tandem stage experiences a drop in total pressure and stall margin under radial distortion. In the case of radially hub distortion, maximum losses are observed at a different mass flow rate. At the

Fig. 21 Total pressure rise coefficient versus flow coefficient (ϕ) for tandem rotor



design mass flow rate, the tandem stage exhibits a drop of 6.55% in total pressure rise under radial hub distortion. In the case of radially tip distorted inflow, the stall range is largely affected. Tandem stage sees a drop off around 3% in the stall margin under hub distorted inflow. In the case of radial tip distortion, a sudden stall is observed.

5 Conclusion

The paper analyzes the effect of radial hub distorted and radial tip distorted inflow condition on the performance of tandem rotor stage in comparison with clean inlet flow condition. The paper also compares the performance of tandem rotor stage with baseline stage for different inlet flow condition. Various key findings from the present study are

1. At design point, tandem stage achieved higher total pressure rise and higher efficiency in comparison with the baseline stage at different inflow conditions. In comparison with single blade, higher diffusion factor can be achieved with the help of tandem blade.
2. In comparison with tandem stage, better stall margin is observed for the baseline stage. Performance of both stages drop substantially under radial distorted inflow.
3. Due to the low hub to tip design and higher flow turning, tandem stage experiences a substantial drop in a total pressure rise and isentropic efficiency under hub distorted inflow. In case of hub distorted inflow, migration of higher mass flow toward the tip region results in drop of the stall margin in comparison with the clean flow.
4. The stall margin of Tandem rotor stage under a clean flow inlet condition is 20%. In comparison with baseline stage drop of around 13% is observed in the stall margin of the Tandem rotor stage under clean inlet flow condition. Tandem rotor stage stall margin drops by 3% in case of radial hub distorted inflow condition in comparison with clean inlet flow condition. Both stages experience a drop in stall margin under tip distorted inflow. However, the effect of tip distorted region is more pronounced on the tandem rotor, where stall margin drops to 2% under tip distortion. A sudden stall is observed under tip distortion, which is attributed to the highly loaded tip design of the tandem rotor.
5. In case of the tandem rotor, strong tip leakage vortices from both forward and aft blade create a large blockage region. Further, wakes emanating from the forward and the aft blade mix with the tip leakage flow and result in a large flow blockage area under radial tip distortion, which leads to sudden stall.
6. The tandem blade needs to be designed with lower blade loading near the tip region. The strength of TLV can be further reduced by reducing the tip gap size. This will improve the performance of tandem blade near tip region, which will further help in improvising the stall margin.

References

1. Saha UK, Roy B (1997) Experimental investigation on tandem compressor cascade performance at low speeds. In: *Experimental thermal and fluid science*. Elsevier Inc
2. Falla G A C (2004) Numerical investigation of the flow in tandem compressor cascades. Diploma thesis, Universidad Nacional de Colombia, written at Institute of Thermal Powerplants, Vienna University of Technology
3. McGlumphy J, Ng W, Wellborn S, Kempf S (2007) Numerical investigation of tandem airfoils for subsonic axial-flow compressor blades. In: *ASME Paper IMECE2007-43929*, accepted for *ASME J Turbomach*
4. McGlumphy J, Ng W, Wellborn S, Kempf S (2008) 3-D numerical investigation of tandem airfoils for a core compressor rotor. In: *Proceedings of ASME turbo expo*, Berlin, Germany, 9–13 June 2008
5. Hasegawa H, Matsuoka A, Suga S (2003) Development of highly loaded fan with tandem cascade. In: *AIAA paper 2003-1065*
6. Linnemann H (1964) *UntersuchungeneineinstufigenAxialgelblasesmitTandemgittern*, Konstruktion, Heft 4, S 128
7. Brent JA, Clemmons DR (1974) Single-stage experimental evaluation of tandem airfoil rotor and stator blading for compressors. *NASA CR-134713*
8. Bammert K, Staude R (1979) Optimization for rotor blades of tandem design for axial flow compressors. In: *ASME paper 79-GT-125*
9. Weber A, Steinert W (1997) Design, optimization, and analysis of a high-turning transonic tandem compressor cascade. In: *ASME 1997 international gas turbine and aeroengine congress and exhibition*. American Society of Mechanical Engineers
10. Lee K-J, Lee B-H, Kang S-H, Jung J-H, Yang S-S, Lee D-S, Kwak J-S (2007) Development of block type inlet distortion simulating device for gas turbine engine inlet distortion test. *Int J Aeronaut Space Sci* 8:121125. <https://doi.org/10.5139/IJASS.2007.8.2.121>
11. Lee K, Lee B, Kang S, Yang S, Lee D (2010) Inlet distortion test with gas turbine engine in the altitude engine test facility. In: *AIAA paper*, 4337. <https://doi.org/10.2514/6.2010-4337>
12. Liu K, Sun Y, Zhong Y, Zhang H, Zhang K, Yang H (2014) Numerical investigation on engine inlet distortion under crosswind for a commercial transport aircraft. In: *29th congress of the International Council of the Aeronautical Sciences*, St. Petersburg, Russia
13. Kumar A, Pradeep AM (2019) Design and off-design behaviour of a tandem rotor stage. In: *Proceedings of IMechE (accepted for publication)*, Part G J Aerosp Eng

Design and Analysis of Outlet Air Collector Duct for Axial Compressor Test Rig



Kirubakaran Purushothaman, N. R. Naveen Kumar, P. K. A. Geetha, C. Kishore Kumar, and Ajay Pratap

Abstract Compressor test rigs are commonly used for evaluating the performance of axial and centrifugal compressors at different operating conditions. Axial flow compressors are tested in rigs by driving the test compressor and throttling the exhaust flow, thus creating a higher back pressure or loading to the compressor. Collector box is an important unit which collects the exhaust air from compressor outlet and directs the flow to throttling valves present at downstream location. It plays a major role in compressor testing by providing intended aerodynamic loading at the exit of compressor. This paper discusses in detail about the design of collector box for a given compressor configuration and the influence of various geometrical parameters on compressor loading. A baseline collector box configuration was studied and compared with other similar configurations. Static pressure distortion and total pressure loss coefficient were considered as major design parameters. 3D RANS analysis was carried out to estimate the performance of collector box. Further, the effect of collector box length, outlet configuration, and outlet duct area on collector box performance is studied. Greitzer 'B' parameter is evaluated for all cases to estimate the dynamic instability effects of flow inside the ducting system. Finally, a new configuration with variable outlet duct volume was designed which gave better static pressure uniformity at the compressor exit.

Keywords Collector box · Axial flow compressor · Compressor testing · Static pressure distortion · Greitzer 'B' parameter

K. Purushothaman (✉) · N. R. Naveen Kumar · P. K. A. Geetha · C. Kishore Kumar · A. Pratap
DRDO-Gas Turbine Research Establishment, Bengaluru, India

e-mail: kirubakaran.gtre@gov.in

C. Kishore Kumar

e-mail: kk.gtre@gov.in

A. Pratap

e-mail: ajaypratap.gtre@gov.in

Nomenclature

m	Mass flow rate
P_o	Total pressure
P	Static pressure
λ	Total pressure loss coefficient
SPD	Static pressure distortion
B	Grietzler 'B' parameter
ω	Helmholtz frequency
L	Compressor duct length
D	Collector box outer annulus diameter
A	Compressor duct cross section area
V	Plenum volume
CB	Collector box
S_o	Total outlet area of CB
S	Area of individual CB outlet

Subscripts

in	Inlet plane of collector box
out	Outlet plane of collector box
r	Reference plane (located 40mm from inlet)
r_{\min}	Minimum point in reference plane

1 Introduction

Aerodynamic performance of a gas turbine compressor is evaluated in a compressor test rig facility. Major subsystems of test rig include (i) inlet air flow system, (ii) outlet air flow system, (iii) power driving system, and (iv) lubrication system. The compressor test rig layout shown in Fig. 1. Collector box is an important component of outlet air flow system and is placed at the exit of the compressor. Primary function of collector box is to pass the air from test compressor to outlet ducting system. The main function of collector box is to achieve high-static pressure uniformity around the annulus at exit of compressor and let compressor exit flow to pass uniformly with minimum pressure loss whilst changing the direction of flow from axial to radial direction. Test compressor should be loaded with uniform exit back pressure to evaluate the performance. Non-uniformity of exit back pressure will lead to imbalance in compressor loading. Hence, it is imperative to have an efficient collector box with appropriate size and shape to provide maximum flow uncertainty for proper and effective testing of compressor in test rig.

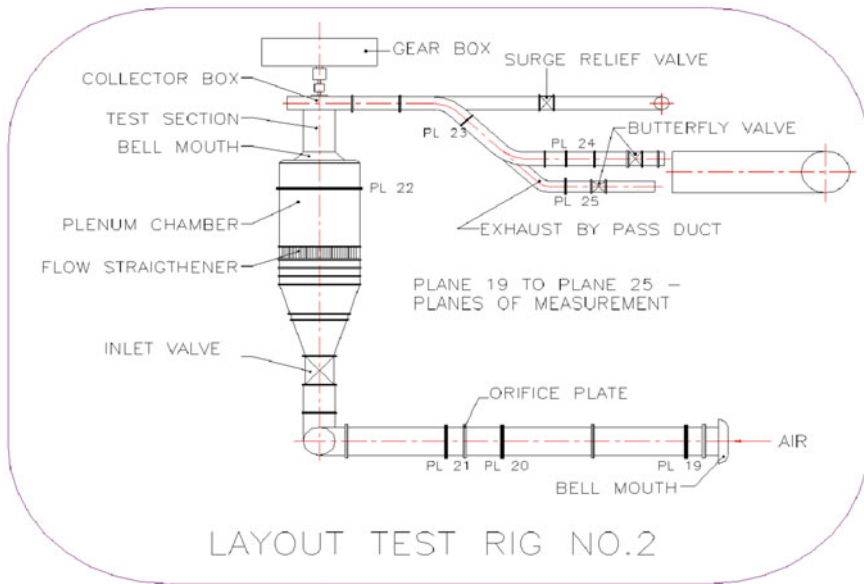


Fig. 1 Compressor test facility layout

This study focusses at design improvement of existing air collector box to achieve high-static pressure uniformity at compressor outlet with minimum pressure loss. 3D RANS analysis was carried out initially to evaluate the static pressure distortion and total pressure loss at the compressor exit. Further, design improvement was done by varying the length of collector box, increasing the outlet area, increasing the number of outlets, and shape of the collector box.

The stability of the system depends on primarily on the volume ratio of exhaust ducting system and compressor flow path. A non-dimensional parameter called ‘*B*’ parameter was formulated by Greitzer [1] to determine the stability of the test rig system. It depends on duct, plenum volume, blade rotational speed, and operating temperature. Premature stall and surge shall be avoided by maintaining the ‘*B*’ parameter below a value of 0.7. ‘*B*’ parameter was evaluated for all the cases, and the instability criteria were calculated for all designs. Moses and Kazberovich studied the effect of size and number of outlet pipes on design of collectors for testing axial flow compressors [2]. Yasutoshi et al. examined pressure recovery in axisymmetric, annular curved diffusers [3]. Lu Xingsu et al. performed aerodynamic design and experimental studies on marine gas turbine exhaust volutes [4]. AM Pradeep et al. studied gas turbine exhaust diffuser performance and its enhancement by shape modifications [5]. Sultanian et al. carried out experimental and CFD investigation in gas turbine exhaust system [7]. Brian C. Bernier et al. studied the impact of a collector box on the pressure recovery of an exhaust diffuser system [8].

Further, a variable outlet duct volume configuration was designed around the circumference of the collector box which provided much higher flow uniformity and low-static pressure distortion at compressor exit.

2 Design Requirement

Primary requirements of collector box design are to improve the static pressure uniformity at test compressor exit with minimum total pressure loss. Two important parameters considered for design are static pressure distortion (SPD) and total pressure loss coefficient (λ). Sectional view and 3D view of baseline collector box design are shown in Figs. 2 and 3, respectively. Volume ratio of compressor duct and exit plenum of collector box plays an important role in determining the stability limit of the test compressor. Greitzer 'B' parameter was fixed less than 0.7 for all the design cases.

The main design parameters considered for the analysis are the mass flow rate, total pressure loss coefficient, and static pressure distortion coefficient (SPD). Reduction in total pressure loss was intended mainly to ensure the sensitivity of throttle valves present at the outlet ducting system. Analysis has been carried out to determine the design parameters like total pressure loss coefficient and SPD. The corrected mass

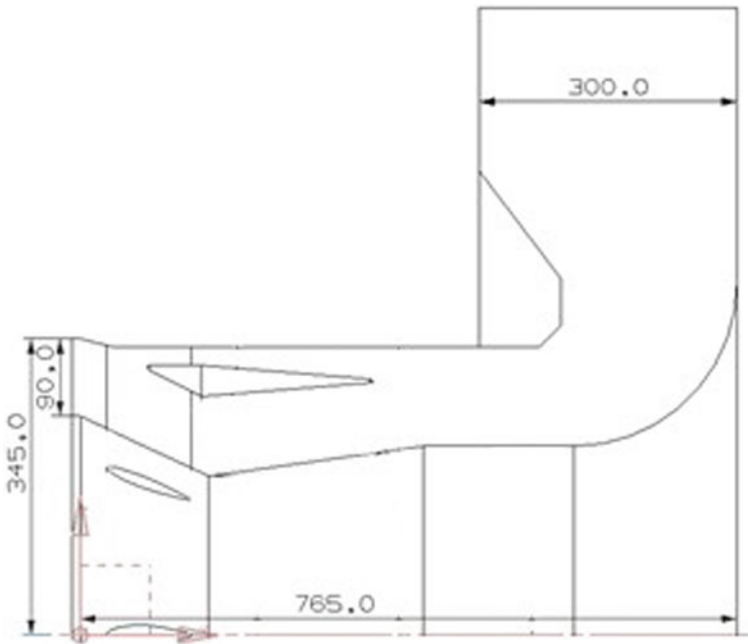


Fig. 2 Sectional view of baseline collector box configuration

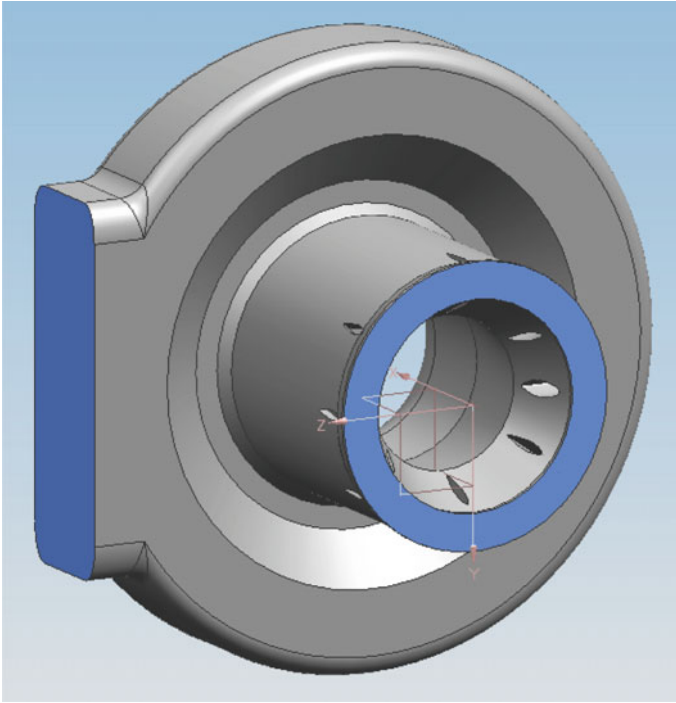


Fig. 3 3D view of collector box

flow rate for collector box was calculated to be 28 kg/s.

$$\lambda = (P_{o,\text{in}} - P_{o,\text{out}})/(P_o - P)_r \quad (1)$$

$$\text{SPD} = (P - P_{\text{min}})_r/(P_o - P)_r \quad (2)$$

$$B = U/2\omega L \quad (3)$$

$$\omega = a\sqrt{A/LV} \quad (4)$$

3 Collector Box Configuration

Compressor test rig layout and other subsystems are shown in Fig. 1. The exhaust flow is throttled using butterfly valves to evaluate the performance of compressor.

The compressor is driven by a power plant and free power turbine (not shown in the layout). Compressor characteristics are generated by throttling the exhaust valves and increasing the loading on test compressor. The collector box outlet is connected to three ducts of different diameters which contains throttling valves of different sizes to evaluate the performance precisely.

4 Computational Domain

Steady-state numerical investigation was performed using 3D RANS solver. A full scale 180° sector collector box was modelled with 1.26×10^6 tetrahedral elements.

Prism elements were used to capture the near wall flow regions. Minimum cell thickness near wall boundary was maintained at y^+ of 4. Turbulence model with $k-\omega$ shear stress transport was used for the analysis. CFD solutions for these configurations were obtained for peak speed test values. Convergence criteria up to 1×10^{-6} residual target were maintained for RMS values during steady-state analysis. Maximum imbalance in mass flow rate at in inlet and outlet was fixed at 0.5% for convergence criteria. Computational grid for baseline configuration is shown in Fig. 4.

The reference plane for static pressure measurement is taken at a distance of 40 mm from the inlet plane. The boundary conditions specified at inlet were total pressure and total temperature. The exit static pressure was varied to achieve the target corrected mass flow rate of 28 kg/s.

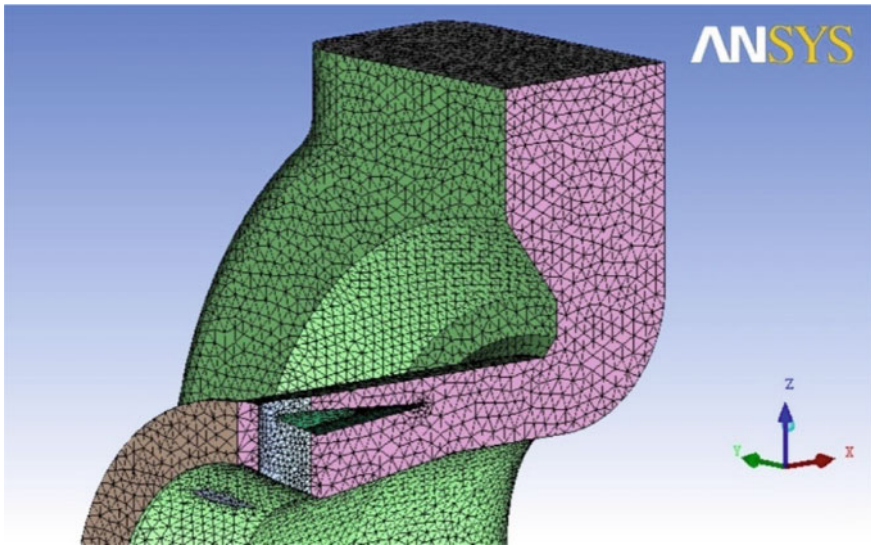


Fig. 4 Computational grid for baseline collector box configuration

Table 1 Performance of baseline CB configuration

Boundary condition	
$P_{o \text{ in}}$	101.325 kPa
$T_{o \text{ in}}$	288.2 K
P_{out}	68 kPa
Results	
m	28 kg/s
λ	1.156
SPD	0.109

5 Performance of Baseline Collector Box

Analysis was first carried out with the existing configuration, and essential parameters like mass flow, SPD, and total pressure loss coefficient were calculated. The existing baseline collector box (configuration 1) thus analysed indicates that it requires improvement in SPD characteristics as it is much higher than the recommended value of 0.05 (Table 1). The total pressure loss coefficient of CB also found to be on the higher side for the target mass flow of 28 kg. Flow velocity contour of baseline configuration is shown in Fig. 5.

Based on the performance of baseline configuration, two more design iterations were carried out to reduce the SPD and pressure loss coefficient. Modified designs of collector box are shown in Figs. 6 and 7.

Analysis was repeated for both the modified designs, and performance was compared with the baseline design. Configuration 3 design was showing total pressure loss reduction. As the flow path was smoothened in configurations 2 and 3, compared to baseline configuration, the total pressure loss was reduced significantly.

Further, parametric study was carried out by varying the length and outlet area of CB.

6 Effect of Length Variation

In the next design iteration, analysis was carried out for varying length. Length of the CB was increased from 760 mm to a maximum of 1500 mm. It has been observed that increasing length has got substantial positive influence on SPD, and remarkable improvement was observed for all the configurations. The variation of SPD with length is plotted in Fig. 8. It can be seen that improvement of SPD with the increase in length is more prominent up to the length of 1200 mm length and beyond that value increasing length does not have much influence on SPD, as shown in Fig. 8. The non-uniformity in the flow gets decreased with increase in the duct length, and flow velocity increases only near the vicinity of the collector box outlet.

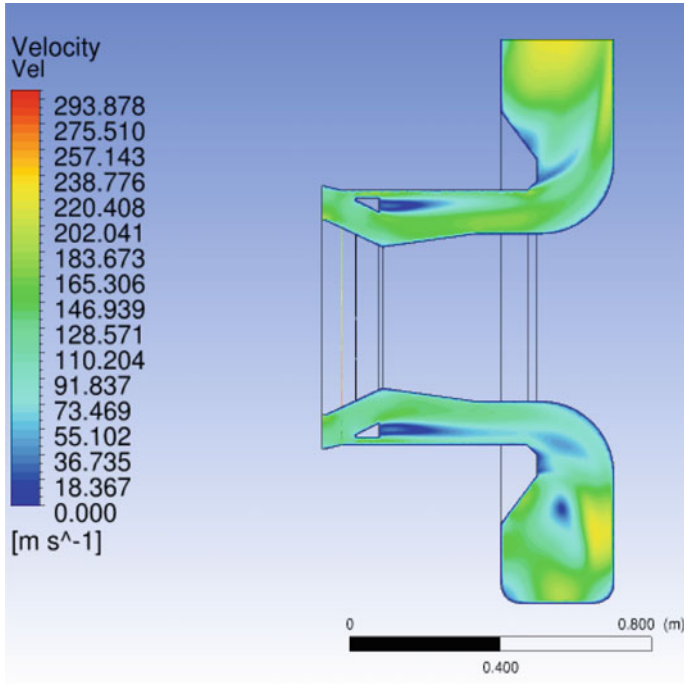


Fig. 5 Velocity contour of baseline CB configuration

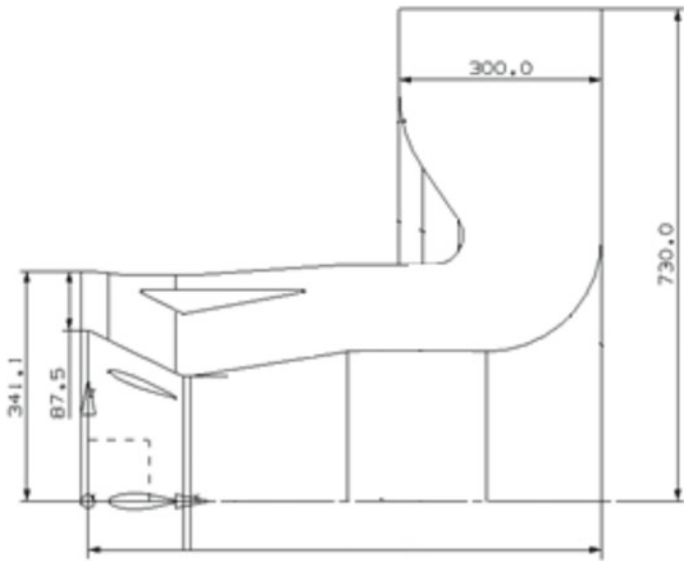


Fig. 6 Sectional view of collector box configuration no. 2

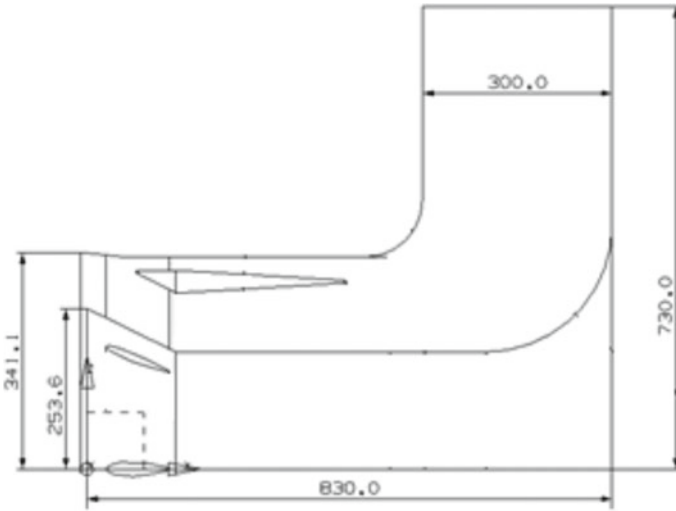
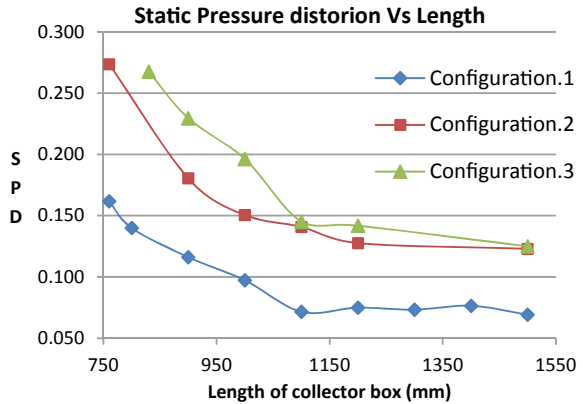


Fig. 7 Sectional view of collector box configuration no. 3

Fig. 8 Variation of SPD with length



Total pressure loss coefficient tends to remain constant with increase in length for all the three configurations as can be seen from the plot shown in Fig. 9.

Static pressure contour along the length of the collector box for two different lengths is shown in Figs. 10 and 11. As shown in the figures, with increasing length, the static pressure non-uniformity decreases towards the compressor exit. Hence, uniform back pressure shall be maintained and equal aerodynamic loading around the annulus can be provided at the exit of compressor. By this way, compressor characteristics shall be generated during testing in an appropriate way with uniform exit conditions. In both the figures, low-static pressure at the top is due to the reason that outlet is present at the top of the collector box, which leads to high-flow velocity at the top portion of CB.

Fig. 9 Variation of total pressure loss coefficient with length

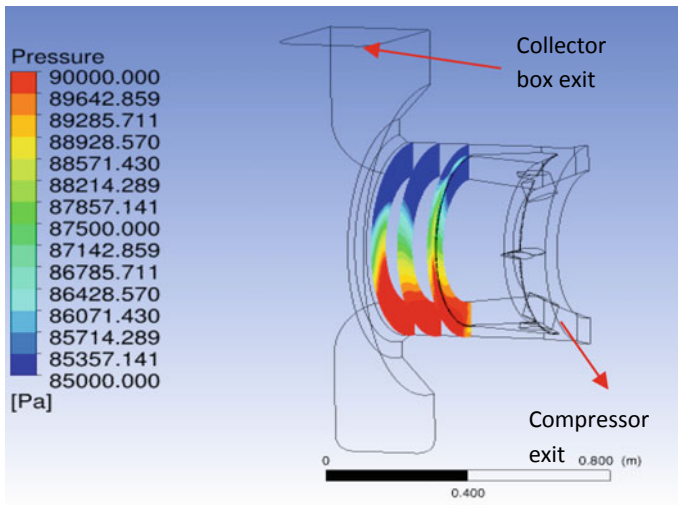
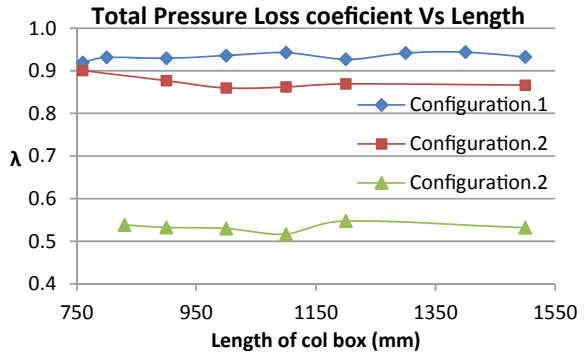


Fig. 10 Static pressure contour along CB length for baseline configuration (760 mm length)

7 Effect of Outlet Size and Configuration

Further, studies were carried out to find the effect of outlet area and orientation of outlet area on the SPD and mass flow. In first case, the total outlet area was fixed same, but the number of outlets were increased from 1 to 4. In the next case, the total outlet area was a multiple of number of outlets. The schemes with various outlet orientations and its area are shown in Figs. 12 and 13, and the respective results are shown in Tables 2 and 3.

In this analysis, the corrected mass flow was kept constant at 28 kg/s, and the length of CB was kept fixed at 900 mm length. A remarkable improvement in SPD was observed. The pressure loss coefficient λ also found to decrease with increased number of outlet.

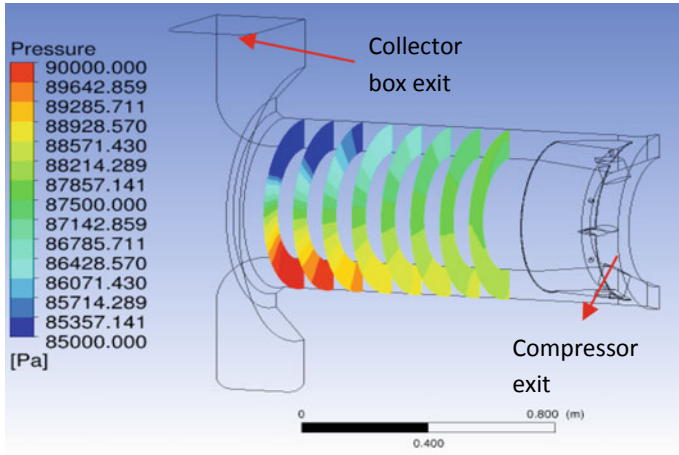


Fig. 11 Static pressure contour along CB length for increased length (1500 mm length)

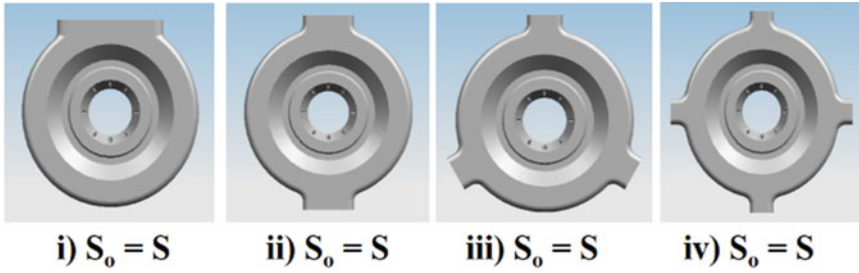


Fig. 12 Multiple CB outlet with constant total area

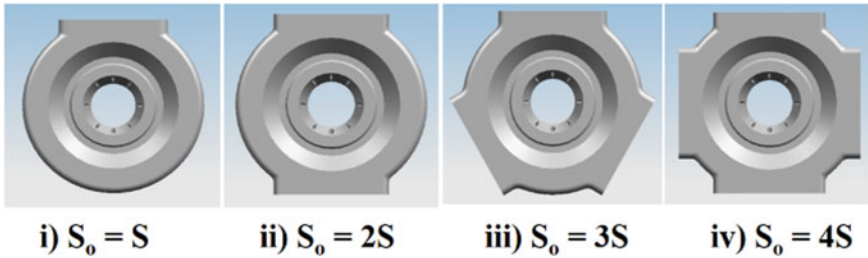


Fig. 13 Multiple CB outlet with increasing total area

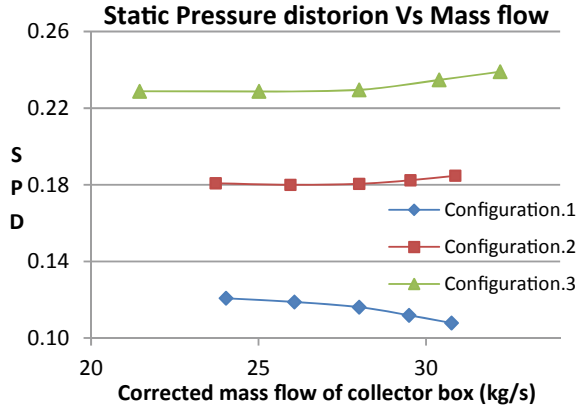
Table 2 Results of multiple CB outlet with constant total area

No. of outlets	1	2	3	4
λ	0.924	0.998	1.013	0.82
SPD	0.162	0.073	0.076	0.075

Table 3 Results of multiple CB outlet with increasing total area

No. of outlets	1	2	3	4
λ	0.924	0.656	0.553	0.472
SPD	0.162	0.082	0.073	0.074

Fig. 14 Variation of SPD with mass flow rate



With multiple outlets, the outlet flow is more uniform at the exit and provided low SPD at the compressor exit. In the initial case, where total outlet area was kept same, SPD was reduced to a minimum of 0.075, but total pressure loss was more due to high-exit velocity comparatively.

8 Effect of Mass Flow Variation

Finally, study was carried out for all three configurations for various mass flow by varying the exit back pressure of the collector box when the inlet pressure was kept fixed at sea level static (SLS) condition. Again, the length of the CB was fixed for a length of 900 mm. The SPD versus mass flow and pressure loss coefficient λ versus mass flow are shown in Figs. 14 and 15, respectively. The variations of SPD and λ with mass flow were not were not remarkable.

9 Variable Outlet Duct Configuration

Further trials were carried out on CB rear profile modification. Since the flow was having higher velocity near the outlet, low-static pressure was observed at one portion of the compressor exit. This lead to high-SPD value at compressor exit and resulted

Fig. 15 Variation of total pressure loss coefficient with mass flow

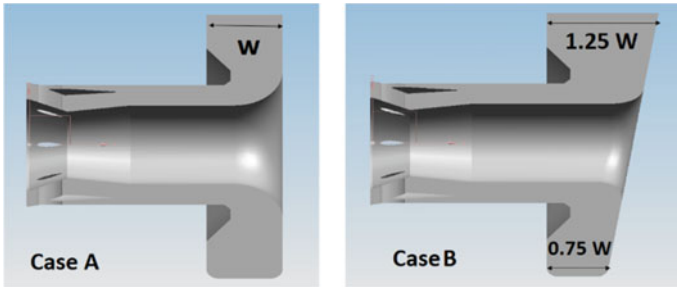
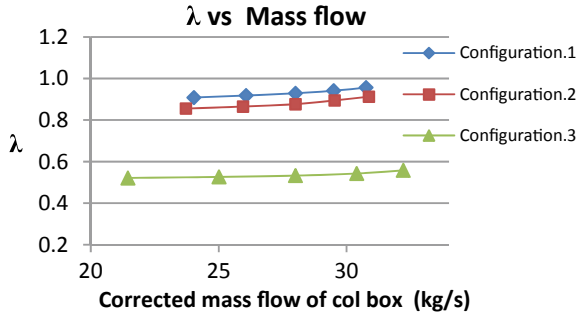


Fig. 16 Baseline and variable outlet duct collector box configuration

in non-uniform loading. Hence, an attempt was made to vary the outlet area of the CB such that static pressure uniformity is preserved at the compressor exit.

The baseline and variable outlet duct volume configuration of collector box are shown in Fig. 16. With such a configuration, the duct volume was increased near the outlet leading to low-velocity and high-static pressure when compared with baseline configuration. This resulted in less SPD near the compressor exit, thus providing more uniform loading to the compressor. The static pressure contour near compressor exit for baseline and variable outlet duct volume configuration are shown in Fig. 17. SPD and total pressure loss coefficients are shown in Table 4 for both the cases.

10 Volute Shaped Duct Configuration

In the final trials, collector box was designed similar to a centrifugal compressor volute. The collector box cross section area was adjusted to vary linearly in the circumferential direction as shown in Fig. 18. This resulted in best performance achieving target value less than 5% static pressure distortion at compressor outlet region. In this configuration, the duct volume was subjected to increase from bottom to top region leading to low-velocity and high-static pressure in top region when

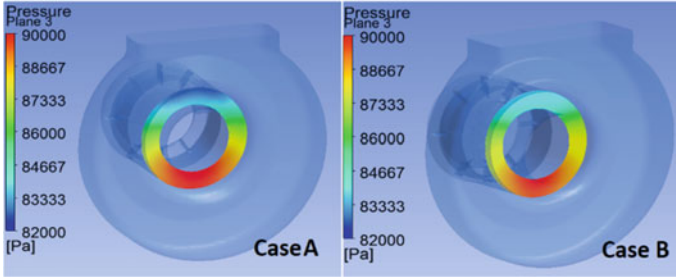


Fig. 17 Static pressure contour near compressor exit for baseline and variable outlet duct collector box configuration

Table 4 Results of variable CB exit area configuration

Configuration	λ	SPD
Case A	0.943	0.072
Case B	0.738	0.056

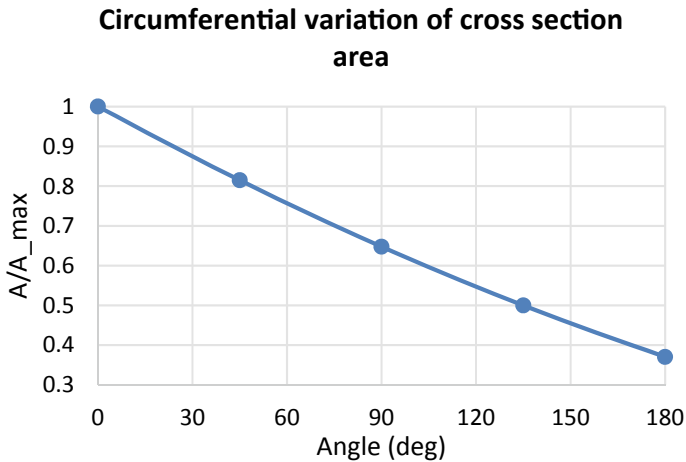


Fig. 18 Circumferential variation of duct cross section area (non-dimensional)

compared with baseline configuration. Due to increased area in the top portion, the velocity of fluid leaving the outlet is decreased resulting in more uniformity in static pressure around the annulus. This resulted in less SPD near the compressor exit, thus providing more uniform loading to the compressor. The volute shaped collector box models are shown in Fig. 19. The static pressure distribution in the aerodynamic interface plane is shown in Fig. 20 and static pressure distortion value is mentioned in Table 5.

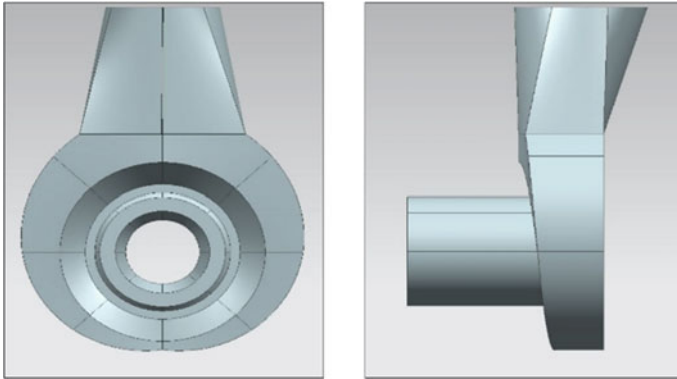


Fig. 19 Volute shaped collector box model

Fig. 20 Static pressure distribution at compressor outlet

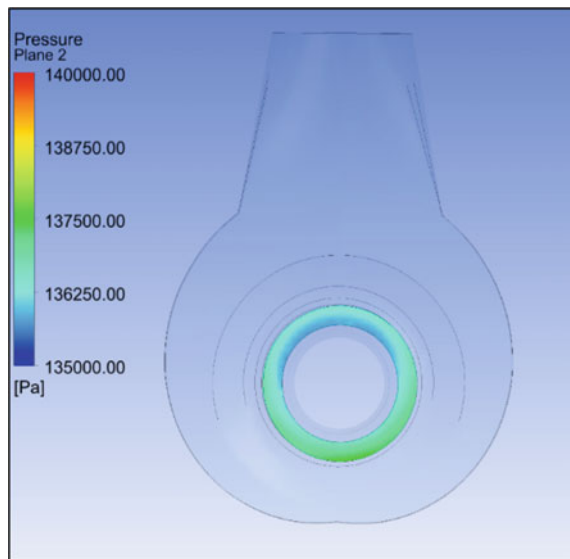


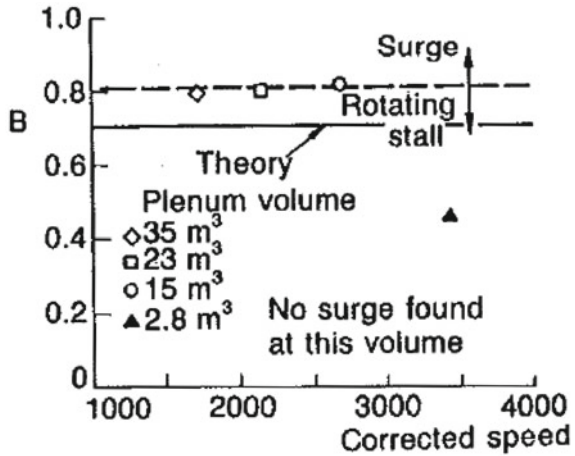
Table 5 Results of volute shaped CB duct configuration

Configuration	λ	SPD
Volute shaped duct	0.608	0.0415

11 Greitzer B Parameter

Greitzer B parameter is used to examine the stability of the system in a one-dimensional approach [1]. The test system mainly consists of compressor duct, to give inertia to the flow, a plenum to give storage to the compressed gas and a throttling

Fig. 21 Comparison of measured and predicted boundary between rotating stall and surge for a 3-stage low-speed compressor showing overriding dependence on B parameter [1]



device. The collector box volume and the downstream volume till throttling valves are considered as the plenum for calculation of B parameter. This non-dimensional parameter is generally used for determining the stability of the system. Maximum value of B parameter to be maintained is 0.7 to ensure stability of the system (Fig. 21).

B parameter was calculation for baseline collector box design is shown below.

$$B = \frac{U}{2a} \sqrt{\frac{V_{\text{collector}}}{V_{\text{compr duct}}}}$$

$$B = \frac{320 \text{ ms}^{-1}}{2 * 405 \text{ ms}^{-1}} \sqrt{\frac{1318 \text{ e} - 3 \text{ m}^3}{217 \text{ e} - 3 \text{ m}^3}}$$

$$= 0.268 * \sqrt{6.1}$$

$$= 0.66$$

12 Conclusions

A detailed CFD analysis of baseline CB and two different configurations of CB has been carried out. Due to high SPD and total pressure loss coefficient, parametric study was carried out in CB configurations to evaluate the influence of geometry parameters on performance. Further, the study was extended to evaluate the performance on variable outlet duct and volute shaped collector box.

- With increasing length of CB, static pressure distortion near compressor exit was decreasing with almost constant total pressure loss coefficient.

- Baseline configuration with 0.51 L/D ratio was resulting in 0.162 SPD and for increased length configuration of 0.75 L/D ratio, SPD was decreased to 0.07.
- Additional outlets with increased/fixed total outlet area substantially decrease SPD and total pressure loss coefficient. For all configurations, Greitzer 'B' parameter was maintained less than 0.7.
- In the variable outlet duct configuration, duct was designed to improve the flow uniformity at the exit of compressor. For 0.75 L/D ratio and variable outlet duct configuration, 0.056 SPD was achieved.
- Finally in the volute type collector duct configuration, best performance was achieved with 0.041 SPD and 0.61 total pressure loss coefficient. This was achieved by reducing the outlet velocity and improving the static pressure uniformity at compressor outlet.

Acknowledgements The authors would like to acknowledge Shri. SA Krishnan, Sc 'G' (Retd) for his valuable contributions and guidance in this collector ducting system study.

References

1. Cumpsty NA (1989) Compressor aerodynamics. Longman Scientific & Technical, U.K
2. Moses JJ, Kazberovich TI (1948) Effect of size and number of outlet pipes on design of collectors for rating and testing axial flow compressors. In: NACA technical note no.1607, Flight Propulsion Research laboratory Cleveland, Ohio. Samnders AJ, Hassan KK, Rabe DC (2004) Experimental and numerical study of stall flutter in a transonic low aspect ratio fan blisk. In: ASME
3. Senoo Y, Kawaguchi N (1983) Pressure recovery of collectors with annular curved diffusers. The American Society of Mechanical Engineers. ASME Paper No. 83-GT-35. Chiang HD, Keilb RE (1993) An analysis system for blade forced response. ASME J Turbomachinery 115(4):762–770
4. Xingsu L, Kunyuan P, Zuomin W (1981) Aerodynamic design and experimental study of marine gas turbine exhaust volutes. The American Society of Mechanical Engineers. ASME Paper No. 81-GT-143. Vahdati M, Simpson G, Imregun M (2009) Mechanisms for wide chord fan blade flutter. In: ASME Turbo Expo 2009, GT 2009-60098
5. Pradeep AM, Roy B, Vaibhav V, Srinivasu D (2010) Study of gas turbine exhaust diffuser performance and its enhancement by shape modifications. In: Proceedings of ASME Turbo Expo 2010. ASME Paper No. GT2010-22088
6. Bottenheim S, Birk AM, Poirier DJ (2006) The Effect of an entraining diffuser on the performance of circular-to-slot exhaust ducts with a 90 degree bend. In: Proceedings of ASME Turbo Expo 2006. ASME Paper No. GT2006-90017
7. Sultanian BK, Nagao S, Sakamoto T (1999) Experimental and three-dimensional CFD investigation in a gas turbine exhaust system. ASME J Eng Gas Turbine Power 121:364–374

8. Bernier BC, Ricklick M, Kapat JS (2011) Impact of a collector box on the pressure recovery of an exhaust diffuser system In: Proceedings of ASME Turbo Expo 2011. ASME Paper No. GT2011-46455
9. Theory Documentation of CFX-ANSYS 16.0, ANSYS Inc

Gas Turbine Propulsion—Turbines

Aerodynamic Design of Axial Flow Turbine for a Small Gas Turbine Engine



D. Harish, R. D. Bharathan, Sharad Kapil, S. V. Ramana Murthy,
and D. Kishore Prasad

Abstract Small gas turbines have been used in many unmanned aerial vehicle (UAV) applications. For UAV, the design of gas turbine engine is driven by its simplicity, cost-effectiveness and reliability, and moderate fuel efficiency. This paper describes the aerodynamic design and salient features of a single-stage axial turbine designed for powerplant of UAV application. Profile, secondary and tip clearance losses are dominant due to reduced blade heights, Reynolds number, and manufacturing constraints. The transonic axial turbine is designed with low-aspect ratio and moderate stage loading. The design point pressure ratio is 2.3, and the target efficiency is 86%.

Nomenclature

C	Chord (mm)
C_p	Specific heat at constant pressure (J/Kg-K)
R	Radius (mm)
S	Pitch (mm)
T_{\max}	Maximum thickness of aerofoil (mm)
X	Axial distance from leading edge (mm)
ΔT	Total temperature drop across turbine (K)

D. Harish · R. D. Bharathan (✉) · S. Kapil · S. V. Ramana Murthy · D. Kishore Prasad
DRDO-Gas Turbine Research Establishment, Bengaluru, India
e-mail: bharathan.gtre@gov.in

D. Harish
e-mail: harishd.gtre@gov.in

S. Kapil
e-mail: sharadkapil.gtre@gov.in

S. V. Ramana Murthy
e-mail: ramanamurthy.gtre@gov.in

D. Kishore Prasad
e-mail: kishoreprasadd.gtre@gov.in

k	Turbulence kinetic energy
ω	Turbulent frequency
η	Efficiency

Subscripts

m	Mean section
h	Hub section
t	Tip section

1 Introduction

In last few decades, small gas turbine engine (SGTE) has been increasingly used as powerplant for UAV application. Specific fuel consumption (SFC) is not of prime importance for this application as its operational time is limited. The following requirements are proposed to be met during developmental phase as proposed by Barbeau [1], Kidd [2], and Rideau [3]:

- Simplicity in design and robustness reduced part count to enhance reliability.
- High specific thrust for compactness.
- Low manufacturing cost.
- Long-term storage and no maintenance.

This paper describes the aerodynamic design of single-stage axial flow turbine for SGTE. A single-stage turbine is designed for the target efficiency of 86% with a pressure ratio of 2.3 such that all the above requirements are considered at preliminary design stage.

The drivers of this design are aerodynamic performance, producibility, low cost, and high reliability. These are achieved by incorporating manufacturing constraints at design phase, reducing weight, part count, and using integrated castings as much as possible. The component shall be designed to guarantee performance requirement.

2 Mean-line Design

The design point is chosen from several operating conditions based on higher rotational speed, turbine entry temperature, and pressure. Turbine stage is designed for nondimensional parameters shown in Table 1, which is obtained from thermodynamic cycle of SGTE. Once the spool speed is agreed upon between compressor and turbine designers, stage loading, flow coefficient, and mean reaction are selected to meet

Table 1 Turbine stage thermodynamic quasi nondimensional parameters

S. No.	Parameters	Units	Values
1	Mass flow function	kg√K/kPa	0.31
2	Specific work function	J/kg-K	186
3	Speed function	(rev/min)/√K	1172.0
4	Pressure ratio	–	2.3
5	Efficiency	%	86

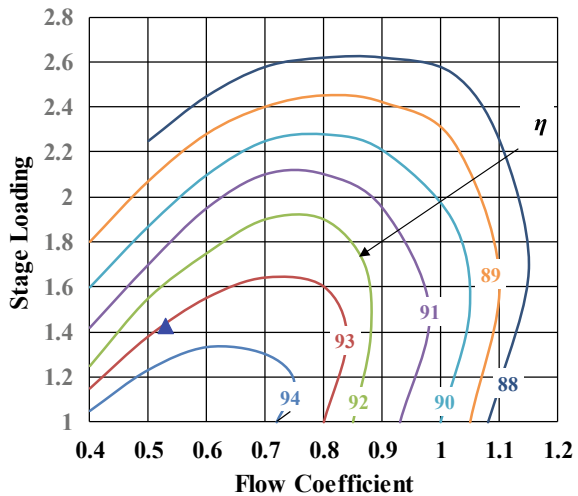
the required aerodynamic performance, dimensional, and weight constraints. The selected parameters are shown in Table 2. Smith [4] proposed correlations between stage loading, flow coefficient, and efficiency of turbines with 0.5 mean reaction based on experimental results. These correlations serve as a qualitative tool to estimate the performance of the turbine stage during preliminary design phase. Figure 1 shows the Smith chart plotted based on the correlations indicating the chosen value of stage loading and flow coefficient.

Mean-line calculation is performed using in-house code based on Horlock [5], Denton [6] and modified based on Ramana Murthy et al. [7, 8]. Loss models, correlations for choice of chord and stagger and blade spacing as mentioned in Kacker and Okapuu [9] are incorporated in the in-house code.

Table 2 Turbine stage overall parameters

S. No.	Parameters	Values
1	Stage loading	1.43
2	Flow coefficient	0.53
3	Mean section reaction	0.45

Fig. 1 Smith chart



3 Flowpath Design

Flowpath geometry, mean-line velocity triangle, number of blades are obtained from mean-line analysis. During this phase, multiple design iterations were carried out by adjusting the parameters to obtain cylindrical endwalls especially for the rotor which allow for constant tip clearance to be maintained and allow for easier inspection. The hub-endwall of the stator is suitably profiled to interface with the upstream combustor. Figure 2 shows the mean velocity triangle. Low mean reaction might lead to negative reaction at hub section (where gases may undergo compression instead of expansion). Hence, mean reaction of 0.45 is chosen.

Profile loss is minimized by choosing an optimal value of S/C and from this, the number of stators and blades can be determined. Zweifel coefficient is calculated from the velocity triangle, S/C and found to be in optimal range. The stagger angle is determined based on the flow angles between inlet and outlet from method proposed by Kacker and Okapuu [9]. Figure 3 shows the flowpath of the turbine stage.

Fig. 2 Mean-line velocity triangle

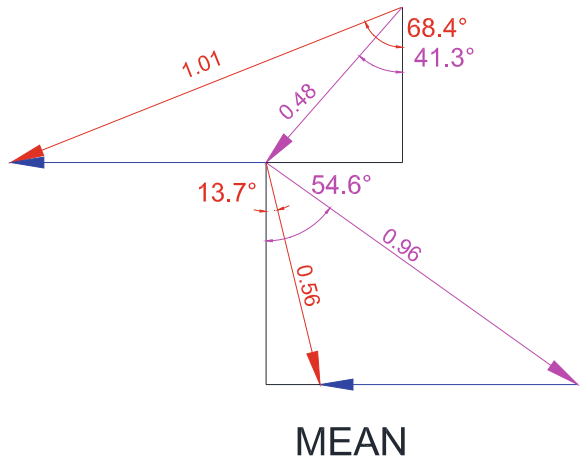
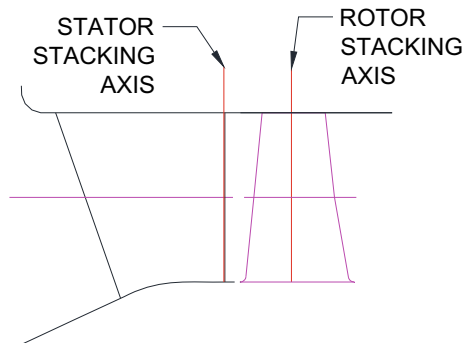


Fig. 3 Turbine stage flowpath



4 Hub-to-Tip Design

In hub-to-tip design, velocity triangles at hub, mean, tip section are obtained. An in-house streamline curvature code based on Denton [10] that solves steady, inviscid, axi-symmetric flow and satisfies radial equilibrium is used. Secondary flows dominate the flow at the endwalls of the turbine stage. Yoon et al. [11] studied the effect of tip clearance leakage flows due to tip reaction. It was suggested that increase in tip reaction will leads to increase tip clearance losses. Therefore, a spanwise controlled vortex with parabolic work distribution with maximum work extraction near the mean and minimum work extraction near the endwalls is adopted. This will help to minimize the secondary losses as well as tip clearance losses. Other parameters such as stator exit Mach number and angle, rotor inlet, and exit Mach numbers and angles as obtained from hub-to-tip analysis are found to be within the limits of industry best practices.

5 Profile Generation

Aerofoil profiles are generated using eleven parameters method by Pritchard [12]. This method is modified by Ramana Murthy and Kishore Kumar [13] to incorporate Bezier curves for constructing pressure and suction side curves instead of polynomials. This provides the flexibility to change the T_{\max}/C while ensuring slope continuity over the generated profile. Table 3 shows some of the salient parameters of the profiles that was generated at this stage.

After completion of each section profile generation, in-house 2-D inviscid blade-to-blade time marching solver formulated by Denton [10] is used to estimate the surface Mach number over the profiles for both design and off-design conditions.

5.1 Stator

In SGTE, TET is much less compared to that of modern military jet engine. Hence, simple convective cooling is sufficient for stators. The stators are hollow and forms flowpath with combustor. The stators are designed using constant S/C ratio at all radii and stacked at the trailing edge circle center. The exit angle is maintained constant. In terms of manufacturing constraints, trailing edge (TE) thickness plays an important

Table 3 Salient profile parameters

S. No.	Parameters	Stator	Rotor
2	S/C	0.69	0.64
3	T_{\max}/C (%)	18	20
4	h/C	0.85	2.0
5	Rh/Rt	0.65	0.65

role. Thicker TE is easier to manufacture but it leads to increase the TE losses. TE thickness is chosen such that it is easy to manufacture and minimizes the losses. Weiss and Fottner [14] suggested that aft-loading of stator reduces the profile and secondary losses. Hence, stator was designed for aft-loading by adjusting the Bezier control points. Three sections for stator are generated at three radial heights. The profiles are stacked at the trailing edge circle center. Figure 4 shows mean section profile designed using the method described above, and Fig. 5 shows the surface Mach number distribution over stator—hub, mean, and tip profiles.

Fig. 4 Stator mean section

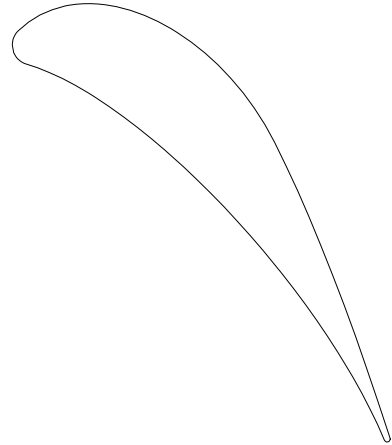
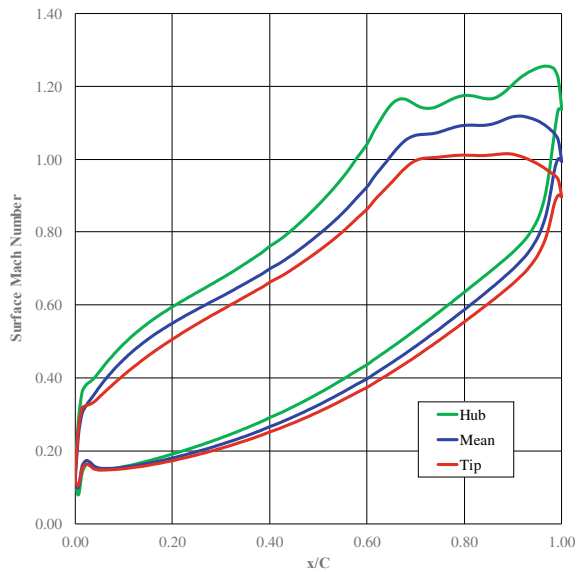


Fig. 5 Surface Mach number distribution over stator mean section



5.2 Rotor

Rotor blades are designed for an aspect ratio of two and stacked at the center of gravity of each section to eliminate bending stress. TE thickness is 20% higher as that of stator so that stresses at the TE of hub section is lower. Rotor blades metal temperature is always close to that of relative total temperature. During preliminary design, based on the estimated metal temperature, it is decided to design a solid blade without any cooling passage. Rotor blisk design was adopted as it significantly reduces weight and the number of components compared to conventional blade and disk design, thereby increasing reliability. The Bezier control points are adjusted such that the rotor sections are mid-loaded. Three sections for rotor blade were generated at three radial heights. The profiles are stacked over the centroid of each section to eliminate the bending stress due to centrifugal loads. Figure 6 shows the mean cross-section profile of rotor blade. Figure 7 shows the surface Mach number distribution over rotor—hub, mean, and tip profiles.

Fig. 6 Rotor mean section

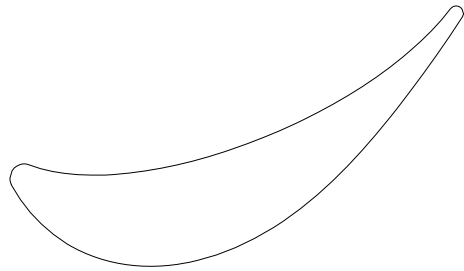
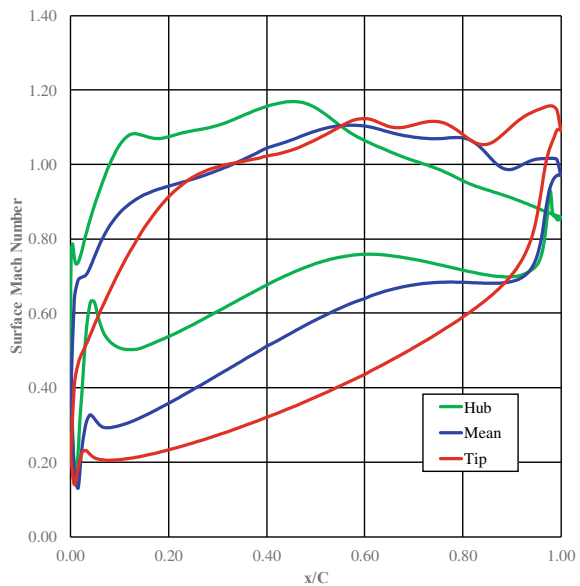


Fig. 7 Surface Mach number over rotor mean section



6 CFD Analysis

ANSYS CFX—commercial three-dimensional Navier–Stokes solver is used during the design phase. Reynolds averaged Navier–Stokes equation is discretized using finite volume method and solved for a steady state solution. Shear stress transport model is used for modeling the turbulence. In this k -epsilon, turbulence model is used in far field and k - ω turbulence model is used near the viscous regions, solutions are merged using blending function. A second order accurate skew upwind differencing scheme with physical advection correction is employed.

6.1 Grid Generation

The computational grid is generated using ANSYS CFX turbogrid. Automatic topology and meshing (ATM) method is used for stator and rotor blade. Sufficient grids are placed at the walls to capture the boundary layers. Grid independence was carried out. The skewness angle of the generated grid is kept between 35 and 155° , y plus less than 1, aspect ratio is kept below 100 and expansion ratio is below 1.2. Tip clearance value is set to be 1% of blade height, and it is modeled separately. The computational grid is shown in Fig. 8.

6.2 Boundary Condition

In stator domain, constant total pressure and radially varying total temperature based on the radial pattern factor are imposed at inlet. At inlet, 10% of blade height is used for eddy length scale and 10% is used for fractional intensity.

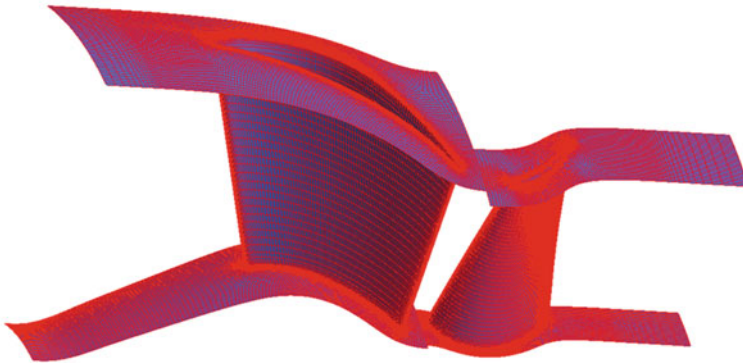


Fig. 8 Computational grid of turbine stage

At rotor domain, static pressure outlet is used. Mixing plane model is used between stator and rotor grid at the interface. Rotational periodicity along the axis of rotation is used at both stator and rotor.

Gas properties such as C_p , kinematic viscosity, thermal conductivity are calculated based on the fuel-to-air ratio and average temperature at inlet and exit plane.

7 Results and Discussion

The designed stage is analyzed using CFX and post-processed using CFX-post. Multiple CFD iterations were carried out to ensure the stage passed the required mass flow, and the blade angles were adjusted to minimize incidences and deviation. Figure 9 shows the blade-to-blade Mach number variation at midspan section. It can be observed that there is no sudden deceleration or flow separation bubble over the suction side of stator and rotor at midspan. The acceleration of the flow is smooth over the suction side on stator. The peak Mach number over the stator is higher compared to that of rotor because of reaction being 0.45. Iterations in CFD were carried out to avoid rotor blade leading edge local acceleration.

Figure 10 shows the surface streamline over stator suction side. Interaction of the secondary flow with the main flow is minimized as shown in Fig. 10. Figure 11 shows the streamline in the tip clearance region. The leakage flow over the tip clearance leads to formation of vortex structure which contributes to tip clearance losses.

The stator exit Mach number varies from 1.2 to 0.9 from hub-to-tip as seen from Fig. 12, corroborating the stator surface streamline pattern observed in Fig. 10.

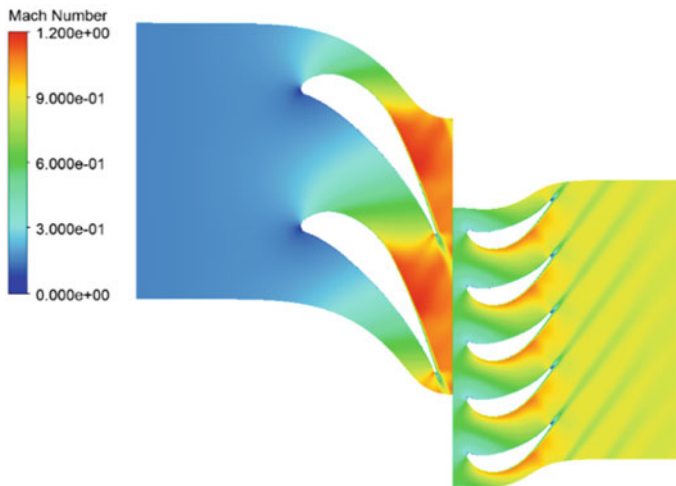


Fig. 9 Blade-to-blade Mach number distribution at midspan

Fig. 10 Streamline over stator

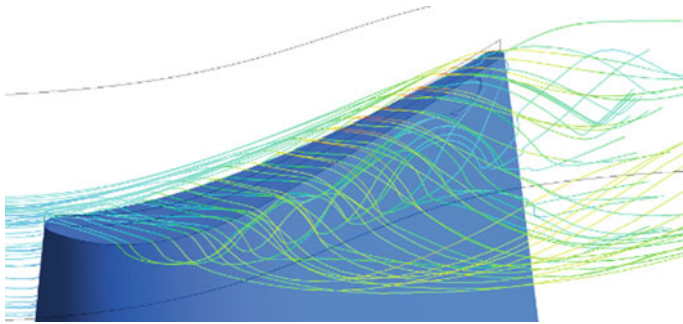
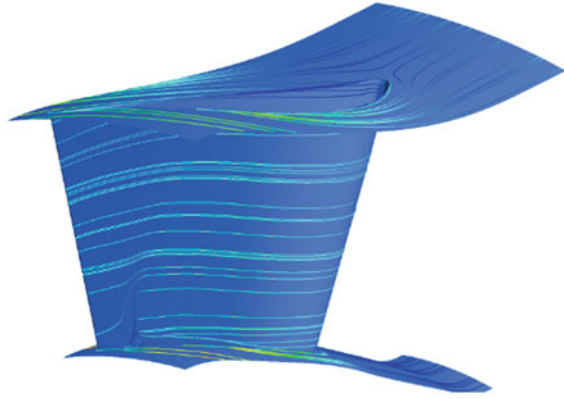
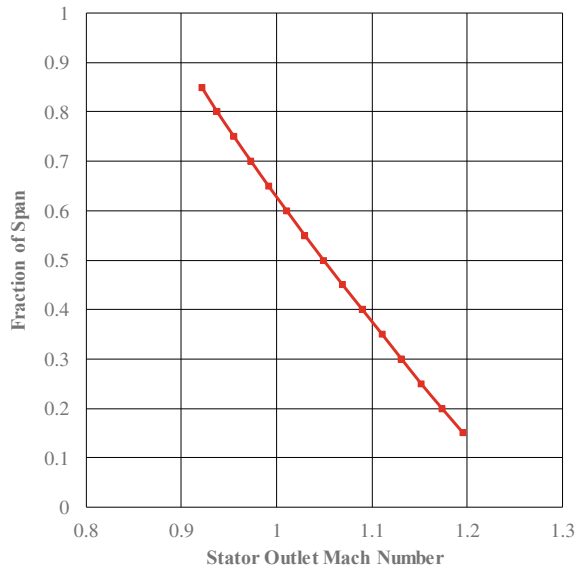


Fig. 11 Streamline in tip clearance region

Fig. 12 Spanwise variation of stator outlet Mach number



Figures 13 and 14 show the rotor outlet relative flow angle and relative Mach number, respectively. The outlet angle varies within -45° and -55° degrees across the span, and the outlet relative Mach number varies from 0.7 to 0.95.

Fig. 13 Spanwise variation of rotor outlet relative flow angle

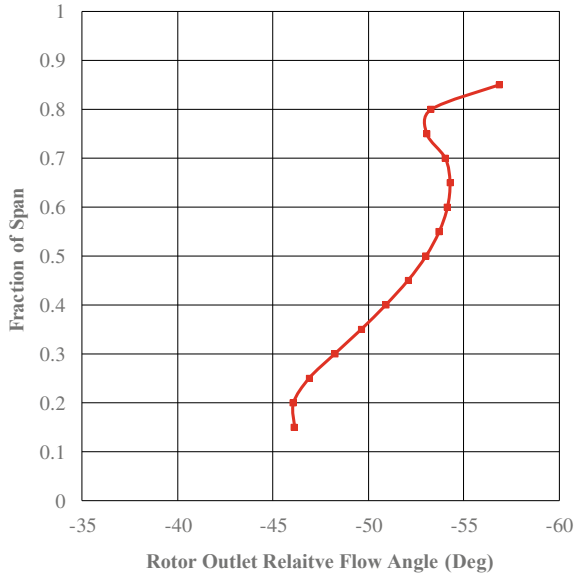


Fig. 14 Spanwise variation of rotor outlet relative Mach number

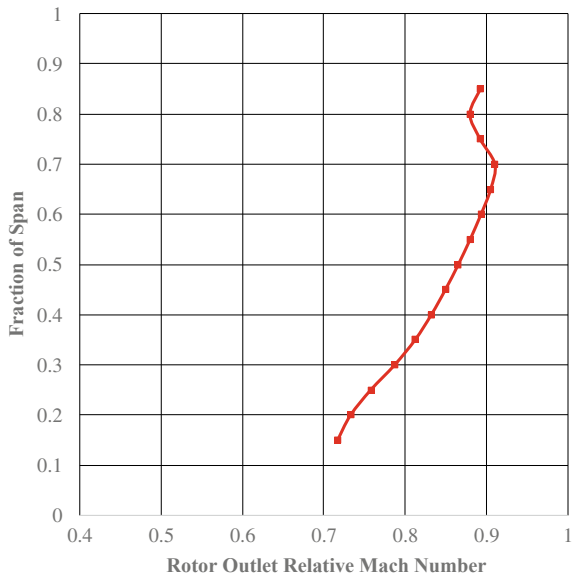


Fig. 15 Spanwise pressure loss coefficient of stator and rotor

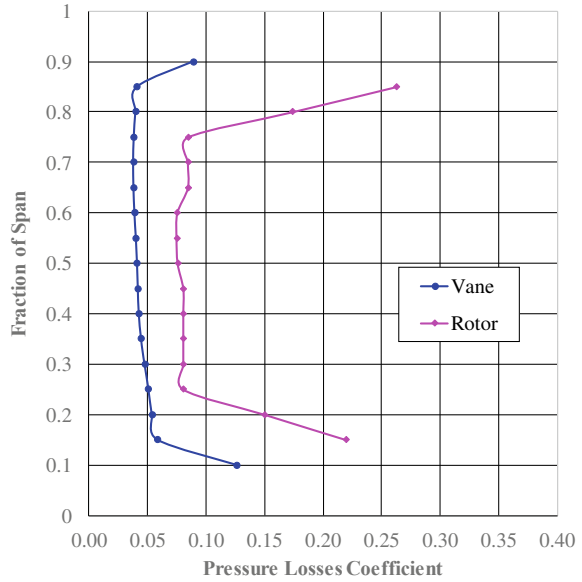
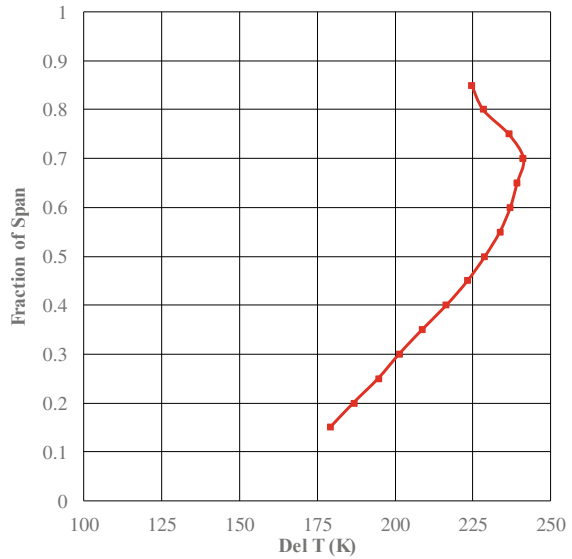


Figure 15 shows the pressure loss coefficient variation for stator and rotor. For stator, losses increase near the endwall regions because of secondary flows. For rotor, secondary and tip leakage flows increase the losses near the endwall. During the preliminary design phase, parabolic work extraction is used and Fig. 16 shows

Fig. 16 Spanwise distribution of temperature drop



the total temperature drop across stage obtained from CFD results. And it can be seen that work extraction at the hub and tip are minimum as per design intent.

8 Conclusions

A single-stage transonic turbine is designed by considering all the constraints during design phase, and it meets the required performance parameters. The stage efficiency with tip clearance of 1% of blade height is estimated to 89% which is 3% higher than target efficiency.

Acknowledgements The authors thank Director, GTRE for giving permission to present this work.

References

1. Barbeau DE (1981) A family of small, low cost turbojet engines for short life applications. ASME paper 81-GT-205
2. Kidd WE (1973) Turbine powerplants for missiles—cost improvement requirements. SAE Transactions, pp 1250–1257
3. Rideau JF, Guyader G, Cloarec A (2008) MICROTURBO families of turbojet engine for missiles and Uav's from the TR60 to the new bypass turbojet engine generation. In: 44th AIAA/ASME/SAE/ASEE joint propulsion conference and exhibit, p 4590
4. Smith SF (1965) A simple correlation of turbine efficiency. J R Aeronaut Soc 69:467–470
5. Horlock JH (1966) Axial flow turbines. Butterworths
6. Denton JD (1972) A computer program for steam turbine performance prediction. ARC 34-229, Turbo 248
7. Ramana Murthy SV, Ganesh R, Krishnaiah TV (2007) Aerodynamic improvement of low pressure turbine using 3D viscous flow computation. ISABE
8. Murthy SR, Kumar SK (2012) Parametric study of axial flow turbine for mean-line design and blade elements. In: Gas turbine India conference, vol 45165. American Society of Mechanical Engineers, pp 131–137
9. Kacker SC, Okapuu U (1982) A mean line prediction method for axial flow turbine efficiency. ASME J Eng Power 104(1):111–119
10. Denton JD (1983) An improved time marching method for turbo machinery flow calculation. J Eng Power 105:514–524
11. Yoon S, Curtis E, Denton J, Longley J (2010) The effect of clearance on shrouded and unshrouded turbines at two levels of reaction. In: Proceedings of the ASME turbo expo 2010: power for land, sea, and air. Volume 7: turbomachinery, parts A, B, and C. Glasgow, UK, pp 1231–1241. ASME
12. Pritchard LJ (1985) An eleven parameter axial turbine airfoil geometry model. ASME paper 85-GT-219
13. Ramana Murthy SV, Kishore Kumar S (2014) Development and validation of a Bezier curve based profile generation method for axial flow turbines. IJSTR 3(12)
14. Weiss AP, Fottner L (1995) The influence of load distribution on secondary flow in straight turbine cascades. ASME J Turbomach 117(1):133–141

Effect of Hub Clearance on Performance of Radial Turbine



R. D. Bharathan, P. Manigandan, Sharad Kapil, S. V. Ramana Murty, and D. Kishore Prasad

Abstract Scalloping of turbine wheel blisk of a radial turbine is done to reduce the centrifugal stress on the disc portion of the blisk, reduce weight and to decrease turbo lag in turbochargers. An attempt has been made to model the effect of scalloping of the turbine wheel on the performance of the radial turbine. The scallops have been modelled as hub clearances and analyses with various depths of scalloping and hub clearances have been analyzed using commercial 3D NS solver. The decrease in efficiency with increased scalloping and hub clearances has been plotted, and the results have been qualitatively compared with experimental results of similar but different radial turbines with and without scalloping. The results of the analyses are found to follow the same trend as those of the experiments.

Keywords Scalloping · Partial hub clearance · Tip clearances · Rotor blisk and twin scroll volute

Nomenclature

C_p	Mean specific heat capacity, J/kg-K
C_0	Spouting velocity, m/s
C_3	Rotor outlet mean absolute speed, m/s
M	Mach number

R. D. Bharathan (✉) · P. Manigandan · S. Kapil · S. V. Ramana Murty · D. Kishore Prasad
DRDO—Gas Turbine Research Establishment, Bengaluru, India
e-mail: bharathan.gtre@gov.in

S. Kapil
e-mail: sharadkapil.gtre@gov.in

S. V. Ramana Murty
e-mail: ramanamurthy.gtre@gov.in

D. Kishore Prasad
e-mail: kishoreprasadd.gtre@gov.in

N	Rotational speed, rpm
N _s	Specific speed, radian
PS	Pressure Side
R ₂	Rotor inlet radius, mm
R _{3h}	Rotor outlet hub radius, mm
R _{3s}	Rotor outlet tip radius, mm
R _C	Volute corner radius, mm
R _{MAIN}	Volute main radius, mm
R _s	Volute scroll wall radius, mm
S	Blade pitch, mm
SS	Suction side
T _{in}	Inlet total temperature, K
T _{max}	Maximum thickness
U ₂	Rotor inlet mean blade speed, m/s
V ₂	Rotor inlet mean relative speed, m/s
V ₃	Rotor outlet mean relative speed, m/s
W	Mass flow rate, kg/s
W _{ax}	Axial rotor width, mm
b ₂	Rotor inlet width, mm
ts	Scroll wall thickness, mm
ΔT	Temperature drop across turbine, K
δ	Volute section half angle, deg

1 Introduction

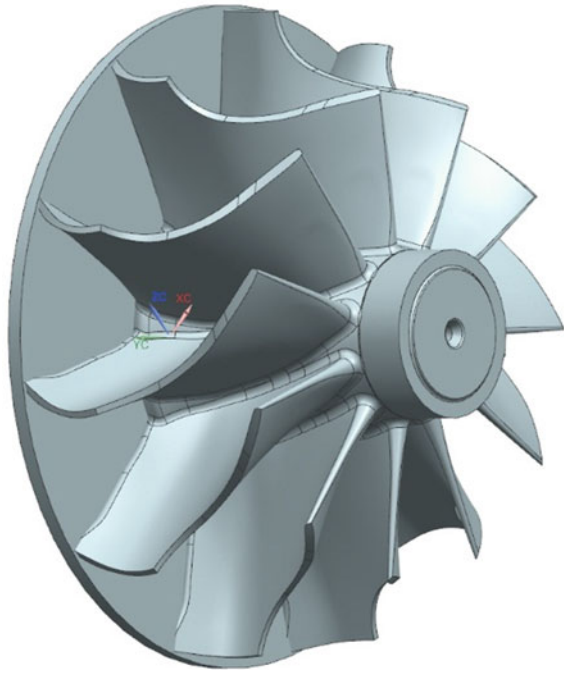
The radial turbine of a turbocharger performs the function of extracting power from the exhaust gases of the internal combustion engine in order to power the centrifugal compressor through a shaft. For its part, the compressor compresses the air at the inlet to the engine and so enhances the engine's volumetric efficiency. A typical vane-less radial turbine comprises a volute and rotor. The exhaust gases from the engine are accelerated by the volute and fed to the rotor the required inlet Mach number and flow angle with the least possible variation of flow properties along the circumferential direction. The gases in turn expand in the rotor, and thus, power is extracted.

Euler's turbine equation states that power extracted by the turbine is as follows:

$$\text{Power} = W(U_2 * C_{2\text{swirl}} - U_3 * C_{3\text{swirl}}) \quad (1)$$

Power extraction in a radial turbine wheel happens both through reduction in blade speed through reduction in radius from inlet to outlet and through a reduction in swirl velocity. The part of the turbine wheel that has the highest radius is its inlet. Most turbocharger turbine wheels are produced as integral blisks through casting route.

Fig. 1 Turbine wheel without scalloping



As the temperature of exhaust gases from the engine is high, they are made of nickel-based superalloys to withstand the high temperature and to meet the life requirement. Therefore, they are typically heavier than the centrifugal impeller and shaft. Excess weight in the inlet hub location which forms the hub endwall of the turbine wheel can lead to high centrifugal stresses on its solid disc portion; see Fig. 1. It can also increase the moment of inertia of the wheel which can lead to a slow response to accelerations and decelerations of the engine, also known as turbo lag; see [1].

In order to reduce the centrifugal stresses in the disc portion of the turbine wheel and to reduce turbo lag, the hub endwalls at the inlet between turbine blades are scooped out by introducing scallops between them as shown in Fig. 2. The stationary heat shield which protects the bearing housing and shaft from the hot turbine gases also performs the function of an endwall separated from the turbine wheel by an axial clearance which shall henceforth be called hub clearance as shown in Fig. 3.

The scalloping of the turbine wheel is accompanied by reduction in efficiency of the radial turbine because, similar to what happens in the tip clearance region, the introduction of a hub clearance provides a short cut for the gases to flow across the clearance from pressure side to suction side which leads to vortices which increase the losses in the stage which translated to a reduction in turbine efficiency. If maps of the radial turbine generated through analysis do not cater to the effect of scalloping, they may lead to overestimation of the performance of the turbine and erroneous matching of radial turbine with centrifugal compressor. Therefore, it is important to

Fig. 2 Scalloped turbine wheel

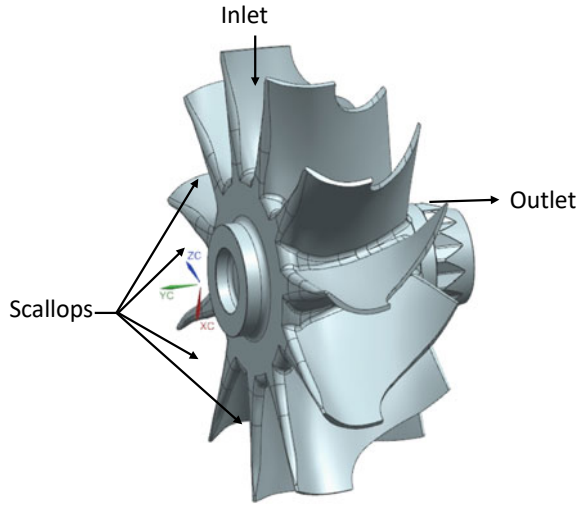
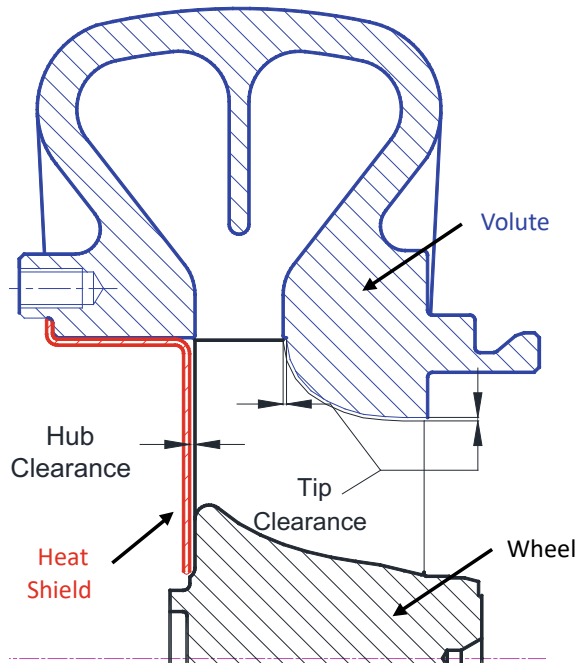


Fig. 3 Radial turbine stage



qualitatively and quantitatively understand the effect of scalloping and hub clearance on the aerodynamic performance of a radial turbine.

2 Description of Radial Turbine Stage

The design of the radial turbine under study was explained in [2]. The methodology for mean-line design of the radial turbine volute and wheel is provided in [3–5]. A vane-less design is favored because of the reduction in part count and weight as well as increase in reliability. To harness the effect of pulsation from the engine cylinders which fire in sequence, a twin scroll volute was designed as discussed in [1]. Appropriate cut-water angle was chosen based on producibility and aerodynamic consideration; see [6]. Table 1 gives the non-dimensional design parameters:

A previously designed and tested rotor wheel is analyzed using an analysis code developed based on [7]. Figure 4 shows the flow path of the turbine wheel, and Table 2 lists the salient non-dimensional turbine wheel parameters. The velocity triangles of the mean streamline of the turbine wheel are shown in Fig. 5.

Table 1 Turbine non-dimensional design parameters [2]

Parameter	Value
Specific speed, N_s	0.8 radians
Flow function, $W\sqrt{T_{in}}/P$	63.09 kg $\sqrt{K/s}$ MPa
Specific work output ($C_p\Delta T/T_{in}$)	216.8 J/kg-K
Total-to-static pressure ratio	3.28
Total-to-static efficiency	73%

Fig. 4 Turbine wheel flow path [2]

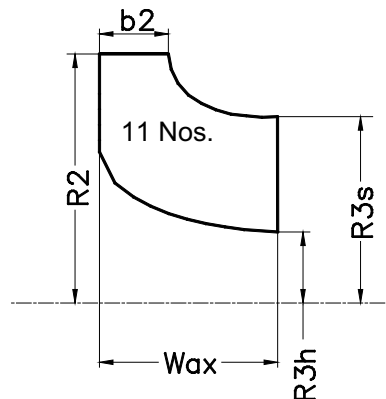
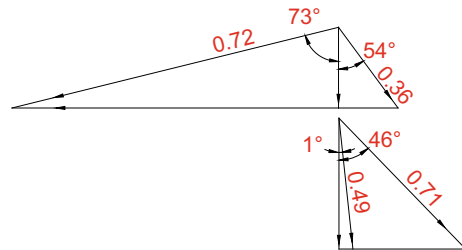


Table 2 Turbine wheel design parameters [2]

Parameter	Value
R3h/R3s	0.38
R3s/R2	0.75
$b2/R2$	0.276
$U2/C0$	0.70
$V3/V2$	1.9
$C3/U2$	0.5

Fig. 5 Mean velocity triangle

3 Modelling and Grid Generation

The computational grid is generated using ICEM-CFD software [9]. The grids are unstructured tetrahedrals. Care is taken to ensure that sudden changes in geometry and flow are captured by locally introducing finer grids. After grid sensitivity analysis, the size of the volute grid is fixed at 2 million. The 3D computational grid used in the analysis for the volute is shown in Fig. 6.

The rotor domain is modelled such that it includes both the hub clearance and tip clearance regions. Whereas the tip clearance is contiguous from the inlet of the rotor to the exit, the hub clearance is partial. This calls for the hub region from the inlet to the end of scalloping to be modelled as a stationary wall with a clearance from the rotor blade and the heat shield wall. The region from the end of scalloping to the outlet is modelled as a rotating wall along with the rotor blades themselves. Due to such complexity, it is not possible for the grid generation process to be carried out in a template-based software such as ANSYS turbogrid.

Therefore, the modelling of the fluid domain a single rotor blade domain with partial hub clearance and full tip clearance is carried out in UG NX 10.0 software as shown in Fig. 7. The modelled geometry is exported to ICEM-CFD software, and grid is generated. The grids are blade-centered multi-block, structural hexahedrals. The grid topology is a combination of O , C and H topologies. The grids are made finer at the regions where high gradients are expected in the flow field.

The grid size for each rotor is fixed after the grid sensitivity analysis at 0.5 million. Figure 8 shows the grid independence plot for the rotor plotted against mass flow rate. Sufficient grid points are placed close to the aerofoil surfaces to resolve the boundary layer. The y^+ values for the finalized grid are less than 12. The achieved skew angles

Fig. 6 3D computational grid of volute

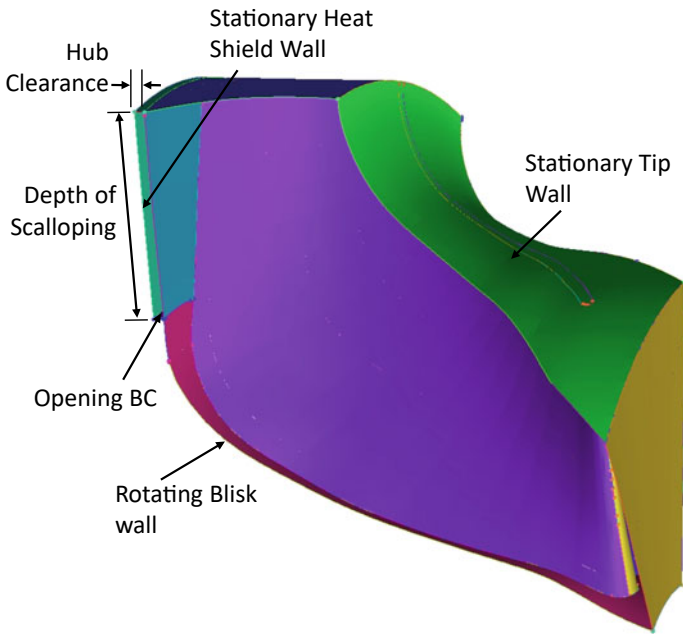
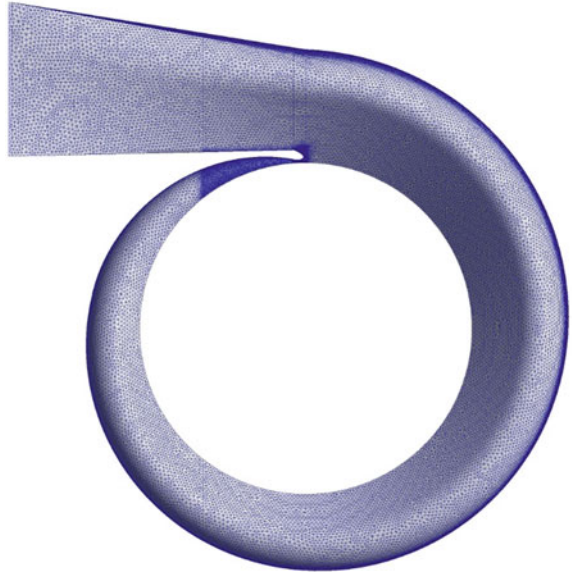
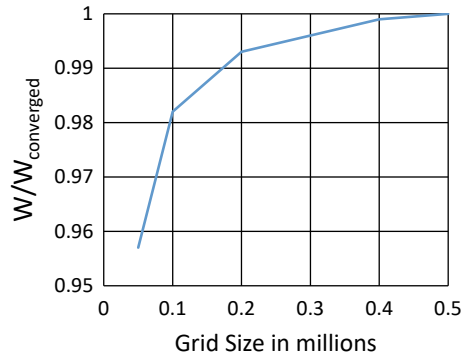


Fig. 7 Rotor blade domain

Fig. 8 Rotor grid independence plot



for the grids are between 30 and 150 degrees, the aspect ratios are less than 100, and expansion ratios are less than 1.2. The outlet domain of the grid is placed one chord downstream of the exit plane for the rotor grid. Multiple rotor meshes are generated to study five different depths of scalloping and three different hub clearances.

4 Computational Methodology

The analysis is carried out for the radial turbine by using the commercial 3D NS solver ANSYS CFX-19 [10] on an IBM DX 360 parallel computing system. The three-dimensional, multi-block, parallel flow solver CFX-19 developed by ANSYS is used for this analysis.

The Reynolds averaged Navier–Stokes equations are solved in the solution procedure. The governing equations are discretized using finite volume method. The solution algorithm is based on an implicit scheme coupled with multi-grid acceleration techniques. The effects of turbulence are modelled with two equations k - ω turbulence model with shear stress transport model. The significant advantage of this model is to predict improved wall shear stress in adverse pressure gradient flows and robustness for complex flows.

The boundary conditions are inlet total pressure, inlet total temperature, inlet flow angle and exit static pressure. The walls are assumed adiabatic. The blisk walls including the surface of the blade and the hub region from the end of scalloping to the outlet are treated as rotating walls. The tip clearance wall formed by the volute exit and the partial hub clearance wall created by the heat shield are treated as stationary walls. The clearance wall which bridges the hub clearance wall with the blisk wall separates the blade domain from the other side of the heat shield which is a closed chamber. Therefore, this is modelled as an opening across which the net mass flow is zero as shown in Fig. 7.

In order to capture the non-uniformity of the exit flow from the volute (especially at the tongue region), all the blades are modelled. Frozen rotor analysis is carried out

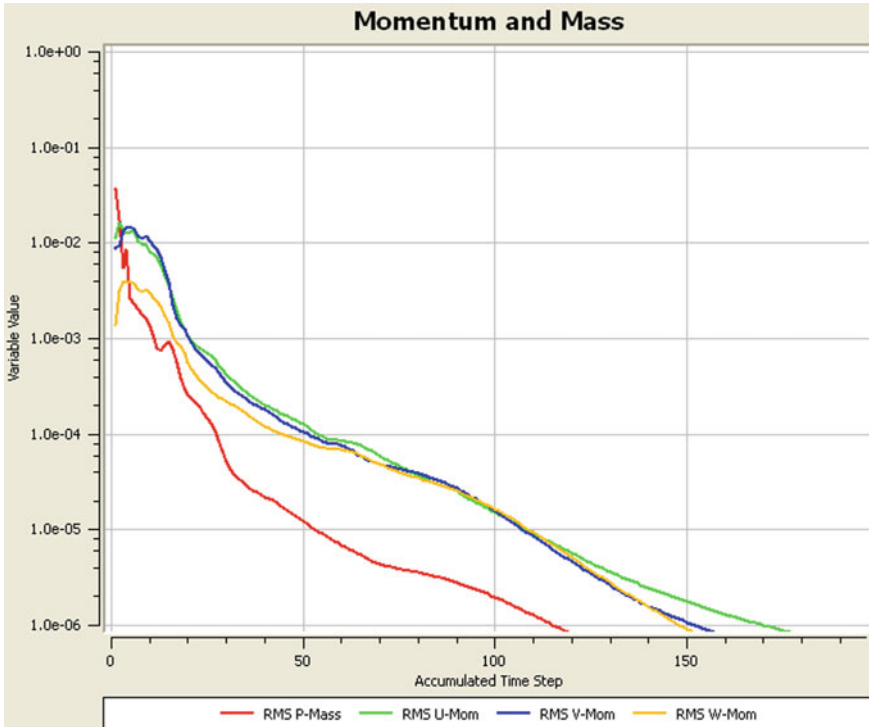


Fig. 9 Typical convergence history

for this purpose. The convergence criterion is set for the maximum residuals below 1E-4. The typical convergence history for the analysis is shown in Fig. 9.

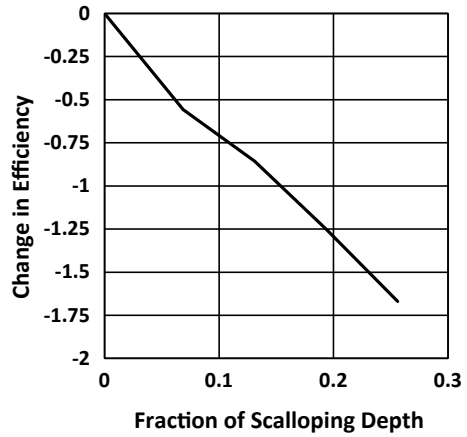
5 Results and Discussion

3D NS analyses are carried out for various depths of scalloping and hub clearances with the finalized volute. The effect of the scalloping and hub clearance on the aerodynamic performance of the radial turbine stage is studied through the non-dimensional performance parameters of the turbine like mass flow function and efficiency.

All analyses are converged to same pressure ratio at the same non-dimensional turbine rotor speed function to enable comparison of the overall turbine stage parameters. The variation of efficiency with depth of scalloping is shown in Fig. 10.

Change in efficiency with increase in scalloping has been plotted against scalloping depth non-dimensionalized with hub meridional length. It can be observed that the drop in efficiency follows a nearly linear trend with increase in scalloping

Fig. 10 Variation of efficiency with scalloping depth



depth. It is also seen that for an increase in depth of 25%, the efficiency reduces by about 1.75 percentage points.

As the depth of scalloping increases, the proportion of flow which cross-flows through the hub clearance region thereby not fully participating in the work production proportionally increases. This wasted flow can be visualized in the form of streamlines that are observed in the hub clearance region representing the cross-flow in Fig. 11. In a non-scalloped turbine wheel, this flow would be completely absent and the entire flow (minus the tip clearance flow) would pass through the turbine channel and contribute to work.

To observe the effect that such scalloping has in turbine work extraction, it is required to analyse the blade loading of the rotor blade near the hub. Figure 12

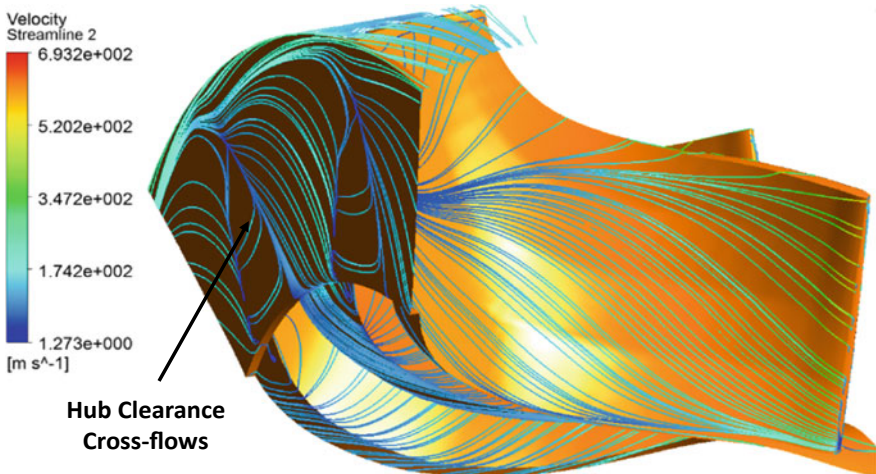
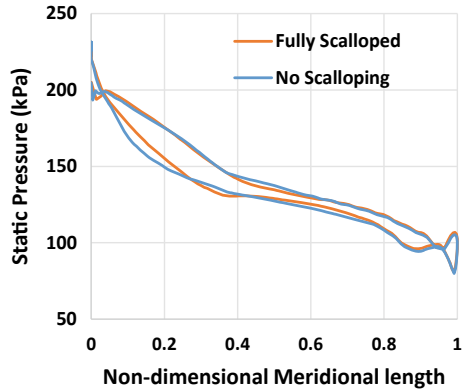


Fig. 11 Cross-flows in hub clearance region

Fig. 12 Rotor blade loading

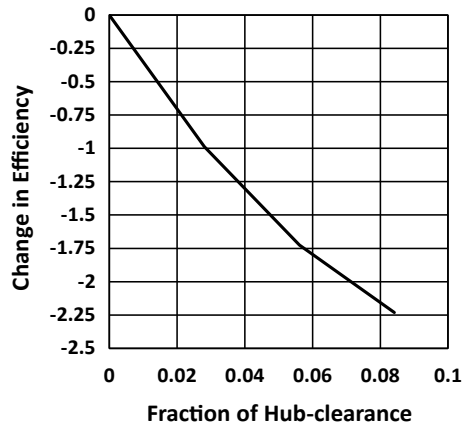


shows a comparison of blade loading of turbine blade at the hub location between a fully scalloped blade and a blade with no scalloping. The area enclosed by the blade loading curve is a measure of the work extracted by the turbine blade at this section.

As stated earlier, all analyses are converged for the same pressure ratio. It can be observed that the area enclosed by the curve is distinctly lesser in the case of the fully scalloped turbine blade as compared to the blade with no scalloping. Especially near the leading edge where the scalloping is done, this difference is marked. This translates to a reduction in power generated by the turbine which, for the same pressure ratio, translates to a reduction in stage efficiency as shown in Fig. 10.

To understand the effect of hub clearance on the performance of the radial turbine, analyses were carried out by varying the hub clearance values for a fixed depth of scalloping. Figure 13 shows the plot of hub clearance non-dimensionalized with inlet blade height versus change in efficiency. As expected, the efficiency decreases monotonically with increased hub clearance. It can be observed that the decrease in efficiency can be as high as 2.25% points in case of 8% hub clearance.

Fig. 13 Variation of efficiency with hub clearance



In the experimental investigation of the effect of various geometrical features of a radial turbine wheel on its performance, [8] observed that scalloping can contribute to a decrease in efficiency of 2 to 4 percentage points. This is in qualitative agreement with the numerical analyses that have been carried out as explained in this paper.

6 Conclusions

The effect of scalloping and hub clearance on the aerodynamic performance of a typical radial turbine stage of a turbocharger is studied using 3D NS analysis. Various depths of scalloping and hub clearances are modelled and meshed and analyzed using commercial software. It is observed that efficiency monotonically decreases with increase in both depth of scalloping and hub clearance. If the turbine wheel is scalloped to 25% of its meridional length, a drop in efficiency of 1.75 percentage points is observed. If the hub clearance is increased to 8% of inlet blade height, a drop in efficiency of 2.25% is observed. Thus, both of these parameters have considerable effect on the performance of the radial turbine and by extension, the turbocharger. The findings of this paper will help the designer to arrive at an optimal design which can take into account conflicting requirements such as aerodynamic efficiency, weight and inertia.

Acknowledgements The authors thank Director, GTRE, for giving permission to present this work.

References

1. Baines NC (2005) Fundamentals of turbocharging. Society of Automotive Engineers Inc
2. Bharathan RD, David John R, Sharad Kapil SV, Murty R, Kishore Prasad D (2017) Design and analysis of radial turbine for turbocharger application. In: Proceedings of the ASME Gas Turbine India Conference 2017
3. Rodgers C (1987) Small high pressure ratio radial turbine technology. VKI presentation
4. Rohlik H (1968) Analytical determination of radial inflow turbine design geometry for maximum efficiency. In: NASA-TN-D 4384
5. Whitfield A, Mohd Noor AB (1994) Design and performance of vaneless volutes for radial inflow turbines. Part 1: non-dimensional conceptual design considerations. Proc Instn Mech Engrs 208:199–211
6. Gu F, Engada A, Benisek A (2001) A comparative study of incompressible and compressible design approaches of radial inflow turbine volutes. Proc Instn Mech Engrs 215(A):475–486
7. Aungier RH (2006) Turbine aerodynamics: axial-flow and radial-inflow turbine design and analysis. ASME Press
8. Hiett GF, Johnston IH (1963) Experiments concerning the aerodynamic performance of inward flow radial turbines. Proc Instn Mech Engrs 1963–64:178
9. ICFD 19.2; “User Documentation,” ANSYS India Inc
10. ANSYS CFX 19.0; “User Documentation”, ANSYS India Inc

Effect of Various Periodic Surface Concepts for Numerical Investigation of Flow Field Through Variable Area LP Turbine Nozzle



Hardikkumar Bhavsar and Chetankumar Mistry

Abstract The gas turbine engine performance can be improved in off-design condition by using variable area nozzle turbine (VANT) concept as mass flow rate varies in off-design conditions. In order to analyze the flow field through VANT, second-stage LPT nozzle geometry was selected from EEE proposed by Pratt and Whitney, and its endwalls were modified. In the present study, meshing of the nozzle domain was done in ICEM CFD[®] due to the limitation of TurboGrid[®] which is discussed. For the numerical analysis, two-passage and one-passage fluid models were analyzed. It was found from two-passage analysis that due to the 3D geometry of the vane at LE, incidence effect was not properly captured. Hence, flow physics is not identical in two passages. Further, one-passage numerical analysis with and without varying the periodic surfaces at -5° , 0° , and $+5^\circ$ vane setting angle is performed. The results were analyzed in terms of static pressure field in the part clearances and total pressure loss coefficient. It is found that mass flow averaged total pressure loss coefficient changes within 3% range with change of different periodic surface concepts.

Nomenclature

C_{ax}	Axial chord
C_{pt}	Total pressure loss coefficient = $\frac{\overline{p_{0,in}} - p_0}{\overline{p_{0,in}} - p_{in}}$
C_{ps}	Static pressure coefficient = $\frac{p - \overline{p_{in}}}{\overline{p_{0,in}} - \overline{p_{in}}}$
p	Static pressure
$\overline{p_{in}}$	Mass flow averaged inlet static pressure
p_0	Total pressure
$\overline{p_{0,in}}$	Mass flow averaged inlet total pressure
EEE	Energy-efficient engine
LE	Leading edge

H. Bhavsar (✉) · C. Mistry

Department of Aerospace Engineering, Indian Institute of Technology, Kharagpur, West Bengal, India

e-mail: csmistry@aero.iitkgp.ac.in

LPT	Low-pressure turbine
LV	Leakage vortex
PS	Pressure surface
PSHSV	Pressure side horseshoe vortex
PV	Passage vortex
SS	Suction surface
SSHSV	Suction side horseshoe vortex
TE	Trailing edge
VANT	Variable area nozzle turbine

1 Introduction

The gas turbine engine is composed of several components. The performance of these components is dependent on the 3D, complex flow passing through their passage. In order to improve the performance of the components, flow physics of each component needs to be understood. This can be done by performing measurement of several parameters on the actual engine components. However, this task is very difficult as well as expensive. Also, in order to develop testing facility, it is a prior requirement to decide which parameters are required to measure and at which location. This can be understood by performing detail computational study on the selected component.

It is known that gas turbine engines are being used in several applications. Also, demand of shaft/thrust power of the gas turbine engine changes with time and operating conditions. Hence, for a quite vast period of life, engine needs to perform in the off-design condition where its mass flow requirement changes. This affects the performance of the engine. In order to operate engine near its design conditions, component flow area is required to change with change in mass flow rate. Variable area nozzle turbine (VANT) concept actively controls the performance of the gas turbine engine with change in power demand suggested by Roy-Aikins [1]. Karstensen and Wiggins [2] described the successful use of variable power turbine nozzle in various applications. Moffit et al. [3] investigated the VANT concept in single-stage turbine by varying the stator area from 70 to 130%. They found that turbine efficiency reduces at a given pressure ratio as vane setting angle was changed from design angle. Razinsky and Kuziak [4] used variable nozzle power turbine concept in GT 225 for various operating point including braking position. They observed improvement in specific fuel consumption at part-load condition as turbine inlet temperature can be kept higher. However, for mechanical movement of the vanes, part clearances are required to be accommodated near hub as well as tip endwalls and vane ends. These part clearances near both ends are responsible for occurrence of leakage flow due to the pressure gradient from PS to SS of the vane. Further, part of the leakage flow passing near the vane end surfaces has rotationality, which forms the leakage vortex within the nozzle passage. This leakage vortex mixes with the primary flow and passage vortex and increases the losses at the exit of the

nozzle. Razinsky and Kuziak [4] also observed increase in the efficiency of 0.7–4.0% when they sealed the vane ends.

Various researchers have performed study to analyze the leakage flow through turbine tip clearances. They have also concluded that 30% losses in the turbine passage are due to tip leakage flow. Hence, several studies have also been performed to mitigate or minimize the tip leakage flow by various methods. However, prior to apply some technique to inhibit the leakage flow, leakage flow field needs to be analyzed. For the VANT concept, as part clearances are required near hub and tip of the vane, leakage flow field needs to be analyzed at both the locations. Hence, present study aims to numerically investigate the leakage flow field near hub as well as tip clearance for the VANT concept. In the present study, second-stage 3D vane of the LPT from EEE proposed by Pratt and Whitney was selected. Details of which are given by Leach et al. [5]. The details about turbine stage and cascade are shown in Table 1. The effect of free stream turbulence and incidence angle on the selected original geometry was performed and reported by Bhavsar and Mistry [6]. Further, for the VANT, vane pivot is present in the either part clearances which also influences the flow within the part clearances. The modification of the hub and casing endwalls for VANT concept was done and reported by Bhavsar and Mistry [7]. In the ANSYS TurboGrid[®], it was not possible to define the vane with the pivot in either clearances for the domain discretization to numerically solve the flow field. Hence, fluid flow domain needs to be defined with periodic surfaces in the ICEM CFD[®] consisting of one or two passages. So far, various CFD studies for linear as well as annular cascade are reported, which mainly focus on the effect of change of incidence angles. In this study, as the vane is turned for the VANT concept, effect of periodic surface needs to be analyzed. Tallman and Lakshminarayana [8] used two passages for their numerical investigation on linear cascade using numerical method given by Basson and Lakshminarayana [9]. They defined one full blade, the periodic surface adjacent to PS of the central blade was formed as SS, and the periodic surface adjacent to SS of the central blade was formed as PS up to tip clearance region. In the tip clearance region, they define the periodic surface as mean camber line on both sides of the main blade.

Hence, in the present study, fluid domain with two passages (case—a) and one passage (cases b and c) was selected for the numerical analysis. Further, in case—b, periodic surfaces of fluid domain were kept constant as vane settling angle was

Table 1 Cascade and turbine parameters

	Hub	Quarter hub	Mean	Quarter tip	Tip
Inlet metal angle	32.7°	37.2°	41.7°	47.7°	52.2°
Exit metal angle	27.7°	21.5°	21°	20.5°	19.8°
Axial chord	4.907 cm				
Aspect ratio	2.65				
Flow coefficient	0.76				
Mean reaction	0.45				

changed. The case—b was not able to accommodate the variation of vane setting angle beyond $\pm 7^\circ$. Whereas in case—c, periodic surfaces were also varied with vane setting angle, and hence, it enables to investigate variation in vane setting angle beyond $\pm 7^\circ$.

2 Numerical Setup

This section discusses the construction of fluid flow model for three cases. It is followed by multiblock domain discretization in ICEM CFD[®] and is discussed with their limitations. The boundary conditions are discussed at the end of this section.

2.1 Fluid Flow Model

The fluid flow model with two passages is shown in Fig. 1a and denoted as case—a throughout the text. In this model, one 3D vane was placed and adjacent vanes were modeled as SS and PS at an angular pitch distance away from central vane. Hence, this model was able to capture the effect of vane turning for wide range of different setting angles. However, the fluid model of case—a has certain limitations in terms of domain discretization and effect of incidence angle as 3D vane in the annular passage was being analyzed here. This is discussed in the subsequent sections. The fluid model with one passage was analyzed having periodic surfaces at half angular pitch distance from the vane with two different cases, i.e., b and c.

In the case—b, the periodic surface was constructed using mean camber line and was kept for design vane setting angle as shown in Fig. 1b. Hence, this methodology imposes limit to perform numerical analysis on the vane setting angle beyond $\pm 7^\circ$. Further, in the case—c, periodic surface was constructed from mean camber line, and it was also changed with vane setting angle as shown in Fig. 1c.

2.2 Domain Discretization

In the present study, as mentioned earlier, part clearance flow field through VANT is numerically analyzed. Also, for VANT, pivot is an essential part which influences the part clearance flow field. Hence, multiblock domain discretization was done in the ICEM CFD[®]. H-type topology was used within the passage, and O-type topology was used near LE, TE, and around the pivot. From the grid sensitivity test performed in the previous study, a total of 40 elements were selected to be kept in the part clearance for all the cases. However, based on the change of geometry, minor re-distribution of the grid elements was done in various directions in each case. Overall comparison of number of elements is given in below Table 2. It is observed that case—a with

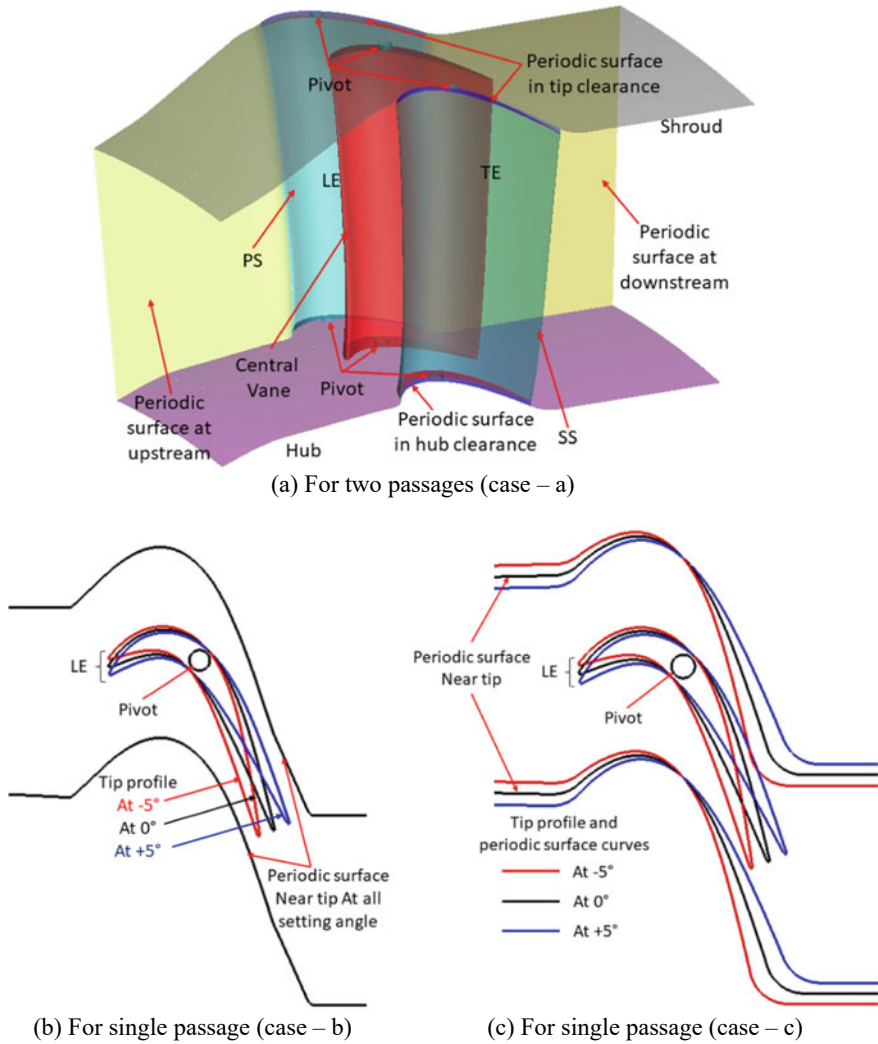


Fig. 1 Fluid domain definition for various cases

Table 2 Overall element count

	Case—a	Case—b	Case—c
Elements (millions)	6.88	3.2	4.3

two passages required 60% more elements than case—c. Hence, it demands more computational power and/or time. The discrepancy in the number of elements from case—b to case—c was due to the increase of spanwise number of grid elements. However, it is required to be noted that in the part clearances, all cases have same

number of elements. Further, limitation to analyze wide VANT setting angle range was limited as discussed in the previous sub-section for case—b.

2.3 Boundary Condition

The steady-state RANS equations were solved in commercially available software ANSYS CFX[®]. For the turbulence closure, two-equation shear stress transport (SST) model was selected. The experimental investigations are planned at IIT Kharagpur using sector annular cascade tunnel based on the present numerical study. Hence, boundary conditions were selected based on the real experimental condition. The inlet velocity of 50 m/s was given with the flow component based on the vane metal angle. The outlet static pressure was given as the atmospheric pressure, i.e., 101,325 Pa. All the walls, i.e., hub and casing endwall, vane surface, and pivot surfaces were given as adiabatic no-slip condition. The periodic surfaces were given as rotational periodic. Further, the RMS convergence criteria were kept as 10^{-6} , and pressure ratio across the passage was also monitored.

3 Results and Discussion

In this section, numerical results are analyzed for the various cases initially. The limitation of case—a to not properly capture the incidence effect in different passage is discussed first. The results of case—b are thoroughly discussed by Bhavsar and Mistry [7]. However, as mentioned earlier, using case—b analysis of $\pm 10^\circ$ setting angle change was not able to perform. Hence, detailed flow field for -10° to $+10^\circ$ setting angle change is discussed using geometry made by case—c.

3.1 Case—a

The flow field through two-passage case for design setting angle is shown in Fig. 2a and b using total pressure loss coefficient, C_{pt} near casing, and hub endwall, respectively. The C_{pt} contour at 0, 50, and 100% C_{ax} location from LE of the vane is shown. In Fig. 2a, total pressure loss due to the formation of the horseshoe vortex is observed near the casing endwall. However, it can be observed that the formation of the horseshoe vortex in both the passages is not identical.

This is denoted by A1 and A2 in the streamwise plane of Fig. 2a at LE of the vane. Further, the formation of the leakage vortex is also differed in streamwise plane shown at 50% C_{ax} distance downstream of the LE. It is observed that the leakage vortex in the region denoted by B1 is extended tangentially away from the suction side compared to leakage vortex denoted by B2. However, core of the leakage vortex

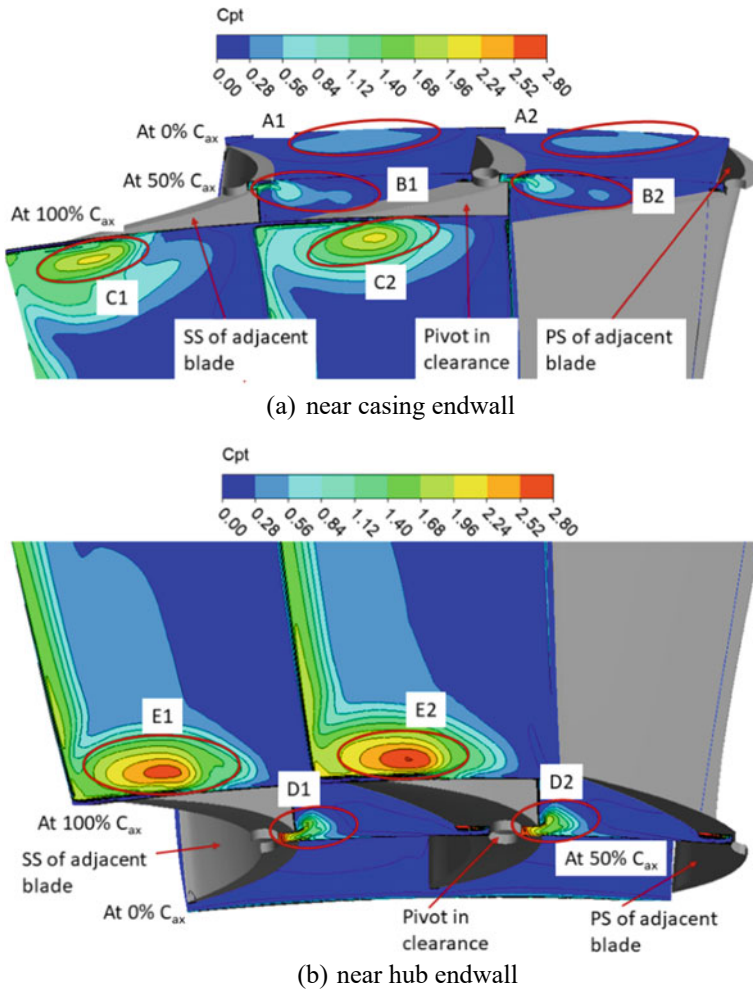


Fig. 2 Streamwise C_{pt} contour

remains near the SS as shown by $B1$. The significant effect of this can be observed in the plane located at TE of the vane. It is observed that the core of the total pressure loss region is elongated in the tangential direction as shown by $C1$. However, as leakage vortex (denoted by $B2$) was away from the SS at 50% C_{ax} location, total pressure loss region in the plane at TE is shifted away from the SS (denoted by $C2$).

Figure 2b shows the C_{pt} contour at similarly located plane near hub endwall. The plane located at LE of the vane does not show much discrepancy. The formation of leakage vortex differs minutely from each other at 50% C_{ax} location downstream of vane LE. The plane located at TE of the vane shows higher total pressure loss in the core shown by $E2$ compared to $E1$.

As the two passages are numerically analyzed, ideally contours should be identical in both the passages. However, the present numerical analysis is not able to capture ideal behavior. This can better be illustrated by observing the velocity distribution at different spanwise locations. It gives the effect of differences in flow incidence at the LE of central vane and partially modeled adjacent vanes. The Mach number contours at 25, 50, and 75% spanwise locations are shown in Fig. 3a–c, respectively.

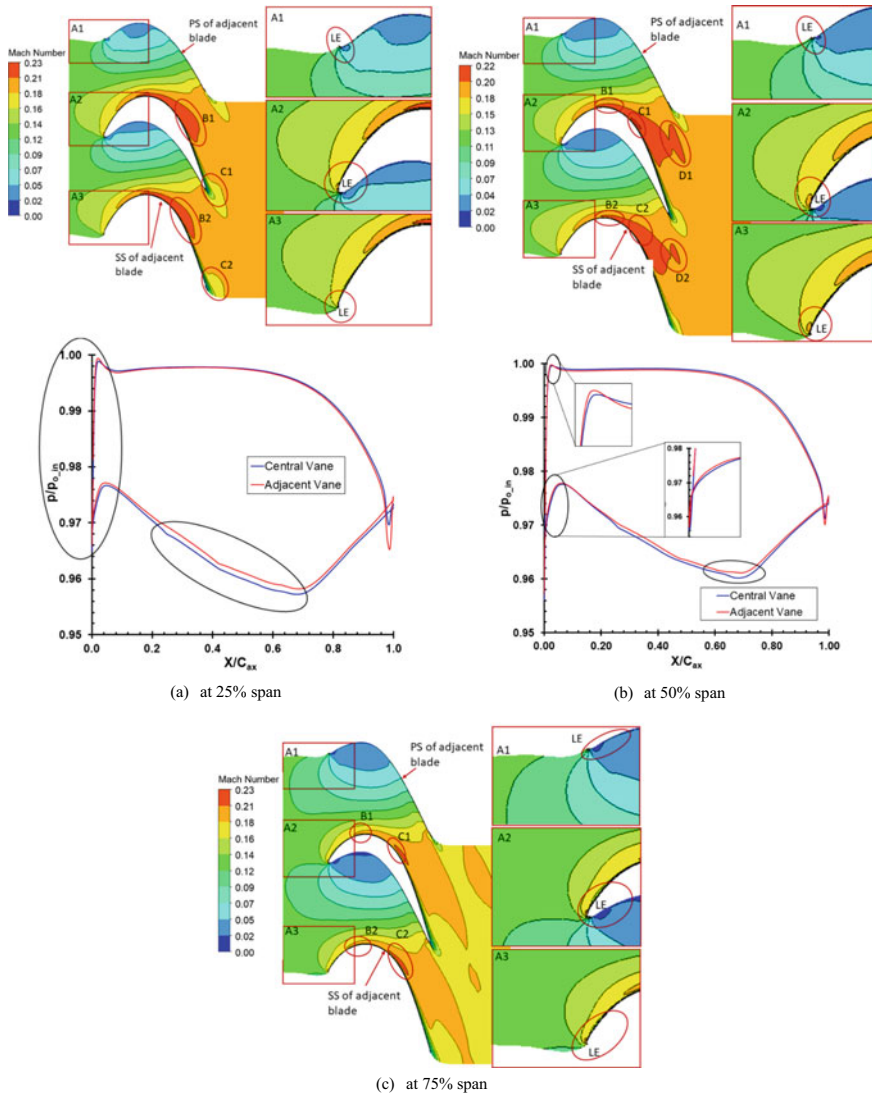


Fig. 3 Mach number contour at different spanwise locations

The enlarged view of LE of adjacent vane PS is denoted by A1, LE of central vane is denoted by A2, and LE of adjacent vane SS is denoted by A3 in all the figures.

Figure 3a shows the Mach number contour (upper part) and loading distribution (below part) at 25% span location. The discrepancy in the Mach number distribution at LE of central vane and adjacent vanes is clearly visible. From region denoted by A1, it is observed that on the PS of adjacent vane, flow accelerates just downstream of the LE and it again decelerates around 15% C_{ax} location from LE. However, A2 region shows that flow gradually accelerates downstream of LE on the PS of the central vane. Further, on the SS of central vane (region denoted by A2), minute region of acceleration is observed which is followed by deceleration, and around 15% C_{ax} location downstream of LE acceleration on the SS is observed. However, this kind of behavior is not observed on the SS of adjacent vane shown by region A3. Also, acceleration of the flow on the SS of central vane is observed earlier than on the SS of the adjacent vane. This change of flow incidence at the LE of central and adjacent vane affects the flow physics within the passage. However, these effects are clearly observed on the SS of the vane which are denoted by B1 and B2 near the throat and C1 and C2 near TE of the vane. This can also be seen from the pressure distribution shown in the below part of Fig. 3a.

Figure 3b shows the Mach number distribution at 50% span location. From A1 and A2 regions, it can be observed that on the PS, downstream of the LE, slightly larger extent of flow deceleration region is observed on the central vane compared to adjacent vane. This can also be seen in loading distribution shown in below part of the figure. This is seen by reduction of pressure value in the loading distribution. Further, on SS, downstream of the LE, larger extent of flow acceleration region is observed on the central vane compared to adjacent vane shown in A3. Due to this minor discrepancy in the incidence angle on the central and adjacent vanes, early acceleration at B1 is observed compared to B2. Similarly, higher Mach number in C1 region is seen compared to C2. Also, near TE, acceleration of larger portion of flow in the tangential direction is observed, which is denoted by D1 compared to D2.

Figure 3c shows the Mach number distribution at 75% span location. Here, discrepancies observed are: near LE, on PS of adjacent blade and central blade; early acceleration in B2 region compared to B1 region; and larger extent of acceleration in C2 region compared to C1 region.

Hence, from the above observed phenomenon, it can be concluded that numerical analysis of required vane turning angle for the VANT concept can be accommodated. Further, simulation of two passages requires 60% more grid elements compared to single passage as mentioned earlier. The increase in the number of grid elements increases the computational cost. However, the numerical results show that the flow field in both the passages is not identical. Hence, in the present study, further investigations of flow field are done using one-passage method.

3.2 Comparison of Case—B and Case—C

The comparison of numerical results obtained for case—b and case—c is discussed using Mach number contours. Due to the geometrical constraint of case—b, the comparison for -5° , 0° , and $+5^\circ$ vane turning angle is shown by Mach number contour at 50% span location in Fig. 4.

It should be noted that actual domain was made for one passage only. However, for better visualization, two passages are shown using instant transform tool of ANSYS CFD Post[®]. For all vane turning angles, it can be observed that most of the flow features are captured quite similar in both the cases. However, minor discrepancy is observed between cases b and c near LE and in the wake region for -5° vane

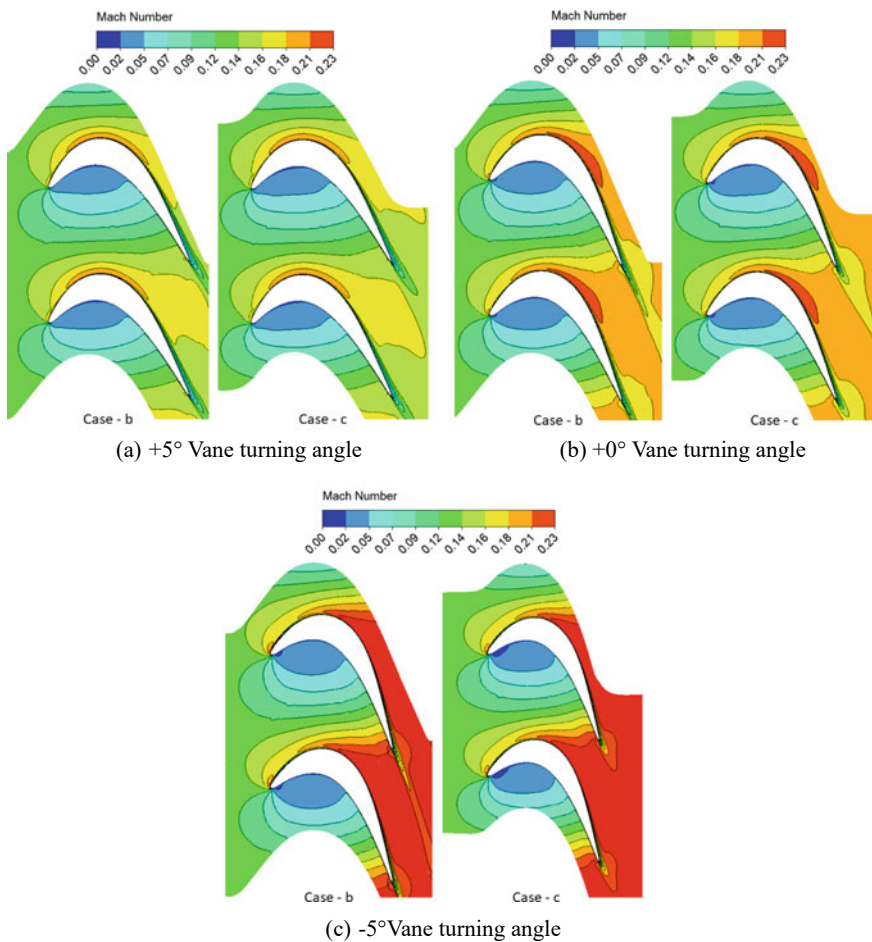


Fig. 4 Comparison of Mach number contour at 50% span for case—b and case—c

turning angle. It should be noted that both the cases were discretized and simulated individually. Hence, computational error of the numerical solution might lead to such small discrepancies in the Mach number contours. Further, it is seen that as the vane setting angle is changed from $+5^\circ$ to -5° , the throat area reduces and Mach number increases.

The static pressure coefficient— C_{ps} comparison between case—b and case—c in the hub as well as tip side part clearances are shown with velocity vectors in Figs. 5 and 6, respectively. Figure 5a–c shows the C_{ps} contour for $+5^\circ$, 0° , and -5° setting angles. As the vane setting angle is changed from $+5^\circ$ to -5° , the throat area reduces. Hence, flow velocity increases within the passage and static pressure reduces. Also, the throat area shifts from 73% C_{ax} to 84% C_{ax} location downstream of the LE as vane setting angle changed from $+5^\circ$ to -5° . The leakage flow through the hub side part clearance occurs due to the presence of pressure gradient from PS to SS. The maximum pressure gradient for the leakage flow to be occurred is observed near PS of the vane in both hub as well as tip side part clearances. The flow gets deflected due to the presence of the circular pivot in the part clearance. Hence, flow recirculation region is observed toward the SS from the pivot. This region is denoted by the ‘RC’ in all the figures. The recirculation region reduces in extent as vane setting angle is changed from $+5^\circ$ to -5° . Further, the presence of pivot puts discontinuity in the favorable pressure gradient near PS. The favorable pressure gradient region in the upstream of the pivot is denoted by A1 and in the downstream of the pivot is denoted by A2. There is a greater effect of vane turning angle observed on the region A2 compared to A1. As the vane turning angle is changed from $+5^\circ$ to -5° , the magnitude and extent of favorable pressure gradient increase significantly in the downstream direction of the pivot location, i.e., region A2.

The C_{ps} distribution for the case—b and case—c is compared in Fig. 5a for $+5^\circ$ vane turning angle. The discrepancy in the value of C_{ps} is observed mainly from the RC region to the throat region. This discrepancy reduces for the 0° vane setting angle case shown in Fig. 5b and vanishes for the -5° vane setting angle case which is shown in Fig. 5c. The difference of C_{ps} distribution in the tip side part clearances is observed between case—b and case—c for all the vane turning angles as shown in Fig. 6. This difference is clearly seen in the favorable pressure gradient region upstream of the pivot denoted by region A1 as well as between the RC and throat location. The difference of C_{ps} distribution near throat region reduces as vane turning angle is changed toward -5° . Further, very minor difference in the region A2 is observed for all the cases.

3.3 Exit Flow Field Comparison

The total pressure loss coefficient, i.e., C_{pt} , at the exit of the cascade is shown for cases—a, b, and c at $+5^\circ$ vane turning angle using contour plot in Fig. 7a–c, respectively. Due to the provision of part clearances near hub and casing endwalls, leakage flow occurs and part of it forms the leakage vortex. This leakage vortex

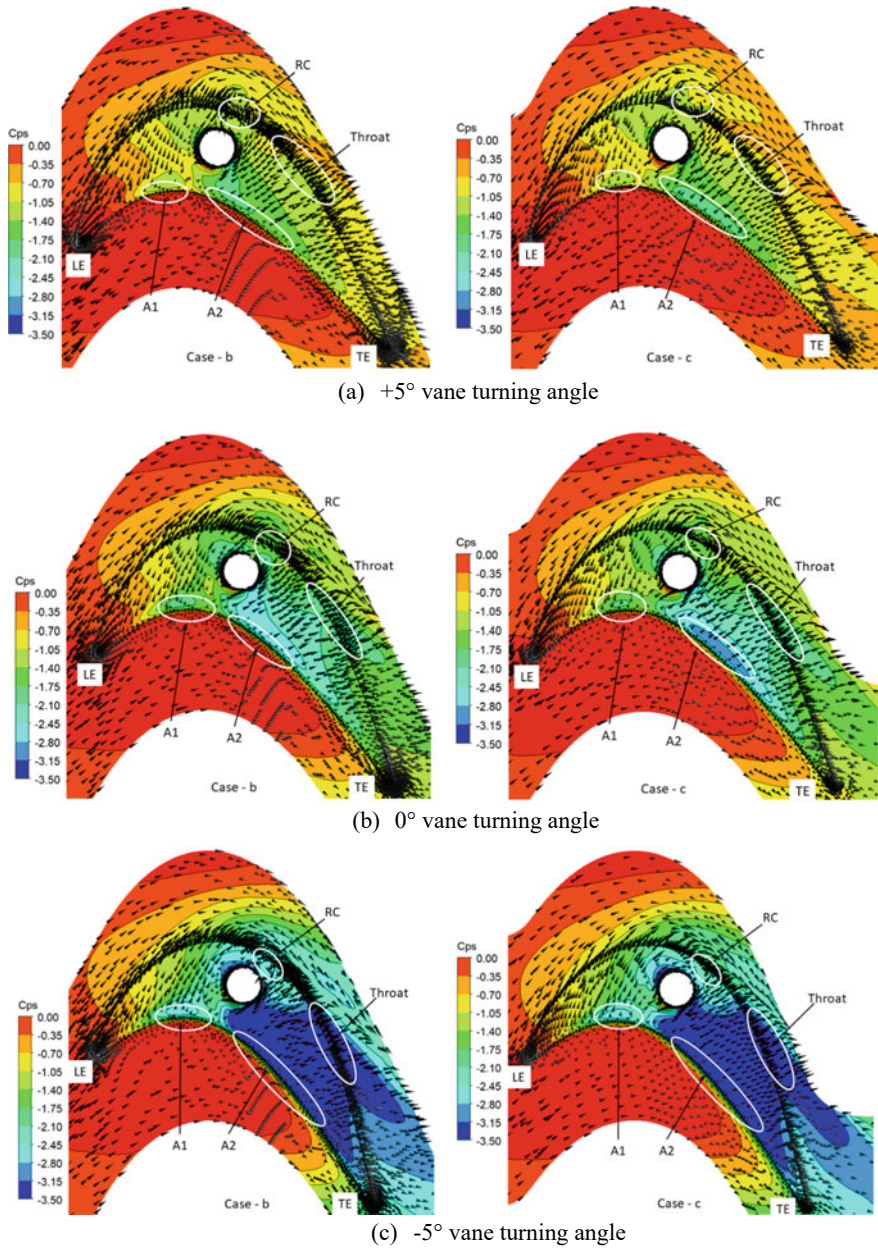
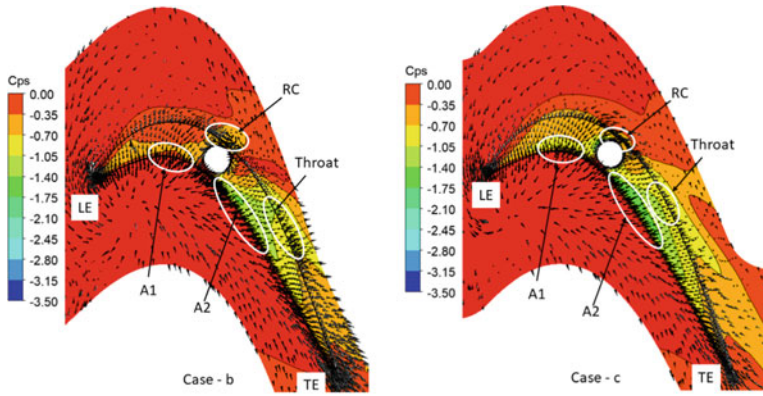
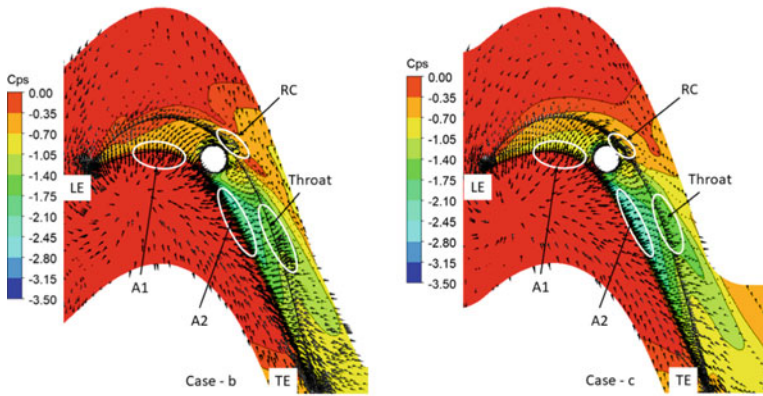


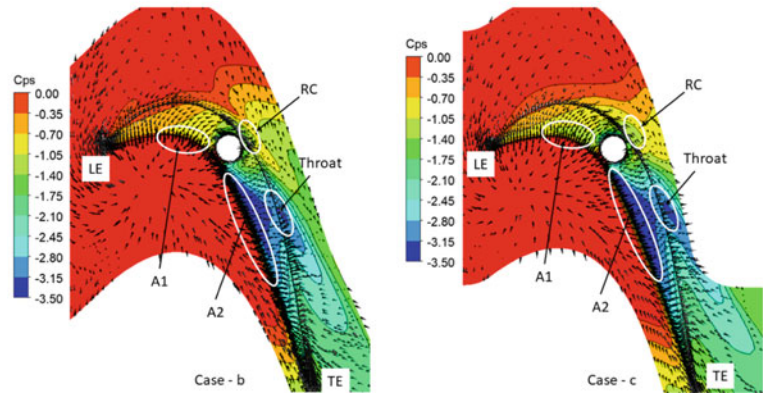
Fig. 5 Static pressure coefficient and velocity vector in hub side part clearance



(a) +5° vane turning angle



(b) 0° vane turning angle



(c) -5° vane turning angle

Fig. 6 Static pressure coefficient and velocity vector in tip side part clearance

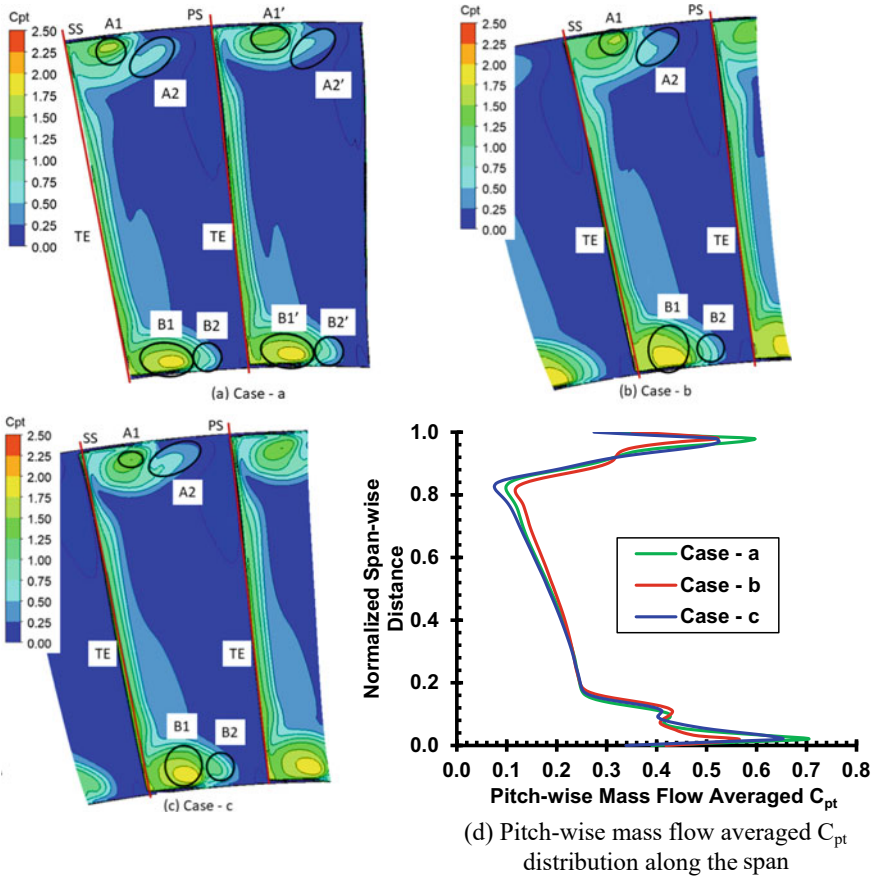


Fig. 7 C_{pt} comparison at the exit of the cascade for $+5^\circ$ vane turning angle

merges with the passage vortex, and hence, two loss regions are seen near each endwalls. These are denoted by A1 and B1 near casing and hub endwall, respectively. It is evident that for case—a, due to the non-identical prediction of incidence angle and flow field in two different passages, total pressure loss region associated with hub and tip leakage vortex differs in size. This is denoted by A1 and A1', A2 and A2', and B1 and B1'.

It can be observed that case—b predicts the larger extent of loss core in the region A1. Also, near the casing endwall, larger spanwise extent of the loss region is observed for case—b, i.e., from casing endwall to 84% of span compared to case—c, i.e., up to 86% of span. However, case—c predicts the larger extent of the loss region in the tangential direction, which is denoted by A2. This can be observed by higher pitch-wise mass flow averaged C_{pt} value in Fig. 7d, from 92% of span to 97% of span for case—c. Further, almost similar pitch-wise mass flow averaged C_{pt} peak value is predicted at 97 and 98% of the span for case—c and case—b, respectively,

(shown in Fig. 7d) whereas case—a predicts 13% higher peak value of C_{pt} . Similar to casing endwall region, extent of the core loss region near hub endwall denoted by $B1$ reduces for case—c. The spanwise extent of the loss region is up to 16% of span for case—b compared to 14% of span for case—c, and for case—a, it is near 12% of span. However, extended loss region in the tangential direction is seen for case—c which is denoted by $B2$. Further, peak in pitch-wise mass flow averaged C_{pt} value is observed for case—a at 2% span.

Figure 8a–c shows the C_{pt} contour for cases—a, b, and c, respectively, for 0° vane turning angle. Here also, core of the loss region is not seen as identical for case—a ($A1$ and $A1'$, $A2$ and $A2'$). Near the casing endwall, larger extent of the core loss region denoted by $A1$ is observed for case—b compared to cases—a and c. Further, the loss region from casing endwall is extended up to 82.5% of span for case—b compared to 85% of span for case—a and 86.5% of span for case—c.

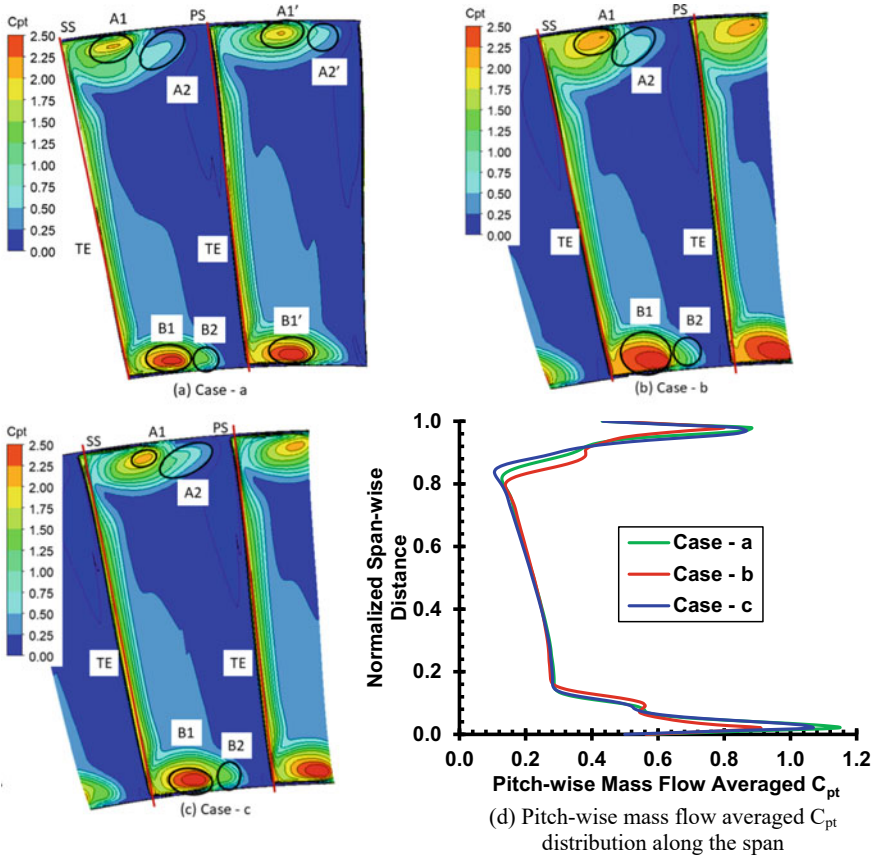


Fig. 8 C_{pt} comparison at the exit of the cascade for 0° vane turning angle

Also, cases—*a* and *c* predict the larger extent of loss region in the tangential direction denoted by *A2* and *A2'* compared to case—*b*. Hence, higher pitch-wise mass flow averaged C_{pt} value is seen in Fig. 8d from 92% of span to peak at 97% of span for case—*c* and peak at 98% of span for case—*b*. The peak C_{pt} value increased by 8.5% near casing endwall for case—*c*. Further, case—*a* predicts even higher peak C_{pt} value by 10% at 98% span. Near the hub endwall, extent of the core loss region denoted by *B1* reduces for case—*c* compared to case—*b*. The spanwise extent of loss region is observed up to 15% of span for case—*b* and 13% of span for case—*c*. However, for case—*c*, due to the larger extent of loss region denoted by *B2* increases the pitch-wise mass flow averaged C_{pt} value from hub endwall to 7% of span. The peak C_{pt} value increases by 17% for case—*c* compared to case—*b*. Here also, case—*a* predicts 25% higher peak C_{pt} near hub endwall.

Figure 9*a–c* shows the C_{pt} contour at the exit of the cascade for cases—*a*, *b*, and *c* at -5° vane turning angle, respectively. Figure 9*d* shows the pitch-wise mass flow averaged C_{pt} distribution for both the cases along the span at the exit of the cascade.

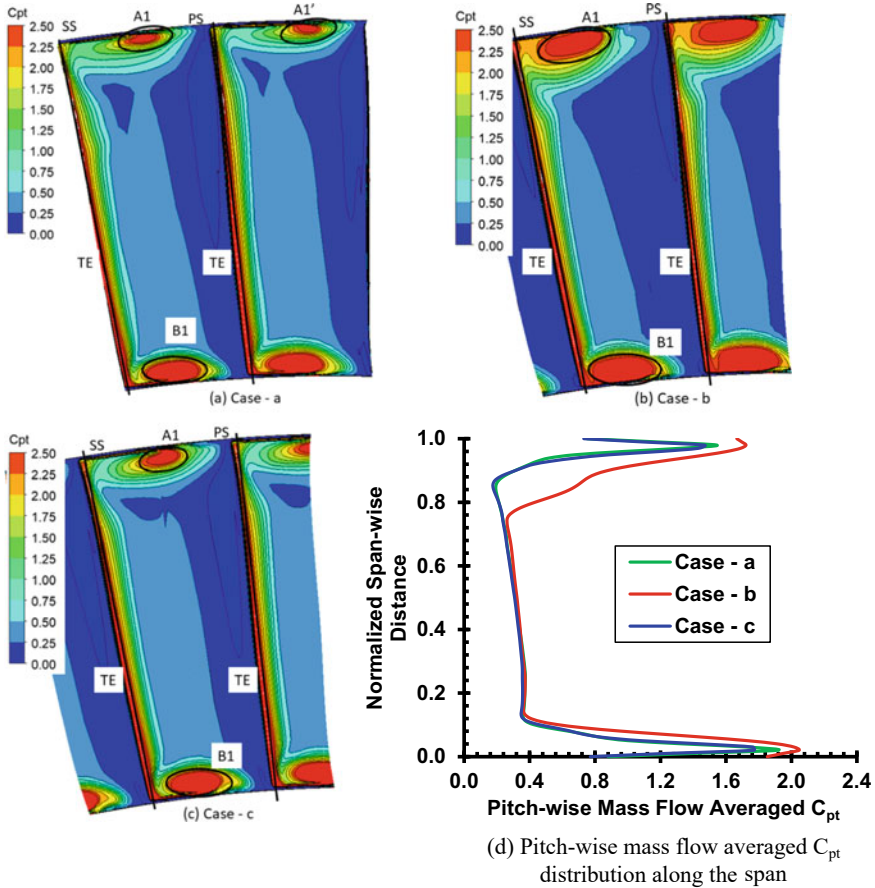


Fig. 9 C_{pt} comparison at the exit of the cascade for -5° vane turning angle

It is seen that core loss region near casing endwall denoted by $A1$ starts by 0.7° away from the SS for case—b compared to 1.8° away from SS for cases—a and c. Further, in the tangential direction, it occupies 2.2° for case—b compared to 1.5° and 1.4° for cases—a and c, respectively. The loss region lies from casing endwall to 84% of span for case—b compared to 88.5% of span for cases—a and c. The pitch-wise mass flow averaged C_{pt} increases from 75% span for case—b, and 17% higher peak value is predicted at 98% of span for case—b. The case—a predicts 5% higher peak C_{pt} value at 98% span. The extent of the loss region near hub is denoted by $B1$ reduces for cases—a and c insignificantly. However, peak value of mass flow averaged C_{pt} increases by 8% for case—a and by 15% for case—b compared to case—c.

The effect of change of periodic surfaces on the exit velocity flow angle is shown in Fig. 10a–c for $+5^\circ$, 0° , and -5° vane turning angle, respectively. The exit velocity flow angle changes linearly with change in vane turning angle, i.e., at $+5^\circ$ vane turning angle, it is around 30° , at 0° vane turning angle, it is 25° , and at -5° , it is 20° . However, at particular vane turning angle, pitch-wise mass flow averaged exit velocity flow angle shows discrepancy from 78% span to 95%.

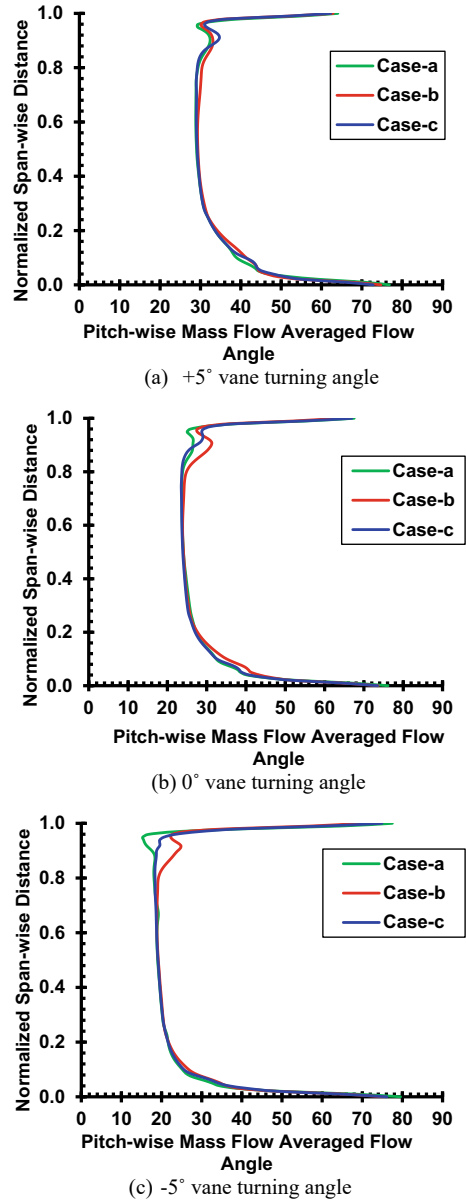
In order to quantify overall total pressure loss, mass flow averaged total pressure loss coefficient is obtained at the exit of the cascade for various vane turning angle in cases—a, b, and c. The obtained values are shown in Fig. 11. As already seen from the total pressure loss contour and its pitch-wise mass flow averaged distribution along the span, for -5° vane turning angle, highest total pressure loss is observed. The mass flow averaged total pressure loss reduces to minimum at $+5^\circ$ vane turning angle due to reduction of mixing and viscous dissipation as kinetic energy reduces for the opening position. The case—a predicts higher losses for all vane turning angles. Also, it can be noted that the difference in the mass flow averaged C_{pt} values for various vane turning angles in cases—a, b, and c is not more than 3%. However, method used in case—c gives wide range of VANT to be analyzed with lesser number of grid points.

4 Conclusion

The present study focuses on the numerical investigation of part clearance flow field near hub as well as casing endwall for the VANT concept. In order to numerically investigate the VANT concept, three different methods were used for the modeling of periodic surface. Based on the results, certain conclusions are made which are shown below:

1. Case—a was modeled with two passages that can accommodate wide range of vane turning angle for the VANT concept. This method includes one central vane and either side adjacent vanes were partially modeled with PS/SS. As the

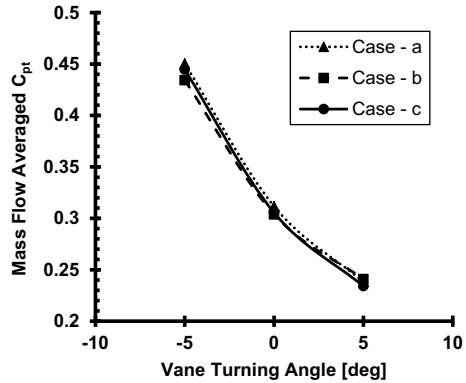
Fig. 10 Exit velocity flow angle distribution



adjacent vanes were partially modeled, due to the 3D geometry of the vane, incidence angle was not captured identically in both the passages. Also, it required 60% more grid elements which increases the computation cost.

2. Case—b was modeled with one vane and constant periodic surfaces of designed setting angle at half angular pitch distance on either side of the vane. However,

Fig. 11 Mass flow averaged C_{pt}



using this concept was not able to accommodate wide range of vane setting angle.

3. In the case—c periodic surfaces were modified as per change of vane setting angle. Hence, this method accommodates wide range of vane setting angle for the VANT concept.
4. From the comparison Mach number contour plot at 50% span location for case—b and case—c, it was observed that due to unavoidable computational errors, minor discrepancies were observed. Also, as the static pressure coefficient contours were compared in the tip side part clearance, discrepancies in the upstream part of the pivot were observed. This discrepancy reduces as the vane turning angle was changed toward -5° .
5. From the C_{pt} distribution at the exit of the cascade, it is seen that case—b predicts higher loss in the core of the loss region. Also, it predicts larger extent of the loss region in the spanwise direction, whereas case—c predicts larger extent in the tangential direction.
6. The difference in the overall mass flow averaged total pressure loss coefficient value at the exit of the cascade within 3% for $\pm 5^\circ$ vane turning angles between cases—a, b, and c. This difference is 0.54% for 0° vane setting angle when periodic surfaces remain almost similar in both the cases between case—b and case—c. This difference increases between cases—a and c for 0° vane turning angle to 2%. This might be due to incorrect prediction of incidence angle in two passages and unavoidable numerical errors.

References

1. Roy-Aikins JEA (1988) A Study of variable geometry in advanced gas turbines. PhD. Thesis, Cranfield Institute of Technology
2. Karstensen KW, Wiggins JO (1989) A variable geometry power turbine for marine gas turbines. In: Gas turbine and aeroengine congress and exposition. Toronto, Ontario

3. Moffitt TP, Whitney WJ, Schum HJ (1969) Performance of a single stage turbine as affected by variable stator area. In: AIAA 5th propulsion joint specialist conference. Colorado, pp 69–525
4. Razinsky EH, Jr WRK (1977) Aerothermodynamic performance of a variable nozzle power turbine stage for an automotive gas turbine (77):587–592
5. Leach K, Thulin R, Howe D (1982) Energy efficient engine turbine intermediate case and low pressure turbine component test hardware detailed design
6. Bhavsar HM, Mistry CS (2019) Numerical study of part clearance and free stream turbulence on high end-wall LP turbine nozzle annular cascade. In: Proceeding of the ASME 2019 gas turbine India. IIT Madras
7. Bhavsar HM, Mistry CS (2020) Numerical investigations on the effect of pivot shapes in part clearance flow field of variable area LP turbine nozzle vane. In: Proceeding of the ASME 2020 turbo expo virtual conference
8. Tallman J, Lakshminarayana B (2001) Methods for desensitizing tip clearance effects in turbines. In: Proceeding of the ASME turbo expo 2001. New Orleans
9. Basson AH, Lakshminarayana B (1995) Numerical simulation of tip clearance effects in turbomachinery. ASME J Turbomach 109(4):545–549

Numerical Investigation of Aerodynamic Performance Parameters in Linear Blade Cascade for High-pressure Turbine



Nitish Kulkarni, D. Harish, R. D. Bharathan, Sharad Kapil,
S. V. Ramana Murthy, R. Senthil Kumaran, and D. Kishore Prasad

Abstract The function of the turbine aerofoil is to turn the flow to a certain angle and provide smooth flow acceleration to a certain Mach number with minimum pressure loss. The flow field in the blade passage is complex, unsteady, transonic, and three dimensional. So, to aerodynamic designer, it is necessary to evaluate the profile losses and other aerodynamic performance parameters to improve the efficiency of the turbine stage. In the present study, CFD simulation has been carried out for the high-pressure turbine nozzle guide vane (NGV) profiles for design and off-design conditions. Parameters such as profile loss coefficient, surface Mach number distribution, and flow deflections are investigated. The results obtained from numerical analysis are compared with experimental data from transonic cascade tunnel.

Keywords CFD analysis · Pressure loss coefficient · Surface Mach no distribution · Flow deflection · Cascade test results

N. Kulkarni · D. Harish · R. D. Bharathan (✉) · S. Kapil · S. V. Ramana Murthy ·
D. Kishore Prasad

DRDO-Gas Turbine Research Establishment, Bengaluru, India

e-mail: bharathan.gtre@gov.in

D. Harish

e-mail: harishd.gtre@gov.in

S. Kapil

e-mail: sharadkapil.gtre@gov.in

S. V. Ramana Murthy

e-mail: ramanamurthy.gtre@gov.in

D. Kishore Prasad

e-mail: kishoreprasadd.gtre@gov.in

R. Senthil Kumaran

CSIR-National Aerospace Laboratories, Bengaluru, India

e-mail: rsk@nal.res.in

Nomenclature

C	Blade Chord
C_{ax}	Axial chord
h	Blade height
HP	High Pressure
I	Incidence angle
k	Turbulence kinetic energy
M_2	Outlet Mach number
M_{is}	Surface Mach number
NGV	Nozzle Guide Vane
P_{01}	Inlet Total Pressure
P_{02}	Outlet Total Pressure
P_s	Outlet static Pressure
s	Pitch
SST	Shear Stress Transport
X	Axial distance from leading edge
Y_p	Pressure loss coefficient
γ	Specific heat ratio

1 Introduction

Gas turbine engines used in advanced fighters need high thrust to weight ratio and low-specific fuel consumption to meet high maneuverability, long range, and low-life cycle cost requirements. To meet high thrust to weight ratio and low-specific fuel consumption, aerogas turbine engines demand high-turbine entry temperature and compressor pressure ratio. A highly efficient turbine is required to maximize the work that can be extracted for a given pressure ratio. The flow in the turbine is highly complex, unsteady, transonic, and three dimensional. The reduction in efficiency is due to a variety of losses such as profile losses, secondary losses, tip clearance losses, and cooling losses. Hence, understanding the contribution from each of these losses is of prime importance.

During preliminary design, correlations are extensively used to predict the losses in the sections. Ainley and Mathieson [1] proposed correlations to calculate the pressure losses and deviation angle. The authors assumed that pressure loss correlations are independent of Mach numbers, and exit angle is independent of incidence angle. Dunham and Came [2] suggested Mach number and Reynolds number correction factors to earlier proposed correlations by Ainley and Matheson [1]. Kacker and Okapuu [3] further modified these correlations to improve the loss prediction. Denton [4] carried out a detailed study on losses in turbomachines and derived the correlation for increase in entropy due to losses. Mee et al. [5] experimentally investigated losses of transonic turbine blade cascade and provided the effect of Mach no. on

Table 1 NGV mean section parameters

Parameters	Values
h/C	2.9
S/C	0.73
Design Mach no.	0.98
Outlet angle	71.25°

boundary layer losses and also gave the effect of shock loss and mixing loss. At the midspan of the blade, the aerodynamic performance of a transonic turbine cascade for different exit Mach no. and for different incidence angles was studied by Jouini et al. [6]. Andrey Granovski et al. [7] examined both experimentally and numerically the influence of unguided turning angle and trailing edge shape on profile loss of transonic turbine blades. Over the last 70 years, these correlations have been updated based on the rig test data that are available to the authors. These studies suggest that the losses in high- and low-pressure turbine aerofoil are influenced by flow turning angle, blade loading, number of aerofoils, and inlet boundary layer profile.

In this study, numerical investigation is carried out to estimate the pressure loss coefficient and aerodynamic parameters like surface Mach number distribution, exit flow deflection for midspan section of the HP turbine NGV for different outlet Mach numbers. These parameters are estimated for -10 , 0 , and 10° incidences. Also computational results are compared with the experimental results obtained for the same profile in transonic cascade tunnel (TCT).

2 Methodology

2.1 Modeling

The fluid domain has modeled in CAD software and same geometrical dimensions maintained as per aerofoils tested in TCT, National Aerospace Laboratories (NAL). The geometrical features for the NGV are given in Table 1.

The fluid domain consists of two NGVs which are placed at 1 pitch distance to define proper boundary condition and for ensuring adequate flow development, inlet and outlet are extended one axial chord from leading and trailing edge, respectively.

2.2 Grid Generation

The computational grid is generated using ICEM-CFD 16.0 software. The grid is passage centered, multiblock, structured, and hexahedral. The grids are made finer at the regions where high gradients are expected in the flow field. Grid independence

analysis is carried out, and the variation of profile loss with grid size is shown in Fig. 1. At 1.5 million grids, the solution becomes grid independent. Therefore, it is finalized for the NGV domain.

Sufficient grid points are placed near the aerofoil to resolve the boundary layer. The skewness achieved for the grid is between 25 and 150°, and $y+$ value for finalized NGV grid is maintained below 1. The aspect ratio is less than 100, and expansion ratio is less than 1.2. The passage centered grid for NGV is as shown in Fig. 2.

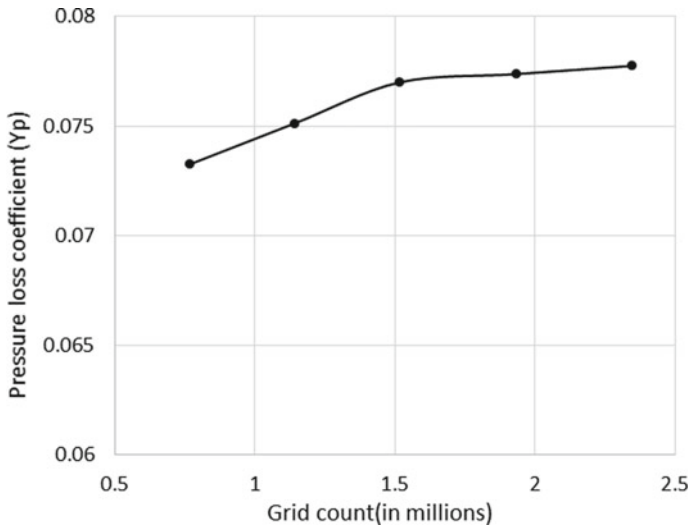


Fig. 1 Grid independency study for NGV fluid domain

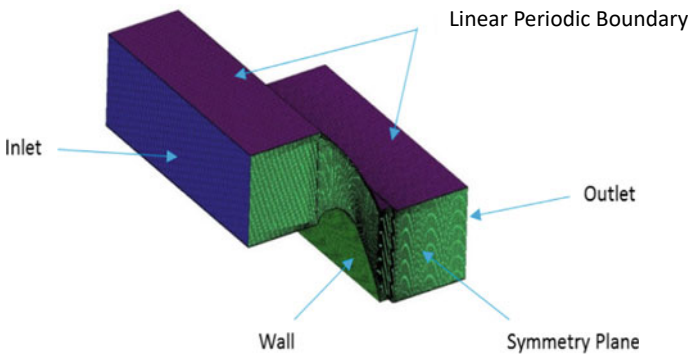


Fig. 2 Computational domain for NGV

2.3 CFD Solver and Boundary Condition

Ansyes CFX-16.0 solver is used to solve the Navier-Stokes equation. CFX solver is based on finite volume approach and is capable of solving complex multidimensional fluid flow problems. The turbulence effect is modeled by using $k-\omega$ SST turbulence model. The advantage of two equation $k-\omega$ SST turbulence model is that it predicts highly accurate flow separation at adverse pressure gradient conditions.

The boundary conditions are inlet total pressure, inlet total temperature, and outlet average static pressure. The top and bottom surfaces are symmetrically placed at one pitch distance and provided with translational periodicity to obtain similar flow condition as linear cascade test. The walls are assumed to be adiabatic and no slip walls.

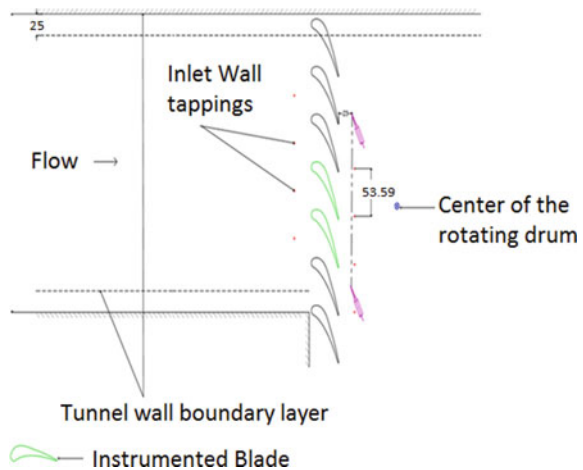
2.4 Linear Cascade Testing

Linear cascade testing is the simplified experimental method for evaluating aerodynamic performance of turbo machinery aerofoils where Coriolis forces and curvilinear effects are ignored. Three dimensional flows can be simplified to two dimensional flows by eliminating the radial component of velocity using linear cascade. A linear cascade is an array of aerofoils stacked at uniform pitch and stagger representing a section of turbo machinery blade rows.

The present study is carried out in TCT, NAL, Bangalore. TCT is a quasi-continuous blow down tunnel. The size of test section is 153×500 mm. The height of the test section is adjustable from 500 to 200 mm.

The schematic view of the mean cascade assembly in the transonic cascade tunnel is shown in Fig. 3. Flow velocity in the test section can be varied by controlling the

Fig. 3 Schematic view of NGV mean cascade in TCT



pressure in the settling chamber with the help of an automatic pressure regulator valve. Inlet total pressure and total temperature are measured in a settling chamber using a pitot tube and thermocouples, respectively. Inlet static pressure and outlet static pressure are measured from test section side wall tapings. A five-hole wedge probe is mounted downstream of the blade trailing edge at the expected outlet flow angle to measure the wake flows. One aerofoil is instrumented along the suction side for surface static pressure measurements, while another aerofoil is instrumented on the pressure side. Scanivalve system and electronic pressure scanners are used for blade surface pressure measurement. The pressures were measured with an accuracy of $\pm 172 \text{ N/m}^2$, and the flow angle was measured with an accuracy of $\pm 0.2^\circ$. Maximum uncertainty in the Mach number was ± 0.02 .

3 Results and Discussion

In this section, the effect of incidence angle and exit Mach no. on the NGV cascade has been numerically predicted and compared with the experimental data.

There are many different loss coefficient definitions to study the turbine losses, but the pressure loss coefficient is most commonly used in cascade studies, because it is easy to calculate from cascade test data. The stagnation pressure loss coefficient for turbine is defined as

$$Y_p = \frac{(P_{01} - P_{02})}{(P_{02} - P_s)} \quad (1)$$

Figure 4 shows the variation of pressure loss coefficient for mean section of the cascade with the exit Mach no. ranging from 0.6 to 1.1 and for incidence angles -10° , 0° , and 10° . The pressure loss coefficient at midspan of the NGV is calculated using Eq. (1) by obtaining area-averaged total and static pressures at cascade exit. The results obtained from CFD investigation have been compared with experimental data, and the experimental results closely match the numerical results for subsonic exit Mach number 0.6–0.9.

There is steep rise in pressure loss in the transonic outlet Mach no. regime due to formation and strengthening of the shock wave, but surprisingly, the loss coefficient observed from computational studies is lower compared to experimental results for Mach no. 1.0 and 1.1. There is no variation observed in pressure loss coefficient for different incidence angles between Mach no. 1.0 and 1.1. This shows that shock losses dominate over the incidence losses in this regime.

The blade to blade Mach number distribution for mean section of the NGV at the exit Mach number 1.0 is shown in Fig. 5. From the contour plot, it is clearly observed that there is no flow separation in the flow passage. Also, wake and shock formation downstream of the blade passage is captured in this contour plot.

The surface Mach number plot shown in Figs. 6 and 7 is obtained using surface static pressure measurement as well as upstream total pressure measurement as shown in Eq. (2).

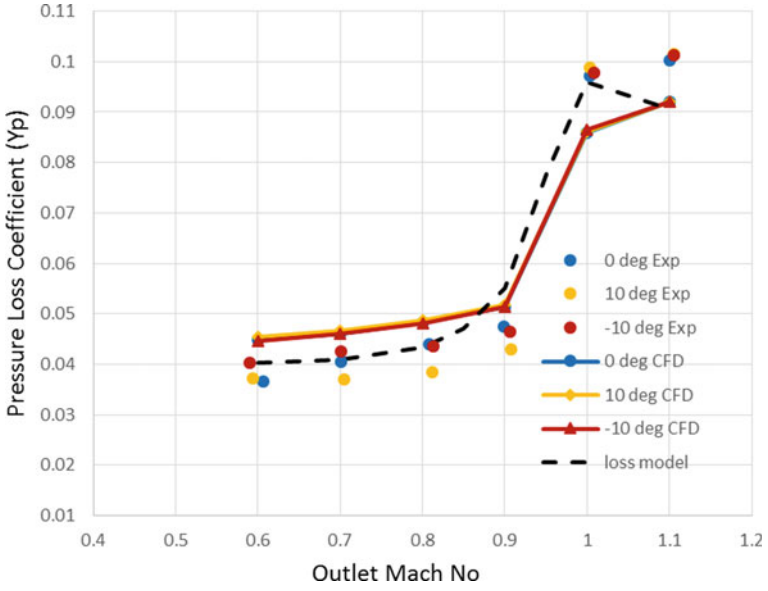


Fig. 4 Variation in pressure loss coefficient for different outlet Mach number

Fig. 5 Mach number contour for the NGV $M_2 = 1.0$

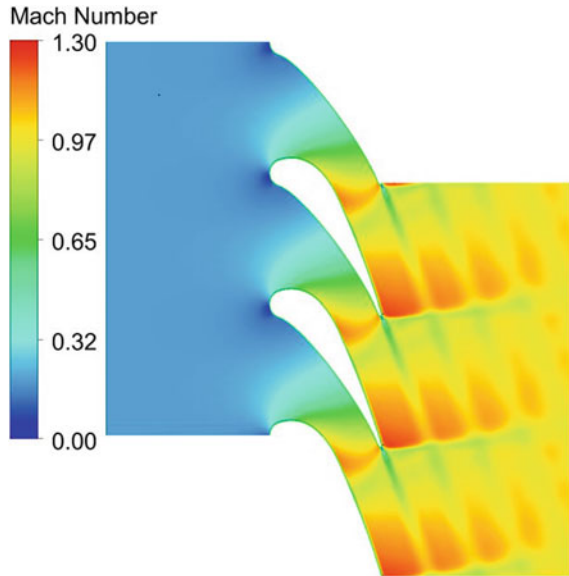


Fig. 6 Surface Mach number distribution of NGV for $M_2 = 0.6$

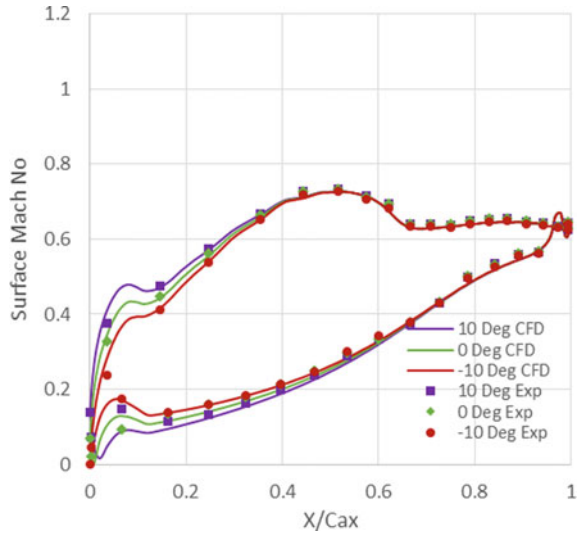
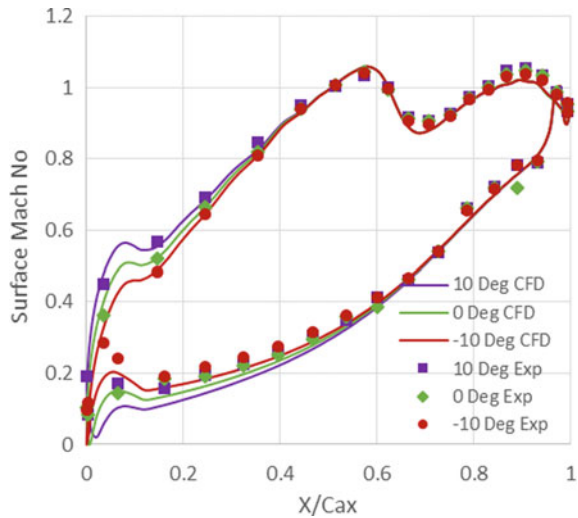


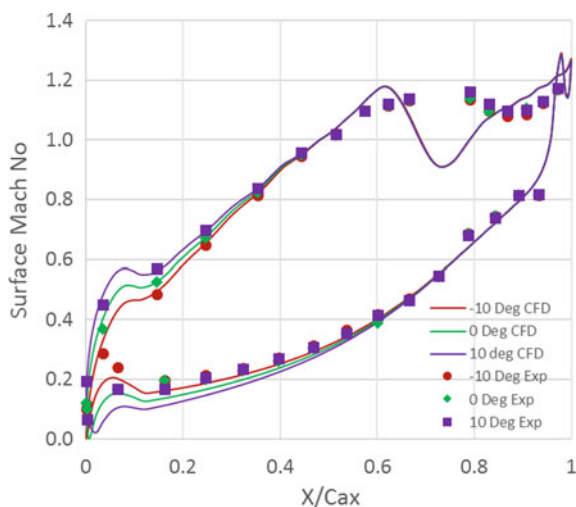
Fig. 7 Surface Mach number distribution of NGV for $M_2 = 0.9$



$$M_{is} = \sqrt{\frac{2}{(\gamma - 1)} \left\{ \left(\frac{P_{01}}{P_s} \right)^{\left(\frac{\gamma - 1}{\gamma} \right)} - 1 \right\}} \quad (2)$$

Figures 6, 7, and 8 show the surface Mach number plot for exit Mach number of 0.6, 0.9, 1.0 and different incidence $-10^\circ, 0^\circ, 10^\circ$. It can be observed that the drop in local Mach number passed the throat point on the suction side becomes increasingly sharp with increase in exit Mach number. At around 0.6 Mach number, the slight drop

Fig. 8 Surface Mach number distribution of NGV for $M_2 = 1.0$

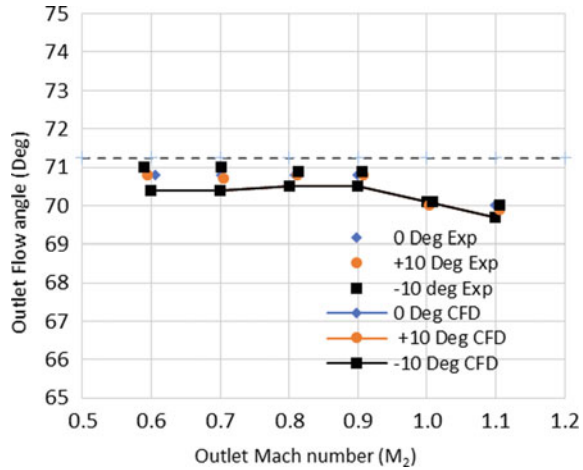


in local Mach number at the throat is due to flow not being guided by the neighboring aerofoil. At around Mach number 1.0, a shock is observed (see Fig. 5) near the throat region which results in a sharp decrease in local Mach number. The surface Mach number is calculated for mean section of the NGV cascade using Eq. (2). There is good match found between computational and experimental results. It can be seen that CFD captures the initial acceleration and the peak Mach number on the suction side of the aerofoil with reasonable accuracy for the Mach number range of 0.6–0.9. In Fig. 7, at around 60% of axial chord, the surface Mach number reaches 1.

The effect of incidence on the surface Mach no. distribution can be seen from Figs. 6, 7, and 8, near the leading edge of the NGV. And its effect on the surface Mach number reduces toward the throat section. For the aerofoil used in this study, the inlet blade angle is 0° . The incidence of $+10^\circ$ shifts the stagnation point move toward the pressure side of the aerofoil. As a result, the flow has to cover more distance over the leading edge circle and experiences strong acceleration. Because of this, the surface Mach number over the pressure side is less compared to incidence of 0° .

The inability of the NGV to turn the flow to the required outlet angle is a measure of the losses in the NGV. Figure 9 shows the outlet flow angle variation for exit Mach number of 0.6–1.1 and different incidences of -10° , 0° , 10° , and it is observed that there is a good agreement between CFD and experimental results. The NGV profile was designed for 71.25° . The CFD and experimental results closely match the design blade angle for exit Mach number below 0.9. Kibsey [8] experimentally and computationally investigated the effect of exit Mach number on outlet flow deflection for different linear blade cascades and stated that outlet flow deflection reduces with increase in exit Mach number beyond the sonic region. Similarly, in present study, outlet flow angle remains more or less constant for the range of exit

Fig. 9 Outlet flow angle variation along the outlet Mach number



Mach no. 0.6–0.9 but it reduces continuously beyond the sonic condition due to formation of shock.

The flow deflection also is shown with respect to different incidence angle in Fig. 9. Very minor variation is observed for different incidences.

4 Conclusions

Computational analysis for NGV cascade has been carried out in commercial CFD software and compared with cascade test results. There is good agreement found between CFD and experimental results for pressure loss coefficient, surface Mach no. distribution, and deviation angle for different incidence angles.

The loss coefficient is lower at subsonic regime but increases steeply in supersonic regime. This is due to formation of shocks which can be observed from Mach number contour plots.

The surface Mach number distribution predicted from numerical analysis shows good match with experimental results. It is observed that the surface Mach number locally exceeds 1 on the suction side in the throat region (minimum area) for exit Mach number of 0.9. CFD captures the shock patterns downstream of the throat.

The deviation angle fairly remains constant at low Mach numbers but it reduces for exit Mach number higher than 0.9.

References

1. Ainley DG, Mathieson GCR (1951) A method of performance estimation for axial-flow turbine. Issue 2974 of Report and memoranda, Aeronautical Research Council
2. Dunham J, Came PM (1970) Improvements to the Ainley-Mathieson method of turbine performance prediction. *ASME J Eng Power* 92(3):252–256
3. Kacker SC, Okapuu U (1982) A mean line prediction method for axial flow turbine efficiency. *ASME J Eng Power* 104(1):111–119
4. Denton JD (1993) Loss mechanisms in turbomachines. *ASME Int Gas Turbine Aeroengine Congr Exposition* 115:621–656
5. Mee DJ, Baines NC, Oldfield MLG, Dickens TE (1992) An examination of the contribution to loss on a transonic turbine blade in cascade. *ASME Int Gas Turbine Aeroengine Congr Exposition* 114:155–162
6. Jouini DBM, Sjolander SA, Moustapha SH (2001) Aerodynamic performance of a transonic turbine cascade at off-design conditions. *ASME Int Gas Turbine Aeroengine Congr Exhibition* 123:510–518
7. Granovskiy A, Gribin V, Lomakin N (2018) Experimental and numerical study of transonic cooled turbine blades. *Int J Turbomach Propul Power*
8. Kibsey MD (2015) Influence of mach number on profile loss of axial-turbine blade cascade. Thesis, Carlton University, Ottawa, Ontario

Aerodynamic Design of a Axial Turbine Stage for a Small Gas Turbine Engine



S. N. Agnimitra Sunkara, Prathapanayaka Rajeevalochanam,
and N. Vinod Kumar

Abstract Compact high speed turbomachines are complicated in aerodynamic design, mechanical construction, and fabrication. Design choices made during the aerodynamic design are strongly coupled to the mechanical integrity due to high rotational speeds and thermal gradients. In the present paper, aerodynamic design of a turbine with a low pressure ratio of 2:1 is presented. The turbine designed is a compact single stage machine, intended to be used in a 1 kN thrust small gas turbine engine. For the present work, the flow path is a constant hub and shroud radius rotor design, with a hub-tip ratio of 0.72. Overall guidelines used for parameter selection in velocity triangles, mean-line design and blade geometry are discussed. The turbine is designed for a mean section reaction of about 25%. Performance evaluation and flowfield analysis for the turbine geometries are carried out using a three-dimensional RANS solver. Performance characteristics of the turbine are generated for a range of pressure ratio at design speed. The intended efficiency of the turbine stage at design point is 88%. Challenges during the design process to obtain blade geometries with wide blade passage throat are put forth. The choices made in aerodynamic design which affect the ease of machining of the stator and rotor components are also brought out.

Nomenclature

C	Velocity
C_p	Specific heat at constant pressure
CFD	Computational fluid dynamics
P	Pressure [kPa]
M	Mass flow rate [kg/s]
MFF	Mass flow function $(M\sqrt{T_{01}})/(P_{01})$ [(kg/s) $\sqrt{\text{K/kPa}}$]
N	Rotational speed [rpm]

S. N. Agnimitra Sunkara · P. Rajeevalochanam (✉) · N. Vinod Kumar
Propulsion Division, CSIR-NAL, Bangalore, Karnataka, India
e-mail: prathap@nal.res.in

RANS	Reynolds averaged Navier–Stokes
SF	Speed function = $N/\sqrt{(\gamma T_{01})}$ [rpm/ $\sqrt{\text{K}}$]
SST	Shear stress transport
SWF	Specific work function = $(C_p \Delta T_0)/T_{01}$ [kJ/kg K]
T	Temperature [K]
Tmax	Maximum blade thickness [mm]
U	Blade speed
y^+	Non-dimensionalized wall cell width

Subscripts

a	Axial component
m	Related to mean radius
0	Stagnation quantity
1	Turbine inlet station

Greek

η	Efficiency = $\Delta T_0/(T_{01} (1 - (1/\pi)^{(\gamma-1)/\gamma}))$
π	Turbine total pressure ratio
φ	Flow coefficient = C_a/U_m
ψ	Stage loading coefficient = $(C_p \Delta T_0)/(U_m)^2$
Λ	Turbine stage reaction (pressure based)
ξ	Pressure loss coefficient = $\Delta P_0/(P_0 - P)_{\text{exit}}$

1 Introduction

Small gas turbines are a promising source of energy in power generation and UAVs. There is an ever increasing need for efficient power plants at all scales. Small gas turbines have been used as turbojets in both civilian and strategic applications [1–3]. They also have found their place in portable and micro-power generation units [4, 5]. CSIR-NAL, propulsion division has been developing small gas turbine for a 1 kN thrust UAV application. A high speed axial turbine is designed for the same. The salient parameters of the turbine are as shown in given Table 1.

With the advent of computer aided techniques, it has become easy-to-design, analyze and model almost anything with basic knowledge of a system. Recent day programs enable design software to have several discrete design modules packed into a suite. In the present work, mean-line design, blade profile generation, and 3D blade

Table 1 Turbine salient parameters

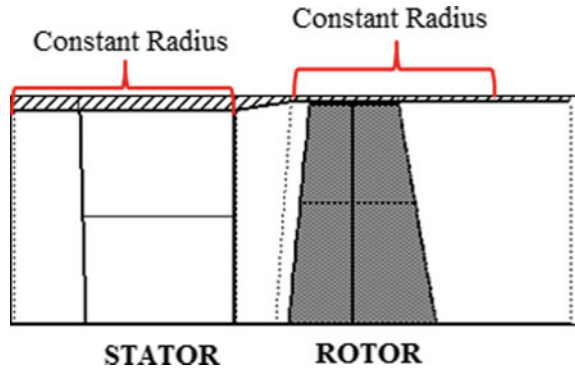
Parameter	Value
π	2.00
ψ	1.3
φ	0.66
Λ	25%
η	88%
MFF	0.1466
SWF	161.19
SF	1265.77
Hub–tip ratio	0.72
Exit flow angle	5°

stacking are carried out using a commercial turbo-machinery design suite of concepts NREC. For this purpose, a few open source turbo-machinery design software T-AXI [6], TBlade-3 [7, 8], MULTALL [9] developed by academics using legacy programming languages are also available with limited features. Turbo-machinery design and development is still seen as a very complicated affair due to the expense of money, time, and expertise, and it requires for a satisfactory design. Often times, a quick ‘design-manufacture’ turn-around is due to expertise gained and standardized methodology developed over a span of time. Majority of literature available on turbo-machinery design is focused only on very specific aerodynamic or mechanical aspects. But it is rare to mention about the problems or challenges faced during initial design phase where majority of choices are made. It is not unusual for designers to face a dilemma in terms of assigning weightage to aerodynamic performance, structural integrity, and manufacturing concerns. But most of the times factors like manufacturing cost, component mechanical reliability, simplicity in design, and ease in assembly outweigh the benefits of a minor aerodynamic performance increment. This work is an attempt by the authors to share their experiences in aerodynamic design with emphasis on arriving at an easy-to-manufacture design for a high speed axial turbine.

2 Aero-thermodynamic Design of Turbine

2.1 Meridional Flowpath Sizing

Turbine sizing is carried out based on meridional Mach number distribution along axial direction. For the present design, an inlet Mach number of maintained around 0.25–0.27 is maintained. Turbine nozzle exit Mach number is fixed for an average value around one. The stage outlet absolute Mach number at rotor outlet is maintained less than 0.55. The swirl angle at the turbine exit is targeted to be less than 20°. Based

Fig. 1 Meridional flowpath

on these preliminary flowpath sizing guidelines the hub and shroud dimensions are arrived. This provides initial estimates of the flow and loading coefficients. If the flow and loading coefficients are too high or too low, the mean radius needs to be altered and checked for stress parameter AN^2 , endwall flare angles, and flow swirl. A constant hub and constant shroud configuration eases the manufacturing or machining of shroud. A rotor configured to be encased within the shroud of stator reduces an extra part as shown in Fig. 1. A constant shroud allows the rotor to move axially without having to reduce the tip clearance.

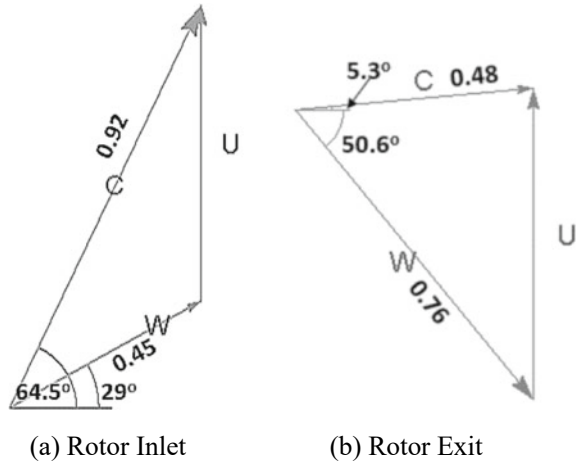
2.2 Mean-Line Design

Mean-line design, velocity triangle selection is carried out by choosing the most optimum reaction level. The effectiveness of a mean reaction is not purely an aerodynamic design choice. Stage reaction influences spanwise distribution of swirl and Mach number. A lower mean reaction gives better turbine starting characteristics due to impulse to hot gas from starter cartridge. Low reaction at hub gives higher hub shock losses in nozzle but a cooler rotor hub. In addition, a low reaction at hub with low exit flow angle makes it difficult to obtain decent blade passage convergence. For the present design, a mean reaction of 25% is chosen. Velocity triangles generated from mean-line design are as shown in Fig. 2. The absolute, relative, and blade velocities are represented by 'C', 'W', and 'U', respectively.

2.3 Blade Parameter Selection

After arriving at velocity triangles, the parameters required to generate blade profiles are selected. The guidelines for these have been laid by empirical loss models by Ainley and Mathieson [10], Dunham and Came [11], Kacker and Okapuu [12],

Fig. 2 Velocity triangles:
mean section



Moustapha et al. [13] which have been in use since decades with due respect and acceptance in the turbo-machinery community. Most important primary blade parameters like blade count, chord, Tmax, and stagger are selected based on least profile loss, maximum possible passage width at the blade throat location. Stagger angle and the throat width dictate the ease with which the tool can pass through the blade passage for machining. Smaller blade passages make it difficult to achieve tight profile tolerances (through machining) which can affect the mass flow and thereby other stage performance parameters. The throat width can be estimated during this stage itself to avoid turn-around in detailed design. Most critical locations are hub throat width for both stator and rotor. It is a very good practice to consider further reduction in the throat passage at the hub/shroud locations due to introduction of fillets in final stages. If this is foreseen at the early stage, a serious shortcoming in the mass flow rate due to reduction in the flow area can be avoided. Initial estimates of blade count can also be obtained from Zweifel criterion [14] and further, looked into reducing the blade count.

Table 2 gives the choice of blade parameters used for stator and rotor mean section airfoils.

Table 2 Blade mean section parameters

Parameter	Stator	Rotor
Stagger angle	50°	30.48°
Pitch/chord	0.71	0.73
Throat/pitch	0.42	0.61
Tmax/chord	0.11	0.13
Tmax location (%C)	16.00	19.00
Aspect ratio	0.917	1.65

2.4 Blade Airfoil Design for Aerodynamic Performance and Manufacturing Ease

For the present work, blade airfoil profiles have been generated using a modified form of Pritchard [15] parametric blade generation model. The blade chord-wise thickness distribution is dictated by leading edge radius, maximum thickness, location of maximum thickness and, inlet and exit wedge angles. Unguided turning being a critical parameter which controls the flow diffusion after the blade passage throat should be kept to a minimum as it influences the surface velocity distribution and flow deviation. As a thumb rule UGT less than six degrees is recommended, but this may sometimes yield a thin profile. For flat back transonic profiles, the UGT is almost equal to exit wedge angle. It is very essential to maintain a flat unguided surface to avoid continuous acceleration till trailing edge [16]. Nevertheless, these blade profiling guidelines are not very strict and their choice of the blade shape purely depends on profile continuity and thickness distribution. The two-dimensional airfoil losses can be assessed using a blade-to-blade CFD solution. The blade profile continuity can be improved at the leading and trailing edges by ensuring smoothness at the junction points of the LE and TE circles with the pressure and suction surfaces. For the present design, elliptical blade leading edges with 2:1 ratio are used. Any discontinuity over the blade suction surface at the throat location is smoothed by conversion to Bezier curves.

Due to constrained design parameters like low reaction and constant radius hub, the airfoil design poses challenges in surface velocity distribution. High stagger configurations yield fore-loaded airfoils which can be used as long as they do not compromise overall performance [17]. The choice of stagger of rotor blades needs to be made with ease of tool reach. A reduced twist from hub to tip also simplifies the blade geometry. But there is an aerodynamic performance penalty by using constant airfoil section rotor blades.

Nevertheless, it is possible to have a constant airfoil section blade for the stator vanes without compromising the aerodynamic efficiency. This may change the design point velocity triangles obtained during variable profile design, but it can be compensated by providing a positive lean. Having constant section stator vanes allows them to be drawn or machined as single blanks easily. Further, the inner and outer rings of the stator shroud can be machined separately reducing the cost. The rings and the blades can be joined using high temperature brazing or electron beam welding, etc. Custom made fixtures would be required to hold the rings perfectly concentric during this process.

Apart from structural considerations, blade thickness also needs to be decided based on the possible warpage or distortion withstanding machine tool loads. An easy-to-machine rotor will have tool access from the top so as to avoid several tool and work piece axis rotation operations. For a BLISK (bladed disk) rotor configuration, it is the easiest to machine a rotor blade, whose blade passages when viewed normal from the top, the pressure surface of one blade and the suction surface of neighboring blade should be visible. Blades designed with this target will have better

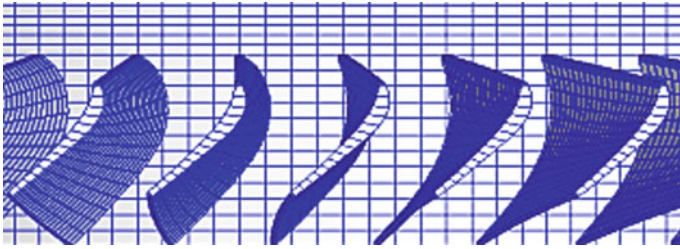


Fig. 3 Rotor blade passage

tool access and ease in machining. For moderate volume production using machining, this multiplies as a huge time saving.

Figure 3 shows the rotor blade passage whose majority of passage is accessible easily using a machining tool on a 5-axis CNC machine.

2.5 Three-Dimensional Blade Design

To obtain complete geometry, the stator airfoils are stacked about their trailing edges and the rotor blade is obtained by stacking the airfoils about their centers of gravity. Sometimes, it becomes difficult to deviate from the mean-line design dimensions owing to efficiency, reaction, swirl, and dimensional constraints. For this, a positive lean around $15\text{--}30^\circ$ gives an excellent flexibility in achieving improved efficiency due to spanwise relaxation in the reaction distribution. Increase in number of geometric features increases design complexity, manufacturing time and cost. For a low cost design, choice of material needs to be solely based on availability. Simple design and reduced number of geometric features in turbine disk cross-section, seal give a significant cost reduction. Detailed design considerations in aerodynamic and thermo-structural aspects of turbine using state-of-the-art design and analysis tools are dealt in [18].

3 Numerical Set Up and Analysis

Turbine aerodynamic performance is predicted using steady RANS CFD solver ANSYS-CFX. The turbine domain is modeled as single passages of stator and rotor connected via a stage interface, through which circumferential averaging of mass, momentum, and energy fluxes is performed. A no-slip, adiabatic wall condition is applied to all the hub, shroud, and blade endwalls.

3.1 *Boundary Conditions*

At the domain inlet; total pressure, temperature, and swirl angle are enforced. Turbulence intensity of 8% and length scale of 1% blade height are assigned. An exit static pressure is assigned at mean radius by considering radial equilibrium. Shear stress transport (SST $k - \omega$) model [19] is used to model the RANS equation.

3.2 *Grid Generation*

Grid generation for the turbine domain is performed using AutoGrid5 tool of NUMECA software. O4H topology is used in generation of structured grid using hexahedral elements. Grid is generated with a near wall expansion ratio of 1.2 and minimum orthogonality of 20° . Grids are generated along with fillets ensuring excellent grid connectivity and orthogonality as shown in Figs. 4, 5, 6, 7 and 8. It is ensured that the grids used for CFD simulations yield $y^+ < 11$ for SST turbulence model as per the solver requirements [20].

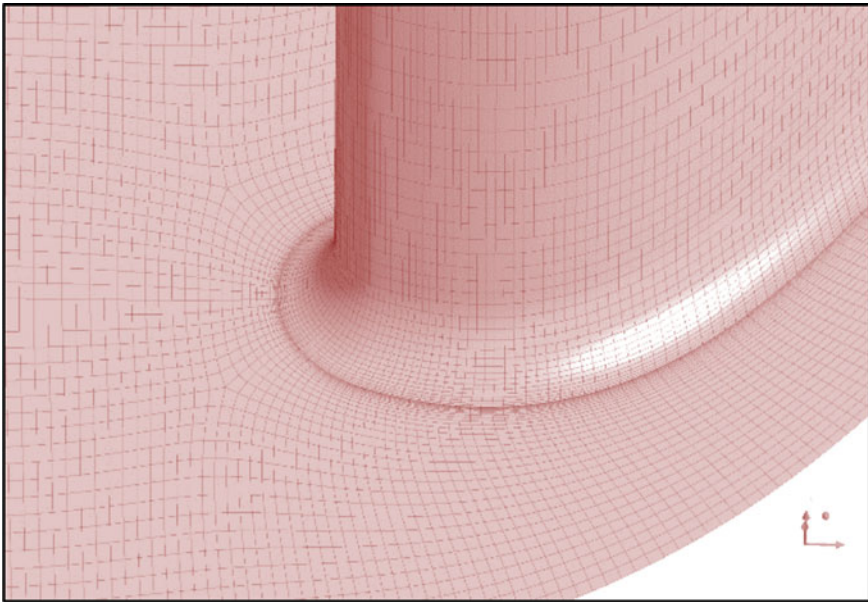


Fig. 4 Stator grid detail—leading edge

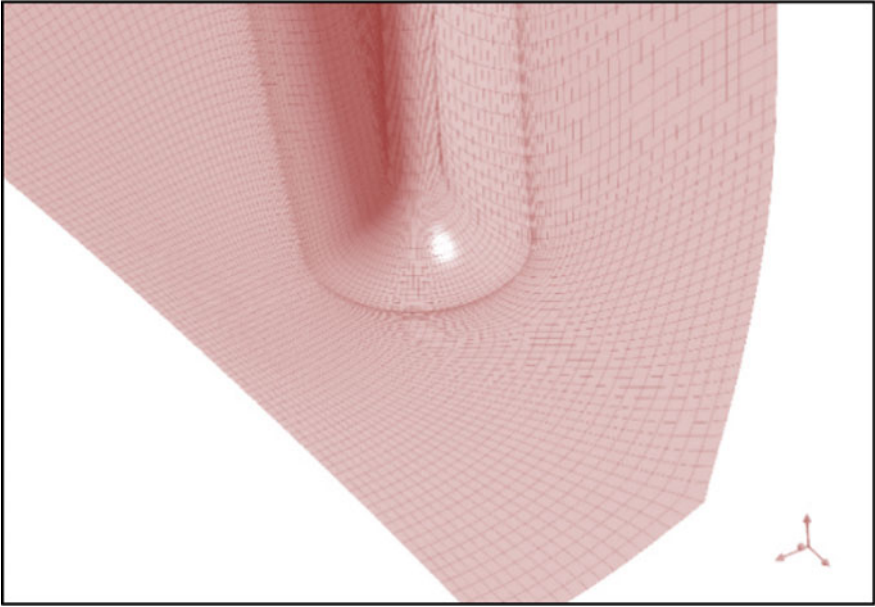


Fig. 5 Stator grid detail—trailing edge

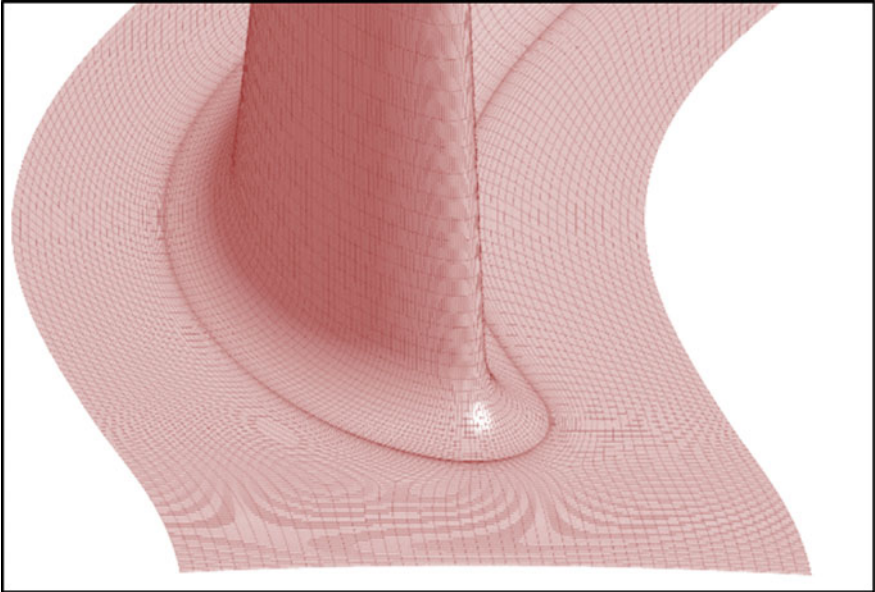


Fig. 6 Rotor grid detail—leading edge

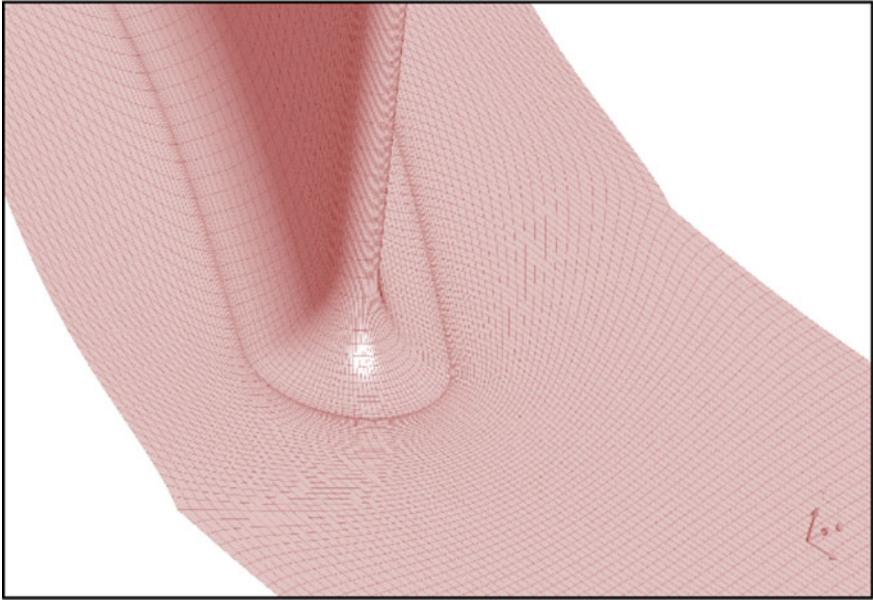


Fig. 7 Rotor grid detail—trailing edge

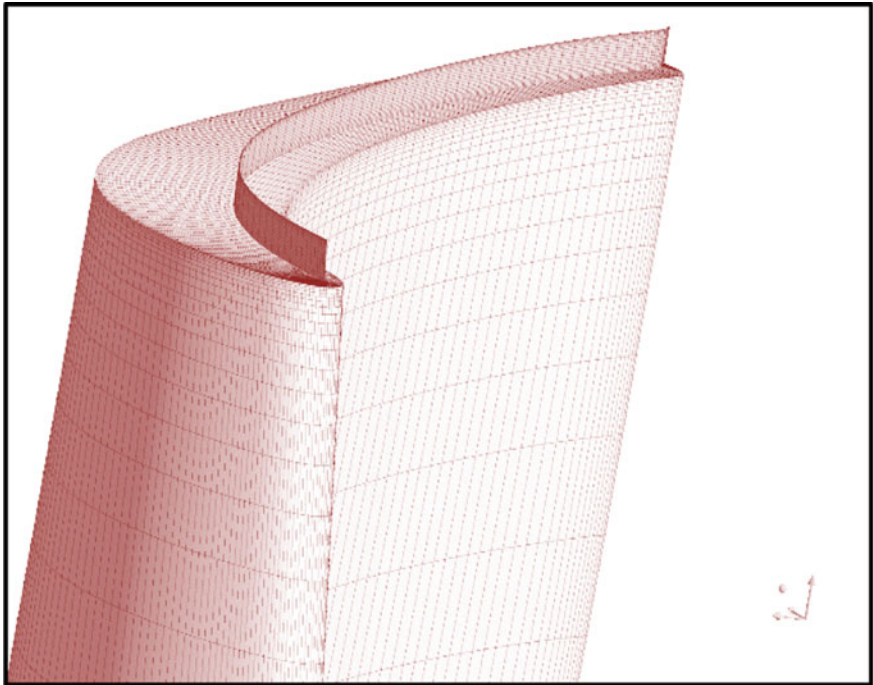


Fig. 8 Rotor tip clearance grid detail

3.3 Grid Independence Study

Size refinement is carried out, and the turbine performance is assessed. The grids are doubled successively and checked for a change in the performance variables. The criterion used is that the deviation of mass flow and the specific work should be by less than 0.2% for two consecutive meshes. From the grid dependence study as shown in Table 3, grid with size 2.7 million is chosen for further detailed analysis.

A distortion free grid is obtained for both the stator and rotor fillet endwall regions.

The tip clearance region (as shown in Fig. 8) of the size independent mesh (2.7 million) consists of about 21 grid points radially.

Figure 9 shows that the grids used for CFD simulations yield a wall $y^+ < 5$. From the detailed study of grid parameters, it can be summarized that the chosen grid is sufficient to carry out detailed performance studies.

Table 3 Grid dependence study

Grid size	MFF	SWF
0.7 million	0.1466	162.93
1.3 million	0.1467	163.55
2.7 million	0.1468	163.61
5.9 million	0.1467	163.38

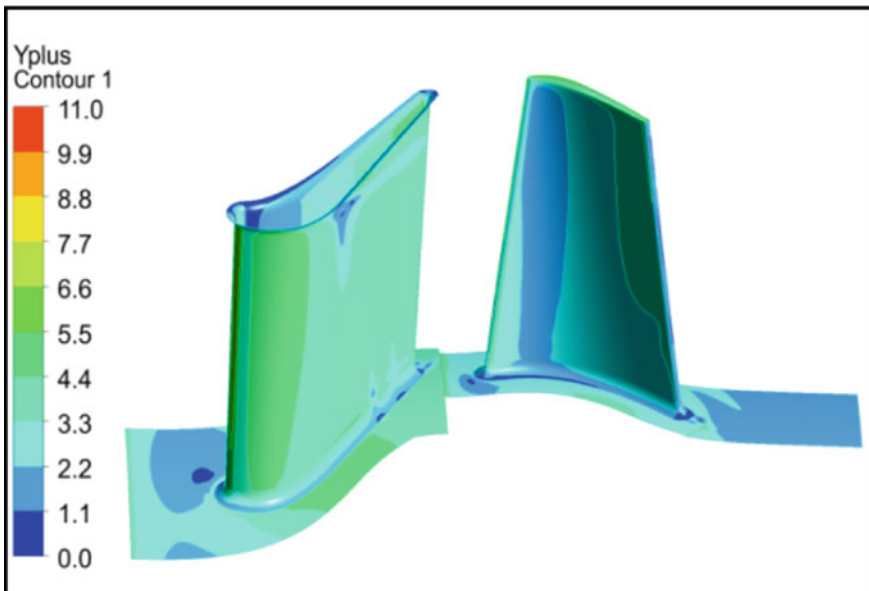


Fig. 9 Endwall y^+ distribution

4 Turbine Performance and Flowfield Results

4.1 Turbine Performance

The aerodynamic performance of the axial turbine is assessed for a range of pressure ratio at design speed. For verification purposes, simulations are carried out for both filleted and non-filleted turbine geometries at design point and the comparative performance is shown in Table 4.

For the same exit static pressure, the presence of fillet caused a mass flow reduction of 0.3% with respect to the no-fillet case. The overall pressure ratio and specific work also changed slightly causing shift in the efficiency by 0.08%. As it is more accurate to analyze the performance considering the blade fillets as they take into consideration the actual reduction in area at the blade endwall junctions, performance of the filleted turbine geometry is assessed for a range of pressure ratio at design speed.

The turbine is clearly operating in choked region as shown in Fig. 10.

The work and efficiency characteristics in Figs. 11 and 12 show that the turbine performance is better than the design intent by approximately 1%. In addition, the turbine also exhibits a flat performance curve over a range of operating pressure ratio adjacent to the design point. This can be attributed to the incidence tolerance and thin leading edges possible through the use of elliptical leading edges.

Table 4 Aerodynamic performance

Parameter	No-fillet	Fillet
π	1.99	1.988
MFF	0.1473	0.1468
SWF	163.57	163.61
η	89.99	89.91

Fig. 10 Turbine mass flow characteristics

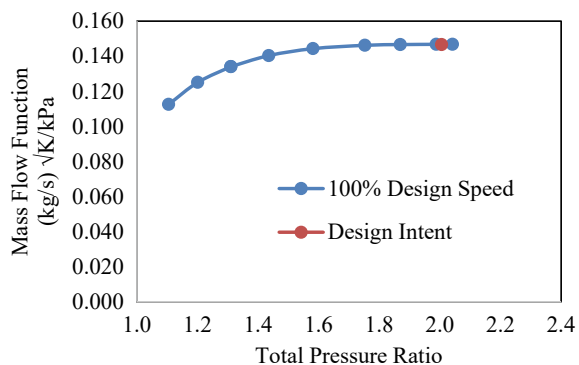


Fig. 11 Turbine work characteristics

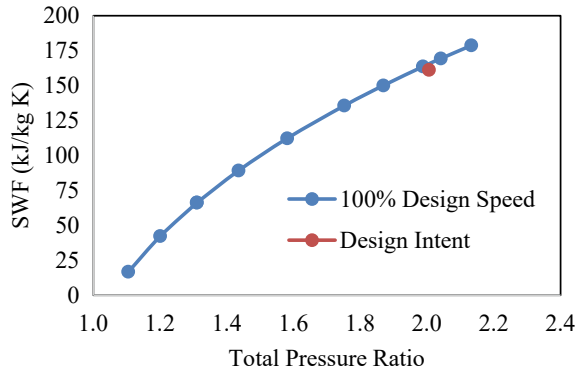
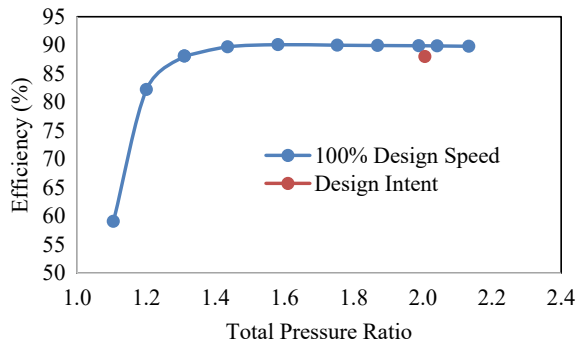


Fig. 12 Turbine efficiency characteristics



4.2 Turbine Mean Section Flowfield

Blade loading of the mean sections of stator and rotor rows is expressed as normalized surface pressure variation across blade axial chord.

For the stator vane, both the suction and pressure surfaces are free from any serious shocks as shown in Fig. 13. This can also be observed in the Mach number distribution in Fig. 15. There are no serious accelerations after the throat location around 52% of axial chord.

From the rotor blade, mean pressure loading as shown in Fig. 14 and it can be observed that the suction surface of the rotor is fore-loaded due to highly staggered rotor blades. But, there are no strong shocks on the suction surface, complemented by velocity distribution in mean section represented by Mach number contour as shown in Fig. 15. This can be owed to a combination of low stage pressure ratio and low rotor reaction.

Also, there is no significant flow deviation in stator or row rows as seen in Fig. 15.

Fig. 13 Blade loading—stator vane mean section

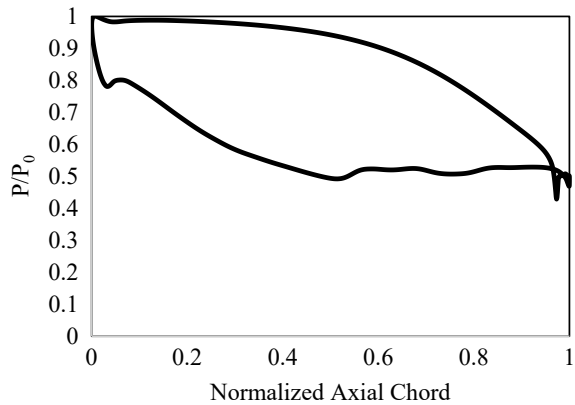
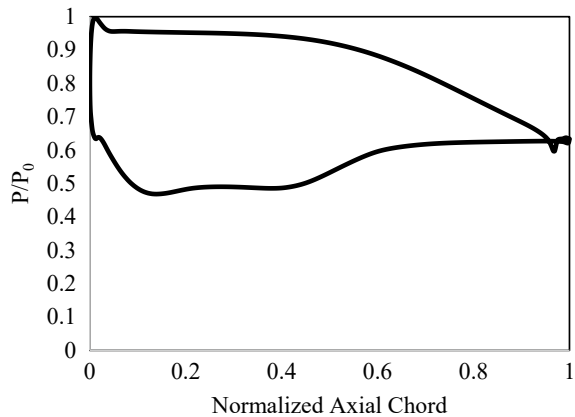


Fig. 14 Blade loading—rotor blade mean section



4.3 Turbine Spanwise Flow Analysis

The circumferentially averaged spanwise distribution of total pressure loss across stator and rotor blade rows is shown in Figs. 16 and 17.

As per the CFD result at design point, mean section loss is 4.7% and 6.9%, respectively, for stator and rotor blades. The average losses across the stator and rotor rows are 8.07% and 11.9%, respectively. From Fig. 16, it is inferred that the endwall effects in stator are well contained within 10% of blade span from both hub and shroud.

The rotor exhibits localized peak loss regions at nearly 30% and 80% of blade span, attributed to the hub passage vortex, and tip leakage vortex, respectively, as shown in Fig. 17. It can be said that from mean to nearly 70% of blade span is a vortex free zone. This is common in blades with very less annular height. The endwall flow features significantly affect the core flow. These can be mitigated using

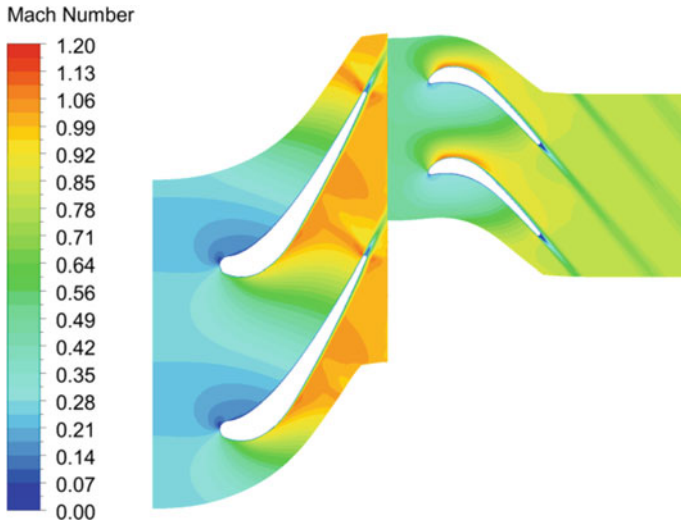
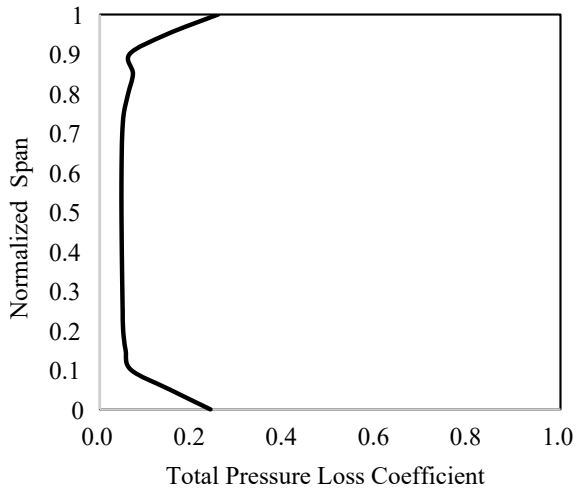


Fig. 15 Mach number distribution—mean section

Fig. 16 Spanwise stator loss distribution



several secondary and tip clearance treatment methods. But these increase the design complexity of the turbine vanes and blades.

Figure 18 outlines that the spanwise reaction of the turbine varies linearly from hub to shroud and the mean section reaction is of 25% and is achieved as per the target. The hub reaction is maintained at 8%.

Fig. 17 Spanwise rotor loss distribution

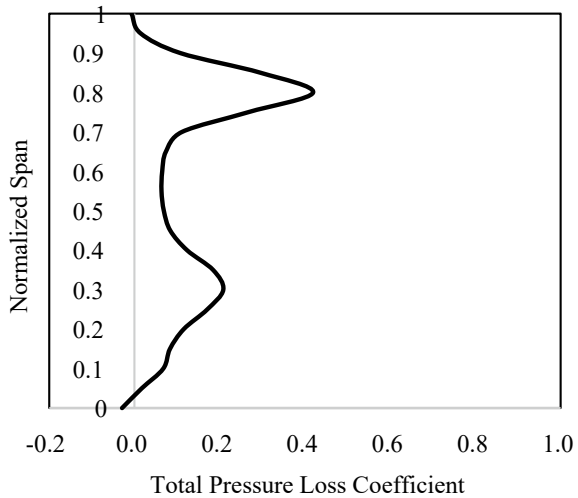
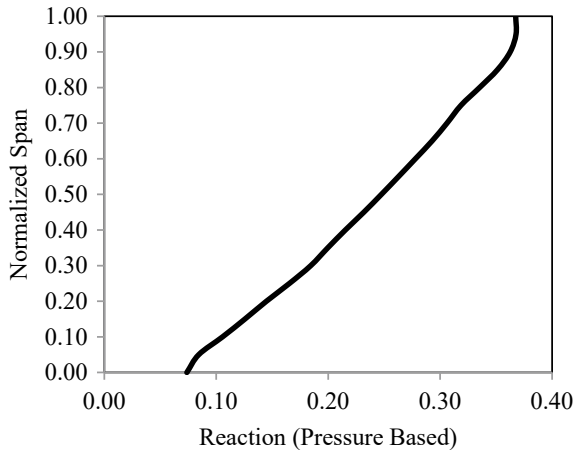


Fig. 18 Spanwise reaction distribution



5 Conclusions

A compact turbine design for a given set of salient parameters is designed, and methodology is demonstrated. The choice of basic flow path and blade parameters influencing the aerodynamic performance, and machining complexity are discussed in detail. The turbine efficiency from RANS CFD predictions is 90% against intended 88% from mean-line design. The targeted mean reaction of 25% is achieved. This is achieved due to improved aerodynamic performance of stator and rotor airfoils by incorporating elliptic leading edges, thin trailing edges, flat unguided turn, and stator positive lean. Various possibilities in simplifying the geometry for machining point of view, in terms of tool reach and reduced number of operations are put forth. Detailed

analysis over and across the turbine stator and rotor rows yields a satisfactory flow field distribution.

References

1. Jean-François R, Gilles G, Alain C, “MICROTURBO families of turbojet engine for missiles and UAV’s from the TR60 to the New bypass turbojet engine generation”, AIAA 2008–4590. In: 44th AIAA/ASME/SAE/ASEE Joint Propulsion Conference & Exhibit 2008
2. Razinsky E “The J402-CA-702-A modern 1000 lb thrust RPV engine”. In: Proceedings of AIAA 24th Joint Propulsion Conference-1988, Paper No. AIAA-88-3248
3. Barbeau DE (1981), “A family of small, low cost turbojet engines for short life applications” In: Proceedings of ASME-Gas Turbine Conference-1981, Paper No. 81-GT-205
4. McDonald CF, Rodgers C (2002), “The ubiquitous personal turbine—a power vision for the 21st century”. *J Eng Gas Turbines Power* 124:835–844,2002
5. De Paepe W, Carrero MM, Bram S, Parente A, Contino F (2017), “Towards higher micro gas turbine efficiency and flexibility—humidified mGTs: a review”, *J Eng Gas Turbines Power* 140(8):081702(8),2017
6. Turner MG, Merchant A, Bruna D, University of Cincinnati T-Axi website. <http://gtsl.ase.uc.edu/T-AXI/>
7. Siddappaji K, Sharma M, Nemnem A, Hussain Mahmood SM, Balasubramanian K, Galbraith MC, Turner MG, University of Cincinnati T-Blade3 website. <http://gtsl.ase.uc.edu/t-blade3/>
8. Siddappaji K, Turner MG, Merchant A, “General capability of parametric 3D blade design tool for turbomachinery”. In: Proceedings of ASME Turbo Expo 2012, GT2012-69756
9. Denton JD, “Multall-An open source, cfd based, turbomachinery design system”. In: Proceedings of ASME Turbo Expo 2017, GT2017-63993
10. Ainley DG, Mathieson GCR (1951), “A method of performance estimation for axial flow turbines”. *British ARC, R & M* 2974
11. Dunham J, Came PM (1970), “Improvements to the Ainley/Mathieson method of turbine performance prediction”. *ASME J Eng Power* 92(3):252–256,1970
12. Kacker SC, Okapuu U (1981), “A mean line prediction method for axial flow turbine efficiency”. ASME paper no. 81-GT-58,1981
13. Moustapha SH, Kacker SC, Tremblay B (1990), “An improved incidence losses prediction method for turbine airfoils”. *ASME J Turbomach* 112(2):267–276,1990
14. Zweifel O (1945), “The spacing of turbomachine blading especially with large angular deflection, the brown Boveri review”, pp 436–444,1945
15. Pritchard LJ, “An eleven parameter axial turbine airfoil geometry model”. ASME paper 85-GT-219,1985
16. Rajeevalochanam P, Senthil Kumaran R, Agnimitra Sunkara SN, Kalita N, Sharath PP, “Experimental and numerical studies on a curved back transonic airfoil”, V001T02A013, Paper No. GTINDIA2017-4874,2017
17. Korakianitis T (1993), “Prescribed-curvature-distribution airfoils for the preliminary geometric design of axial-turbomachinery cascades”. *ASME J Turbomach* 115/325,1993
18. Rajeevalochanam P, Agnimitra Sunkara SN, Mayandi B, Ganesh Banda BV, Chappati VSK, Kumar K, “Design of highly loaded turbine stage for small gas turbine engine”. In: Proceedings of ASME Turbo Expo 2016, GT2016-56178
19. Menter FR, Kuntz M, Langtry R (2003) Ten years of experience with SST κ - ω Turbulence model. *Turbul Heat Mass Transf.*,2003
20. ANSYS CFX User Manual

Gas Turbines—Systems, Components and Structures

Development of Test Bench for Micro Gas Turbine Engine



Prathapanayaka Rajeevalochanam, N. Vinod Kumar,
S. N. Agnimitra Sunkara, Narendra Sharma, Swaroop Shashidhar,
and R. Jai Maruthi

Abstract Performance evaluation of gas turbine engine on the test bed is of prime importance during the engine developmental stage. It is prudent to study the rotor dynamics, lube system, fuel system, vibratory characteristics of the engine along with its performance on the test bed. Micro Gas Turbine (MGT) Engine of 50 N thrust is being under development at CSIR-NAL. To carry out performance tests of MGT, a test bench has been developed. The test bench is equipped with (i) Lubrication system, (ii) Fuel system, (iii) Starting system, (iv) Data acquisition and measurement system. The test bed is designed to measure thrust directly using movable bed and a 'S' type load cell of 100 N capacity. A miniature fuel pump is used to supply fuel to engine. Air-oil lubrication system is used to lubricate the engine bearings. External compressed air supply system is developed to assist the starting of engine. DAQ and instrumentation layout has been designed and developed specific to the existing module. Test bench is configured so as to cater the measurement and online condition monitoring requirements with required sensors to measure thrust, temperature, speed and vibration. Sensors are integrated to the National Instrument data acquisition hardware. DAQ system software is developed on the LabVIEW platform.

Nomenclature

DAQ	Data acquisition
EGT	Exhaust gas temperature
FSO	Full scale output
GUI	Graphical user interface
MGT	Micro gas turbine
PWM	Pulse width modulation
RPM	Rotations per minute

P. Rajeevalochanam (✉) · N. Vinod Kumar · S. N. Agnimitra Sunkara · N. Sharma ·
S. Shashidhar · R. Jai Maruthi
Propulsion Division, CSIR-NAL, Bangalore, Karnataka, India
e-mail: prathap@nal.res.in

1 Introduction

Micro gas turbine (MGT) engines are being explored in various applications in defense [1, 2] power generation applications [3, 4]. MGT engines are in forefront now due to increased research and usage of unmanned air vehicle for different applications in strategic applications. Usually MGT engines are designed to operate at very high speeds in the order of a few lakh rpm. These engines are very compact and lighter (Fig. 1).

CSIR-NAL, Propulsion Division has developed a micro gas turbine engine of 50 N thrust. The developed MGT named 'NAL-PR-MGT-50' is configured with a single stage centrifugal compressor, axial turbine, straight flow vaporizer combustor and a convergent propelling nozzle. The engine is designed for a rated speed of 100,000 rpm. The rotor system is mounted on a pair of ball bearings, one each on compressor and turbine sides. A fuel-lube mixture or oil-air lubrication system can be used. The engine is designed for operation using Jet-A fuel. Separate systems are required for fuel supply, engine control and lubrication.

Therefore, in addition to the core engine, there are three systems involved.

- (a) Lubrication System
- (b) Fuel System
- (c) Data Acquisition and Online Monitoring System.

The existing MGT under development is lubricated using an oil-air lubrication system. A DC motor powered miniature gear pump is used for variable fuel supply. Engine parameters such as speed, thrust, exhaust temperature and vibration are acquired and monitored continuously through dedicated a data acquisition system (DAQ). References [5, 6] provide insights into the design and selection of thrust stand

Fig. 1 Photograph of the developed MGT



for the MGT. Online vibration monitoring and analysis is carried out to assess the engine health during operation. Conventional health monitoring techniques referred in [7–11] are employed in configuring the vibration sensor scheme and analysis.

2 Engine Test Bed

The engine required a dedicated test bench for mounting of the complete engine structure, corresponding sensors and sub-systems. A dedicated test bed is designed and configured suitable for the MGT as shown in Fig. 2. The test bench is designed comprising of an engine mounting structure, fuel and lubrication system, data acquisition unit.

The test bed layout is designed and configured based on easily available off-the-shelf components. The designed test bed consists of a fixed bed and a movable bed. Movable bed is supported by two parallel linear motion guide rails which are mounted on the fixed bed. THK make linear motion guide rails with least frictional resistance are selected based on the thrust, and weight of the engine. It consists of two guide rails of length 700 mm and four LM blocks. The movable bed is coupled to a ‘S’ type load cell of 100 N capacity which is capable of measuring both compressive as well as tensile loads. Micro gas turbine is fixed to a 4 inch ‘U’ type pipe clamp. The thrust load generated by the engine is transferred to movable bed and in turn to the load cell. Thus the load cell will record the thrust produced by the engine (Fig. 3).

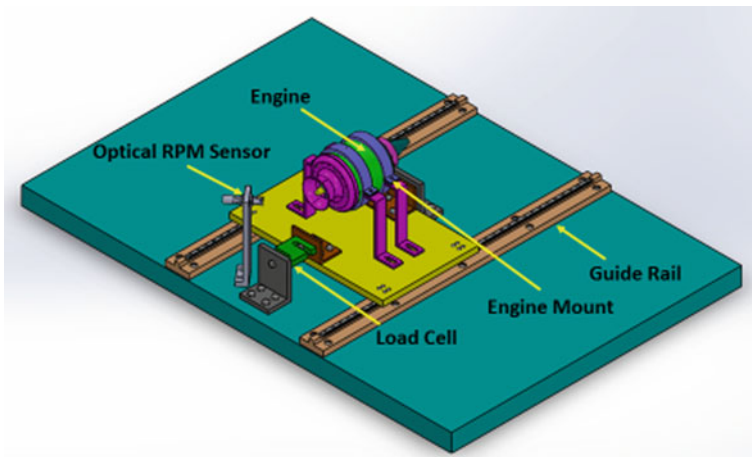


Fig. 2 MGT test bed model



Fig. 3 Photograph of MGT test bed

2.1 Engine Operation Procedure

Engine starting is done by assistance through external compressed air to rotate it to a certain speed, with lube system ON. Lube system continuously injects oil-air mixture to both bearings of the engine rotor system. Simultaneously, ignition is first done using propane gas with glow plug ON. After successful ignition, temperature rises quickly and the engine spools up. After sustained combustion, glow plug is switched OFF. Thermocouple placed at exit of nozzle measures exhaust gas temperature (EGT). Subsequently, after ensuring sustained combustion Jet-A fuel is slowly injected and propane gas supply is gradually cut off. Solenoid valves are operated for any emergency cut down of gas or fuel. Engine control inputs are systematically operated to initialize sustained combustion, running at different speeds and shutting down engine safely. The input control loop for safe engine operation is as shown in Fig. 4. After engine is sustained, speed increases with increase in fuel supply. Fuel pump voltage is initially tuned to maintain sustained combustion and varied using a manual PWM Circuit. Experiments are carried out to acquire thrust data at different speed points. Engine is shut down by slowly decreasing speed and switching off the pump at lower speed. External air supply is continued along with lube system to cool down the engine. The thrust bed is placed in a dedicated room to protect the surrounding personal from any debris in case of a catastrophic failure. For better flow control and to avoid excessive fuel supply a bypass valve is incorporated in the fuel line. In case of engine over-speeding, the fuel pump is cutoff immediately. Fire extinguishers are kept in place for fire safety.

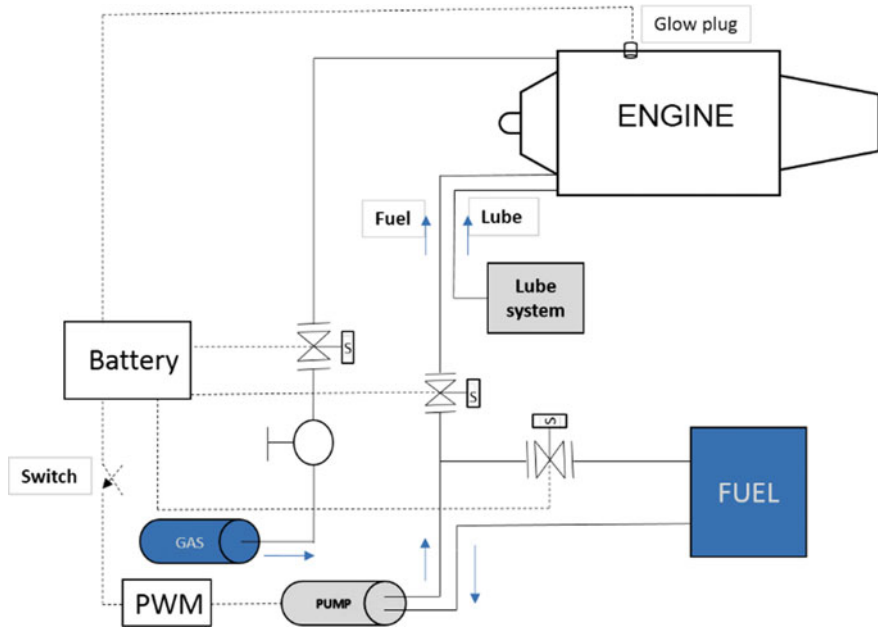


Fig. 4 Engine fuel and lubrication system schematic

2.2 Fuel System

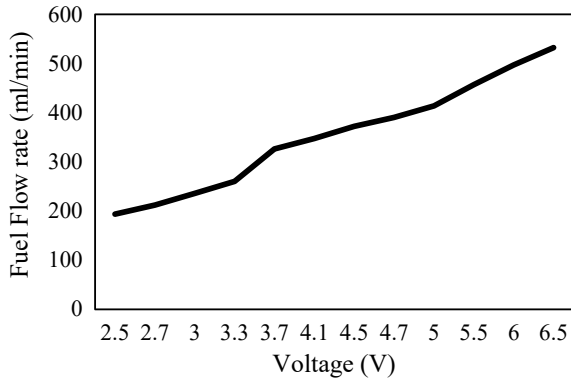
The fuel is pumped to the engine fuel delivery system using a DC powered miniature gear pump as shown in Fig. 5. Engine nominal fuel flow rate is 300 ml/min approximately.

Fuel rates are controlled by a Pulse Width Modulation (PWM) circuit. Pressure transducer in fuel line measures fuel pressure flowing to combustion chamber. To avoid sudden increase in flow of fuel, a bypass to fuel tank is also configured. This can be controlled manually or through a solenoid valve. Though the fuel pump characteristics are furnished by the manufacturer, it is very important to calibrate the fuel pump and generate ‘Voltage’ versus ‘Flow rate’ with the fuel supply system

Fig. 5 Fuel pump



Fig. 6 Fuel pump characteristics



of engine connected. Figure 6 is the characteristic obtained for fuel pump in bypass fully closed condition.

2.3 Lubrication System

For the MGT under development, an oil-air lubrication system is employed for bearing lubrication. It consists of a lube tank, pump, mixing valve with metering unit and tubes with hose coils. A line distributor unit pumps a set quantity of lubricant to a mixing valve. Air flow feeds the lubricant through the secondary line and to the lubrication point in the form of oil streaks. Figure 7 shows a photograph of the oil-air lubrication unit used. The over pressure due to the air flow and prevents the ingress of contaminants into bearing assembly. The ability to tune the oil-air quantity is the reason to chose such a lubrication units during the developmental testing of MGT.

2.4 Sensors and Instruments

Temperature, thrust and speed sensors are installed at different sensing points of the engine. Figure 8 shows detailed location of the sensors and Table 1 provides sensor specifications.

A K-type thermocouple is used for the exhaust gas temperature measurement at the exit of engine nozzle. A 10 kg range S-type load cell is used for the thrust measurement. One end of the Load cell is attached to static fixture and other end is fixed to the moving rail of the engine mounting structure. Load cell is compressed during thrust generation and 4–20 mA Current Output load cell transducer produces the equivalent thrust generated by engine. Optical speed sensor generates pulse signal



Fig. 7 Oil air mixture generator

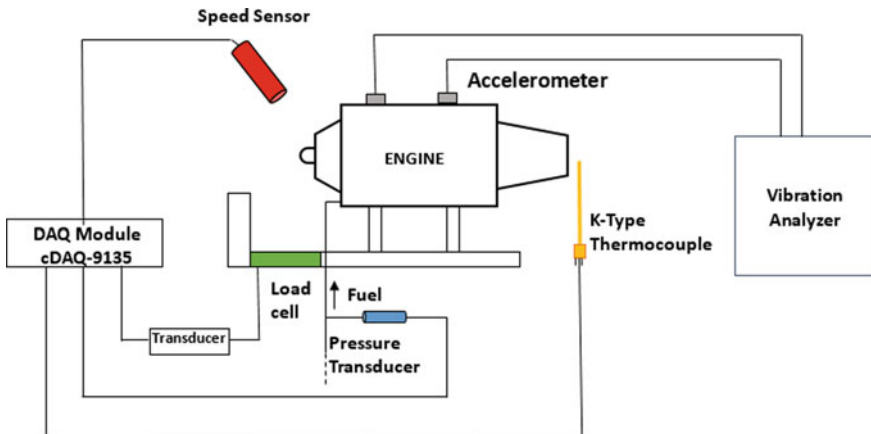


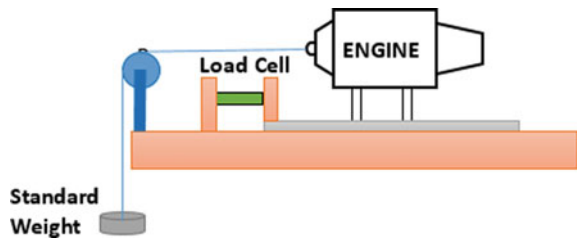
Fig. 8 Sensors schematic

for every one rotation and converted to RPM. Figure 9 shows the calibration methodology adapted for the thrust stand. The engine along the thrust axis is loaded with the standard weights with the help of a pulley and string. The measured load by the load cell is recorded and calibrated with standard weights.

Table 1 Engine sensor details

Parameter	Sensor	Measuring signal	Acquisition module	Range	% Error	Signal output
Temperature	Thermocouple	Voltage	NI 9134	-200 ~ +1250 C	±0.75%	0-54 mV
Thrust	Load cell	Ampere	NI 9205	0-10 kg	-	4-20 mA
Speed	Tachometer	TTL pulses	NI 9401	0-250,000 RPM	-	0-3 kHz
Pressure	Pressure transducer	Ampere	NI 9205	0-50 psi	0.25% full scale	4-20 mA
Vibration	Accelerometer	Acceleration	OROS	0-100 g	±1.5% to 900 Hz	IEPE

Fig. 9 Setup for thrust calibration



2.5 Data Acquisition System

Sensor signals are acquired through the National Instruments compact DAQ controller 9135 with sensor specific modules as shown in Fig. 10. Sensor Signals are carried in Teflon cables for avoiding any interference noise signal to hardware.

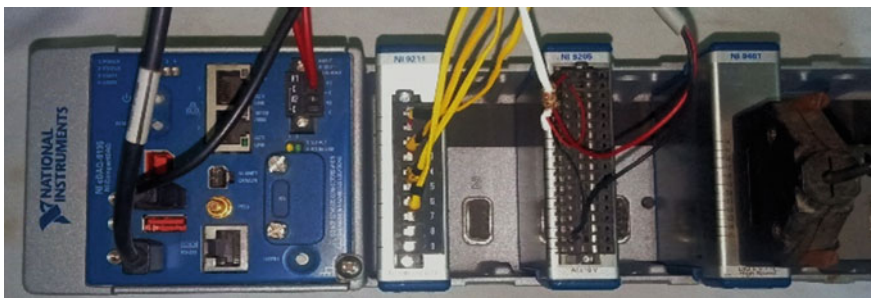


Fig. 10 cDAQ-9135 data acquisition hardware with module

3 Online Engine Condition Monitoring

The engine exit temperature, thrust and speed are acquired at 10 Hz and continuously monitored through the GUI developed in LabVIEW software as shown in Fig. 11. The block diagram of the LabVIEW program is shown in Fig. 12. Engine exit temperature and RPM is monitored to gain sustained combustion. Speed and thrust data are monitored during the incremental fuel injection to reach the required speed. These data are stored with time and date stamping. Engine vibration signals are acquired by two tri-axial accelerometers mounted at the plane of two bearings using OROS Vibration analyzer.

Each accelerometer constitutes of 3 axis data which are axial, radial and transverse signals as shown in Fig. 13. These individual signals are processed online to obtain

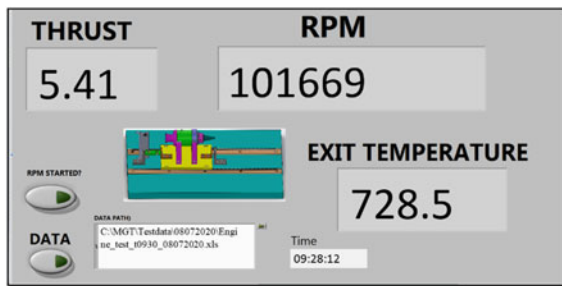


Fig. 11 Front panel of LabVIEW program

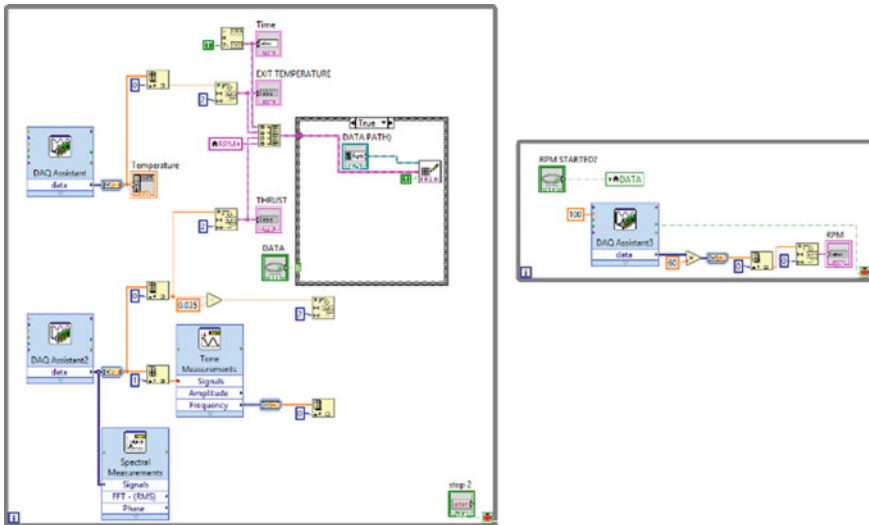


Fig. 12 Block diagram of LabVIEW program

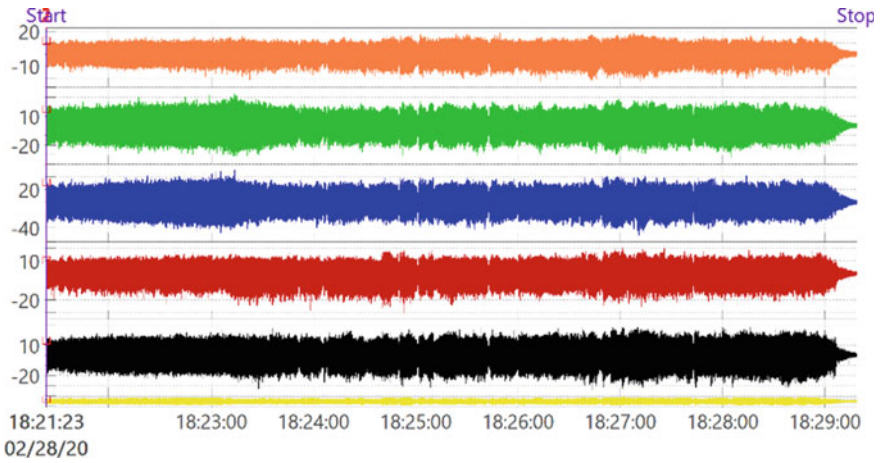


Fig. 13 Raw accelerometer data

instantaneous FFT plots as shown in Fig. 14. FFT plots of each direction are analyzed to get individual frequency acceleration and displacement values. In the post analysis these FFTs are summarized for a period of time and consolidated as a water fall plot as shown in Fig. 15. These plots help in providing a deep understanding of the rotor

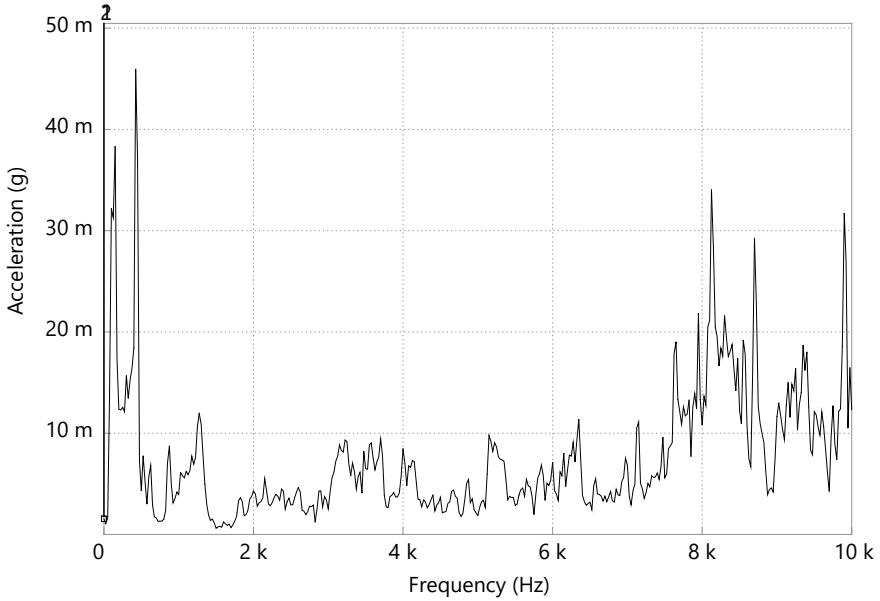


Fig. 14 Instantaneous FFT plot

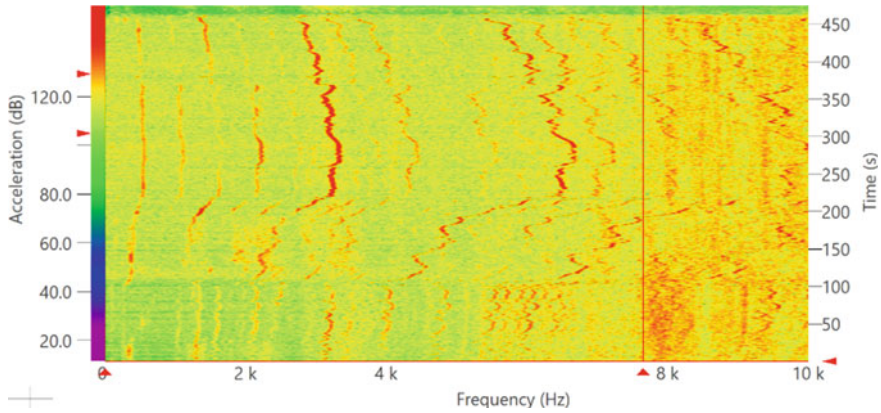


Fig. 15 Waterfall plot of MGT vibration

dynamic vibration modes excitation and analyse engine orders at different speeds and the reasons can be ascertained by analysing the signature.

4 Results and Discussions

The developed Micro Gas Turbine engine was able to deliver thrust of 5.4 kg at the design speed of 100,000 rpm. The performance of the engine is plotted in Fig. 16.

Uncertainty of the measurements is estimated as per guidelines by Abernathy et al. [12]. Both the fixed and random errors have been considered for the calculation of uncertainty. The values of uncertainty for the measured quantities are reported in Table 2 with a confidence level of 95%. Though the uncertainty levels are satisfactory, they need to be further reduced. It is found that improving the fuel supply can help

Fig. 16 Engine performance plot

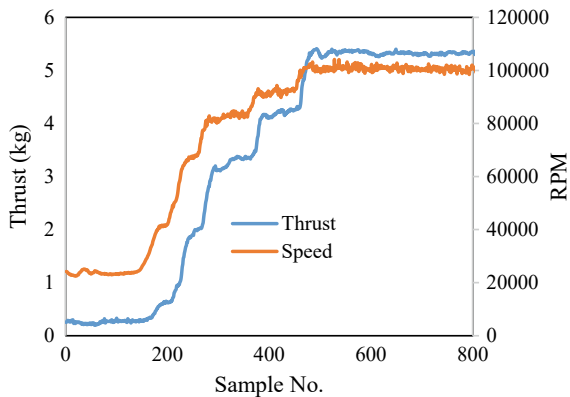


Table 2 Uncertainty of measurements

Quantity	Value	% Uncertainty
Thrust (kg)	5.4	1.38
Speed (RPM)	100,617	0.68
Temperature (°C)	755	1.61

reduce the variations in the speed and thrust. In addition to the engine performance, a few important points pertaining to the operation have been established specific to the existing MGT module. The engine is capable of successfully starting using compressed air till light-off condition. The engine can self-sustained at 25,000 rpm. As the MGT is in a developmental phase, the fuel and compressed air supply are not completely automatic at present. It is planned to automate these systems. The MGT engine test bed developed for performance evaluation is operating satisfactorily.

5 Conclusions

A simple and economical engine test bed has been designed and developed indigenously to test micro gas turbine engines up to 100 N. Manual control fuel system has been developed to test the engines. Currently, the test bench is not capable of automated fuel control which is under development. Data acquisition system for the test bench is configured and developed to acquire data of various engine parameters during testing. It is designed to be flexible to take additional measuring inputs for future changes in the sensors by adding the required control and measurement modules. NAL-PR-MGT-50 is successfully tested using this test bench for a continuous speed of 1 lakh RPM and generating a thrust of 5.4 kg. The test bench has proven to be very useful in the performance characterization, monitoring of the engine.

References

1. Razinsky E (1988) The J402-CA-702-A modern 1000 lb thrust RPV engine. In: Proceedings of AIAA 24th joint propulsion conference, Paper No. AIAA-88-3248
2. Barbeau DE (1981) A family of small, low cost turbojet engines for short life applications. In: ASME-gas turbine conference, Paper No. 81-GT-205
3. McDonald CF, Rodgers C (2002) The ubiquitous personal turbine—a power vision for the 21st century. *J Eng Gas Turbines Power* 124:835–844
4. De Paepe W, Carrero MM, Bram S, Parente A, Contino F (2017) Towards higher micro gas turbine efficiency and flexibility—humidified mGTs: a review. *J Eng Gas Turbines Power* 140(8):081702(8)
5. Kho S, Ki J, Park M, Kong C, Lee K (2009) Development of condition monitoring test cell using micro gas turbine engine. <https://doi.org/10.1115/GT2009-59931>
6. Runyan RB, Rynd Jr JP, Seely JF (1992) Thrust stand design principles. In: Proceedings of 17th AIAA aerospace ground testing conference, AIAA-92-3976

7. Turne KY, Bajwa A (1999) A survey of aircraft engine health monitoring systems. In: Proceedings of AIAA 99-2528. <https://doi.org/10.2514/6.1999-2528>
8. Beneda K (2016) Development of a modular FADEC for small scale turbojet engine. In: SAMI 2016, IEEE 14th international symposium on applied machine intelligence and informatics, 21–23 January 2016
9. Volný O, Pecinka J (2017) Analysis of engine monitoring system report. In: 2017 international conference on military technologies (ICMT), May 31–June 2 2017, Brno, Czech Republic
10. Rahman M, Zaccaria V, Zhao X, Kyprianidis K (2018) Diagnostics-oriented modelling of micro gas turbines for fleet monitoring and maintenance optimization processes
11. Djaidir B, Hafaifa A, Kouzou A (2017) Faults detection in gas turbine rotor using vibration analysis under varying conditions. *J Theor Appl Mech* 55(2):393–406. Warsaw, <https://doi.org/10.15632/jtam-pl.55.2.393>
12. Abernathy RB, Thomson Jr JW (1973) Handbook of uncertainty in gas turbine measurements. AEDC-TR-73-5

Development Strategy for Evaluating Gas Turbine Driven High-speed Alternator



Poonam Kumari, V. Prabakar, and A. N. Vishwanatha Rao

Abstract In this paper, strategy for development of high-speed rig for performance evaluation of gas turbine driven alternator is discussed. In aeronautical systems, only high-speed alternator is the power generating unit, which is directly or through gear train coupled with variable speed gas turbine engine. Performance evaluation of this type of alternator needs to be conducted on bench to validate its rating. Development of high-speed (30,000–60,000 rpm) rig is really demanding to meet this performance evaluation requirement. Apprehension and challenges for development of high-speed rig, instrumentations, and its rig characterizations are presented in details.

Keywords Air turbine · Current transducer · Drive · Data acquisition · Gas turbine · High-speed motor · High-speed alternator · Power supply

1 Introduction

Gas turbine driven alternators are specially designed for high-speed applications and also considered for high-temperature environment. Basically, permanent magnet technology-based alternator is the best candidate for this condition, but homo-polar technology-based alternator also plays good role for such kind of application in less efficient way [1, 2]. Evaluation of these types of alternator is a great challenge because its characterization completely depends on rotor speed. Variable speed control of rotor can be achieved by means of integrated high-speed drive. Development of high-speed drive or rig totally depends on the prime mover capability to provide sufficient mechanical power to the coupled alternator without losing its control.

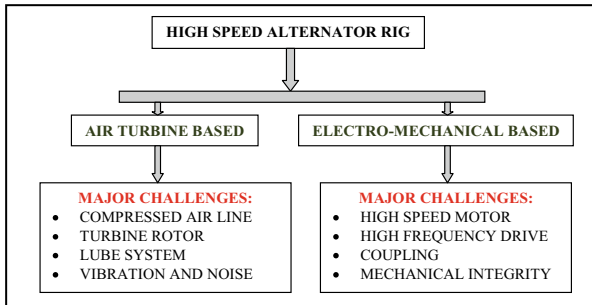
Air turbine and electric motor on this speed range can act as appropriate prime mover to meet the performance criteria. Many factors are influencing the development strategy for these kinds of prime movers. Air turbine-based prime mover demanding the capability of its turbine rotor to support the high-speed, whereas in case of electro-mechanical type prime mover, high-speed motor is used to produce enough

P. Kumari (✉) · V. Prabakar · A. N. Vishwanatha Rao
GTRE, DRDO, Bangalore, India
e-mail: poonamkumari.gtre@gov.in

© The Author(s), under exclusive license to Springer Nature Singapore Pte Ltd. 2023
G. Sivaramakrishna et al. (eds.), *Proceedings of the National Aerospace Propulsion Conference*, Lecture Notes in Mechanical Engineering,
https://doi.org/10.1007/978-981-19-2378-4_12

191

torque [3, 4]. Turbine rotor dynamics and motor inertia are important factors that affect the integrated sub-systems in terms of vibration, temperature, and its coupling. Challenges for both kinds of rig are depicted below:



This paper describes only air turbine-based high-speed alternator rig and also focuses on difficulties faced during rig development.

2 Air Turbine-Based Rig Setup

Rotation of shaft at high speed by means of any kind of prime mover introduces multifaceted technology. Air turbine-based rig was used to produce high speed to the shaft. This type of rig development associates many challenges with respect to development of air turbine rotor, compressed air supply and lube system, etc. System integration, mechanical integrity, and its operability are additional effort. To maintain and regulate the compressed airline pressure for long duration, it needs huge air reservoir with pressure regulator. This airline composed of a manual gate valve, a motorized gate valve for mass flow control, an orifice for mass flow measurement, a quick shut off butterfly valve to avoid over speeding of rotor in case of load interruptions, and a rubber bellow for vibration isolation. Precise operation and control of such a long air pressure line involve continuous monitoring and expertise.

After iterations, rig setup was attained to integration level to characterize the high-speed alternator. Major integration issue was related with turbine rotor assembly with alternator rotor. To achieve this, air turbine rotor was inserted into the hollow shaft of the alternator rotor and locked on the other side by using lock nut to transfer the torque. Another challenge was development of lubrication system to provide cooling and lubrication requirements of the alternator and its bearings, respectively. After continuous efforts and facing the multi-technological challenges, rig was developed. Rig layout and actual view of air turbine rig are shown in Figs. 1 and 2, respectively.

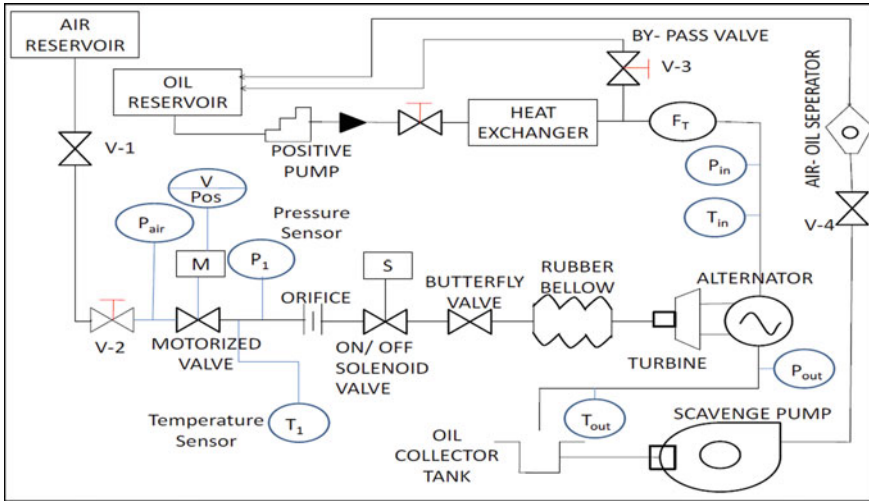


Fig. 1 Air turbine rig layout

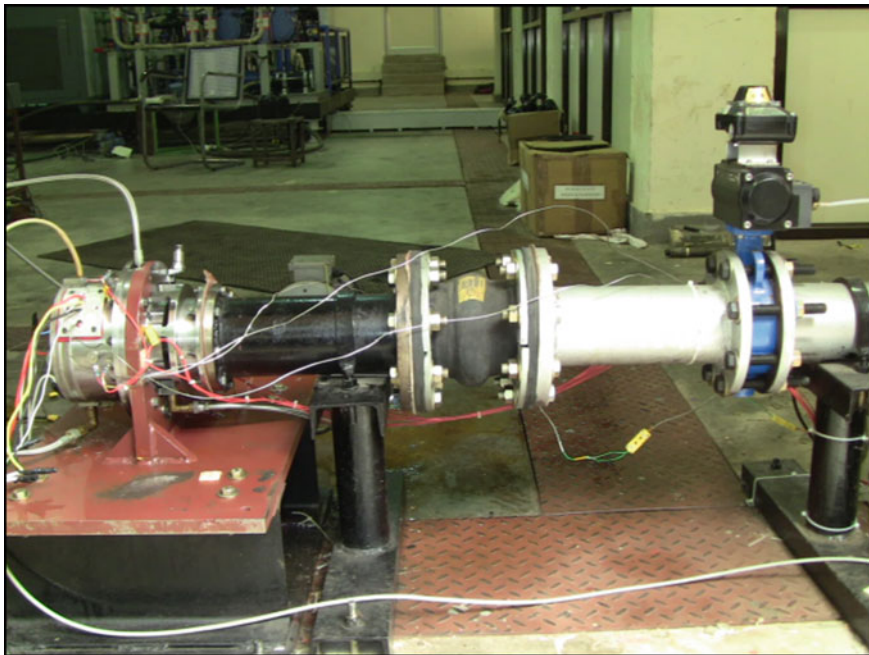


Fig. 2 Air turbine rig setup—actual view

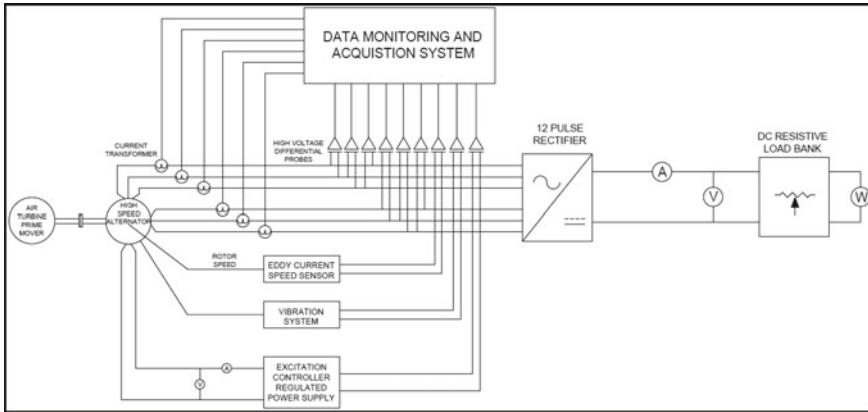


Fig. 3 Electrical instrumentation layout

3 Rig Instrumentations

Rig instrumentations for measurement of critical parameters are necessary before evaluation of integrated system. Hence, complete rig was instrumented with proper measuring device to capture the rig behavior. Significant mechanical and electrical parameters were measured and recorded in high-speed data acquisition system. Electrical instrumentation for system evaluation is shown in Fig. 3.

4 Measurements and Monitoring System

Measuring instruments and data acquisition system details are given below.

4.1 For Mechanical Parameters

4.1.1 Pressure

Turbine inlet air pressure and lubrication oil inlet pressure were measured by pressure transducer. All the pressure transducers/transmitters were calibrated by using pneumatic pressure and dead weight calibrator before use.

4.1.2 Temperature

All temperatures were measured using K-type thermocouples in the range of 0–200 °C. Thermocouples were placed at various locations like lubrication oil inlet, lubrication oil outlet, alternator casing at front side, bearing housing, etc.

4.1.3 Vibration

To monitor the vibration levels of the test rig and the integrated alternator, piezo-electric type accelerometers were mounted at critical locations on the test rig. The vibration data were acquired by using a multi-channel DSP base PROSIG system. Sensor with 31.6 mV/g sensitivity is used. The sensor outputs were connected to PROSIG system to monitored vibration level.

4.1.4 Speed

Eddy current probe was used and mounted at rear side of the drive shaft. Output signal from the probe was conditioned through signal conditioner and given to the timer/counter unit, which was programmed to display the speed in rpm. Speed measurement is also possible by deriving the frequency from alternator output voltage.

4.1.5 Flow

Measurement of lubrication oil inlet flow rate to the alternator is also important, and it was done by using a turbine flow meter.

4.2 For Electrical Parameters

4.2.1 Voltage Measurement

Differential voltage probes with suitable attenuation ratio were used for voltage measurement purpose. All output voltages of the alternator were continuously monitored, and same signals are taken to the high-speed acquisition system for data logging and processing.

4.2.2 Load Current Measurement

High-frequency AC currents were measured by Hall effect current transducers with nominal output of 4 volts at full range. All transducers were located in proper place, and outputs were given high-speed data acquisition system for measurement and record purpose.

5 Data Acquisition System

A high-speed data acquisition system (34970A) with a high bandwidth was designed by using a PXI-based embedded controller and data acquisition cards. All steady-state parameters were measured and given to the data acquisition card, which measures voltage, current, and frequency. All the process and instrumentation parameters were integrated to this system. All time domain signals, namely AC line voltages and AC line currents, were measured using two high-speed simultaneously sampling cards. This sampling card receives the raw data from high-speed instruments and after processing provides data to LabVIEW. Full alternator load test architecture is defined in LabVIEW in such a way that critical parameters like transients in voltage/current with respect to loading/unloading, output power, waveforms, etc., can be seen in real time and can also store data simultaneously for future analysis.

6 Rig Considerations

Rig was developed for performance evaluation of high-speed alternators. Rig characterization was carried out to ascertain its capabilities to achieve the desired requirements. Without alternator integration, preliminary checks like mechanical integrity, vibration, oil leakage, shaft rotation at various speeds were checked to assure rig operability. Shaft rotation at rated speed along with all controllable parameter was also conducted many times to avoid system failure during integral trial. Rig was subjected for no load test and load test separately. Details are given in succeeding paragraph.

6.1 No Load Test

Under no load test, turbine rotor system was first rotated at low speed and gradually increased to higher speed by means of increasing the air mass flow rate to the air turbine-alternator rotor system. This run was carried out without electrical load to understand the dynamics of the rig. Considering very high speed of alternator, the rotor was expected to have some critical speeds within its rated speed. Hence, the

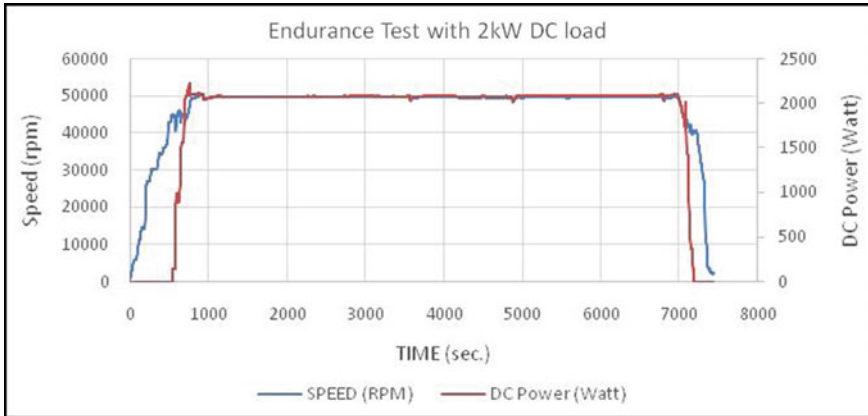


Fig. 4 Endurance test plot

vibration levels were monitored carefully to full speed, and resonant frequencies were identified to decide safe operational regimes during the run and to draw the test schedule. With this dynamic behavior of rotor system, safe test schedule is drawn to accelerate the alternator quickly while passing through resonant speed band. No load run up to full speed was carried out.

6.2 Load Test

After rig dynamic stability at high speed and confirming the comfortable region of vibration level, load test was carried out at 50,000 rpm. First, alternator was loaded in step up to 2 kW DC load by DC load bank, and parameters were measured. Subsequently, endurance test for continuous 2 h with 2 kW DC load was conducted to validate the alternator design parameters. All performance data were monitored and captured in data acquisition system for further analysis. Test results are plotted separately in Figs. 4 and 5.

7 Conclusion

Alternator was evaluated on air turbine-based rig with rated DC load. Common difficulties were observed with respect to critical speed, high vibration, bearing failure, and synchronizations with electrical equipment. Due to these great challenges, rig behavior was very unusual. Hence, all rig modules were subjected for many design iterations to meet development strategies. Multi-technology-based high-speed rig is successfully developed and evaluated with integrated alternator.

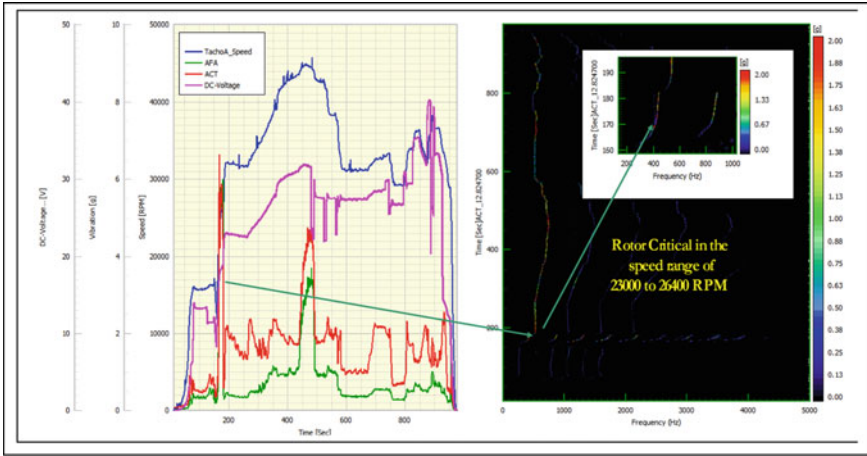


Fig. 5 Vibration plot

Acknowledgements The authors wish to thank, The Director, GTRE, Bangalore-93, for his constant encouragement and valuable guidance. Thanks to the entire GTRE team members for their valuable suggestions and support. Special thanks to propulsion division NAL, CSIR, Bangalore for extended cooperation and involvement in rig development and its operation, without which it could not have been possible.

References

1. Tapani J (1988) High speed electrical machines. In: Proceedings of the conference on high speed technology, Lappeenranta, Finland, pp 175–185
2. Chudi P, Malmqvist A (1989) Development of a small gas turbine-driven PM high speed generator (HSG). Thesis, KTH, Sweden
3. Pyrhonen J (1988) Some aspects of high-speed rotor design in electrical machines. In: Proceedings of the conference on high speed technology, Lappeenranta, Finland, pp 231–246
4. Claire S Gas turbine, a hand book of air, land and sea applications

Independent Verification and Validation of Aero Engine Propulsion System Software



Sonal Shekhawat , Arshad Iqbal , Usha Srinivasan ,
and Sreelal Sreedhar 

Abstract With the evolving technology and extensive software usage, aircrafts have become a software embedded flying contrivance. Navigation system, landing gear system and propulsion system are some of the major subsystems of the aircraft. Propulsion system is one of the vital sub-systems with demarcated purpose to propel the aircraft. Earlier, the control unit of the engine was completely controlled by mechanical means but with the technical advancements it has been automated by software embedded control unit. Software has become so important these days that its safety, complications and risks cannot be ignored. The embedded software in digital engine control unit is a safety critical software as its failure can lead to hazardous state that can cause loss of property, damage to environment and even loss of human life. Therefore, intensive care needs to be taken while ensuring the safety and reliability of such software. The traditional testing approach needs to be fortified with more firm and rigid standardized methodology in order to diminish the probability of failure of the system. This paper throws light on the Independent Verification and Validation process followed to ensure safety, reliability and robustness of aero engine propulsion system software.

Keywords Verification and Validation · DO-178B · Traceability · Static testing · Dynamic testing

1 Introduction

Over recent years, software has gained its importance in more or less every field of engineering. Across all the disciplines including aviation systems, engineers rely on software these days for seamless interaction with the hardware. Various subsystems such as aircraft propulsion system, aircraft structural system, air data and flight instrumentation, navigation system and communication system constitute the complex machinery known as aircraft [1].

S. Shekhawat (✉) · A. Iqbal · U. Srinivasan · S. Sreedhar
Gas Turbine Research Establishment, DRDO, Bangalore, India
e-mail: sonalshekhawat209@gmail.com

© The Author(s), under exclusive license to Springer Nature Singapore Pte Ltd. 2023
G. Sivaramakrishna et al. (eds.), *Proceedings of the National Aerospace Propulsion Conference*, Lecture Notes in Mechanical Engineering,
https://doi.org/10.1007/978-981-19-2378-4_13

Aircraft propulsion system is one of the vital subsystems to propel the aircraft. Propulsion means to push or to drive forward. It works on Newton's 3rd law of motion, which states that for every action there is an equal and opposite reaction. To drive the aircraft in the preferred direction, adequate amount of thrust is required to be generated in the opposite direction which is attained by an engine.

As per the various implementations and principles followed, different kinds of engines can be used for aerospace propulsion system such as piston engine and gas turbine engine. The piston engine works on the principle of converting the pressure into rotating motion using pistons, whereas the gas turbine engine uses the pressure generated from fuel ignition to produce thrust. The gas turbine engines have got quite a few advantages over piston engine such as very high power to weight ratio and much lighter weight [2]. It follows the principle of Brayton's cycle and has got three main sections, namely compressor, combustor and turbine. Each of these sections has a well-delineated purpose such as compressing the incoming air, air/fuel mixture, ignition timing, idle speed and energy extraction from the heated air to turn the compressor [3].

Before the introduction of electronic control units, each of the above-mentioned functionality was accomplished with mechanical coupling and control. However, as the avionics system evolved, the usage of software has secured a vital footing by enhancing system's reliability and performance.

In today's aircraft design, Digital Electronic Control Unit (DECU) is designed with the embedded software to autonomously control the engine all through its operating range in both normal and off-normal conditions. In case of mechanical equipments, each operation needs to be executed mechanically by the pilot, which might result in distraction and lesser attention toward another prominent task.

During a risky situation at 35,000 feet, pilot cannot be expected to take the complete charge of the mechanical control system. For that matter, DECU decreases pilot's workload by providing self-operating, self-monitoring, redundant and failsafe setup. With all these advancements in the airborne systems technology, the aircraft has become a flying machine, controlled and monitored by complex software. Avoiding aircraft accidents and providing air safety is the need of the hour of aviation system development. In this context, the safety critical software needs to have a very high assurance of the quality with respect to system's safety, reliability and security which is ensured by Independent Verification and Validation (IV and V).

The Patriot missile system shutdown, Ariane five rocket explosion, Ethiopian Airlines Flight 302 crash and Lion Air Flight 619 crash are some of the known examples from the past where software errors have certainly led to loss of irrecoverable human life and critical missions. This paper talks about the IV and V process followed to ensure the exactitude of safety critical embedded software which in turn assures its quality, reliability and safety.

2 Why IV and V?

Undeniably, software is one of the most intricate man-made piece. Unlike hardware, software errors are not realistically visible. Software does not follow any proved laws of physics, so as to predict the type and the consequences of the error. Some bugs still remain in the software even after meticulous and rigorous testing. Verification and Validation is often mistaken as testing. Testing is only a part of V and V process and not the V and V as a whole.

The development team also tests the software before delivering it, then, what is the need of an Independent V and V activity? Developer works with constructive mind-set, whereas the verifier works with a destructive mind-set. While developer needs out-of-the-box thinking and creates lens in finding better ways to optimize the solution, testing needs patience, discipline and relentlessness in doing repetitive work.

Every human being thinks that he is right and developer is no exception to that. With a default attitude to authenticate the efforts, the developer articulates the test cases which are adequate to demonstrate the intended functionality. On the contrary, the independent verifier creates a wave of negativity to disagree with the developer's testing regarding the correctness and completeness of the envisaged objectives.

What is IV and V? IV and V stands for Independent Verification and Validation. Verification ascertains the correctness of the software in terms of the process followed to ensure the intended functionality. Validation guarantees the mapping of the software functionality to the user requirements and assures the completeness of the software [4]. As per Boehm: Verification: "*Are we building the product right?*" Validation: "*Are we building the right product?*" [5].

Moreover, an independent test resource would rule out any misunderstanding in the requirement by reviewing, analyzing and testing the software without any preconceived notion about the software, thereby enhancing the confidence in the delivered product.

3 Do-178b

To ensure the global acceptance of any product, the development process should adhere to some standard guidelines which are accepted worldwide. A standard is a commonly agreed upon technical document which is formulated to provide uniform guidelines. All the stakeholders of a specific process, product or service come together to form a standard [6].

Accomplishment of quality goals, improved software management, overcoming the schedule and budget constraints are some of the potential benefits attained by the usage of standards. There are various standards laid out for different safety critical system software such as automotive standard—ISO 26262, railway standard—CENELECEN 50,126, nuclear standard—IEC 60,880 and medical standard—IEC

Table 1 Categorization of software as per criticality levels

Criticality level	Design assurance levels	Examples
When software failure results in catastrophe events	Level A	Flight and engine control system
When software failure leads to hazardous or severe major failure conditions of aircraft	Level B	Flight management system
When software failure leads to major failure condition of the aircraft	Level C	Collection of internal built-in test equipment (BITE) faults
When software failure leads to minor failure conditions of the aircraft	Level D	Flight history, keyboard monitor command
When software failure does not hamper the operational capability of aircraft or pilot workload	Level E	Entertainment equipment

62,304. Similarly, DO-178B is an aerospace standard for airborne systems and software considerations. It categorizes the software in different levels based on the failure conditions and the criticality levels of the software as given in Table 1.

Each level of the software has its own specific set of objectives defined. The focus of this paper is toward the level A objectives mandated for aero engine propulsion system software.

4 Software Verification

Software verification is an integral process that is applied throughout the entire software life cycle. It starts in the planning phase and goes all the way through product release and even into maintenance [7]. As per the glossary of DO-178B, “*Verification is the evaluation of the results of a process to ensure correctness and consistency with respect to the inputs and standards provided to that process*”[8].

It ensures that uncovered and unidentified errors do not propagate to the next step of the activity, thereby reducing the amount of work that the developers need to redo in case the error propagates to the next level. A combination of reviews, analysis and thorough testing satisfies the objectives of software verification which will be elaborated further.

4.1 Review

Review is a holistic process which scrutinizes the activity through a different perspective and provides a qualitative assessment of the correctness [8]. It helps uncovering the defects and errors at early stage. Reviewing an activity is carried out at every stage of the software development life cycle, beginning from requirement gathering and all the way through design, development and testing. The cost incurred to rectify the defect is inversely proportional to the software development detection phase. After evaluating multiple projects, Barry Boehm [5] approximated the cost impact analysis as depicted in Fig. 1 [9].

The considerable increase in the cost encountered to detect and resolve the bugs during the requirements phase to testing phase can heftily increase the software expenditure.

The robust review process across the software development life cycle (SDLC) enhances efficiency and confidence in the product being delivered. There are various review activities which are carried out at different stages such as code review, design review and requirements review to ensure that the developed software meet its requirements and has been represented as per the agreed standards.

4.1.1 Document Review

It involves reviewing all the SDLC artifacts such as software requirements document (SRD) and software design document (SDD). Document review ensures readability, understandability, completeness and traceability with respect to its SDLC counterparts. Apart from ensuring the bidirectional traceability across SDLC, review also handles the assessment of compliance to its corresponding standards.

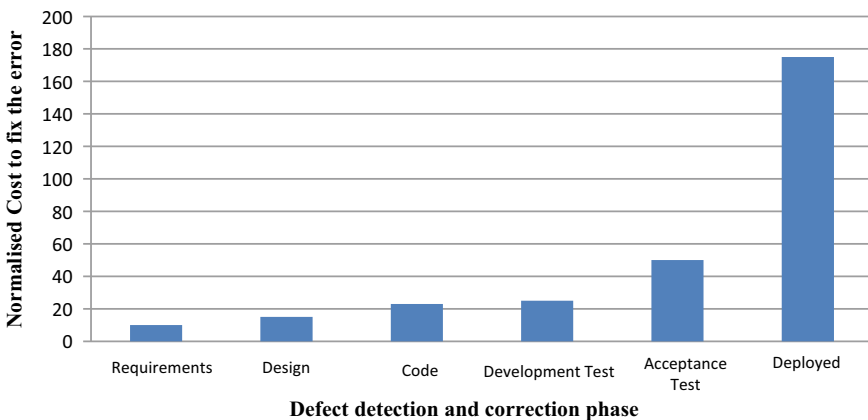


Fig. 1 Increase in cost to fix during SDLC

4.1.2 Code Review

In order to assure the completeness and accuracy of the software, the source code is reviewed with respect to the low-level requirements in code review. It makes sure that the coding standards followed in the code are in compliance with software design plan (SDP). Reviewing the code also ensures the bidirectional traceability between the low-level requirements and code. After each review, problem reports are generated by incorporating all the review results and shared with the developer team for rectification. This iterative process continues until the code becomes bug-free.

4.2 Analysis

As per DO-178B, analysis concentrates on the obtained results of the software development and software verification. It provides repeatable evidences of correctness [8]. There are various types of analysis performed during the safety critical software life cycle. Analysis not only inspects the completeness and the intended task of the software but also scrutinizes its association to the other components in the aero engine system [8].

In order to report repeatable evidences of the correctness, analysis should be perfectly documented and maintained. The procedure followed to carry out the analysis should have well-defined purpose, criteria and all the other related requirements to identify the analysis methodology and data items to be analyzed. Detailed instruction set is required to perform analysis. The artifacts generated as a result of analysis procedure are further scrutinized and corrective actions are suggested. There are various kinds of analysis which are performed as per the requirements [7]:

- (1) Worst case execution analysis,
- (2) Memory margin analysis,
- (3) Link and memory map analysis,
- (4) Load analysis,
- (5) Interrupt analysis,
- (6) Math analysis,
- (7) Errors and warning analysis,
- (8) Partitioning analysis.

4.3 Testing

4.3.1 Static Testing

Static testing is a testing technique which detects the defects without having the code executed. This testing is also known as non-executable testing as code execution is

not required for this testing. Static testing comprises of software inspection, code walkthrough and static analysis.

IEEE defines the software inspection technique as: a visual examination of a software product to detect and identify software anomalies, including errors and deviations from standards and specifications. Inspections are peer examinations led by impartial facilitators who are trained in inspection techniques. The goal of software inspection is to detect the software flaws by scrupulous peer examination, whereas code walkthrough aims at evaluating the source code file, detecting bugs, omissions and discrepancies. The output of code walkthrough process documents the anomalies and corresponding action items [10].

Static analysis is a procedural analysis of detecting anomalies, checking code complexity and analyzing data flow in the source code. It is usually performed by using tools like data flow analyzers, rule checkers and complexity analysis tools. It analyzes the complexity of the code by computing a variety of metrics which can be used to enforce appropriate standards. Data flow analysis analyzes the action on the variables in the source files and reports any kind of problem with the usage.

4.3.2 Dynamic Testing

Dynamic testing is a testing approach which focuses on testing the dynamic behavior of the software. This testing needs the code to be executed; hence, it is termed as executable testing. Dynamic testing being implemented at a later phase of the SDLC, its associated cost impact on error addressal is relatively high. In this methodology, the source code is probed by providing various inputs to the software to ensure the reliability and robustness of the software.

4.3.3 Unit Testing

In unit testing, individual modules of the source code are tested at component level. Test Cases are designed and executed to ensure the accurate functionality of each module. It tests each module independently against the expected results as per the code and ensures that the generated results; i.e., the actual results are identical to the expected results. Hundred percent structural coverage, dead code elimination and deactivated code analysis are accomplished by means of unit testing.

4.3.4 Software–Software Integration Testing

In Software–software integration (SSI) testing, independent modules are integrated and tested for the apt functionality. It uncovers all the errors which have been introduced as a result of the integration of the modules. It aims at testing the interface between the modules. To perform the integration testing, a well laid-out plan should be in place which includes the designing of test cases, test scenarios and test scripts

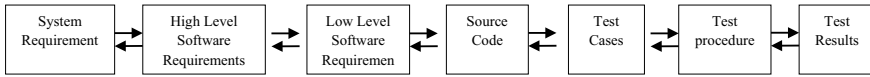


Fig. 2 Bidirectional traceability

followed by the execution of test cases. The detected defects are further traced and documented, and this continues till the source code is completely tested.

4.3.5 Hardware–Software Integration Testing

Once the application software is ready, it is imported on the hardware. Hardware–software integration (HSI) testing aims to expose the errors which occur when software is executed in the target operating environment. Different kinds of tests are executed to certain the robustness and reliability of the system. Various dynamic errors such as control loop behavior, interrupt handling, timing, memory faults are uncovered during HSI testing [7].

5 Traceability

As per DO-178B, traceability is the evidence of the association between items, such as between process outputs, between an output and its originating process or between a requirement and its implementation [8].

Establishing traceability across SDLC is crucial in order to guarantee that no unwanted functionality is introduced in the code. Traceability ensures that every low-level software requirement is traceable to some system requirement. Traceability verification at each stage starting from system requirements to test results assures that only the intended requirements have been implemented. Bidirectional traceability as shown in Fig. 2 assures that no unwanted task has been coded in the software. Traceability, once established, gives the confidence that each and every requirement specified in the SRD has been implemented in the source code. If some changes take place, traceability helps to detect impacted modules or data that need to be verified again.

6 Conclusion

The invention of aircraft with demarcated subsystems, such as landing gear, propulsion system, navigation system and telemetry system, is an extremely intricate research that humans have ever attempted. The convoluted functionality of the aircraft propulsion system depends on the complex gas turbine engine controlled by crucial

software embedded DECU which is the concealed brain behind the safe travels. Ensuring the quality, reliability, impregnability and security of such safety critical software is mandatory. Propulsion system, being one of the most intricate functionalities of the aircraft system, contributes to the criticality and complexity of the embedded software. In this software reliant era, performing IV and V activity has become a must to muddle through the exponential increase in the complexity and criticality of the source code and rapid technology changes to accommodate the capability enhancement. Would any one risk the human life to a complex machine after knowing that it could have been subjected to another perspective before flying but hadn't? [11].

IV and V is that another perspective which brings the destructive view into the picture to track down the design shortcomings and code bugs by diligently reviewing and analyzing the results. IV and V gives the confidence about the correctness of the software being deployed and makes sure that the final software is meeting user requirements [12]. It ensures that the software is reliable and serves no extra functionality, thereby eliminating the risk of failure. It is an efficacious risk alleviation strategy that effectively exposes the faults and looks out for the opportunities for improvement throughout the SDLC [13].

IV and V also results in significant reduction in overall cost of the project savings by augmenting the odds of exposing the high-risk errors early in SDLC [14].

An oversight is an open invitation to safety risks, vulnerable data, security issues and fatal errors that are sufficient enough to break the system down causing financial loss, mission failure, loss of irrecoverable human life and atrocious destruction. A well-defined IV and V when in place serves as a mitigation strategy to avoid these disastrous scenarios and to confidently deploy the safety critical software in the airborne systems.

Acknowledgements The author expresses the gratitude to Director GTRE for his consent to demonstrate this work. The author would like to thank Mrs. Pratibha Menon Sc "D," for her continuous moral support and encouragement in pursuing this activity.

References

1. <http://assets.press.princeton.edu/chapters/s9497.pdf>
2. <https://www.differencebetween.com/difference-between-gas-turbine-engine-and-vs-reciprocating-engine-piston-engine/>
3. https://www.cast-safety.org/pdf/3_engine_fundamentals.pdf
4. Pressman RS, Software engineering, a Practitioner's approach
5. Boehm B (1981) Software engineering economics. Prentice Hall, pp 463–365
6. <https://www.cen.eu/work/endev/whatisen/pages/default.aspx>
7. Rierson L, Developing safety-critical software: a practical guide for aviation software and DO-178C
8. DO-178B Document/RTCA DO-178B (EUROCAE ED-12B)
9. <https://pdfs.semanticscholar.org/d236/2d97f419c29c5ad78df4f79d4e7061c19155.pdf>
10. Khurana H (2016) Software testing. Pearson India Education Services Pvt. Ltd., pp 14–24

11. Lewis RO (1992) Independent verification and validation—a lifecycle engineering process for quality software. A—Wiley Interscience Publication, pp 3–10
12. <https://www.nasa.gov/centers/ivv/services/whativv.html>
13. <https://panorama-consulting.com/wp-content/uploads/2016/07/Independent-Validation-Verification.pdf>
14. <https://www.belmero.com/2017/06/the-benefits-of-ivv/>

Influence of Chiral Lattice on Modal Characteristics of Structures



Rukmangad S. Barad, B. K. Nagesh, Sanjay Barad, and T. N. Suresh

Abstract Design of mechanical structures for aeronautical applications is mainly aimed towards maximizing the strength-to-weight ratio and alleviating the vibratory response to the maximum extent so that the stresses are well below the endurance limit. The present paper aims to bring out features that fulfil these requirements. An innovative approach is the introduction of a chiral lattice in the structure that can enhance the damping in structure through intentional deformations in the chiral webs and that can also be tuned to act as vibration absorbers to reduce the overall vibratory response of the structure. The design features suggested can be successfully implemented in components like aerofoils, engine carcass, blisks and disks. This is possible due to the advent of 3D printing technology. The paper aims to bring out these aspects by considering a simple cantilever beam with a chiral lattice internal to it. Further parametrization of geometric designs is undertaken to understand the vibratory response characteristics.

Keywords Chiral lattice · Modal analysis · 3D printing

Nomenclature

C	Damping coefficient
K	Stiffness
M	Mass
Q	Qualification factor
W	Total kinetic energy
C_c	Critical damping
F_d	Damping force

R. S. Barad (✉)
PES University, Bangalore, Karnataka, India
e-mail: ruks1999@yahoo.com

B. K. Nagesh · S. Barad · T. N. Suresh
GTRE, Bangalore, Karnataka, India

© The Author(s), under exclusive license to Springer Nature Singapore Pte Ltd. 2023
G. Sivaramakrishna et al. (eds.), *Proceedings of the National Aerospace Propulsion Conference*, Lecture Notes in Mechanical Engineering,
https://doi.org/10.1007/978-981-19-2378-4_14

$F(t)$	Dynamic force
ΔW	Energy dissipated in one cycle
β	Hysteretic damping constant
δ	Logarithmic decrement
ϕ	Phase
ζ	Damping factor
η	Loss factor
φ	Specific damping capacity
ω_n	Natural frequency
ω_d	Damped natural frequency
μ	Mass ratio
γ	Optimal damping ratio
ϵ	Optimal frequency ratio

1 Introduction

Any dynamic system/structure is described by the storage element that stores energies in the form of potential or kinetic energy and the energy dissipative element, also popularly referred to as a non-conservative element. In addition, the forcing function is an external excitation that the system experiences in due course of its operation. The response of the system is a function of all these elements and type of excitation. It is this characteristic of the system that is defined by the ratio of the response to the excitation in the Laplace domain and what is called the transfer function (TF) of the system. The same characteristics when represented in the frequency domain are called a frequency response function (FRF). In other words, the geometric definition in terms of mass distribution, the material properties in terms of density, Young's modulus and interfaces between the mating parts define the stiffness, mass and damping elements of the system. This generalized system equation is given by Eq. (1).

$$[M]\{\ddot{x}\} + [C]\{\dot{x}\} + [K]\{x\} = \{F(t)\} \quad (1)$$

wherein the M , C and K represent the mass, damping and stiffness matrices of the system, respectively, and the terms x and $F(t)$ are the response and forcing vectors, respectively.

The present paper aims at controlling these system parameters by the introduction of chiral lattices in the structure to alleviate the vibration response of the structure. This is with the aim of enhancing intentional deformations, resulting in increased damping in specific modes and also making it to behave as a vibration absorber, thereby alleviating the overall vibratory response.

The paper focuses initially on the estimation of damping and later on brings about the vibration absorber concept to be integrated into the final structural configuration for study.

2 Modelling of Damping in Mechanical Systems

Damping is a non-conservative energy element in a dynamic system. These elements represent the various energy dissipation mechanism in a system, viz. friction at interfaces, viscous drag, internal friction in the lattice, electrical resistance, collision, electromagnetic, radiation, etc. The energy is dissipated to the surrounding in the form of energies like thermal, acoustic, etc. The amount of energy dissipated is a measure of damping in the system and is defined by a term called “damping capacity”. This damping capacity is a ratio of the energy dissipated in one cycle to the maximum amount of energy accumulated in the structure.

Most of the systems, though not necessarily, demand maximization of this damping so that the structure limits its amplitude of vibration response. This in turn minimizes stresses in structural members, thus enhancing the life of the system.

There are phenomena wherein the damping can be negative, in which case the system leads to unstable vibratory response. In this case, the mechanism is a regenerative field wherein the energy is fed back into the system, resulting in continuous increase in the amplitude of the response. Few examples of such unstable or self-excited phenomena are aeroelastic flutter and thermoacoustic instabilities like screech in jet engine combustors or jet pipes, etc. However, this aspect is not considered in this paper.

Depending on the mechanism of damping existing in the system, the damping element is modelled. This could be a viscous damper model or friction damper or hysteric damper model, etc. The viscous damper model with a constant coefficient is the most common and simple. The other models also play a role when a close simulation is required. But, for a start, an equivalent viscous damper model has been arrived at so that the solution is rather simple and approachable.

2.1 Viscous Damping

For a system with a viscous damper, the damping force is given by;

$$F_d = -C\dot{x} \quad (2)$$

The negative sign indicates that the force is opposite to velocity. In the present context, the underdamped case where $\zeta < 1$ is of more interest. The generalized solution for this underdamped free vibration case is given by

$$x(t) = X_0 e^{-\zeta\omega_n t} \cos\left(\sqrt{1 - \zeta^2}\omega_n t + \phi\right) \quad (3)$$

The oscillation amplitude gradually decreases with time. This is shown in Fig. 1.

For a forced vibration with harmonic excitation, the generalized solution for the SDOF system is given by

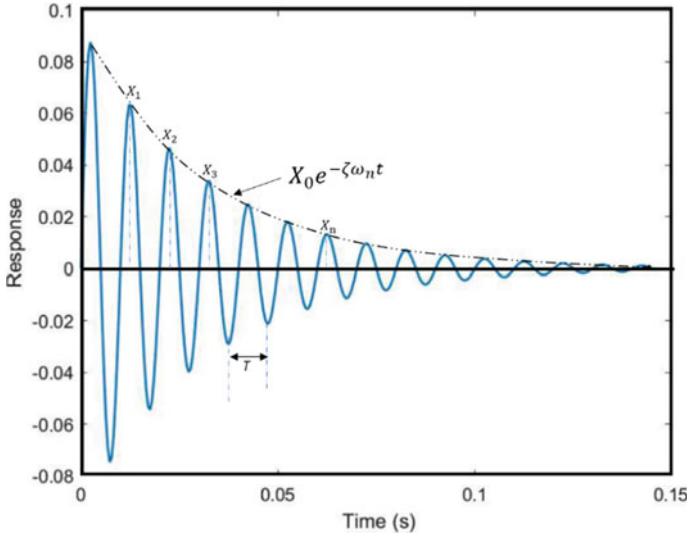


Fig. 1 Time response of SDOF system for free vibration

$$\begin{aligned}
 x(t) = & e^{-\zeta \omega_n t} \left(C_1 e^{-i \omega_n t \sqrt{1-\zeta^2}} + C_2 e^{-i \omega_n t \sqrt{1-\zeta^2}} \right) \\
 & + \frac{F}{\sqrt{(K - \omega^2 M)^2 + (\omega C)^2}} e^{i(\omega t + \phi)}
 \end{aligned}
 \tag{4}$$

This consists of a complimentary solution as a transient part that persists only for a limited time and the particular integral representing the steady-state part that exists as long as the forcing function remains active. The information can be represented in frequency domain as shown in Fig. 2. This is called the frequency response function (FRF).

This FRF is used for evaluating the damping characteristics in addition to the other modal parameters, viz. mode shapes, modal mass, modal stiffness and frequencies. Experimentally, this is arrived by performing a ping test if the structure has low damping. For structures with higher damping, a continuous excitation using a shaker is beneficial.

The excitation is measured using a force transducer, while the measurement of the responses is done using accelerometers. There are also different types of excitations one may use for better results, viz. step sine, random, burst random, chirp, etc., each having its own advantages.

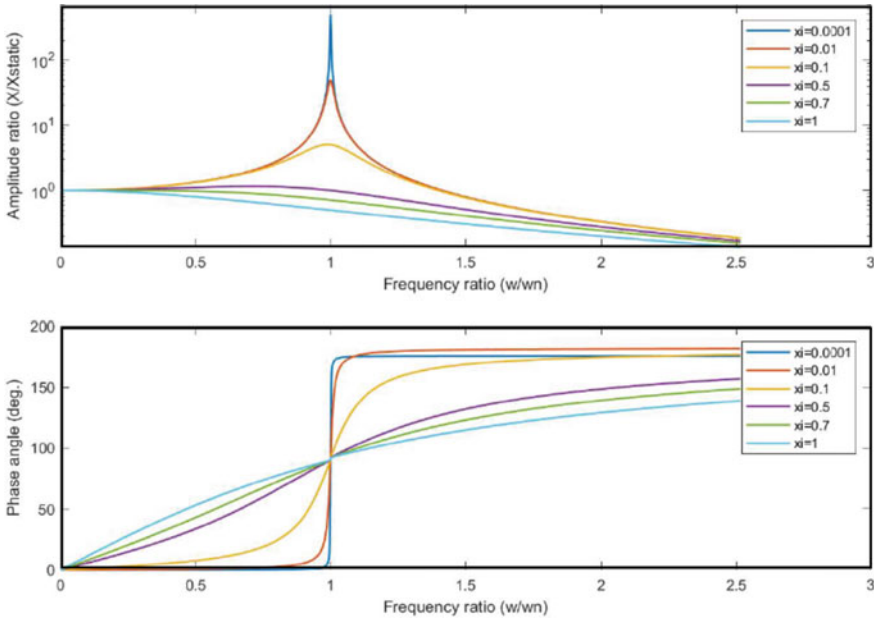


Fig. 2 Frequency response function for SDOF system under forced excitation

2.2 Hysteric Damping

In this case, the energy is dissipated through the friction between the internal planes that slip or slide during the deformation/vibration. This exhibits a hysteric loop in the stress–strain or force displacement curve. The area enclosed by this curve is the energy loss per cycle per unit volume of the material. This material damping is a function of stress amplitude, internal forces, number of cycles, geometric parameters, quality of surfaces and temperature. This damping is related with the stress amplitude by the expression

$$D = J \cdot \sigma^n \tag{5}$$

where J and n are constants. The typical value of “ n ” lies between 2 and 4, but generally a value of 2.3 is used. Damping increases with number of cycles, and finally a fatigue collapse occurs. The value of J varies significantly as per the literature survey [1].

The hysteric damper is only a linear device in the sense that it is described by a linear frequency response relationship. This alternative damping model has the advantage of not only describing more closely the energy dissipation mechanism exhibited by most real structures, but also provides a much simpler analysis when dealing with multiple degree of freedom systems.

2.3 Structural Damping

This is a more generic term that encompasses the energy dissipation through internal friction within the material as well as the dissipation due to the friction at the interfaces like riveted joints, lamination, welding joints, spigots, bolted joints, etc. As the energy dissipation mechanism is through friction, this is governed by the friction force. The friction force is governed by the normal force and the coefficient of friction at the interface between the components and is not dependent upon velocity or displacement. More details are available in literature.

3 Techniques for Evaluating Damping

This damping parameter can be experimentally determined by various techniques; the most popular and simple ones are the logarithmic decrement technique and the half power point technique.

3.1 Logarithmic Decrement Technique

The logarithmic decrement represents the rate at which the amplitude of free damped vibration decreases. For viscous damping, this is given by Eq. (6).

$$\delta = \frac{1}{M} \ln \left(\frac{x_1}{x_{n+1}} \right) \quad (6)$$

It is a dimensionless quantity and is related with the damping factor ζ by Eq. (7)

$$\delta = \frac{2\pi\zeta}{\sqrt{1-\zeta^2}} \simeq 2\pi\zeta \quad (7)$$

Similar decrement can be arrived for hysteric damping, and this is given by Eq. (8)

$$\delta = \ln(1 + \pi\beta) \quad (8)$$

where β is called as the hysteretic damping constant.

This procedure can be used for built-up structures. However, this β then established includes the effect of material damping, friction damping, aerodynamic damping, etc. in short, it is the combined damping.

In order to evaluate the material damping specifically, one may use a long strip of the metal with defined geometry and subject it to a free decay on excitation by an impulse. This decay is predominantly due to the material damping, as the

aerodynamic damping is meagre, and there is no boundary condition imposed. This material damping is a material property and is available in literature for various materials, refer [2]. These can be used as a first cut value for any solution if required. However, for precise models, an experimental evaluation is must.

3.2 Half Power Point Technique

The half power point technique uses the FRF plot for estimation of damping. This FRF is generated during the experimental modal testing of a component. The damping is estimated by establishing the amount of energy dissipated per cycle at each of the resonances.

The half power points on the curve are the point where the energy dissipated is half the value at resonance. In that case, these points on the response curve should be at 0.707 of the peak value at resonance, refer Fig. 3. The corresponding frequency values at these half power points and the peak response points can be used for establishing the loss factor. The loss factor is given by Eq. (9);

$$\text{Loss factor } \eta = \frac{\omega_2^2 - \omega_1^2}{2\omega_n^2} = \frac{1}{Q} = 2\zeta \tag{9}$$

This expression involves only the frequency values, and hence, an accurate estimation of the peak response is must. To overcome this, one resorts to the curve fitting techniques wherein one can precisely get the peak response, refer Fig. 8. The half power points can be located and the precise value of the natural frequency— ω_n and corresponding frequency values ω_1 and ω_2 at half power points can be read, refer Fig. 3.

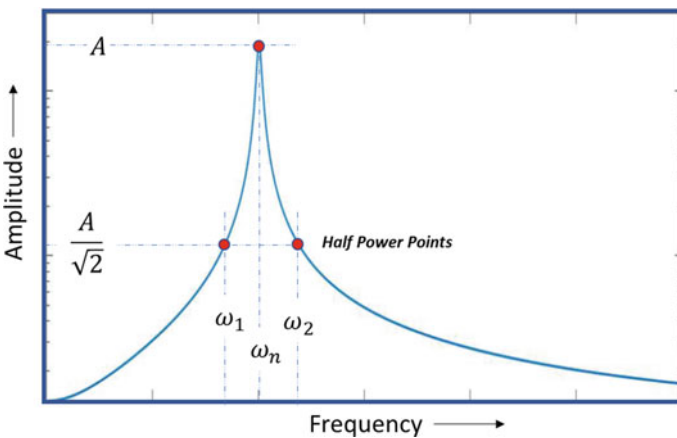


Fig. 3 Frequency response function for estimation of Q -factor

4 Equivalence Between Viscous and Other Damping Mechanisms

Very often, the damping is modelled as an equivalent viscous damping for various forms of energy dissipation mechanisms. This is because of its simplicity to model. The equivalence is arrived at by considering the energy dissipated in one cycle and equating it to the energy dissipated in one cycle of viscous damping. For a viscous damper, this is given by Eq. (10);

$$\Delta W = \pi C \omega_d X^2 \quad (10)$$

As observed in viscous dampers, the energy dissipation is proportional to the square of the amplitude of vibration. This is not constant for a given value of damping constant and amplitude but rather depends on the frequency of oscillation— ω_d .

This energy dissipation is also often expressed as fraction of the total kinetic energy of the vibrating system and is called the specific damping capacity. This gives Eq. (11);

$$\begin{aligned} \frac{\Delta W}{W} &= \frac{\pi C \omega_d X^2}{\frac{1}{2} M \omega_d^2 X^2} = 2 \left(\frac{2\pi}{\omega_d} \right) \left(\frac{C}{2M} \right) \\ &= 2\delta = \frac{4\pi\zeta}{\sqrt{1-\zeta^2}} \approx 4\pi\zeta = \varphi \end{aligned} \quad (11)$$

This specific damping capacity φ is useful in comparing the damping capacity of various materials and also arriving at the equivalent damping model.

The other term that is used for expressing the damping is the loss coefficient, which is defined as the ratio of energy dissipated per radian to the total strain energy, and this is given by Eq. (12).

$$\eta = \frac{(\Delta W/2\pi)}{W} = \frac{\Delta W}{2\pi W} \quad (12)$$

So, we have the relations, and these are given in Eqs. (13)

$$\eta = \frac{\varphi}{2\pi} = \frac{\delta}{\pi} = \frac{1}{Q} = 2\zeta \quad (13)$$

A similar approach can be followed for hysteretic damping. In this case, the energy is dissipated through the friction between the internal planes that slip or slide during the deformation/vibration. This exhibits a hysteretic loop in the stress–strain or force displacement curve. The area enclosed by this curve is the energy loss per cycle per unit volume of the material.

Experimentally, this energy loss is observed to be independent of frequency but is approximately proportional to the square of the amplitude. The energy dissipation

per cycle is given by Eq. (14):

$$\Delta W = \pi K \beta X^2 \quad (14)$$

Here, β is the dimensionless hysteretic constant of the material and is a material property. This is called the loss factor.

The product $K\beta$ is related to the size, shape and material properties of the system. The constant π is used as a convenience to have a similarity with the viscous damping equation of work dissipation given in Eq. (14). The log decrement for this is given by Eq. (15)

$$\delta = \frac{2\pi\zeta}{\sqrt{1-\zeta^2}} \approx 2\pi\zeta = \pi\beta \quad (15)$$

Similarly, if we equate the energy dissipated in both cases, we have Eq. (16);

$$\begin{aligned} \Delta W &= (\pi C \omega_d X^2)_{\text{viscous}} \\ &= (\pi K \beta X^2)_{\text{hysteretic}} \end{aligned} \quad (16)$$

Implies Eq. (17)

$$C_{\text{equivalent}} = \frac{K\beta}{\omega_d} \quad (17)$$

This is the equivalent hysteretic damping coefficient given by Eq. (17) and is represented as viscous damping in the basic equation of dynamics.

5 Representing the Chiral Lattice-embedded Cantilever in State-space Form

The vertical chiral-embedded cantilever can be represented using a lumped parameter model and formulating the state-space equation. The advantage is to understand the influence of each parameter or system variable on the dynamic characteristics. The central chiral core is represented by mass $M2$, and the adjoining cantilever body that is connected by the chiral webs is represented by the masses $M1$ and $M3$. The associated damping and stiffness of the cantilevers and the chiral webs are represented by the damping and stiffness elements in the system. Figure 4 shows a schematic representation of the same.

The same is represented in the matrix form by Eq. (18) and can be solved numerically or by SIMULINK, refer Fig. 5. The iterations can be performed for various parameter variations to have a better understanding.

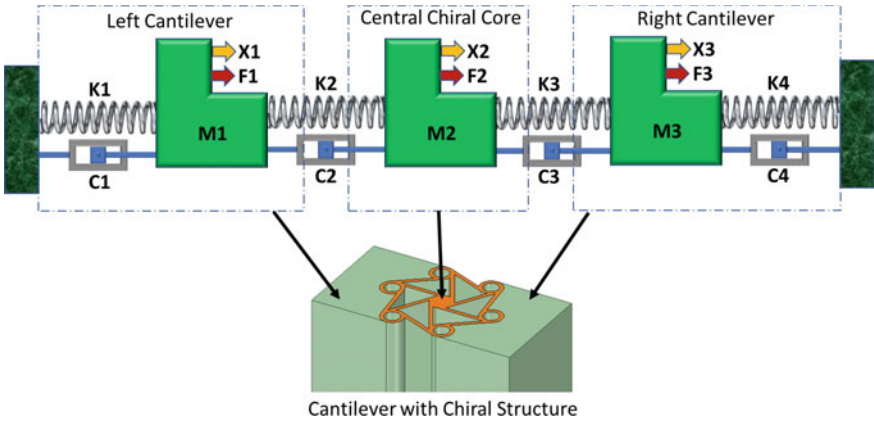


Fig. 4 Discrete representation of the dynamic system for cantilever with vertical chiral structure

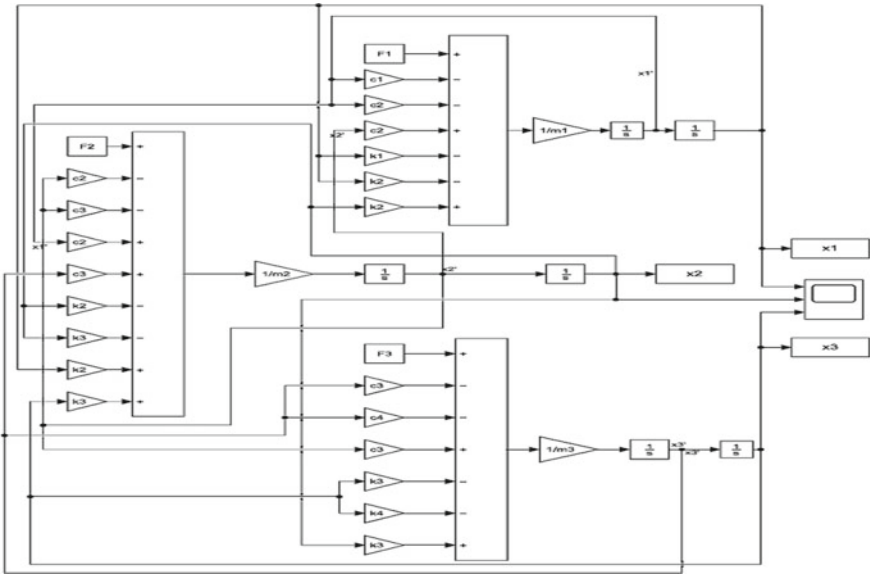


Fig. 5 SIMULINK model for the described 3DOF system

Being a 3 DOF system, as seen in Fig. 4, it has three modes of vibration Fig. 6. The central core and webs can be tuned in a manner so that it can act as a vibration absorber and thereby enhance the damping. The webs can be made to deform intentionally so that the energy dissipation is maximized. This has to be within the design constraints imposed, such as max deflections permitted, material strength, etc.

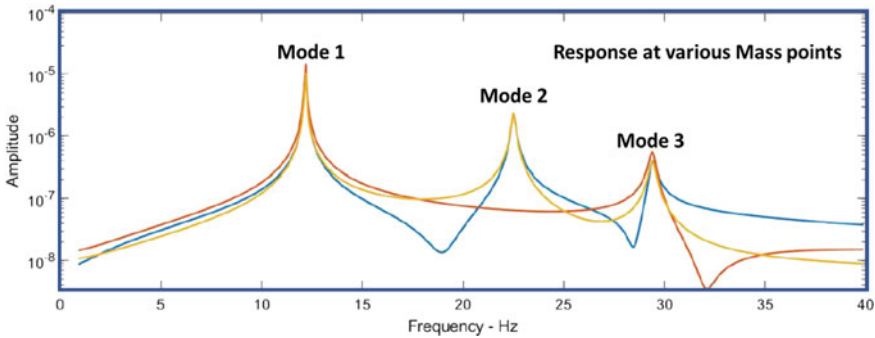


Fig. 6 Simulated response for 3DOF system

$$\begin{aligned}
 & \begin{bmatrix} M1 & 0 & 0 \\ 0 & M2 & 0 \\ 0 & 0 & M3 \end{bmatrix} \begin{bmatrix} \ddot{X}1 \\ \ddot{X}2 \\ \ddot{X}3 \end{bmatrix} + \begin{bmatrix} C1 + C2 & -C2 & 0 \\ -C2 & C2 + C3 & -C3 \\ 0 & -C3 & C3 + C4 \end{bmatrix} \begin{bmatrix} \dot{X}1 \\ \dot{X}2 \\ \dot{X}3 \end{bmatrix} \\
 & + \begin{bmatrix} K1 + K2 & -K2 & 0 \\ -K2 & K2 + K3 & -K3 \\ 0 & -K3 & K3 + K4 \end{bmatrix} \begin{bmatrix} X1 \\ X2 \\ X3 \end{bmatrix} = \begin{bmatrix} F1 \\ F2 \\ F3 \end{bmatrix} \tag{18}
 \end{aligned}$$

With this basic understanding, the study is undertaken on a simple cantilever. The various cantilever configurations, refer Fig. 14, are studied and analysed. The formulation can be extended for multiple chiral unit cells that can act as individual vibration absorbers and also have enhanced damping in specific modes because of deformation in the chiral webs.

These chiral lattice cells act as vibration absorbers and reduce the overall vibratory response of the main structure. The energy dissipation is through these chiral cells. The popular model of this vibration absorber for the undamped case was given by Farhm in 1909, while, later on, the damped model for the same was given by Den Hartog in 1943. Figure 7 shows a simple damped vibration absorber system.

For a tuned mass damper system, Den Hartog derived an approximate formula for the absorber stiffness and damping. The optimal frequency ratio ϵ (i.e. the ratio between the frequency of the tuned mass damper and the main structure) and the optimal damping ratio γ of the tuned mass damper are given by Eqs. (19) and (20), respectively.

$$\epsilon^{opt} = \frac{\omega_2}{\omega_1} = \frac{\sqrt{K_2 M_1}}{\sqrt{K_1 M_2}} = \frac{1}{1 + \mu} \tag{19}$$

$$\gamma^{opt} = \frac{C_2}{2M_2\omega_2} = \sqrt{\frac{3\mu}{8(1 + \mu)^3}} \tag{20}$$

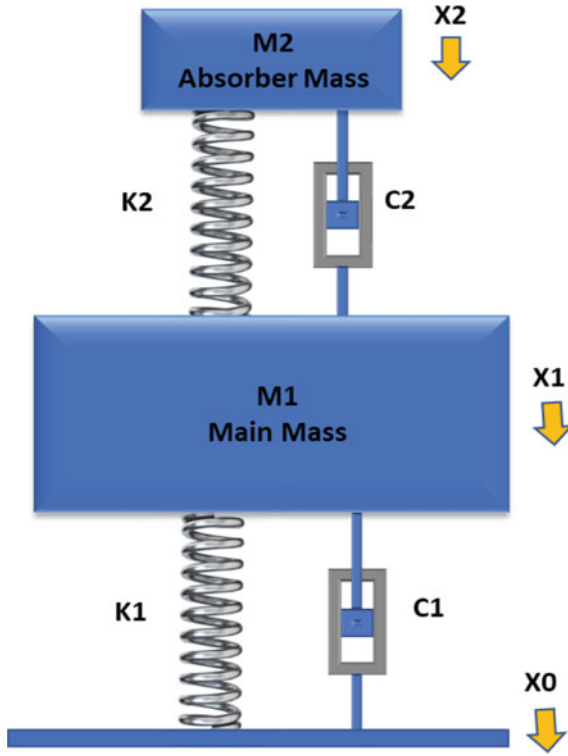


Fig. 7 Tuned damped vibration absorber model

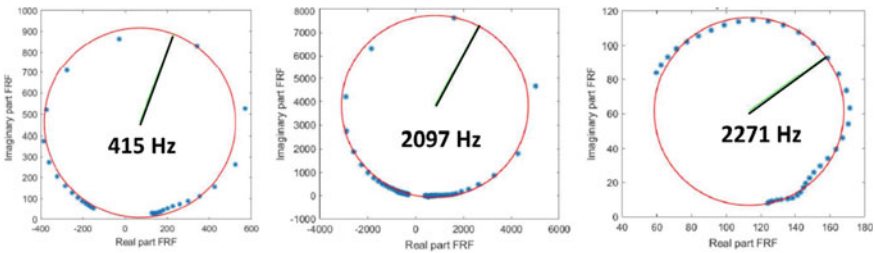


Fig. 8 Nyquist plot used for circle fitting the individual modes and estimate the damping

where μ is mass ratio, i.e. the ratio between the absorber mass and the main body mass.

The popular solution results for this indicate a suppression of the resonant peak of the main system while diverting the energy into the absorber with a different frequency. Basically, resulting in a 2DOF system.

The concept can be extended to multi-degree of freedom system. However, the mass distribution needs to be optimized in terms of its locations with a possible

constraint of net mass not exceeding a given limit. The overall vibration response does reduce. This is discussed during the analysis of specific cantilever design with chiral structures embedded with absorber masses, refer Fig. 18.

6 Theoretical and Experimental Modal Studies on a Solid Cantilever

In order to establish the process of modelling and analysis, a basic cantilever design, refer Fig. 9, is considered that is subjected for theoretical and experimental studies. The analysis was undertaken using the ANSYS 19.0 software package. The component was subjected to modal and harmonic analysis.

The experimental modal analysis (EMA) is performed using the impact hammer technique. The hammer excitation impulse is measured using a force transducer embedded in an instrumented impact hammer, while the response is measured using a miniature accelerometer mounted at a free end corner of the cantilever. The time data block captured for the excitation and the response is then used to establish the frequency response functions (FRFs). A roving force technique is used to measure the response at a location due to excitation at various points on the structure. These FRFs generated are then used to extract the modal parameters, viz. frequencies, damping and mode shapes. The processing is done using the MATLAB software. In the present case, a circle fit technique has been used to establish the modal parameters as there were no closely spaced modes, refer Fig. 8.

For further refinement of the mode shapes, a Polytech Laser Vibroscanner system has been used to get the precise modal parameters. The results are tabulated in Fig. 9.

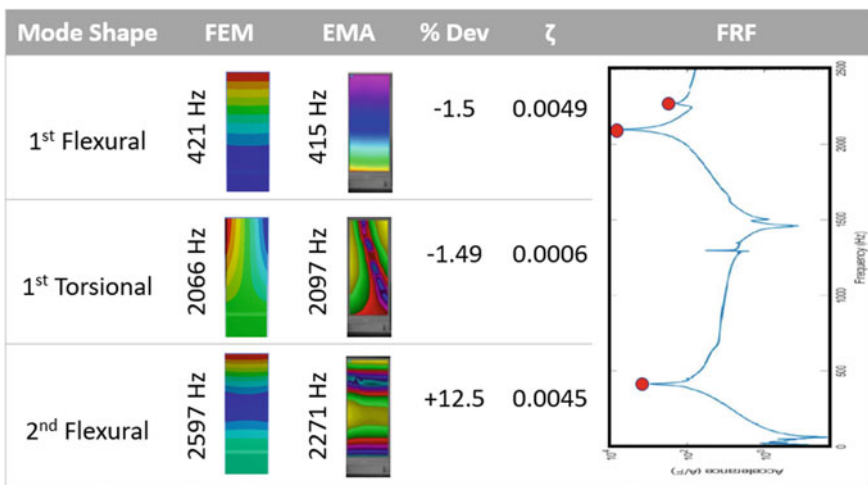


Fig. 9 Correlation of experimental and theoretical modal analysis results

A good correlation exists between the analytical (FEM) and experimental (EMA) results in terms of prediction of frequencies and mode shapes. The damping/loss factor arrived from the experiment has been used for updating the theoretical model for response study evaluation. With the finalization of this procedure, further theoretical studies were undertaken for various chiral-embedded cantilever configurations. These are shown in Fig. 13.

7 Modelling and Analysis of Chiral Structures

An object is said to be chiral, or with handedness, if it cannot be superimposed over its mirror image by rotations and translations alone [3]. These chiral designs are used in the form of a lattice structure that exhibits coupling between local rotation, bending and bulk deformation. This results in origin of many unusual properties such as high shear rigidity, negative Poisson's ratio, high compressibility, a negative effective density and a negative effective bulk modulus [4].

Figure 10 shows the deformations of the ligaments and the overall deformation pattern for various types of loading. Similar studies are undertaken for modal behaviour also to understand the various modes of vibration of these chiral cells. The results for the first ten modes are shown in Fig. 11.

Meanwhile, with the progress of advanced manufacturing techniques, various types of advanced additive manufacturing (AM) are widely employed for biomedical, aerospace, automotive, marine and offshore industrial sections. These low-cost AM techniques demonstrated superior manufacturing efficiencies and economic advantages for advanced lightweight industrial components with unlimited arbitrary topological layouts and complex internal microstructures and are proposed for fabrication of auxetic materials and structures.

The effectiveness of these chiral structures can be optimized based on the various geometrical parameters (viz. the ligament length and thickness, inner and outer diameter of circular nodes, central node diameter, chiral angles Θ and φ , pitch diameter of the nodes) and the depth of the unit chiral as shown in Fig. 12. In addition, the orientation based on the constraints imposed by modal characteristics in terms of frequency placement and loading patterns/excitations on the structural member also plays a vital role.

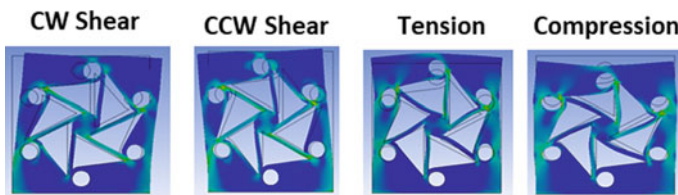


Fig. 10 Deformation of a unit hexachiral cell under various loading

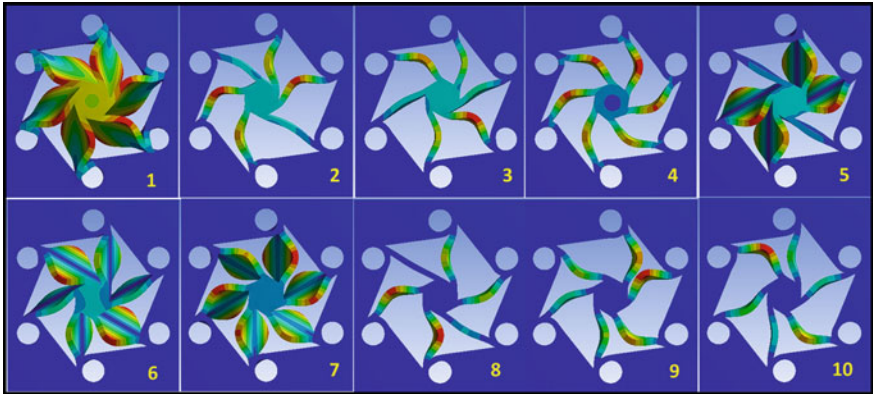
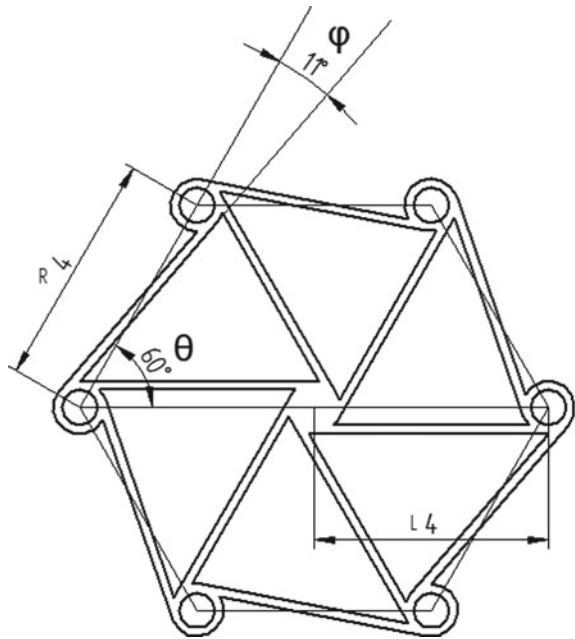


Fig. 11 Mode shapes of a unit hexachiral cell considered

Fig. 12 Geometric detailing of a unit chiral cell



8 Theoretical Studies on Chiral-embedded Cantilevers

The studies undertaken are for three configurations of cantilever.

1. A solid cantilever.
2. Solid cantilever with vertical chiral structure.
3. Solid cantilever with transverse chiral structure.

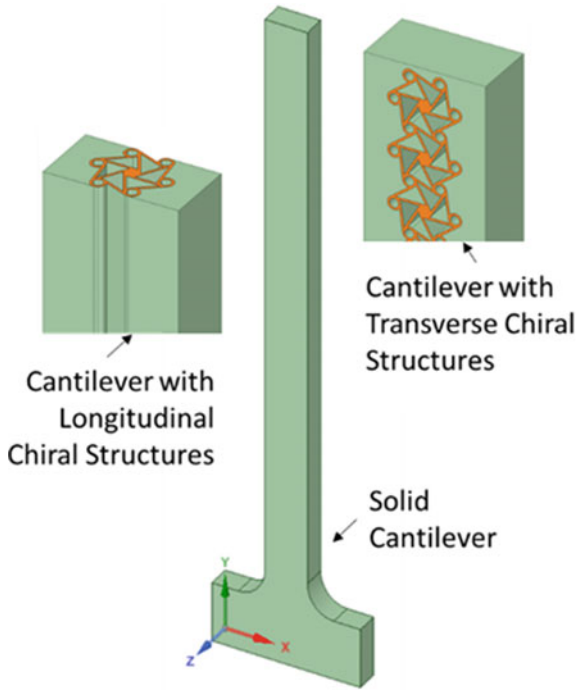


Fig. 13 Orientation of chiral lattice in the cantilever

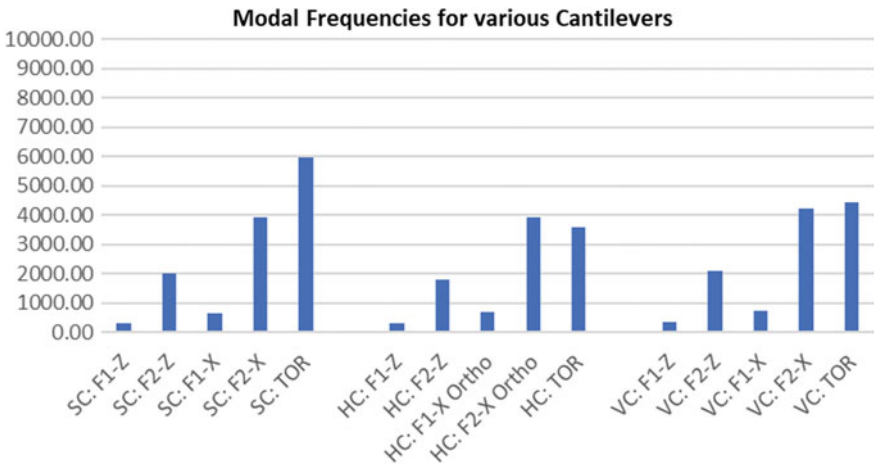


Fig. 14 Modal frequencies for various modes of vibration for different cantilever configurations

All these configurations are of same dimensions and material, i.e. steel. This was essential to undertake comparative studies of the responses.

With the procedure already established, the modal analysis and then the harmonic analysis for the cantilevers were undertaken for these configurations. The harmonic analysis is performed for a unit load at the tip with load direction selected specifically to excite a particular mode of interest and get the FRF. As a part of this analysis, the damping was incorporated in the form of a Raleigh damping that considers damping proportional coefficients α and β to mass and stiffness, respectively, as given in Eq. (21). These coefficients can be established by considering the damping and the frequency information from the experimentally established transfer function through the use of Eq. (22). Note that these coefficients are mode dependent, and one needs to determine these coefficients for specific modes of interest. The modal mass can be obtained through ANSYS.

$$[C] = \alpha[M] + \beta[K] \quad (21)$$

$$\zeta_n = \frac{\alpha}{2} \frac{1}{\omega_n} + \frac{\beta}{2} \omega_n \quad (22)$$

This was essential as the chiral ligaments are prone to deformations during its local vibratory modes, refer Fig. 10. These act as elements to dissipate the vibrational energy through its oscillations and deformations. These results are discussed in the following section. Note that the conventions used in the discussion are as per Fig. 13, which indicates the co-ordinate axes.

9 Results and Discussion

The observations and conclusions are drawn specific to the geometric configuration considered. However, on similar lines, conclusions can be drawn for specific structural configurations. As observed in Fig. 14, the modal frequencies for the initial four modes for the various cantilever configurations are intentionally kept almost practically same, except for the torsional mode of vibration.

A significant reduction in the weight of the structure is achieved, and in the present case, it is around 17% compared to solid cantilever. In fact, this optimization study can be undertaken based on the structural and material property constraints, viz. permissible stresses, permissible deflections, placement of frequencies and type of mode shapes.

As observed from Fig. 15, the Q -factor is relatively higher for the solid cantilever $F1$ - X and TOR . This is because the chiral lattice deformations are significant in these modes. This can also be seen in Fig. 16, wherein the max stress location for the X -direction mode has shifted from the cantilever root location to the chiral geometry location. Similar observation is there for the Z -direction mode, but it is not that

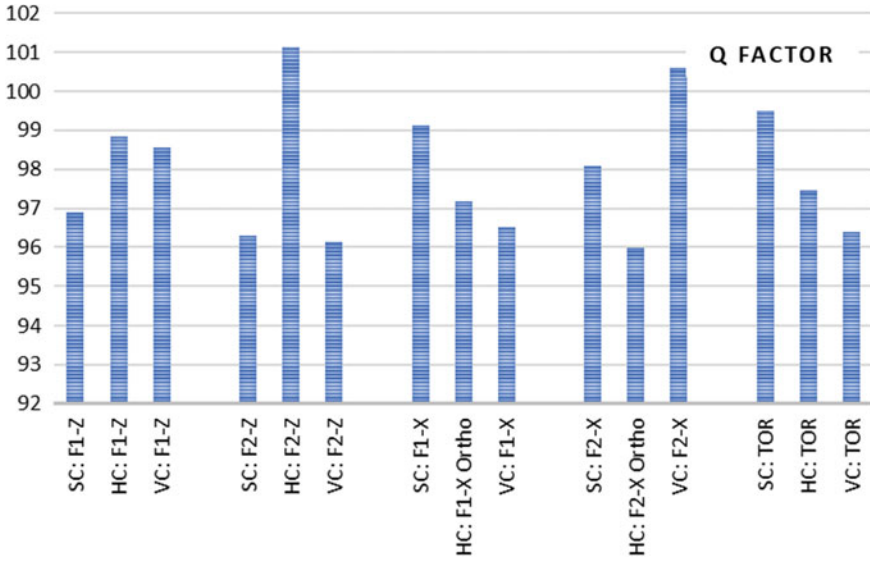


Fig. 15 Q-factor for various modes of vibration

X- IF Mode	Z – IF Mode	Torsional Mode	Remarks
			Solid Cantilever : Stresses maximum at Root in all the modes
			Vertical Chiral : Torsional mode exhibit shift in the stress pattern to central core in the chiral structure
			Transverse Chiral: Max stress location shifted to the chiral structure. Clear deformation in the webs observed. This is also reflected in the increased damping/loss factor.

Fig. 16 Stress patterns for various modes of cantilever configurations

significant. For torsional mode, a significant reduction is observed with the same reason as the max stress is shifted to the central chiral structures.

The orientation of the chiral lattices also plays an important role in enhancing the specific damping capacity, refer Fig. 17. The orientation of the chiral lattice can be done based on the requirements and constraints. Placement and orientation of the chiral lattices can be optimized as a future study depending on constraints. In

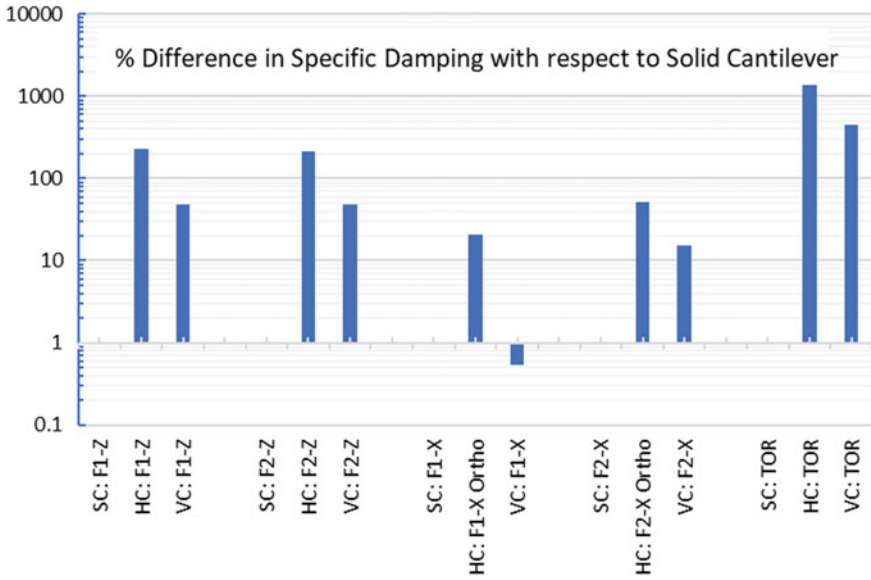


Fig. 17 Percentage difference in specific damping with respect to solid cantilever

In addition to this, as the chiral structures have a great sensitivity to impact, these can be used to absorb the impact energy in structures with an added benefit of weight reduction. There is also a potential to fill this hollow structure with a viscoelastic material to further enhance the damping.

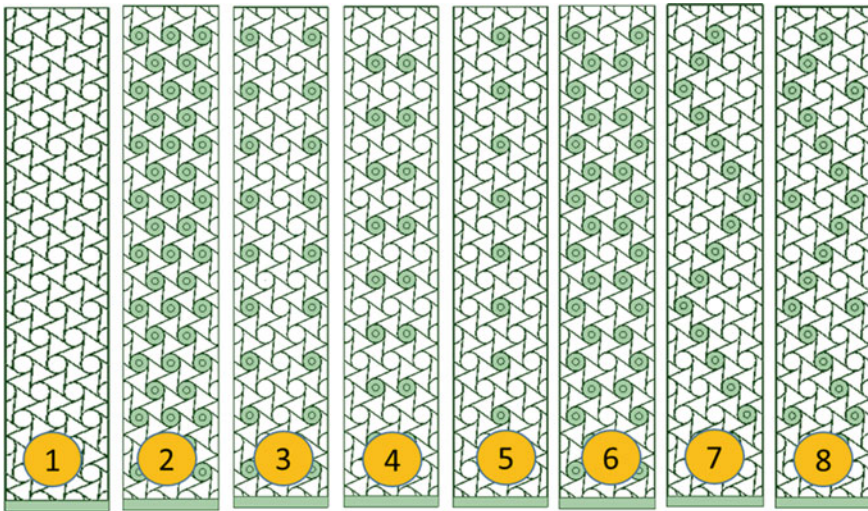


Fig. 18 Various chiral configurations analysed for response studies

These chiral structures are difficult to produce through conventional machining techniques, but due to the recent development of additive manufacturing technology, this can be easily achieved.

With this study undertaken, further configurations were analysed to understand the effect of the absorber masses embedded in the chiral structures. The absorber geometry is with a central steel mass surrounded by neoprene rubber.

The various configurations analysed are given in Fig. 18. With the basic modal analysis completed, the harmonic analysis was undertaken to understand the response behaviour for various modes.

In this paper, the response study for one of the modes that is critical has been presented in Fig. 19. The chiral pattern number four as indicated in Fig. 18 with absorber is shown. This has the maximum benefit in terms of reduced response with limited penalty on the mass increase. Figure 20 shows the response plots for the various eight configurations indicated.

As observed, a chiral pattern number four gave the maximum benefit, with minimum optimum masses. Further increase in the number of absorbers do reduce the response, but one needs to look at the frequency shift and the net mass that needs to be limited.

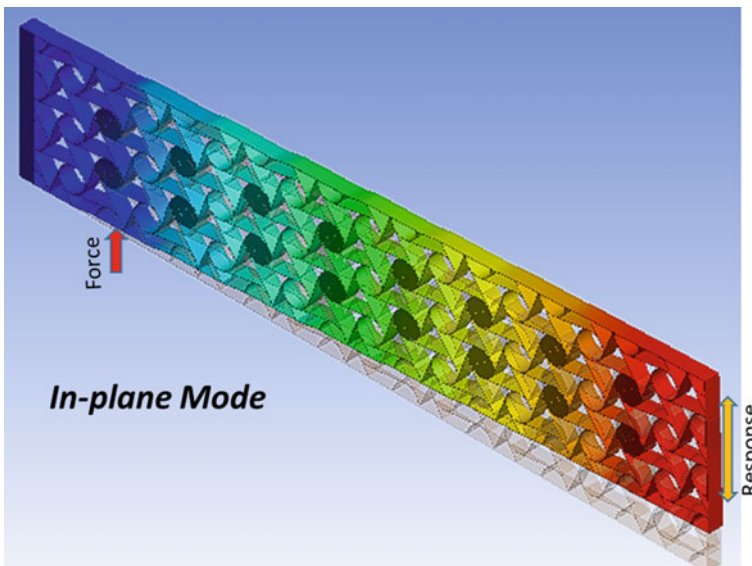


Fig. 19 Fundamental in-plane mode of the of the cantilever configuration

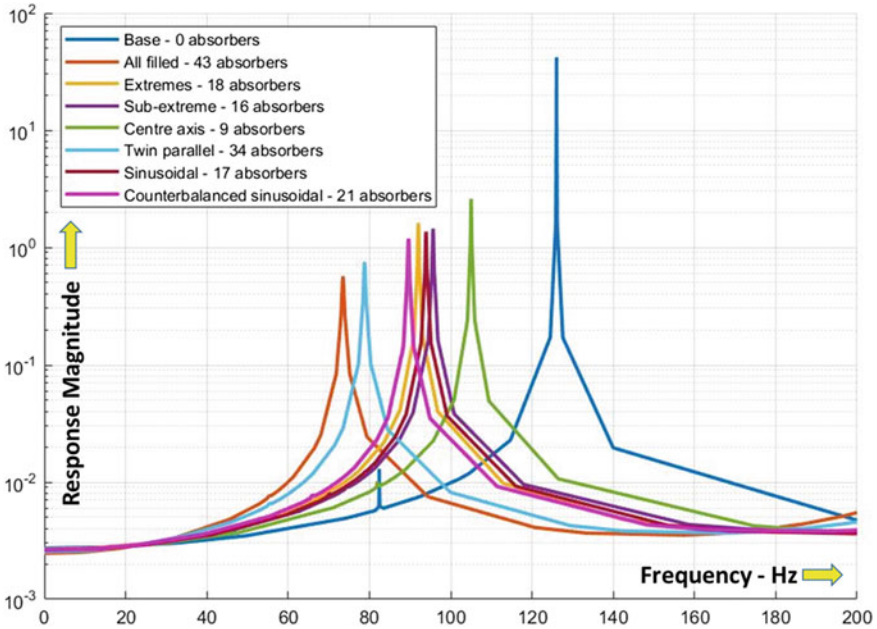


Fig. 20 Response plots for various configuration patterns of absorber mass locations

10 Conclusions

The chiral structures are one of such potential mechanical design features that can be incorporated in the structural members to have a significant reduction in weight while maintaining the stress margins within the requirements. The max stress locations can be altered and relocated in the chiral lattice so as to enhance the local deformations due to vibrations. The inherent deformation of these chiral structures does benefit in dissipating the vibratory energy or enhancing the loss factors.

There could be a minor loss of structural stiffness in the process, but as an integrated design analysis, one can optimize the chiral lattice design for structural dynamic response by considering various constraint parameters like strength to weight ratio, loss factor, response levels, maximum stresses, etc.

What is more interesting is that this chiral lattice structure core can be designed or exploited to act as a vibration absorber by tuning the frequency for a specific mode and intentionally ensuring bifurcation of the frequency. This can alleviate the response of the system for a specific mode.

Coupled with this observation of the property of chiral structures, the overall vibratory response can be controlled for various modes ensuring a reduction in overall vibratory response. This added benefit makes it a potential candidate for optimization of the structure. The study undertaken here does indicate a possible optimization of

these chiral structures with absorber masses to meet the design constraints of response levels, mass limitations and frequency placement.

The major benefit can be seen in the aircraft structures, turbo machinery discs, engine carcasses, airfoils, etc., where one targets for lowering the weight to the maximum extent possible, thereby enhancing the thrust to weight ratio of the aircraft. Specific to the rotor structures like discs and blades, this can play a vital role as a slight reduction in weight can gain significantly in reducing the centrifugal stresses. With the current trend towards smaller gas turbine engines, the rotors are designed to have blisks instead of a traditional bladed disc assembly. These blisks do have a basic limitation of low damping and are purely dependent on the material damping. The only way remains then is to intentionally increase this damping by providing such lattice structures that act as vibration absorbers that reduce the weight and intentionally deform, leading to enhance loss factors.

There are other parameters like bandgap increase during this process. That has its utility in the case of acoustic treatment. However, this has not been discussed in this paper.

Acknowledgements The authors acknowledge Director GTRE, Bangalore, for extending his support in motivating and permitting to undertake this work on chiral lattice structure behaviour for its potential application in the field of gas turbine technology.

References

1. Silva J, Maia N (1998) Modal analysis and Testing. In: Proceedings of the NATO advanced study institute. Springer Publication, Portugal
2. Orban F (2010) Damping of materials and members in structures. In: Journal of physics: conference series 268 012022, 5th international workshop on multirate processes and hysteresis—MURPHYS 2010.
3. Wenwang W et al (2019) Mechanical design and multifunctional application of chiral mechanical metamaterials: a review. *J Mater Des* 180:107950
4. Zhu D et al (2016) Vibration isolation characteristics of finite periodic tetra-chiral lattice coating filled with resonators. *J Mech Eng Sci* 230(16):2840–2850
5. Bacigalupo A, Ambarotta LG (2016) Simplified modelling of chiral lattice materials with local resonators. *Int J Solids Struct* 83:126–141

Micromechanics Approach to Determine Fatigue Life of Ceramic Matrix Composite



Kumar Rajesh and Rajeev Jain

Abstract With the increase in demand of light and durable material, composite materials are replacing conventional materials in aerospace industries. Efficiency of aeroengine can be increased by increasing turbine entry temperature of an engine. Composites are replacing conventional materials for low- and high-temperature applications due to their high-specific strength. It consists of reinforce fiber along with suitable matrix. Unlike monolithic material, the mechanical behavior of composite depends on the properties of its main constitutes, i.e., fiber and matrix. This paper uses micro and mesoscale modeling techniques to develop fatigue behavior of composite material. A novel technique has been developed to estimate fatigue life of composite components using progressive damage by propagation of crack through matrix and fiber under cyclic loading.

Keywords CMC · FEM · Composite · Multi-scale · Micro-meso

1 Introduction

Performance of gas turbine aeroengine can be increased using materials which poses high-specific strength at elevated temperature. As per study on futuristic materials, ceramic matrix composites (CMC) reinforced with woven and braided fabric preforms are the potential materials for the futuristic lightweight aerospace turbo machinery [1, 2]. It has produced a great interest among the scientists and engineers working in the field of aeronautics to develop CMC to gains engine performance. These materials have high stiffness, strength and high-fracture toughness and therefore make them suitable materials for hot engine components [3–5]. Ceramic materials not only maintain their strength up to 1300 °C but are lighter and possesses

R. Kumar (✉) · R. Jain
Gas Turbine Research Establishment, CV Raman Nagar, Bangalore 560093, India
e-mail: rajeevjain.gtre@gov.in

R. Jain
e-mail: rajeevjain63@gmail.com

material damping. Ecologically, these materials possess high resistance to oxidation and creep behaviour and therefore highly suitable for hot components of gas turbine engine. Also, these materials have oxidation and creep resistance, as well as thermal shock stability at elevated temperatures.

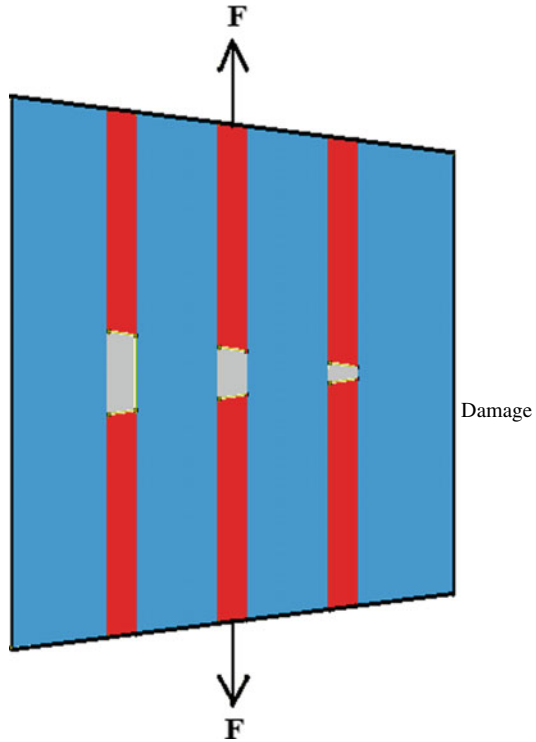
Extensive work [6, 7] has been carried out in the development of analytical tools for accessing the static properties of fabric reinforced composite. There is a biggest challenge to use CMC for the development of rotating blades due to high vibratory stresses which can result failure of component due to high-cycle fatigue (HCF). It is highly challenging to predict initiation and growth of damage in a composite due to existence of multiple damage mechanism. Damage in composite can occur due to fiber fracture, matrix cracking, failure at the interface of fiber and matrix, fiber buckling, and delamination etc. Numerous research work [6–9] has been done to understand complex phenomena of fatigue behavior of fiber-reinforced composite materials.

Limited work is available to evaluate the useful life of a component based on fatigue strength of composite material. There is a big challenge to develop a systematic approach based on feasible analysis procedure to design a composite structures such as bladed disk (Bling) for compressor. Paley and Aboudi [10] developed generalized method of cells (GMC), and later, Aboudi et al. [11] developed High-Fidelity Generalized Method of Cells (HFGMC) assuming linear and quadratic field, respectively, to predict effective properties of the composite and local fields. Naik [12] developed a general geometry model based on fabric architectures to obtain mechanical properties of CMC. Wang et al. [13] used cohesive zone technique of the extended finite element model (XFEM) to simulate the fracture damage within the fine aggregate matrix of finer-reinforced composites. They showed that failures in composite are different than metals [14]. Metals show no reduction in stiffness and linear stress-strain relation during fatigue process [15, 16]. On contrary, fatigue behavior of fiber-reinforced composite materials is highly complex due to inhomogeneous and anisotropic characteristics of composites. Fatigue performance of composite depends on types of fibre and matrix, and shows influence of reinforced structure (unidirectional, mat, fabric braiding), stacking sequence of the laminate, environmental conditions (temperature and moisture).

Fatigue phenomena demands extensive mechanical testing at coupon and component level for the certification of the product, which is difficult for the manufacturers due to lack of time for launching their new product. Numerical simulation consisting of fiber and matrix properties is only a viable solution to predict product performance. Simulation of these materials for fatigue loading, however, is not yet quite perfect. Several developments in modeling techniques for fatigue damage assessment have been presented in the scientific literature. Multi-scale modeling based on representative volume element approach is used by several authors [17] to predict fatigue life of epoxy composite.

Physics of micromechanisms damage in fiber-reinforced composites is interesting. In fiber-reinforced composite with ductile matrix, load acting on composite is shared by the filers of the composite. Due to whole load born by the filers, filers tend to fail first. Due to failure of the weakest filers, loading increases in the neighbouring intact

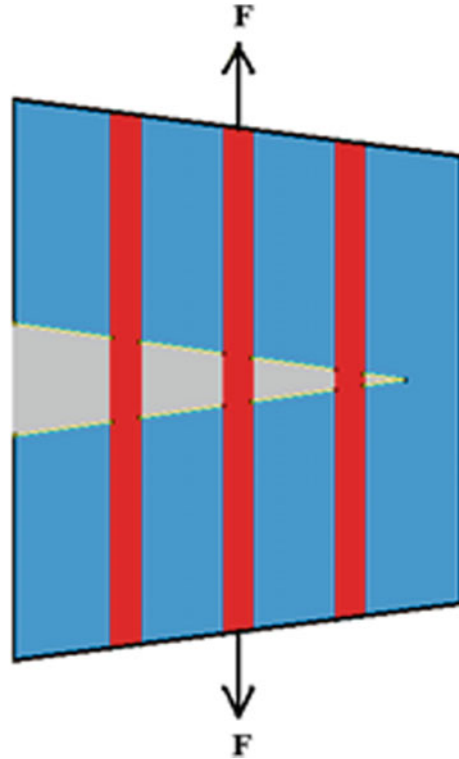
Fig. 1 Crack growth in ductile matrix



filers which fail subsequently as indicated in Fig. 1. These filers failure lead to higher stress concentration in the matrix and result in matrix cracking. Damage mechanics operate differently in composite having brittle matrix material [16, 17] like CMC. In such types of composites, crack is first developed in the matrix region and thereafter it grows along the interface due to weak matrix interface as revealed in Fig. 2. The crack bridging mechanism is operative due to availability of intact filers behind the crack front as discussed by Min et al. [18]. Load acting on the composite is shared by the bridging filers and crack tip, and therefore results in reduction of stress intensity factor at the crack tip. A higher amount of bridging filers leads to the lower stress intensity factor at the crack tip, and thereby increasing the crack resistance due to increase in crack length. If intact fibers are available behind the crack front and they are connecting the crack faces, the crack bridging mechanism is operative. In this case, the load is shared by the bridging fibers and crack tip.

This paper presents a novel technique to predict fatigue life of fabric-reinforced ceramic matrix composite structures. Analysis is based on assumption that the woven fabric consists of periodicity of the repeated pattern, therefore single unit cell is sufficient to describe the complete fabric architecture. Multi-scale modeling technique is used to evaluate anisotropic properties and later predict failure behavior of composite. Fiber yarn modeling (micro-scale) and the woven fabric modeling (mesoscale) are used to gain much deeper insight into the complex failure mechanism of woven

Fig. 2 Crack growth in brittle matrix



composites under loading. Finite element analysis has been performed by subjecting the micro and mesoscale models under uniform global strain to obtain mechanical properties of the composite. Propagation of crack causes damage in the fiber yarn/tow which finally leads to fatigue failure of the components. The progressive damage [18] in the CMC component is modeled using fatigue crack growth in representative volume element (RVE) of woven fabric composite and determining component life based on progressive reduction in load carrying capacity with increasing crack length under cyclic loading.

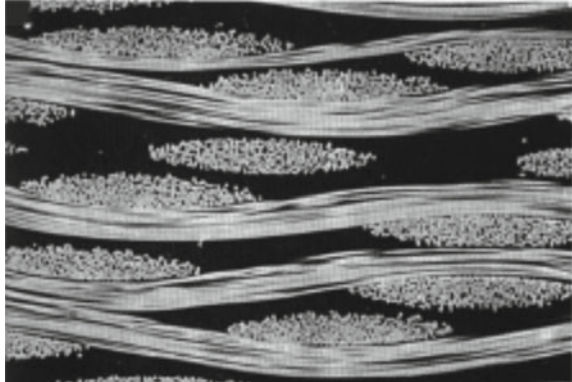
2 Mathematical Formulation and Modeling Methodology

Composite material is fabricated using pre-impregnated layers of woven fabric which are cured and joined together similar to tape laminates. Figure 3 shows scanning electron microscope (SEM) picture of composite laminate indicating weave yarn. Cross-sectional view of this weave structure is shown in Fig. 4. Each yarn is packed with almost identical filers with indistinguishable properties, and size of each yarn is measured by number of fibers in the yarn.

Fig. 3 Composite laminate with representative unit cell [23]



Fig. 4 Cross-sectional view of composite lamina [23]



Fabric-reinforced composite has very complicated geometry structures for numerical analysis. It is highly difficult to model this geometry using conventional finite element techniques without making certain assumptions. Microstructure of woven composite composed of interlacing warp and weft yarns surrounded by matrix. Also, each yarn contains bundles of fibers surrounded by matrix, schematic sketch explain it in Fig. 5.

This numerical model assumes iso-strain assumption to calculate mechanical properties of the composite. This section describes modeling procedure to obtain mechanical properties of 2-D plain weave unit cell composite and overall component based on assumption. Micro-scale model consists of fiber and matrix, and it is used to derive mechanical properties of the weave yarn. Analysis ignores existence of voids in-between adjacent fibers. Mesoscale model consists of yarn and matrix.

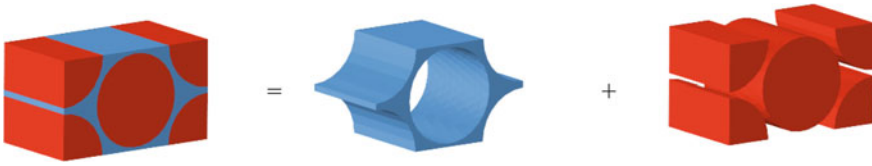


Fig. 5 Micro-scale model of single fiber and matrix

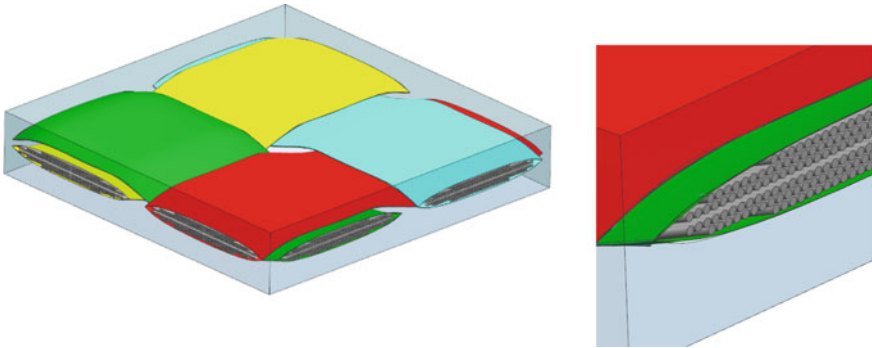


Fig. 6 Mesoscale model of 2D plane weave and close-up view of fibers in yarn

2.1 *Micro-scale Modeling*

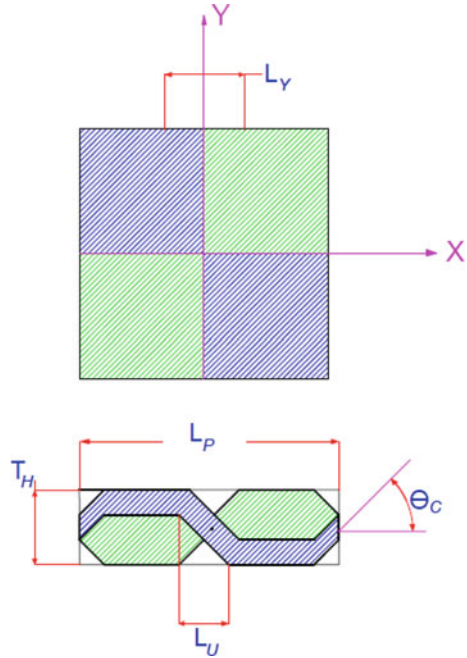
Micro-scale modeling is used to determine effective properties of yarns, which can be considered as fibers surrounding by matrix. Numerical analysis has been done using representative volume element shown in Fig. 5.

2.2 *Mesoscale Modeling*

The mesoscale model is established to describe the stress–strain curve and failure mechanism of woven composite under axial and transverse tensile loading. Based on the periodical characteristic of the woven composites, the meso-scale schematic figure of one layer of the 2D plain weave RVE is illustrated in Fig. 6. Close-view of this figure stipulates single yarn consists of several fibers along with matrix of composite material.

Figure 7 shows unit cell of weave yarn along with cross-sectional view. This figure indicates the undulation of a warp yarn as it crosses over and under the fill yarns. Material properties of the composite depend on yarn spacing, L_Y , in both fill and warp directions; yarn filament count, N , for the fill and warp yarns; yarn packing density, P_D ; filament diameter, D_F .

Fig. 7 Unit cell of plain weave composite



Packing density (P_D) of the yarn can be estimated using image analysis of photomicrographs of sections through the thickness of the composite. If there are (N) fibers of identical diameter (D_F) in a single yarn of packing density (P_D), then cross-sectional area of yarn (A_Y) can be calculated as

$$A_y = \frac{\pi D_F^2 N}{4 P_D} \tag{1}$$

Projected length of each yarn is $L_P = 2L_Y$. If it is assumed that yarn spacing and yarn filament counts for the fill and warp directions are equal. Also, the cross-sectional area (A_Y) of the yarn is assumed to be the same in both (warp and fill) directions and remains constant along the entire composite yarn path, then the volume occupied by the four yarns within the unit cell is given as

$$V_Y = 4A_Y L_P \tag{2}$$

Dimension of unit cell is $L_P \times L_P \times T_H$. Space not occupied by the yarns can be assumed to be interstitial matrix. The overall volume fraction of this unit cell can be derived as

$$V_F = \frac{\pi D_F^2 N}{P_D L_P T_H} \tag{3}$$

Equations (1) and (3) can be used to determine thickness (T_H) of the lamina for a given fiber volume fraction (V_F).

The cross-section of the yarn is a lenticular shape consisting of two symmetrical arcs. The maximum thickness of the yarn is designated to $T_H/2$. Yarn path consists of two straight portion and three undulated portions. The yarns path generally follows sinusoidal path, the yarn center line path can be expressed as

$$Z_C = \pm \frac{T_H}{4} \sin\left(\frac{X_C \pi}{L_U}\right) \tag{4}$$

where X_C is the quantity measured from the corresponding cross over point along the warp yarn direction.

2.3 Mechanical Properties

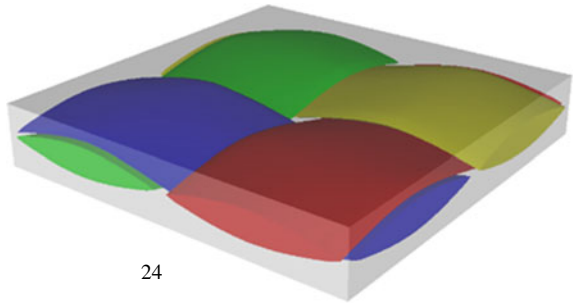
As per assumption, the mechanical properties for a unit cell can be considered as the same of the whole specimen. Composite properties is determined by discretizing all the yarns within the unit cell.

In finite element modeling of this lamina, the straight portion of each yarn path is modeled as a single slice length, L_s . Along an undulated portion, the yarn is divided into, q_N , equal, piecewise straight slices made perpendicular to its in-plane direction and normal to the $X-Y$ plane. Thus, the sinusoidal yarn undulated portion is approximated by q_N interconnected straight yarn slices. The volume of each yarn slice (V_Y) of the undulated portion is computed as

$$V_Y = \frac{A_Y L_U}{q_N} \tag{5}$$

Unit cell of composite consists of spatially oriented yarn slices and an interstitial matrix material slice as shown in Fig. 8. Each yarn within the unit cell has been approximated by straight yarn slices and orientation angles. Volume occupied by

Fig. 8 Geometry model of composite



the interstitial matrix pockets in the unit cell can be obtained by subtracted volume occupied by all the yarn slices from the volume of the unit cell.

It is assumed that matrix is isotropic, while the yarn slices transversely isotropic [19]. The three-dimensional elastic stress–strain relations in global coordinates for the unit cell has been defined using effective material properties to relate the average values of the stress–strain state variables. The average stress technique [20] based on an iso-strain assumption within the unit cell has been used to compute the overall composite properties.

Three-dimensional stiffness matrix $[E']_k$ for the can be formed from given material constants. The five independent material constants of composite (E_{11} , E_{22} , G_{12} , ν_{12} , and ν_{23}) are required to define $[E']_k$ matrix for the yarn slice. Here, subscript 1 corresponds to the axial direction of the finer. Assuming uniform strains inside the unit cell, the stress–strain relation can be given as

$$\{\sigma\} = [E]\{\varepsilon\} \tag{6}$$

where the $[E]_{6 \times 6}$ matrix is the overall stiffness matrix of the unit cell, which can be expressed as a summation over all the q yarn and matrix slices in terms of the materials slices stiffness matrix:

$$[E] = \sum_{k=1}^q (V_k [T]_k^T [E']_k [T]_k) \tag{7}$$

where V_k is the fiber volume fraction of the k th material slice, $[T]_k^T$ is the transformation matrix between the global coordinates and the local coordinates of the k th material slice. Equation (6) can be used to evaluate average strains in a unit cell The stress components in global coordinates of each material slice can be obtained and transformed to the local material coordinates as

$$\{\sigma\}_k = ([T]_k [E']_k [T]_k^T) \{\varepsilon\} \tag{8}$$

This formulation enables the calculation of stresses and strains of each material slice when the thermal or mechanical loads are given. This forms the foundation for the damage analysis and failure analysis of fabric-reinforced composites.

2.4 Damage Criterion

Due to high-longitudinal strength and stiffness of fibers, the damage initiation of fibers can be characterized by the non-interactive maximum principal stress criterion given as

$$\frac{\sigma_f}{T_f} = 1 \quad (9)$$

where T_f is the fiber tensile strength, and σ_f is the maximum principal stress of the fiber.

Failure criterion for matrix is formulated as

$$\frac{\sigma_{Vm}^2}{T_m} + \frac{J_{1m}}{T_m} = 1 \quad (10)$$

where T_m is the tensile strength of the matrix; J_{1m} is the first stress invariant and σ_{Vm} is the von-Mises stress of the matrix.

3 Finite Element Analysis

Commercially, available finite element software ABAQUS [21] is used to analyze micro-scale and meso-scale models of ceramic matrix composite and determine effective mechanical properties and crack growth in ceramic matrix composite. Hyper-mesh pre-processor is used to model micro-scale (fiber and matrix) and meso-scale (yarn and matrix) finite element models.

3.1 Micro-scale Model

Effective properties of fiber yarns are essential to simulate failure mechanism of meso-scale model. Yarn consists of bundles of fibers along with matrix, they are assumed to be transversely isotropic. Therefore, the micro-scale model has been generated to predict the axial and transverse effective properties of fiber bundles. These properties have been used in the mesoscale model to evaluate properties of composite.

Material properties of carbon fiber and matrix used to evaluate effective mechanical properties of yarn are shown in Tables 1, 2 and 3, respectively. Convergence study has been done to understand effect of mesh density on mechanical properties.

Periodic boundary condition is used to determine mechanical properties of fiber for micro-scale model. Figure 9 indicates stress distribution of micro-scale model in axial and transverse directions. The stress field of the model is harmonious under tensile loading due to major load taken by the fiber. In transverse direction due to tensile load, matrix plays a major bearing force, and therefore, there is non-uniformity in stresses. This analysis evaluates homogenized material properties indicated in Table 4.

Table 1 Properties of carbon and silicon-carbide matrix for yarn and plain weave

<i>Yarn properties</i>	
Fiber volume fraction	80%
Yarn void volume fraction	3%
Yarn packing structure	Square
Fiber	T-300
<i>Weave properties</i>	
Fiber volume fraction	43%
Void volume fraction	15.3%
Weave void volume fraction	10%, 80%
Thickness	6.55 mm
Matrix	CVI-SiC

Table 2 Material properties of carbon (C) fiber [22]

Property	Magnitude
E_{11} (GPa)	231.0
$E_{22} = E_{33}$ (GPa)	28.0
$G_{12} = G_{13}$ (GPa)	24.0
G_{23} (GPa)	10.7
$\nu_{12} = \nu_{13}$	0.26
ν_{23}	0.30

Table 3 Material properties of matrix (SiC)

E (GPa)	G (GPa)	ν
3.51	8.13	0.20

Fig. 9 Stress distribution in RVE in axial and transverse directions

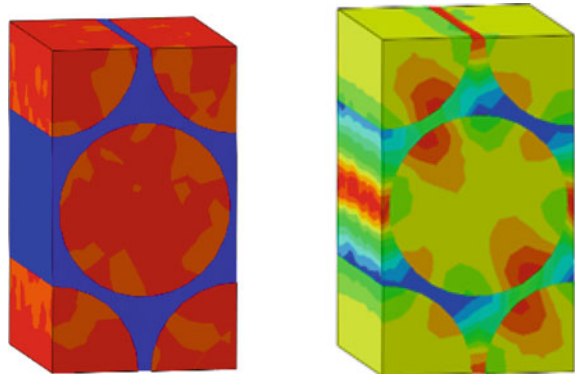


Table 4 Homogenized material properties of fiber and matrix unit cell

Property	Magnitude
E_{11} (GPa)	184.0
$E_{22} = E_{33}$ (GPa)	14.8
$G_{12} = G_{13}$ (GPa)	9.26
G_{23} (GPa)	5.83
$\nu_{12} = \nu_{13}$	0.25
ν_{23}	0.26

3.2 Meso-Scale Model

Geometry architecture of composite unit cell is shown in Fig. 8. This figure indicates weave pattern of yarn inside matrix. Hyper-mesh pre-processor has been used to model unit cell of the composite yarn and matrix using C3D8R brick elements. The mesoscale model of lamina shown in Fig. 11 consists of 64,676 eight-noded finite elements and 83,739 nodes. Table 4 indicates material properties of the yarn shown in Table 4 indicates material properties of the yarn used to evaluate effective material property of the composite using repeated boundary conditions.

Homogenized material property of composite is shown in Table 5.

As CMC are porous matrix materials, the stiffness of porous materials is lower than the pure matrix listed above, resulting in the lower modulus in the beginning. After the matrix failure, the fibers begin to bear the load, and due to the higher strength of the fibers, the ultimate strength of the material is slightly raised.

The damage in matrix initiates at 0.08% strain, but the stress–strain curve has no significant change, which reveals that matrix damage has little effect on the elastic behavior of the woven composites under axial tensile load. When the global strain level is 0.2%, the axial fiber bundles crack and finally result in ultimate failure of the material at 0.22% strain.

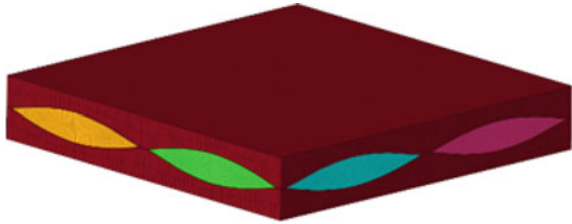
Table 5 Homogenized material properties of the composite

Property	Magnitude
E_{11} (GPa)	21.0
$E_{22} = E_{33}$ (GPa)	5.5
G_{12} (GPa)	0.83
$G_{13} = G_{23}$ (GPa)	0.20
$\nu_{12} = \nu_{13}$	0.07
ν_{23}	0.23

Fig. 10 Finite element model of yarn



Fig. 11 Finite element model of lamina



4 Results and Discussion

Commercially available finite element solver ABAQUS has been used to evaluate mechanical properties of plain weave laminate unit cell of ceramic matrix composite under uniaxial tension.

4.1 Static Crack in Micro-model

Figure 12 shows geometrical configuration of single fiber embedded inside ceramic matrix. It has fiber and matrix diameter of 7 and 8 μm , respectively. This 3-D micro-model is subjected to quasi-static loading in axial direction at one end and restrained on the other side to suppress rigid body mode. Finite element model of this geometry consists of 70,400 elements as shown in Fig. 13.

This geometry contains pre-crack of 0.1 μm length around the circumference of cylindrical geometry to study crack propagation characteristics as the cracks grow from the surface to fiber/matrix interphase. Loading was considered strain-controlled with uniform displacements applied at the boundaries parallel to the initial crack. The remaining boundary conditions were assumed to be traction free.

Fig. 12 Geometrical configuration of micro-model of fiber and matrix

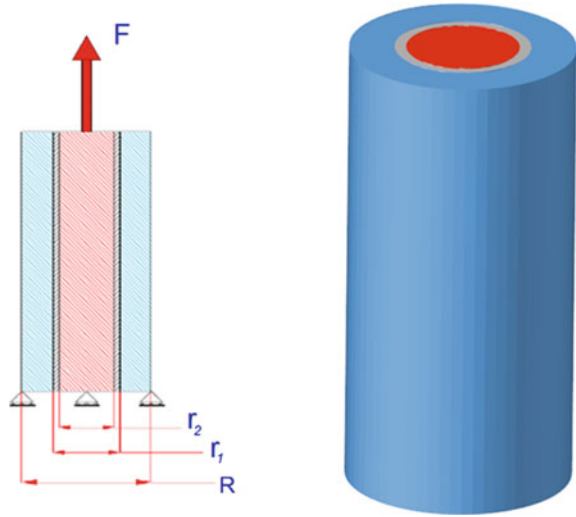
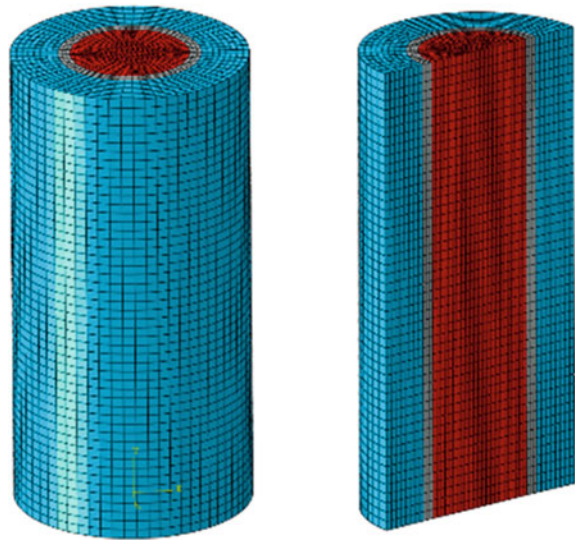


Fig. 13 Finite element micro-model of fiber and matrix composite

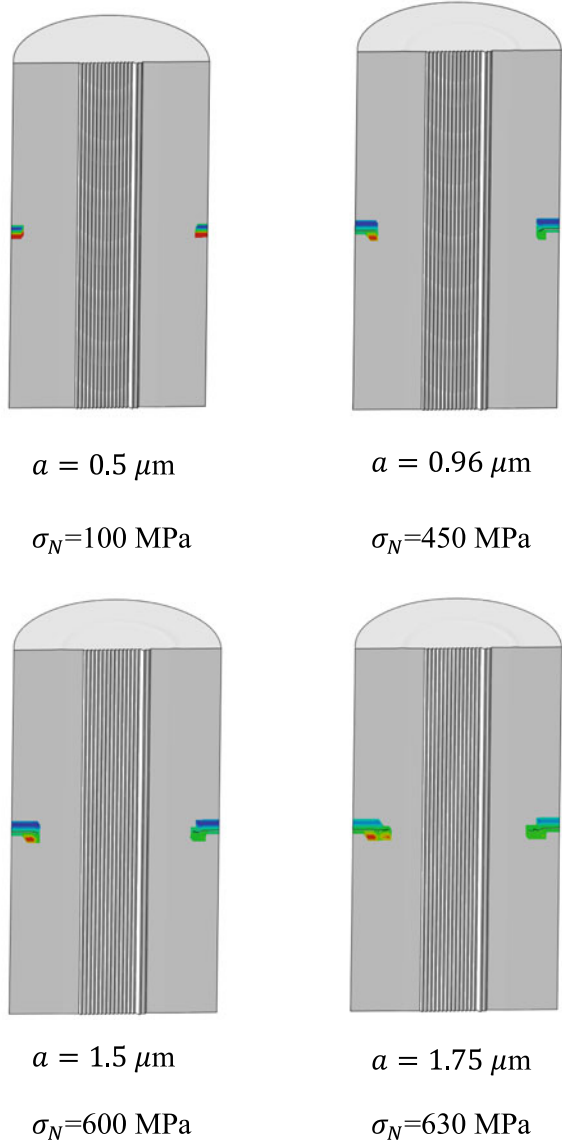


Commercially available ABAQUS software XFEM module is used to simulate crack propagation in the micro-FE model. Initiation of damage is predicted based on maximum principal stress taken as 2600 and 800 MPa for fiber and matrix, respectively. Crack evolution is governed by cohesive laws where the fracture energy defines the rate at which cohesive stiffness is degraded once the initiation criterion is met. Viscous regularization was employed to aid convergence of the solution at each integration time step. Damage stabilization control parameter of the software is used to control the viscous regularization.

Figure 14 reveals variation in crack length (a) due to application of nominal stress (σ_N) at one end of the fiber-matrix micro-model. This figure indicates crack length increases to $0.5 \mu\text{m}$ on application of 100 MPa nominal stress at one end. This magnitude increases to $1.75 \mu\text{m}$ crack length at 630 MPa nominal stress.

During first cycle of monotonic loading, the initial crack extends due to severe stress concentration near crack tip. When cyclic load is applied, the crack will further propagates from this extended crack length.

Fig. 14 Crack propagation due to monotonic tensile load



4.2 Crack Propagation in CMC Material

Fatigue behaviour of ceramics matrix composite (CMC) is invariably controlled by the progressive damage in matrix and fiber under cyclic loading. Initially, the toughening of CMC is increased by crack tip shielding mechanisms associated with extensive crack bridging from undamaged fiber. Since gas turbine engine components are subjected to cyclic loading undergo fatigue crack growth leads to progressive damage of such bridging fiber in the crack wake. This results in reduction of σ as well as loading carrying capacity of the composite.

In the present analysis, Paris power-law is used to define the fatigue properties of the woven fabric. The plot of da/dN (fatigue crack growth rates) and ΔK (stress intensity range) at 1150 °C is shown in Figs. 14 and 15. The Paris law constants are determined by fitting the curve and used it in ABAQUS, XFEM [21] to calculate fatigue crack growth in the CMC.

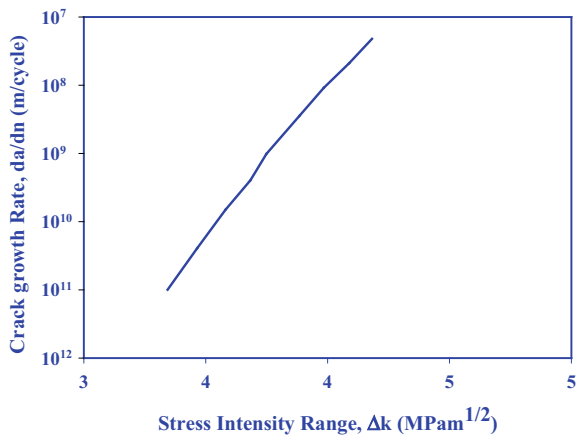
$$\frac{da}{dN} = C(\Delta K)^m \tag{11}$$

where C and m are material constants of the composite.

Figure 16 shows variation in stiffness with crack length. This figure reveals that there is reduction of 6% stiffness with 0.5 mm increase in crack length.

Crack surface composite at 400, 500, and 600 MPa nominal stress under 0-max-0 cyclic loading is shown in Figs. 17, 18 and 19.

Fig. 15 Variation is crack growth rate with stress intensity range



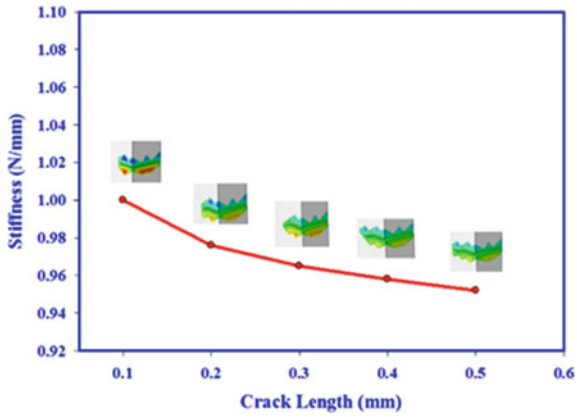


Fig. 16 Variation in stiffness with crack length in composite



Fig. 17 Progressive crack growth in lamina due to 0-400-0 MPa load up to 1000 cycles

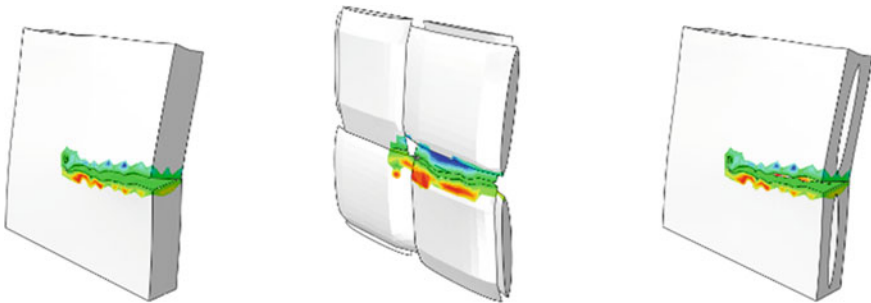


Fig. 18 Crack in composite, fabric, and matrix due to 0-500-0 MPa load after 169 cycles

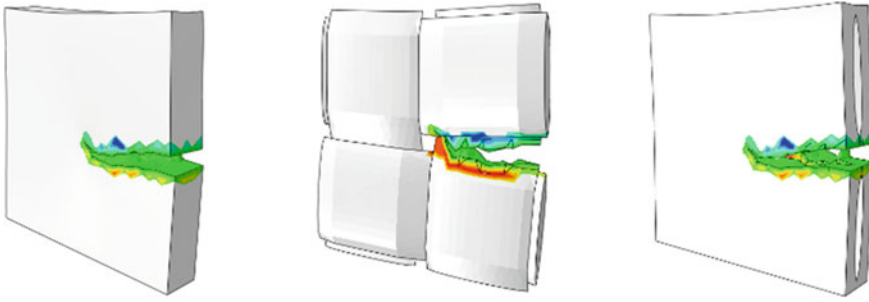


Fig. 19 Crack in composite, fabric, and matrix due to 0-600-0 MPa load after 43 cycles

5 Conclusions

Paper presents multi-scale modeling technique to evaluate homogenized material properties of yarn and weave. Commercial software ABAQUS [21], XFEM module is used to evaluate number of cycles due to present of existing crack in the composite. Analysis reveals decrease in stiffness of the composite due to increase in crack length. Micromechanics-based model defining the laminate geometry and constitutive relations, as well as failure criteria for several damage modes are proposed. Micro and mesoscale-based simulation has been done to determine fatigue life of CMC component based on dynamic crack propagation under different cyclic load.

Acknowledgements Authors are thankful to the Director, GTRE for providing permission to present this paper for the National Conference on Air-breathing Engines.

References

1. Herbell TP, Eckel AJ, Brockmeyer JW (1994) Composites in high speed turbines for rocket engines. In: High temperature high performance materials for rocket engines and space applications, pp 13–20
2. Brockmeyer J (1996) Fiber-reinforced ceramic matrix composites for earth-to-orbit rocket engine turbines. Cleveland, OH
3. Inghels E, Lamon J (1991) An approach to the mechanical behaviour of SiC/SiC and C/SiC ceramic matrix composites. *Mater Sci* 26:5403–5410
4. Camus G, Guillaumat I, Baste S (1996) Development of damage in a 2D woven C/SiC composite under mechanical loading. *Compos Sci Technol* 52(12):1363–1372
5. Aboudi J (2011) The effect of anisotropic damage evolution on the behavior of ductile and brittle matrix composites. *Int J Solids Struct* 48(14):2102–2119
6. Reifsnider KL (1990) Fatigue of composite materials. In: Composite materials series, vol 4. Elsevier
7. Harris B (2003) Fatigue in composites, woodhead publishing series in composites science and engineering
8. Vassilopoulos AP (2010) Fatigue life prediction of composites and composite structures. Woodhead Publishing Limited

9. Degrieck J, Paepegem VW (2001) Fatigue modeling of fibre-reinforced composite materials. *Appl Mech Rev* 54:279–300
10. Paley M, Aboudi J (1992) Micromechanical analysis of composites by the generalized cells model. *Mech Mater* 14:127–139
11. Aboudi J, Pindera MJ, Arnold SM (2003) Higher-order theory for periodic multiphase materials with inelastic phases. *Int J Plast* 19:805–847
12. Naik RA (1994) Analysis of weave and braided fabric reinforced composite
13. Wang H, Wanga J, Chen J (2014) Micromechanical analysis of asphalt mixture fracture with adhesive and cohesive failure. *Eng Fract Mech* 132:104–119
14. Liu KC, Chattopadhyay A, Bednarczyk B, Arnold SM (2011) Efficient multiscale modeling framework for triaxially braided composites using generalized method of cells. *Aerosp Eng* 24(2):162–169
15. Min JB (2013) Micromechanics fatigue damage analysis modeling for fabric reinforced ceramic matrix composites. In: 54th AIAA/ASME/ASCE/AHS/ASC structures, structural dynamics, and materials conference
16. Naik RA (1994) Analysis of woven and braided fabric reinforced composites. National Aeronautics and Space Administration, Washington, DC
17. Huang ZM (2002) Fatigue life prediction of a woven fabric composite subjected to biaxial cyclic loads. *Compos A* 33(2):253–266
18. Pineda EJ, Bednarczyk BA, Waas AM, Arnold SM (2013) Progressive failure of a unidirectional fiber-reinforced composite using the method of cells: Discretization objective computational results. *Int J Solid Struct* 50:1203–1216
19. Jones RM (1975) *Mechanics of composite materials*. Hemisphere Publishing Corporation, New York
20. Rosen BW, Chatterjee SN, Kibler JJ (1977) An analysis model for spatially oriented fiber composites. In: *Composite materials: testing and design*, ASTM, pp 243–254
21. ABAQUS Software Version 6.12-1 Ed, Providence RI, USA: Simulia, 2019
22. Borkowski L, Chattopadhyay A (2015) Multiscale model of woven ceramic matrix composites considering manufacturing induced damage. *Compos Struct* 126:62–71

Space and Missile Propulsion

Design and Analysis of KIIT Nanosatellite's Micro-Pulsed Plasma Thruster



Dibyesh Satpathy, Shalika Singh, Subham Mahanty, Sidhant Patra, and Isham Panigrahi

Abstract Mechanical and electrical designs for a micro-pulsed plasma thruster have been presented here, which is to be accommodated in the KIIT University's Nanosatellite for technological demonstration in space. Design-related calculations based on dimensional limitations, power constraints, and optimal thruster performance have been done and laid out. Mechanical design includes accurate computer-aided design (CAD) and physical calculations of thruster casing, miniature spark plug, and electrodes. The electrical design includes the printed circuit board (PCB) design and circuit-related calculations. The thruster being considered here uses a flared electrode and casing in order to achieve optimal thruster performance. Thrusters are well known for their issues of erosion which hamper the thruster lifetime, therefore, the correct choice of materials for electrode, casing, and spark plug has been considered after a wide survey in order to limit the erosion as much as possible. Analysis of both the mechanical and electrical system has been done using SOLIDWORKS and PROTEUS software, respectively, for critical validation. A space grade micro-pulsed plasma thruster weighing only 130 g capable of surviving loads of a polar satellite launch vehicle (PSLV) by Indian Space Research Organization (ISRO) and providing a specific impulse of 600 s has been concluded.

Nomenclature

μ PPT Micro-pulsed-plasma thruster
PTFE Polytetrafluoroethylene

D. Satpathy (✉) · S. Patra
Graduate Student, University of Tokyo, Tokyo, Japan
e-mail: dibyesh1996@gmail.com

S. Singh · S. Mahanty
School of Electronics Engineering, KIIT University, Bhubaneswar, Odisha, India

I. Panigrahi
School of Mechanical Engineering, KIIT University, Bhubaneswar, Odisha, India

- PPT Pulsed plasma thruster
- AVX Advanced electronics components
- CW Cockcroft-Walton

1 Introduction

Pulsed plasma thruster (PPT) is an electric propulsion system which works based on the acceleration of plasma through Lorentz force. Plasma is generated when the arc of electricity passing through PTFE ablates and sublimates the propellant; the heat generated turns the gas into plasma. The plasma is propelled between the anode and the cathode, due to the force of ablation. Since the plasma is charged, the fuel effectively completes the circuit between the two plates, allowing a current to flow through the plasma. This generates the Lorentz force required for the acceleration of plasma at high velocities (Fig. 1).

The attractiveness of a PPT lies on its ease of operation, effective thruster performance, and efficient power usage. In addition to this, a PPT is also highly modifiable as per the requirements of a specific mission. The objective of this paper is to present a micro-pulsed plasma thruster which can be accommodated in small satellites for attitude control and drag compensation. The purpose of μ PPT here is for technological demonstration via tilting the satellite, and the least possible angular distance moved can prove the demonstration, which can be detected by an onboard magnetometer. For the mission, we plan to use it for technological demonstration in low earth orbit. The critical designs are based on the tight dimensional limitations of a

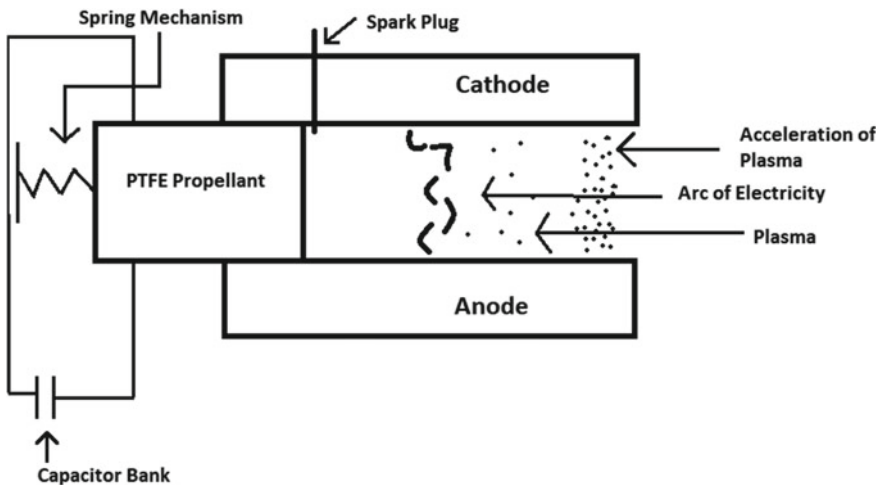


Fig. 1 Schematic layout of a pulsed plasma thruster

nanosatellite and the mass budget. Application of material research has been considered for enhancing thruster performance. Similarly, for limiting the carbonization and erosion issues choosing better materials for thruster walls is the best solution. Finally, as the considered PPT is an ablative one, this is a solid-pulsed plasma thruster; polytetrafluoroethylene (PTFE) has been well researched for application in PPT as a propellant. Therefore, PTFE has been employed as the propellant for this thruster. The KIIT nanosatellite is an 8U satellite with the intended purpose of earth mapping and demonstrating the thruster technology. The nanosatellite structure has a mass of 2.2 kg and is $212 \times 212 \times 224$ mm in dimensions. The overall mass of the nanosatellite (including the payload) is intended to be about 5 kg. The thruster is fixed on the plate adjacent to the single solar panel and is kept at a distance from the centre of the satellite to create a moment for demonstration when the thruster is fired. The PCB will be mounted separately in a box, but close to the thruster.

2 Micro-Pulsed Plasma Thruster (μ PPT)

- Before calculating the dimensions of important aspects of the PPT, it is necessary to decide upon certain present conditions. An ablative PPT has 2 kinds of configuration, breech fed, and side fed. The main distinguishing factor is that in case of breach fed, there is only a single unit of propellant supply, whereas in case of side fed, there can be multiple propellant supply units. Using the side fed system, with 2 propellant supply unit is being chosen. The propellant supply unit is to be a rectangular bar, as it is relatively easy to operate upon a rectangular bar and has a simpler design than other kinds of the bar such as cylindrical bars.
- Various studies have proven that the ratio of inductance variance to initial inductance is directly linked to the acceleration of plasma [1–10]. Inductance variance can be increased by increasing the aspect ratio that is the ratio of electrode spacing to electrode width [2, 5, 6, 11, 12] and by mounting the capacitors close to the thrust chamber will ensure reduced initial inductance, and therefore, maximum thruster performance can be attained. To get an estimated idea of inductance variation with respect to the electrode aspect ratio, Kohlberg and Couburn approach can be considered [11].
- Electric propulsion systems are well known for their drawbacks of contamination and erosion. The erosion can be limited through a suitable choice of wall or housing materials, however, there is always a possibility of contamination flyback, which could certainly damage the electronic components of the satellite and could probably lead to short-circuiting. Therefore, a nozzle shaped wall has been introduced here to counter these particular drawbacks [1, 13]. Overall thrust also includes a gas dynamic component apart from the electromagnetic one. Therefore, the electrodes were also designed in accordance with the nozzle to maximize performance. The electrodes follow a simple design of rectangular ends [2, 8, 14–16] although other variations like semi-circular and tongue-shaped end also exist and have their pros and cons.

- Generally, spark plugs design consists of an electrode which is surrounded by a semiconducting material and is inserted through an electrode. The same concept also applies to the spark plug of PPT. Shot to shot variation in thruster performance has been reported in such spark-based systems [15]. To counter this, it is recommended that the spark plug size should be much smaller than the propellant bar length [17]. Coaxial spark plugs have been considered for this project, which are conventionally used in most PPTs [18], although a rectangular one is relatively easier to manufacture [17].
- However, realistically, the shot energy to exposed area ratio has been found to be of relevance to specific impulse [2, 10, 13, 19]. Therefore, the semi-empirical relations as given by other studies should be taken into consideration if the design and nature of the project permit it.
- AVX ceramic capacitors are being used in the electrical system because of their proven high reliability. To prove that required voltages for ablation and acceleration are acquired by the chosen electrical components, the use of 555 timer has been mentioned here, as the nanosatellite's onboard computer data are beyond the scope of this paper.
- A potential difference of 0.7–5 V (taken from the power subsystems of a given nanosatellite) is fed to the 555 timer IC. The 555 timer provides a pulsating input to a XP POWER Q-15, which helps obtain an output of 1500 V. The 1500 V voltage is then redirected to the bank of capacitors made from AVX ceramic capacitors of 10 nF capacitance.
- Another input of 5 V is taken from the power subsystems and is fed to another 555 timer IC to produce a pulsating voltage. The pulsating output of the 555 timer is fed to XP POWER Q-60, which helps to produce an output of 6 kV. The 6 kV output is in turn fed to a Cockcroft-Walton (CW) generator. This ladder system produces a high-voltage spark of nearly equal to 12 kV which serves to provide electrons to bridge the vacuum gap between the electrodes and eventually cause the main discharge to occur.

3 Design Specifications of the Thruster

3.1 Mechanical Design of Thruster

3.1.1 Electrode Design

- An electrode length of 1.7 cm has been considered here. With a longer electrode, the wall friction could slow down the plasma and therefore reduce the thruster performance. If the electrodes are too short, then the plasma would be expelled when energy is still in the capacitor. It is assessed that the maximum available space in axial direction would be about 2 cm; giving some free space to the back wall. For low-electrical resistance, high-melting point, low-thermal expansion,

and optimal erosion resistance, tungsten-copper alloy is being chosen as the material [20]. Other alternatives like thoriated tungsten, tungsten coated copper, pure tungsten, or copper could also have been considered [21]. For perfect mechanical and electrical resistance, electrode thickness of 0.2 cm is being pitched on. Also, flared shaped electrodes at an angle of 25° have been opted for maximum output.

- For optimum performance, the electrode aspect ratio can be taken to be 2. If the electrode ratio is too high, many non-uniformities could arise which could reduce performance and increase plasma resistance. If the ratio is too small, the system could get uncontrollable [1]. Also, if the electrode spacing is increased, there should also be corresponding increase in voltage to keep the electric field optimized. It is critical to choose the correct value for electrode spacing. That is so because a higher value of the space will lead to inefficient discharge when the spark plug is in action. Hence, an electrode spacing of 1.1 cm and a corresponding electrode width of 0.55 cm is being settled upon (Fig. 2).

3.1.2 Solid Propellant Dimensions

As per calculations, the total mass of PTFE being carried by the nanosatellite should be 14 g. A propellant height of 1.2 cm has been selected, which is slightly more than the electrode spacing of 1.1 cm. This has been done to avoid getting the propellant bar directly beneath the spark plug which could lead to incomplete ablation. The PTFE bar will be kept linear, and each arm length of the PTFE bar is 5.84 cm. Since the ratio of energy to the area is an important factor, the propellant width here is considered as 0.46 cm, giving a small clearance of 0.02 cm on either side of the bar; that is, the width of the propellant port is 0.5 cm (Fig. 3).

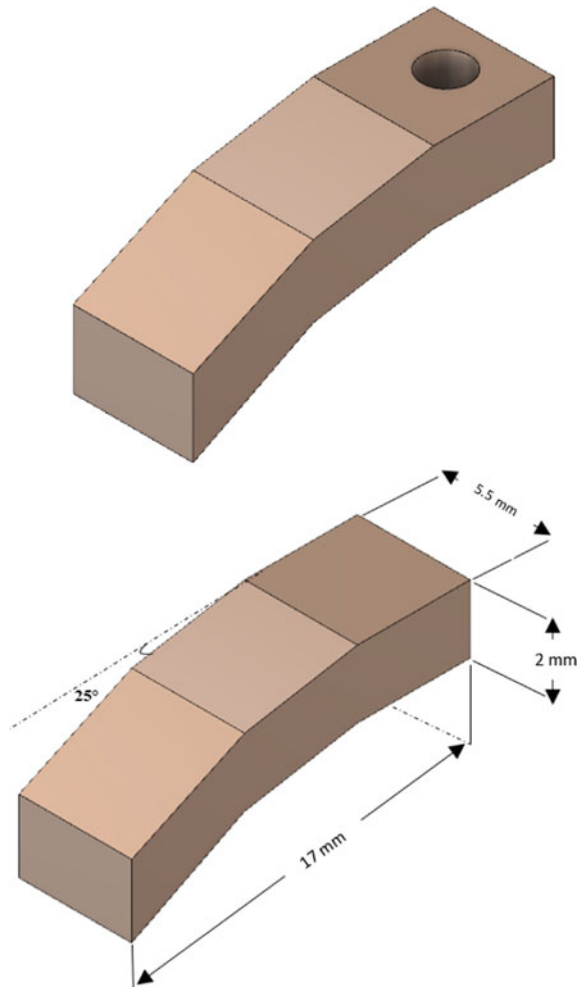
3.1.3 Spark Plug Design

In a coaxial spark plug, there is an inner electrode which is connected to a high-voltage supply and is surrounded by a semiconducting material [15, 22, 23]. Tungsten has been selected as the material for the inner electrode, and it has a diameter and a length of 1.5 mm and 1 cm, respectively. The surrounding semiconducting material is made of PTFE and has an interior diameter of 1.5 mm and an exterior diameter of 2 mm. The spark plug electrode is fixated at the origin of the cathode (Fig. 4).

3.1.4 MPPT Structure Design

- Starting from the origin (initial position of the PTFE propellant), after 0.5 cm of the thruster chamber (out of 1.7 cm), the side walls begin. To minimize the carbonization [13] of the walls, a diverging angle of 10 is introduced. About halfway later for the nozzle shape, another 25-degree divergence is introduced. Many authors consider 20 to 30-degree divergence for optimal performance [24]. To ensure

Fig. 2 Upper and lower electrodes



uniform velocity profile, and the plasma sheet being expelled with synchronization to energy stored in the capacitor, flared electrodes with 25° divergence are accommodated in the nozzle. A thickness of 0.1–0.2 cm for walls is considered for proper insulation both electrically, thermally, and also for surviving static loads. Instead of leaving the design with edges, proper filleting has been done beside the nozzle walls to reduce stress concentrations and to make the structure more rigid against the load brought in by a launch vehicle.

- In order to ensure a constant supply of propellant, a suitable propellant feeding system is necessary to be designed. This can be done by using springs to push the solid propellant towards the spark plug. However, compression springs and torsion springs would not be suitable as when subject to buckling, they would not perform the required job properly. Therefore, a constant force spring like a negator

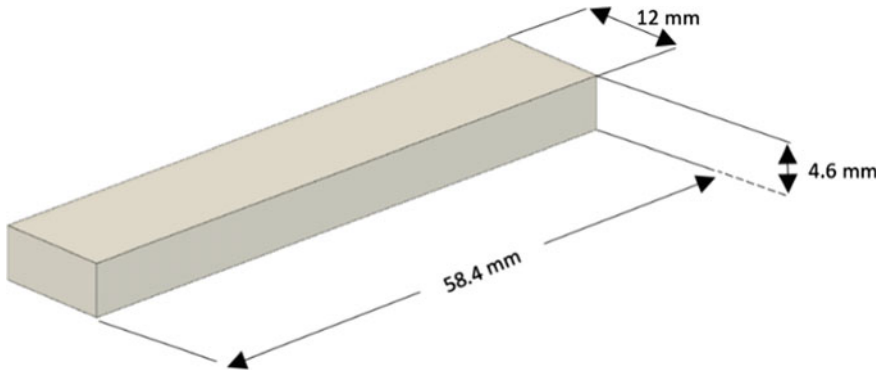
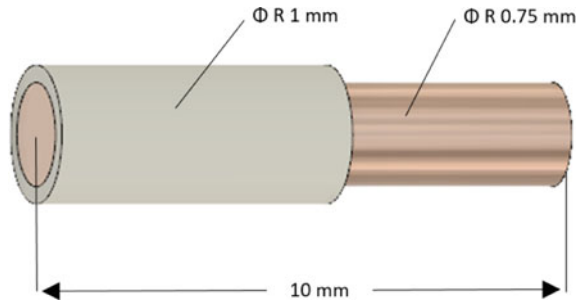


Fig. 3 PTFE bar

Fig. 4 Spark plugs



spring has to be used [14, 25, 26]. The total length of the negator spring should be more than the length of propellant, to ensure the propellant rod is consumed till the end. Commercially available negator springs of the smallest size made of stainless steel by ASRAYMOND have been opted for the thruster

- Due to the carbonization issue, which is highly critical in pulsed plasma thruster, we are considering Torlon 4203™ for manufacturing the final model. ShapalM™ (machine able aluminium nitride ceramic) is a good alternative for Torlon 4203 (Figs. 5, 6, 7, and 8).

3.2 Electrical System of the Pulsed Plasma Thruster

3.2.1 Initiation of Spark Plug

We will apply a pulsed input of 5 V to the 555 timer connected to flyback XP POWER Q-60. The pulsating input is boosted to 6000 V which in turn is fed to the CW [27]. We are using the CW of 2 stages in cascade which further boosts the 6–12 kV. The high voltage of 12 kV is sufficient to produce the high-voltage spark at the PTFE

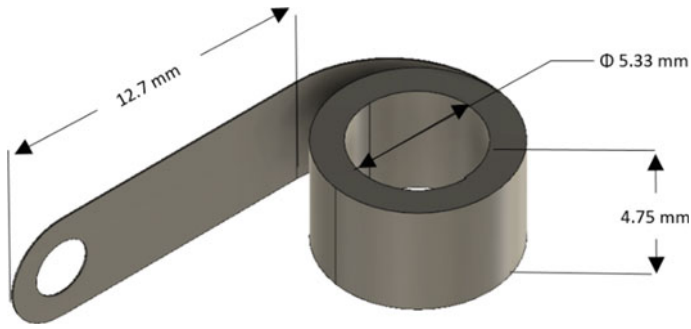


Fig. 5 Negator springs

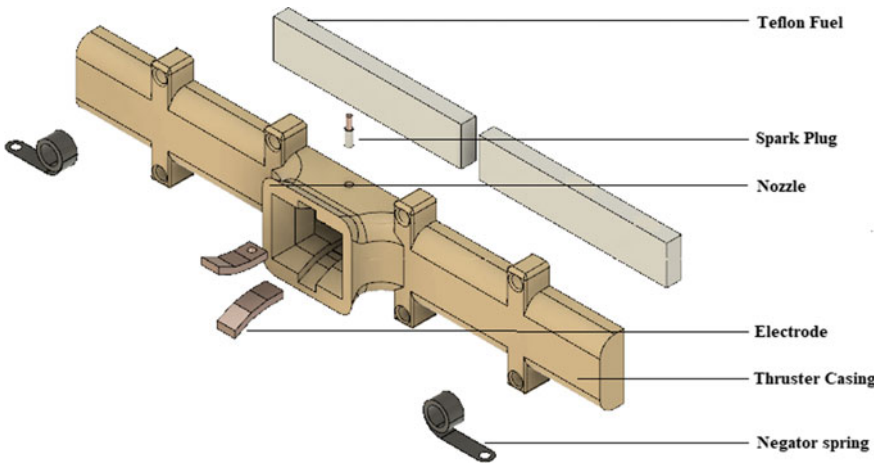


Fig. 6 Schematic of the thrusters with markings

surface to initiate its ablation. The ladder comprises 2 stages in a cascade made of 10 nF capacitors and diodes, as depicted in Fig. 17 (Table 1).

$$E_{out} = 2 * n * 1.4 * E_{rms} \tag{1}$$

Voltage drop under load is calculated as

$$E_{drop} = \frac{I_{Load}}{f * C} \left(\frac{2}{3}n^3 + \frac{n^2}{2} - \frac{n}{6} \right) \tag{2}$$

The ripple voltage in the case where all stage capacitance (C1 through C(2 * n)) may be calculated from

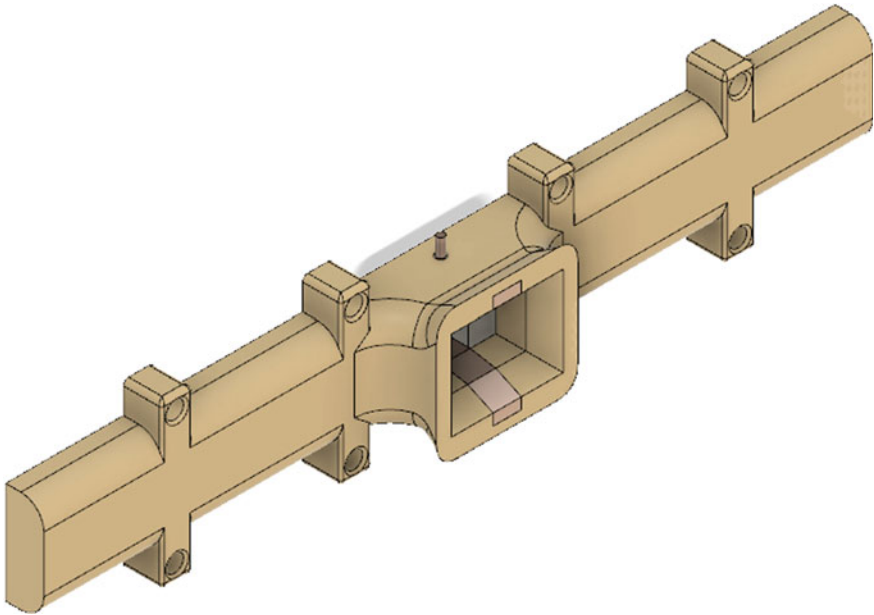


Fig. 7 Isometric view of micro-pulsed plasma thruster

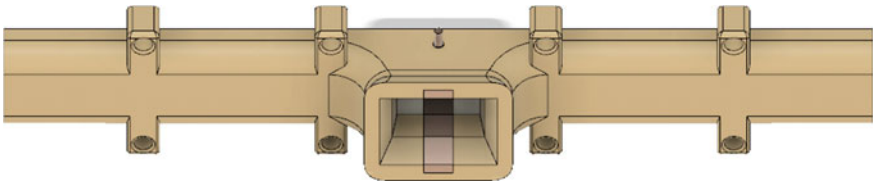


Fig. 8 View showing the use of curved surfaces beside the nozzle walls

Table 1 Spark plug specifications

Specifications	Value
Input voltage range	0.7–5 V
Maximum output voltage	6 kV
Maximum output current	83 μ A
Power	0.5 W
Voltage isolation	500 V

$$E_{\text{ripple}} = \frac{I_{\text{Load}}}{2f * C} * n * (n + 1) \tag{3}$$

It is observed that ripple increases rapidly with increase in the no. of stages (here n is squared).

Table 2 Specifications of diode used in CW

Specifications	Value
Repetitive-peak in reversed voltage	20 kV
Average forward current	5 mA
Max surge-current	0.51 A
Average forward-voltage drops	44 V
Reversed recover time	100 ns
Terminal	Axial lead

We will be using 2 stages in cascade in order to produce a voltage nearly equal to 12 kV that would be sufficient enough to produce the high-voltage spark from the output of the flyback Q-60, at the PTFE surface. So according to our calculations, we considered the capacitors of capacitance 1 μF and 20 kV rated to be used in the CW. We will be using 2 high-voltage diodes and 2 capacitors in a ladder and then each ladder in cascade (Table 2).

3.2.2 Initiation of Electrodes

We will apply a pulsed input of amplitude 1.5 kV with rise time as 1 μs , fall time as 1 μs , and pulse width as 10 ms. The input is boosted to 1500 V. The boosted output is then fed to the bank of capacitors which in turn starts loading the capacitors. The output voltage of 1500 V from the bank is applied across the electrode plates in pulsed form to generate the pulsed plasma thrust (Table 3).

For the bank of capacitors, we are using a parallel of six, series of two 1 μF , 1000 V rated capacitors to form a 3.0 μF as total capacitance of the bank, as depicted in Fig. 18. The capacitor that we are using is of X7R dielectric. When the Q-15 supplies the boosted voltage, the PPT circuit will begin loading capacitors. The main capacitor is loaded to the full output voltage that needs to be applied in a pulsating manner between the electrode's plates. If more than one thruster is considered, a switching mechanism using 4H-SiC IGBT [28] across the output of the CW can be considered.

Table 3 Electrode charging circuit data or specification of Q-15

Specifications	Value
Input voltage range	0.7–5 V
Maximum output voltage	1.5 kV
Maximum output current	333 μA
Power	0.5 W
Voltage isolation	500 V

3.3 Result and Analysis

The section shows the specifications of components, static load simulations, and electrical simulations (Tables 4, 5, and 6).

3.3.1 Static Load Simulation

To check whether the system can handle the extreme stresses of a rocket launch, a total load of 15 G is considered for the static load simulation, in addition to gravity acting against the load. Yield stress of Torlon is 137 MPa and of PTFE is 7 MPa. As it can be seen in the simulation results below, the maximum stress formed is much less than the yield stress of the considered materials. Therefore, the design is safe for use in space (Figs. 9 and 10).

3.3.2 Simulation of Voltage to Be Applied Across the Electrodes

Amplitude 1.5 kV, rise time = 1 μ s

Fall time = 1 μ s, pulse width = 10 ms

Table 4 Specification of mechanical components

PTFE bar geometry: Linear	Electrode length: 1.7 cm
PTFE mass: 14 g	Electrode spacing: 1.1 cm
Propellant bar length: 5.8 cm each arm	Electrode width: 0.55 cm
Propellant bar height: 1.1 cm	Electrode thickness: 0.2 cm
Propellant bar width: 0.5 cm	Electrode division: Follows Nozzle
Nozzle middle wall divergence: 10°	Interface to satellite: Nut and bolts
Nozzle outer wall divergence: 25°	Spark plug holder: 1 mm radius
Spark plug: 0.75 mm radius, 1 cm long	PPT dry mass: 40 g

Table 5 Material considerations of various components

Components	Materials	Composition	Alternative
Electrode	Tungsten-copper alloy	75%–25% W-Cu	Tungsten coated copper
Spark plug electrode	Pure tungsten	99.5% W	Pure copper
Spark plug holder	PTFE	PTFE	ShapIM™
Thruster casing	Torlon 4203™	PAI	ShapIM™
Negator springs	Steel wire	Stainless steel	–

Table 6 Specifications of electrical components

Items	Quantity	Mass (gm)	Dimensions
XP POWER pulse transformer Q-15	1	4.3	12.7 mm L * 12.7 mm H * 12.7 mm W
XP POWER pulse transformer Q-60	1	28.3	21.59 mm L * 21.59 mm H * 21.9 mm W
AVX capacitor (for BNC)	15	1	19.6 mm L * 18.3 mm H * 5.08 mm T
HVGT diode	12	0.45	Φ3 mm * 12 mm
Capacitor (for CW)	6	2	Φ18 mm
8.2 MΩ (for 555 timer) (JAMECO VALUE PRO)	4	1	6.8 mm L * 28 mm H * Φ2.5 mm
2.8 MΩ (for 555 timer) (VISHAY INTER TECHNOL OFY)	4	1	6.5 mm L * Φ2.5 mm
AVX Capacitor 10nF (for 555 Timer)	4	0.45	3.81 mm L * 2.54 mm W * 3.81 mm H
AVX capacitor 22nF (for 555 timer)	4	0.5	4.83 L * 2.29 W * 4.83 mm H

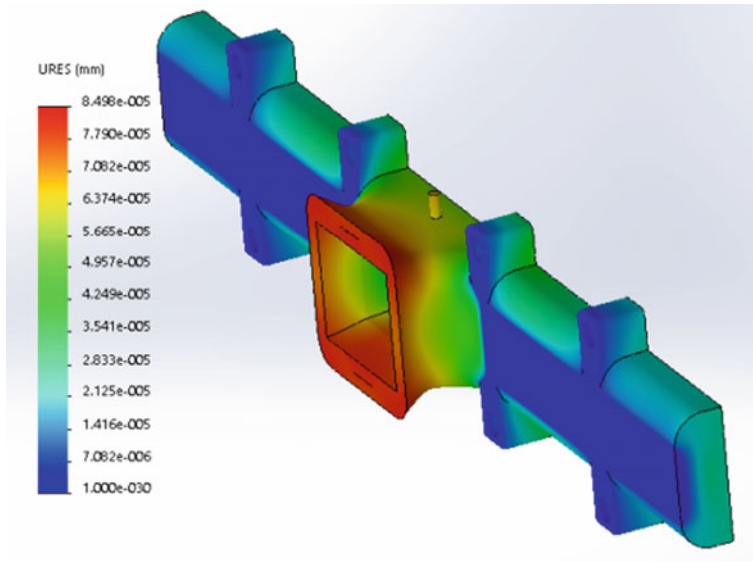


Fig. 9 Maximum deformation plot

Frequency = 1 Hz, to the bank of capacitors. It produced an output voltage of 1500 V (Figs. 11 and 12).

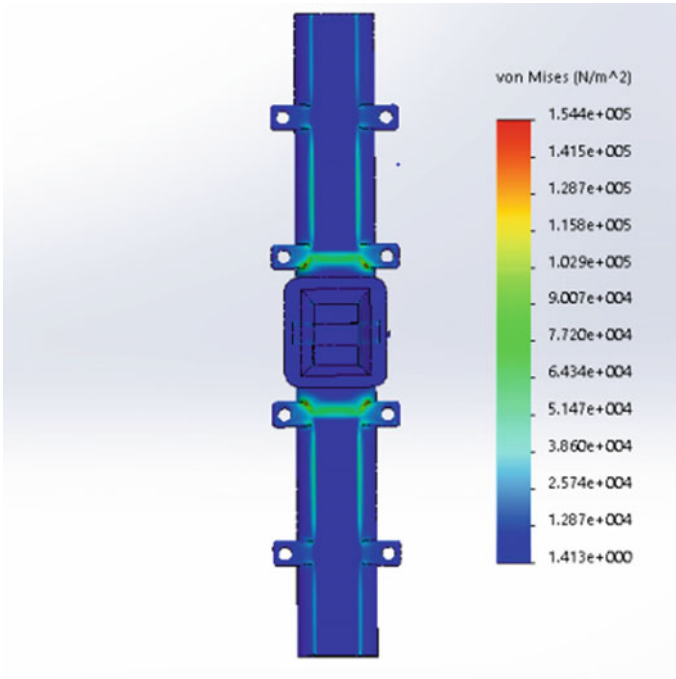


Fig. 10 Maximum stress plot

3.3.3 Simulation of Voltage to Be Used for the High-voltage Spark

Amplitude 6.0 kV, rise time = 1 μ s

Fall time = 1 μ s, pulse width = 10 ms

Frequency = 1 Hz, to the CW. It produced an output voltage of 12 kV (Figs. 13, 14, and 15).

3.4 Thruster Performance Calculation

From the graph below [13], we find that for an E/A ratio of $\sim E/A$ ratio of $\sim 3 \text{ J/cm}^2$, $I_{sp} = 600 \text{ s}$.

$$E = 0.5 CV^2 = 0.5 \times 3 \times 10^{-6} \times 1500^2 = 3.375 \text{ J}$$

$$E/A = \frac{3.375}{(2 \times 1.2 \times 0.46)} = 3.06818 \text{ J/cm}^2$$

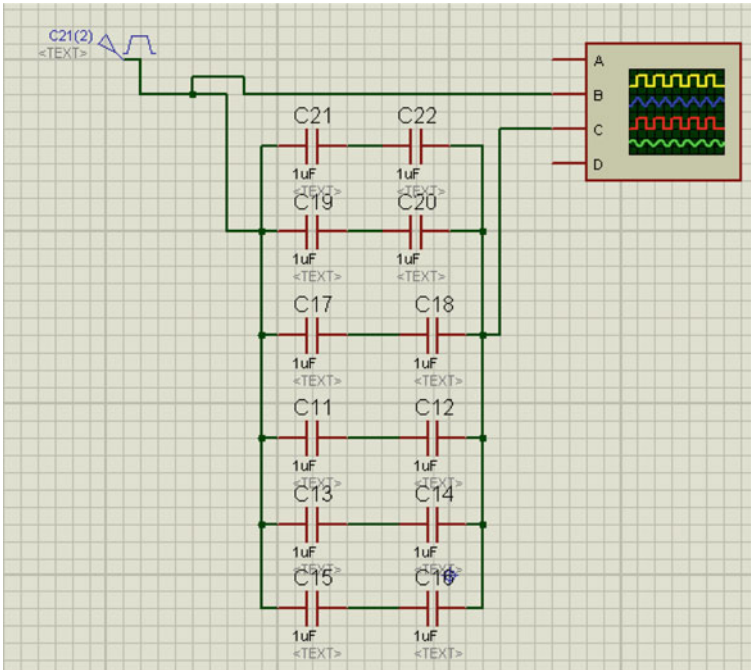


Fig. 11 Circuit diagram and pulse generator properties for bank of capacitors

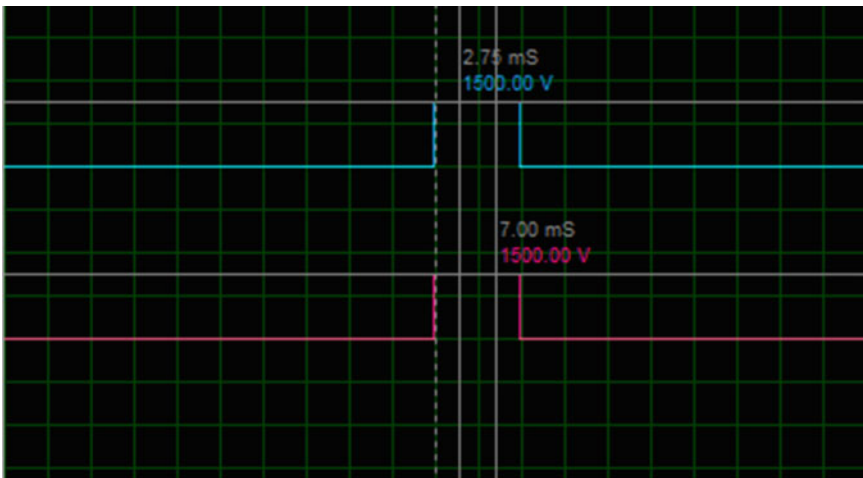


Fig. 12 Simulation result produces a voltage of 1500 V as the output of the bank

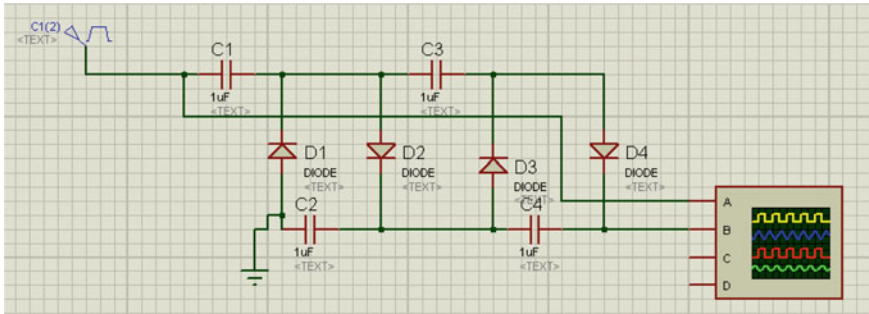


Fig. 13 Circuit diagram and pulse generator properties for CW

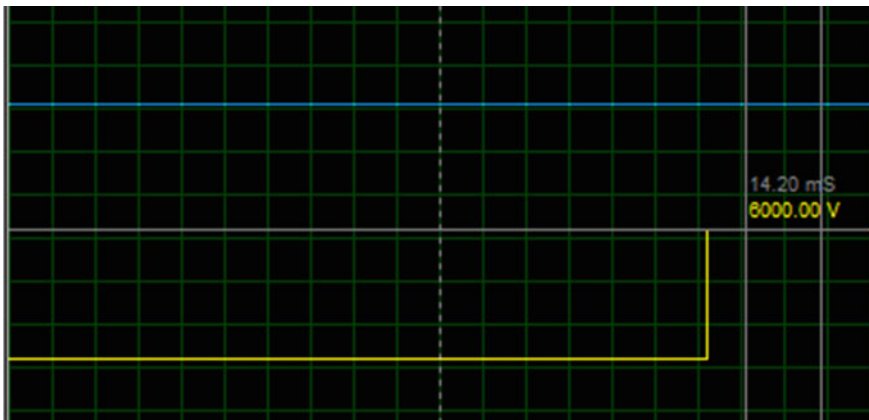


Fig. 14 Simulation of the input 6 kV given to CW

By studying the graph, it can be estimated that for this thruster system, the specific impulse is 600 s (Fig. 16).

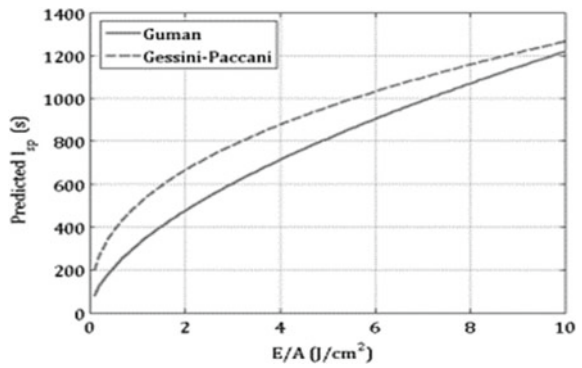
4 Conclusions

The mechanical and electrical design of a micro-pulsed plasma thruster have been presented. Various parameters and models have been considered for this design to work properly in integration with a nanosatellite. In addition, theoretical analysis of the thruster performance has been presented. Furthermore, manufacturing and experiments in vacuum chamber will help in realizing the true feasibility and capability of the thruster.



Fig. 15 Simulation of the output of high-voltage spark (12 kV)

Fig. 16 I_{sp} versus E/A graph



Acknowledgements We would like to thank Prof. Loganathan Muthuswamy and Prof. Marappa Krishnaswamy for their invaluable suggestions and corrections during our work on the Micro-pulsed plasma thruster.

Annex

See Figs. 17, 18, 19, 20, 21, and 22.

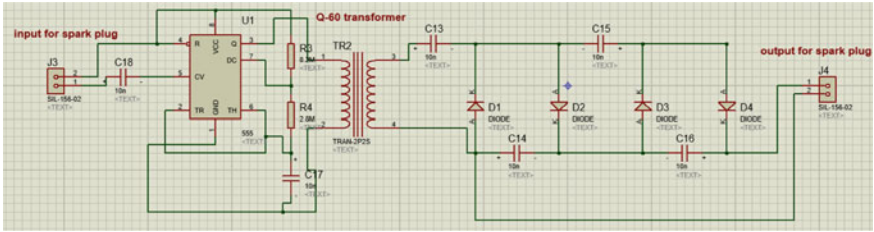


Fig. 17 Circuit diagram for spark plug

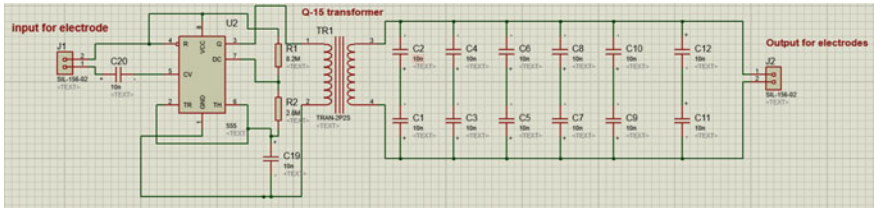


Fig. 18 Circuit diagram for electrode charging

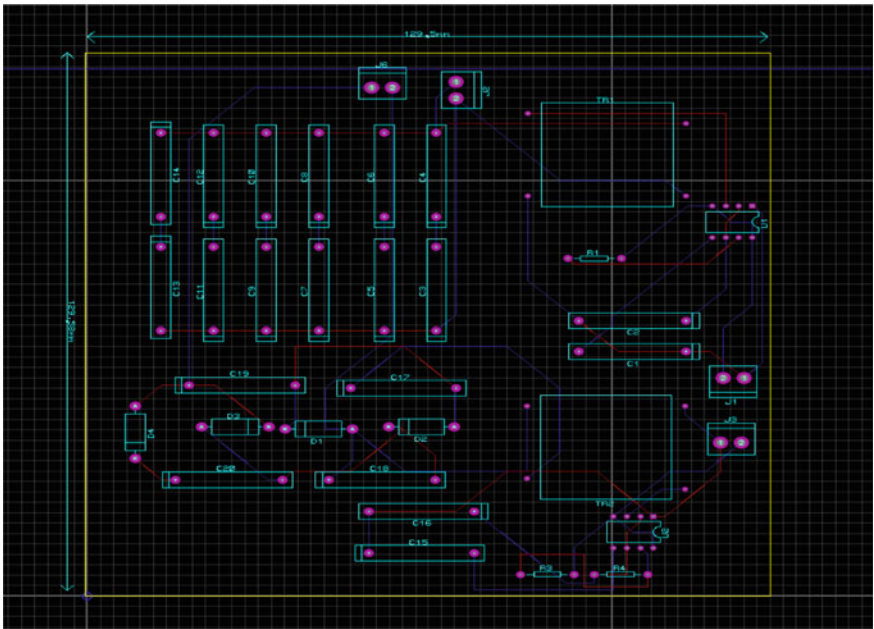


Fig. 19 PCB design of the μ PPT electrical system

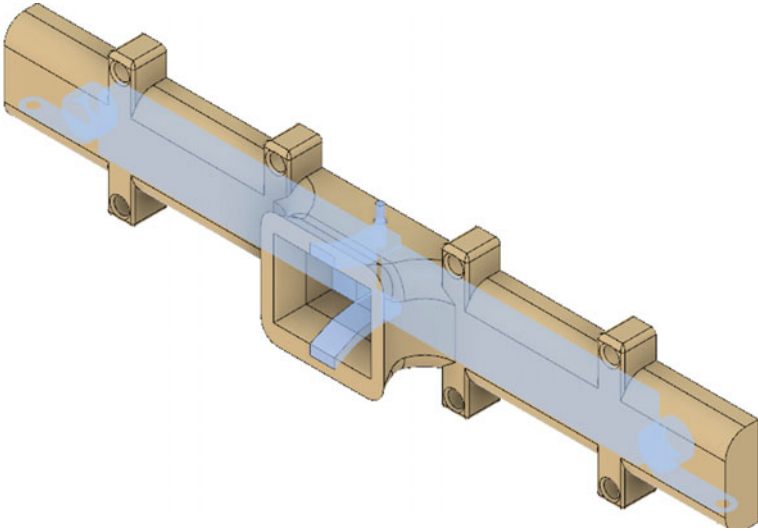


Fig. 20 Highlighted internal components of the micro-pulsed plasma thruster

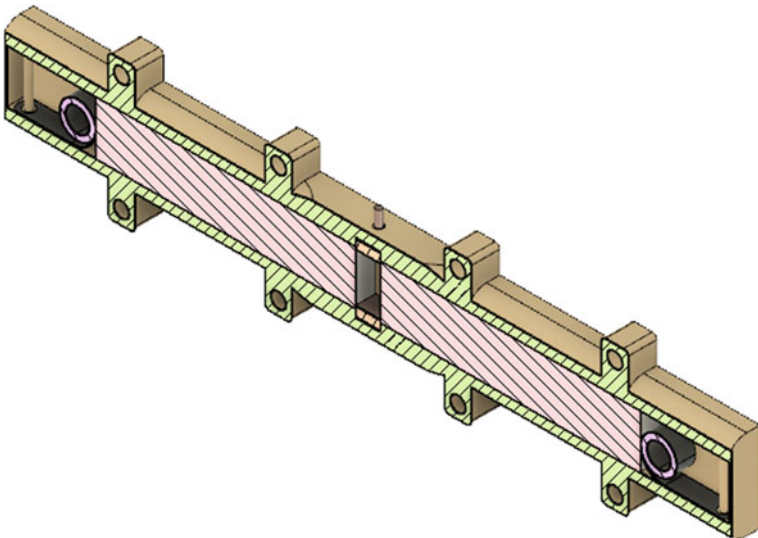
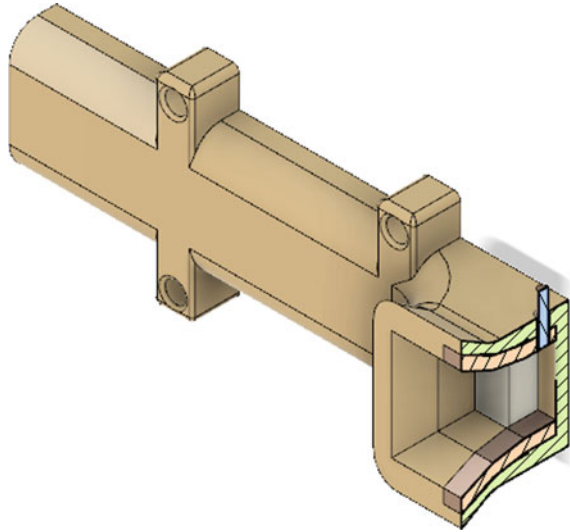


Fig. 21 Cross-sectional view depicting the propellant bars and the negator springs

Fig. 22 Cross-sectional view depicting the electrodes and spark plug



References

1. Jahn R (1968) Physics of electric propulsion. McGraw–Hill, NewYork
2. Burton RL, Turchi PJ (1998) Pulsed plasma thruster. *J Propul Power* 14(5):716–735
3. Guman WJ (1976) Solid propellant pulsed plasma propulsion system design. *J Propul Power* 13(1):51–53
4. Burton RL, Wilson MJ, Bushman S (1998) Energy balance and efficiency of the pulsed plasma thruster. In: 34thAIAA/ASME/SAE/ASEE joint propulsion conference and exhibit, Cleveland, OH, USA
5. Pottinger SJ, Scharlemann CA (2007) Micro pulsed plasma thruster development. In: 30th international electric propulsion conference, Florence, Italy
6. Pottinger SJ, Krejci D, Scharlemann CA (2010) Pulsed plasma thruster performance for miniaturised electrode configurations and low energy operation. *Acta Astronaut*
7. Dali H, Wansheng Z, Xiaoming K, Pingyang W (2008) Effect of ceramic nozzle on performance of pulsed plasma thruster. *Aerosp Sci Technol* 12:573–578
8. Vondra RJ, Thomassen K, Solbes A (1970) Analysis of solid PTFE pulsed plasma thruster. *J Spacecr Rocket* 7(12):1402–1406
9. Palumbo DJ, Guman WJ (1976) Effects of propellant and electrode geometry on pulsed ablative plasma thruster performance. *J Spacecr Rocket* 13(3):163–167
10. Gessini P, Paccani G (2001) Ablative pulsed plasma thruster system optimization for microsatellites. In: 27th international electric propulsion conference, Pasadena, CA, USA
11. Kohlberg I, Coburn WO (1995) A solution for three dimensional rail gun current distribution and electromagnetic fields of a rail launcher. *IEEE Trans Magn* 31:628–633
12. Nawaz A, Auweter–Kurtz M, Herdrich G, Kurtz HL (2005) Experimental setup of a pulsed MPD thruster at IRS. In: European conference for aerospace sciences (EUCASS), Moscow, Russian Federation
13. Guman WJ (1975) Designing solid propellant pulsed plasma thruster. 11th electric propulsion conference, New Orleans, LA, USA
14. Guman WJ, Williams TE (1973) Pulsed plasma microthruster for synchronous meteorological satellite. In: 10th international electric propulsion conference, Lake Tahoe, NV, USA
15. Vondra RJ, Thomassen K (1974) Flight qualified pulsed electric thruster for satellite control. *J Spacecr Rocket* 11(9):613–617

16. Guman WJ, Vondra RJ, Thomassen K (1970) Pulsed plasma propulsion system studies. AIAA Paper 70-1148
17. Coletti a,n M, Guarducci b F, Gabriel SB (2011) A micro PPT for Cubesat application: design and preliminary experimental results. *Acta Astronautica* 69:200–208
18. Brady ME, Aston G (1983) Pulsed plasma thruster ignitor plug ignition characteristics. *J Spacecraft Rockets* 20(5)
19. Palumbo DJ, Guman WJ (1972) Continuing development of the short pulsed ablative space propulsion system. In: 8th AIAA–SAE joint propulsion conference, New Orleans, LA, USA, November 29–December 1, 1972
20. Nawaz A, Albertoni R, Auweter-Kurtz M (2010) Thrust efficiency optimization of the pulsed plasma thruster SIMP–LEX. *Acta Astronaut* 67:440–448
21. Palumbo D (1979) Solid propellant pulsed plasma propulsion system development for N-S stationkeeping. In: 14th International electric propulsion conference, IEPC, Princeton, New Jersey
22. Brady ME, Aston G (1983) Pulsed plasma thruster ignitor plug ignition characteristics. *J Spacecraft Rockets* 20(5):450–451
23. Aston G, Pless LC (1982) Ignitor plug operation in a pulsed plasma thruster. *J Spacecr Rocket* 19(3):250–256
24. Iio J, Uezu J, Fukushima T, Kamishima Y, Takegahara H (2005) Evaluation! On impulse bit characteristics of pulsed plasma thruster by single impulse measurement. In: 29th international electric propulsion conference, Princeton University, NJ, USA
25. Guman WJ (1974) Development of a short pulsed solid propellant plasma thruster. Fairchild Republic Company, Farmingdale, NY
26. TY-BOOK AU-Cassady R. AU - Hoskins, William AU - Campbell, Mark AU - Rayburn, Christopher PY - 2000/02/01 SP - 7 EP - 14 vol.4 SN - 0-7803-5846-5 T1 - A micro pulsed plasma thruster (PPT) for the “Dawgstar” spacecraft VL - 4 DO. <https://doi.org/10.1109/AERO.2000.878359> JO - IEEE aerospace conference proceedings ER
27. Kang B, Low K (2015) A single-switch high voltage quasi-resonant DC-DC converter for a pulsed plasma thruster. In: 2015 IEEE 11th international conference on power electronics and drive systems, Sydney, NSW, pp 509–513
28. Hrbud IA, Rose MF, Meqman SA (1997) A simple Marx power system for pulsed plasma thrusters

Use of N₂O–O₂ as the Oxidizer for the Hybrid Rocket Application



Rajiv Kumar and K. Thamizarasan

Abstract Present study deals with the study on the effect of Nitrox oxidizer which is the combination of both gaseous oxygen and gaseous nitrous oxide with the wax as a fuel on regression rate, combustion efficiency, and sliver loss. The oxygen was injected through the axial or showerhead injector, and for the nitrous oxide, two different injectors were used, i.e., radial and swirl injector. The study had been carried out with three different combinations of the N₂O and oxygen, i.e., 50:50, 70:30, 80:20 ratio. It was further compared with the GOX and N₂O. It has been observed that the pure N₂O gave lower regression rate compared to the oxygen unless swirl injector was used with N₂O. Among the injectors used, most effective in enhancing performance was swirl, then the radial and last was the showerhead injector. Among the combination of all the three oxidizers used, the 50:50 ratio was the most promising in all respect of performance improvement.

Keywords Hybrid rocket · Radial injector · Regression rate · Combustion efficiency · Nitrox oxidizer

Nomenclature

O/F	Oxidizer to fuel ratio
PVC	Poly Vinyl Chloride
LOX	Liquid oxygen
HTPB	Hydroxyl-terminated polybutadiene
RFNA	Red Fuming Nitric Acid
m_f	Mass of fuel burnt, g
t_b	Burn time, s
r, \dot{r}	Regression rate, mm/s

R. Kumar (✉) · K. Thamizarasan
Department of Space Engineering and Rocketry, Birla Institute of Technology, Mesra, Ranchi,
Jharkhand 835215, India
e-mail: rajiv@bitmesra.ac.in

G_{ox}	Oxidizer mass flux, $g/cm^2 s$
d_f	Final diameter, mm^2
d_i	Initial port diameter, mm^2
X	Axial location, mm
P_c	Average chamber pressure, P_{si}
L, L_g	Length of the motor, mm
$\eta\%$	Combustion efficiency
n	Mass flux exponent
A_t	Throat area, mm^2
\dot{m}_t	Total mass flow rate, g/s
A_P	Area of port, mm^2
\dot{m}_{ox}	Oxidizer mass flow rate, g/s
A_t	Nozzle throat area, mm^2
ρ_f	Density of fuel, kg/m^3

1 Introduction

Hybrid rocket is a type of propulsion system in which fuel and oxidizer are used in two different physical states. It generally uses liquid or gaseous oxidizer and fuel in the solid phase. This type of hybrid rocket is called direct hybrid system. In reverse hybrid system, solid oxidizer is used along with liquid or gaseous fuel. In the case of solid fuels that do not contain any oxidizers is termed as true hybrid system [1, 7].

The hybrid rocket consists of a pressurized oxidizer in the propellant tank, and the solid fuel grain is stored separately inside the combustion chamber. The oxidizer is fed from the tank to the combustion chamber using an injector, and the flow rates are controlled by the control valves of the feed system. An igniter is used to initiate the combustion process, and the combustion persist till the oxygen supply is stopped. In the hybrid rocket during the combustion process, oxidizer flows over the fuel surface. It forms the turbulent diffusion boundary layer over the surface. The flame exists within the boundary layer above the fuel grain surface. During the combustion, heat is generated and it is transferred to the fuel surface, so that the vaporization of fuel occurs. This vaporized fuel further diffuses with the oxidizer within the boundary layer. If the boundary layer keeps increasing the flame, height also increases and so the heat transfer rate decreases. This combustion model was established by Marxman and Gilbert [5].

Hybrid rockets are safer to handle and manufacture compared to other chemical rockets. It is an intermediate type rocket compare to both the chemical rockets, i.e., solid and liquid in many aspects like high performance, able to control the thrust instantly compared to solid rockets. Density impulse is higher compared to the liquid rocket engine which actually means the higher compactness compared to the liquid rocket engine. In a hybrid rocket during the operation, the port diameter starts increasing due to the burning of fuel grain surface. Hence, the heat transfer

rate decreases, and the regression rate tends to be decreased. This problem can be rectified by various methods that improvise the regression rate of the fuel grains and the efficiency [1].

Some of the common polymeric fuels used in hybrid rocket are polyethylene, hydroxyl-terminated polybutadiene (HTPB), and it is considered as one of the high-energetic fuels. It has good mechanical properties. In the hybrid fuels, energetic metals such as aluminum and magnesium are also used in the form of very fine particles to improve the overall properties and performance of the system. Basically, the hybrid fuels have also been split into two categories; liquefying and non-liquefying or polymeric fuels. The combustion behavior of liquefying fuel (paraffin wax) is slightly different from the non-liquefying fuel. In a liquefying fuel, when the fuel surface is exposed to the heat, it forms a thin melt liquid layer over the solid grain surface. As the oxygen enters into the combustion chamber through the fuel port with high velocity, a thin melt layer is sheared off into the fine droplets. These droplets will vaporize and mix with the incoming oxygen by providing additional mass of fuel for combustion. Apart from the boundary layer combustion, it provides additional combustion due to the disturbance experienced by the liquefied fuels [1].

The most common oxidizer used in hybrid rocket is liquid oxygen. Liquid oxygen is a high-performance oxidizer compared to the other oxidizers, and the specific impulse for LOX is over 3000 Ns/kg. However, to maintain oxygen in liquid form is a complex work. The second most useable oxidizer is nitrous oxide. Its critical temperature is 36 °C, and this allows the storing of nitrous oxide at liquid phase without any special heat treatment. The vapor pressure of nitrous oxide is 5.85 MPa at 20 °C. The specialty of nitrous oxide is that it does not require any additional pressure devices to pressurize the oxidizer during the combustion process, and hence, nitrous oxide is referred as self-pressurant. Apart from the storable oxidizers, few others are applied in hybrid systems. These are red fuming nitric acid (RFNA), nitrogen tetroxide, and hydrogen peroxide. The interesting part of hybrid application is the use of hydrogen peroxide, and it is a transparent liquid with density equals to 1463 kg/m³. As a rocket propellant, it has been used in the concentration range of 80–98% H₂O₂ and so-called high-test peroxide. Hydrogen peroxide decomposes both catalytically and thermally on water vapor and oxygen. The decomposition temperature of high-test peroxide ranges from 900 to 1100 K. It is high above the ignition temperature of the polymeric hybrid fuels and produces environmental friendly decomposition products [1].

Patnala et al. [6] had studied using nitrous oxide and gaseous oxygen as oxidizer with paraffin wax as a fuel. In their study, they used swirl injection to inject the oxidizers into the combustion chamber. They observed lower local regression rate with nitrous oxide as compared to the gaseous oxygen. The reason was claimed to be the less oxygen content available for the complete combustion in nitrous oxide. Grosse [2] had studied the combination of carbon hydrogen series-based fuel with nitrous oxide as oxidizer. He used diaphragm within the combustion chamber to mix the combustion product effectively and produce higher regression rate and higher combustion efficiency. It was reported that the use of diaphragm improves the mixing significantly, and overall regression rate also increases. Simurda et al.

[8] had discussed about the importance of the nitrous oxide and oxygen combinations as the oxidizer for hybrid rocket applications. He used fuel as the paraffin wax. Oxidizer and fuel were tested with the medium scaled hybrid rocket, and the grain length was 470 mm. The pre-combustion chamber was used to conduct experiments only with nitrous oxide instead of Nytrox due to safety checks and later with very minimal percentage of oxygen (90% of nitrous oxide and 10% of oxygen) and produced successful results. Karabeyoglu [3] had worked with the nitrous oxide and oxygen mixtures as oxidizers for rocket propulsion applications. In this, they carried out study with the mixture of both the oxidizers (N_2O , O_2) and found the practical advantages over a pure form. The major advantage of this new mixture over the pure one was that it has self-pressurizing capability, high density and high-density impulse, various operational temperatures, improved safety, etc. To examine it, they worked with ATK's GEM60 motor. They reported that the Nytrox systems have a major weight and length advantages over other systems.

It is observed from the above study that among the various oxidizers available for the hybrid rocket system, the nitrous oxide has the best possibilities for the practical applications. It is mainly due to its self-pressurizing behavior. It has only disadvantages that it gives lower regression rate compared to other oxidizer due to the lower oxygen content. Hence, research has been focused on adding oxygen as oxidizer with it to improve its performance. Thus, an attempt has been made in the present study to explore the performance characterization by using the mixture of nitrous oxide and the oxygen system. Further, attempts were also made to compare it with pure N_2O and O_2 oxidizer. The fuel used for the studies was paraffin wax. The experiments are conducted by using two different injectors, i.e., radial and swirl. The injector used for the oxygen supply is axial type. The main aim of having two different combinations of injectors is that the mixing between N_2O and O_2 would be better, once oxidizer combination experiments would be conducted. Parameters used for the studies are regression rate, combustion efficiency, and sliver loss with the selected injectors and the oxidizers.

2 Experimental Procedure

The fuel used in the present study is the mixture of paraffin wax and microcrystalline wax of 70:30 ratio. Both the paraffin wax (straight chain structure) and microcrystalline wax (branched structure) are odorless, white in color, and sticky type, but the melting point is higher for microcrystalline wax (54–95 °C) compare to paraffin (48–70 °C). Also the tensile strength comparison, it is plastic and malleable for microcrystalline, whereas for paraffin, it is brittle in nature. The wax used here has a density of 890 kg/m³, congealing point of 337.3 K, and a melting point of 337.1 K.

The oxidizer used is the gaseous oxygen and the gaseous nitrous oxide. The gaseous oxygen has a density of 1.43×10^{-6} kg/m³, and also it is easily commercially available. Further, the combination of gaseous oxygen and nitrous oxidize has been

used. The combination percentage used for N_2O and O_2 is in the ratio of 50:50, 70:30, and 80:20.

2.1 Experimental Setup

Since two oxidizers have been used for the experimentation purpose, and thus, two separate connections have been made from the cylinder to the injector that is connected to the rocket motor as shown in Fig. 1. The pressure regulator is connected to the oxygen cylinder to control the downstream pressure and the mass flow rate. A pipe line is connected from regulator to the motor through a ball valve and the solenoid valve. The ball valve is used for emergency closure purposes, if the solenoid valve fails during experimentations. The solenoid valve used is normally closed type and has the pressure capacity of 50 bar. Similar arrangements have been made for the supply of nitrous oxide from the N_2O cylinder to the combustion chamber. A N_2O pressure regulator is connected to the N_2O cylinder to control the downstream pressure. It was passed through the ball valve, solenoid valve, the non-return valve, and then to the combustion chamber through the injectors. The ball valve is used for safety purposes to close the supply of N_2O if solenoid fails similar to the oxidizer pipe line. The non-return valve helps to prevent any back flow of flame toward the cylinder. Both the solenoid valves used to control the flow of oxygen and N_2O have been connected to sequential timer. A DC power supply used for ignition purposes has also been connected to this sequential timer. Ignition time is thus controlled by the sequential timer. For ignition, the solid propellant pellet of around 0.5 gm has been used. It was inserted to the nichrome wire, and 16 V DC power supply was

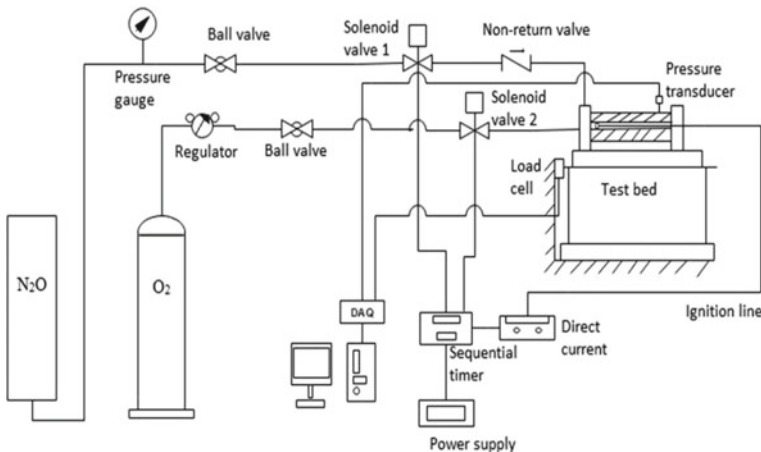


Fig. 1 Schematic diagram of experimental setup

given to it for the ignition through the sequential timer. Now, all these connections such as solenoid valve and the ignition power supply will operate in a series.

For pure oxygen, totally two channels will be in operations: channel 1 used for ignition power supply which will be connected through the timer and channel 2 will be connected to operate the solenoid valve. For nitrous oxide, totally three channels have been used. Channel 1 will be used same as for ignition power supply, channel 2 will be used to operate the oxygen solenoid valve (utilized to support ignition for N_2O combustion with fuel) for few fractions of second, and channel 3 will be operated for nitrous oxide solenoid valve. For the another set of experimentation, totally two channels have been used: channel 1 for ignition power supply and the channel 2 used for both the oxygen and nitrous oxide solenoid valves to operate together at the same time. The DC power supply for the ignition, solenoid valves, and the timer with the complete experimental set up is shown in Fig. 1.

2.2 Experimental Hybrid Rocket Motor

The combustion chamber consists of the flanged cylindrical tube with the internal diameter of 50 mm and the external diameter of 68 mm. The motor is made up of mild steel, and at its head end for the oxidizer, supply injector was fasten to the combustion chamber. At the aft end of the motor, the graphite convergent divergent nozzle was connected to the combustion chamber.

The graphite was used as it can withstand high temperature and also resists the erosion of the material after repeated experiments. The igniter pellet was connected to igniter wire with the help of a nichrome wire, and it is inserted into the combustion chamber via nozzle portion. Also, while assembling the motor, China clay was provided in between the head end flange and the nozzle end flange. This assures the leak proof assembly between these two flanges and prevents leaking of the hot product gases during the combustion of the propellant. Finally, the motor is completely fixed to the test bed with the help of belt, bolts, and nuts. A fully assembled motor is shown in Fig. 2, and its complete geometry details are given in Table 1.

2.3 Injectors Used for Study

Two different types of injector were used for the nitrous oxide (radial and swirl) and for the oxygen, showerhead or axial type of injector was used. Oxygen and nitrous oxide were injected separately without any premixing. It can be seen from Fig. 3a. In order to get the radial or swirl injector, only bottom flange part of the injector shown in Fig. 3a would be changed with the injectors shown in Fig. 3b, c. It shows the injector flange of radial and swirl type.

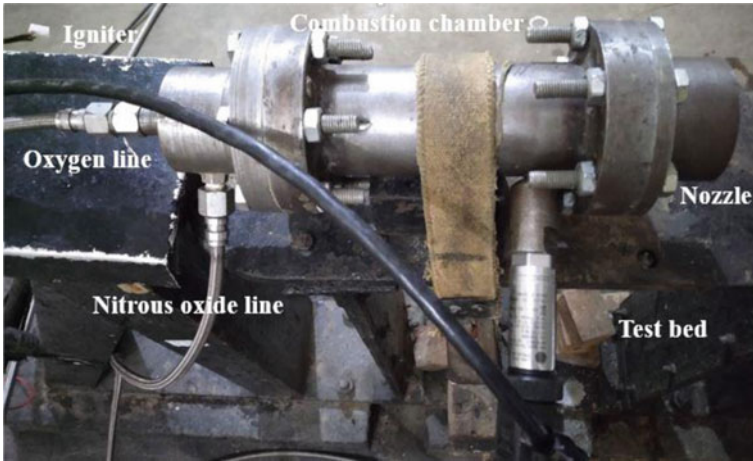


Fig. 2 Hybrid rocket motor fixed to the test bed

Table 1 Dimensions of the hybrid rocket motor

Parameters	Values
Fuel grain length	188 mm
Inner diameter of the chamber	50 mm
Port diameter	15 mm
Area ratio of nozzle	4.34
Throat diameter of nozzle	12 mm
Convergent diameter of nozzle	45°

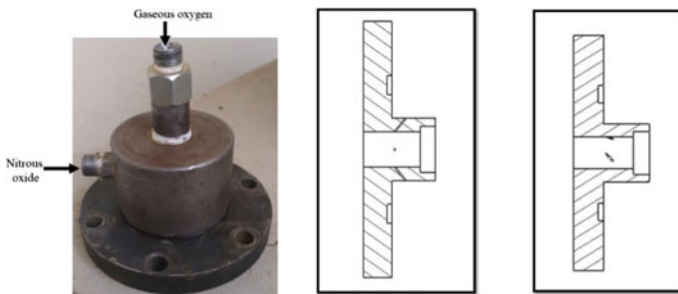


Fig. 3 a) Injector assembly, cross sectional view of b) radial injector, and c) swirl injectors

2.4 Performance Parameter Determination

Regression rate was measured using the weight loss method as explained in Ref. [4]. The weight of the motor before the combustion and after the combustion was

recorded. With this known information about the mass of fuel consumed (m_f), density of fuel (ρ_f), initial port diameter (d_i), and length of the fuel grain (L_g), the final diameter after the combustion was calculated (d_f). Further, knowing the initial port diameter (d_i), final diameter (d_f) which is calculated earlier and the known burn time (t_b) from all these parameters will be obtained the regression rate (\dot{r}) using Eqs. 1 and 2. The oxidizer mass flux was calculated from the mass flow rate of the oxidizer and the average port area of the combustion chamber after the test experiment using Eq. 3.

$$d_f = \sqrt{\frac{4m_f}{\pi\rho_f L} + d_i^2} \quad (1)$$

$$\dot{r} = \frac{(d_f - d_i)}{2t_b} \quad (2)$$

$$G_{ox} = \frac{\dot{m}_{ox}}{A_p} \quad (3)$$

The calculation for the combustion efficiency is done using theoretical approach, where NASA SP273 software had been used. With the known experimental chamber pressure and the total fuel burnt, experimental characteristic value has been obtained. Further, combustion efficiency is obtained using Eqs. 4 and 5. The combustion chamber pressure was measured using the pressure transducer. The power supply is given as 12 V and connected to the NI 9171 DAQ as shown in Fig. 3. The data are acquired using this system through the LabVIEW signal express. The pressure transducer used was UNIK 5000, and the pressure range was between 0 and 50 bar.

$$\eta = \frac{C^*_{exp}}{C^*_{the}} \quad (4)$$

$$C^*_{ex} = \frac{P_c A_t}{\dot{m}_t} \quad (5)$$

The sliver loss study has also been conducted by measuring the regression rate along the length of fuel grain after the combustion.

3 Results and Discussion

3.1 Studies of Regression Rate

Regression rate of hybrid rocket fuel is defined as the surface regression of the fuel grain during the combustion over a given burn time of the hybrid rocket motor.

Mainly, three different aspects of the regression rate have been studied. Initially with the pure oxidizers using the both the type of injectors, then the combinations of both oxidizer with both the types of injectors, finally overall comparison of the pure oxidizers and their combinations with both the injectors.

3.1.1 Regression Rate with Pure Oxidizer

In the present work, interrupted static test was conducted after evaluating the thermal response time of paraffin wax which was around 0.0143 s, and hence, the burn time for gaseous oxygen was 1 s, and for gaseous nitrous oxide, the burn time was 1.5 s.

Before initiating the experimentation, the mass flow rate of the oxidizer requires to be known. The mass flow rate was calculated by mass loss method. The initial and final mass of the cylinder after allowing the gas to pass through the injector for 10 s were recorded. By knowing the mass loss and time, the mass flow rate was obtained. For experimentations, the total burn duration was chosen as 4 s based on the Web thickness available with the given fuel grain. Regression rate is measured here using the weight loss and interrupted test method [4]. The experimental setup used for this study is shown in Fig. 1 in Sect. 1. The hybrid rocket used for this study has a length of 188 mm. The initial port diameter was 15 mm. Detailed experimental procedure is explained in Sect. 4. The experimental results with the gaseous oxygen obtained are shown in Fig. 4. The results shown are for the total burn time of 4 s interrupted after each 1 s. It means the motor is stopped after each 1 s, and its result is analyzed, and then, the same motor is restarted for the next 1 s. It continued for the total burn time of 4 s.

From Fig. 4, it is observed that the regression rate decreases as the oxidizer mass flux is decreased during the combustion process, as the port diameter increases with the progress in burn time. The power fit curve of the oxidizer mass flux versus regression rate for gaseous oxygen and wax combination is also shown in Fig. 4. The n values obtained for this combination are 0.51. This n value indicates that the O/F ratio does not change with the burn time. It is to be noted that the axial or shower head type of injector has been used for this study. This type of injector has been used for this fuel-oxidizer combination, and same has been used for other combination too. Figure 4 also compares the results obtained with the gaseous nitrous oxide. With gaseous nitrous oxide, the experiments have been carried out with two different types of injectors: radial and swirl injector. The total burn time for radial injector was 6 s, and for the swirl injector, the burn time was restricted to 2.75 s. The reason for restricting to 2.75 s is the higher regression rate with this fuel, hence beyond this, burn time fuel might be fully consumed in the combustion chamber. The swirling phenomenon makes big change in the regression rate is due to the oxidizer flow attachment over the grain surface, and heat transfer rate is much improved to the fuel surface, hence the pyrolysis process happens in instant manner. This is the reason it has higher regression rate, and hence, the burn time has been reduced at consecutive testing process. Whereas in the radial injection, it acts like an impingement type and after that, it becomes central motion in the port diameter like the axial injector,

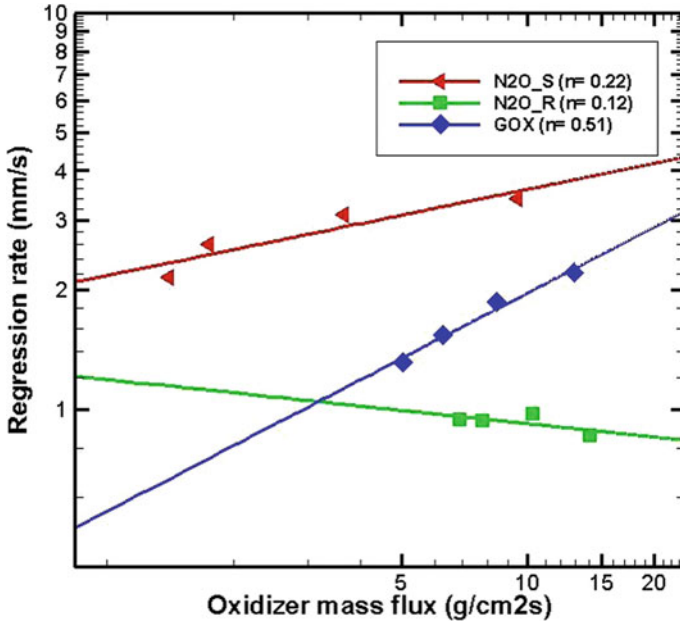


Fig. 4 Regression rate variation with Gox for gaseous oxygen and gaseous nitrous oxide with the wax fuel for hybrid rocket using radial and swirl injector type

but it will flow with less velocity due to its neutralization of velocity during the impingement process. That is the reason even at 1.5 burn time constantly, it gives very low regression rate. It has also been observed that igniting the wax fuel with N_2O as oxidizer was difficult with solid propellant bead. Thus, to achieve stable combustion with fuel-oxidizer combination, initial ignition has been sustained by supplying oxygen for a fraction of sec, then N_2O was supplied as per the burn time requirement. The solid propellant igniter bead and the gaseous oxygen both are used for the ignition with nitrous oxide as it has the higher activation energy compared to the gaseous oxygen due to less content of oxygen level. It can be seen from Fig. 6 that the swirl injector gives around 3 times higher regression rate compared to the radial injector. And also, with the radial injection of nitrous oxide, the regression rate increases as the oxidizer mass flux is decreased as compared to the swirl injection and axial injection of gaseous oxygen. This trend is rarely observed in hybrid rocket, where decrease in Gox regression rate increases. The reason for this could be that as the port diameter increases or the Gox decreases, the radial injection pattern is such a way that it is always impinging over the fuel surface and thus improving the regression rate. Still, the radial injector has very weak effect on the improvement of regression rate due to the lower actual oxidizer mass flux in the combustion chamber compared to the swirl injector. Thus, it gives lower regression rate compared to the swirl injectors. It is to be noted that the regression rate of wax with N_2O is lower compared to gaseous oxygen, if shower head type of injector is used. This is the reason

in practical application gaseous oxygen is preferred compared to N_2O . But due to the self-pressurization capability of N_2O , it is in demand for practical application. If the swirl injector is used, the regression rate is higher than the regression rate obtained with gaseous oxygen. Thus, the use of swirl injector can overcome the reduced regression rate due to the use of N_2O as the oxidizer. It is also to be noted, in the present study, the main aim of selecting two different combinations of injectors for gaseous oxygen and N_2O is to enhance mixing between these two oxidizer combinations. It is useful, when combination oxidizer is used. For the gaseous oxygen, the n value is close to the 0.5, whereas for the N_2O swirl injection and radial injection, it is much lesser than 0.5 making the total mass flow rate more dependent on the port diameter. Here, n is called the mass flux exponent; its significance is that it indicates the dependency of regression rate with the oxidizer mass flux. The dependency of oxidizer mass flux with n is also linked with the change in the O/F ratio with burn time. In hybrid rocket required values of n is 0.5 for getting the constant O/F ratio with the burn time.

3.1.2 Regression Rate with Oxidizer Combinations

It is known from the above study that N_2O along with shower head injection gives lower regression rate compared to oxygen system. Thus, attempts were made to study the effect of oxygen in combination with N_2O system; it is termed as Nytrox system. For this study, three different combinations have been selected. It includes ratios as 50:50, 70:30, and 80:20 for N_2O and gaseous oxygen, respectively. The results obtained with these combinations are given in Figs. 5 and 6. Figure 5 shows the results obtained with radial injector, while Fig. 6 describes about swirl injector.

It can be seen from Fig. 5 that regression rate with N_2O is lower compared to gaseous oxygen. It is mainly because of the lower concentration of oxygen in the N_2O gas. If it is compared with Nytrox with varying concentration of each oxidizer, it is observed that the 50:50 ratio gives highest improvement compared to other combinations such as 70:30 and 80:20. It is also to be noted that the regression rate with all the combination gives higher or close to pure oxygen. In reality, the regression rate with all the combination should be lower compared to the pure oxygen. The reason for this difference is that the injector used for pure oxygen is shower head type, but for N_2O , it is radial injector. Thus, when N_2O is used or even with the combination, the effect of radial injector is improving the regression rate.

Similarly, it can be seen from Fig. 6 that the regression rate with pure oxygen is lower compared to other combinations even lower than the pure N_2O condition. It is mainly because for pure oxygen shower head injector was used, whereas for N_2O , swirl injector was used. It is known that swirl injection improves the regression rate. Thus, even in the combination of the oxidizers, always N_2O swirl effect will help in enhancing the regression rate as observed in Fig. 6. Although the results obtained with 70:30 ratio gives contrary results. Thus, details study needs to be done to understand this. It is interesting to note that even with N_2O and combination with O_2 , regression rate can be achieved as 5 mm/s at around 15 GOX. This is highly useful for hybrid

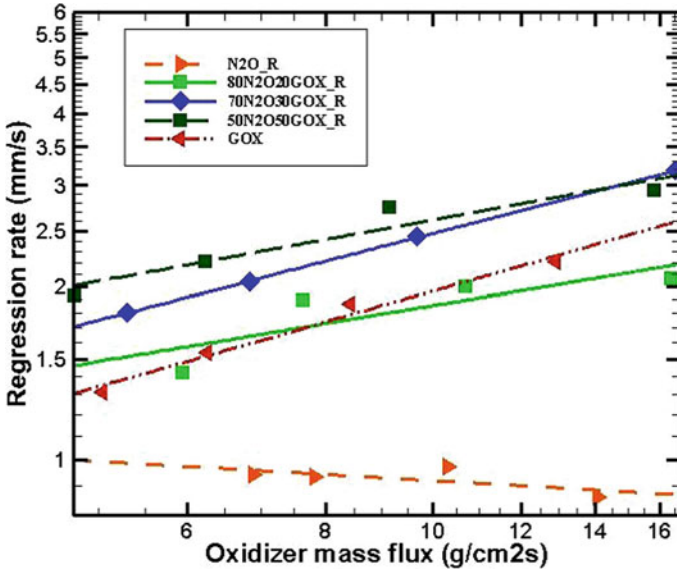


Fig. 5 Regression rate variation with Gox for the pure oxidizers and their various combinations using axial radial injector

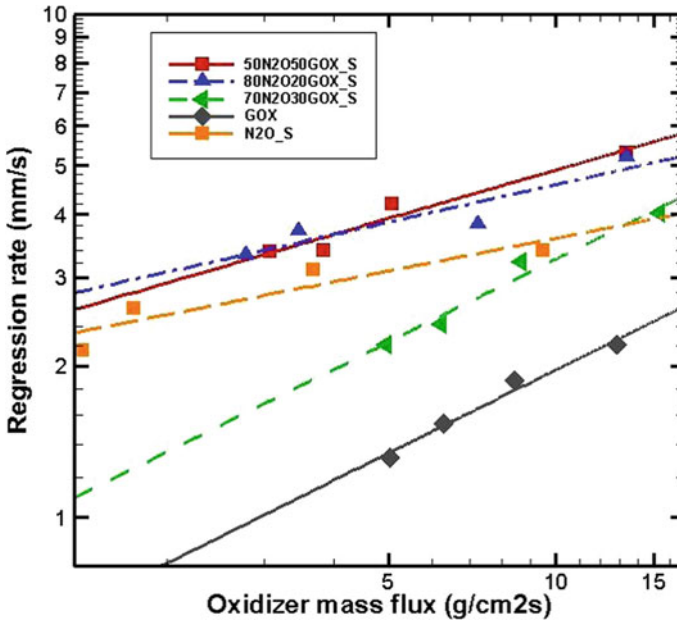


Fig. 6 Regression rate variation with Gox for the pure oxidizers and their various combinations using axial swirl injector

rocket for practical applications as high regression rate is required for hybrid fuel. It can also be seen from Figs. 5 and 6 that the regression rate improvement is significant with swirl injector compare to the radial injector.

3.1.3 Studies on Combustion Efficiency

The combustion efficiency for pure oxidizers and their combinations is discussed in this section. The procedures for obtaining the efficiencies are discussed in Sect. 4. To get the combustion efficiency, experiments were conducted for the continuous burn time of either 1 s or 3 s, based on the Web thickness of the fuel available in the combustion chamber. The pressure time has been obtained for the given burn time and based on the mass flow rate of propellant and chamber pressure, efficiency has been obtained. The results obtained are given in Table 2. As it is known that for the oxygen supply, a showerhead type of injectors has been used. For the N₂O and its combination with O₂, two types of injector have been used. Results for both the types injectors for N₂O and its combination are also given in Table 2. It is also observed from Table 2 that the burn time used for the swirl injector was restricted to only 1 s of the burn time, and it is due to higher regression rate of the fuel. Apart from this, it is also to be noted that with the pure N₂O, the burn time is only 0.5 s. The reason for this is that to sustain the steady combustion with radial injector for longer burn time beyond this was very difficult. It has been stated earlier that the ignition for pure N₂O system was difficult with the igniter as the solid propellant alone. Thus, to sustain proper combustion with N₂O, for a fraction of sec, oxygen was supplied and then N₂O was supplied such that stable combustion is possible with it. It could be seen from the pressure time graph shown in Fig. 7. The pressure time shows a certain fraction of time for the ignition with oxygen supply and then with the N₂O system as alone. Here, 0.5–1 s is the gaseous oxygen as it is given for the additional ignition as mentioned earlier higher ignition energy required for nitrous oxide than the oxygen since oxygen content is less in it. And then from 1 to 1.5 s, actual gaseous

Table 2 Combustion efficiencies obtained with various combinations of oxidizer

S. No	Oxidizer type	Injector used	Burn time	O/F ratio	P_c	η (%)
1	O ₂	Shower type	3.5	1.61	62	42.50
2	N ₂ O	Radial	0.5	1.90	25	28.34
		Swirl	1.0	0.90	40	39.10
3	50N ₂ O50O ₂	Radial	3	1.20	60	52.85
		Swirl	1	0.97	99	65.38
4	70N ₂ O30 O ₂	Radial	3	1.33	55	49.70
		Swirl	1	0.99	87	57.65
5	80N ₂ O20 O ₂	Radial	3	1.31	40	46.80
		Swirl	1	1.11	77	52.08

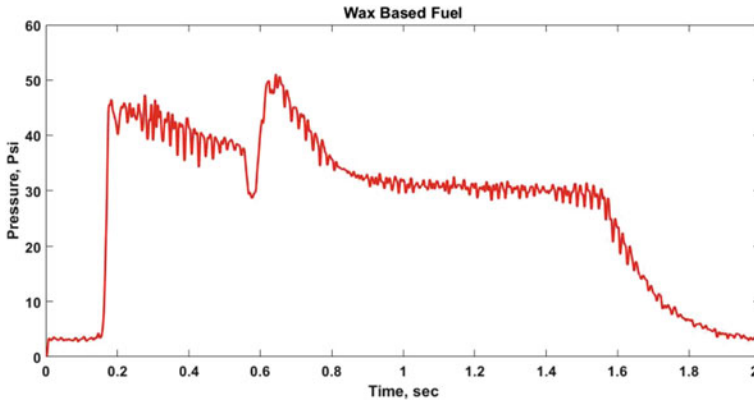


Fig. 7 Pressure time graph showing the ignition time and N_2O oxidizer supply

nitrous oxide is used for the combustion (only this duration of data was used for the combustion efficiency percentage calculation for N_2O oxidizer). Similar, procedure is adopted for other test of experiments where pure N_2O has been used.

It is seen from Table 2 that the efficiency obtained with pure N_2O system having radial injector is very low. Its efficiency with the use of swirl injector improves, but still it is very low. The reason for it is that the N_2O has lower oxygen content. The efficiencies obtained with the pure O_2 are higher than the N_2O system. Its efficiencies would be higher, if the injector used here would be either radial or the swirl injector. Further, it is also observed that as the oxygen content is improved in the N_2O oxidizer, its efficiencies have improved significantly. The efficiencies obtained with 50 N_2O 50 O_2 combination give the highest improved in efficiencies with the swirl injector. Relatively, the highest improvement is observed with the radial injector.

3.1.4 Sliver Loss Study

It is known that non-uniform regression rate along the length of hybrid fuel is one of the drawbacks in hybrid rocket. This non-uniform regression rate along the length gives higher sliver loss in hybrid rocket. The sliver loss is studied by calculating the local regression rate along the axial location. It is done by the taking X-ray image after the combustion of fuel grain and then measuring its unburnt thickness. The regression rate along the length is normalized with the maximum regression rate, and it is presented in Figs. 8 and 9.

It is clearly seen from Fig. 8 that the trend of regression rate for both the cases with the pure oxidizer is completely different. With oxygen, the regression rate at the head end is lower compared to the nozzle end. The higher regression rate at the nozzle end is due to higher mass flux at the downstream toward the nozzle end. For the radial type of injector with N_2O , the regression rate is higher at the head end compare to

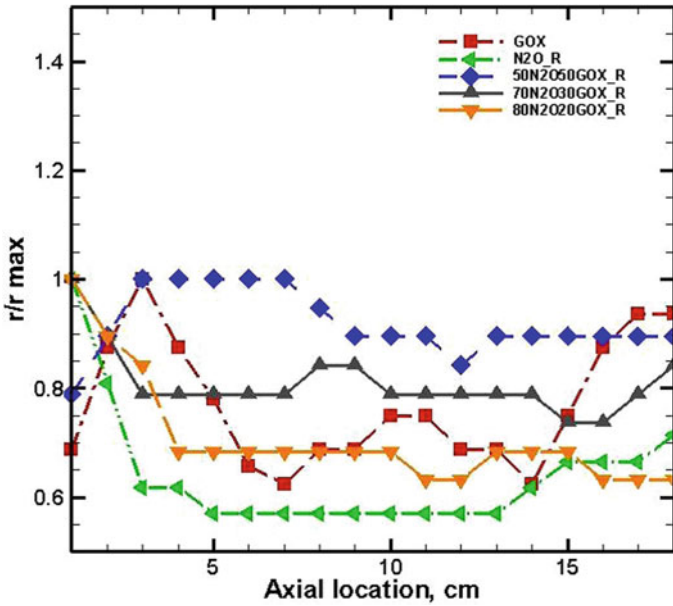


Fig. 8 Normalized regression rate along the axial length of the grain for gaseous oxygen, nitrous oxide, and their three combinations using axial radial injection

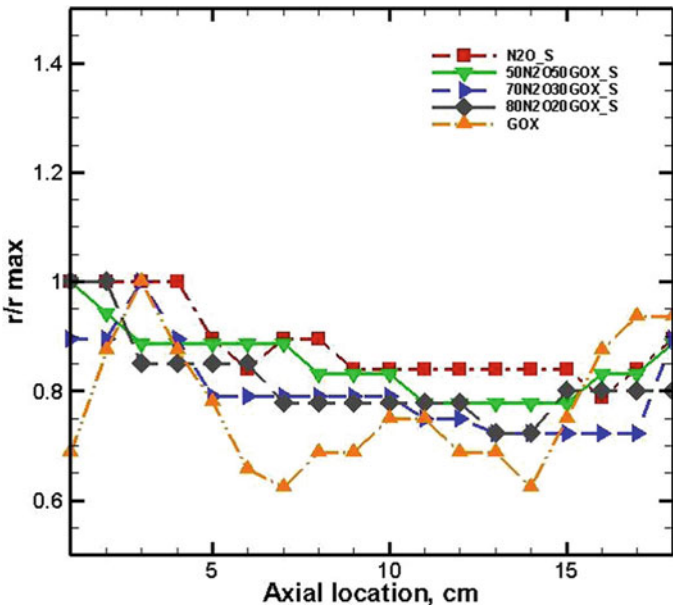


Fig. 9 Normalized regression rate along the axial length of the grain for gaseous oxygen, nitrous oxide, and their three combinations using axial swirl injection

the nozzle end. In this, lower regression rate is seen in the middle. The reason for this type of trend is that the radial injector is directly impinging over the surface at the head end, and thus, higher regression rate is observed. Further downstream regression rate is reduced as its impingement effect is absent only mass flux effect is seen. Far downstream near nozzle end due to higher mass flux (mass of oxidizer and mass of fuel), the regression rate is further enhanced. In overall, it is observed that the uniformity with radial injector among O_2 and N_2O system, the N_2O system is better than axial injector with gaseous oxygen.

From Fig. 9, it is observed that higher mass is burnt with nitrous oxide due to the swirl injection effect as the flow is attached over the fuel surface, and so the heat transfer rate to the fuel surface had been improved giving higher regression rate. It is observed that the regression rate is highest at the head end and decreases toward the nozzle end. It is just opposite to that is seen with gaseous oxygen. Relatively better uniformity is observed with nitrous oxide compared to the gaseous oxygen.

Further, the results were compared with other combinations of the oxidizer having radial and the swirl injector as shown in Figs. 8 and 9, respectively. It is seen from Figs. 8 and 9 that all the combination gives higher uniformity compared to the pure N_2O or O_2 case with both the types of injectors used. While comparing between the radial and swirl, the uniformity obtained with swirl injector is better than the radial types of the injector. Further, when compared among these three combinations, 50% of gaseous oxygen and 50% of nitrous oxide have shown the highest uniformity compare to other combinations for both the types of injectors. Thus, it has been observed from all the study that 50:50 ratio combinations are the best to be used for practical applications.

4 Conclusions

The present study deals with the effect of the Nytrox (N_2O and oxygen mixer) oxidizer on the performance of the hybrid rocket motor. Mainly, three different oxidizer combinations of the N_2O and oxygen, i.e., 50:50, 70:30, 80:20 ratio with the wax as a fuel have been used for the study. From the results obtained of experimental work that was carried out in the present studies, the following conclusions can be drawn.

1. For the gaseous nitrous oxide, the regression rate was 3 times higher for the swirl injector compared to the radial injector.
2. For the 50:50 ratio using the axial radial injection, it shows an increase of 41% of average regression rate compared to GOX and 164% rise using the radial injection of N_2O .
3. With the use of 50:50 ratios using the axial swirl injection, it shows an increment of 135% of average regression rate compared to GOX with axial injection and 45% using swirl injection of N_2O .

4. Increase in combustion efficiency for 50:50 ratio using axial swirl injection was 54% when compared to gaseous oxygen and 67% compared to gaseous nitrous oxide using swirl injection and for axial radial injection, it was 24% higher than the gaseous oxygen and 86% higher than the gaseous nitrous oxide using radial injection.
5. Uniform burning of fuel grain from head end to the nozzle end was observed with 50:50 combinations when compared to the other combinations using both the axial radial and axial swirl injectors.

References

1. Chiaverini MJ, Kuo KK (2007) Fundamentals of hybrid rocket combustion and propulsion, vol 218. American Institute of Aeronautics and Astronautics, Inc
2. Grosse M (2009) Effect of a diaphragm on performance and fuel regression of a laboratory scale hybrid rocket motor using nitrous oxide and paraffin. American Institute of Aeronautics and Astronautics, Paper 2009-5113
3. Karabeyoglu MA (2014) Nitrous oxide and oxygen mixtures (Nytrox) as oxidizers for rocket propulsion applications. *J Propul Power* 30(3):696–706
4. Kumar R, Ramakrishna PA (2012) Enhancement of regression rate using bluff body in hybrid fuels. In: Ninth international conference on flow dynamics, Sendai
5. Marxman GA, Gilbert M (1963) Turbulent boundary layer combustion in the hybrid rocket. In: Ninth international symposium on combustion, vol 9(1), pp 371–383
6. Patnala S, Chatterjee AK, Joshi PC (2012) Combustion studies on paraffin wax in gaseous oxygen and nitrous oxide. *ARPN J Eng Appl Sci* 7(7):806–811
7. Sutton GP, Biblarz O (2000) Rocket propulsion elements. Wiley, Weinheim
8. Simurda L, Stober KJ, Boiron AJ, Hornstein K, Jens E, Fletcher A (2012) Design and development of a thrust vector controlled Paraffin/Nytrox hybrid rocket. American Institute of Aeronautics and Astronautics, Paper 2012-4310

Effect of Protrusion Configuration on Combustion Stability of Hybrid Rocket Motor



Mengu Dinesh and Rajiv Kumar

Abstract In the present study, attempts were made to investigate the effect of the protrusion configuration on the performance and combustion stability behavior of the hybrid rocket motor. The protrusion configurations used for study include circular, star, multi-hole and fin. All the protrusion configurations were tested by placing at 0.7X/L location in a hybrid rocket motor. The wax and gaseous oxygen were used as a fuel and oxidizer, respectively. The regression rate and combustion efficiency were improved upon inserting the protrusion in hybrid rocket motor. Among the protrusion configurations, multi-hole case showed the highest improvement in regression rate and combustion efficiency. The hybrid rocket with/without protrusion case exhibited the first and second longitudinal acoustic modes which are dominant throughout the combustion. Upon inserting the protrusion, the stability of the combustion was improved significantly. Among all the protrusion cases, the star case exhibited the higher stable combustion. The frequency range of longitudinal acoustic modes was changing while changing the protrusion configuration.

Keywords Hybrid rocket · Regression rate · Combustion efficiency · Protrusion configuration · Combustion instabilities

1 Introduction

Hybrid rocket is the combination of solid and liquid rocket engine, where the fuel and oxidizer are stored in two different phases. Generally, fuel is in solid phase and oxidizer is in liquid or gaseous phase. Hybrid rocket possesses many advantages over the solid and liquid rocket engines due to its inherent nature of safety and simplicity [1, 2]. However, hybrid rocket suffers with drawbacks such as low fuel regression rate, low combustion efficiency, O/F shift and higher sliver loss [1, 2]. These drawbacks are restricting its utilization in practical applications.

M. Dinesh · R. Kumar (✉)

Department of Space Engineering and Rocketry, Birla Institute of Technology, Mesra, Ranchi, Jharkhand, India

e-mail: rajiv@bitmesra.ac.in

Till date, several methods have been adopted to improve the performance of the hybrid rocket [3–11]. Some of these methods being used frequently are addition of energetic metal additives [4] and oxidizer particulates [5], using swirl injection [6], protrusions [7–10] and cavities [11] in the midst of combustion chamber and pre- and post-combustion chambers [12]. Among these methods, protrusion method has attracted most to investigate only due to its simple configuration, cost effectiveness and suitability for the different applications [13]. Also, it can act as the flame holder in the combustion chamber [14]. Generally, protrusion method comes under the category of turbulence generators as it disturbs the flow inside the combustion chamber of the hybrid rocket [8–10]. Due to this, the heat transfer to the fuel surface improves by reducing the average boundary layer thickness, and the turbulence generated by protrusion improves the mixing of burnt gaseous species [8–10]. Thus, using the protrusion technique, regression rate and combustion efficiency can be enhanced concurrently [8]. More detail explanation regarding the protrusion method in hybrid rocket can be found in Ref. [8]. In most of the studies, the shape of the protrusion core used in hybrid rocket was circular [7–10]. Using the protrusions other than circular shapes (non-conventional configurations) such as star, fin and multi-hole shapes could increase the turbulence level in the flow field [15]. Because of this, the mixing efficiency of the combustion gasses can be enhanced further. The studies regarding the non-conventional protrusion configurations are rarely found in hybrid rocket literature.

So far, the studies related to protrusion method in literature relate to only improvement in the regression rate and the combustion efficiency [7–10]. There have been no studies found addressing the issue of combustion instabilities when the protrusion method has been used in the hybrid rocket. In general, if the chamber pressure oscillations are above or below the 5% of the mean chamber pressure, then the combustion process of that system is considered as unstable [16]. The combustion instabilities in hybrid rockets are not catastrophic as in the case of solid and liquid rockets [16]. In hybrid rockets, the intrinsic low-frequency instabilities (ILF) are commonly observed which are typically in the order of <50 Hz [16]. In addition to these, the instabilities related to oxidizer feed system coupled with chamber pressure oscillations, atomization and vaporization of liquid oxidizers and bulk mode instabilities were also found in hybrid rockets [17]. The classification of hybrid rocket combustion instabilities and its driving mechanism are summarized in Table 1. Karabeyoglu et al. [16] reported that the intrinsic low-frequency instabilities are driven by the fuel mass production oscillation during the combustion. Experimental studies of Park et al. [18] showed that the initiation and amplification of low-frequency instabilities (range is 10–20 Hz) were related to vortex shedding which occurs due to the flow modifications and the variation of volume ratio of combustion chamber to post-combustion chamber. Lee et al. [19] observed the raise in the pressure oscillations when protrusion is inserted in a hybrid rocket. In the presence of protrusion, the source for exciting the pressure oscillations was found to be the edge tone instability.

Thus far, there are no explicit research efforts found related to combustion instabilities of protrusion inserted hybrid rocket. Also, while attempting to increase the turbulence in flow field in combustion chamber by using non-conventional protrusion

Table 1 Classification of combustion instabilities in hybrid rocket motor

Classification	Frequency range ^a	Driving mechanism
Low-frequency instabilities	<200 Hz	Incomplete atomization/feed system coupled [20] Fuel grain chuffing (<10 Hz) [20] Coupling of transient events such as thermal lag in solid fuel, diffusion combustion and chamber gas dynamics or fuel production oscillations (<50 Hz) [16] Bulk mode or Helmholtz mode [17]
Hydrodynamic instabilities	200–2000 Hz	Vortex shedding [21, 22]
Acoustic instabilities	200–2500 Hz	Longitudinal acoustic modes linked with the combustion process including unsteady heat release, flame holding effects and the vortex impingement on chamber walls [23]

^aFrequency range depends on the size and operational parameters of the hybrid rocket motor

configurations, the stability behavior of the motor is expected to change. Thus, the present study aims to emphasize on the combustion stability behavior of protrusion inserted in hybrid rocket motor. In the present study, the protrusion configurations used are circular, star, fin and multi-hole. These protrusion configurations were tested using a 12.5 L/D (length to diameter) laboratory scale hybrid rocket motor. The paraffin wax and gaseous oxygen were used as fuel and oxidizer, respectively. Apart from the combustion instabilities, the regression rate and combustion efficiency were also measured for various protrusion cases.

2 Experimental Methodology

In the present study, the wax used was the combination of paraffin and microcrystalline wax at 70:30 ratio. The properties of the wax are given in Table 2. In order to prepare the wax fuel grains, first the wax should be melted using induction heater above its melting point (65 °C). This melted wax is then casted in the mold and kept at room temperature for 3 h. Once the wax is solidified, it needs to be taken out from

Table 2 Properties of wax

Properties	Values
Melting point	337.1 K
Congearing point	337.7 K
Density (ρ_f)	890 kg/m ³
Viscosity	6.60 cSt
Tensile strength	1.48 MPa @ 5 mm/min
Percentage elongation	4.5% @ 5 mm/min

Table 3 Dimensions of the hybrid rocket motor and fuel grain

Geometrical parameters	Dimensions
Throat diameter (mm)	10
A_e/A_t	5.76
L^* (m)	0.42
Fuel grain length, L (mm)	188
Initial port diameter, D or d_i (mm)	15
L/D	12.5
Fuel grain outer diameter, d_o (mm)	50

the mold carefully. Prior to cast the fuel grains, grease should be applied to avoid the sticking to the mold and mandrel. The dimensions of the fuel grain are given Table 3.

2.1 Hybrid Rocket Experimental Setup

The geometrical representation of laboratory scale hybrid rocket motor can be seen in Fig. 1. It has shower head injector, motor casing where fuel grain was inserted and C-D nozzle made of high density graphite covered with mild steel casing. The dimensions of the motor and fuel grain can be seen in Table 3. The experiments on hybrid rocket motor were conducted using the laboratory scale experimental facility as shown in Fig. 2. The experimental setup consists of two commercially available gaseous oxygen cylinders, weighing balance, pumping system, electrical systems and test bed. The gaseous oxygen was supplied to the motor at the rate of 30 g/s. The oxidizer mass flow rate was measured by taking the weight of the oxygen cylinders before and after combustion over the anticipated time. The oxidizer flow was controlled using the solenoid valve which was connected to sequential timer. The sequential timer controls the timing required to open and close the solenoid

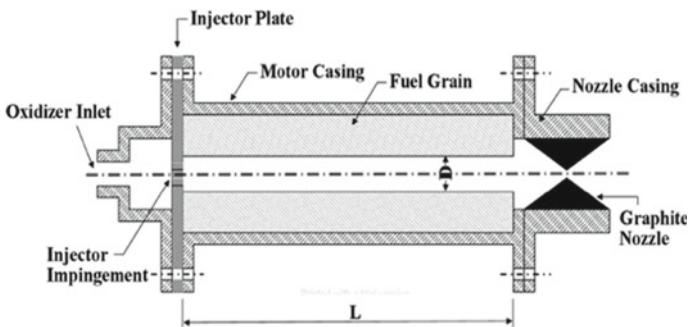


Fig. 1 Schematic view of hybrid rocket motor [14]

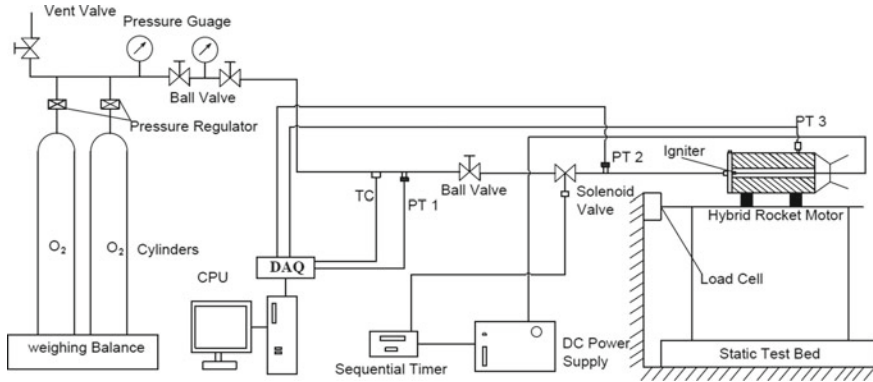


Fig. 2 Schematic view of hybrid rocket motor [8, 14]

valve. The ignition of the motor was achieved by igniting the solid propellant bead embedded with Nichrome wire. This Nichrome wire was connected to electrical wire. The electrical wire was then inserted into the combustion chamber through the nozzle in such way that the propellant bead was at injector end. A 12 V DC power is supplied through the electrical wire to ignite the solid propellant bead. Once the propellant bead is ignited, the solenoid valve will be open to inject the oxidizer. The mass of the igniter was around 0.5 g. The entire sequence was controlled using the sequential timer.

2.2 Protrusion Configurations

The protrusion configurations used in the present study are circular, star, wagon wheel and multi-holes which are depicted in Fig. 3. The high density graphite was used to fabricate the protrusions. The inner diameter and thickness of the protrusion were 10 and 2.5 mm, respectively. The point of depth (P) for both star and fin configurations was 5 mm. In multi-hole configuration, the diameter of each hole adjacent to inner diameter of the protrusion was 4 mm. In the process of preparing the fuel grain along with protrusion, the protrusion was sandwiched between the fuel grain segments at preferable location. The length of each fuel grain segment was depending on the location of the protrusion to be inserted. The location of the protrusion was given as X/L in which X is the distance from the head end of the fuel grain and L is the length of the fuel grain. Since this study is mainly to compare the performance and stability behavior of the motor, the axial locations have been fixed at single location of 0.7 X/L for the current study.

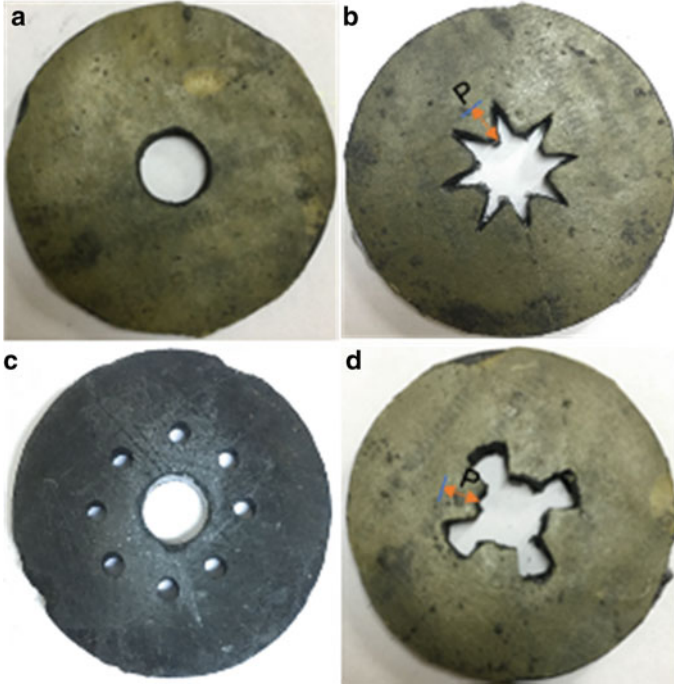


Fig. 3 Protrusion configurations before the combustion: **a** circular, **b** star, **c** multi-hole and **d** fin

2.3 Data Reduction

In the current experimental study, regression rate (\dot{r}) is deduced using weight loss method [24]. In this method, the mass of the fuel (m_f) consumed during combustion is determined by measuring the weight of the motor before and after combustion. Using the known mass of the fuel consumed after certain burn time (t_b), the final diameter (d_f) of the fuel grain will be measured using Eq. 1. Further, this final diameter will be helpful to calculate the regression rate and oxidizer mass flux (G_{ox}) using Eqs. 2 and 3.

$$d_f = \sqrt{\frac{4m_f}{\pi\rho_f L} + d_i^2} \quad (1)$$

$$\dot{r} = \frac{(d_f - d_i)}{2t_b} \quad (2)$$

$$G_{ox} = \frac{16\dot{m}_{ox}}{\pi(d_i + d_f)} \quad (3)$$

The combustion efficiency is determined using Eq. 4. The experimental characteristic velocity (C_{ex}^*) is calculated with the help of Eq. 5. In Eq. 5, the average chamber pressure is measured using piezo-resistive pressure transducer (Model: UNIK 500 Make: GE) at the sampling rate of 2 kHz. This pressure transducer is connected at the nozzle end of the motor as shown in Fig. 3. The response of pressure transducer is recorded using NI-9215 module and LabVIEW signal express software. The theoretical characteristic velocity (C_{th}^*) is determined using NASA SP-273 chemical equilibrium software [25] at corresponding chamber pressure and O/F ratio.

$$\eta = \frac{C_{ex}^*}{C_{th}^*} \quad (4)$$

$$C_{ex}^* = \frac{P_c A_t}{\dot{m}_t} \quad (5)$$

The combustion stability behavior of the motor was determined with the help of the fast Fourier transformation (FFT) plots of the chamber pressure data. The chamber pressure was recorded using the high response piezo-electric pressure transducer (Make: PCB, Model: 124A24). The piezo-electric pressure transducer was mounted at the nozzle end of the motor. The chamber pressure was recorded at sampling rate of 13 kHz using NI-9215 module and LabVIEW signal express software. The pressure data was converted to FFT using Tecplot software.

3 Results and Discussion

3.1 Studies on Regression Rate and Combustion Efficiency

The performance parameters such as regression rate, oxidizer mass flux and combustion efficiency for without protrusion (WOP) and other protrusion configurations are given in Table 4. The regression rate was measured using the weight loss method as discussed in earlier section. The mass flow rate of the oxidizer was 30 g/s.

The burnt time used in the present study was 4 s. It can be seen in Table 4 that the regression rate and combustion efficiency for the protrusion cases were improved

Table 4 Performance parameters of hybrid rocket with various protrusion configurations

Protrusion	\dot{r} (mm/s)	G_{ox} (kg/m ² s)	P_c (bar)	O/F	η (%)
WOP	1.94	73.68	6.96	1.29	63.90
Circular	2.12	67.47	7.17	1.09	67.07
Star	2.03	71.35	7.19	1.21	66.76
Fin	2.27	66.82	7.42	1.07	69.19
Multi-hole	2.29	65.33	7.50	1.03	69.52

compared to the without protrusion case. The regression rate and combustion efficiency obtained for the fin and multi-hole case were higher than the circular case. However, in the case of star configuration, both the parameters were lower than the circular case. The reason for this might be the interruption in the formation of the recirculation zone behind the protrusion. Generally, in a hybrid rocket with conventional (circular) protrusion configuration, the recirculation zone behind the protrusion re-attaches to the fuel surface by dragging the hot gaseous products from the reaction zone (or flame zone) [14]. As a result of this, the heat transfer to the fuel surface increases followed by this the regression rate also improves. Further, the regressed fuel recirculates within the recirculation zone and transits axially downstream of the motor. The mixing of gaseous products occurs in the recirculation zone which helps in improving the combustion efficiency of the motor (Table 5).

Although the protrusion with star configuration is disturbing flow field inside the combustion chamber, it is expecting that the spikes (extruded portions in star configuration) were restricting the formation of the recirculation zone. As the formation of recirculation zone is diminished, the heat transfer to the fuel surface and effectiveness in the mixing of product gases were reduced. Hence, the regression rate and combustion efficiency obtained for star configuration were lower than the circular configuration. On the other side, in the multi-hole case, the formation of recirculation might not be diminished as occurred in the case of star. Also, as the combustion proceeds, the adjacent holes start exposing to combustion chamber; therefore, the secondary recirculation zones develop within the primary recirculation zone due to the adjacent holes. As a consequence of this, the product gases in the primary

Table 5 Theoretically predicted and experimentally obtained frequency modes for the WOP case

Frequency mode	Analytical expression	Theoretical frequency (Hz)	Experimental frequency (Hz)
Boundary layer mode or fuel production oscillations	$f_b = \frac{0.48}{\tau_{bl}} = 0.234 \left(2 + \frac{1}{O/F} \right) \frac{4}{\pi} \frac{\dot{m}_{ox}(RT)_{av}}{L_f PD^2}$	190 Hz	10–230 Hz
Bulk mode	$f_H = \frac{C}{2\pi} \sqrt{\frac{\pi}{4} \frac{D_t^2}{V(U+0.8D_t)}}$	580 Hz	550 Hz (observed in Fig. 5c)
Longitudinal acoustic modes	$f_l = \frac{C}{2L} = \frac{\sqrt{r(RT)_{av}}}{2L}$	First mode = 2250 Hz Second mode = 4500 Hz	First mode = 2200 Hz Second mode = 4300 Hz
Vortex shedding	$f_v = \frac{S_t U}{D} = \frac{S_t \dot{m} RT}{\pi PD^3}$	2500 @ S = 0.5	–

Symbols related to this table: P = chamber pressure (N/m^2), D = port diameter (m), R = specific gas constant, T = chamber temperature (K), V = chamber volume (m^3), l = convergent length (m), C = speed of sound (m/s), in which $\gamma = 1.24$ [26], $(RT)_{av}$ is $6.89 \times 10^5 \text{ m}^2/\text{s}^2$ [26], L = length of the combustion chamber (m), D_t = throat diameter (m), S_t = Strouhal number ($0.25 \leq S_t \leq 0.5$) [22], \dot{m} = total mass flow rate (kg/s), L_f = length of the fuel grain (m)

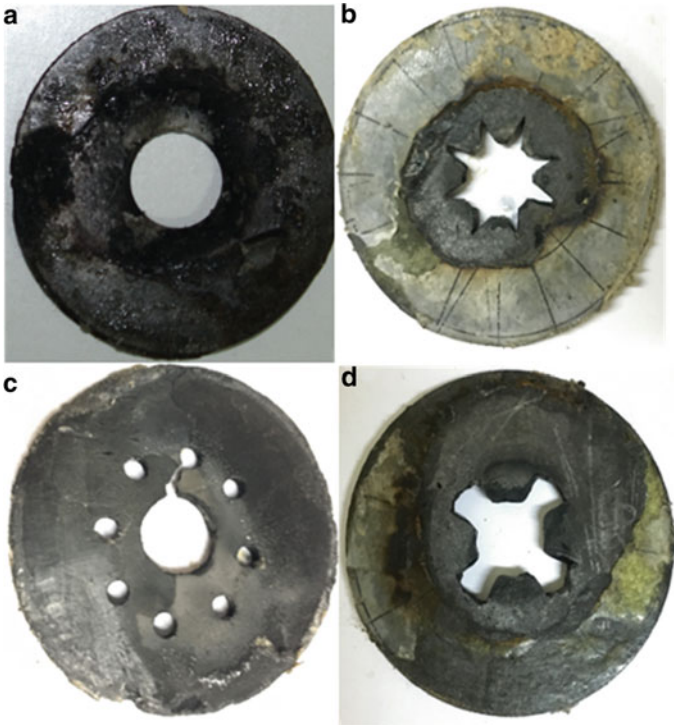


Fig. 4 Protrusion configurations after the combustion: **a** circular, **b** star, **c** multi-hole and **d** fin

recirculation zone further mixed in the secondary recirculation zones. Hence, the performance of the hybrid rocket motor improved effectively compared to circular and star configurations. Therefore, it is observed from these results that the formation of recirculation zone behind the protrusion has the significant influence on performance of the hybrid rocket. Further to support the aforementioned analysis, the detailed computational fluid dynamic (CFD) studies need to be conducted in future. Furthermore, the protrusions were taken out of the fuel grains after the combustion and inspected for any structural defects. The protrusions were appeared to be in good condition, and it can be seen in Fig. 4.

3.2 Studies on Combustion Instabilities

In this section, the combustion stability behavior of the hybrid rocket motor without and with protrusion cases was discussed. The studies were done with the protrusion cases of various configurations such as circular, star, multi-hole and fin. The stability behavior of the hybrid rocket motor was determined using the FFT plots. These FFT plots were obtained with the help of chamber pressure data and converted

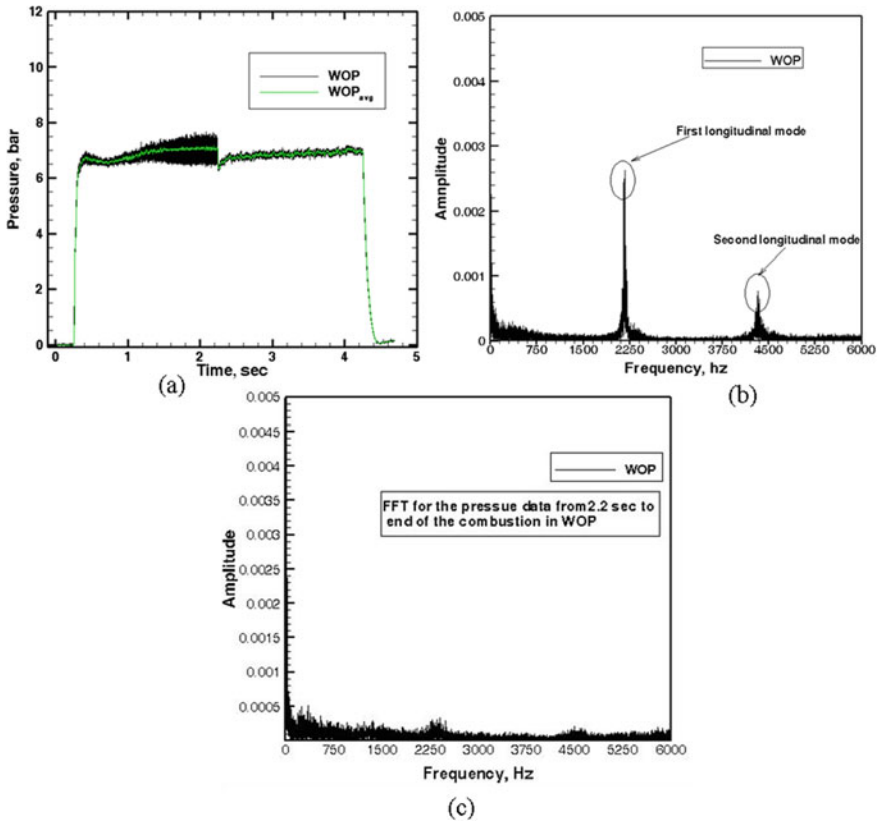


Fig. 5 Pressure versus time and FFT plot for the WOP case

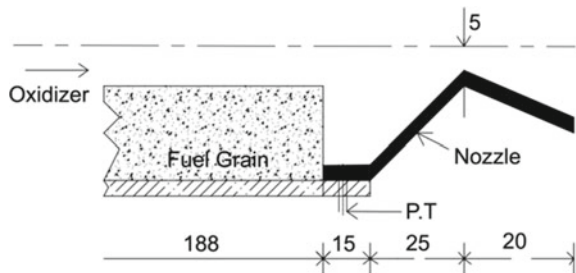
using Tecplot software. The details of pressure sensor were given in experimental methodology section.

The chamber pressure versus time and FFT plots for the without protrusion case is shown in Fig. 5. In Fig. 5a, after a little time of the beginning of the combustion, the chamber pressure starts oscillating and reaches it maximum and then suddenly dampened. After this, till the end of the combustion, no oscillations were observed. The FFT plot for this chamber pressure data is shown in Fig. 5b. The two distinctive frequency peaks at around 2200 Hz and 4300 Hz can be observed in Fig. 5b. These frequency peaks are corresponding to the longitudinal acoustic modes of the combustion chamber. These frequency values are in good agreement with the analytically calculated longitudinal acoustic modes of the motor as given in Table 3. Furthermore, the FFT (Fig. 5c) has been plotted for the chamber pressure data starting from the 2.2 s to till the end of the combustion. It can be seen in Fig. 5c that the peaks corresponding to longitudinal modes are present; however, the amplitude of the peaks was reduced significantly. The large amplitude of the acoustic modes in Fig. 5b is attributed to the coupling of unknown energy source with longitudinal

acoustic modes. This unknown energy is further decoupled after 2.2 s which leads to the stable combustion; however, the acoustic modes are present with lower amplitude (Fig. 5c). This unknown energy might be due to the vortex shedding which occurs at the nozzle end. Carmicino [22] reported that when the interaction between the vortex shedding in post-combustion chamber and longitudinal acoustics takes place, a sudden rise in the amplitude can be observed. During the vortex shedding at the exit of the fuel grain, the vortex impinges on the nozzle walls, and it leads to the breakup of the vortex which further augments the fine scale mixing of fuel and oxidizer in the post-combustion chamber. This mixing results in a sudden heat release in post-combustion chamber and increase in the strength of the acoustics in the chamber. In this process, the vortical energy converts into acoustic energy, due to impulse in heat release changes the acoustic velocity which further enhances the heat flux to the fuel surface [21, 22]. As a consequence of this, the regression rate increases which further increases the chamber pressure [22]. Although the hybrid rocket motor used in the present study is not having the post-combustion chamber, there is a small space between the exit of the fuel grain and nozzle entrance as shown in Fig. 6. This space was used for mounting the piezo-electric pressure transducer. Therefore, in the present study also it is expecting that the vortex formation is occurring after the exit of the fuel grain. As the exit diameter of the fuel grain increased, the energy associated with vortex shedding might be dampened. Hence, the pressure oscillations were reduced, and stable combustion is achieved. In Fig. 5c, besides the longitudinal acoustic modes, the frequencies in the range of 500–600 Hz are also observed. As per the theoretical predictions, this frequency range has matched with the bulk mode oscillations as listed in Table 1. However, the bulk mode oscillations have the lower amplitude. Also, the oscillations due to fuel production (10–220 Hz) are present in a hybrid rocket motor with without protrusion case.

The FFT plots for the various protrusion configurations studied in the present study are shown in Fig. 7. Compared to the without protrusion case in Fig. 5b, the protrusion cases exhibited the stable combustion. Upon inserting the protrusion, the amplitude of the longitudinal acoustic modes was reduced significantly. The reason for this is that when protrusion is placed, it dampens the amplitude of the oscillations because it increases the energy dissipation in the combustion chamber as the protrusion acts as the baffle. Moreover, protrusion reflects the acoustic waves and partially leaves the part of it pass through.

Fig. 6 Schematic view of fuel grain exit and nozzle interface



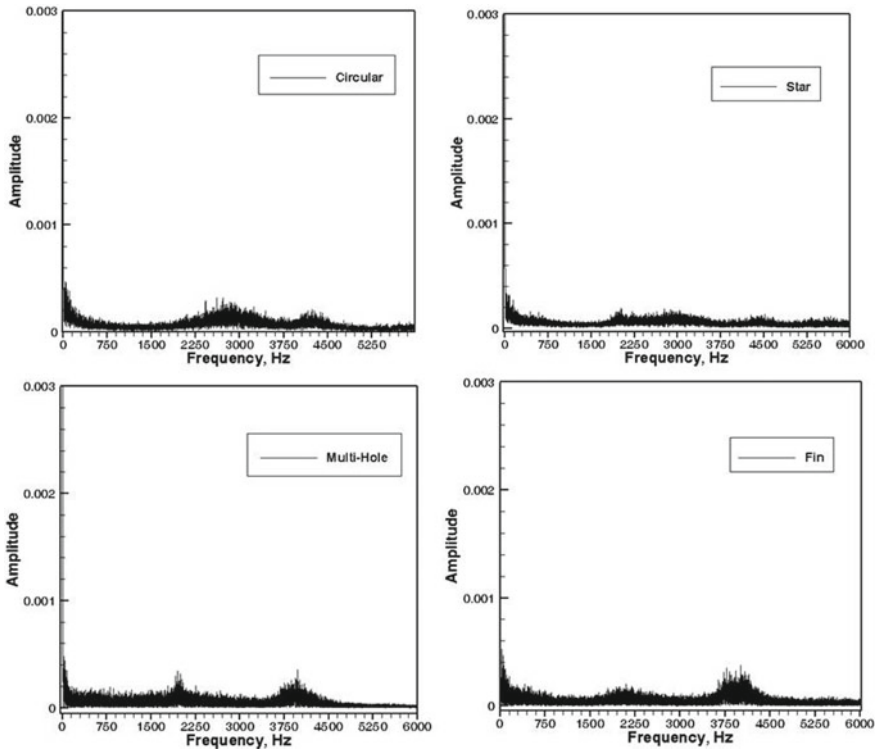


Fig. 7 FFT plots for the various protrusion configurations

Also, the decoupling of the flow field between the sections before and after the protrusion is also expected. Furthermore, the protrusion at $0.7X/L$ might have influenced the vortex shedding at the exit of the fuel grain as it is near the nozzle end. Therefore, the coupling of vortex shedding frequency with acoustic modes might be diminished. Hence, the amplitude of longitudinal acoustic frequencies was reduced upon inserting the protrusion in hybrid rocket. Among the protrusion configurations, the star case has shown more stable combustion.

In all the protrusion configurations, the frequencies of the longitudinal acoustic modes were modified compared to the without protrusion case. These frequency peaks are given in Table 6. This might be due to the change in wavelength of the acoustic waves as the protrusion reflects it or partially part of it passes through the inner diameter of the protrusion. Depending on the shape of the protrusion, the frequency range and its amplitude are observed to be varied.

Table 6 Frequency range of longitudinal acoustic modes for all the protrusion configurations

Protrusion configurations	Longitudinal acoustic modes	Frequency range (Hz)
WOP	1st Mode	2200
	2nd Mode	4300
Circular	1st Mode	2700
	2nd Mode	4200
Star	1st Mode	–
	2nd Mode	4500
Multi-hole	1st Mode	2100
	2nd Mode	4000
Fin	1st Mode	2200
	2nd Mode	3900

4 Conclusions

An attempt has been made to investigate the effect of protrusion configuration on the stability behavior and on the performance of the laboratory scale hybrid rocket motor. The circular, star, fin shape and multi-holes type protrusion configurations were studied. The combustion performance parameters such as regression rate and combustion efficiency were determined. The important conclusions that can be drawn from the present study are given below:

1. Regression rate and combustion efficiency were enhanced upon inserting the protrusion.
2. Among the protrusion configurations, the multi-hole case showed better improvement in regression rate and combustion efficiency.
3. Among without protrusion case, longitudinal acoustic modes were found to be dominant.
4. Vortex impingement on nozzle walls is expected to be the reason for excitation of acoustic modes amplitude in without protrusion case.
5. Combustion oscillations were reduced after inserting the protrusion in hybrid rocket motor.
6. Among all the protrusion configurations, star case exhibited the more stable combustion.
7. The frequency range of the longitudinal acoustic modes is observed to be varied depending on protrusion configuration.

Acknowledgements This work was supported by Council of Scientific and Industrial Research (CSIR)—Human Resource Development Group (HRDG) under the scheme of Senior Research Fellowship (SRF)—Direct, File No: 09/554(0049)/2019EMR-1, Government of India.

References

1. Sutton GP, Biblarz O (2000) Hybrid propellant rockets. Rocket propulsion elements. Wiley-VCH, Weinheim, pp 417–607
2. Altman D, Holzman A (2006) Overview and history of hybrid rocket propulsion. Fundamentals of hybrid rocket combustion and propulsion. American Institute of Aeronautical and Astronautics Inc., Roston, VA, pp 1–36
3. Veale K, Adali S, Pitot J, Brooks M (2017) A review of the performance and structural considerations of paraffin wax hybrid rocket fuels with additives. *Acta Astronaut* 141:196–208
4. Karabeyoğlu M, Arkun U (2014) Evaluation of fuel additives for hybrid rockets and SFRJ systems. AIAA paper, AIAA 2014–3647
5. Faderick RA Jr, Whitehead J, Knox LR, Moser MD (2007) Regression rate study of mixed hybrid propellants. *J Propul Power* 23(1):175–180
6. Kumar CP, Kumar A (2013) Effect of swirl on the regression rate in hybrid rocket motors. *Aerosp Sci Technol* 29:92–99
7. Grosse M (2009) Effect of a diaphragm on performance and fuel regression of a laboratory scale hybrid rocket motor using nitrous oxide and paraffin. AIAA Paper 2009–5113
8. Dinesh M, Kumar R (2019) Utility of multi-protrusion as the performance enhancer in hybrid rocket motor. *J Propul Power* 35(5):1005–1017
9. Kumar R, Ramakrishna PA (2014) Effect of protrusion on the enhancement of regression rate. *Aerosp Sci Technol* 39:169–178
10. Kumar CP, Kumar A (2013) Effect of diaphragms on regression rate in hybrid rocket motors. *J Propul Power* 29(3):559–572
11. Wu Y, Yu X, Lin X, Li S, Wei X, Zhu C, Wu L (2018) Experimental investigation of fuel composition and mix-enhancer effects on the performance of paraffin-based hybrid rocket motors. *Aerosp Sci Technol* 82: 620–627
12. Boardman TA, Abel TM, Claffin SE, Shaeffer CW (1997) Design and test planning for a 250 klbf thrust hybrid rocket motor under the hybrid propulsion demonstration program. In: AIAA Paper 1997–2804
13. Mon K, Park C, Lee C (2014) Modification of flow characteristics on the blowing surface by inserting a diaphragm. *J Propul Power* 30(6):1683–1691
14. Dinesh M, Kumar R (2020) Experimental studies of protrusion inserted hybrid rocket motor with varying L/D ratio. *J Spacecraft Rockets*
15. Ramamurthi K (2016) Hybrid rockets. In: Rocket propulsion. Trinity Press
16. Karabeyoglu A (2006) Combustion instability and transient behaviour hybrid rocket motors. Fundamentals of hybrid rocket combustion and propulsion. American Institute of Aeronautical and Astronautics Inc., Roston, VA, pp 351–406
17. Zilwa SD, Karabeyoglu A, Zilliac G, King L, Reinath M (2003) Combustion oscillations in high-regression-rate hybrid rockets. AIAA paper 2003–4465
18. Park KS, Lee C (2015) Low frequency instability in laboratory-scale hybrid rocket motors. *Aerosp Sci Technol* 42:148–157
19. Leea J, Rhee S, Kimc J, Moond H, Shynkarenkoe O, Simonef D, Morita T (2019) Combustion instability for hybrid rocket motors with a diaphragm. In: 8th European conference for aeronautics and space sciences (Eucass)
20. Helmy AM (1994) Chronical review of the hybrid rocket combustion. AIAA paper 94–2881
21. Greiner B, Frederick Jr RA (1994) Experimental investigation of lab-scale hybrid instability. AIAA paper 94–2878
22. Carmicino C (2009) Acoustics, vortex shedding, and low-frequency dynamics interaction in an unstable hybrid rocket. *J Propul Power* 25(6):1322–1335
23. Messineo J, Lestrade JY, Hijlkema J, Anthoine J (2019) Hydrodynamic instabilities modeling in hybrid rocket engines. *J Spacecraft Rockets* 56(5)
24. Kumar R, Ramakrishna PA (2013) Issues related to the measurement of regression rate of the fast burning hybrid fuels. *J Propul Power* 29(5):1114–1121

25. Gordon S, McBride BJ (1996) Computer program for calculation of complex chemical equilibrium compositions and applications. NASA RP-1311
26. Karthikeyan G, Shimada T (2018) Numerical parametric analysis of combustion instability in axial-injected hybrid rocket motors. J Propulsion Power 34

Prediction of Wake Structure Transition for a Linear Plug Nozzle Using Detached Eddy Simulation (DES)



M. Manu Mohan, N. Balakrishnan, and N. Munikrishna

Abstract The base flow of a truncated plug nozzle exhibits a phenomenon called Wake Structure Transition (WST), where in an open base wake develops into a closed wake as the pressure ratio is increased. From design point of view, it is important to predict this transition. There are empirical models available for predicting WST but they are inaccurate for routine use in design. One physics-based model proposed by CAad lab of IISc, shows a potential to do the same with a great accuracy. However, its utility is limited by the requirement that accurate base pressure at two operating conditions, one in open and other in closed wake are to be known. The inherent limitations of RANS (or URANS)-based CFD solvers in predicting base pressure for large separated flows, limits the utility of aforementioned models. The present attempt explores the use of high-fidelity DES tool for the simulation of base flow and thereby WST prediction. The preliminary results obtained are very encouraging both from the view point of accuracy of the predicted base flow and its use in the physics-based model for predicting WST.

Keywords Truncated plug nozzle · Supersonic base flow · Wake structure transition · Detached Eddy simulation · Spalart Almaras model

1 Introduction

Plug nozzles are one of the viable replacement for conventional De-Laval nozzles in Single Stage To Orbit (SSTO) kind of missions where a single nozzle has to perform consistently over a wide range of altitudes [1]. It consists of a primary

M. Manu Mohan (✉)

Liquid Propulsion Systems Center, ISRO, Thiruvananthapuram, Kerala, India

e-mail: manu.lpsc@gmail.com

N. Balakrishnan

Department of Aerospace Engineering, IISc, Bangalore, Karnataka, India

N. Munikrishna

S & I Engineering Solutions Pvt. Ltd., Bangalore, Karnataka, India

nozzle where the flow expands internally to sonic condition and a plug surface over which flow expands externally to supersonic condition (refer Fig 1a). Even though the full-length plug nozzle shows a consistent performance, its thrust to weight ratio is poor compared to conventional nozzle because of high plug length. To overcome this deficiency, the practically realizable plug nozzles are designed with a shorter length by truncating its sharp end. This will introduce a wake region (refer Fig. 1b) in plug nozzle flow field where some interesting flow dynamics can be observed.

The contour of full-length plug nozzle is designed in such a way that at design condition the flow expands continuously and there will not be any wave reflection from the nozzle surface. But at off-design condition, there will be wave interactions with in core jet flow which makes the flow much more complex. In case of truncated plug nozzle, along with these complexities, flow exhibits a phenomenon called Wake Structure Transition (WST), where in an open base wake develops into a closed wake as the pressure ratio is increased. At lower pressure ratios, the wake will be completely open and it will be under the influence of atmospheric pressure. As the pressure ratio increases the wake will be transformed into a closed one and then onward the base pressure normalized by stagnation pressure will be independent of pressure ratio. From design point of view, it is important to predict this transition since the base thrust critically dependent on WST. The best way to predict the transition curve like the one shown in Fig. 2 is to carry out experiments at different pressure ratios. But this is not a viable option since it demands large vacuum facilities to simulate high altitude condition.

In the past, researchers have proposed empirical models for prediction of base wake transition based on their experimental results. But they lack in generality and accuracy for routine use in design. In the CA d lab, IISc a physics-based model for WST has been proposed by Chutkey et al. [2]. This model has potential to predict WST to required accuracy. However, its utility is limited by the fact that it requires a two-point data set (base pressure), one in the closed wake regime and the other in the open wake regime. This data, in fact, can be predicted using CFD. The inherent limitation of the RANS (or URANS)-based turbulence models to predict the turbulent

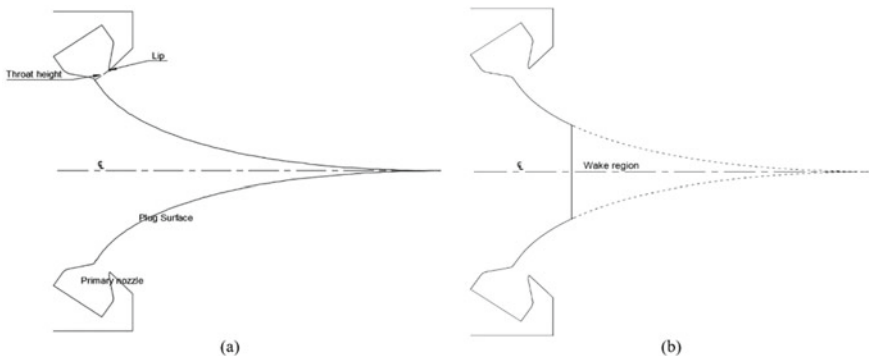


Fig. 1 Plug nozzle geometry. **a** Full-length. **b** 20% Truncated

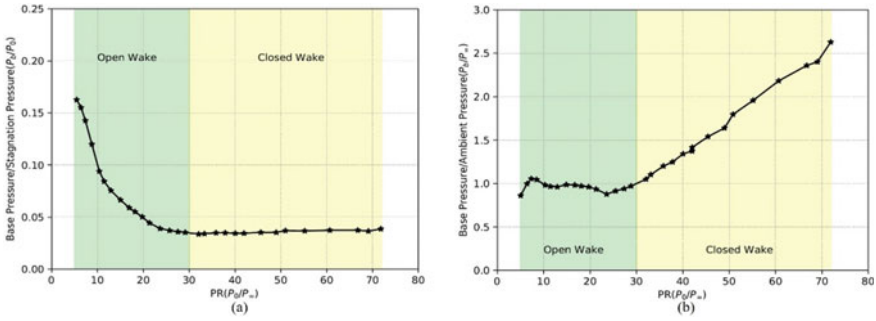


Fig. 2 Base pressure vs Pressure ratio of 20% truncated plug nozzle (from experiments conducted by Chutkey et al. [2]). **a** Base pressure normalized by stagnation pressure. **b** Base pressure normalized by ambient pressure

viscosity at large separated regions (since they are fine tuned to capture the physics behind wall-bounded flows), does not allow accurate prediction of the base flows limiting the utility of this physics-based model.

The present attempt explores the use of high-fidelity DES tool for the base pressure estimation in case of a truncated linear plug nozzle and prediction of WST with the help of aforementioned physics-based model. The DES computations have been performed in conjunction with Spalart–Allmaras (SA) model with compressibility correction proposed by Paciorni et al. [6] for turbulence. The SA model with its robustness has already become a standard for industrial computations (Ref. the AIAA CFD Drag Prediction Workshop summary by Tinoco et al. [8]) and therefore the same has been adopted in this work also. Owing to the unsteady nature of DES computations and the required grid resolution, these computations were carried out on the Cray XC 40 (SahasraT) platform available in SERC, IISc.

2 WST Model

An experimental outcome of base pressure (normalized by ambient pressure and stagnation pressure) for different pressure ratios (PR) are shown in Fig. 2. Two regimes can be identified in this. In first (open wake) base pressure (P_b) is almost equal to ambient pressure (P_∞) or P_b/P_∞ is nearly equal to 1 and in second (closed wake) it (P_b/P_∞) is varying linearly with respect to pressure ratio (Fig. 2b). It can also be noted that ratio of base pressure to stagnation pressure (P_b/P_0) is almost constant in closed wake regime (Fig. 2a) and this implies the base pressure is independent of ambient pressure. The pressure ratio which marks the transition of open wake to closed wake is called transition pressure ratio (PR_{tr}). Based on these observations, an empirical model was proposed by Chutkey et al. [2] to predict base pressure of a truncated plug nozzle for any pressure ratio.

As per this model, the slope (m) of P_b/P_∞ vs PR curve in closed wake regime is approximated as

$$m = (P_b/P_o)_{\text{closed}}$$

where $(P_b/P_o)_{\text{closed}}$ is a constant value corresponding to closed wake regime. This approximation is validated with different experimental results available in open literature (Ref: Chutkey et al. [2] Table 3). Now if we know the base pressure in open wake regime, by using simple geometric relations, we can estimate the transition pressure ratio.

$$PR_{\text{tr}} = \left(\frac{P_o}{P_\infty} \right)_{\text{tran}} = \frac{k}{m} \tag{1}$$

where $k = P_b/P_\infty$ corresponding to open wake regime and its value approximately equal to 1 in present case.

The model is graphically represented in Fig. 3. Hence, if we know base pressure at two different pressure ratios (one at open wake regime and other at closed wake regime), we can predict the transition and base pressure corresponds to all other pressure ratios using this model.

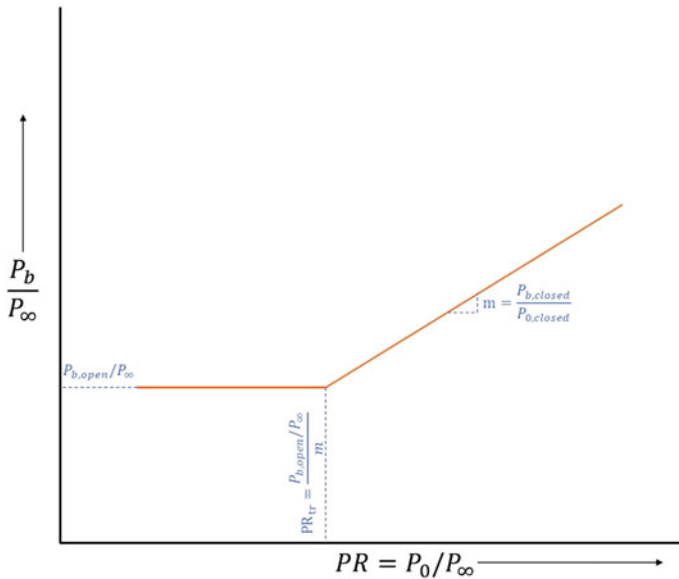


Fig. 3 Base pressure transition model

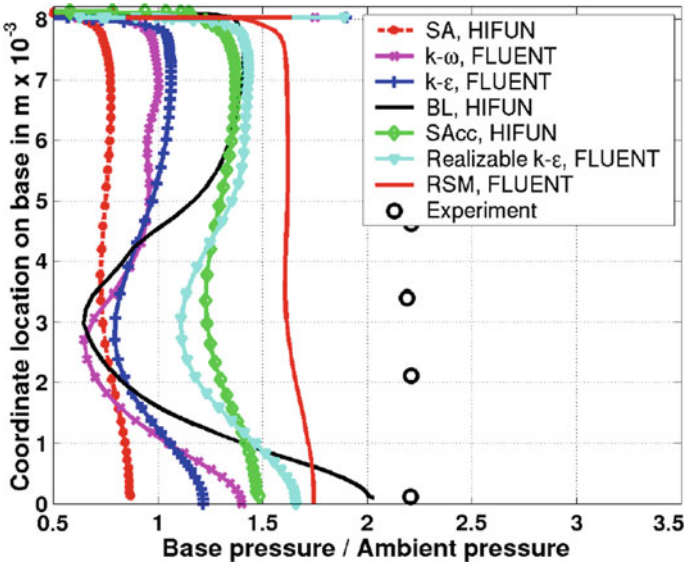


Fig. 4 Base pressure distribution at PR = 60 [3]

3 Base Pressure Estimation Using RANS

Several attempts have been made to predict the base pressure of truncated plug nozzle using RANS-based CFD solvers. But none of them were successful in predicting it with reasonable accuracy. Figure 4 shows a comparison of base pressure estimation using different RANS models with experimental values made by Chutkey [3]. With respect to average base pressure, Reynolds stress equation model (RSM) performs the best with 23% deviation followed by Spalart–Allmaras model with compressibility correction (SAcc) with 36%. As discussed in introduction, this deviation is mainly due to the limitation of conventional turbulence models in predicting eddy viscosity at the large separated regions.

4 Detached Eddy Simulation

Detached Eddy Simulation (DES) is a three-dimensional unsteady numerical solution using a single turbulence model, which functions as a subgrid-scale model in regions where the grid density is fine enough for an LES, and as RANS model in near wall region. The conventional Spalart Allmaras (SA)-based DES model which originally proposed by Spalart [7] with compressibility correction is used here for all simulations. In which the driving length scale of RANS-SA model (distance to the closest wall) is replaced by another length scale \bar{l} , which is defined as:

$$\tilde{l} = \min(d, C_{DES} \Delta) \quad (2)$$

where d is cell distance to the closest wall, Δ is the largest among all three cell dimension of local grid and C_{DES} is an adjustable model constant.

For wall-bounded separated flows, the above formulation results in a hybrid model that functions as the standard RANS SA model inside the whole attached boundary layer, and as its subgrid-scale version in the rest of the flow including the separated regions and near wake [4]. Indeed, in the attached boundary layer, due to the significant grid anisotropy (other two-dimensions will be much higher than the wall normal dimension) $\tilde{l} = d$, and the model reduces to the standard RANS SA model. Otherwise, once a field point is far enough from walls ($d > C_{DES} \Delta$), the length scale of the model becomes grid-dependent, i.e., the model performs as a subgrid-scale version of the SA model.

Value of C_{DES} is taken as 0.65 for all simulations. This value is based on the numerical experiments conducted by Strelets [4] on massively separated flows.

5 Grid Generation Methodology

Grid generation is the most crucial step for Detached Eddy Simulation. Even though the flow is almost 2-D in case of a linear plug nozzle, we have to generate 3-D grids because of the inherent 3-D nature of DES. It is also necessary to generate cells equally fine in all three-dimensions in the near wake region where the flow physics is to be captured more accurately.

Based on these considerations, a 2-D mesh is generated in x - y plane and extruded in z direction by maintaining uniform cell dimensions (for cells in recirculation region) in all 3 directions. To resolve large eddies in all 3 directions, the total height of extrusion in z direction is maintained as 1.5 times of base height.

Structured mesh topology is considered in the primary and secondary nozzle flow regions to accurately resolve the boundary layer and mixing layer effects in wall and free shear regions, respectively, by aligning the grids with streamlines as closely as possible (Fig. 5b). Incorporating structured mesh in recirculation region helped in controlling the cell dimension more accurately in all 3 directions. At truncated base lip, the grid lines were aligned to the local centered expansion fan as per the guidelines given by Childs et al. [5]. In far-field, triangular unstructured mesh is considered to reduce the total cell count and it is progressively coarsened toward the far-field boundary. Far-field boundary dimension is maintained of the order of 10,000 times plug throat height to avoid wave reflection from far-field to computational domain.

The boundary names of plug nozzle computational domain are shown in Fig. 5. The boundary conditions applied on each of these boundaries are given in Table.1. The two parallel planes (normal to z axis) created while extruding this 2-D mesh to 3-D are treated as periodic pairs.

Two types of grids were identified for simulation, as listed in Table.2.

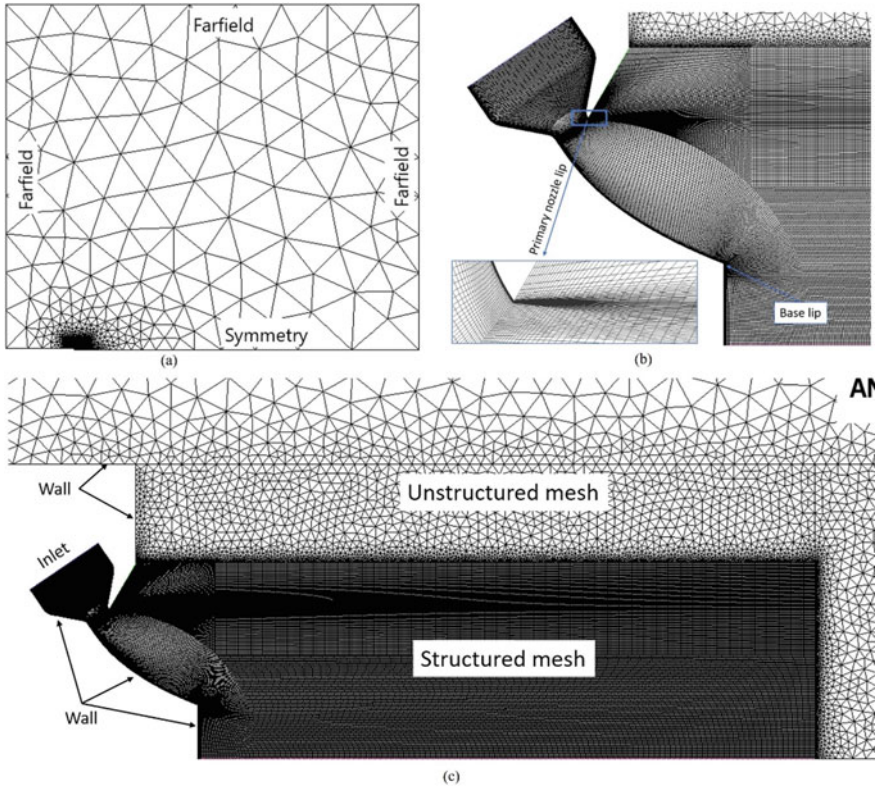


Fig. 5 Plug nozzle computational domain in x - y plane. **a** Full domain showing far-field and symmetry boundaries. **b** Showing grid alignment in base lip. **c** Showing structured and unstructured domains

Table 1 Boundary names and conditions

Boundary name	Boundary condition
Wall	No-slip and adiabatic
Symmetry	Symmetry
Inlet	Subsonic inlet based on far-field Riemann
Far-field	Non-reflecting constant pressure (ambient) outlet
Two parallel planes generated after extruding to 3-D	Periodic

Table 2 Grid details

Grid Id	No. of cells	Cell size in wake
Grid1	7.8 million	0.2 mm
Grid2	36 million	0.1 mm

Table 3 Experimental conditions

Parameter	Value
Design PR	60
Primary nozzle inlet Mach number	0.184
Primary nozzle exit Mach number	1.0
Primary nozzle area ratio	3.2
Tilt angle	55.78 deg
Throat height	3.84 mm
Ambient pressure	101,325 Pa
External flow Mach number	0.0

6 Experimental Details

Plug nozzle flows for a wide range of pressure ratios were experimentally investigated by Chutkey et al. [2]. Using Free Jet Facility at Hypersonic Laboratory of Department of Aerospace Engineering, Indian Institute of Science and published the details in reference [2]. These experimental results are the reference for the computational simulation detailed in this paper. Dimensions and flow conditions of plug nozzles used in experiment are detailed in Table 3.

7 Simulation Results

The experimental conditions in terms of stagnation pressure, temperature and Mach number at inlet of primary nozzle are imposed for RANS and DES simulations. Pressure ratio selected are 20 and 60 for open and closed wake simulations, respectively. Inlet Mach number is taken as 0.184 and ambient pressure as 101,325 Pa. Initial CFL for RANS is kept as 1×10^{-4} and gradually increased with iteration. Average y^+ observed over plug surface is 0.5 which is well enough for resolving viscous sub layer accurately. From converged RANS solution, DES is initiated and continued until the base pressure drag converges. A physical time step of 10^{-6} s is considered for DES and results are time averaged for 0.5 ms.

The base pressure (normalized by ambient pressure) distribution for two pressure ratios (20 and 60) obtained in RANS and DES simulations are plotted in Figs. 6 and 7. Percentage deviation of average base pressure from experimental result in each case is tabulated in Table 4. It can be observed that while RANS results show insensitivity to the mesh refinement, DES provide more and more accurate results suggesting that even a finer grid help in achieving better accuracy.

Total core hours utilized for one steady RANS simulation followed by unsteady DES simulation for 36million grid (Grid2) was about 120,000. Since the simulations were carried out in 10,000 cores the wall time demanded was nearly 12 h.

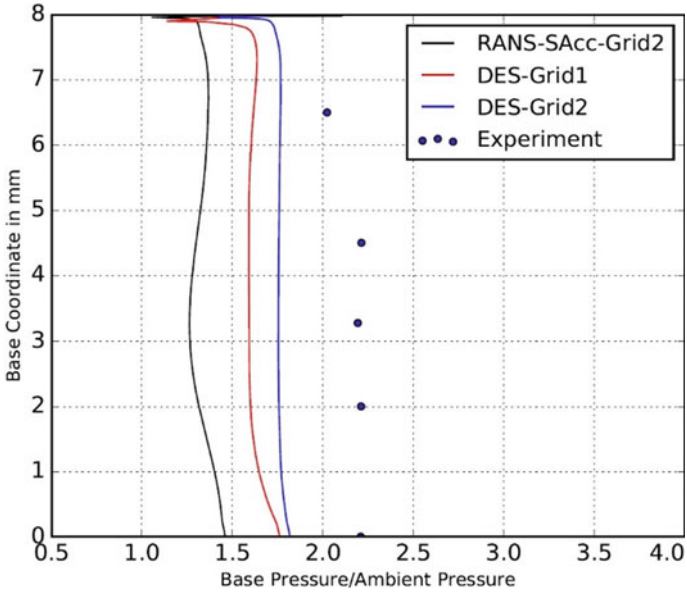


Fig. 6 Base pressure comparison for PR60 (closed wake)

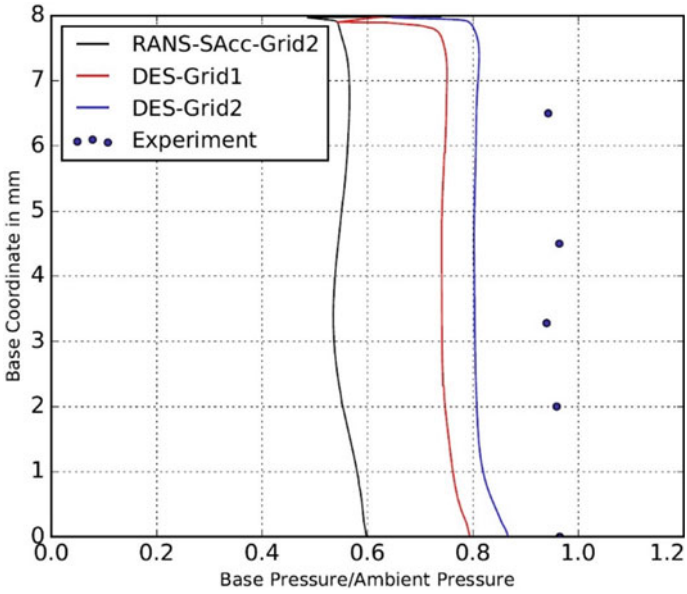


Fig. 7 Base pressure comparison for PR20 (open wake)

Table 4 Deviation in base pressure prediction

Average base pressure $\left(\frac{P_b}{P_\infty}\right)$			
Grid Id	Experiment	RANS-SAcc	DES
PR = 60			
Grid1	2.170	1.350 (-37.8%)	1.617 (-25.4%)
Grid2		1.340 (-38.2%)	1.762 (-18.8%)
PR = 20			
Grid1	0.954	0.558 (-41.5%)	0.750 (-21.3%)
Grid2		0.557 (-41.6%)	0.811 (-15.0%)

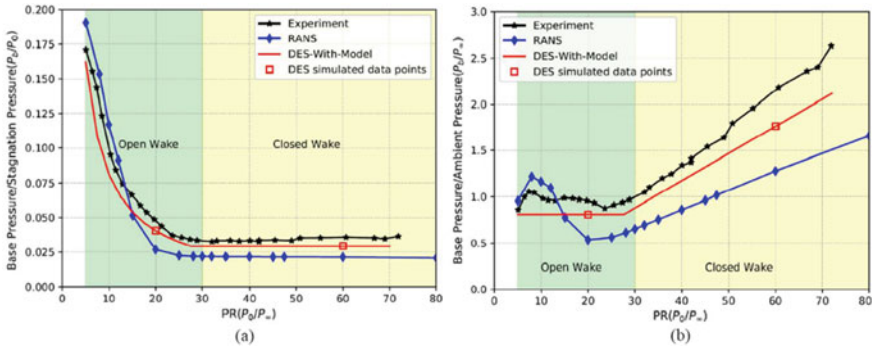


Fig. 8 Comparison of transition curve predicted against experimental data. **a** Base pressure normalized by stagnation pressure. **b** Base pressure normalized by ambient pressure

8 Prediction of WST

Based on DES predicted average base pressure, the transition pressure ratio is calculated using Eq. 1. PR_{tr} estimated is 27.61 against an experimental value of 30. The transition curve predicted using wake transition model is shown in Fig. 8, which shows a better match with experimental results.

9 Conclusions

The objective of current study was to predict the wake structure transition of a truncated plug nozzle, using an empirical model proposed by Chutkey et al. [2]. Which demands an accurate prediction of base pressure at two operating regimes (open and closed wake). Due to the limitations of RANS-based solvers for predicting the same, feasibility of DES is studied in detail and reported.

DES predicted the average base pressure with an accuracy of 15–19% and it also predicted the uniform nature of pressure distribution along the base surface. Based

on the DES predicted average base pressure, the transition pressure ratio (PR_{tr}) calculated using Eq. 1 is 27.61 which is nearly 8% less compared to the experimental value of 30.

With emerging technology like DES which has great relevance to industry, it is important to understand its limitations and applications. The present study can be considered as a step in that direction. With this objective, attempts are being made to carry out DES on a 200 million grid with base cell size equal to 0.05 mm which is expected to provide a better prediction of WST. But the expected computational cost for such an experiment is nearly of the order of 600 k core hours. Having established a DES procedure for base pressure prediction of plug nozzles, it would be interesting to consider clustered annular and linear plug nozzles in future.

Acknowledgements The authors acknowledge the Supercomputer Education and Research Center (SERC), Indian Institute of Science, Bangalore, India, for providing the supercomputer facilities to carry out the simulations.

References

1. Hagemann G, Immich H, Nguyen TV, Dumnov GE (1998) Advanced rocket nozzles. *J Propul Power* 14(5):620–634
2. Chutkey K, Vasudevan B, Balakrishnan N (2012) Flowfield analysis of linear plug nozzle. *J Spacecrafts Rockets* 49(6):1109–1119
3. Chutkey K (2013) Investigation of plug nozzle flow field. PhD Thesis, IISc Bangalore
4. Strelets M (2001) Detached eddy simulation of massively separated flows. In: 39th AIAA aerospace science meeting and exhibit
5. Childs RE, Caruso SC (1991) Assessment of modeling and discretization accuracy for high-speed afterbody flows. *J Propul Power* 7(4):607–616
6. Paciorri R, Nasuti F, Sabetta F (2003) Compressibility correction for the spalart-allmaras model in free-shear flows. *J Spacecr Rocket* 40(3):326–331
7. Spalart P, Jou WH, Strelets M, Allmaras S (1997) Comments on the feasibility of LES for wings, and on a hybrid RANS/LES approach. In: First AFOSR international conference on DNS/LES
8. Tinoco E, Brodersen O, Laffin K, Feltrop E, Vassberg J, Mani M, Rider B, Wahls R, Morrison J, Hue D, Roy C, Mavriplis D, Murayama M (2017) Summary data from the sixth AIAA CFD drag prediction workshop: CRM cases. *J Aircr* 55:1–28

Computational Study of Aero-acoustic Feedback in Supersonic Cavity Flow



Priyansh Jain , Tarun Chavan, Mayukhmali Chakraborty, and Aravind Vaidyanathan 

Abstract Experimental and computational analysis has been already carried out by many researchers on supersonic flow past cavities, but detailed analysis of computational results still needs some insight. For this purpose, an open rectangular cavity with a length to depth ratio of 2 ($L/D = 2$) and inlet Mach number 1.71 was considered for an unsteady computational analysis in ANSYS FLUENT, using SST $k - \omega$ turbulence model. The two dimensional structured grids were generated in Point-wise grid generation software. FFT using Power Spectral Density (PSD) was carried out on the unsteady pressure data for 10,000 time-steps, with a total flow time of 10 ms. Many modes were observed, with dominant frequency at 10.5 kHz. The mode frequencies obtained were validated from experimental results and from the corresponding Rossiter's Modes. Correlation between the unsteady pressure data was also found to analyze the flow dynamics. Many flow visualization techniques were employed such as density gradient-based numerical schlieren, which revealed many flow features associated with the flow. Vortex Shedding Visualization was carried out in terms of the lambda 2 criterion, where the vortex core ($\lambda_2 < 0$) can be observed moving downstream in the shear layer. Lastly in the acoustic pressure contour, an acoustic wave can be observed moving within the cavity. The analysis was extended for different shapes of subcavities on the front and aft wall. As the front wall subcavity act as a passive control device, reducing the overall sound pressure level inside the cavity, whereas the aft wall subcavity acts as a passive resonator with distinct harmonic fluid-resonant modes. A more detailed analysis on these configurations with different shapes will give a comparative and better understanding on the flow

P. Jain (✉) · A. Vaidyanathan

Department of Aerospace Engineering, Indian Institute of Space Science and Technology,
Thiruvananthapuram, Kerala 695547, India
e-mail: jpriyansh786@gmail.com

A. Vaidyanathan

e-mail: aravind7@iist.ac.in

T. Chavan

ISRO Propulsion Complex, Mahendragiri, Tirunelveli, Tamil Nadu 627133, India

M. Chakraborty

Agnikul Cosmos Pvt Ltd, NCCRD, IIT Madras, Chennai, Tamil Nadu 600036, India

features, mode frequencies, Rossiter's coefficients, and fluid-resonant oscillations in a supersonic cavity. Also, the applicability of Rossiter's Modes has been compared with the Closed-Box acoustic model for different configurations.

Keywords Supersonic cavity flow · Fast Fourier transform · Numerical Schlieren · Lambda 2 criterion

Nomenclature

FD	Fluid-dynamic
FR	Fluid-resonant
PSD	Power spectral density
OASPL	Overall sound pressure level

Subscripts

∞	Free stream conditions
c	Inside cavity conditions

1 Introduction

Supersonic flow over cavity is a widely researched area with many applications such as scramjet flame holders, aircraft landing gear, weapons bay, and high-speed cars. Scramjet flame stabilization and mixing phenomena has been very important in the development of various variants of the elite technology, in which supersonic cavity has played a crucial part. A general review of the emergence and maturing of supersonic combustion ramjet (scramjet) engine technologies over the last 40 years is very well presented by Curran [1].

In general, cavity flow produces increased drag and strong pressure fluctuations within the cavity. These oscillations sometimes give rise to high amplitude modes which need to be considered seriously for the structural safety of the overall system and also increase the aerodynamic noise associated. The existence of aero-acoustic feedback and resonance in few cases leads to these high amplitude modes. Similarly, the fluid–structure interactions and loading can lead to structural vibrations.

Cavity flow studies started in 1950s. Krishnamurthy [2] found that 2D cavities cut onto aerodynamic surfaces emit intense acoustic radiation in high-speed flow. The acoustic fields due to different gaps in varying flow conditions were studied by means of schlieren, hot-wire, and optical interferometric techniques. Krishnamurthy [2] has also explained the feedback loop which drives fluid-dynamic oscillations inside the cavity. Some of the early researchers properly identified the actual mechanism and modes of this fluid-dynamic oscillations [3–5]. The closed-box acoustic

modes, based purely on acoustic model, were first mentioned in Heller et al. [6], and later in Rona [7] worked well with supersonic flows. This was verified by Unalms et al. [8] and was also simulated with cover plate configuration. Rockwell and Nau-dascher [5] categorized these cavity oscillations in fluid-dynamic, fluid-resonant, and fluid-elastic oscillations, with possible configurations. Zhang and Edwards [9] suggested that the transverse vortex governed mechanism was observed in the deep cavity, whereas the longitudinal shear layer governed mechanism was seen in shallower cavities. Kumar and Vaidyanathan [10] observed that the transition between the two feedback modes is found to occur between L/D 1.67 and 2, marked by the existence of different subtones for these transitional cavities. Plentovich et al. [11] properly classified cavity configurations, on the basis of various experiments and parameters, which will be discussed in detail, in upcoming sections. Similarly, many other researchers did experimental studies on different variants and observing different kinds of phenomena. Schlieren photography and planer laser imaging were used by Murray and Elliott [12] for vortex visualization. Thangamani [13] experimentally observed the mode switching phenomena in supersonic flow, using wavelet coherence for cavity configuration of $L/D = 2$. For different flame-holding configurations, a comparative steady analysis based on RANS model was conducted by Gruber et al. [14]. Barnes and Segal [15] created a complete picture of flame-holding in different types of injections, cavity geometries, and combustor inlet conditions with their effects on local mixing. For flame stability, it is required to minimize the inherent aero-acoustic feedback for different cavity configurations, as the instability caused by the feedback can inhibit the flame. Further, Cai et al. [16] has reviewed the cavity ignition in supersonic flows, explaining different ignition strategies and their industrial applications.

As suppression of cavity oscillations has quite an importance, many researchers including Vikramaditya and Kurian [17], Maurya et al. [18], Lad et al. [19], and Xiansheng et al. [20] did experiments using different front wall ramp geometries, aft wall offset, subcavities, and front wall blowing. Similarly more wide ranged computational analysis has been carried out, on suppression phenomenon. Zhang et al. [21] suppressed the oscillation amplitudes by implementing wedged and curved ramp, aft wall configurations. Finally, Alam et al. [22] through computational results introduced controlling of cavity-induced pressure oscillations using subcavity, at the front wall, in a deep cavity with $L/D = 1$. This phenomenon was further explored by Lad et al. [19] and Panigrahi et al. [23], with both experimental and computational analysis, showing that the presence of subcavity in different configurations can inhibit or enhance the feedback. A computational study with novel flow visualization techniques, such as Lambda 2 criterion and Acoustic Pressure contour, will be helpful to get better insight on the flow physics associated with the aero-acoustic feedback. Further, this understanding can lead to new configurations, which can inhibit the feedback and enhance flame stability.

For this purpose of interpreting the Rossiter's Equation, its coefficients and the mechanisms proposed by Rossiter [3], Heller et al. [6], and Unalms et al. [8], CFD simulations on rectangular cavity of $L/D = 2$ are being performed. Further objective

was extending the numerical study to aft and front wall subcavities of different shapes with $l/L = 0.2$ so that the presence of FD and FR oscillations can be studied and compared with experimental results from Panigrahi et al. [23].

2 Computational Details

2.1 Geometry and Meshing

The baseline configuration was chosen with $L/D = 2$, $L = 26$ mm and duct height as 25.4 mm, as shown in Figs. 1 and 2. A 50 mm length was given before the leading edge of the cavity so that the flow stabilizes, and boundary layer is properly developed before it. Square subcavities both for aft as well as front wall have been chosen of $l/L = 0.2$. The triangular subcavity for aft and front walls is such that the base and the height of triangle are equal to “ l ” corresponding to $l/L = 0.2$. Also, the semi-elliptical subcavity is considered with semi-major axis and the minor axis length equal to “ l ” corresponding to $l/L = 0.2$, as shown in Fig. 3.

The meshing was performed in Pointwise V18.1 R2 and has approximately 20,000 structured quad cells for baseline and 30,000 structured quad cells for all subcavity geometries. The grids generated here have been designed for the wall-resolved turbulence modeling. Hence, the near wall meshing was such that the wall $y+$ is less than unity for all the walls.

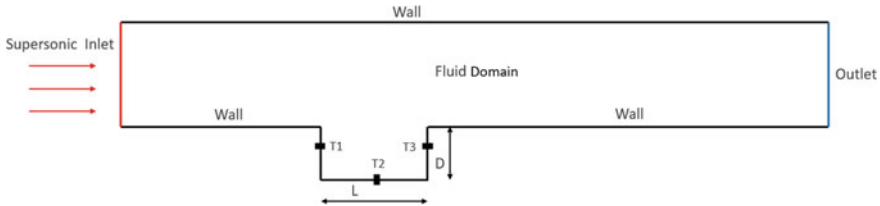


Fig. 1 Computational domain—baseline configuration

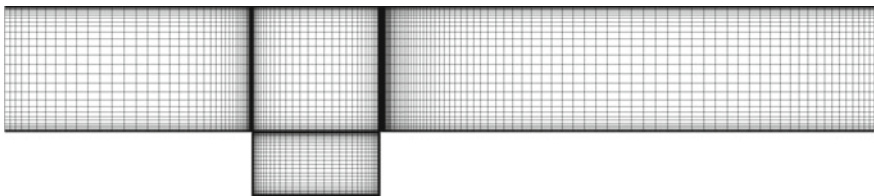


Fig. 2 Computational mesh—baseline configuration

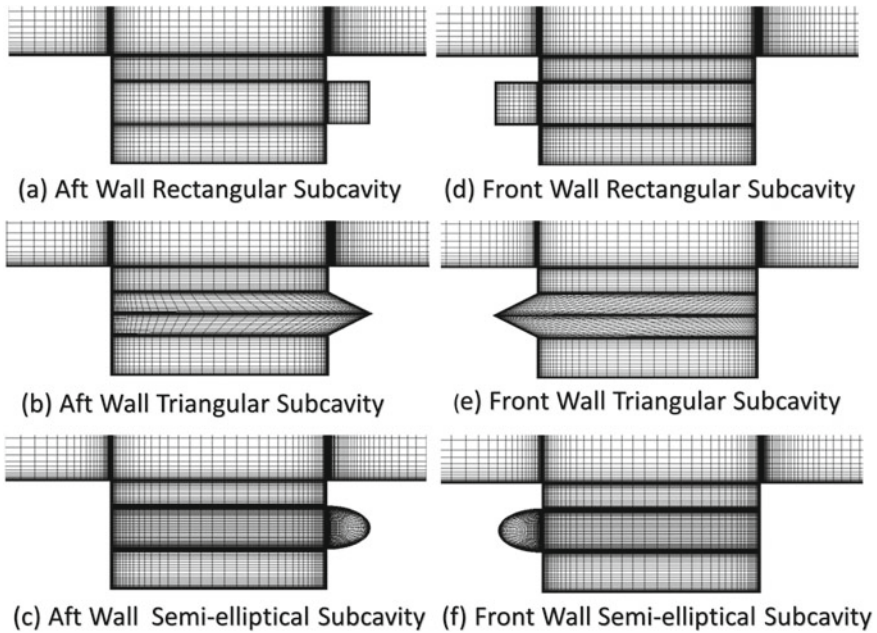


Fig. 3 Different subcavity configurations

Table 1 Free stream conditions

Fluid	Air
Mach number	1.71
Static pressure	99,779.24 Pa
Static temperature	189.45 K
Mass flow rate	0.5584 kg/s

2.2 Boundary Conditions

The free stream conditions are as shown in Table 1. The boundary conditions are as shown in Fig. 1 with there specified locations.

The supersonic pressure inlet had been implemented with total pressure of 500,000 Pa, supersonic gauge pressure of 99,779.24 Pa, and total temperature of 300 K. Also, a simple back pressure boundary condition is applied at the outlet in which the gauge pressure is 101,325 Pa and total temperature of 300 K. The overall operating pressure has been taken as 0 Pa, and all the walls have adiabatic no slip conditions with standard roughness model.

2.3 CFD Setup

The grids were generated in Pointwise grid generation software (Pointwise V18.1 R2). The commercially available software ANSYS FLUENT-Workbench 2020 R1 was used for unsteady numerical computation, which uses the Reynolds Averaged Navier Stokes (RANS) flow equation on the grid by means of a finite volume approach. The URANS simulation is justified based on the availability of solution controls such as Courant number, explicit relaxation factors, and under relaxation factors, which can be used if solution becomes stiff or diverges. Out of the other available simulation models, LES actually is not recommended for 2D analysis and DNS being very computationally intensive, were not considered against URANS. The post processing was done in ANSYS CFD-Post, MATLAB R2018b, and Tecplot 360 EX 2017 R3. A pressure-based transient analysis has been carried out on two dimensional planar domain, neglecting the spanwise variations, as the oscillatory nature of a supersonic cavity flow are not influenced notably by the three dimensionality of the flow, as suggested by Rizzetta [24]. The two equation $k - \omega$ Shear Stress Transport model was chosen after turbulence modeling validation, along with energy equation. Considering the reduced mixing levels associated with high convective Mach numbers, the compressibility corrections of Wilcox have been employed. The compressible ideal gas with specifications of air and Sutherland viscosity model was used as the working fluid. A coupled solver was chosen, solving the continuity and momentum equations simultaneously and later energy and turbulence equations in decoupled manner. All the parameters follow second order upwind method in spatial discretization and second order implicit transient formulation for unsteady simulation. Appropriate flow Courant number with some under-relaxation factors is chosen depending upon the problem, for better results and the convergence rate. The steady flow result was taken as initialization for the transient simulation, as followed by Lee et al. [25] in solving 3D LES problems on passive techniques to alleviate oscillations in supersonic cavity flow. The transient simulation has been done for 10,000 time-steps each of 1×10^{-6} s with 50 internal sub-iterations. This gives a sampling rate of 1000 kHz, which according to Nyquist criteria can measure maximum bandwidth of 500 kHz.

2.4 Turbulence Modeling Validation

The turbulence modeling validation on the baseline configuration with 30,000 grid count, after steady flow simulation with different turbulence models, was performed as unsteady simulation is computationally intensive. The static pressure values on the three walls are plotted for all the models in Fig. 4, and $k - \omega$ SST model was chosen among them due to better convergence rate and consistency with Gruber et al. [14].

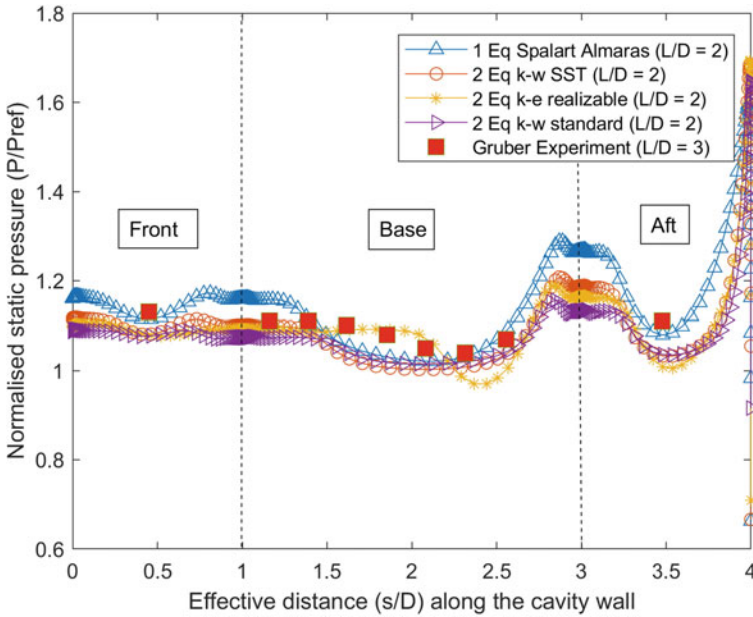


Fig. 4 Turbulence modeling validation

2.5 Grid Independence Study

The grid independence study was carried out on the baseline configuration with $k - \omega$ SST model, after steady flow simulation with different grid counts. The static pressure values on the three walls are plotted for all the grids in Fig. 5 which shows that all the grids are consistent among each other. Hence, 20,000 mesh size grid was chosen among them for baseline configuration to minimize the computational effort and 30,000 mesh size grid for all the subcavity configurations, due to their inherent requirement of more grid count to cover more computational domain.

3 Analysis Techniques

3.1 Power Spectral Density

Power spectral density function (PSD) measures the strength of the energy/power as a function of frequency by transforming from time domain to frequency domain. PSD describes the amplitude of vibrations at frequency, which varies randomly with time. The “welch” method is used for estimating the Power Spectral Density in MATLAB to obtain SPL versus frequency plot. The square root of the output from

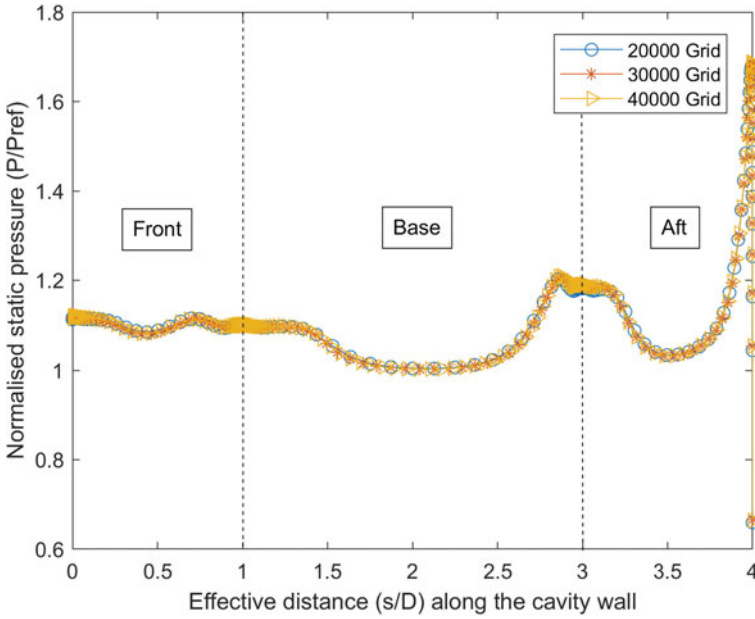


Fig. 5 Grid independence study

“welch” method was converted to dB scale and plotted as SPL versus frequency in kHz. Equation 1 is used to perform Discrete Fourier Transform.

$$X(\omega_k) = \sum_{n=0}^{N-1} x(t_n)e^{i\omega_n t_k} \tag{1}$$

where $x(t_n)$ is Pressure value at sampling instant t_n , t_n is the n th sampling instant, $X(\omega_k)$ is amplitude of pressure signal in frequency domain, ω_k represents frequency.

3.2 Correlation

Correlation is a statistical method that measures similarity between two signals within time domain. Correlation of a signal with itself is known as auto-correlation, whereas with the other signal is known as cross-correlation. Normalized correlation coefficient is defined as

$$C_r(\tau) = \frac{r_{12}(\tau)}{\frac{1}{N} \sqrt{\sum_{n=0}^{N-1} x_1^2(n) \sum_{n=0}^{N-1} x_2^2(n)}} \tag{2}$$

$$r_{12}(\tau) = \frac{1}{N} \sum_{n=0}^N x_1(n)x_2(n - \tau) \quad (3)$$

where $r_{12}(\tau)$ is correlation coefficient of mean removed signals x_1 and x_2 . N is number of samples. τ represents time lag of one signal relative to other. Normalized correlation coefficient ranges from -1 to $+1$. Larger the value of normalized correlation coefficient, more similar two signals are.

3.3 Mean Pressure Level and Overall Sound Pressure Level (OASPL)

Mean pressure level defines average pressure of all sampling data acquired for a given duration. Normalized mean pressure is a ratio of the mean pressure to the free stream stagnation pressure. Root Mean Square Pressure Level or RMS pressure represents the deviation from the mean value.

It is defined as the square root of mean square deviation and denoted by p_{rms} . Overall sound pressure level (OASPL) represents root mean square pressure level in dB. Overall sound pressure level is defined in Eq. 4, where p_{ref} is the reference pressure of $20 \mu\text{Pa}$.

$$\text{OASPL} = 20 \log_{10} \left(\frac{p_{\text{rms}}}{p_{\text{ref}}} \right) \quad (4)$$

3.4 Numerical Schlieren

Tecplot 360 EX 2017 R3 was employed to plot density gradient-based numerical schlieren. X direction and Y direction density gradients were used to calculate the density gradient magnitude at each node in the domain. Flow features are boundary layer, shear layer, front wall compressive shock-expansion wave, aft wall reattachment shock, bow shock and reflected shocks.

3.5 Lambda 2 Criterion

The lambda 2 criterion was used for vortex shedding visualization, plotted in Tecplot 360 EX 2017 R3. The eigen value 2 of the result has been plotted for characterization of vortex cores in the domain, by using the sufficient condition of $\lambda_2 < 0$, according to the definition of vortex core given by Jeong and Hussain [26].

3.6 Acoustic Pressure Contour

The static pressure at each node inside the cavity was used to calculate the acoustic pressure at each node by subtracting the mean pressure level at each node obtained from the unsteady pressure data, as shown in Eq. 5. The unsteady acoustic pressure contour is used to observe the presence of acoustic wave inside the cavity, and its role in the aero-acoustic feedback inside the cavity. Also by this analysis, the spatial variation of SPL strength can also be compared among points inside the domain.

$$p(\bar{x}, t) = P(\bar{x}, t) - P_{\text{mean}}(\bar{x}) \tag{5}$$

3.7 Static Temperature Contour

The static temperature inside the cavity was plotted, as it plays a critical role in the closed-box acoustic model, for finding the actual value of cavity recovery and its variation inside the cavity. It also gives an idea if the material inside the cavity will be able to withstand the heating effects of the flow.

4 Results and Discussion

Unsteady static pressure at each time-step for some predefined points on the front, aft, and base wall (as shown by T_1 , T_2 , and T_3 in Fig. 1) was processed according to methods proposed by Vikramaditya and Kurian [17], for all the cases. The unsteady pressure data (Fig. 6) suggested that after the initial 2 ms of development the flow attained the sustained pressure fluctuations; hence, to reduce computational requirements the flow time was taken as 10 ms.

Power spectral density (SPL vs. Frequency) plots for different configurations are shown in Figs. 7, 12, 16, 20, 24, 25, and 26. The peaks at different frequencies

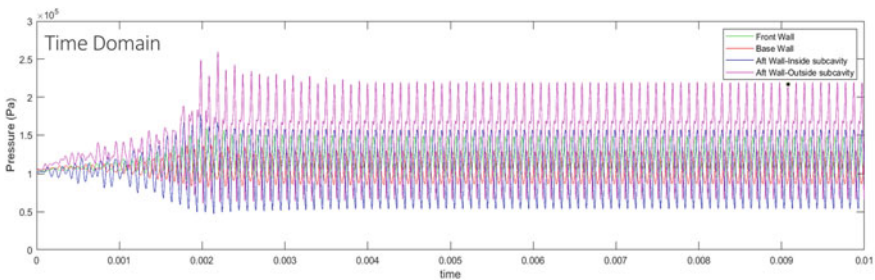


Fig. 6 Unsteady pressure data—aft wall rect. subcavity

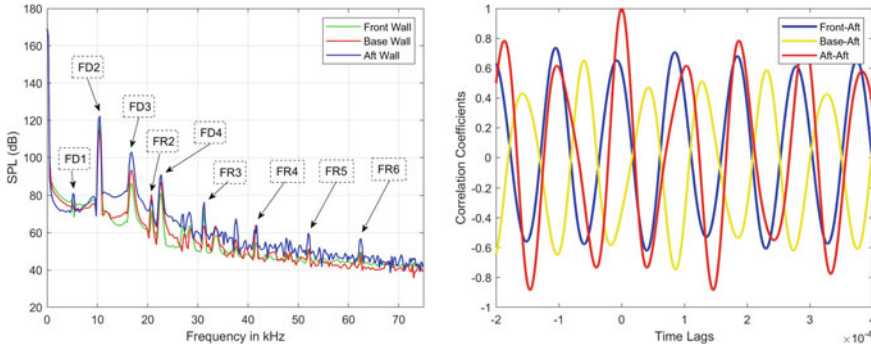


Fig. 7 PSD and correlation—baseline configuration

correspond to the cavity modes or tones. When the SPL of the signals obtained from the points located at three different locations inside the cavity are compared, cavity mode naturally turns out to be at the same frequency for all three locations. Hence, it was deduced that the cavity tone is independent of the location of the pressure measurement, illustrating a global instability of the flow field. The direct impingement of the turbulent shear layer on the aft wall and intermittent impingement of the bow shock at the aft wall results in high amplitudes of cavity tones at the aft wall with respect to the front and base wall, which can be clearly identified from the PSD plots. Figure 7 for baseline configuration indicates the presence of high amplitude cavity tones corresponding to those predicted by the semi-empirical formula by Rossiter [3] and later modified by Heller et al. [6] based on FD oscillations and low amplitude modes harmonic in nature corresponding to the FR oscillations.

Considering the cavity recovery factor (r), as given in Eq. 6 the generalized form of Heller’s formula, also used by Vikramaditya and Kurian [17], is given in Eq. 7

$$r = \frac{T_c - T_\infty}{T_o - T_\infty} \tag{6}$$

$$f = \frac{U_\infty(m - \alpha)}{L \left(\frac{M_\infty}{\sqrt{1+r(\frac{\gamma-1}{2})M_\infty^2}} + \frac{1}{k} \right)} \tag{7}$$

In Eq. 6, T_c , T_o , and T_∞ are Cavity, Stagnation, and Free stream temperatures and in Eq. 7, L represents the cavity length while U_∞ and M_∞ are the free stream velocity and Mach number, respectively, m is mode number for cavity oscillation and r is the cavity recovery factor.

The empirical constant, k , is the ratio of convective velocity of vortices to free stream velocity, while α is the phase delay between acoustic wave and new vortex, and will vary depending on L/D . Rossiter derived the values of these constants empirically as $k = 0.57$ and $\alpha = 0.25$ for a $L/D = 4$ [3].

Table 2 Comparison of computational modes, Rossiter modes, and closed-box mode for certain cavity configurations

Mode number	Rossiter's mode (kHz)	Baseline (kHz)	Aft wall rect. (kHz)	Aft wall tri. (kHz)	Aft wall semi-ell. (kHz)
FD1	4.499	5.127	4.639	4.639	4.639
FD2	10.498	10.5	–	–	–
FD3	16.496	16.85	14.65	15.14	15.14
FD4	22.495	22.71	–	–	–
FR1	–	–	10.01	9.89	10.25
FR2	–	20.75	20.02	19.78	20.51
FR3	–	31.25	30.03	29.54	31.01
FR4	–	41.75	40.04	39.55	41.26
FR5	–	52	50.29	49.32	51.76
FR6	–	62.5	60.3	59.33	62.01
Closed-box model					
First mode	–	6.1193 ± 0.48	5.232 ± 0.4	5.197 ± 0.4	5.23 ± 0.4

The Closed-Box Acoustic modes, based purely on acoustic model, were first mentioned in Heller et al. [6] derived by solving the wave equation for 3 dimensional rectangular cavities to determine possible resonance frequencies of a flow-cavity system. The consistency of those equations with higher Mach numbers was verified by Unalmis et al. [8], by considering only the longitudinal standing waves and simplifying the equation to Eq. 8. This phenomena was also simulated with cover plate configuration, which was geometrically similar to the aft wall subcavity investigated by Panigrahi et al. [23] and to be analyzed in further sections.

$$S = \left(\frac{a_c}{2U} \right) n = \frac{\sqrt{1 + \frac{r(\gamma-1)M^2}{2}} n}{2M} \quad (n = 1, 2, 3, \dots) \quad (8)$$

Table 2 clearly illustrates and classifies the Fluid-Dynamic modes and Fluid-Resonant modes for baseline and aft wall subcavity cases. The flow mechanism can be easily predicted corresponding to the highlighted dominant frequencies. For the reference baseline configuration, the correlation plot, numerical schlieren, static temperature, lambda 2 criterion and acoustic pressure contour are shown in Figs. 7, 8, 9, 10, and 11, respectively.

Further analysis on the unsteady pressure data was carried out by auto and cross-correlation of aft wall data with itself and front or base wall data, respectively (Figs. 7, 12, 16, 20, 24, 25, and 26). The dominant frequencies obtained from the reciprocal of time lag between two consecutive peaks of aft wall auto-correlation as suggested by Vikramaditya and Kurian [17] have been presented in Table 3 for baseline and aft wall cases. Its comparison with highlighted dominant frequencies obtained from PSD

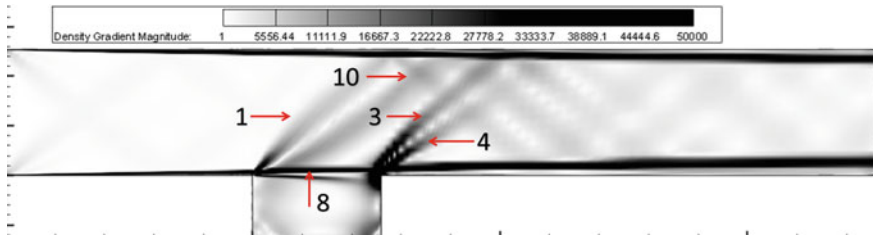


Fig. 8 Numerical Schlieren—baseline configuration

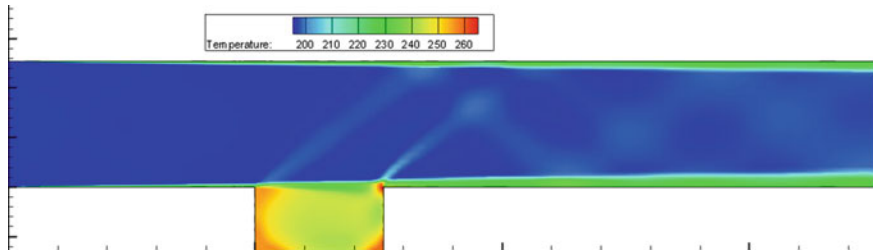


Fig. 9 Static temperature contour—baseline config

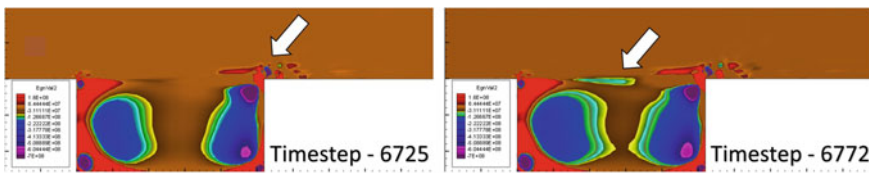


Fig. 10 Lambda 2 criterion—baseline configuration

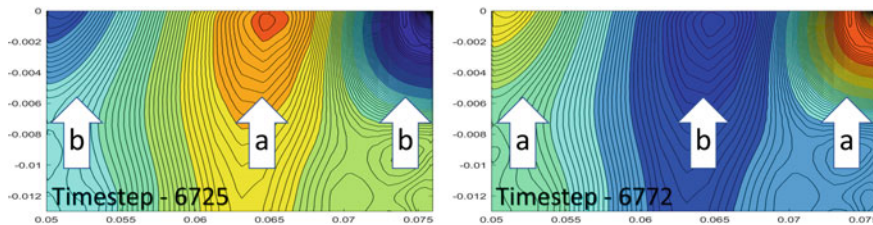


Fig. 11 Acoustic pressure—baseline config

suggests clearly that both methods are consistent with each other within acceptable accuracy. The auto-correlation of the aft wall data and the cross-correlation of the aft wall and front wall data should be in phase for the subcavity at the aft wall due to the presence of dominant fluid-resonant modes and the existence of prominent resonant standing waves inside the cavity (as shown in Figs. 15, 19, and 23) for the cases of $l/L = 0.20$ subcavity placed at the aft wall. But the existence of phase difference

Table 3 Comparison of dominant frequency obtained from auto-correlation of the aft wall signal with PSD

	Baseline (kHz)	Aft wall rect. (kHz)	Aft wall tri. (kHz)	Aft wall semi-ell. (kHz)
Time lag (ms)	0.0935	0.1	0.101	0.097
Dominant frequency obtained from auto-correlation (kHz)	10.695	10	9.9	10.31
Dominant frequency obtained from PSD (kHz)	10.5	10.01	9.89	10.25

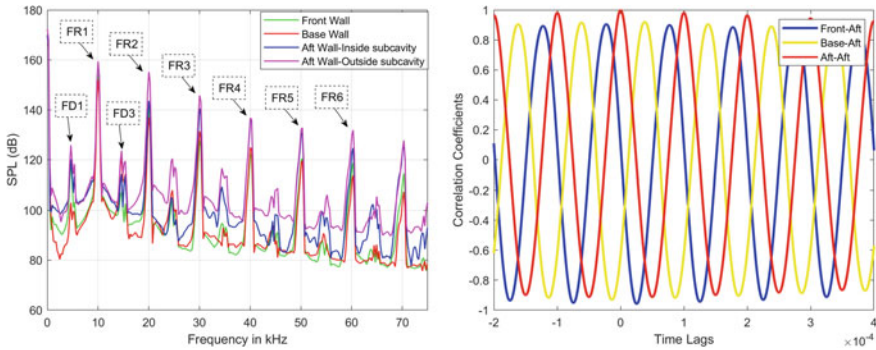


Fig. 12 PSD and correlation—aft wall rect. subcavity

here should be accounted on the simultaneous existence of FD and FR oscillations, which can also be verified by the presence of FD modes in lower frequency range of PSD plots. The presence of a strong recirculation region, mass exchange at the trailing edge, and other effects associated with the fluid-dynamic oscillations produce deviations from the ideal resonating behavior of rectangular enclosures with no mean flow [5].

For rectangular aft wall subcavity, the correlation plot, numerical schlieren, lambda 2 criterion, and acoustic pressure contour are shown in Figs. 12, 13, 14, and 15, respectively.

The instantaneous density gradient-based numerical schlieren are presented in Figs. 8, 13, 17, 21, 27, 28, and 29 for baseline and different subcavity configurations. The flow direction in all of them is from left to right. For the baseline and all front wall subcavity cases, the spatial variations between two time-steps were not easily distinguishable, results of only one time-step are shown here, unlike the aft wall cases which have large spatial variation between two time-steps, the difference of whom is same as half of the time scale corresponding to the dominant frequency of that configuration.

Five different types of waves are clearly observed in all of the configurations. The time-steps for aft wall case are chosen such that the first will have the shear layer deflected above the aft wall whereas the second will have the shear layer

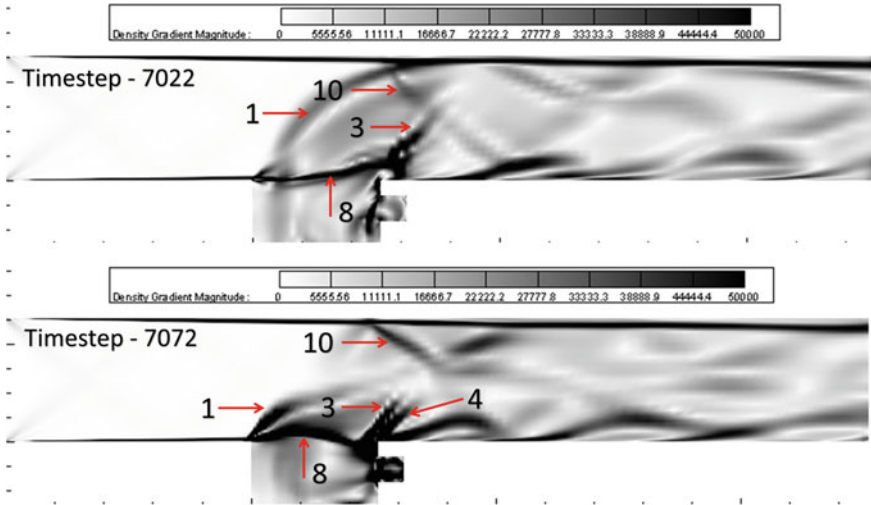


Fig. 13 Numerical Schlieren—aft wall rect. subcavity

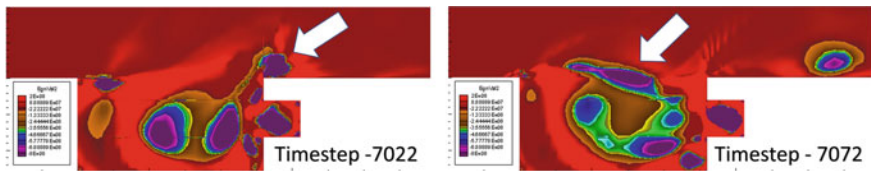


Fig. 14 Lambda 2 criterion—aft wall rect. subcavity

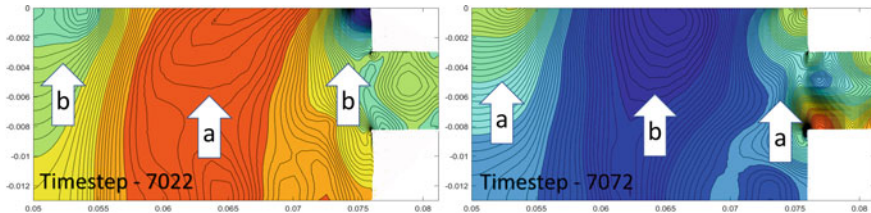


Fig. 15 Acoustic pressure—aft wall rect. subcavity

deflected below aft wall, directly impinging at the corner. **Type-1** wave is the leading edge compression shock-expansion wave, alternatively appearing and disappearing, which is clearly observed in Figs. 13, 17 and 21. Similarly **type-4** wave represents the periodically appearing reattachment shock at aft wall. The **type-3**, **type-8**, and **type-10** waves represent the bow shock at aft wall, shear layer, and reflected shock from upward wall, respectively, which are clearly observed for all the cases.

The vortex visualization technique employed through the condition of negative eigenvalue-2 obtained from lambda 2 criterion algorithm has been shown for the

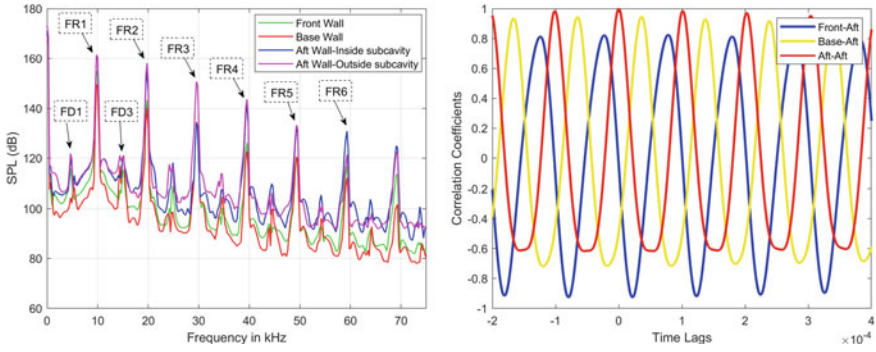


Fig. 16 PSD and correlation—aft wall tri. subcavity

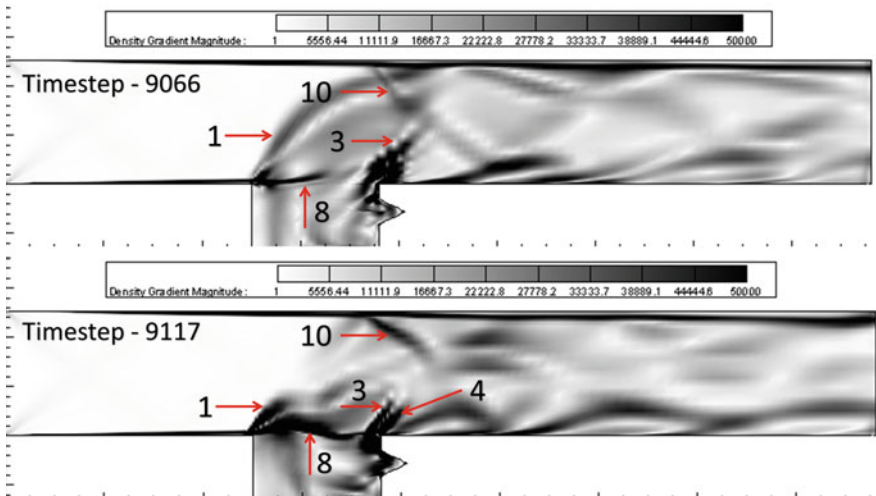


Fig. 17 Numerical Schlieren—aft wall tri. subcavity

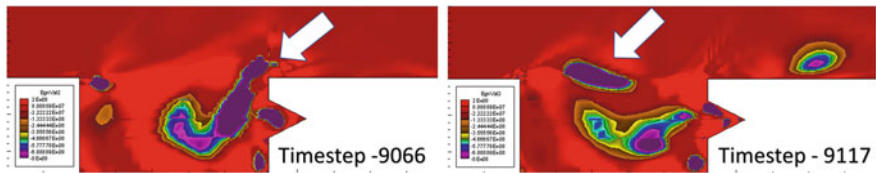


Fig. 18 Lambda 2 criterion—aft wall tri. subcavity

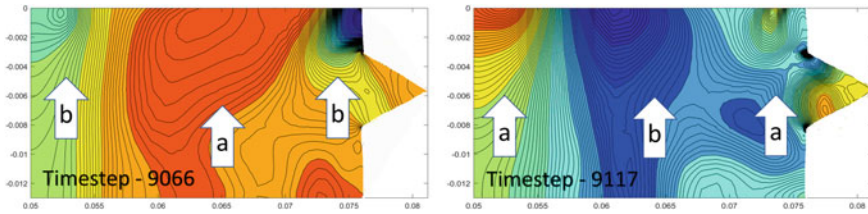


Fig. 19 Acoustic pressure—aft wall tri. subcavity

Table 4 Rossiter’s coefficient “*k*” obtained from different methods

	Baseline (kHz)	Aft wall rect. (kHz)	Aft wall tri. (kHz)	Aft wall semi-ell. (kHz)
<i>k</i> from Eq. 9	0.6059	0.6113	0.6098	0.6111
<i>k</i> from Eq. 10	0.6484	0.7158	0.7066	0.6977
<i>k</i> from Eq. 11	0.6516	0.5524	0.6675	0.5835

baseline and aft wall subcavity cases in Figs. 10, 14, 18, and 22. The time-steps employed here are same as numerical schlieren. The large vortex features inside the cavity as well as inside the subcavities are clearly observed. More importantly, the convective vortex core is also observed moving downstream through the shear layer. The first time-step has a fully developed vortex impinging on the aft wall and also a small vortex generated at the front wall, whereas the second time-step has a large vortex core in between the two walls inside the shear layer, whose exact core can also be obtained by changing the color scheme of the contour.

The acoustic pressure contour also for the time-steps employed for numerical schlieren has been plotted for the baseline and aft wall cases in Figs. 11, 15, 19, and 23. The “a” region illustrates the compression whereas “b” region represents the rarefaction inside the cavity. Strong resonant standing wave inside the cavity can be observed for the aft wall cases, whereas a relatively weaker wave is observed for the baseline configuration. This verifies the already observed phenomena of FD oscillations in baseline configuration and dominant FR oscillations with some effects of FD oscillations in aft wall subcavity cases.

The front wall subcavity cases are acting as passive control devices as the cross-correlation coefficients are observed to an order smaller than unity, showing that the Fluid-Dynamic oscillations are being inhibited by the $l/L = 0.2$ front wall subcavities. The PSD results and the OASPL values support this phenomena, with no proper peaks and very low OASPL, respectively.

The empirical constant *k* which is defined as the normalized value of convective velocity of the vortices with respect to the free stream velocity can be theoretically found by the definition used by Murray and Elliott [12], from Eq. 9

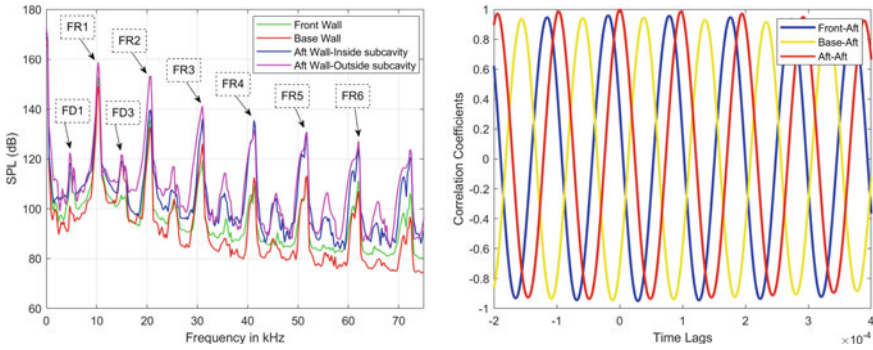


Fig. 20 PSD and correlation—aft wall semi-ell. subcavity

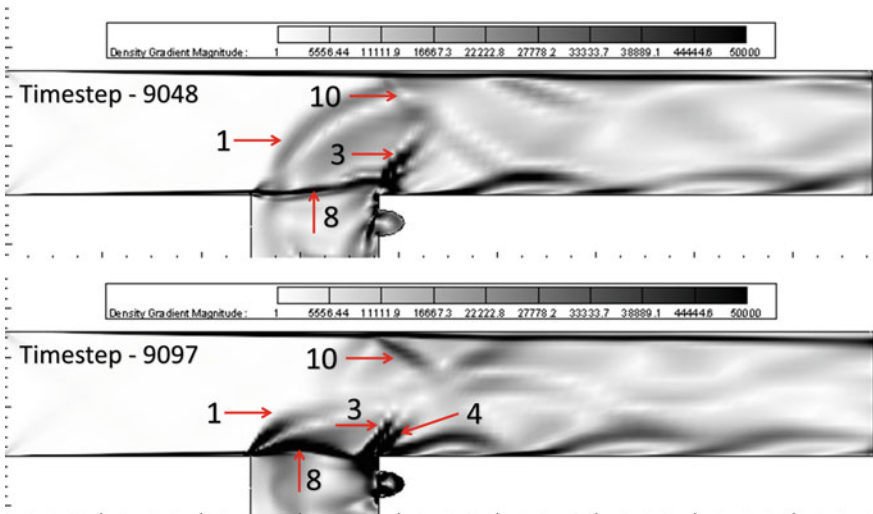


Fig. 21 Numerical Schlieren—aft wall semi-ell. subcavity

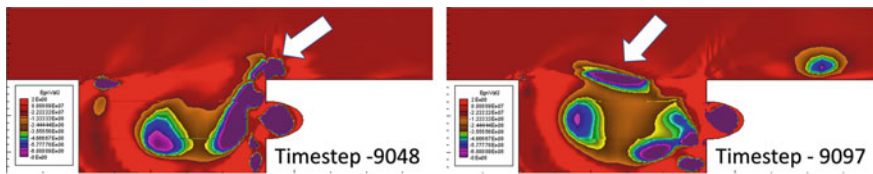


Fig. 22 Lambda 2 criterion—aft wall semi-ell. subcavity

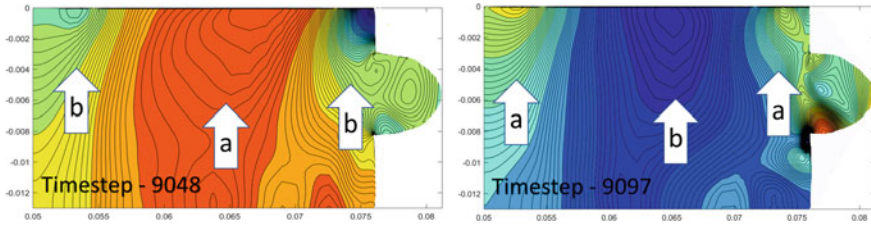


Fig. 23 Acoustic pressure—aft wall semi-ell. subcavity

$$k = \frac{\frac{a_\infty U_c}{a_c U_\infty} + 1}{1 + \frac{a_\infty}{a_c}}; \frac{a_c}{a_\infty} = \sqrt{1 + \frac{r(\gamma - 1)M_\infty^2}{2}} \tag{9}$$

where subscripts ∞ and c represent the free stream and inside cavity properties and “ a ” denoted the speed of sound whereas “ U ” represented the velocity for that region. The “ k ” values shown in Table 4 were calculated based on the spatiotemporal average values of U_c and a_c inside the cavity, obtained from CFD results for the corresponding case.

The “ k ” value was also calculated by the method proposed by Thangamani [13], by using the positive downstream lag (t_d) of the first peak in the cross-correlation plot between aft and front wall signals. Equation 10 was used to calculate “ k ”.

$$k = \frac{L}{t_d U_\infty} \tag{10}$$

Finally, a method based on the lambda 2 criterion is proposed here. As the location of the vortex can be determined with some accuracy for both the time-steps shown in Figs. 10, 14, 18, and 22, the average speed of the vortex and hence the “ k ” value can be found by the simple equation given by Eq. 11.

$$k = \frac{(\Delta x)}{(\Delta t)U_\infty} \tag{11}$$

where Δx is obtained by the horizontal distance between the two locations at different time-steps and Δt is the difference between those time-steps.

Table 4 shows the Rossiter’s Coefficient “ k ” obtained from different methods for the baseline and the aft wall subcavity cases. The three approaches lead to close values of “ k ” for baseline configuration and rather dispersed results for aft wall cases due to the inherent flow instability and large mass exchange phenomena at the trailing edge.

The OASPL comparison between all the configurations at certain points inside cavity as shown in Fig. 30 also infers that an aft wall subcavity ($l/L = 0.2$) of any shape acts as passive resonator, whereas a front wall subcavity ($l/L = 0.2$) for any shape acts as a passive control device with respect to the reference baseline configu-

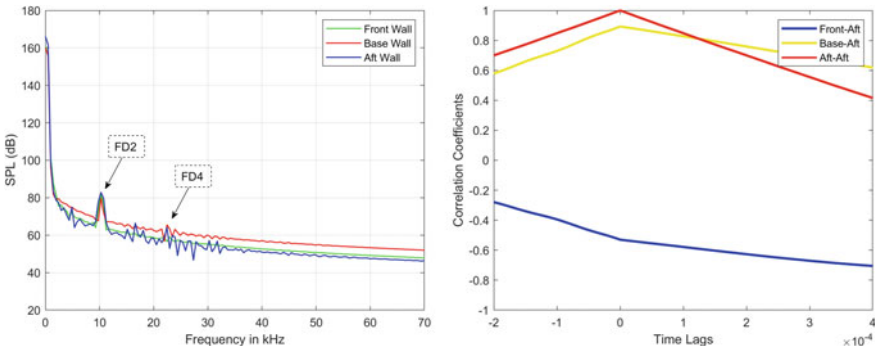


Fig. 24 PSD and correlation—front wall rect. subcavity

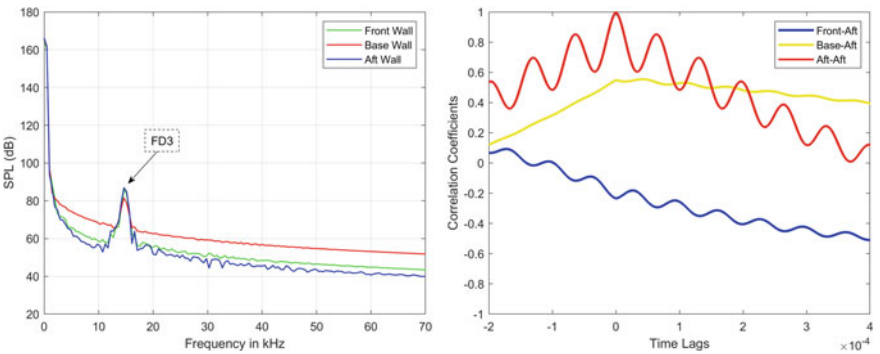


Fig. 25 PSD and correlation—front wall tri. subcavity

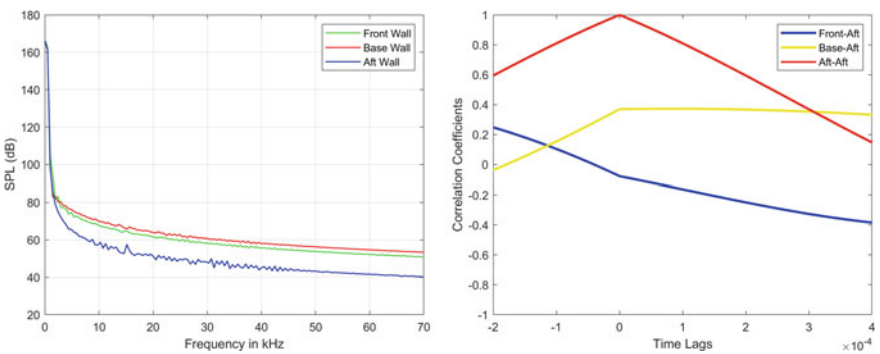


Fig. 26 PSD and correlation—front wall semi-elliptical subcavity

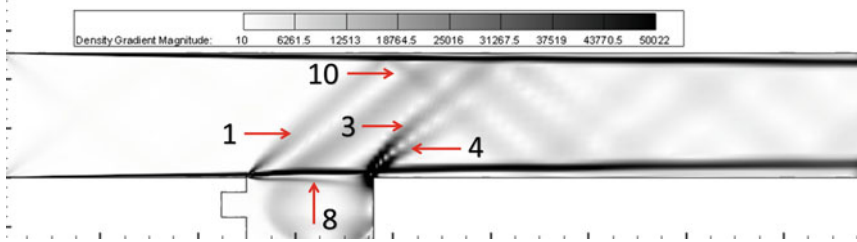


Fig. 27 Numerical Schlieren—front wall rect. subcavity

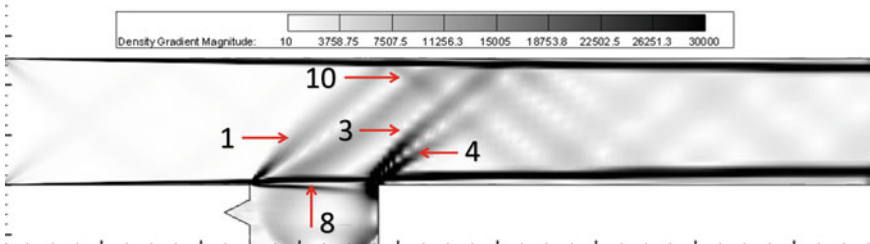


Fig. 28 Numerical Schlieren—front wall tri. subcavity

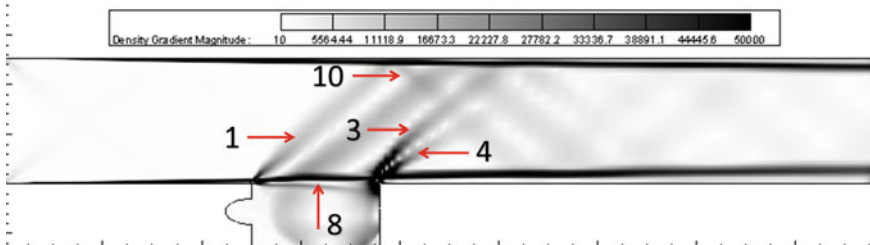


Fig. 29 Numerical Schlieren—front wall semi-elliptical subcavity

ration. As it was observed that the front wall rectangular subcavity reduces the front wall OASPL by 9.6 dB, whereas an increase of 35 dB OASPL has been noted for aft wall rectangular subcavity. The OASPL values with respect to the corresponding experiment [23] are found to be lower which can be accounted by the noise present in the experimental transducer and measurement system, as observed by Sridhar et al. [27].

The normalized mean pressure level noted at certain points inside the cavity is plotted in Fig. 31 for all the configurations and the available experimental data [23]. The highest mean pressure level is found to be at the aft wall due to the direct impingement of the shear layer. Here as well, the aft wall subcavity mean pressure level is more than the reference baseline configuration and mean pressure values of the corresponding experiment [23]. The cause of more value for experimental mean pressure with respect to computational results can be explained on the basis of the

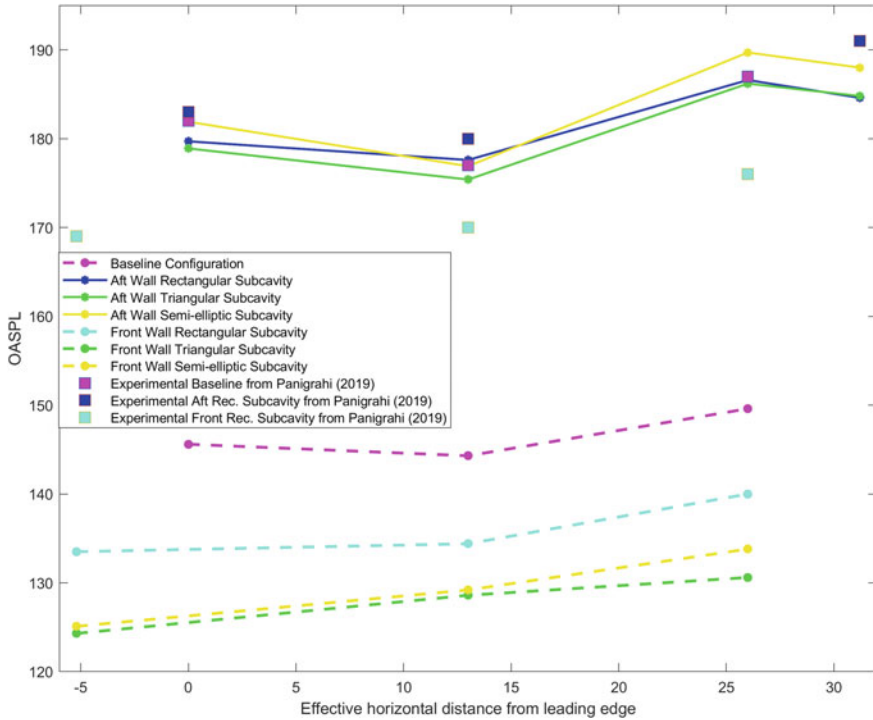


Fig. 30 OASPL for different configurations compared with Panigrahi et al. [23]

position of unsteady pressure transducer in the experimental setup. As the shear layer constantly fluctuates, the flow to be measured near the transducer changes its direction continuously, as shown in Fig. 13. This phenomenon can lead to an overestimation of the measurement of pressure than the actual static pressure, in the experiments. As there is no such ambiguity for static pressure in computational results, it always gives the static pressure value.

A comparative study on the applicability of Rossiter’s formula and Closed-Box Acoustic Model for frequency modes was performed by plotting their frequency vs mode number plot with the CFD results. The exercise was employed for checking if the Closed-Box acoustic modes can be used to estimate the FR oscillation modes. Figure 32a showed that the Rossiter’s modes are quite consistently following the CFD results for baseline configuration. But here the Closed-Box acoustic modes over predicted the CFD results. On a contrary, Fig. 32b–d showed that the Closed-Box acoustic modes are quite consistently following the CFD results and Rossiter’s modes over predict for aft wall cases. This can be easily justified as the baseline configuration has dominantly FD oscillation modes, which is the basis of Rossiter’s modes and the aft wall cases are governed by the dominant FR oscillation modes which require the presence of strong acoustic standing wave. Hence, it has been

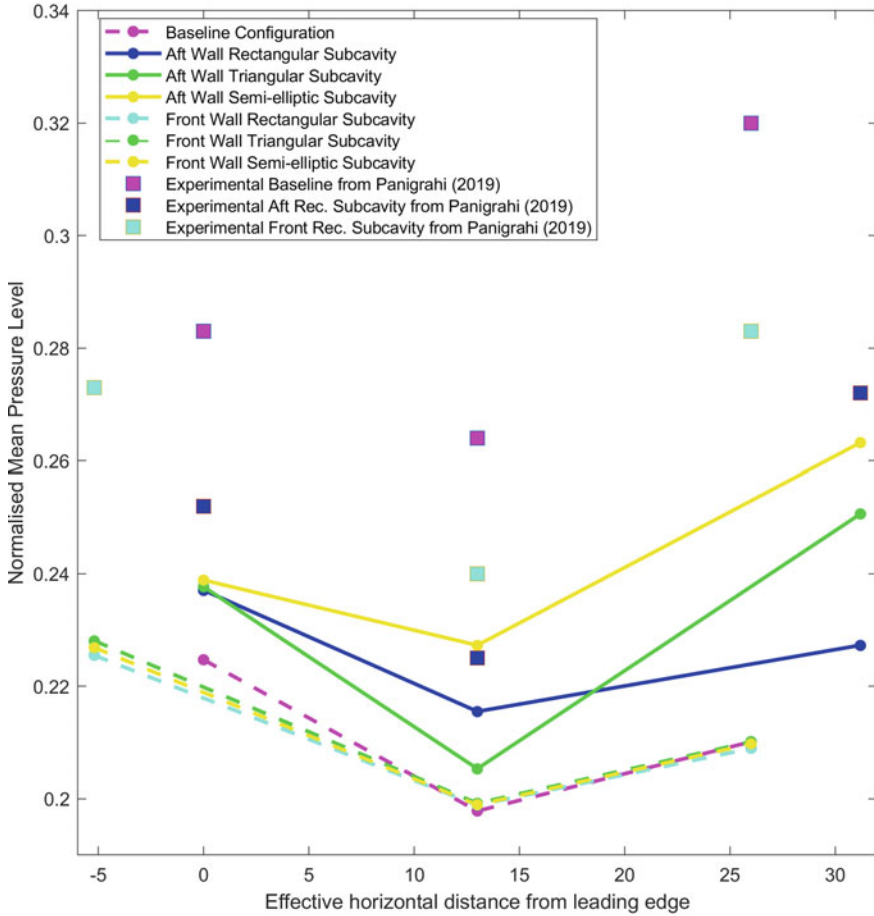


Fig. 31 Mean pressure level for different configurations compared with Panigrahi et al. [23]

clearly shown that the Closed-Box acoustic model can be used for the prediction of FR modes inside a cavity flow field.

5 Conclusion

A computational study has been performed on a supersonic cavity of $L/D = 2$ with baseline configuration as well as with subcavities of $l/L = 0.2$ placed at its aft or front wall at a Mach number of 1.71, and the results are compared with the experimental results as obtained by Panigrahi et al. [23]. Different analysis techniques such as numerical schlieren were employed for flow visualization and different statisti-

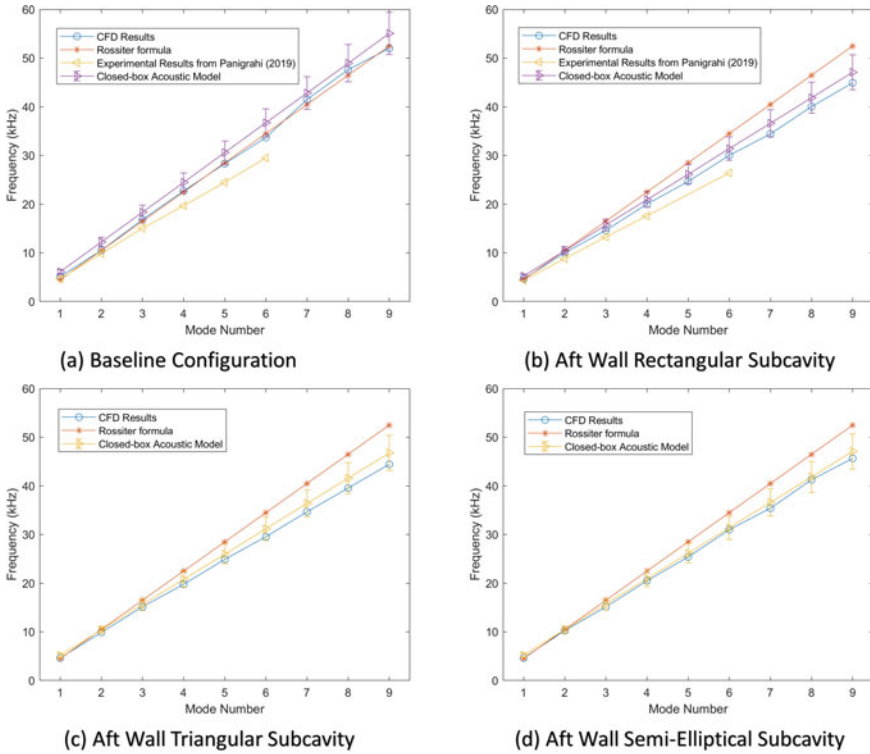


Fig. 32 Frequency versus mode number for different configurations compared with Panigrahi et al. [23]

cal methods were used to process the unsteady pressure data. The flow mechanism was predicted for different configurations based on the PSD results. The baseline configuration also showed the presence of weak FR oscillations whereas when different types of $l/L = 0.2$ subcavities were placed at the aft wall strong harmonic FR oscillations were observed. Validation of the two statistical methods was performed by comparing the dominant frequencies. And the presence of phase lag between the auto and cross correlations was accounted for the simultaneous presence of FD and FR oscillations. Different types of waves were identified in the numerical schlieren. The vortices were visualized by the lambda 2 criterion. And the existence of acoustic standing wave was confirmed by acoustic pressure contour. In-depth comparative analysis was carried out for the Rossiter’s coefficient “ k ”. The OASPL and the mean pressure levels for all the cases were plotted and compared with the experimental data. Finally, a comparative study between the applicability of Rossiter’s formula and Closed-Box Acoustic Model on the frequency modes was performed, and it was shown that the Closed-Box acoustic model can be used for the prediction of FR modes inside a cavity flow field.

References

1. Curran ET (2001) Scramjet engines: the first forty years. *J Propul Power* 17(6):1138–1148. <https://doi.org/10.2514/2.5875>
2. Krishnamurty K (1955) Acoustic radiation from two-dimensional rectangular cutouts in aerodynamic surfaces
3. Rossiter JE (1964) Wind tunnel experiments on the flow over rectangular cavities at subsonic and transonic speeds. RAE technical report no. 64037
4. Heller HH, Bliss DB (1975) Aerodynamically induced pressure oscillations in cavities. Physical mechanisms and suppression concepts AFFDL-TR-74-133
5. Rockwell D, Naudascher E (1978). Self-sustaining oscillations of flow past cavities. <https://doi.org/10.1115/1.3448624>
6. Heller HH, Holmes D, Covert EE (1971) Flow-induced pressure oscillations in shallow cavities. *J Sound Vib* 18(4):545–553. [https://doi.org/10.1016/0022-460X\(71\)90105-2](https://doi.org/10.1016/0022-460X(71)90105-2)
7. Rona A (2007) The acoustic resonance of rectangular and cylindrical cavities. *J Algorithms Comput Technol* 1(3):329–356. <https://doi.org/10.1260/174830107782424110>
8. Unalmsi OH, Clemens N, Dolling D (2004) Cavity oscillation mechanisms in high-speed flows. *AIAA J* 42(10):2035–2041. <https://doi.org/10.2514/1.1000>
9. Zhang X, Edwards J (1990) An investigation of supersonic oscillatory cavity flows driven by thick shear layers. *Aeronaut J* 94(940):355–364
10. Kumar M, Vaidyanathan A (2018) Oscillatory mode transition for supersonic open cavity flows. *Phys Fluids* 30(2):026101. <https://doi.org/10.1063/1.5017269>
11. Plentovich EB, Stallings Jr RL, Tracy MB (1993) Experimental cavity pressure measurements at subsonic and transonic speeds. Static-pressure results
12. Murray RC, Elliott GS (2001) Characteristics of the compressible shear layer over a cavity. *AIAA J* 39(5):846–856, 026101. <https://doi.org/10.2514/2.1388>
13. Thangamani V (2019) Mode behavior in supersonic cavity flows. *AIAA J* 57(8):3410–3421, 026101. <https://doi.org/10.2514/1.J057818>
14. Gruber M, Baurle R, Mathur T, Hsu KY (2001) Fundamental studies of cavity-based flameholder concepts for supersonic combustors. *J Propul Power* 17(1):146–153, 026101. <https://doi.org/10.2514/2.5720>
15. Barnes FW, Segal C (2015) Cavity-based flameholding for chemically-reacting supersonic flows. *Prog Aerosp Sci* 76:24–41, 026101. <https://doi.org/10.1016/j.paerosci.2015.04.002>
16. Cai Z, Wang T, Sun M (2019) Review of cavity ignition in supersonic flows. *Acta Astronaut* 165:268–286, 026101. <https://doi.org/10.1016/j.actaastro.2019.09.016>
17. Vikramaditya N, Kurian J (2009) Pressure oscillations from cavities with ramp. *AIAA J* 47(12):2974–2984, 026101. <https://doi.org/10.2514/1.43068>
18. Maurya PK, Rajeev C, RR VK, Vaidyanathan A (2015) Effect of aft wall offset and ramp on pressure oscillation from confined supersonic flow over cavity. *Exp Therm Fluid Sci* 68:559–573. <https://doi.org/10.1016/j.exptthermfluidsci.2015.06.014>
19. Lad KA, Vinil Kumar RR, Vaidyanathan A (2018) Experimental study of subcavity in supersonic cavity flow. *AIAA J* 56(5):1965–1977, 026101. <https://doi.org/10.2514/1.J056361>
20. Xiansheng W, Dangguo Y, Jun L, Fangqi Z (2020) Control of pressure oscillations induced by supersonic cavity flow. *AIAA J* 58(5):2070–2077, 026101. <https://doi.org/10.2514/1.J059014>
21. Zhang X, Rona A, Edwards JA (1998) The effect of trailing edge geometry on cavity flow oscillation driven by a supersonic shear layer. *Aeronaut J* 102(1013):129–136, 026101
22. Alam MM, Matsuob S, Teramoto K, Setoguchib T, Kim HD (2007) A new method of controlling cavity-induced pressure oscillations using sub-cavity. *J Mech Sci Technol* 21(9):1398, 026101. <https://doi.org/10.1007/BF03177426>
23. Panigrahi C, Vaidyanathan A, Nair MT (2019) Effects of subcavity in supersonic cavity flow. *Phys Fluids* 31(3):036101. <https://doi.org/10.1063/1.5079707>
24. Rizzetta DP (1988) Numerical simulation of supersonic flow over a three-dimensional cavity. *AIAA J* 26(7):799–807, 036101. <https://doi.org/10.2514/3.9972>

25. Lee Y, Kang M, Kim H, Setoguchi T (2008) Passive control techniques to alleviate supersonic cavity flow oscillation. *J Propul Power* 24(4):697–703, 036101. <https://doi.org/10.2514/1.30292>
26. Jeong J, Hussain F (1995) On the identification of a vortex. *J Fluid Mechanics* 285:69–94, 036101. <https://doi.org/10.1017/S0022112095000462>
27. Sridhar V, Gai S, Kleine H (2012) A numerical investigation of supersonic cavity flow at Mach 2. In: 18th Australasian fluid mechanics conference, Launceston, Australia

Numerical Investigation of Blockage of Scramjet Strut Injector Model in a Supersonic Wind Tunnel



Anbarasan Sekar, Mayukhmali Chakraborty, and Aravind Vaidyanathan

Abstract Blockage of strut injector in a supersonic blowdown wind tunnel was studied numerically. Blockage of a model depends mainly on model cross-sectional area, Mach number, shockwave boundary layer interaction, displacement of the boundary layer, and total pressure loss. Simulations were carried out for Mach number of 2 for different chamber pressures while keeping all the other parameters fixed. The blockage phenomenon was simulated using commercial software ANSYS Fluent with SST $K-\omega$ turbulence model. Results showed that increasing the chamber pressure did not help in avoiding blockage. Flow field was also not affected by the change in chamber pressure. Due to the influence of the boundary layer, blockage had appeared for all the cases even though the total pressure recovery was better than the theoretical value.

Keywords Strut injector · Blockage · Supersonic wind tunnel

Nomenclature

A_m	Maximum cross-sectional area of the model
A_t	Throat area
A_{test}	Area of the test section
H	Height of the test section
M_d	Design Mach number
P_0	Total pressure

A. Sekar (✉) · A. Vaidyanathan
Department of Aerospace Engineering, Indian Institute of Space Science and Technology,
Thiruvananthapuram 695547, India
e-mail: anbumsr@gmail.com

A. Vaidyanathan
e-mail: aravind7@iist.ac.in

M. Chakraborty
Agnikul Cosmos Pvt. Ltd., NCCRD, IIT Madras, Chennai 600036, India

© The Author(s), under exclusive license to Springer Nature Singapore Pte Ltd. 2023
G. Sivaramakrishna et al. (eds.), *Proceedings of the National Aerospace Propulsion Conference*, Lecture Notes in Mechanical Engineering,
https://doi.org/10.1007/978-981-19-2378-4_21

P_C	Chamber pressure
R	Gas constant
T_0	Total temperature
u	x component of velocity
ρ	Density
γ	Specific heat ratio
δ	Boundary layer thickness
δ^*	Displacement thickness

Subscripts

- 1, 2 Indicates location of nozzle throat and trailing edge of the model, respectively

1 Introduction

One of the important difficulties in designing a scramjet engine is the stable and efficient supersonic combustion. The working fluid should be injected deeply into the core flow for effective mixing and enhanced thrust generation. This can be achieved using a strut injector. Flame holding is another advantage of using a strut injector. While testing a scramjet strut injector in a supersonic blowdown wind tunnel (SBWT), the blockage of the model should be taken into account. Otherwise, it is possible not to have the design Mach number in front of the model. Not only strut injector, but any model that will be tested in a SBWT should also be given careful attention to the blockage. Blockage in supersonic inlets and supersonic wind tunnel diffusers had been well studied. An empirical equation for self-starting of the supersonic inlet was given by Sun and Zhang [1]. According to that formula, for Mach 2 flow, maximum of 24% model blockage can be allowed without facing unstart problem. This equation fails in problems where the two-dimensional (2D) models are considered because this formula was derived for conical flows. Figure 1 shows a typical normal shock boundary layer interaction. In this figure, the reduction in the core region due to the separation of boundary layer caused by pressure rise due to normal shock was shown. This straightaway has an effect on blockage [2]. Vaisakh et al. [3] studied the effect of aspect ratio on the shock wave boundary layer interactions. Tunnel with an aspect ratio equal to one gives maximum normal shock portion, which means that the penetration of boundary layer effects due to separation was less. This must also imply that the displacement of the boundary layer is less in the square duct. So, this could help in reducing the blockage due to viscous effects. Yu et al. [4] had made the 2D assumption for testing a model and faced blockage problem even for 8% of the model blockage area. The blockage could be overestimated due to the negligence of corner separation and its influence on centreline separation [5].

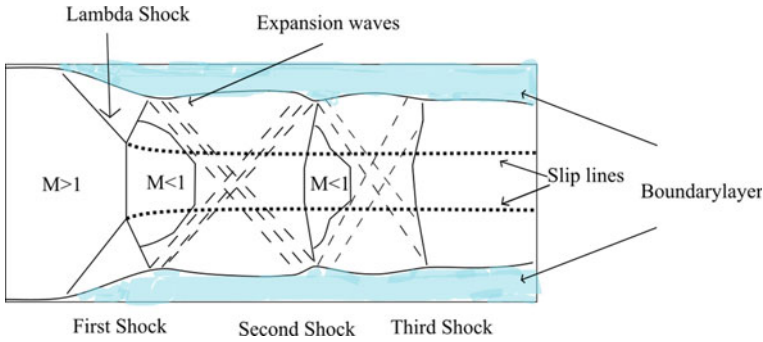


Fig. 1 Typical normal shock boundary layer interaction

If the flow reached sonic condition at the second throat, the intuition would be that the tunnel would suffer from unstart. One more solution exists for the flow to reach the sonic near the second throat and still have supersonic flow. This was achieved by producing a normal shock in the test section, and it was explained clearly by Dayman [6]. This current study has also encountered the same phenomenon.

This blockage phenomenon could be utilized for studying the normal SWBLI due to its stability over pressure variations as will be seen in Sect. 4. Shock holding plate can be used for this study, but it is not possible to study this phenomenon across the whole cross section [7]. The conventional way of controlling the normal shock location is by controlling the pressure ratio, but the oscillations due to pressure fluctuations make it unstable.

2 Theoretical Approach

The maximum possible blockage can be calculated by assuming a normal shock in front of the model. This approach assumes the flow to be inviscid and adiabatic. This approach is mostly used for designing supersonic inlets and supersonic wind tunnel diffusers. If the blockage is such that flow is choked at the second throat, i.e., minimum area after throat, for a particular total pressure, the mass flow rate can be written in terms of total pressure and throat area as given in Eq. (1).

$$\dot{m} = P_0 A_t \sqrt{\frac{\gamma}{RT_0} \left(\frac{2}{\gamma + 1} \right)^{\frac{\gamma+1}{\gamma-1}}} \tag{1}$$

The total pressure recovery across a normal shock for a given Mach number can be given by Eq. (2).

Table 1 Theoretical maximum blockage for Mach 2 flow

Mach number	$\frac{P_{02}}{P_{01}}$	$\frac{A_{test}}{A_{t1}}$	$\left(\frac{A_m}{A_{test}} \times 100\right)\%$
2	0.7209	1.687	17.77

$$\frac{P_{02}}{P_{01}} = \left[1 + \frac{2\gamma}{\gamma + 1}(M_d^2 - 1)\right]^{\frac{-1}{\gamma-1}} \left[\frac{(\gamma + 1)M_d^2}{(\gamma - 1)M_d^2 + 1}\right]^{\frac{\gamma}{\gamma-1}} \tag{2}$$

Since, the mass flow rate is constant, and the flow is adiabatic, Eq. (3) can be obtained.

$$\frac{P_{02}}{P_{01}} = \frac{A_{t1}}{A_{t2}} \tag{3}$$

Area ratio for a design Mach number can be found for isentropic flow using the Eq. (4).

$$\left(\frac{A_{test}}{A_{t1}}\right)^2 = \frac{1}{M_d^2} \left[\frac{2}{\gamma + 1} \left(1 + \frac{\gamma - 1}{2} M_d^2\right)\right]^{\frac{\gamma+1}{\gamma-1}} \tag{4}$$

Using above equation, ratio between maximum allowable cross section of model and test section is derived, and it is given in Eq. (5).

$$\frac{A_m}{A_{test}} = 1 - \frac{A_{t2}}{A_{test}} \tag{5}$$

For Mach 2 flow, the area ratio, total pressure recovery, percentage of maximum allowable cross section of model are given in Table 1.

3 Numerical Methodology

The model was designed with a maximum cross section that was calculated theoretically, i.e., 17.77% of the test section area. The half wedge angle was chosen as 10° which is much lower than the maximum deflection angle (22.97°) for Mach 2 flow. The model was fixed at 1 x/H from the nozzle exit. Model and tunnel dimensions were given in Fig. 2. The cartesian coordinate system was considered with the origin fixed at the center of the YZ plane at the throat. SWBLI is a 3D phenomenon, so the geometry was created in 3D with symmetry boundary conditions in Y and Z directions.

A structured grid with 1.34 million nodes was created using ICM CFD. This mesh was considered a fine grid due to the consideration of symmetry boundaries in Y and Z directions. Nodes near tunnel walls were made very fine with the first layer

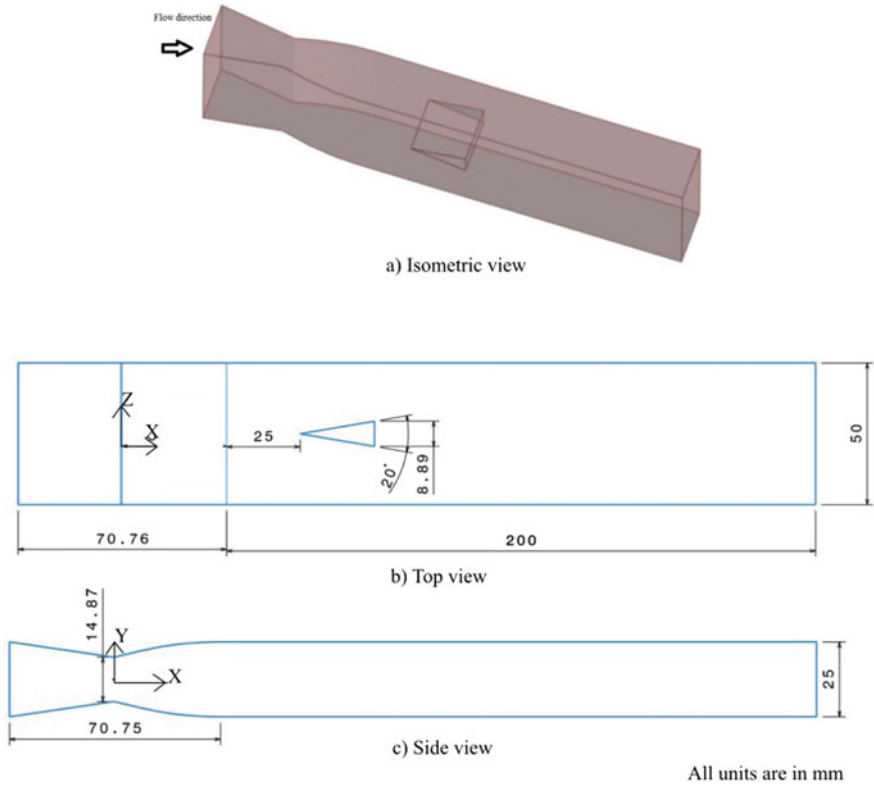
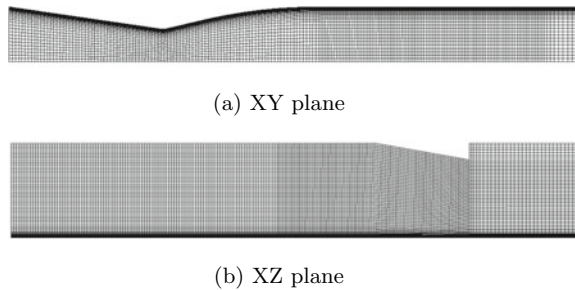


Fig. 2 Different views of geometry with dimensions

Fig. 3 Grids on XY and XZ symmetry planes



thickness of 2×10^{-6} m to keep the wall y plus below 5. Boundary layer effects on the model were neglected. Grids on XY and XZ planes were shown in Fig. 3.

The model cross-sectional area, wedge angle, and the placement of the model were kept constant. Only the chamber pressure was varied. One optimum expansion, two over-expansion, and two under-expansion cases were considered. The chamber pressure values were chosen as per the practical experimental conditions, and the

Table 2 Inlet boundary conditions

Case	1	2	3	4	5
Total gage pressure (bar)	5	6	6.8	8	9

conditions were given in Table 2. For all the cases, the outlet pressure was set to one atmosphere, and the total temperature was fixed to 300 K. No-slip boundary condition was applied to the walls, and symmetry boundary condition was applied to symmetry planes.

Numerical simulation was carried out using commercial software ANSYS Fluent with SST $K-\omega$ turbulence model. Wilcox [8] used $K-\omega$ turbulence model to simulate SWBLI for high-Mach number flows and showed that it captured the separation and wake region closely to experiments. The computational cost of the model is also very less compared to other scale resolving models. Density-based steady-state solver was used in this simulation. The flowfield was initialized with outlet conditions.

4 Results and Discussion

Figure 4 shows the contours of Mach number on the XZ plane for different chamber pressures. From these contours, it was clearly seen that the flow reaches sonic velocities at the trailing edge, and then it expands to supersonic velocities due to the increment in area. All Mach number contours look identical despite having different chamber pressures.

Figure 5 shows the contours of density gradient in the X direction on the XZ plane for different chamber pressures. This clearly shows normal shock interaction with the boundary layer and bifurcated shock structures. A pseudo shock train can also be seen till the end of the trailing edge. As seen in the Mach number contours, density gradient contours also look identical for all the cases.

Figure 6 shows the contours of total pressure on the YZ plane at the trailing edge of the model for different chamber pressures. This shows that the influence of the boundary layer was more in the Z direction compared to the Y direction. This was due to the centerline separation induced by corner separation in the shorter side of the test section. The shape of the boundary layer also looks identical for all the cases.

Table 3 shows maximum Y plus on tunnel walls for different chamber pressures. For all the cases, the maximum wall Y plus was less than 5. Maximum Y plus was encountered in the vicinity of the throat due to high-mass flux. The wall Y plus on the test section walls was near unity, and this shows that the boundary layer was captured closely for all the cases.

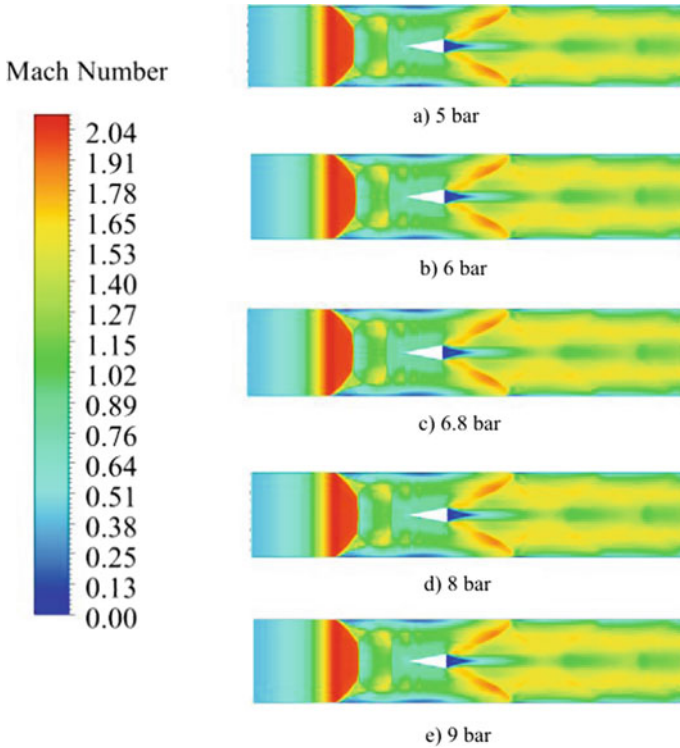


Fig. 4 Contours of Mach number on XZ plane for different chamber pressures

Displacement thickness at a particular location on the YZ plane can be calculated using the following equation.

$$\delta^* = \int_0^\delta \left(1 - \frac{\rho u}{\rho_\infty U_\infty} \right) dy$$

where, ρ_∞ , U_∞ denote free stream density, and axial velocity at that location, respectively.

Figure 7 shows the boundary layer and displacement thickness in Y and Z directions at selected points along the flow direction from throat to trailing edge of the model for a chamber pressure of 5 bar. It clearly shows that the influence of the boundary layer was more in the Z direction than in the Y direction. This was also seen in the total pressure contours. Since increasing the chamber pressure did not change the location of shock waves, boundary layer and displacement thickness for remaining chamber pressures would follow the same trend as shown in Fig. 7.

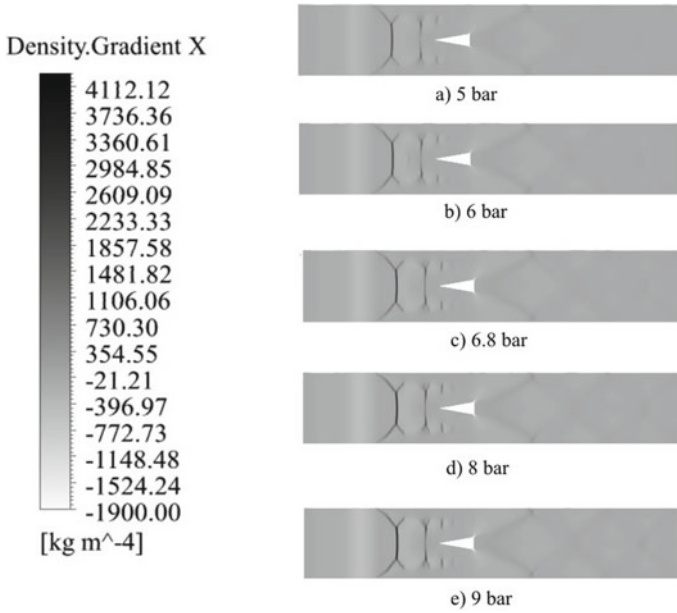


Fig. 5 Contours of density gradient in X direction on XZ plane for different chamber pressures

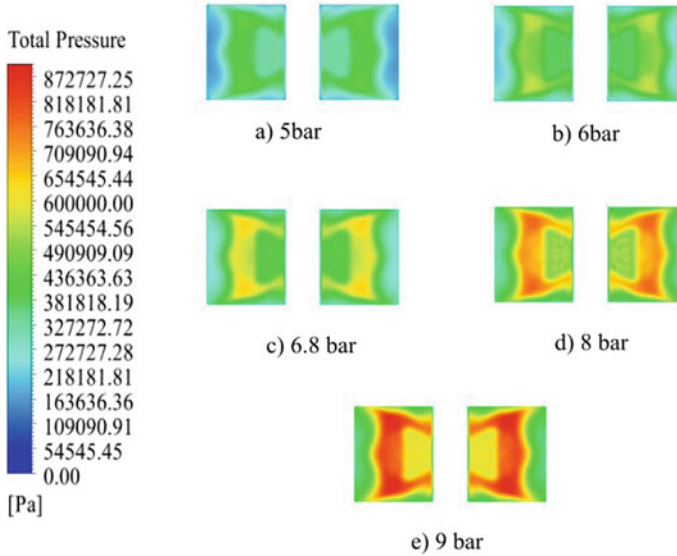


Fig. 6 Contours of total pressure on YZ plane at trailing edge of the model for different chamber pressures

Table 3 Maximum Y plus on tunnel walls

Gage pressure(bar)	Maximum wall Y plus
5	2.69
6	3.09
6.8	3.40
8	3.82
9	4.17

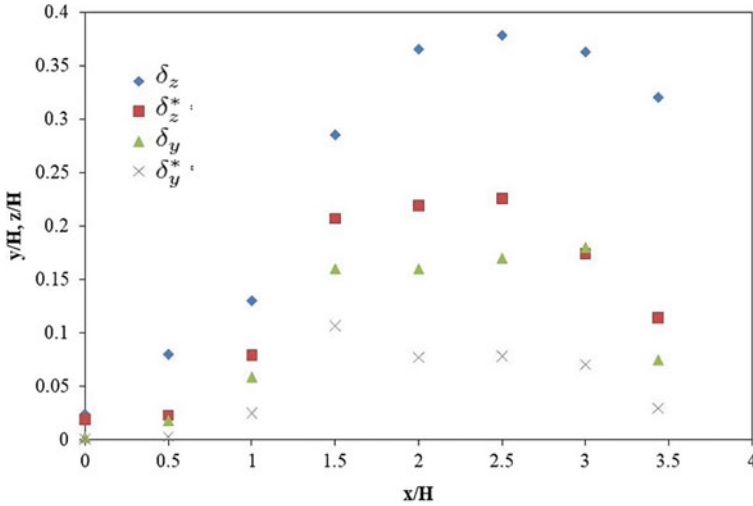


Fig. 7 Boundary layer and displacement thickness in Y and Z directions from throat to trailing edge of the model for chamber pressure of 5 bar

The mass-weighted total pressure was calculated to assess the total pressure recovery. The formula for mass-weighted total pressure is given as follows.

$$P_{0a} = \frac{\int \rho u P_0 dA}{\int \rho u dA}$$

Variation of $\frac{P_{0a}}{P_C}$ along the flow direction from throat to trailing edge for different chamber pressures was shown in Fig. 8. Curves for all chamber pressures merged because the pressure ratio did not influence much on the location of shock waves and the shape of the boundary layer. Even though the total pressure recovery was better than the theoretical value, blockage had appeared for all the cases.

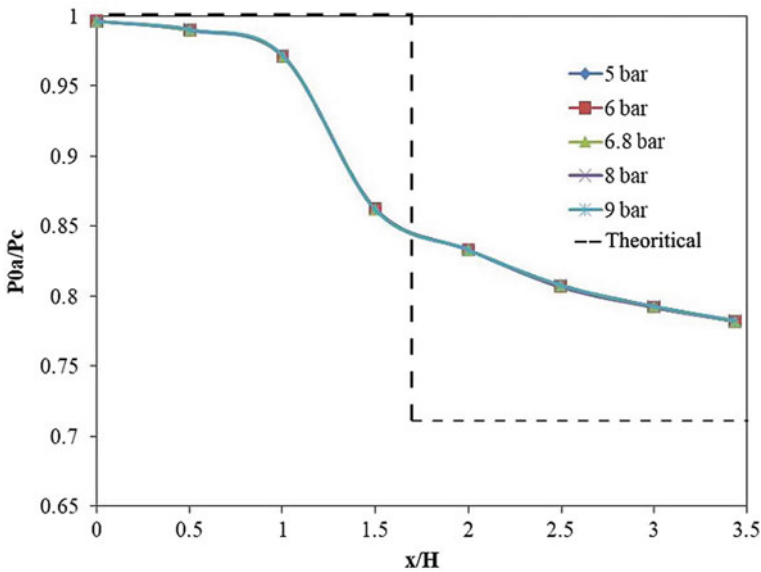


Fig. 8 Variation of ratio of total pressure to chamber pressure along flow direction for different chamber pressures

5 Conclusions

Blockage of strut injector model has been studied numerically for different chamber pressures, and the results were clearly discussed in the previous section. The following conclusions were also drawn from the results.

- The pressure ratio did not influence much on the blockage, so increasing the chamber pressure would not be a solution for the blockage problem if the blockage was experienced for low-chamber pressures.
- When comparing the theoretical and numerical pressure recovery, the shape of the boundary layer seems to be an important parameter in blockage.
- Due to its stability over the pressure variations, the blockage phenomenon could be used for normal SWBLI studies instead of using a shock holding plate, or controlling the location of shock by pressure ratio.

References

1. Sun B, Zhang Ky (2010) Empirical equation for self-starting limit of super-sonic inlets. *J Propuls Power* 26(4):874–875
2. Carroll BF, Dutton JC (1992) Multiple normal shock wave/turbulent boundary-layer interactions. *J Propuls Power* 8(2):441–448

3. Vaisakh S, Namratha P, Muruganandam T (2020) Effect of duct aspect ratio on normal shock wave/boundary layer interaction. *Shock Waves* 30(2):215–219
4. Yu K, Xu J, Liu S, Zhang X (2018) Starting characteristics and phenomenon of a supersonic wind tunnel coupled with inlet model. *Aerospace Sci Technol* 77:626–637
5. Burton D, Babinsky H (2012) Corner separation effects for normal shock wave/turbulent boundary layer interactions in rectangular channels. *J Fluid Mech* 707:287–306
6. Dayman B Jr (1958) Blocking in the supersonic wind tunnel. *J Aerospace Sci* 25(4):264–265
7. Ogawa H, Babinsky H (2006) Wind-tunnel setup for investigations of normal shock wave/boundary layer interaction control. *AIAA J* 44(11):2803–2805
8. Wilcox DC (2008) Formulation of the kw turbulence model revisited. *AIAA J* 46(11):2823–2838

Performance Investigation of a Rectangular Ramjet Intake with Throat Flush Slot Bleed System



Subrat Partha Sarathi Pattnaik and N. K. S. Rajan

Abstract Results of numerical investigation of flow and performance characteristics of a rectangular mixed-compression intake with boundary-layer bleed are presented. A flush slot configuration applied at the intake throat has been studied to evaluate its effect on the compression performance. The viscous flowfield has been obtained by solving Favre-averaged Navier–Stokes equations with SST $k-\omega$ turbulence model. The analysis has been carried out at a range of freestream Mach numbers of 1.7–2.8 and 0° angle-of-attack, corresponding to a unit Reynolds number of approximately $1.8\text{--}3.0 \times 10^7 \text{ m}^{-1}$. The results show that with the use of bleed, the low energy boundary layer and the secondary cross flows are successfully removed near the throat as well as the terminal shock gets stabilized at its entrance. Consequently, the exit flowfield uniformity as well as the critical and peak total pressure recovery improves considerably compared to the intake without bleed system. Furthermore, the critical area-averaged intake exit Mach number reduces by about 0.04 in the complete operating regime. As well as the overall mass capture is found to increase at all operating conditions prior to “unstart because of SWBLI”, since the throat separation bubble is reduced and hence the cowl shock is pushed downstream.

Keywords Mixed-compression intake · Shock wave/turbulent boundary-layer interaction (SWBLI) · Total pressure recovery · Flush slot bleed · CFD

Nomenclature

BL Boundary layer
BMFR Bleed mass flow ratio

S. P. S. Pattnaik (✉) · N. K. S. Rajan
CGPL, Department of Aerospace Engineering, Indian Institute of Science,
Bangalore, Karnataka 560012, India
e-mail: subrat@iisc.ac.in

N. K. S. Rajan
e-mail: nksr@iisc.ac.in

DI	Distortion index, $\frac{P_{0f \max} - P_{0f \min}}{\bar{P}_{0f}}$
Δ /EBR	Throttling degree/exit blockage ratio
FANS	Favre averaged Navier-stokes equations
H_j	Height at j th station w.r.t ramp surface
M_j	Mach number after j th station
MFR	Mass flow ratio
p	Static pressure, Pa
P_0	Total pressure, Pa
\bar{P}_{0f}	Area weighted average total pressure at combustor face
$P_{0f \max}$	Maximum total pressure at the exit of intake
$P_{0f \min}$	Minimum total pressure at the exit of intake
Re	Reynolds number
SWBLIs	Shock wave boundary-layer interactions
SST	Shear stress transport (SST k - ω model)
TPR	Total pressure recovery, $\frac{\bar{P}_{0f}}{P_{0\infty}}$
w	Intake width (mm)
Y^+	Non-dimensional wall distance, $y_{\text{wall}} \times u^*/\nu$, $u^* = \sqrt{(\tau_{\text{wall}}/\rho)}$
X, Y, Z	Axis in the stream-wise, vertical and span-wise direction
3D	Three-dimensional

Subscripts

c	Cowl station
f	Intake exit/combustor entrance station
t	Throat entrance
0	Stagnation/total condition
∞	Freestream condition

1 Introduction

Supersonic air intake is an essential component of a ramjet engine. The internal flow in the supersonic intake usually gets compressed through a series of oblique shocks in the supersonic diffuser, a complex shock/expansion fan interaction pattern followed by a terminal normal shock (or pseudo-shock) close to the throat. The subsonic flow after the normal shock is compressed further in the subsonic diffuser, bringing it to the required combustor conditions [1, 2]. Practically, the internal flowfield is highly complicated due to the adverse flow conditions related to shock–shock interactions, shock wave/boundary-layer interactions (SWBLIs) [3, 4] and many other flow phenomena (secondary cross flows or vortices [5]), affecting the performance

parameters such as pressure recovery, mass flow capture, drag, flow distortion at its exit and the stability margin or the flow unsteadiness (buzz) in the subcritical modes of operation (discussed in Sect. 2.3) [6–8].

Apart from the complex SWBLIs, mixed-compression intake configurations (preferred above Mach 2) also suffer from an aerodynamic phenomenon known as intake unstart. When unstart occurs, usually a normal or bow shock is induced ahead of the cowl to allow mass spillage, resulting in a large reduction in the mass flow ratio (MFR) and total pressure recovery (TPR). Unstart might occur because of (i) geometric effects: (a) over contraction or variation in operating conditions to lower Mach number such that the flow becomes subsonic before throat [9, 10] and (b) unexpected distortion of the incoming inlet flow because of separation of boundary layer due to SWBLIs (glancing or incident) as a result of variation in angle-of-attack, Reynolds number and wall temperature conditions [10]. However, it should be noted that practically in the presence of the cowl shock, in all the above cases the triggering mechanism is mostly SWBLI. Secondly, because of (ii) operational effect: that is excess combustor backpressure condition when the terminal shock is expelled upstream of the cowl [8]. For the convenience of reference, in this paper we shall name the first unstart mechanism as “unstart because of SWBLI” and second type as only “unstart”.

A number of studies have been carried out in the literature to provide an understanding of the effects of various internal geometric concepts (for supersonic diffuser, throat and subsonic diffuser) [1], upstream flow conditions [1, 2], unstart [6], buzz oscillations [4, 5] as well as various active and passive boundary-layer control methods [7, 8] on intake performance. According to these studies, out of various boundary-layer control methods, the active control using a bleed system is the most preferred method for practical usage because of its strong impact on performance improvement. A number of investigations have shown that use of bleed and bypass systems lead to (i) an improvement in pressure recovery and flow uniformity because of the decrease in losses across the SWBLIs and (ii) a delay in buzz oscillations (increase in stable operating range) because of shock stabilization [7–15]. Fujimoto et al. [14] have shown the shock stabilization effect and hence a delay in buzz through numerical analysis. Obery et al. [7] reported that even though bleed improves the total pressure recovery (TPR) compared to no-bleed case, maximum gain in critical TPR is obtained with least amount of bleed sufficient to remove the low energy boundary layer. Moreover, it is shown that in rectangular intakes by locally enlarging the throat slot bleed width close to the sidewalls, the adverse effects of the sidewall boundary layer (secondary flows/stream-wise vortices) can be appreciably reduced. Consequently, the use of sidewall bleed systems can be avoided. In another effort, Fisher [5] concluded that out of various flow control methods throat slot bleed extended at the sidewalls leads to maximum improvement in performance. A few other studies have shown that, with the use of bleed since the flow separation around the SWBLIs as well as the effective internal contraction decreases (when applied upstream of the throat), the “unstart because of SWBLI” can be delayed [11–13]. Similarly, Herrmann and Triesch [12] concluded that bleed helps in expanding the manoeuvre range by delaying the “unstart because of SWBLI” at high angles-of-attack.

According to the above discussion, all the previous studies agree that bleed can prevent the flow separation around the SWBLIs as well as remove the boundary-layer upstream of it leading to an improvement in performance, alleviate the “unstart because of SWBLI” and delay the initiation of buzz at design conditions. However, a very few research studies have considered the impact of fixed-exit (or passive) bleed systems used in missiles at off-design operating conditions in detail. Therefore, the objective of the present study is set to provide a better understanding of the effects of bleed system on the flow and performance characteristics at off-design Mach numbers. Here, a 3-ramp rectangular mixed-compression intake with a flush slot bleed applied at the intake throat has been considered and is numerically analysed in the freestream Mach number range of 1.7–2.8, and 0° angle-of-attack.

Consequent to this introductory note, the paper has been organized as follows: Sect. 2 describes the intake model, boundary-layer bleed configuration as well as the numerical methodology adopted to obtain viscous flowfield. Further, the methodology deployed has been validated with the experimental data from literature. In Sect. 3, a detailed comparison of the performance parameters is presented and the internal flowfield is described in terms of the contours derived from the flowfield. And in the final section, the conclusion of the work is summarized. The analysis shows that with the use of bleed, the exit flowfield uniformity as well as the sustainable backpressure ratio improves considerably at all upstream conditions leading to an extension of the stable flight operation.

2 Computational Methodology

The intake model, bleed configuration and the numerical methodology adopted for the CFD analysis are discussed in this section.

2.1 Intake Model

A three-ramp rectangular mixed-compression intake model has been considered for the study, and the same is schematically shown in Fig. 1. Its major dimensions are presented in Table 1 and are normalized with respect to the cowl height (H_c). The intake is designed for a shock-on-lip condition at Mach 2.2. The ramp and cowl angles of the model have been obtained using a 1D optimization criterion for maximum total pressure recovery (at Mach 2.2), that results in an angle of about 21° for the third ramp and a cowl internal angle of 11° relative to the freestream. The cowl upper surface is designed with a taper angle of 7° . These angles are selected to ensure that the flow separation at the design condition is minimal. Moreover, to reduce the effects of aerodynamic heating blunt ramp and cowl lips are used, with a radius of 0.2 mm each. A small internal contraction ratio of about 1.05 has been considered

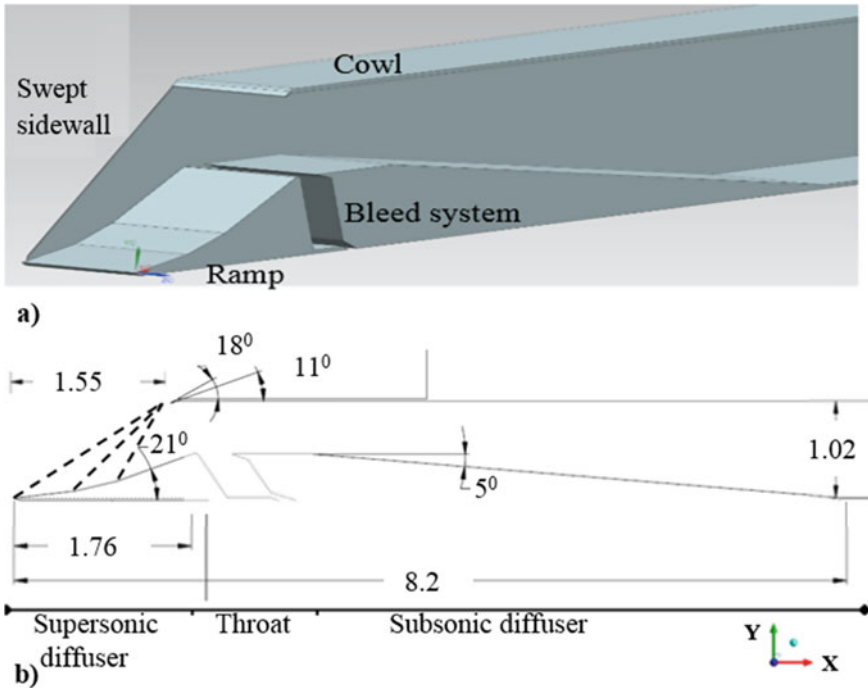


Fig. 1 a Model and b boundary line diagram of the intake

Table 1 Intake geometric dimensions (normalized)

Overall length	Inner width	Cowl angle	Throat height	Throat length	Subsonic diffuser		Internal CR
					Length	Lower wall div. angle	
8.2	1.06	11°	0.55	1.21	6.06	5°	1.05

for the design, for which the intake theoretically self-starts up to a freestream Mach number of 2.1 according to Kantrowitz limit [9] (see Eq. 1). Below this limit, the intake “unstarts because of SWBLI”; that is, a normal/bow shock is formed ahead of cowl to allow spillage. It should be noted that, as shown in Ref. [10], though the Kantrowitz self-starting limit becomes conservative at high speeds, is valid up to a cowl lip Mach number close to 1.6. The sidewalls considered for the model are swept back at an angle corresponding to first ramp shock from its lip. The normalized throat height (H_t) of the model is about 0.55 and has a length of approximately 2.2 times its height. This length has been chosen such that the flow separation due to normal SWBLI completely reattaches at the freestream Mach number of 2.2 and holds the shock train portion of the pseudo-shock at higher off-design Mach numbers up to 2.5 without bleed. The subsonic diffuser used after the throat has a lower wall divergence angle of about 5°, that results in a configuration with good compromise between

pressure gradient and total length. The overall normalized length of the model is about 8.2.

$$\left(\frac{A_t}{A_c}\right)_{\text{Kantrowitz}} = \left[\frac{2 + (\gamma - 1)M_c^2}{(\gamma + 1)}\right]^{0.5} \left[\frac{2\gamma}{\gamma + 1}M_c^2 - \frac{\gamma - 1}{\gamma + 1}\right]^{(1-\gamma)} M_c^{(\gamma-1)/(\gamma+1)} \quad (1)$$

where M_c denotes the average Mach number at the cowl lip station.

2.2 Bleed System Design

In this study, a flush slot configuration has been considered for the bleed system design. To remove the compression ramp boundary layer, it is applied downstream of the throat entrance at a close proximity of the point of impingement of the cowl shock at Mach number of 2.2 and matches the complete width of the intake. As shown in Refs. [16–23], the chosen location (a) helps in better pumping characteristics due to higher static pressure realized after the compression shocks, (b) augments in eliminating the flow separation due to incident cowl shock and hence improves the starting characteristics [19–21], (c) avoids the formation of shock train at the throat and (d) stabilizes the terminal shock within the intake entrance such that the captured mass flow is not altered and the buzz oscillation is delayed [6–8]. The exit of the bleed system has been designed in the shape of a convergent-divergent nozzle to dump the flow supersonically and approximately in line with the external flow to reduce the bleed drag. Dumping the flow supersonically ensures that the external pressure waves do not enter the plenum via the exit and affect the plenum static pressure [24]. The mass flow through the bleed is regulated by the throat area of the exit nozzle and is retained as a fixed geometry (no throttling). To reduce the total pressure loss due to the barrier shock [25] that forms at the bleed rear edge, its structural thickness has been reduced with a taper angle of 20° . The schematic view of the geometrical design of the bleed system is shown in Fig. 1. The entrance and exit throat areas of the model (optimized in the earlier study) are about 54% of the intake throat area and 17% of the bleed entrance area, respectively, and is located at an axial position of 9.1% of the throat height downstream of intake entrance. These geometric parameters result in a 2.7% supercritical bleed mass flow ratio and removes the complete boundary layer at its peak operation at the design Mach number of 2.2.

2.3 Performance Evaluation

The operation of a ramjet air intake can be divided into three different modes, the subcritical, critical and supercritical modes of operation, characterized by the position

of the “terminal” normal shock (or pseudo-shock [4, 26]) in the system [1]. In order to simulate the different modes of operation (with subsonic flow at the intake exit), “a simulated combustion chamber with a variable area exit throttle” has been connected at the intake exit to control the backpressure [14]. It should be noted that the use of duct with throttle provides two specific advantages; first, the question of specifying the exact pressure at different operating conditions is eliminated and, secondly, this technique more closely models the practical system with combustor and a nozzle downstream of the intake system (also see Sect. 2.5) [14]. For each geometric or flow parameters studied, the simulation is first carried out without considering the throttle and then the backpressure is increased by gradually closing the throttle area till the intake is forced to “unstart”. The effect of throttle on the flowfield in the complete domain can be seen in Fig. 2. The throttling condition corresponding to a throttle area is described in terms of throttling degree (Δ) or, exit blockage ratio (EBR), is defined as the ratio of the exit duct area blocked by the throttle to the total area of the exit duct as described in Eq. 2 [27]. To have a systematic discussion in the subsequent sections, we shall name the intake stations as ∞ , c , t and f that corresponds to the freestream condition, cowl lip station, throat and intake exit, respectively. Further, the domain after the intake exit will not be shown.

$$\Delta(\%) = \left(1 - \frac{A_{\text{throttle}}}{A_{\text{exit}}} \right) \times 100 \tag{2}$$

The parameters that have been used to evaluate the steady internal performance of the intake are defined in Eqs. 3–7 [27, 28].

- (i) *Total pressure recovery (TPR)*: The TPR is defined as the ratio of mean (area-averaged) total pressure delivered to the combustor to the freestream total pressure.

$$\text{TPR} = \frac{\bar{P}_{0_f}}{P_{0_\infty}} \tag{3}$$

- (ii) *Capture ratio/mass flow ratio (MFR)*: The MFR is defined as the ratio of actual freestream mass flow rate captured by the intake to the maximum air

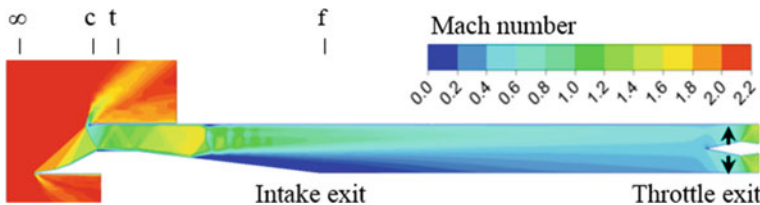


Fig. 2 Exit throttle arrangement to back pressurize the model; and its effect on the flowfield in the complete domain at a fixed EBR; M_∞ 2.2

mass flow rate that can be captured at a supercritical mode of operation and at zero-degree angle-of-attack.

$$\text{MFR} = \frac{\dot{m}_\infty}{\dot{m}_c} \quad (4)$$

- (iii) *Bleed mass flow ratio (BMFR)*: The BMFR is defined as the ratio of mass flow rate of air diverted through the bleed to the maximum air mass flow rate that can be captured by the intake at a supercritical mode of operation and at zero-degree angle-of-attack.

$$\text{BMFR} = \frac{\dot{m}_{bl}}{\dot{m}_c} \quad (5)$$

- (iv) *Distortion index (DI)*: The flow distortion at the combustor face or the intake exit is measured using distortion index and is defined by considering the stagnation pressure profile at the intake exit as given in Eq. 6.

$$\text{DI} = \frac{P_{0f \max} - P_{0f \min}}{\overline{P_{0f}}} \quad (6)$$

- (v) *Sustainable backpressure ratio (PR_b)*: The ratio of maximum backpressure that can be sustained in the intake prior to unstart or the normal shock moves upstream of the cowl, leading to complete separation of the ramp boundary layer and forcing a large mass spillage is called as sustainable backpressure ratio [27]. This is an indication of the backpressure up to which the intake can operate steadily. It should be noted that the peak TPR (discussed in Sect. 3) and the sustainable backpressure ratio correspond to the same operating point and are used interchangeably.

$$\text{PR}_b = \frac{P_{f_{\text{back}}}}{P_\infty} \quad (7)$$

2.4 CFD Analysis

The mathematical equations that govern the flow inside a supersonic intake are the conservation of mass, momentum, energy and the equation of state frequently referred to as compressible form of Navier–Stokes equations. In the present study, to properly represent the effect of turbulence with least computational cost, Favre-averaged Navier–Stokes (FANS or compressible RANS) equations are solved [29].

In the FANS/RANS approach, there has been an increasing thrust to model the turbulence stresses and heat fluxes using minimum number of equations, such that the computational effort is reduced and the model can be used as a design tool.

Therefore, a number of validation studies have been carried out in the literature to demonstrate the prediction capability of various eddy viscosity models like the one-equation SA (Spalart–Allmaras), two-equation $k-\omega$, BSL and SST $k-\omega$ models to capture the canonical SWBLIs and the supersonic intake flowfield. As shown in these studies, the SST $k-\omega$ turbulence model shows superior capability to predict the onset and the amount of flow separation under adverse pressure gradient conditions with least computational cost [26, 30, 31] and, hence, has been chosen here over other models. The model combines the standard $k-\omega$ model near the wall and transformed $k-\varepsilon$ model in the outer region with some blending function. The transport equations for turbulent kinetic energy (k) and specific dissipation rate (ω) and the modelling constants can be found from Ref. [32].

The Governing equations (FANS equations with SST $k-\omega$ model [33]) have been solved using commercial CFD solver: CFX-17.0 [34]. The solver uses an element-based finite volume technique and has been verified previously for 3D supersonic and hypersonic flow configurations [34]. By using higher order schemes, though the numerical error reduces faster with the mesh or time step refinement, they are generally less numerically stable than their low-order counterparts. Therefore, to avoid the dispersive and diffusive discretization errors associated with the schemes, the convective fluxes are computed using high resolution scheme given by Barth and Jespersen [35]. This is a blend of first order upwind and bounded central difference schemes. The local time marching has been obtained using second order backward Euler scheme considering CFL criteria to reach the steady solution.

The intake flowfield has been simulated in the freestream Mach number range of 1.7–2.8 and 0° angle-of-attack at an altitude condition of 8 km. The freestream parameters at these conditions are $p_\infty=35,650$ Pa, $T_\infty=236$ K and a unit $Re_\infty: 1.8\text{--}3.0 \times 10^7 \text{ m}^{-1}$. The high freestream Reynolds number indicates that the flowfield remains fully turbulent in the major part of the intake; thus, the boundary layer is assumed to be turbulent from the beginning.

In the simulated operating condition, as the stagnation temperature remains below 700 K, the working fluid air has been modelled as an ideal gas, with the fluid properties like specific heat capacity (C_p), thermal conductivity (λ) and viscosity (μ) are defined as a function of temperature. Here, the viscosity is modelled using the model provided by Sutherland (1893) [34], obtained from kinetic theory for dilute gases. The specific heat variation with temperature has been modelled using a curve fit. However, it can also be modelled using NASA polynomial format. And the thermal conductivity of air has been modelled using the modified Eucken Model (2001) [34]. The models and the corresponding constants are as follows:

$$\mu(T) = \mu_0 \frac{T_0 + C}{T + C} \left(\frac{T}{T_0} \right)^{1.5} \quad (8)$$

$$C_p(T) = 955.63 + 0.1761 T; \quad 50 - 1500 \text{ K} \quad (9)$$

$$\lambda(T) = \mu C_v \left(1.32 + \frac{1.77R}{C_v} \right) \tag{10}$$

where T_0 is the reference temperature, 291.15 K; μ_0 is the reference viscosity at T_0 , 1.827×10^{-5} Pa s; C is the Sutherland's constant, 120 K, C_p and C_v are the specific heat at constant pressure and volume, respectively.

Grid generation: The computational domain used for the study is shown in Fig. 3a. The domain with symmetry at the span-wise midplane has been considered, since the geometry and the flowfield are symmetric about it. To provide accurate boundary conditions, an outer flow domain is created above, below and in the span-wise direction of the intake geometry up to an extent of about 8, 4 and 4 times the cowl height, respectively. The outer domain boundaries are so placed to ensure that the leading edge shocks pass through the outer boundary and avoid any shock reflection at off-design operations.

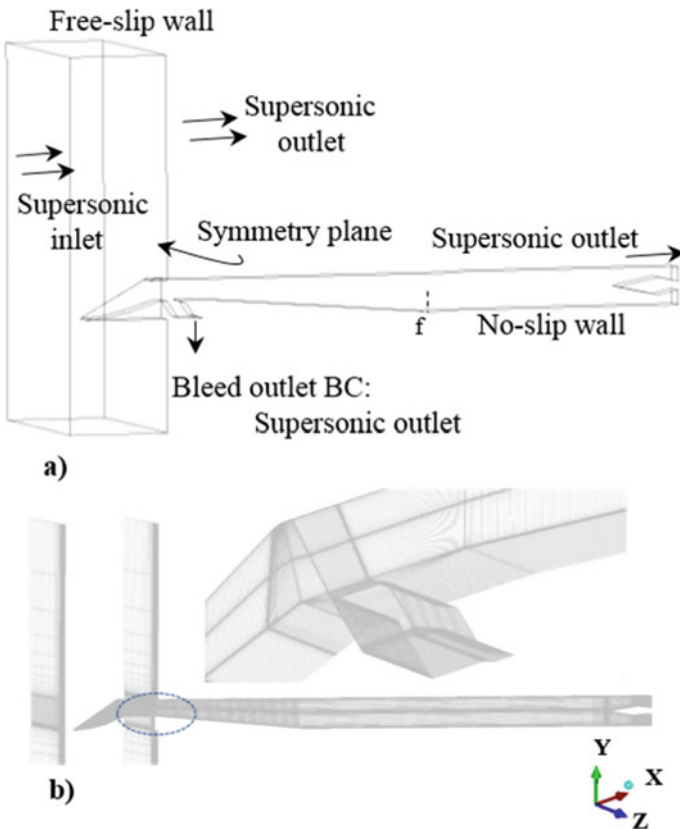


Fig. 3 a Computational domain with applied B.C. b A schematic of the mesh used for 3D computation

The CAD utility NX 9 has been used for modelling the computational domain and the domain has been meshed completely with hexahedral cells using ICEM CFD grid generation tool within the ANSYS Workbench [34], as shown in Fig. 3b. All the geometric features including cowl and ramp lip radii are captured in the modelling and proper cell quality is maintained using suitable block structures. To capture the turbulent boundary layer and the complete flow physics of SWBLIs, a systematic approach with mesh refinement has been carried out and numerical sensitivities were tested at the ramp corner, throat and the walls. In particular, a finer mesh resolution is used for all the grids at the geometric corners, bleed plenum and near the walls to resolve the steep gradients. For the near wall refinement, a grid stretching factor (the rate of increase in grid spacing from the wall) of about 1.3 is maintained. Further, since the flow through the intake alone is of interest, a coarse mesh resolution is used for the outer domain.

2.5 *Boundary Conditions*

The boundary conditions applied for the domain are as shown in Fig. 3a. All the solid walls are modelled as stationary and no-slip adiabatic boundary, where the velocity components, pressure gradient and heat flux are assigned as zero. At the inlet to the supersonic intake, the freestream conditions are applied as a supersonic velocity inlet boundary that includes assigning of static pressure, static temperature and velocity. The turbulence quantities at the inlet are specified in terms of eddy viscosity ratio and turbulence intensity, where a value of about 5% and 0.5%, respectively, is used. The outlet boundary after the downstream throttle has been modelled as supersonic outlet, where the flow variables are determined from the interior of the domain by extrapolation. It should be noted that though the flow at the intake exit is subsonic, because of the presence of the throttle the subsonic flow accelerates to supersonic Mach numbers at its outlet and hence eliminates the requirement to specify the exit pressure (see Fig. 2) [14]. The flow below the ramp lip is predominantly supersonic after the lip bow shock. However, the flow above the cowl could be transonic in nature depending on the freestream Mach number and the shock structure ahead of the cowl. In order to avoid specifying the exact flow conditions for subsonic flow, the outlet boundary in the external domain above the cowl has been placed sufficiently downstream such that the high pressure regions dissipate, or the flow expands to supersonic conditions. The supersonic flows at the outlet boundaries in the outer domain now can be handled easily and have been assigned as supersonic outlet, where the flow variables are determined from the interior of the domain by extrapolation. As discussed in Sect. 2.2, the exit of the bleed system has been designed in the shape of a convergent–divergent nozzle to achieve supersonic flow at its outlet. Therefore, the bleed outlet is also modelled as supersonic outlet. The far-field boundaries are assigned as slip-walls, where the velocity normal to it and the shear stress are assigned as zero. And the symmetry plane is assigned with zero-gradient of flow variables.

Initial Conditions. To reduce the run time, for the first simulation at each upstream conditions without throttle, the domain is initialized with flow properties obtained from 1D shock calculations. For the subsequent simulations at different throttling conditions, the previous converged solutions are used for initialization.

The point of convergence of the numerical simulations have been identified by (i) considering the overall mass, momentum and energy balance in the domain, with a criterion of RMS (root mean square) residuals below 10^{-5} and (ii) the stabilization of several flow property monitors used at the intake throat and exit sections. In the converged solutions, the difference between the mass flow rates at the intake entrance, and the intake as well as bleed exit (inflow minus outflow divided by inflow) are found to be within 0.3%, which is a good indicator of convergence.

2.6 Grid Independence Study

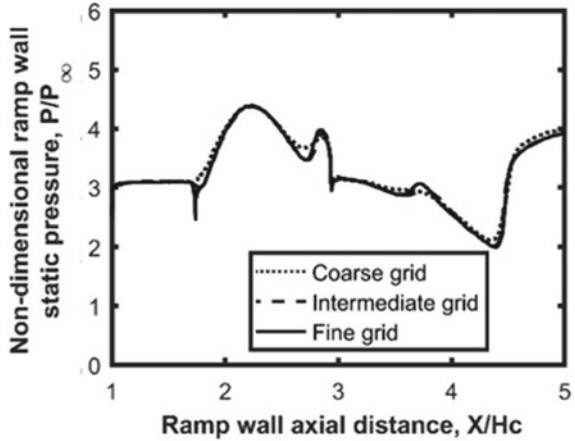
To accurately capture the internal flowfield with optimal number of cells and minimum error, three sets of grids have been considered for the simulation. The detail strategy used for grid generation is explained in Sect. 2.4. The computational results for the coarse mesh having 7.45 million cells showed a maximum wall Y^+ of about 11. In order to reduce the wall Y^+ and properly capture the shocks, the grid is successively refined twice close to no-slip boundaries, at regions of sharp geometrical transitions and axially at the zones of steep pressure gradients (shocks) across the intake. The details of the maximum wall Y^+ at EBR—30.7% and the approximate cell count for all the three grids are presented in Table 2. Moreover, Fig. 4 shows the ramp wall static pressure distribution for all the three grids. As shown in the figure, the pressure peaks are predicted quite accurately with the intermediate grid and going to fine grid does not show any significant improvement. Thus, the grid convergence is achieved with the intermediate mesh and has been considered for all remaining simulations.

Estimation of grid convergence (GCI). To quantify the numerical error in the computational result because of discretization, a verification analysis has been carried out using grid convergence index (GCI), as suggested by Celik et al. [36]. The analysis shows that the discretization error for the maximum intake exit Mach number converge at an order of 1.455. In addition, the uncertainty in its prediction in the fine

Table 2 Details of mesh resolution of all three grids

Level of resolution	3D cells (millions)	First cell distance, y (mm)	Max. wall Y^+
Coarse, G1	7.45	0.01	11
Intermediate, G2	13.67	0.005	2.5
Fine, G3	15.4	0.002	1

Fig. 4 Comparison of non-dimensional ramp wall static pressure for three different grids; $M_\infty=2.2$, EBR—30.7%



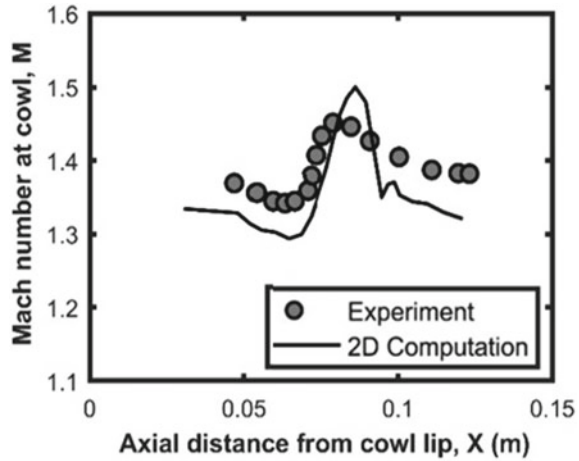
grid solution and the intermediate grid solution are 0.762% and 1.03%, respectively. As well as the relative error is found to be below 0.01 for the intermediate grid solution.

2.7 Validation Study

To further ensure the effect of turbulence model and boundary condition uncertainties, the numerical methodology has been validated with the supersonic intake experimental data of Neale and Lamb [37]. For this, a rectangular intake geometry with a flush slot bleed located at the upstream of the throat has been considered for the simulation. The model consists of a supersonic diffuser, a throat followed by a subsonic diffuser. The supersonic diffuser consists of two external ramps with a deflection angle of 7° each relative to the upstream flow, and a cowl angle of 4° relative to the freestream. The subsonic diffuser consists of a straight upper wall with three different lower wall divergence angles. Moreover, out of the different bleed configurations tested, the case with 1.8% supercritical bleed mass flow has been considered. Further details on the geometry can be found in Ref. [37]. The simulation has been carried out at the test conditions of $M_\infty = 2.2$, $P_{0\infty} = 1.355$ bar and $T_\infty = 153$ K (altitude of 18.3 km).

The computational domain for the model and the grid generation strategies are maintained similar to that explained above. Further, a grid independence study has been carried out to have optimum number of cells. Figure 5 shows the comparison of the predicted Mach number close to the cowl above the bleed with the experimental data, for a supercritical mode of operation. As shown in the figure, the overall trend of slight drop in Mach number ahead of the throat followed by the Mach number increase across the expansion fans and then the reduction because of barrier shock are captured quite accurately. However, the profile is slightly shifted to the right, which

Fig. 5 Comparison of Mach number distribution close to the cowl wall with experiment [23]; $M_\infty=2.2$



could be because of the uncertainties in the exact location of measurement. Further, the peak Mach number because of the expansion fans is slightly over predicted. This discrepancy is probably because of the mismatch in the exact rear edge radius not known from the experiment, or the unsteady nature of the SWBLIs not captured in the simulation. However, the overall difference is within 4% of the data. The overall favourable agreement between the predicted results with the data demonstrate that FANS calculations with SST $k-\omega$ model are capable of predicting the supersonic intake mean flowfield as well as the flow through the bleed system quite accurately. For a detailed validation study, the reader should follow the earlier studies by the author [38].

3 Results and Discussion

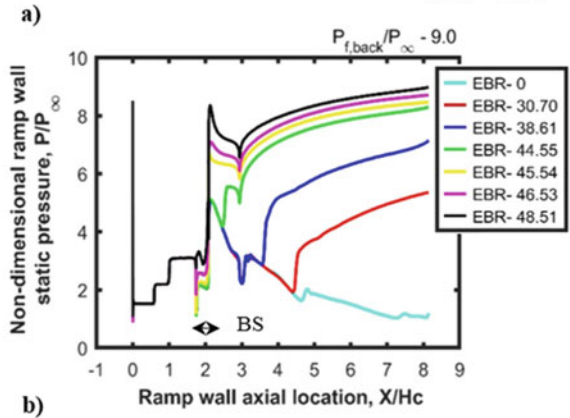
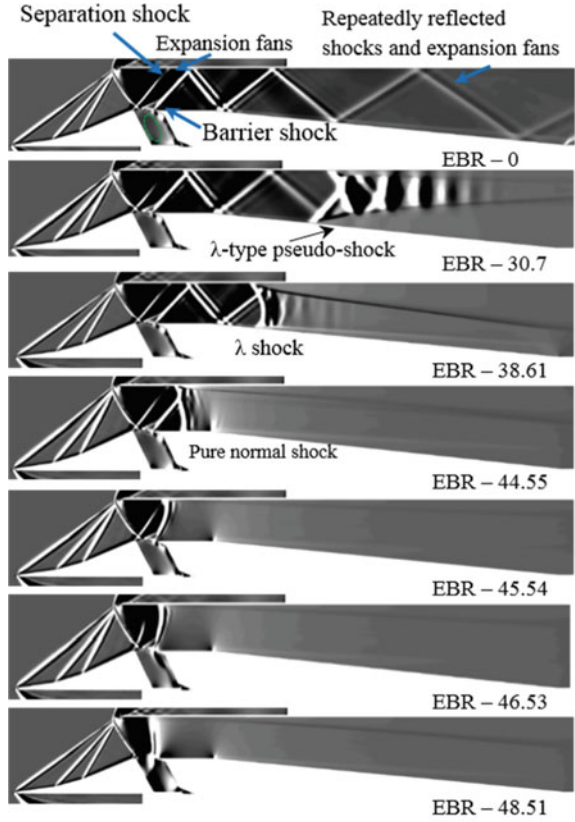
In this section, the detailed results of numerical simulation describing the internal flowfield and the intake performance parameters are presented.

3.1 Internal Flow Characteristics

3.1.1 Design Conditions, $M_\infty=2.2$, $AoA=0^\circ$

The internal flowfield of the intake has been investigated at different modes of operation starting from an un-throttled condition (EBR—0%) till the flow unstarts, by gradually increasing the degree of throttle. Figure 6 shows the contours of axial density gradient ($d\rho/dx$) and the corresponding ramp wall static pressure on the

Fig. 6 Contours of **a** axial density gradient and **b** ramp wall static pressure distribution at different EBRs till the flow unstarts; $M_\infty=2.2$



symmetry plane of the intake, for different EBRs at a freestream Mach number 2.2. In the contours, the shocks are visibly thicker because of the numerical interpolation, and the black colour shows the regions of flow acceleration or expansion. As shown in the figure, the incoming flow is first compressed across the ramp lip bow shock followed by two oblique shocks, and then the cowl lip shock that turns the flow back into the system. The cowl shock then impinges at the throat just downstream of the ramp shoulder. It can be seen that in the presence of the bleed, the throat separation bubble because of the incident cowl SWBLI has reduced. The supersonic flow downstream of the cowl shock then expands at the bleed entrance resulting Prandtl–Meyer expansion fans, and a part of the low energy boundary layer gets diverted into the bleed plenum. Following this, as the flow turns around the bleed rear edge a bow shock is generated, called as barrier shock [25]. It should be noted that since the boundary-layer growth is controlled at the throat, its thickness in the subsonic diffuser reduces. Consequently, the SWBLIs weaken and hence lower the stagnation pressure loss. Downstream of the bleed, the barrier shock and the expansion fans impinge on the cowl wall and keep reflecting till the intake exit. The repeatedly reflected shocks and expansion fans are found to get weakened and the mean flow expands in the subsonic diffuser (un-throttled); similar to that observed in the case without bleed system. The flowfield in the bleed plenum shows that the low momentum boundary layer only enters close to its rear edge, and a large recirculation region is observed at the upstream wall. The diverted supersonic flow then encounters a fluidic compression and expansion close to the trailing wall like a supersonic jet before diffusing to low subsonic speed. The subsonic flow reaccelerates in the converging–diverging section at the plenum exit and gets choked at its throat.

With the application of exit throttle, a terminal shock is induced in the flowfield across which the static pressure increases to the backpressure conditions; however, the flowfield upstream of it remains the same, as explained for the un-throttled case. For EBR—30.7%, the normal shock stands at an axial location of about $X/H_c = 4.5$. At this location, since the Mach number upstream of the shock is close to 1.7, a very strong normal SWBLI occurs and instead of a single shock a λ -type pseudo-shock is observed in the subsonic diffuser; downstream of which the flow becomes subsonic. It should be noted that as per the available research literature on canonical normal SWBLI [3, 4, 38], for a nominal boundary-layer thickness, a single bifurcated shock is observed in the Mach range of 1.3–1.5, that changes to a λ -type (normal) pseudo-shock in the Mach number range of about 1.5–1.9 and above this the structure changes to a X -type (oblique) pseudo-shock. As described by Matsuo et al. [4], the pseudo-shock in general can be divided into a region of shock train followed by a mixing region, where the shock train consists of a series of shocks with a strong bifurcated leading shock followed by a number of weak secondary shocks. In the λ -type pseudo-shock, the leading shock shows a bifurcated normal shock (λ) pattern, which form a “X” pattern with stronger interactions. For EBR—30.7%, it can be seen that downstream of the primary λ -shock four secondary shocks are induced followed by a mixing zone. Moreover, the last three shocks are pure normal shocks with a gradual reduction in the distance between them. Clearly, all the characteristic features of the λ -type pseudo-shock are captured in the computation. It should be

noted that the large separation region produced in the subsonic diffuser due to the strong SWBLI leads to a higher flow distortion at its exit. With increase in EBR, the terminal shock is found to move upstream with a gradual reduction in the exit Mach number. In this process, since the flow Mach number as well as the boundary-layer thickness ahead of the terminal shock decreases, the strength of the terminal SWBLI and the flow separation keep decreasing. Consequently, the structure of the shock train progressively changes to a train with lower length, a single λ -type shock and then to a pure normal shock, similar to that observed for the intake without bleed. For EBR—44.55%, the normal shock starts to interact with the barrier shock resulting in a complex shock structure after interaction. And with a further increase in throttling to EBR—45.54%, the shock gets stabilized at the bleed entrance. The operational point just before the normal shock stabilization that leads to optimum mass flow capture and total pressure recovery is called as the critical mode of operation. And the operational modes prior to critical point is known as the supercritical modes of operation. It should be noted that in the supercritical modes, since the terminal shock is positioned downstream of the bleed, the bleed entrance Mach number, the plenum pressure and the bleed mass flow ratio (BMFR) remain the same. As the terminal shock gets stabilized, a higher amount of boundary-layer mass flow is expelled through the bleed because of the higher static pressure difference between the entrance and the plenum; consequently, the plenum pressure and the TPR keep increasing (see Fig. 9a). The stabilization of shock continues up to a point where the plenum pressure matches the pressure upstream of it (EBR—48.51%), and then, the shock moves upstream of the cowl leading to unstart. At this condition, the mass flow capture is found to drop and the flow started to oscillate (buzz [8]). Therefore, as described in Sect. 2.3, further higher subcritical modes are not simulated here. For the convenience of reference, we shall call the point of unstart as peak operation.

The ramp wall static pressure distribution clearly indicates that the static pressure increases in steps across the ramp shocks. Following this, there is a drop in pressure across the expansion fans produced at the throat shoulder as well as the bleed entrance, and then, it increases sharply across the barrier shock produced at the bleed rear edge, raising the pressure ratio to about 5.0. Further downstream, alternate pressure peaks can be seen across the repeatedly reflected oblique shocks and expansion fans with a mean value decreasing because of flow expansion in the subsonic diffuser (EBR—0%). At different EBRs, the static pressure rises sharply across the leading terminal shock and then increases monotonically till the exit of the subsonic diffuser. Further, it can be seen that with increase in EBR the terminal shock keeps moving upstream, maintaining a fixed distribution ahead of it. At EBR—45.54%, the shock stabilization process is indicated by the step rise in pressure at the bleed rear edge as well as in the plenum. It can be seen that, as the shock gets stabilized, the static pressure at the throat downstream of the bleed decreases marginally, indicating that the throat length downstream of the bleed does not contribute to the sustainable backpressure. This is because, since the boundary-layer thickness and the separation bubble due to the terminal SWBLI at the throat are reduced in the presence of the bleed, the subsonic flow downstream of the terminal shock reaccelerates in the constant area duct, leading to a decrease in wall static pressure.

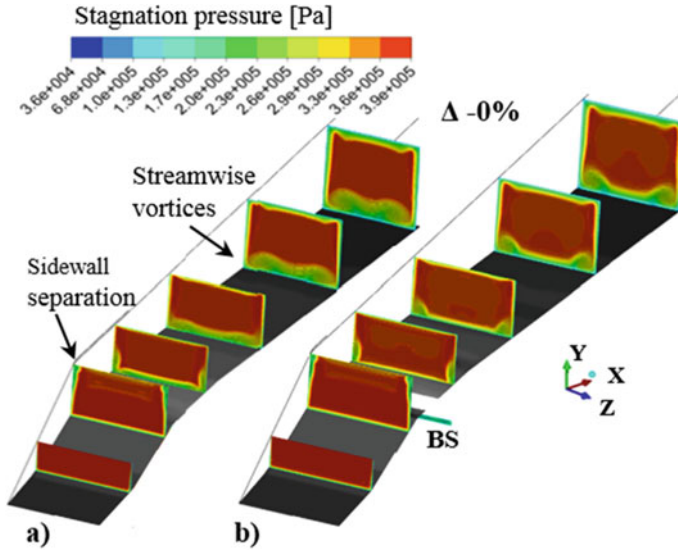


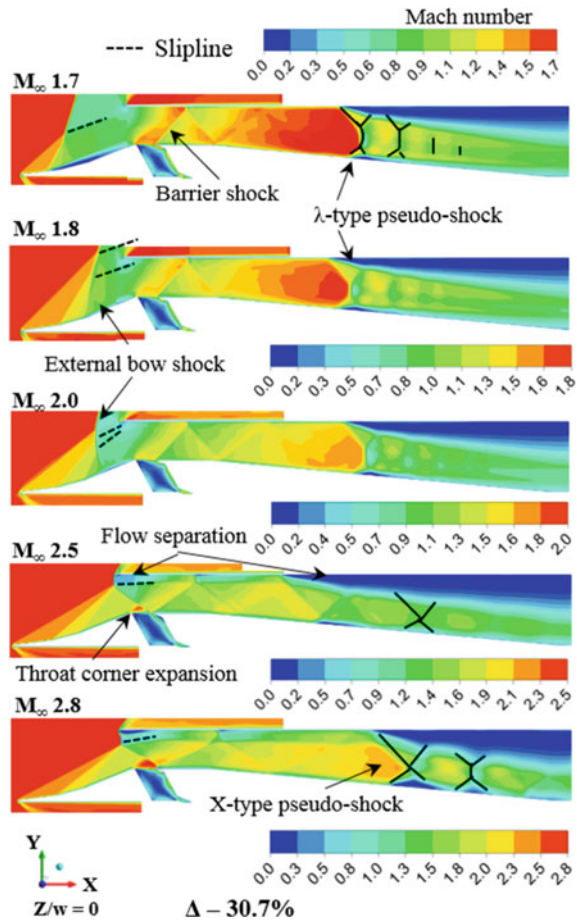
Fig. 7 Contours of stagnation pressure on selected cross-sectional planes **a** without and **b** with bleed system (X/H_c : 0.7, 1.6, 2.5, 3.4, 5.4, 7.9); $M_\infty=2.2$, $EBR_s=0\%$

Figure 7 shows the contours of stagnation pressure on the cross-sectional planes of the intake at selected axial locations (X/H_c : 0.7, 1.6, 2.5, 3.4, 5.4, 7.9) for the cases with and without the use of bleed, at $EBR=0\%$. As shown in Fig. 7a, a separation bubble is induced near the sidewall as a result of the interaction of the cowl shock with sidewall boundary layer (sidewall swept SWBLI). Following the separation, secondary cross flows are produced and are found to get deflected downwards at the throat. Further downstream, the secondary flows can be seen to migrate towards the symmetry plane resulting in two stream-wise vortices, that interact with the ramp boundary layer and grows in size as it propagates in the subsonic diffuser. In the presence of the bleed, it can be seen that a part of the secondary cross flows is diverted into the plenum leading to a decrease in the strength of the two stream-wise vortices. Consequently, the flow distortion as well as the stagnation pressure loss reduces.

3.1.2 Off-Design Conditions, $M_\infty: 1.7-2.8$, $AoA=0^\circ$

To study the effectiveness of the bleed system at off-design operations, the flowfield has been simulated at a range of off-design Mach numbers. Figure 8 shows the contours of Mach number on the symmetric plane of the intake at different freestream Mach numbers of 1.7, 1.8, 2.0, 2.5 and 2.8, and 0° angle-of-attack, for a supercritical mode of operation ($EBR=30.7\%$). It should be noted that the flowfield at higher EBRs is not presented here; however, a similar upstream movement of the terminal

Fig. 8 Contours of Mach number at off-design operations for EBR—30.7%; M_∞ :1.7–2.8, $AoA=0^\circ$

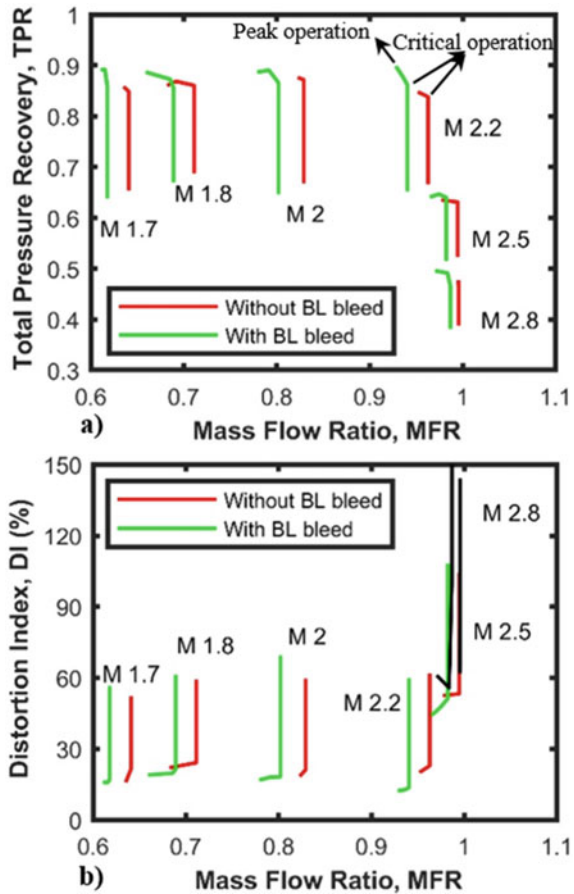


shock to match to the backpressure with a corresponding variation in its structure depending on the flow Mach number and its stabilization at the bleed entrance are observed at each upstream conditions till the intake unstarts, as explained for Mach 2.2 (Sect. 3.1.1). As shown in the figure, with the variation in the freestream Mach number the external compression shock structure as well as the flowfield around the bleed entrance changes depending on the shock strength. However, downstream of the bleed of the flowfield involving the repeatedly reflected shocks and expansion fans followed by a terminal shock remain almost similar at all upstream conditions. At the low off-design Mach number of 2.0, the ramp shocks become steeper and are expected to pass above the cowl. However, it can be seen that an additional bow shock is formed upstream of the cowl lip, since the post ramp shock Mach number is such that the flow “unstarts because of SWBLI”. The subsonic flow downstream of the bow shock then accelerates in the converging zone till the throat and finally goes through a series of shock and expansion waves. Moreover, since the flow remains subsonic

close to the cowl wall, no shock is produced from the cowl lip and its shoulder. At further lower Mach numbers of 1.8 and 1.7, a similar flowfield is observed except that the bow shock moves upstream leading to a higher mass as well as stagnation pressure loss across it. On the contrary, at high off-design Mach numbers the ramp shocks pass below the cowl. Consequently, two streams of flow having different level of compression enter the intake as well as the cowl shock keeps moving downstream towards the bleed rear edge. Because of the displacement of the incident cowl shock, a strong flow expansion is observed above the bleed entrance leading to a decrease in the static pressure difference that drives the flow into the bleed (Fig. 8).

Several differences in the flow characteristics at low and high off-design conditions can be noted. At high off-design Mach numbers (i) for EBR—30.7%, since the flow Mach number ahead of the terminal shock is above 1.9, a X-type pseudo-shock structure is observed leading to a higher flow distortion (see Fig. 9); whereas at the low off-design Mach numbers, a λ -type pseudo-shock is produced similar to that at

Fig. 9 Comparison of **a** performance characteristics, **b** DI with and without bleed; M_∞ : 1.7–2.8



the design condition. Moreover, (ii) the strength of stream-wise vortices produced at the sidewalls increase adding to the flow distortion effect, compared to that at the low off-design Mach numbers. However, it is found that at all upstream conditions (a) the pseudo-shock weakens to form a single normal shock close to the critical operation at the bleed and (b) the ramp and bow shocks interact ahead of the cowl lip resulting in sliplines or vortex sheets that enter into the intake close to the cowl surface. Downstream, the sliplines form a mixing layer leading to a relatively lower stagnation pressure region close to the cowl wall compared to that at the ramp. It should be noted that the presence of sliplines in the domain results in little buzz or low amplitude oscillations in the system (Ferri criterion), as shown in the previous studies in Refs. [6–8].

The wall static pressure at various off-design conditions shows a similar trend as shown in Fig. 6b. However, it is found that the sustainable backpressure, critical exit Mach number and the flowfield distortion keep increasing with the operating Mach number. The flowfield in the subsonic diffuser indicates that, at the off-design Mach numbers, the major flow separation downstream of the terminal shock occurs close to the cowl wall compared to that at the ramp wall for the design condition. This is because of the ingestion of sliplines at the off-design Mach numbers resulting in a lower stagnation pressure near the cowl wall compared to that because of thick boundary layer at the ramp, where the flow separation is triggered.

3.2 Performance Characteristics

Figure 9 shows the comparison of performance characteristics and the variation in DI at the intake exit with and without the boundary-layer bleed system, in the Mach number range of 1.7–2.8. It should be noted that, since the supercritical MFR at high off-design Mach numbers are close to unity, for the clarity in visualization the curves at Mach 2.8 are presented by black lines. The performance curve (cane curve) shows the variation in total pressure recovery (TPR) with the captured mass flow ratio (MFR) till the flow unstarts or the last stable operational point. As shown in the figure, for the cases without bleed the curves are in the shape of a vertical line with a constant MFR and increasing TPR, then the turning begins to the left with a reduction in mass flow ratio. The vertical branch of the curve indicates the supercritical modes of operation and the variation in pressure recovery occurs because of the increase in backpressure. At low backpressure, the terminal shock is formed at a higher flow Mach number, thus resulting in a lower TPR. As the backpressure increases, the shock moves upstream to regions of lower Mach number. Hence, the TPR keeps increasing with a fixed MFR. The bend/knee point of the curve shows the critical operation for which the shock strands at the throat entrance and both the TPR and the MFR become maximum. At a slight higher backpressure, the terminal shock moves upstream of the cowl, leading to unstart. This condition leads to a decrease in the MFR because of spillage ahead of the cowl, whereas the TPR remains nearly constant or decreases depending on the losses across the terminal SWBLI. With further increase

in backpressure, both MFR and the TPR are likely to drop; moreover, the flowfield becomes oscillatory in nature [6–8]. Therefore, higher subcritical modes of operation are not simulated here.

In the presence of the bleed, the characteristic curve remains similar to that explained above up to the critical operation, with a slight reduction in supercritical MFR. However, it can be seen that the pressure recovery does not drop after the critical point. This can be explainable from the analysis that, as the terminal shock gets stabilized at the bleed entrance, a higher amount of boundary-layer mass flow (BMFR) is removed through the bleed because of the higher static pressure difference. Consequently, the TPR keeps increasing due to the reduction in stagnation pressure loss across the normal shock as well as in the subsonic diffuser. Hence, the subcritical and supercritical branch of the performance/cane curve is connected by a line with increasing TPR and decreasing MFR, till the intake unstarts. Here, we shall call the point of unstart or the maximum pressure recovery in the presence of the bleed as peak operation.

To have a better understanding of the variation in the performance parameters with operating Mach number, various critical parameters such as supercritical MFR and BMFR, peak TPR and the critical exit Mach numbers are analysed and are presented in Figs. 10, 11 and 12. The variation in the pressure recovery (see Figs. 9a and 10) shows that, at low off-design Mach numbers the critical TPR without bleed remains almost constant. This is because, though the TPR is expected to increase with decrease in the Mach number due to the reduction in the losses across the weaker ramp shocks; it is compensated by the increase in the losses across the bow shock formed ahead of the cowl as a result of “unstart because of SWBLI”. However, it can be seen that at high off-design Mach numbers the TPR drops drastically. Because of the higher losses across the strong compression shocks, SWBLIs as well as the stream-wise vortices induced at the sidewalls. In the similar way, the variation in the supercritical MFR indicates that, at the design and high off-design Mach numbers the value is close to unity, and as the Mach number decreases the MFR drops rapidly

Fig. 10 Variation of critical/peak TPR and supercritical MFR with freestream Mach number; M_∞ : 1.7–2.8

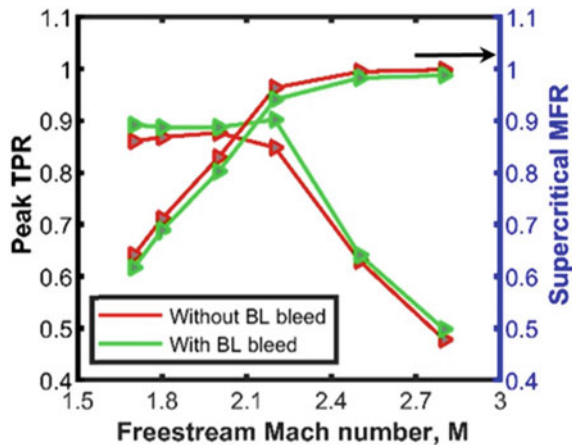


Fig. 11 Variation of supercritical BMFR with freestream Mach number; M_∞ : 1.7–2.8

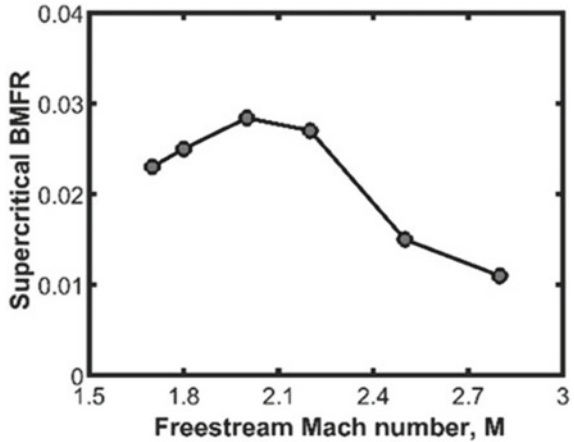
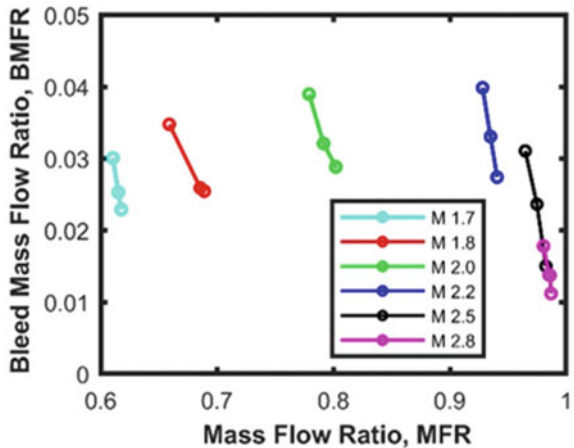


Fig. 12 Variation of BMFR with MFR at different modes of operation; M_∞ : 1.7–2.8



because of the upstream movement of the ramp shocks as well as the “unstart because of SWBLI” approximately below Mach 2.1. The slight drop in MFR at Mach 2.2 is caused by the spillage ahead of the cowl, since the ramp shocks are marginally pushed upstream because of the boundary-layer effects as well as the sidewall swept SWBLI. On the contrary, with the use of bleed, the critical as well as the peak TPR increases at all upstream conditions compared to the case without bleeding system, with a slight loss in boundary-layer mass flow through it. This is because of the reduction in the losses across the SWBLIs as well as the stabilization of the terminal shock at its entrance. The increase in peak TPR indicates that the initiation of buzz oscillation is delayed or the steady operation before the start of buzz is enhanced.

The variation in the DI at the intake exit indicates that a large flow distortion is observed at the supercritical modes of operation that keeps decreasing with increase in backpressure up to the critical operation (see Fig. 9b). Moreover, with the use

of bleed since the SWBLIs weaken, the critical DI further reduces. Clearly, for the present configuration the critical DI varies in the range of 19–25% for the design and low off-design Mach numbers, which decreases to about 15–20% with the use of bleed. However, at high off-design Mach numbers the critical DI increases to about 40%. This is caused by the large separation regions as well as the strong stream-wise vortices induced because of the SWBLIs. In addition to the decrease in the distortion, the critical exit Mach number too decreases with the introduction of bleed. It is found that, in the complete range of operation, the critical area-averaged exit Mach number reduces by about 0.04.

Figure 11 shows the variation of supercritical BMFR with freestream Mach number. It can be seen that the BMFR at high off-design Mach numbers are smaller compared to that at low off-design Mach numbers. This is because of the reduction in the bleed entrance pressure difference (that drives the flow) at high off-design Mach numbers, due to the strong expansion fans produced at the bleed as the cowl shock moves downstream, whereas at low off-design Mach numbers the bleed entrance pressure decreases gradually with the upstream movement of the bow shock. Figure 12 shows the variation in the BMFR with the captured MFR at different Mach numbers up to the peak operation. Clearly, the BMFR as well as the MFR remains the same up to the critical mode. As the normal shock gets stabilized, the BMFR keeps increasing with a corresponding drop in MFR. It can be seen that for the present bleed configuration the BMFR varies between 1 and 4% in the complete range of operation (M_∞ : 1.7–2.8).

To sum up, for the present bleed configuration, at Mach number of 2.2, the peak TPR increases to about 0.9 from 0.84 and the sustainable backpressure increases by about 12% compared to the case without bleed, with a supercritical BMFR of 2.7%. Similarly, the configuration is found to increase the sustainable backpressure by about 5.6%, 3.3%, 5.6%, 7.2% and 7.0% at Mach numbers of 1.7, 1.8, 2.0, 2.5 and 2.8, respectively, with a corresponding supercritical BMFR of 2.3%, 2.5%, 2.7%, 1.5% and 1.1%, respectively. Moreover, with the use of bleed, since the throat separation bubble is reduced and the cowl shock is pushed downstream, the overall mass capture is found to increase marginally at all operating conditions prior to “unstart because of SWBLI”.

4 Conclusions

In the present study, a numerical investigation has been carried out to evaluate the impact of a fixed-exit flush slot bleed system applied downstream of the throat, on the off-design performance characteristics of a rectangular mixed-compression intake. The viscous flowfield has been obtained by solving Favre-averaged Navier–Stokes (FANS) equations with SST $k-\omega$ turbulence model. Moreover, the numerical method deployed has been validated with the experimental data from literature. The analysis has been carried out at several modes of operation till the flow unstarts, in the freestream Mach number range of 1.7–2.8 and 0° angle-of-attack, corresponding

to a unit Reynolds number of approximately $1.8\text{--}3.0 \times 10^7 \text{ m}^{-1}$. The performance has been evaluated in terms of total pressure recovery (TPR), mass flow ratio (MFR), sustainable backpressure ratio (or peak TPR) and distortion index (DI). The highlights of the results are as follows.

The flow features indicate that with the use of the bleed, the low energy boundary layer, throat separation bubble as well as the secondary cross flows (or stream-wise vortices) produced due the sidewall swept SWBLI are successfully removed near the throat at all operating conditions, in the supercritical modes of operation. Consequently, the exit flowfield distortion as well as the critical TPR improves considerably compared to the intake without bleed; because of the reduction in the total pressure loss as well as the flow separation across the SWBLIs. Moreover, since the terminal shock gets stabilized at the bleed entrance after the critical operation, the TPR or the sustainable backpressure further increases up to its peak operation leading to a delay in the initiation of buzz oscillations or the stable flight operation is extended.

The variation the BMFR shows that compared to the low off-design Mach numbers, at high off-design Mach numbers the BMFR is smaller. This is because of the reduction in the pressure difference that drives the flow at high off-design Mach numbers, due to the strong expansion fans produced at the bleed entrance as the cowl shock moves downstream. For the present bleed configuration, the BMFR varies between 1 and 4% in the complete range of operation (M_∞ : 1.7–2.8). Furthermore, it is found that the critical area-averaged intake exit Mach number reduces by about 0.04 in the complete operating regime. The analysis shows that, with the use of bleed, the overall mass capture is found to increase at all operating conditions prior to “unstart because of SWBLI”, since the throat separation bubble is reduced and the cowl shock is pushed downstream. It is observed that at off-design Mach numbers, since the cowl shock incident point changes relative to the bleed entrance, the exact structure of the SWBLI at its entrance varies. Therefore, the effectiveness of the fixed geometry bleed system at off-design operation strongly depends on the bleed location apart from its sizing.

Acknowledgements The authors acknowledge DRDL, Hyderabad, for supporting the work (project code JATP/P-VIII/P-2018/159) and Mr. Vivek R. of DRDL, Ramjet Propulsion Division, for his technical guidance during the study.

References

1. Mahoney JJ (1990) Inlet for supersonic missiles. AIAA education series, AIAA, Washington, DC, 1
2. Seddon J, Goldsmith E (1999) Intake aerodynamics. AIAA
3. Babinsky H, Harvey JK (eds) (2011) Shock wave boundary-layer interactions, vol 32. Cambridge University Press
4. Matsuo K, Miyazato Y, Kim HD (1999) Shock train and pseudo-shock phenomena in internal gas flows. Prog Aerosp Sci 35(1):33–100. [https://doi.org/10.1016/s0376-0421\(98\)00011-6](https://doi.org/10.1016/s0376-0421(98)00011-6)

5. Fisher SA (1986) Three-dimensional flow effects in a two-dimensional supersonic air intake. *J Propul Power* 2(6):546–551. <https://doi.org/10.2514/3.22940>
6. Abedi M, Askari R, Soltani MR (2020) Numerical simulation of inlet buzz. *Aerosp Sci Technol* 97:105547. <https://doi.org/10.1016/j.ast.2019.105547>
7. Yamamoto J, Kojima Y, Kameda M, Watanabe Y, Hashimoto A, Aoyama T (2020) Prediction of the onset of supersonic inlet buzz. *Aerosp Sci Technol* 96:105523. <https://doi.org/10.1016/j.ast.2019>
8. Hirschen CM, Herrmann D, Gülhan A (2007) Experimental investigations of the performance and unsteady behaviour of a supersonic intake. *J Propul Power* 23(3):566–574. <https://doi.org/10.2514/1.25103>
9. Kantrowitz A, Donaldson CD (1945) Preliminary investigation of supersonic diffusers. NACA ACR No. L5D20
10. Sun B, Zhang KY (2010) Empirical equation for self-starting limit of supersonic inlets. *J Propul Power* 26(4):874–875. <https://doi.org/10.2514/1.46798>
11. Abedi M, Askari R, Sepahi-Younsi J, Soltani MR (2020) Axisymmetric and three-dimensional flow simulation of a mixed compression supersonic air inlet. *Propul Power Res* 9(1):51–61. <https://doi.org/10.1016/j.jprr.2020.01.002>
12. Herrmann D, Triesch K (2006) Experimental investigation of isolated inlets for high agile missiles. *Aerosp Sci Technol* 10(8):659–667. <https://doi.org/10.1016/j.ast.2006.05.004>
13. Herrmann D, Blem S, Gulhan A (2011) Experimental study of boundary-layer bleed impact on ramjet inlet performance. *J Propul Power* 27(6):1186–1195. <https://doi.org/10.2514/1.b34223>
14. Chen H, Tan HJ, Liu YH, Zhang QF (2019) External-compression supersonic inlet free from violent buzz. *AIAA J* 57(6):2513–2523. <https://doi.org/10.2514/1.J057811>
15. Titchener N, Babinsky H (2013) Shock wave/boundary-layer interaction control using a combination of vortex generators and bleed. *AIAA J* 51(5):1221–1233. <https://doi.org/10.2514/1.j052079>
16. Zuo F, Huang G (2018) Numerical investigation of bleeding control method on section-controllable wave-catcher intakes. *Acta Astronaut* 151:572–584. <https://doi.org/10.1016/j.actaastro.2018.06.059>
17. Choe Y, Kim C, Kim K (2020) Effects of optimized bleed system on supersonic inlet performance and buzz. *J Propul Power* 36(2):211–222. <https://doi.org/10.2514/1.b37474>
18. Zhang J, Yuan H, Wang Y, Huang G (2020) Experiment and numerical investigation of flow control on a supersonic inlet diffuser. *Aerosp Sci Technol* 106:106182. <https://doi.org/10.1016/j.ast.2020.106182>
19. Haberle J, Gulhn A (2007) Internal flowfield investigation of a hypersonic inlet at Mach 6 with bleed. *J Propul Power* 23(5):1007–1017. <https://doi.org/10.2514/1.29669>
20. Das S, Prasad JK (2010) Unstart suppression and performance analysis of supersonic air-intake adopting bleed and cowl bending. *J Inst Eng (India) Aerosp Eng J* 91:27–35
21. Liu H, Yan C, Zhao Y, Wang S (2019) Active control method for restart performances of hypersonic inlets based on energy addition. *Aerosp Sci Technol* 85:481–494. <https://doi.org/10.1016/j.ast.2018.12.025>
22. Hahn TO, Shih TP, Chyu WJ (1993) Numerical study of shock-wave/boundary-layer interactions with bleed. *AIAA J* 31(5):869–876. <https://doi.org/10.2514/3.11698>
23. Hamed A, Yeuan JJ, Shih SH (1995) Shock-wave/boundary-layer interactions with bleed. II - effect of slot location. *J Propul Power* 11(6):1236–1241. <https://doi.org/10.2514/3.23963>
24. Slater JW, Saunders JD (2010) Modeling of fixed-exit porous bleed systems for supersonic inlets. *J Propul Power* 26(2):193–202. <https://doi.org/10.2514/1.37390>
25. Davis DO, Willis BP, Hingst WR (1998) Flowfield measurements in a slot-bleed oblique shock wave and turbulent boundary-layer interaction. *AIAA paper* 1998-0032. <https://doi.org/10.2514/6.1998-0032>
26. Catalano P, Amato M (2003) An evaluation of rans turbulence modelling for aerodynamic applications. *Aerosp Sci Technol* 7(7):493–509. [https://doi.org/10.1016/s1270-9638\(03\)00061-0](https://doi.org/10.1016/s1270-9638(03)00061-0)

27. Reinartz BU, Herrmann CD, Ballmann J, Koschel WW (2003) Aerodynamic performance analysis of a hypersonic inlet isolator using computation and experiment. *J Propul Power* 19(5):868–875. <https://doi.org/10.2514/2.6177>
28. Soltani MR, Younsi JS, Farahani M (2015) Effects of boundary-layer bleed parameters on supersonic intake performance. *J Propul Power* 31(3):826–836. <https://doi.org/10.2514/1.b35461>
29. Marvin JG (1983) Turbulence modeling for computational aerodynamics. *AIAA J.* 21(7):941–955. <https://doi.org/10.2514/3.8182>
30. Bardina JE, Huang PG, Coakley TJ (1997) Turbulence modeling validation, testing, and development
31. Boychev K, Barakos GN, Stejrl R (2020) Flow physics and sensitivity to RANS modelling assumptions of a multiple shock wave/turbulent boundary layer interaction. *Aerosp Sci Technol* 97:105640. <https://doi.org/10.1016/j.ast.2019.105640>
32. Menter FR (1994) Two-equation eddy-viscosity turbulence models for engineering applications. *AIAA J* 32(8):1598–1605. <https://doi.org/10.2514/3.12149>
33. Menter FR (2009) Review of the shear-stress transport turbulence model experience from an industrial perspective. *Int J Comput Fluid Dyn* 23(4):305–316. <https://doi.org/10.1080/10618560902773387>
34. CFX-Solver ANSYS (2012) Software package, Release 17.0, Ansys Inc.
35. Barth TJ, Jespersen DC (1989) The design and application of upwind schemes on unstructured meshes. AIAA paper 89-0366
36. Celik IB, U. Ghia U, Roache PJ, Freitas CJ, Coleman H, Raad PE (2008) Procedure for estimation and reporting of uncertainty due to discretization in cfd applications. *J Fluids Eng* 130(7). <https://doi.org/10.1115/1.2960953>
37. Neale MC, Lamb PS (1966) Further tests with a variable ramp intake having a design Mach number of 2.2, HM Stationery Office. Ministry of Aviation Report, C. P. No. 826
38. Pattnaik SPS, Rajan NKS (2021) Theoretical design and performance evaluation of a two-ramp and a three-ramp rectangular mixed compression intake in the Mach range of 2–4. Design and development of aerospace vehicles and propulsion systems: 143–166. https://doi.org/10.1007/978-981-15-9601-8_10

Alternative Propulsion Systems

JP-10 Propellant Powered Rotating Detonation Waves for Enhancing the Performance of Hypersonic and Supersonic Missiles



Kiran Ivin and Ajay V. Singh

Abstract The new detonation-based combustors for hypersonic and supersonic missiles could reduce the launch mass (up to 3–4 times) and body length (up to 2 times) of such systems considerably and are most sought after by researchers worldwide. Near future practical detonation-based engines will be based on liquid hydrocarbon fuels. A promising synthetic jet fuel used in many military applications is JP-10. We are interested in improving the performance of JP-10 by using ignition promoters like O_3 and H_2O_2 in trace amounts for applications in detonation-based hypersonic and supersonic missiles. The effect of these promoters is to enhance combustion rates and energy release rates simultaneously. Stable propagation of detonation waves near its limits without the danger of attenuation or failure for continuous operation of detonation-based combustors is an ongoing problem of interest for military and air force researchers worldwide.

Nomenclature

E_a	Activation energy (kJ mol^{-1})
P_{CJ}	Post-detonation pressure (bar)
R	Gas constant ($\text{Jkg}^{-1} \text{K}^{-1}$)
T_{CJ}	Post-detonation temperature (K)
V_{CJ}	CJ detonation velocity (ms^{-1})
V_{VN}	Post-shock velocity (ms^{-1})
\dot{e}	Energy or heat release rate ($\text{MJkg}^{-1} \mu\text{s}^{-1}$)
u_{CJ}	Particle velocity in the shock-attached frame of reference (ms^{-1})
Δ_i	Induction zone length (mm)
τ_i	Induction delay time (μs)

K. Ivin · A. V. Singh (✉)
Indian Institute of Technology, Kanpur, U.P. 208016, India
e-mail: ajayvs@iitk.ac.in

K. Ivin
e-mail: kiranaf@iitk.ac.in

Δ_e	Exothermic zone length (mm)
τ_e	Exothermic time (μs)
Δ_r	Reaction zone length (mm)
$\dot{\sigma}$	Thermicity (μs^{-1})
Δh^0	Heat of reaction extrapolated to zero temperature (MJkg^{-1})
θ	Effective activation energy parameter (—)
χ_i	Stability parameter (—)
ε_i	Activation energy of the induction process (—)
$\dot{\sigma}_{\text{max}}$	Maximum thermicity (μs^{-1})

1 Introduction

The new detonation-based combustors for hypersonic and supersonic missiles could reduce the launch mass (up to 3–4 times) and body length (up to 2 times) of such systems considerably and are most sought after by researchers worldwide. Near future practical detonation-based engines will be based on liquid hydrocarbon fuels. The researchers continue to push the frontiers of propulsion technology in an attempt to discover a better and more efficient fuel for supersonic combustion and detonation-based propulsion systems. On the ground, technology demonstration of JP-10-hydrocarbon-fuelled dual combustion ramjet has been recently tested by the DARPA, US Navy, and Boeing for its exclusive use in supersonic and hypersonic missiles as reported by Andreadis [1]. A leading choice of fuel for scramjets, ramjets, and detonation-based engines that seem to drive the future of propulsion systems is JP-10 ($\text{C}_{10}\text{H}_{16}$). JP-10 is often used in volume-limited scramjet applications due to its high-energy density. It has a high-volumetric energy density due to its strained cyclic geometric structure. It is presently used as missile fuel by the US military [2]. A high-volumetric energy density and superior performance at lower temperatures are critical for high-performance characteristics of supersonic and hypersonic missiles, which makes JP-10 an ideal fuel for missile applications. Its heat of combustion (39.4 MJ/L) is substantially higher than the conventional petroleum-derived fuels, such as JP-8 (34.5 MJ/L). The high-performance characteristics like a density of 0.94 g/cm^3 , a specific impulse of 297.4 s (the thrust per mass flow rate at the nozzle), and a low-freezing point of $-79 \text{ }^\circ\text{C}$ [3] make JP-10 an ideal fuel for applications in high-speed propulsion systems. JP-10 also acts as an excellent endothermic liquid hydrocarbon fuel and can act as an active cooling system to reduce the severe heat loads due to aerodynamic heating. JP-10 decomposes to a set of pyrolysis products that can be quite different from those of conventional jet fuels. It undergoes thermal decomposition at high temperatures to smaller gaseous species like hydrogen, methane, and ethylene, and therefore act as a heat sink during its thermal pyrolysis or decomposition at high temperatures [4]. The present study focuses on the detonation chemistry of JP-10, which is practically a single-component fuel. It is comprised of 96.5

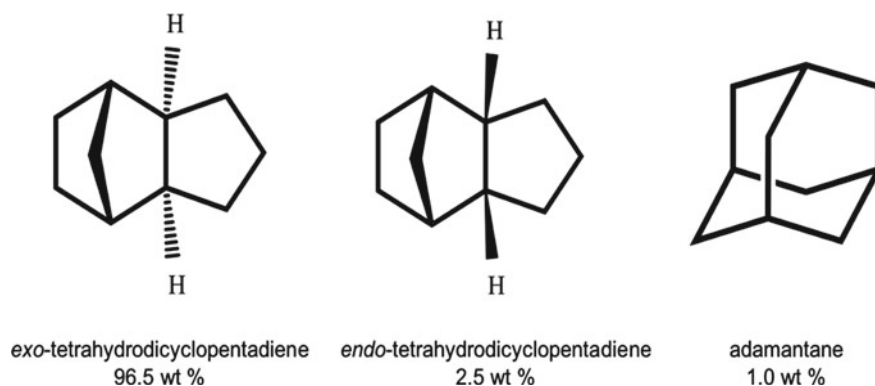


Fig. 1 Molecular structure of major components of JP-10

Table 1 Key properties of JP-10

Property	Value
Average formula	$C_{10}H_{16}$
H/C ratio (mole)	1.6
Average molecular weight (g/mol)	136.2
LHV (MJ/kg)	43.0
Model formula	$C_{10}H_{16}$

wt% exo-tetrahydrodicyclopentadiene, 2.5 wt% endo-tetrahydrodicyclopentadiene, and 1.0 wt% adamantane (Fig. 1). Key properties of JP-10 are listed in Table 1.

The fuel-oxidizer chemistry of a detonating mixture significantly affects the detonation cell size and the ZND length and time scales. In the previous studies, a linear correlation was found to exist between the induction zone length and the detonation cell size. Crane et al. [5] recently studied the effect of ignition promoters on hydrogen–oxygen detonation structure. They observed that the addition of ozone in trace amounts could significantly reduce the induction length and time scales of certain mixtures without affecting their thermodynamic and gas-dynamic properties, allowing the effect of induction time or length to be studied in isolation. It was shown that the addition of ozone could significantly reduce the average cell size of a detonation wave, which, in turn, could make the detonation wave more robust near its propagation limits. Kirillov et al. [6] showed that the addition of hydrogen peroxide in trace amounts (<1% by volume) could reduce the induction length and time scales substantially. Also, the addition of hydrogen peroxide was found to be effective in small concentrations, where its effect on induction length and time scales was substantial. However, at large concentrations, it was found that its impact on induction length and time scales was approximately the same.

It was observed that for fuel-air mixtures, the addition of the ignition promoter like H_2O_2 increases the production of OH radicals. The OH radical, during ignition, accelerates the chain branching process and shortens the ignition delay time. Thus,

production of OH radicals accelerates the chain branching process and results in reduced induction length and time scales as given in the work by Chen et al. [7], Ivin and Singh [8], and Kumar and Singh [9]. Kumar et al. [23] showed that the addition of ignition promoters like ozone and hydrogen peroxide in trace amounts could significantly reduce the induction length and time scales of a detonating mixture. Kumar et al. [23], Ivin and Singh [8], and Kumar and Singh [9] showed that the sensitization of fuel-oxidizer-diluent mixtures in the presence of ozone and hydrogen peroxide could widen the detonability limits of detonation-based engines. These calculations coupled with previous findings of a strong correlation between induction length and detonation cell structure suggest that the addition of dopant levels of ozone and hydrogen peroxide could significantly alter the detonation structure.

A clear understanding of the detonation phenomenon in a given fuel-oxidizer mixture can be explained by various critical parameters like energy release rate (\dot{e}), effective activation energy parameter (θ), and the non-dimensional stability parameter (χ_i) [10]. The energy release rate may be calculated by dividing the heat of reaction by the total time taken for the release of energy, which is approximately equal to the sum of the induction and exothermic time and is given as

$$\dot{e} = \frac{\Delta h^0}{\tau_i + \tau_e} \quad (1)$$

where \dot{e} , Δh^0 , τ_i , and τ_e are the energy release rate, the heat of reaction extrapolated to zero temperature, induction time, and exothermic time, respectively. The effective activation energy parameter may be defined as

$$\theta = \frac{E_a}{RT_{VN}} = \frac{1}{T_{VN}} \left(\frac{\ln \tau_2 - \ln \tau_1}{\frac{1}{T_2} - \frac{1}{T_1}} \right) \quad (2)$$

where θ is the effective activation energy parameter, E_a is the activation energy, R is the gas constant, and T_{VN} is the von Newman temperature. To evaluate the expression in Eq. (2), two constant-volume explosion simulations corresponding to (T_1, τ_1) and (T_2, τ_2) are run for each activation energy data point. Initial conditions for states one and two are generated by varying the shock velocity by Considering the effect of chemistry on stability, it was found that the stability of the reactant mixture depends on factors that effectively dictate the ratio of the induction length to the exothermic recombination zone length. Following the stability studies of previous investigators, Ng et al. [10] defined the stability parameter as the ratio of the induction-to the reaction-zone length. They also incorporated the temperature sensitivity of the induction reaction into the definition of the stability parameter χ_i . According to Ng et al. [10], the non-dimensional stability parameter is defined as

$$\chi_i = \varepsilon_i \frac{\Delta_i}{\Delta_r} \quad (3)$$

where ε_i represents the normalized activation energy of the induction reaction with respect to the post-shock temperature. It must be noted at this stage, that ε_i and θ are the same. Also, Δ_i and Δ_r are the induction and reaction zone lengths, respectively. Since the reaction zone length gradually varies as a function of temperature, it is difficult to define reaction zone length based on a particular post-shock temperature rise, heat release rate, or the local Mach number in the shock-attached frame of reference. Ng et al. [10] defined reaction length as the ratio of the particle velocity of a steady CJ detonation in the shock-attached frame of reference to the maximum thermicity, given by

$$\Delta_r = \frac{u_{\text{CJ}}}{\dot{\sigma}_{\text{max}}} \quad (4)$$

Therefore, the stability parameter can be written as

$$\chi_i = \varepsilon_i \frac{\Delta_i}{\Delta_r} = \varepsilon_i \dot{\sigma}_{\text{max}} \frac{\Delta_i}{u_{\text{CJ}}} \quad (5)$$

The stability parameter is often used in detonation studies to predict cell regularity. It is evident that stability of the detonation is a consequence of the temperature sensitivity of the chemical reactions. Small fluctuations in shock temperature can cause large perturbations in the induction delay time as well as the energy release rate of the recombination reactions. It should be noted that the induction time (or induction zone length) should be measured relative to the recombination time. An extended reaction zone or long reaction time is observed to have a stabilizing effect as it spreads out the energy release and thus reduces the effect of fluctuations in the induction time. Thus, a long reaction time has a stabilizing effect, and this is taken into consideration explicitly in the stability parameter of Ng.

The addition of ignition promoters like ozone and hydrogen peroxide in modest concentrations could fasten the ignition kinetics of JP10-air mixtures. Ignition promoters like ozone and hydrogen peroxide could improve the ignition and combustion kinetics of JP-10 tremendously for applications in ramjets and detonation-based engines. Another problem associated with detonation-based engines is the higher post-detonation temperatures. This grossly affects the operating temperature limits of detonation-based engines. Inert diluents like helium or argon, when added to fuel-air explosive mixtures, decreases the post-detonation temperature at the cost of an increase in the induction length and time scales. This change in the dominant chemical length and time scale could significantly affect the detonation structure, and could result in the weakening or degeneration of a detonation wave into a deflagration wave as shown by Westbrook [13], Westbrook and Urtiew [14], Knystautas et al. [15], and Lee et al. [16]. Ignition promoters, such as ozone (O_3) and hydrogen peroxide (H_2O_2) when added in trace amounts, prove to be ideal for resolving this issue where they alter the ignition kinetics of a given mixture without affecting the thermodynamic and gas dynamic properties of burned or unburned mixtures. The overall effect of such a fuel-sensitization or doping is to significantly reduce ignition

delay time of certain mixtures without affecting their thermodynamic properties, allowing the effect of induction time (or length) to be studied in isolation.

The impact of the addition of ignition promoters like ozone and hydrogen peroxide in the presence of inert diluents like argon and helium was investigated for JP10-air detonations. Induction length and time scales were calculated along with the post-detonation temperatures to investigate the effect of ignition promoters on JP10-air-diluent mixtures. Energy release rates, effective activation energy parameter, and stability parameter were also calculated in the present study. The influence of the addition of dopants has been further elaborated through detailed chemical kinetics and species profiles obtained from the ZND calculations. The effect of variation of equivalence ratio with and without dopants was also studied in the present study. One of the major motivations of this study is to reduce the operating temperatures of detonation-based engines to avoid complex cooling mechanisms to reduce weight penalty and mechanical complexity for applications in hypersonic and supersonic missiles. A reduction in the weight penalty will mean higher payload capacity for hypersonic and supersonic missiles.

2 Methodology: Numerical Calculations

ZND computations were performed in the present study for JP10-air detonations using the HyChem model [17], which comprises 119 species and 841 reactions. Additionally, the Princeton Ozone sub-mod el by Zhao et al. [21] was combined with the HyChem model for calculations with ozone as a dopant. ZND numerical computations were carried out with CANTERA 2.4 [22], an open-source software integrated with MATLAB R2018b and Python Ver 3.7. ZND calculations were performed using a modified version of the CalTech Shock and Detonation Toolbox [20].

3 Results and Discussions

3.1 *Effect of the Addition of Ignition Promoters to JP10-Air Mixtures*

The effects of the addition of O_3 and H_2O_2 were studied numerically by ZND calculations for stoichiometric JP10-air detonations at various dopant levels of 0, 5000, 10,000, and 16,000 PPM (mole fraction based) and the variations in detonation parameters like V_{VN} , T_{CJ} , V_{CJ} , M_{CJ} , P_{CJ} were calculated for JP10-air mixtures (refer to Table 2).

The variation of induction length and time scales as a function of dopant concentration were calculated for stoichiometric JP10-air mixtures at initial conditions of 295 K and 1 atm pressure. Ozone acts as an ignition promoter at small and large

Table 2 Detonation parameters for stoichiometric JP10-air detonations in the presence of ignition promoters at modest concentrations

Fuel-Oxidizer	Mech	X_{O_2} ($\times 10^6$)	$X_{H_2O_2}$ ($\times 10^6$)	V_{VN} (m/s)	T_{CI} (K)	V_{CI} (m/s)	M_{CI}	P_{CJ} (bar)	Δ_j (mm)	τ_{ign} (μ s)	Δ_e (mm)
JP10-air ($O_2/N_2 = 3.76$)	HyChem-JP-10	0	0	1525	2877	1797	5.41	18.90	2.6178	8.1570	0.1978
		5000	-	1530	2894	1801	5.43	19.05	2.0711	6.2807	0.1863
		10,000	-	1534	2908	1805	5.45	19.18	1.5405	4.5108	0.0147
		16,000	-	1538	2921	1808	5.47	19.32	0.0088	0.0325	0.0285
		-	5000	1531	2885	1802	5.43	19.03	2.2533	6.8719	0.1934
		-	10,000	1530	2882	1801	5.43	19.01	2.0338	6.0929	0.1960
		-	16,000	1533	2882	1802	5.44	19.06	1.8155	5.3482	0.1952

The calculations were carried out at initial conditions of $\varphi = 1$, $P_0 = 101,325$ Pa and $T_0 = 295$ K

concentrations where it readily decomposes into O_2 and O through,



During ignition, the O -atom accelerates the chain branching process and shortens the ignition delay time. H_2O_2 also acts as an ignition promoter where it readily decomposes into OH radicals. The OH radicals, during ignition, accelerates the chain branching process and shortens the ignition delay time.



Present ZND calculations show that the addition of O_3 and H_2O_2 at modest concentrations (up to 16,000 PPM) can reduce the Δ_i by 99% and 30%, respectively for JP10-air mixtures (see Fig. 2 and Table 2). It is now evident that the addition of ignition promoters like O_3 and H_2O_2 could significantly alter the chemical length and time scales and can have a significant effect on the detonation structure of JP10-air mixtures.

This is a remarkable result because JP-10 is a higher molecular weight single-component fuel, where it decomposes to a set of pyrolysis products that are quite different from those of conventional jet fuels or heavier liquid hydrocarbon fuels. Its

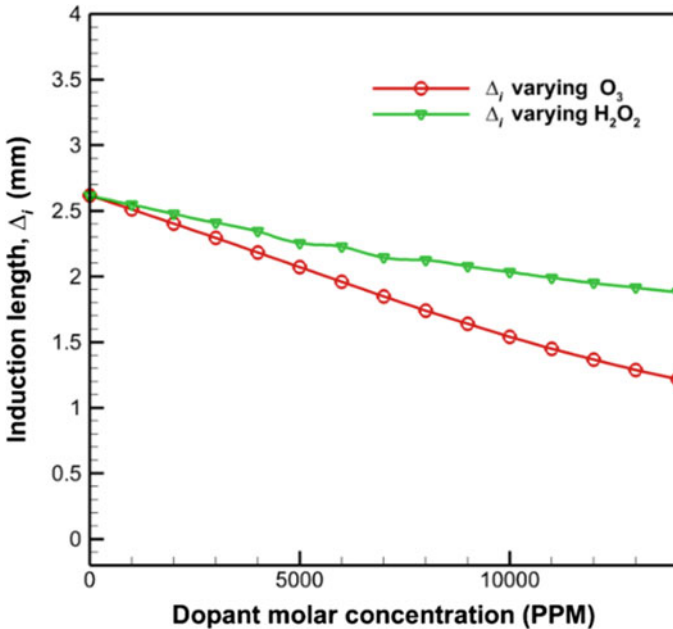


Fig. 2 Effect of the addition of ozone and hydrogen peroxide on induction zone length (Δ_i) for stoichiometric JP10-air detonations. The calculations were carried out at initial conditions of $\phi = 1$, $P_0 = 101,325$ Pa and $T_0 = 295$ K

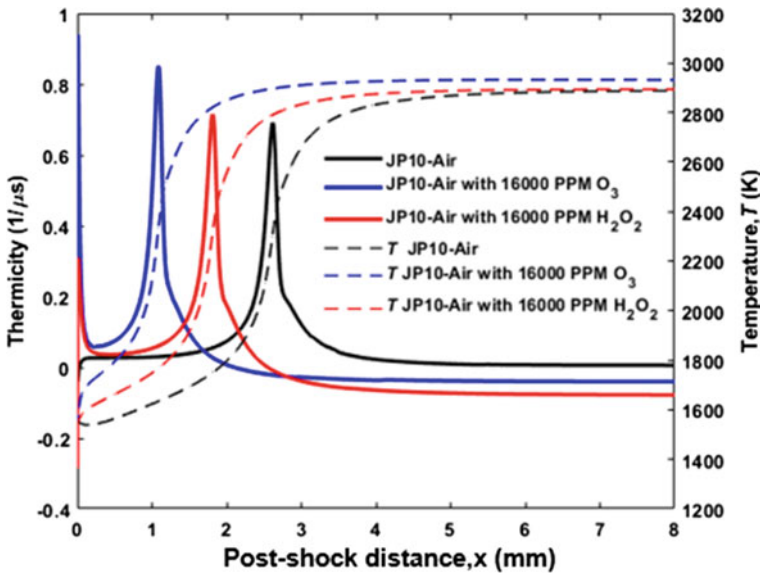


Fig. 3 Thermicity profiles with and without the addition of O₃ and H₂O₂ at modest concentrations (16,000 PPM) for stoichiometric JP10-air detonations. The solid lines represent the thermicity ($\dot{\sigma}$), whereas the dotted lines represent the post-shock temperature profile, T . The calculations were carried out at initial conditions of $\varphi = 1$, $P_0 = 101,325$ Pa and $T_0 = 295$ K

oxidation chemistry is somewhat more complicated than the chemistry of gaseous fuels like ethylene. Yet, our calculations show that the ignition promoters like ozone and hydrogen peroxide do not distinguish between the gaseous and complex heavier hydrocarbon liquid fuels as far as their effect on ignition chemistry is considered. The addition of ozone and hydrogen peroxide in trace amounts to fuel-oxidizer-diluent mixtures could help to establish, stabilize, and sustain detonation waves in small tubes or channels that would otherwise not be able to maintain a detonation wave. Ozone is found to be a better ignition promoter than H₂O₂ for stoichiometric JP10-air detonations at 16,000 PPM. The shift in the thermicity peaks to the left for the addition of ignition promoters at modest concentrations (16,000 PPM of O₃ and H₂O₂), clearly demonstrate the sensitization effect of ignition promoters on induction length, Δ_i . Figure 3 indicates that O₃ is a better ignition promoter than H₂O₂.

3.2 Energy Release Rates and Stability Parameter Analysis—Effect of the Addition of Ignition Promoters

The trend for variation of induction length Δ_i and the corresponding energy release rate is shown in Fig. 4 for JP10-air mixtures doped with O₃ and H₂O₂ at modest concentrations (16,000 PPM). The energy release rate increases as we increase the

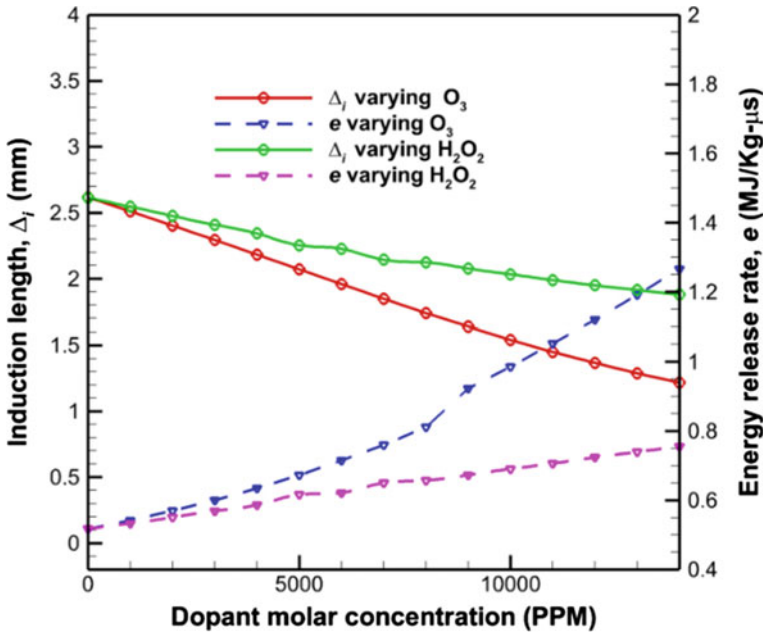


Fig. 4 Variation of induction length (solid lines) and energy release rate (dotted lines) in the presence of ignition promoters like O_3 and H_2O_2 at modest concentrations for JP10-air detonations. The calculations were carried out at initial conditions of $\varphi = 1$, $P_0 = 101,325$ Pa, and $T_0 = 295$ K

concentration of the ignition promoters for JP10-air mixtures. Similarly, an investigation of the stability parameter reveals that it decreases with the increase in the dopant molar concentration for JP-10-air mixtures (see Fig. 5). The stability parameter is lower when ozone and H_2O_2 are used as ignition promoters at a given concentration level, suggesting that ignition promoters could have a strong stabilizing effect on the detonation wave structure (see Fig. 5).

3.3 Species Profiles—Effect of the Addition of Ignition Promoters on JP10-Air Mixtures

The high-temperature combustion of large hydrocarbon fuel molecules, like JP10, occurs in two steps: pyrolysis or oxidative pyrolysis of JP10 first, followed by the oxidation of the decomposed products. The two processes are separable in spatial or time scales. Since the thermal decomposition of the parent fuel molecule is fast when compared to the oxidation of the decomposed products, the oxidation of the pyrolysis products is rate-limiting during the entire course of the reaction leading to ignition. The composition of these pyrolysis products determines the combustion

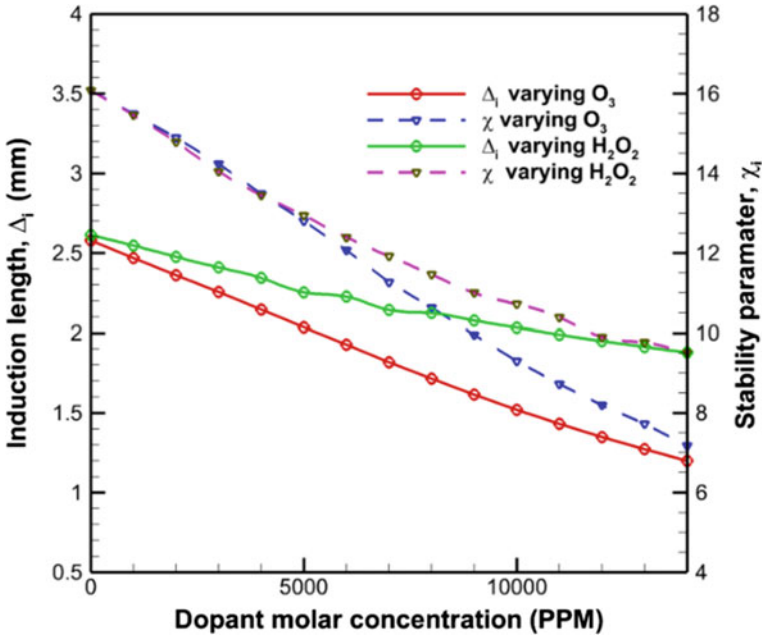


Fig. 5 Variation of induction length (solid lines) and the stability parameter (dotted lines) in the presence of ignition promoters like O_3 and H_2O_2 at modest concentrations for stoichiometric JP10-air detonations. The calculations were carried out at initial conditions of $\varphi = 1$, $P_0 = 101,325$ Pa, and $T_0 = 295$ K

characteristics of the original parent fuel molecule. Due to high-post-shock temperatures, JP10 undergoes decomposition into several small pyrolysis products first, long before the ignition. Major decomposition products of JP10 are cyclopentadiene (C_5H_6), benzene (C_6H_6), toluene (C_7H_8), ethylene (C_2H_4), and propene (C_3H_6), all of which have substantially larger molecular diffusivities than the parent fuel molecule, JP10. The concentrations of the decomposed products peak in the post-shock preheat region. The decomposition zone primarily comprises the region where the parent fuel molecule undergoes rapid thermal decomposition. The region that follows the decomposition zone is known as the oxidation zone, where the pyrolysis products are oxidized as they enter the flame along with molecular oxygen, leading to the production of CO , CO_2 , H_2O , and heat release. The location of the peak thermicity represents the ignition point beyond which radical recombination reactions occur leading to substantial heat release.

The rate of consumption of the JP-10 (in terms of mole fraction) during the detonation phase is significantly higher in the presence of ignition promoters, depicting faster pyrolysis/decomposition kinetics of JP-10 in the presence of ignition promoters. JP-10 comprises a basket-shaped, multi-ring structure and decomposes into a set of pyrolysis products that are quite different from conventional jet fuels. The calculations show that with the addition of ignition promoters, there is an earlier and

higher production of reactive radical species like H, CH₃, O, OH, O, and HO₂ during thermal decomposition or oxidative pyrolysis of JP-10. Since these small species have substantially high-molecular diffusivity, they diffuse rapidly into the decomposition zone from the oxidation and recombination zones due to high-concentration gradients and facilitate the decomposition of parent fuel molecule (JP-10) into a set of pyrolysis products. This happens long before the oxidation of the decomposed or pyrolysis products. The reason for the same may be the ease with which fuel undergoes decomposition in the preheat zone due to high temperatures (roughly between 1600 and 1700 K) and the subsequent effect of ignition promoter that promptly results in the formation of these reactive radical species. The earlier production of these reactive species is responsible for faster pyrolysis and enhances the oxidation of decomposed products. The more rapid production of these active radical species will imply earlier and faster kinetics resulting in smaller induction length and time. The pyrolysis or decomposition zone also shows an early rise in the formation of intermediate species like C₂H₄, C₂H₂, CH₄, H₂, C₃H₆, C₅H₆, C₆H₆, and C₇H₈, suggesting faster decomposition of parent fuel molecule (JP10 in this case). Thus, the addition of ignition promoters is seen to promote and fasten the production of these pyrolysis intermediates in comparison with the unsensitized fuel-oxidizer mixture.

For a no-dopant case, the complete pyrolysis of the fuel takes around 1.54 μs, and after that oxidation of decomposed products takes place, which results in the oxidation of the pyrolysis products with molecular oxygen leading to ignition. The total time taken for the oxidation of pyrolysis products leading to ignition is 6.48 μs (see Fig. 6). Clearly, the thermal or oxidative thermal decomposition of JP-10 is fast, and the oxidation of the pyrolysis products is rate-limiting during the entire course of the reaction leading to ignition. The time scales for the thermal decomposition of JP-10 in the presence of ignition promoters like hydrogen peroxide and ozone (at modest concentrations of 16,000 PPM) are 0.47 μs and 0.09 μs, respectively (see Fig. 6). Thus, thermal decomposition of JP-10 occurs ~3.3 and ~17.1 times faster in the presence of hydrogen peroxide and ozone, respectively (see Fig. 6). Similarly, the time scales for the oxidation of pyrolysis products are 4.79 μs and 3.02 μs, respectively, for hydrogen peroxide-doped and ozone-doped cases. Here again, oxidation of decomposed products occurs ~1.35 and ~2.15 times faster in the presence of hydrogen peroxide and ozone, respectively, (see Fig. 6). Thus, the thermal decomposition of JP-10, as well as the oxidation of pyrolysis products, takes place faster in the presence of ignition promoters like ozone and hydrogen peroxide. The species profile data and respective time scales of fuel decomposition and oxidation show that ozone acts as a better ignition promoter than hydrogen peroxide for JP10-air detonations. Subsequently, induction length and time are smaller for the ozone-doped case when compared to the hydrogen peroxide-doped case, suggesting that ozone is a better ignition promoter than hydrogen peroxide.

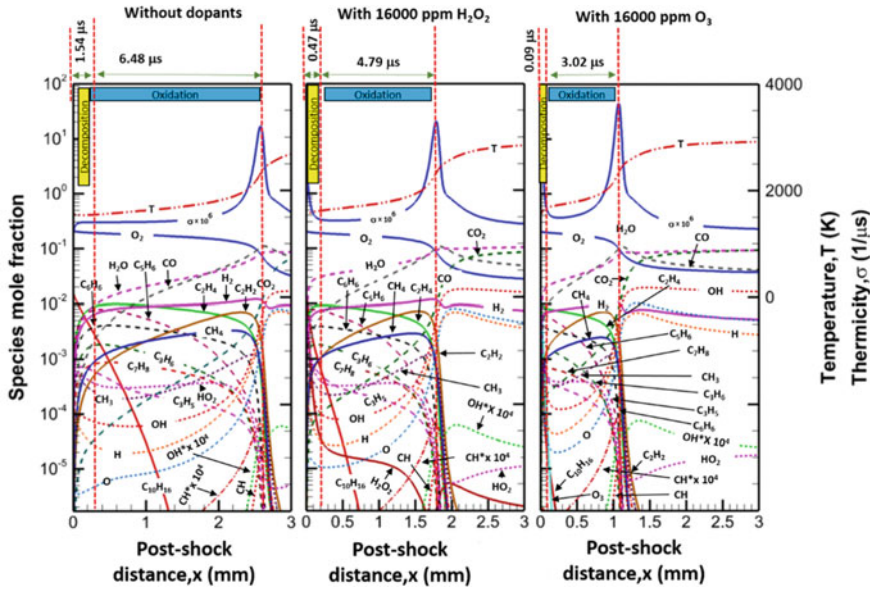


Fig. 6 Variation of species mole fraction with and without the addition of ignition promoters at modest concentrations (16,000 PPM of O₃ and H₂O₂) for stoichiometric JP10-air detonations. The calculations were carried out at initial conditions of $\phi = 1$, $P_0 = 101,325$ Pa and $T_0 = 295$ K

3.4 Effect of the Addition of Inert Diluents in JP10-Air Mixtures

ZND calculations for the addition of argon and helium in percentage molar concentration show an increase in Δ_i by 79 and 166 times at dilution levels of 80%. This can be seen in Table 3. However, we can see a tremendous decrease in post-detonation temperature (T_{CJ}) from 2877 to 1671 K and 1667 K (~42% decrease in temperature) for argon and helium dilution, respectively, for JP10-air mixtures (see Fig. 7). These calculations reveal that the addition of inert diluents like argon and helium can reduce the post-detonation temperatures significantly, thereby reducing the operating temperatures of detonation-based engines. However, this convenience comes at the cost of an increase in the induction length and time scales. This significant increase in length and time scales could attenuate a detonation wave near its propagation limits. The addition of argon and helium to fuel–air mixtures decreases the heat capacity and the energy release of the resulting mixture. On comparing the corresponding rise in induction length and time scales, argon appears to be a better diluent than helium at high-dilution levels (since the corresponding increase in induction length and time scales is less for argon diluted case) for JP10-air mixtures (see Table 3).

In JP10-air mixtures, the induction length Δ_i increases significantly for dilution levels greater than 60% for argon and helium. At 80% dilution of argon and helium,

Table 3 Detonation parameters for JP10-air mixtures in the presence of inert diluents like argon and helium

Fuel-Oxidizer	Mech	X _{Ar}	X _{He}	T _{CJ} (K)	V _{CJ} (m/s)	M _{CJ}	P _{CJ} (bar)	Δ _i (mm)	τ _i (μs)	Δ _e (mm)	% ΔT _{CJ}
JP10-air (O ₂ /N ₂ = 3.76)	HyChem-JP10	0	0	2877	1797	5.41	18.90	2.624	8.172	0.194	
		30	–	2706	1644	5.07	17.02	2.927	8.880	0.302	5.9
		60	–	2325	1446	4.53	13.65	6.862	20.122	0.738	19.2
		80	–	1671	1185	3.72	9.10	207.545	615.798	6.105	41.9
		–	30	2706	2000	5.07	17.02	3.563	8.890	0.367	5.9
		–	60	2326	2277	4.53	13.66	10.875	20.243	1.213	19.2
		–	80	1667	2396	3.72	9.07	434.917	636.509	24.037	42.1

The calculations were carried out at initial conditions of $\phi = 1$, $P_0 = 101,325$ Pa and $T_0 = 295$ K

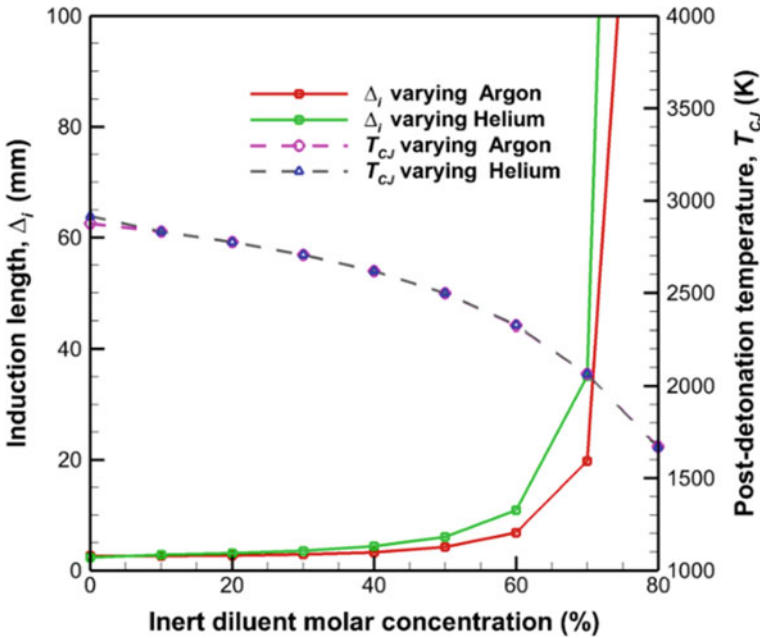


Fig. 7 Variation of induction zone length (solid lines) and post-detonation temperature (dotted lines) in the presence of inert diluents like argon and helium for JP10-air detonations. The calculations were carried out at initial conditions of $\phi = 1$, $P_0 = 101,325$ Pa and $T_0 = 295$ K

the post-detonation temperatures reduce to 1671 K and 1667 K, respectively, for JP10-air mixtures (see Fig. 7). The shift of thermicity peaks to the right, and flattening of these peaks indicates the decrease in the strength or robustness of the detonation wave, for argon and helium dilution at 50% for JP10-air mixtures (see Fig. 8). The increase in induction zone length is associated with a decrease in the detonability of the given mixture. Smaller induction lengths and times are indicative of tighter coupling between the shock wave and reaction zone and quantitatively represent mixtures which are more sensitive to detonation in terms of direct initiation energy. The flattening of thermicity curves for argon and helium dilution indicates a reduction in heat release rate and exothermicity for both the mixtures.

3.5 Energy Release Rate and Stability Parameter *Analysis—Effect of the Addition of Inert Diluents*

The energy release rates decrease with an increase in diluent molar concentration for JP10-air mixtures. The addition of inert diluents like argon and helium has a strong thermal inhibiting effect. The addition of these monoatomic gases decreases

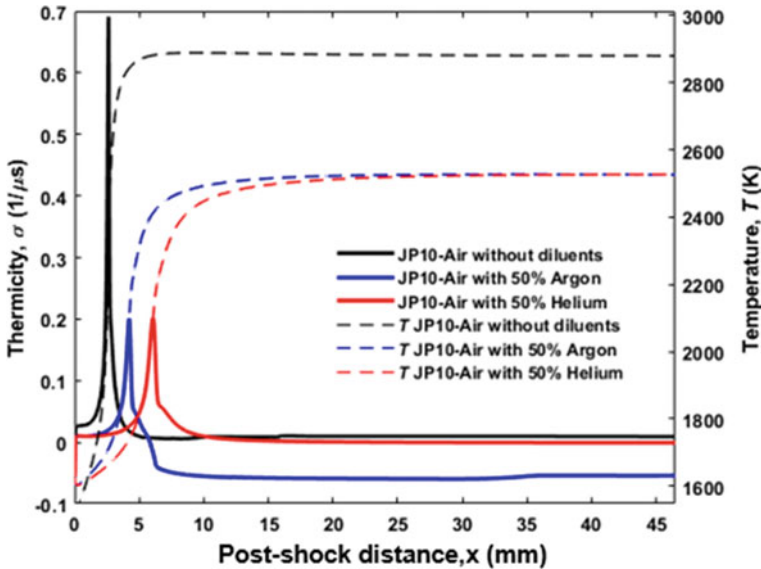


Fig. 8 Thermicity profiles with and without the addition of inert diluents (50% dilution by argon and helium) for stoichiometric JP10-air detonations. The solid lines represent the thermicity ($\dot{\sigma}$), whereas the dotted lines represent the post-shock temperature profile, T . The calculations were carried out at initial conditions of $\varphi = 1$, $P_0 = 101,325$ Pa and $T_0 = 295$ K

the energy release and increases the reaction time scales, thus causing a reduction in the energy release rates.

The stability parameter is often used in detonation studies to predict the regularity of detonation cells. It is observed that the stability of a detonation wave is a result of the temperature sensitivity of the chemical reactions. Small fluctuations in shock temperature can result in large perturbations in the induction delay time as well as the energy release rate of the recombination reactions. An extended reaction zone or long reaction time is seen to have a stabilizing effect as it spreads out the energy release and thus reduces the effect of fluctuations in the induction time. Large values of the stability parameter leads to gasdynamic instabilities in the reaction zone. Thus, chemistry plays a crucial role in detonation instability. As seen in Fig. 9, for JP10-air-diluent mixtures, the stability parameter (χ_i) decreases with the addition of inert diluents (up to dilution levels of 70% when compared to undiluted mixtures), which indicates that the mixture becomes more stable with the addition of inert diluents. It is observed that the addition of diluent like argon and helium has a stabilizing effect on the resulting detonation structure. As observed in Fig. 9, the length of the induction zone does not change noticeably for varying amounts of argon dilution. One of the effects of argon dilution is to raise the post-shock temperature by decreasing the specific heat of the resulting mixture. This would reduce the induction zone length and tend to stabilize the detonation. However, another effect

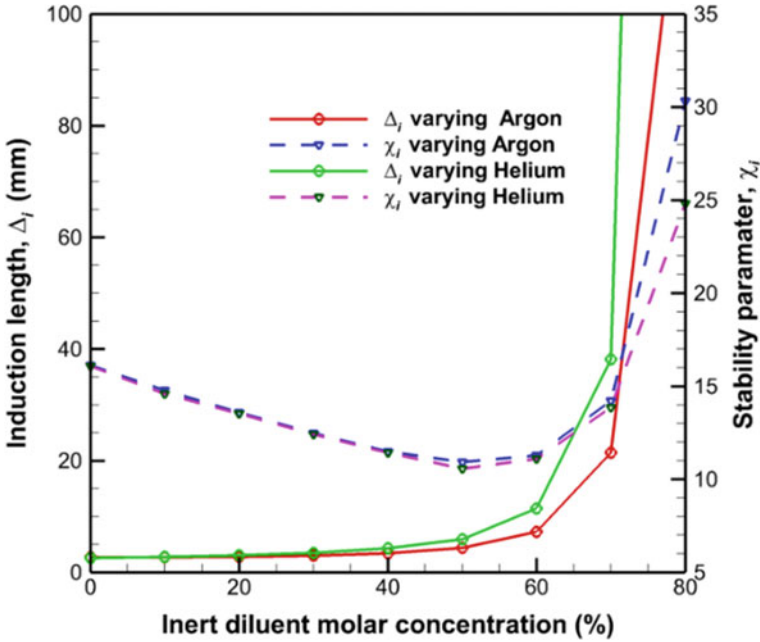


Fig. 9 Variation of induction zone length (solid lines) and stability parameter (dotted lines) in the presence of inert diluents like argon and helium for JP10-air detonations. The calculations were carried out at initial conditions of $\varphi = 1$, $P_0 = 101,325$ Pa and $T_0 = 295$ K

of argon dilution is to reduce the exothermicity of the mixture and hence the detonation velocity and the post-shock temperature. It appears that these two competing effects balance each other, resulting in little change in the post-shock temperature and hence the induction zone length. However, numerically it is observed that the length of the recombination zone increases significantly with increasing argon dilution. With argon dilution, the exothermicity of the mixture is reduced, resulting in a lower temperature rise in the reaction zone. The reaction rates of the exothermic reactions are also reduced, and this increases the reaction time.

Thus, the stabilizing effect of argon dilution is a result of the increase in the reaction zone length and a decrease in exothermicity. Stable mixtures tend to have lower velocity deficits near propagation limits. For JP10-air-diluent mixtures, a dramatic increase in the stability parameter is observed beyond dilution levels of 60%, making the mixture more unstable at higher dilution levels. Since induction length and activation energy parameter increase drastically beyond 60% dilution, the stability parameter rises sharply for dilution levels above 60%.

3.6 Combined Effect of the Addition of Ignition Promoters and Inert Diluents in JP10-Air Mixtures

The CJ calculations for stoichiometric JP10-air mixtures show T_{CJ} of around 2877 K. The addition of O_3 at modest concentrations of 16,000 PPM to stoichiometric JP10-air mixtures and diluting it with either 80% Ar or He can reduce T_{CJ} from 2877 to 1725 K. Also, for stoichiometric JP10-air mixtures, the addition of H_2O_2 at modest concentrations of 16,000 PPM in the presence of 80% Ar or He can reduce T_{CJ} from 2877 to 1704 K and 1674 K, respectively (see Table 4). Here again, τ_i and Δ_i are lower than the length and time scales of JP10-air detonations in the absence of any inert diluents or dopants. This suggests that the combined effects of ignition promoters and inert diluents can help increase the detonability of a given fuel-oxidizer mixture. The numerical computations show that the strong inhibiting effects of inert diluents on τ_i and Δ_i can be nullified by sensitizing a given fuel-oxidizer mixture with promoters like O_3 and H_2O_2 at modest concentrations. Fuel-sensitization in the presence of ignition promoters like O_3 and H_2O_2 could significantly alter the induction length and time scales of a given explosive mixture and can widen the detonability limits even at high-dilution ratios (see Table 4 and Fig. 10). Therefore, for a given explosive mixture, the geometric constraints on the stable propagation of a detonation wave and the related velocity deficit constraints can be removed in the presence of ignition promoters. Specifically, widening the detonation limits would allow a broader use of fuels, lowered constraints on the oxidizer (e.g., the use of air instead of pure oxygen) and more confined engine geometries. Therefore, using ignition promoters to sensitize a given explosive mixture is a viable technique that can help achieve such a widening of detonation limits.

3.7 Energy Release Rate, Activation Energy, and Stability Parameter Analysis—Combined Effect of the Addition of Ignition Promoters and Inert Diluents

From Table 5, it is clear that the addition of inert diluents in the presence of ignition promoters, shows an increase in the energy release rate (\dot{e}) for JP10-air mixtures. However, the energy release rate is sufficiently low with diluent argon and dopant H_2O_2 . The significantly lower values of the stability parameter (χ_i) indicate that the dilution of the mixture with argon and helium in the presence of ignition promoters (at modest concentrations of 16,000 PPM) can help stabilize a detonation wave.

Table 4 Detonation parameters for JP10-air mixtures in the presence of inert diluents and ignition promoters

Fuel-Oxidizer	Mech	X_{O_3} ($\times 10^6$)	$X_{H_2O_2}$ ($\times 10^6$)	X_{Ar}	X_{He}	T_{CJ} (K)	V_{CJ} (m/s)	M_{CJ}	P_{CJ} (bar)	Δ_i (mm)	τ_i (μ s)	Δ_e (mm)	$\% \Delta T_{CJ}$
JP10-air ($O_2/N_2 = 3.76$)	HyChem-JP10	0	0	0	0	2877	1797	5.41	18.90	2.624	8.172	0.194	
		16,000	-	0.80	-	1725	1206	3.81	9.47	0.044	0.140	0.111	40.0
		-	16,000	0.80	-	1704	1201	3.78	9.37	0.164	0.524	0.587	40.8
		16,000	-	-	0.80	1725	2413	3.81	9.48	0.082	0.130	0.203	40.0
		-	16,000	-	0.80	1674	2402	3.75	9.19	0.383	0.607	1.436	41.8

The calculations were carried out at initial conditions of $\phi = 1$, $P_0 = 101,325$ Pa, and $T_0 = 295$ K

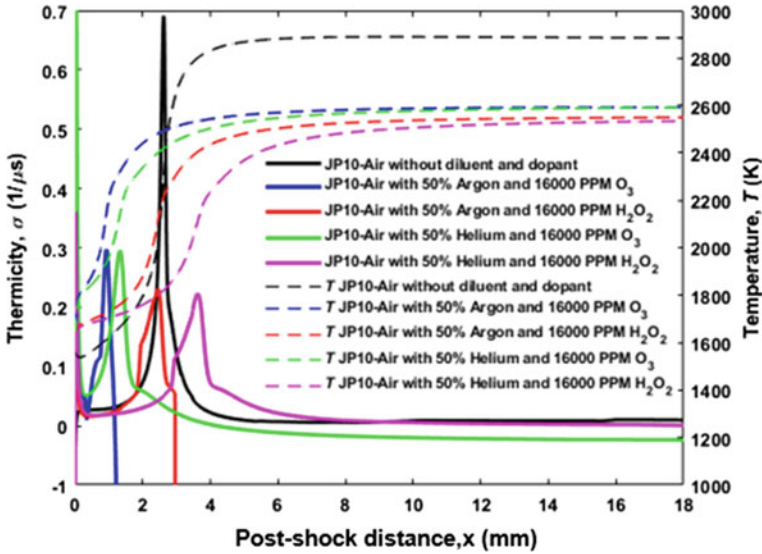


Fig. 10 Thermicity profiles showing the combined effects of the addition of ignition promoters (16,000 PPM of O_3 and H_2O_2) and inert diluents (50% argon and helium) for stoichiometric JP10-air detonations. The solid lines represent the thermicity ($\dot{\sigma}$), whereas the dotted lines represent the post-shock temperature, T . The calculations were carried out at initial conditions of $\phi = 1$, $P_0 = 101,325$ Pa, and $T_0 = 295$ K

3.8 Effect of Lower Equivalence Ratios in the Presence of Ignition Promoters

The induction length and time scales for JP10-air mixtures increase exponentially with decreasing equivalence ratio. In JP10-air detonations, the addition of ozone at concentrations of 16,000 PPM can help reduce Δ_i and τ_i even at an equivalence ratio of 0.3 when compared to the stoichiometric undoped case, resulting in post-detonation temperatures (T_{CJ}) of 1583 K. However, hydrogen peroxide at modest concentrations of 16,000 PPM can help reduce or maintain the Δ_i and τ_i up to an equivalence ratio of 0.8 when compared to the stoichiometric undoped case, as observed in Table 6 and Fig. 11.

At a given equivalence ratio, the sensitized fuel-oxidizer mixtures have shorter induction lengths and time when compared to the unsensitized mixtures. The use of ignition promoters at a given equivalence ratio makes the mixture more sensitive to detonation, thereby preventing the degeneration or attenuation of a detonation wave near its limits. For the JP10-air mixture, ozone is found to be a better ignition promoter, which can enable operations of detonation-based engines at lean equivalence ratios, thereby reducing the operating temperatures of detonation-based combustors.

Table 5 Detonation parameters for JP10-air mixtures in the presence of inert diluents and ignition promoters

Fuel-Oxidizer	Mech	X_{O_3} ($\times 10^6$)	$X_{H_2O_2}$ ($\times 10^6$)	X_{Ar}	X_{He}	Δ_t (mm)	e (MJ/Kg- μ s)	χ_t
JP10-air ($O_2/N_2 = 3.76$)	HyChem	0	0	0	0	2.624	0.498	16.122
		16,000	-	0.80	-	0.044	1.117	0.080
		-	16,000	0.80	-	0.164	0.226	0.087
		16,000	-	-	0.80	0.082	4.860	0.073
		-	16,000	-	0.80	0.383	0.746	0.082

The calculations were carried out at initial conditions of $\varphi = 1$, $P_0 = 101,325$ Pa and $T_0 = 295$ K

Table 6 Detonation parameters for JP10-air mixtures in the presence of ignition promoters at modest concentrations

Fuel-oxidizer	Mech	ϕ	$X_{O_3} (\times 10^6)$	$X_{H_2O_2} (\times 10^6)$	$T_{CJ} (K)$	$V_{CJ} (m/s)$	M_{CJ}	$P_{CJ} (bar)$	$\Delta_i (mm)$	$\tau_{ign} (\mu s)$	$\Delta_e (mm)$	$\% \Delta T_{CJ}$
JP10-air ($O_2/N_2 = 3.76$)	HyChem-JP10	1	0	0	2877	1797	5.41	18.90	2.624	8.172	0.194	
		0.6	16,000	–	2378	1609	4.80	14.63	0.020	0.074	0.061	17.3
		0.8	–	16,000	2699	1730	5.18	17.24	2.752	8.042	0.270	6.2
		0.3	16,000	–	1583	1294	3.82	9.25	0.124	0.467	0.434	45.0
		0.6	–	16,000	2356	1607	4.78	14.49	6.740	19.500	0.695	18.1

The calculations were carried out at initial conditions of $P_0 = 101,325$ Pa and $T_0 = 295$ K

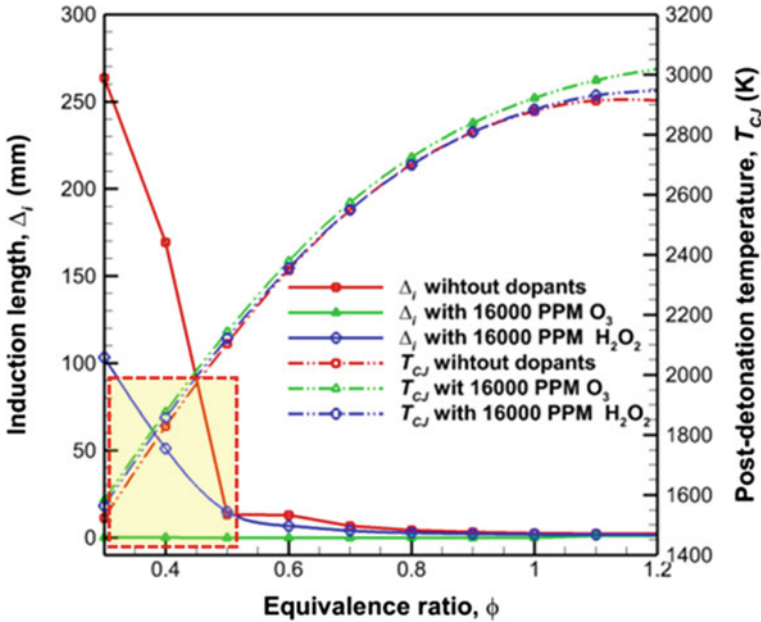


Fig. 11 Effect of varying equivalence ratios on the induction zone length (solid lines) and post-detonation temperature (dotted lines) in the presence of ignition promoters at modest concentrations (16,000 PPM of O_3 and H_2O_2) for JP10-air detonations. The calculations were carried out at initial conditions of $P_0 = 101,325$ Pa and $T_0 = 295$ K

It is feasible for JP10-air mixtures to have a broader operating temperature range in the presence of ignition promoters like ozone and hydrogen peroxide. Operating temperatures below 2000 K are feasible for JP10-air mixtures at leaner conditions when ozone and hydrogen peroxide are used as ignition promoters at modest concentrations (see Fig. 11). However, at a given equivalence ratio, ozone helps in widening the detonability limits and reduces the induction length and time scales to a larger extent when compared to hydrogen peroxide. Thus, using ozone as an ignition promoter is more useful in ultra-lean fuel conditions, where it can be used to lower the operating temperatures of detonation cycle engines. The square boxes in Fig. 11 highlight the proposed operating temperature range for RDEs to keep the post-detonation temperatures low for the continuous operation of detonation-based engines.

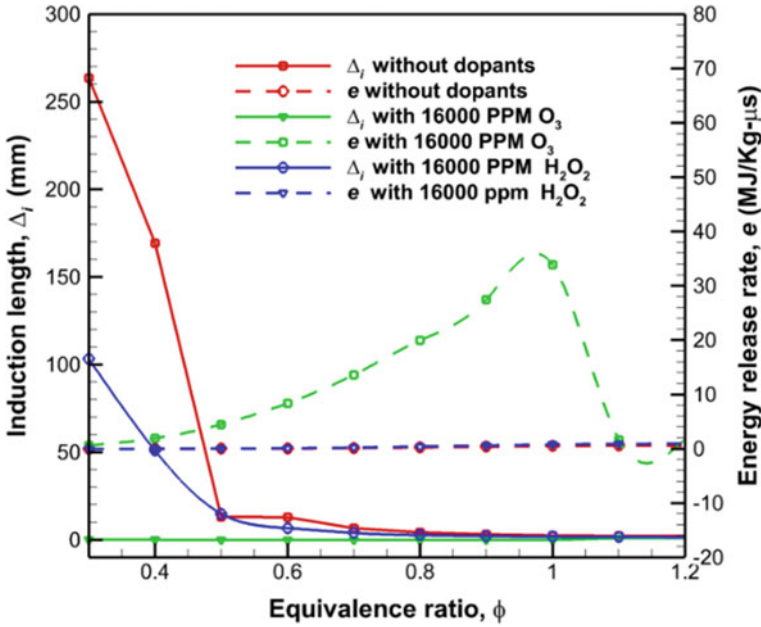


Fig. 12 Effect of varying equivalence ratios on the induction zone length (solid lines) and energy release rate (dotted lines) in the presence of ignition promoters at modest concentrations (16,000 PPM of O_3 and H_2O_2) for JP10-air detonations. The calculations were carried out at initial conditions of $P_0 = 101,325$ Pa and $T_0 = 295$ K

3.9 Energy Release Rate and Stability Parameter Analysis—Effect of Equivalence Ratio

In JP10-air mixtures, the energy release rate (\dot{e}) decreases as we decrease the equivalence ratio of the mixture from stoichiometric to lean values (see Fig. 12). However, at a given equivalence ratio, the energy release rate is always higher for ozone followed by hydrogen peroxide. Rise in the induction times and lower energy release at leaner equivalence ratios is the primary reason for such a decrease in the energy release rate. There is a strong dependence of post-shock temperature (T_{VN}) on the equivalence ratio. The post-shock temperature increases with equivalence ratio and reaches a maximum at stoichiometric or slightly rich conditions and then decreases again on the fuel-rich side. Since the induction time is a sensitive function of post-shock temperature, it increases for a decrease in the post-shock temperature due to slower kinetics. It is now clear that the thermodynamic properties of the leading shock play a significant role in the induction process. Also, the energy release per unit mass is highest in stoichiometric conditions. This can cause higher post-shock and post-detonation temperatures and therefore, higher overall kinetic rates at the stoichiometric conditions.

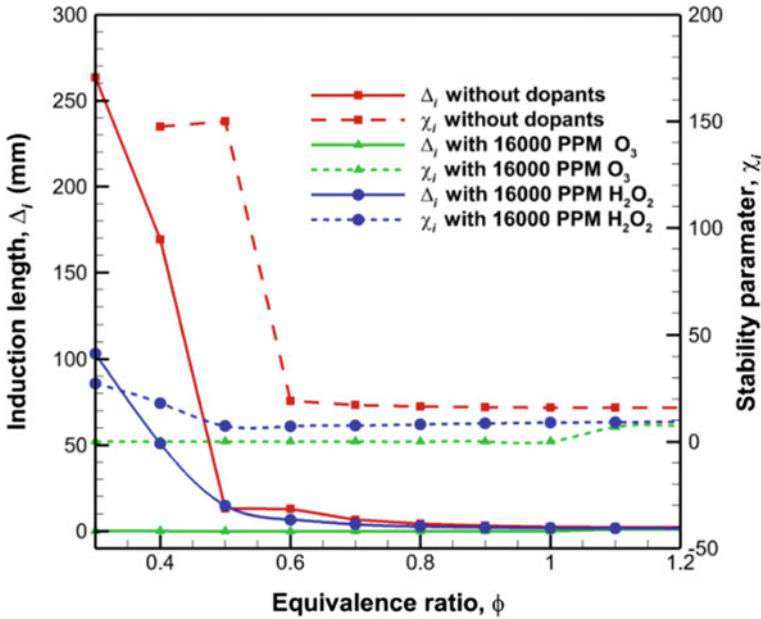


Fig. 13 Effect of varying equivalence ratios on the induction zone length (solid lines) and the stability parameter (dotted lines) in the presence of ignition promoters at modest concentrations (16,000 PPM of O_3 and H_2O_2) for JP10-air detonations. The calculations were carried out at initial conditions of $P_0 = 101,325$ Pa and $T_0 = 295$ K

In JP10-air mixtures, as we approach the fuel-lean conditions, the stability parameter (see Fig. 13) remains approximately the same for the undoped and hydrogen peroxide-doped case up to an equivalence ratio of 0.6 and 0.5, respectively. Beyond that, it increases drastically for the undoped case and somewhat moderately for the hydrogen peroxide case under ultra-lean conditions. Ozone seems to have an interesting behavior on the stability parameter at lean equivalence ratios. For the ozone-doped case, the stability parameter decreases for fuel-lean conditions, suggesting a stabilizing effect of ozone on detonations at lower equivalence ratios.

4 Conclusions

The following conclusions can be drawn from the present study:

1. The addition of the ignition promoters like ozone and hydrogen peroxide to JP10-air mixtures significantly alters the ignition chemistry, without significantly impacting the gas dynamics and thermodynamic states of the given mixture. Ignition promoters also help in reducing the relevant ZND length and time scales and increase the detonability of a given mixture substantially.

2. The addition of diluents like argon and helium can reduce the temperature of the post-detonation products considerably. However, it comes at the cost of an increased τ_i and Δ_i . The increase in τ_i and Δ_i can be compensated by the addition of ignition promoters in trace amounts.
3. Sensitizing fuel-oxidizer mixtures with ozone and hydrogen peroxide at leaner equivalence ratios results in lower post-detonation temperatures and can yield a more robust detonation wave near its propagation limits.
4. It is envisaged that the optimal fuel-sensitization of JP10-air mixtures will enable us to reduce the operating temperatures of detonation cycle engines for practical applications. Complex cooling mechanisms can be avoided in such cases. Thus, a reduction in weight penalty and mechanical complexity can be achieved for applications in hypersonic and supersonic missiles. A reduction in weight penalty will mean higher payload capacity for detonation-based hypersonic and supersonic missiles.

Acknowledgements This work is supported by the start-up research grant of the Indian Institute of Technology Kanpur (Grant # IITK/AE/2017331).

References

1. Andreadis D (2004) Scramjet engines enabling the seamless integration of air & space operations. *The Industrial Physicist*, pp 16–19
2. Xing Y, Fang W, Xie W, Guo Y, Lin R (2008) Thermal cracking of JP-10 under pressure. *Ind Eng Chem Res* 47(24):10034–10040
3. Bruno TJ, Bruno TJ, Huber ML, Laesecke A, Lemmon EW, Perkins RA (2006) Thermochemical and thermophysical properties of JP-10. NISTIR 6640:325
4. Li G, Zhang C, Wei H, Xie H, Guo Y, Fang W (2016) Investigations on the thermal decomposition of JP-10/iso-octane binary mixtures. *Fuel* 163:148–156
5. Crane J, Shi X, Singh AV, Tao Y, Wang H (2019) Isolating the effect of induction length on detonation structure: Hydrogen–oxygen detonation promoted by ozone. *Combust Flame* 200:44–52
6. Kirillov IA, Strelkova MI, Panasenkov AV, Roekaerts D (2005) Sensitivity to detonation and detonation cellular structure of H₂-O₂-air-H₂O₂ gas mixtures. In: *First international conference on hydrogen safety*, Pisa, Italy, pp 8–10
7. Chen GB, Li YH, Cheng TS, Hsu HW, Chao YC (2011) Effects of hydrogen peroxide on combustion enhancement of premixed methane/air flames. *Int J Hydrogen Energy* 36(23):15414–15426
8. Ivin K, Singh AV (2019) Sensitizing ethylene-air and ethylene-oxygen mixtures for optimal performance of detonation cycle engines. In: *33rd National convention of aerospace engineers and national conference on emerging technologies in aerospace structures, materials and propulsion systems*, Nov 16–17, pp 20–26
9. Kumar DS, Singh AV (2019) Sensitizing gaseous mixtures for practical applications in rotating detonation engines. In: *33rd National convention of aerospace engineers and national conference on emerging technologies in aerospace structures, materials and propulsion systems*, Nov 16–17, pp 14–19
10. Ng HD (2005) The effect of chemical reaction kinetics on the structure of gaseous detonations. PhD thesis, McGill University, Montreal, Canada

11. Ng HD, Higgins A, Kiyanda C, Radulescu M, Lee JHS, Bates K, Nikiforakis N (2005a) Nonlinear dynamics and chaos analysis of one-dimensional pulsating detonations. *Combust Theor Model* 9(1):159–170
12. Ng H, Higgins A, Kiyanda C, Radulescu M, Lee JHS, Bates K, Nikiforakis N (2005b) Nonlinear dynamics and chaos analysis of one-dimensional pulsating detonations. *Combust Theor Model* 9(1):159–170
13. Westbrook CK (1982) Chemical kinetics of hydrocarbon oxidation in gaseous detonations. *Combust Flame* 46:191–210
14. Westbrook CK, Urtiew PA (1982) Chemical kinetic prediction of critical parameters in gaseous detonations. In: *Symposium (International) on combustion*, vol 19, no 1, pp 615–623
15. Knystautas R, Lee JH, Guirao CM (1982) The critical tube diameter for detonation failure in hydrocarbon-air mixtures. *Combust Flame* 48:63–83
16. Lee JHS, Jesuthasan A, Ng HD (2013) Near limit behavior of the detonation velocity. *Proc Combust Inst* 34(2):1957–1963
17. Wang H, Xu R, Wang K, Bowman CT, Hanson RK, Davidson DF, Brezinsky K, Egolfopoulos FN (2018) A physics-based approach to modeling real-fuel combustion chemistry-I. Evidence from experiments, and thermodynamic, chemical kinetic and statistical considerations. *Combust Flame* 193:502–519
18. Xu R, Wang K, Banerjee S, Shao J, Parise T, Zhu Y, Wang S, Movaghar A, Lee DJ, Zhao R, Han X (2018) A physics-based approach to modeling real-fuel combustion chemistry-II. Reaction kinetic models of jet and rocket fuels. *Combust Flame* 193:520–537
19. Tao Y, Xu R, Wang K, Shao J, Johnson SE, Movaghar A, Han X, Park JW, Lu T, Brezinsky K, Egolfopoulos FN (2018) A Physics-based approach to modeling real-fuel combustion chemistry-III. Reaction kinetic model of JP10. *Combust Flame* 198:466–476
20. Browne S, Ziegler J, Shepherd JE (2008) Numerical solution methods for shock and detonation jump conditions. *GALCIT Report FM2006* 6:90
21. Zhao H, Yang X, Ju Y (2016) Kinetic studies of ozone assisted low temperature oxidation of dimethyl ether in a flow reactor using molecular beam mass spectrometry. *Combust Flame* 173:187–194
22. Goodwin DG, Moffat HK, Speth RL (2009) *Cantera: an object-oriented software toolkit for chemical kinetics, thermodynamics, and transport processes*. <https://www.cantera.org>, Caltech, Pasadena
23. Kumar DS, Ivin K, Singh AV (2021) Sensitizing gaseous detonations for hydrogen/ethylene-air mixtures using ozone and H_2O_2 as dopants for application in rotating detonation engines. *Proc Combust Inst* 38(3):3825–3834

Design and Analysis of Rotating Detonation Wave Engine



V. Ramanujachari, Rahul Dutta Roy, and P. Amrutha Preethi

Abstract Rotating detonation wave engine (RDE) would be the futuristic engine for air-breathing missile systems and gas turbine systems (aero and stationary applications). The continuous operation of RDE with an operating frequency of 3–15 kHz is attractive for propulsion systems based on rocket, ramjet and turbojet engines. The cell size is the characteristic dimension of the cellular pattern of a propagating detonation wave. The cell size is found to depend strongly on the choice of fuel and oxidizer, its equivalence ratio, initial temperature and initial pressure. Some empirical relations based on cell size are used to design the present detonation combustor. Hydrogen is chosen as the fuel, while air is selected as the oxidizer. The RDE hardware has been realized, and the test facility is being modified at NCCRD, IIT, Madras to carry out static tests. The analysis of the RDE combustor without the nozzle is carried out using the “pressure history model” reported in literature. As the hydrogen fuel and air are entering as two different streams perpendicular to each other, a simple mixing analysis has been carried out to evaluate the mixture properties ahead of the detonation wave. The Chapman–Jouguet (CJ) detonation computations are carried out using the detonation tool box runs in conjunction with Cantera software assuming chemical equilibrium. The fuel-based specific impulse resulted from the present analysis for our configuration using H₂–air is 4733 s compared to a value of 4706 s reported in literature for a stoichiometric composition. The same model has been used to evaluate the C₂H₄–air system. The specific impulse of our study is 2111 s compared to 1975s reported in literature for the fuel-based equivalence ratio of 0.5. This has given credence to the results of the analytical work.

Keywords Rotating detonation wave engine · Pressure history model · CJ detonation · Specific thrust · Specific impulse

V. Ramanujachari (✉) · R. Dutta Roy
National Centre for Combustion Research and Development, IIT Madras, Chennai 600036, India
e-mail: vramanujachari@yahoo.co.in

P. Amrutha Preethi
G. Pulla Reddy Engineering College, Kurnool 518007, India

Nomenclature

A	Area (m^2)
F	Force (N)
H	Mixture layer height (m)
K	Value of integral
P	Pressure (bar)
P_a	Ambient pressure (bar)
\bar{P}_c	Average pressure acting on the thrust surface
\bar{R}	Mean radius of combustion chamber (m)
S	Surface area (m^2)
T	Temperature (K)
V	Velocity (m/s)
W, w	Width of the annular space (m)
X	Azimuthal coordinate
Z, x	Axial coordinate
c_p	Specific heat at constant pressure (J/Kg-K)
h	Enthalpy (MJ/kg)
\dot{m}	Mass flow rate
p	Static pressure (bar)
t	Time (ms)
u	Velocity (m/s)

Greek Symbols

ρ	Density (kg/m^3)
γ	Ratio of specific heats
γ_e	Ratio of specific heats at equilibrium condition
τ_w	Shear stress on the walls (N/m^2)

Subscripts

1	Airflow state
2	Fuel flow state
3	Mixture state
c	Averaged combustion chamber conditions

1 Introduction

The rotating detonation wave engine has emerged as a promising concept due to its high specific power output, thrust to weight ratio and volumetric efficiency [1]. This has been proposed as a substitute for liquid propellant rocket or ramjet/engine [2]. In addition, it can replace gas turbine engines for power generation also [3]. Due to its promising potential as a propulsive and power generation device, it has been researched worldwide based on both numerical and experimental investigations. It has been reported that the detonation wave propagates with high velocity deficit when compared to CJ detonation wave velocity [3]. A lot of countries abroad are working on this concept. In order to understand this RDE and realize an engine to deliver adequate thrust, an experimental work has been initiated. An experimental engine is designed based on the empirical correlations of Bykovskii et al. [4] by the authors at IIT, Madras, [5] and the hardware is being tested. In the present work, it is analysed to obtain the performance of the engine using simple one-dimensional modelling technique. Davidenko et al. [6], Shepherd and Kasahara [7] and Braun [8] have carried out simple modelling of the complex detonation wave phenomena. Universal relationship, based on experimental data on expansion wave pressures downstream of detonation front was evolved by Sichel and Foster [9]. This has been used as a part of the performance prediction method. The objective of this paper is to show how an engine analysis can be carried out for an engine designed based on empirical methods. Hence, no parametric study is reported. This work establishes the conditions to be set for the proposed experiments and the performance expected from the engine tests.

2 Concept of RDE

In RDE concept, a unidirectional detonation wave could be created and the exhaust gases are expanded through an annular nozzle producing necessary thrust. Figure 1 shows the elements of a rotating detonation wave engine concept designed and realized by the authors. In this case, the combustor or the detonation chamber is the annular ring, where the premixed fuel-air mixture is prepared for detonation by injecting axially the hydrogen fuel and radially the air at the one end of the combustor. After initiation of combustion, a detonation wave propagates circumferentially around the annular ring near the plane of the injector. The detonation products are expanded and exhausted out of the other end of the combustor, which could have a nozzle to further increase the thrust. RDE provides steady source of thrust without needing initiation for every cycle. In RDE, the detonable mixture is injected axially and the detonation wave runs circumferentially around the annular combustor making the flow field very complex, leading to the design very difficult. In addition, as the detonation wave is continuously rotating in a particular location

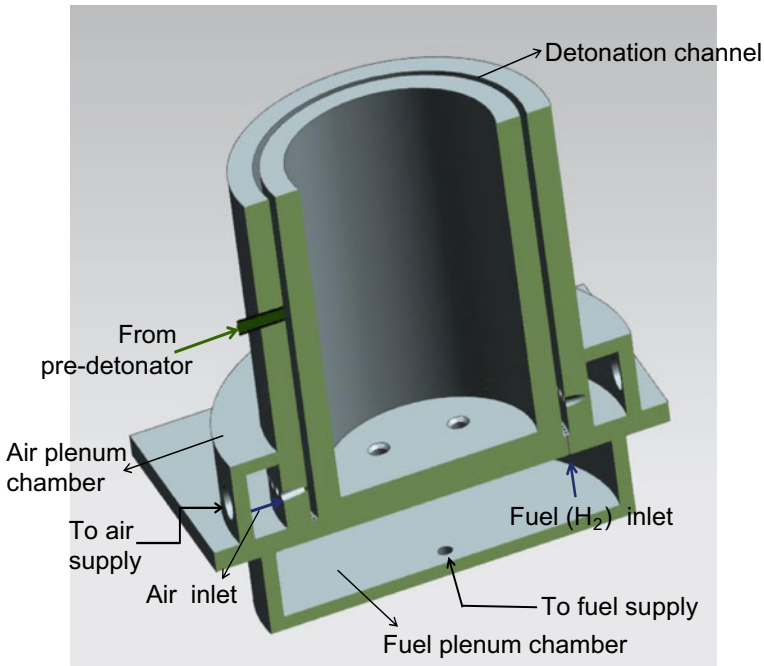


Fig. 1 Elements of a rotating detonation engine

inside the combustion chamber, the heat transfer to the wall and its control would be a major challenge.

As the radial dimension of the RDE is very small compared to the azimuthal and axial dimensions, the variation of flow properties in the radial direction can be considered negligible. The modelling of the flow field behind the detonation wave is quite complex due to oblique shock wave, contact surface between combustion products of detonation wave and shocked combustion products and the expansion waves. Hence, the RDE is “unrolled” into two-dimension as shown in Fig. 2 to make it amenable for simple computations.

3 Pressure History Model of RDE

It is assumed that the fuel and oxidizer are well mixed and supplied at a constant average mass flow rate. The detonation wave propagates at a constant speed equal to CJ detonation speed. The second assumption is that the flow properties are periodic with a period of T (inverse of frequency).

This implies that the flow would be steady in a frame co-rotating with the detonation wave. The third assumption is that the radial variation in the flow may be

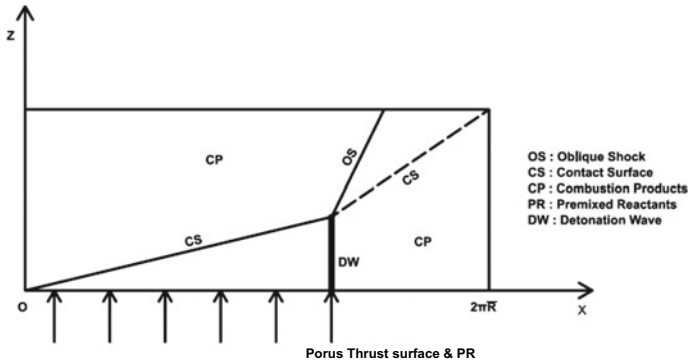


Fig. 2 Unwrapped flow field of RDE

neglected and the flow can be approximated as two-dimensional flow in space. It is reported that the two-dimensional models are adequate for computing average thrust [7]. By averaging over a period, the azimuthal and time dependence of the flow can be eliminated for computing the propulsion parameters. This gives the simplification that the modelling can be quasi one-dimensional and the properties depend on axial direction, Z only. Figure 3 shows the control volume considered for the pressure history model [7]. This encloses the engine but does not cross the exit plane. Here, the control volume is placed along the walls of the combustion chamber and crosses the inlet plane of the combustion chamber. This enables the computation of thrust based on the condition at the porous thrust surface. The forces in the axial direction for this control volume are given below:

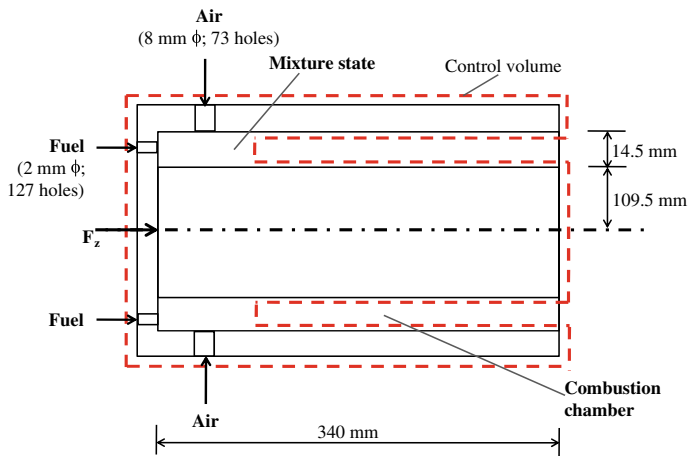


Fig. 3 Control volume for the pressure history model postulated by Shepherd and Kasahara [7]

$$F_Z = \underbrace{\int_{A_c} (P_c - P_{c,1}) dS}_I + \underbrace{\int_{A_c} [\rho_c u_{z,c}^2 + (P_{c,1} - P_a)] dS}_II - \underbrace{\int_{A_w} \tau_w dS}_III \quad (1)$$

First term in the above equation represents the integrated effects of the detonation generated pressure force on the injector surface at the upstream end of the combustion chamber. This can be expressed as

$$F_I = A_c (\bar{P}_c - P_{c,1}) \quad (2)$$

Here, the averaged pressure \bar{P}_c has to be computed. The second term represents the force associated with the momentum flux of the gas at the inlet to the combustion chamber. This can be expressed as

$$F_{II} \approx A_c (P_{c,1} - P_a) + \bar{u}_c \dot{m} \quad (3)$$

Here, the averaged velocity is obtained based on the mass continuity equation. The third term represents the friction due to viscous forces on the combustion chamber walls. This can be neglected and compared to the magnitudes of the first two terms.

4 Modelling of Injection Process

It is essential to obtain an injection model just upstream of the detonation for subsequent modelling based on pressure history model. For simplicity, one-dimensional steady flow equations of continuity, momentum and energy are formulated and solved to obtain the mixture properties of fuel and air prior to detonation in the annular combustor. State 1 is for the air flow; state 2 is for the fuel flow, and state 3 for the mixture conditions. In all the cases, the total pressure of the air is maintained at 4.5 bar(abs) and hence, the flow rate of air is constant at 3.852 kg/s. Depending upon the fuel-based equivalence ratio, the fuel flow rate is varied. As the number and diameter of the fuel injection holes are fixed, the fuel injection total pressure is varied to allow the required amount of fuel flow as shown in Fig. 4.

1. Continuity equation

$$\dot{m}_1 + \dot{m}_2 = \dot{m}_3 \quad (4)$$

$$\dot{m}_3 = \rho_3 A_3 V_3 \quad (5)$$

2. Energy equation

$$\frac{\dot{m}_1}{\dot{m}_3} \left(h_1 + \frac{V_1^2}{2} \right) + \frac{\dot{m}_2}{\dot{m}_3} \left(h_2 + \frac{V_2^2}{2} \right) = c_{p,3} T_3 + \frac{V_3^2}{2} \quad (6)$$

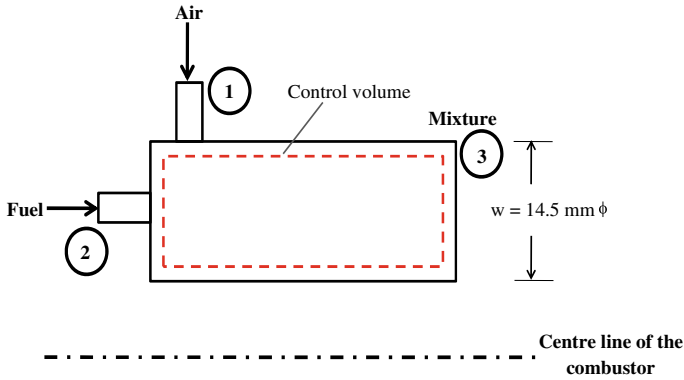


Fig. 4 Control volume for the injection process

3. Axial momentum equation

$$\dot{m}_2 V_2 + p_2 A_2 + p_1 (A_3 - A_2) = \dot{m}_3 V_3 + p_3 A_3 \tag{7}$$

The axial momentum contribution of air flow is not considered as air is injected perpendicular to the axial direction. We have three equations and three unknowns (p_3, T_3, V_3). These equations can be solved using Newton–Raphson method. We can use isentropic equations to obtain the stagnation pressure, stagnation temperature and Mach number at the mixture state. Figures 5, 6, 7 and 8 show the distribution of mass flow rate of fuel, Mach number, total and static pressures and total and static temperatures of the mixtures. As the mass flow rate of air is kept constant for all the fuel-based equivalence ratios, the fuel flow rate continuously increases with increase in equivalence ratio as shown in Fig. 5.

The Mach number of the mixture over the range of equivalence ratios is shown in Fig. 6. A slight decrease in trend is noted. This may be due to the particular gas constant effect of the hydrogen air mixture, which in turn affects the sonic speed of the mixture. The sonic speed marginally increases due to the mixture ratio

Fig. 5 Mass flow rate of fuel versus equivalence ratio

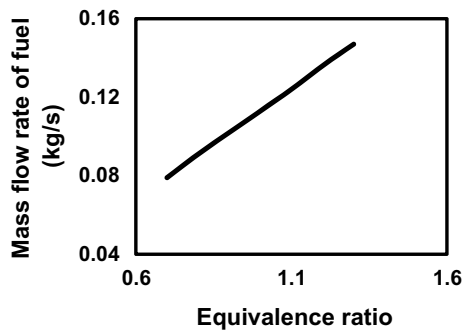


Fig. 6 Mach number versus equivalence ratio

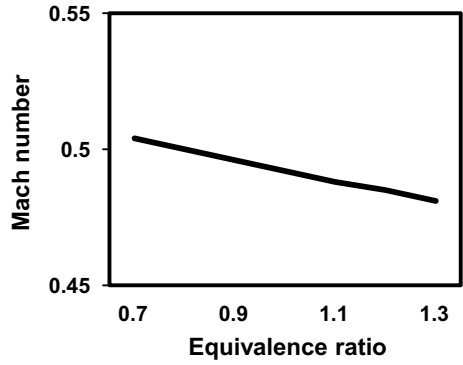


Fig. 7 Total and static pressure of reactants versus equivalence ratio

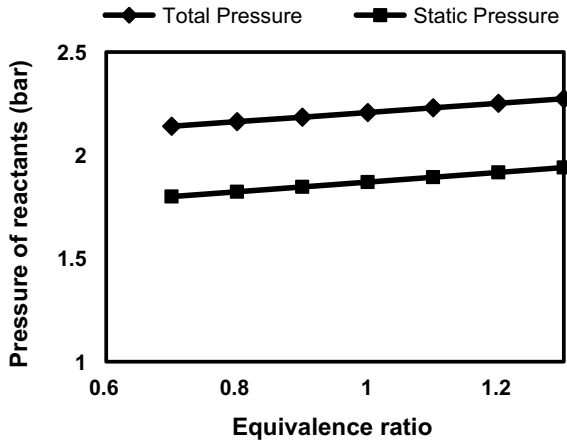
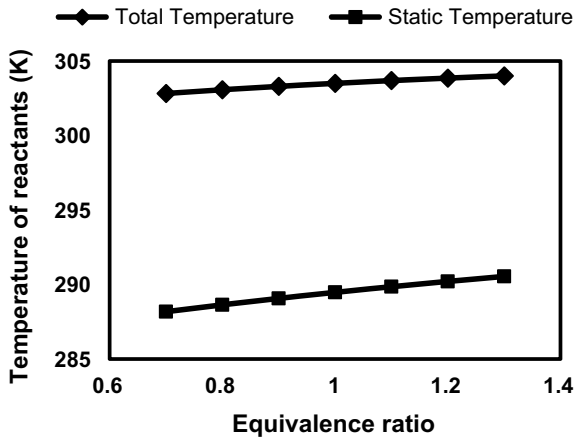


Fig. 8 Total and static temperature of reactants versus equivalence ratio



effect containing low molecular weight hydrogen. Figure 7 shows the distribution of static and stagnation pressures as a function of equivalence ratio. Both of them are almost constant over the equivalence ratios considered. The stagnation value is higher compared to static quantity due to finite Mach number of the flow. Similar trend is seen for the temperatures as shown in Fig. 8.

5 Computation of Detonation Properties

The CJ detonation computations are carried out using the shock and detonation tool box [10] runs in conjunction with Cantera software assuming chemical equilibrium [11]. The quantities of interest are CJ detonation velocity, pressure, temperature and density downstream of detonation wave. Figures 9, 10 and 11 show the CJ detonation velocity, pressure and temperature as a function of fuel-based equivalence ratio. The CJ detonation velocity increases with increase in equivalence ratio. This is due to the increase in sonic velocity of the gases as a result of decrease in molecular weight and increase in temperature. Heat release due to combustion also affects the CJ velocity.

Fig. 9 CJ detonation velocity versus equivalence ratio

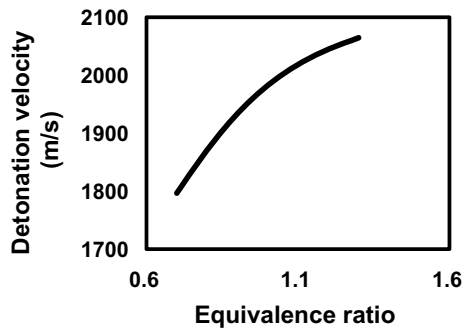


Fig. 10 CJ pressure versus equivalence ratio

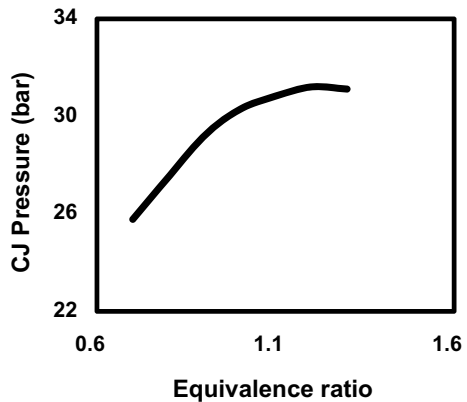
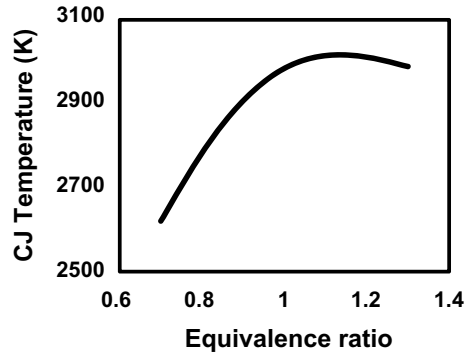


Fig. 11 CJ temperature versus equivalence ratio



Heat release is appreciable as the stoichiometric condition is approached. This in turn increases the CJ pressure and temperature as shown in Figs. 10 and 11. The pressure value becomes almost constant in the fuel excess regime considered in this work. But, the CJ temperature decreases after attaining maximum at stoichiometry.

6 Determination of Averaged Pressure on the Thrust Wall

In order to find the averaged pressure on the thrust wall, one has to model the gas dynamics of the flow field created by the RDE. A simple way is to consider the propagation of the detonation in a layer of height, H over a solid surface. This is equivalent to making an assumption that the flow ahead of the detonation is parallel to the thrust surface, and the detonation wave is normal to the surface. The complex flow field downstream of the detonation wave is shown in Fig. 2. The modelling of the flow field behind the detonation wave is quite complex due to oblique shock wave, contact surface between combustion products of detonation wave and shocked combustion products and the expansion waves. Simplifications reported in literature are utilized to model the above aspects using a self-similar rarefaction wave pressure profile. The flow field was modelled by a few researchers [12] using simple shock solutions and method of characteristics (MOC). Using the data base on rarefaction waves, Sichel and Foster [9] computed impulse function from an infinitely long layer using the parameters, viz., layer height, H and detonation overpressure, ΔP_{CJ} . They gave an expression for pressure along the ground behind detonation wave front. It can be expressed as follows:

$$P(x) - P_{c,1} = (P_{CJ} - P_{c,1})\Psi\left(\frac{x}{H}\right) = \Delta P_{CJ}\Psi(\xi; \gamma_e) \quad (8)$$

The function Ψ depends on the properties of combustion products. The average pressure along the thrust surface is given as follows:

$$\bar{P}_c - P_{c,1} = \Delta P_{CJ} \frac{H}{2\Pi R} \int_0^{2\Pi R/H} \Psi(\xi) d\xi \tag{9}$$

The data of P/P_{CJ} as a function of x/H is curve fitted as a fourth order polynomial (correlation coefficient: 0.99131). The least square fit is given below

$$P/P_{CJ} = -0.0561(x/H)^4 + 0.3455(x/H)^3 - 0.5807(x/H)^2 - 0.153(x/H) + 1.0147 \tag{10}$$

Here, $P/P_{CJ} = \Psi$ and $x/H = \xi$. A few authors have fitted an exponential fit [7] which does not seem to be the best fit to the experimental data. The least square fit for the experimental data is given in Fig. 12 [7]. Using this, the integral term of Eq. 9 can be evaluated to obtain the average pressure on the thrust surface. Figure 13 shows the variation of average pressure as a function of equivalence ratio for hydrogen-air

Fig. 12 Least square fit of experimental data [9]

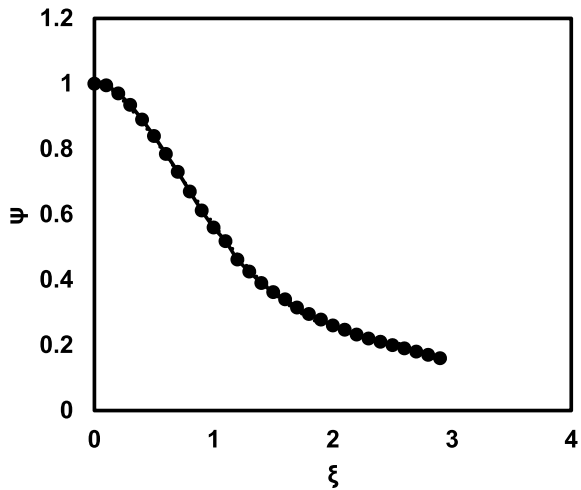
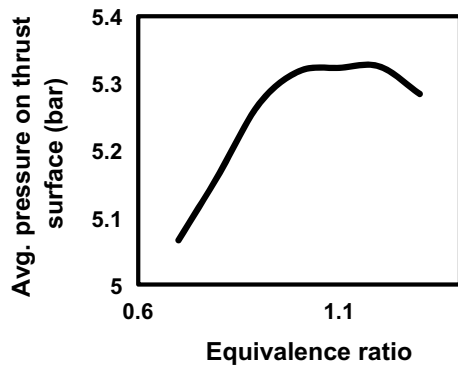


Fig. 13 Average pressure on thrust surface versus equivalence ratio



detonation. The average pressure increases with increase in equivalence ratio due to the strength of the detonation wave as a result of heat release till stoichiometry is reached. Afterwards the pressure value levels off as the fuel rich compositions do not release large energy of combustion. Reduction of pressure is seen for the equivalence ratio of 1.3. The value of detonation layer height, H is shown as a function of equivalence ratio in Fig. 14. The detonation wave height or layer height decreases as the equivalence ratio is increased. This height is inversely proportional to detonation wave velocity for a given mixture flow rate and combustor geometry. The detonation wave velocity increases with increase in equivalence ratio and therefore, the height decreases with increase in equivalence ratio.

Knowing the pressure distribution, the temperature distribution can be evaluated as follows:

$T(x) = T_{CJ} (P(x)/P_{CJ})^{\text{gam}}$ where $\text{gam} = (\gamma - 1)/\gamma$. The pressure and temperature distributions for two detonation cycles at unity equivalence ratio are given in Fig. 15.

Fig. 14 Mixture height versus equivalence ratio

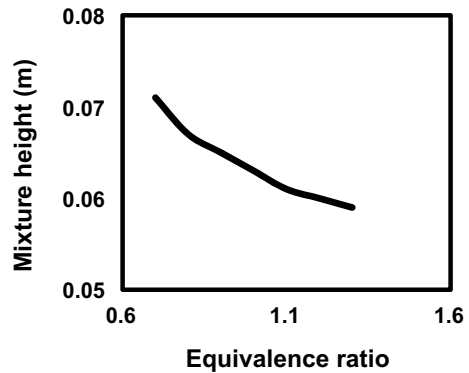
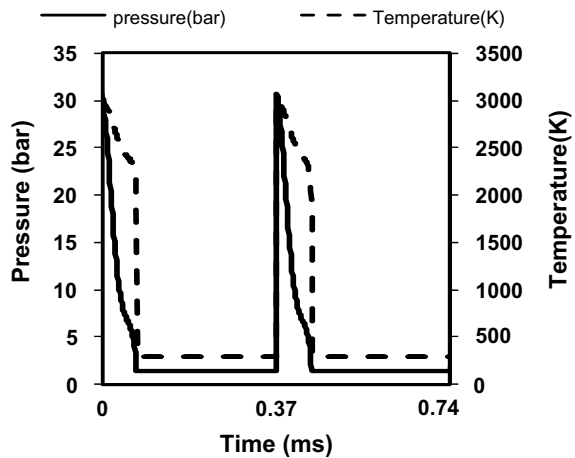


Fig. 15 Pressure and temperature versus time



The starting time ($t = 0$) corresponds to the detonation wave. The pressure and temperature distributions downstream of the detonation wave are shown for two cycles. It is to be seen that the period over which the pressures are in excess of injection static pressure would be the time of blockage of the flow.

The point at which the flow commences until the next detonation cycle getting established can be seen clearly from this detonation cycle diagram based on the downstream expansion waves computed using the experimental least square fit expression explained above. The pressure distributions for varying equivalence ratios of the hydrogen-air detonation are given in Fig. 16. The equivalence ratios are varied from 0.7 to 1.3 to cover either side of the stoichiometry. The value of pressure at the starting point of $x = 0$ is the CJ pressure. The pressure increases with increase in equivalence ratio.

All the pressures merge together after 0.2 m distance from the detonation wave in the circumference of the RDE indicating that the flow of fresh mixture starts entering inside the annular combustor. The corresponding temperature distributions for varying equivalence ratios of the hydrogen-air detonation are given in Fig. 17. In this case, the CJ temperatures are increasing with increasing equivalence ratio

Fig. 16 Pressure versus distance for various equivalence ratios

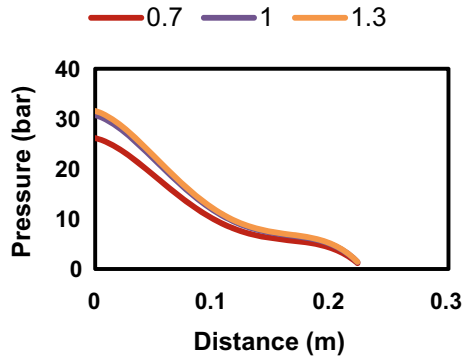
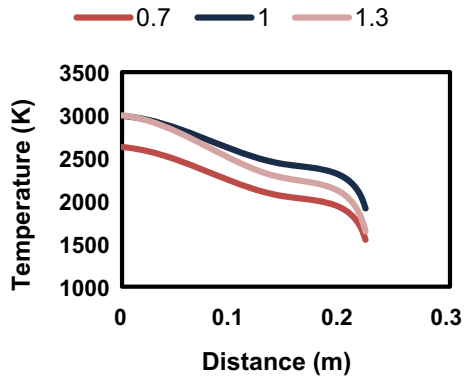


Fig. 17 Temperature versus distance for various equivalence ratios



till stoichiometry. After equivalence ratio equals unity, the temperature starts falling down. The rest of the trend continues as per the distribution function.

7 Propulsion Parameters Under Pressure History Model

Average thrust due to detonation is given by

$$F_I = \Delta P_{CJ} \frac{A_c H}{2 \Pi R} K = \Delta P_{CJ} W H K \quad (11)$$

where K is the value of the integral

$$\text{Thrust}(N) = F_I + F_{II} \quad (12)$$

$$\text{Specific thrust}(N/\text{kg/s}) = \text{Thrust}/\text{Total mass flow rate} \quad (13)$$

$$\text{Specific impulse}(s) = \text{Thrust}/(\text{Fuel flow rate} * g) \quad (14)$$

Figure 18 shows the variation of specific thrust with equivalence ratio. The specific thrust increases in the fuel lean regime, attains a maximum at stoichiometry and then decreases in the fuel rich regime. This follows the trend of the average pressure exerted on the thrust surface. However, the numerical values are not very much different over the equivalence ratios considered. Figure 19 shows the variation of fuel-based specific impulse with equivalence ratio. Specific impulse decreases with increase in equivalence ratio due to the increase of fuel flow rate. The fuel-based specific impulse resulted from the present analysis for our configuration using H_2 -air is 4733 s compared to a value of 4706 s reported in literature [7] for a stoichiometric composition. The same model has been used to evaluate the C_2H_4 -air system. The

Fig. 18 Specific thrust versus equivalence ratio

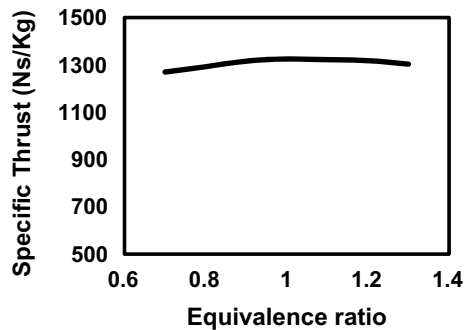
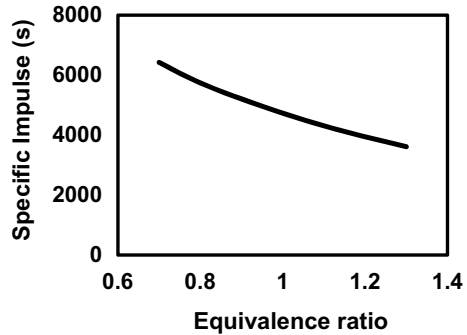


Fig. 19 Specific impulse versus equivalence ratio



specific impulse of our study is 2111 s compared to 1975s reported in literature [7] for the fuel-based equivalence ratio of 0.5.

8 Conclusions

The conclusions of this study are as follows:

1. The objective of obtaining the conditions to be set during the experiments has been fulfilled. The stagnation conditions at the hydrogen fuel and air injection plenum chambers for varying the equivalence ratios over 0.7–1.3 can be set using the flow rates to be handled within the available flow rates of the test facility.
2. As the fuel and oxidiser are injected perpendicular to each other and not injected as a premixed mixture, a simple mixing analysis has been carried out to obtain the conditions ahead of the detonation wave. This was useful in getting the reasonable propulsive performance.
3. The flow properties of detonation wave have been obtained using a well-tested tool box exclusively made for the prediction of shock waves and detonations.
4. The thrust and specific impulse are computed based on “pressure history model” of [7]. This model could yield the performance parameters, which are likely to emerge from the experiments proposed to be conducted at NCCRD, IIT, Madras.
5. The fuel-based specific impulse resulted from the present analysis for our configuration using H_2 -air is 4733 s compared to a value of 4706 s reported [7] for a stoichiometric composition. The same model has been used to evaluate the C_2H_4 -air system. The specific impulse of our study is 2111 s compared to 1975s reported [7] for the fuel-based equivalence ratio of 0.5. These are the reasonable matching values due to certain improvements made in the present study such as incorporation of mixing model and utilizing the curve fit data of the expansion wave pressure decay downstream of the detonation wave in the calculation of average pressure over the porous thrust surface.

6. After obtaining the experimental data, the shortcomings or strength of these simple models can be assessed and corrective actions can be taken using high fidelity models based on CFD.

Acknowledgements The first author expresses his gratitude to CSIR, Government of India for funding the project on RDE under the CSIR Bhatnagar Fellowship Scheme. The support extended by Prof. S. R. Chakravarthy, Coordinator, NCCRD, IIT, Madras for performing the research activities is sincerely acknowledged.

References

1. George AS, Driscoll R, Anand V, Gutmark E (2017) On the existence and multiplicity of rotating detonations. *Proc Combust Inst* 36:2691–2698
2. Yi TH, Lou J, Turangan C, Choi JY, Wolanski P (2011) Propulsive performance of a continuously rotating detonation engine. *J Propul Power* 27(1):171–181
3. Anand V, Gutmark E (2018) Rotating detonations and spinning detonations: similarities and differences. *AIAA J* 56(5):1717–1722
4. Bykovskii FA, Zhdan SA, Vedernikov EF (2006) Continuous spin detonations. *J Propul Power* 22(6):1204–1216
5. Roy RD, Amrutha P, Ramanujachari V (2019) Design of rotating detonation wave combustor based on detonation cell width correlations. In: *Proceedings, 26th national conference on internal combustion engines and combustion*, NIT Kurukshetra, India
6. Davidenko DM, Eude Y, Gokalp I, Falempin F (2011) Theoretical and numerical studies on continuous detonation wave engines. In: *AIAA 2011–2334*
7. Shepherd JE, Kasahara J (2017) Analytical models for the thrust of a rotating detonation engine. *GALCIT Report*, CIT, CA, USA
8. Braun EM (2012) New detonation concepts for propulsion and power generation. PhD Thesis, University of Texas at Arlington, USA
9. Sichel M, Foster JC (1979) The ground impulse generated by a plane fuel air explosion with side relief. *Acta Astronaut* 6:243–256
10. Browne S, Ziegler J, Shepherd JE (2008) Numerical solution method for shock and detonation jump conditions. *GALCIT Report FM 2006.006*
11. Goodwin D (2010) Cantera: object oriented software for reactive flows. <http://code.google.com/p/cantera>
12. Fievisohn RT, Yu KH (2016) Steady state analysis of rotating detonation engine flow fields with method of characteristics. *J Propul Power*, online publication, Article in Advance

Design and Performance Evaluation of Plug Nozzle for Rotating Detonation Wave Engine



V. Ramanujachari, Rahul Dutta Roy, and P. Amrutha Preethi

Abstract In a rotating detonation wave engine (RDE), a unidirectional detonation wave could be created and the exhaust gases are expanded through an annular plug nozzle producing thrust. Empirical relations reported in open literature based on detonation cell size are used to design the combustor. Hydrogen is chosen as the fuel, while air is selected as the oxidizer. The RDE hardware has been realized, and the test facility is being modified at National Combustion Centre for Research and Development (NCCRD), IIT Madras, to carry out static tests. In order to obtain necessary increment in thrust for propulsion applications, a plug nozzle is designed based on simple wave theory under stoichiometric condition. The inlet conditions to the nozzle are established based on “axial flow model” of RDE reported in open literature. As the hydrogen and air are entering as two different streams perpendicular to each other, a simple mixing analysis is carried out to evaluate the mixture properties ahead of the detonation wave. The Chapman Jouguet (CJ) detonation computations are carried out using the shock and detonation toolbox runs in conjunction with Cantera software assuming chemical equilibrium. The modelling of the flow field downstream of the detonation wave is established using the solution of integral mass, momentum and energy equations written for the streamline flow from detonation wave to the exit of the combustor. These conditions are used to evaluate the propulsion parameters at different fuel-based equivalence ratios (0.7–1.3) as a result of expansion through the plug nozzle. The increment in fuel-based specific impulse resulted from the present analysis for our configuration using H₂–air is 18% due to the presence of plug nozzle for the stoichiometric composition at a nozzle entry stagnation pressure of 6.9 bar. The fuel-based specific impulse based on the “axial flow model” reported in the literature for the stoichiometric hydrogen–air mixture at the combustor exit static pressure of 1 bar without plug nozzle is 5383 s. For the present combustor at the same condition, it is 5474 s, which appears to be close while modelling the complex processes using simplified model equations. Several input conditions and

V. Ramanujachari (✉) · R. D. Roy
National Centre for Combustion Research and Development, IIT Madras, Chennai 600036, India
e-mail: vramanujachari@yahoo.co.in

P. Amrutha Preethi
G. Pulla Reddy Engineering College, Kurnool 518007, India

© The Author(s), under exclusive license to Springer Nature Singapore Pte Ltd. 2023
G. Sivaramakrishna et al. (eds.), *Proceedings of the National Aerospace Propulsion Conference*, Lecture Notes in Mechanical Engineering,
https://doi.org/10.1007/978-981-19-2378-4_25

combustor–plug nozzle combined performance parameters would be utilized for setting the conditions for the experiments.

Nomenclature

A	Area (m^2)
A_{annular}	Annular area of combustion chamber (m^2)
a	Speed of sound (m/s)
F	Thrust produced (N)
I_{sp}	Specific impulse (s)
M	Mach number
R	Radius from the plug axis (m)
T	Temperature (K)
V, u	Velocity (m/s)
c_p	Specific heat at constant pressure (kJ/kg-K)
h	Enthalpy (MJ/kg)
\dot{m}	Mass flow rate (kg/s)
p	Pressure (bar)
q_o	Heat release (MJ/kg)
w	Combustion chamber width (m)

Greek symbols

γ	Ratio of specific heats
ε	Expansion ratio of nozzle
ρ	Density (kg/m^3)
Φ_x	Angle between plug axis and Prandtl–Meyer expansion wave
ϕ	Equivalence ratio
μ	Mach angle
ν	Prandtl–Meyer turning angle/expansion angle

Subscripts

CJ	Chapman Jouguet conditions
c	Chamber conditions
d	Downstream conditions of the detonation wave
m	Mixture state
t	Stagnation conditions
x	Location point

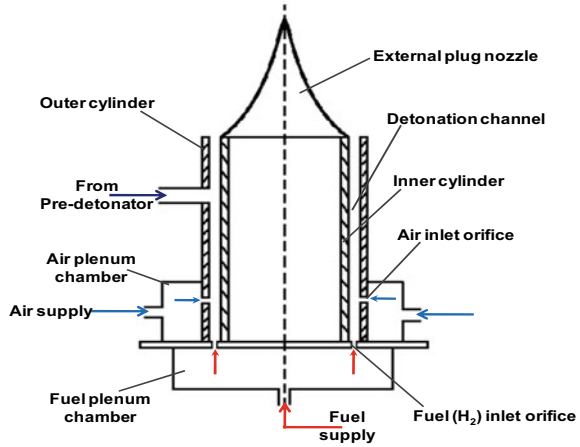
1 Introduction

The propulsive performance increases in detonation mode of engines. Continuous detonation engines can be used for rocket engines and air-breathing engines. It is reported that the constant area combustor using continuous detonation wave combustion delivers 7–18% more specific impulse than the one delivered by a deflagrative mode of combustion [1]. The rotating detonation wave engine has emerged as a promising concept due to its high specific power output, thrust to weight ratio and volumetric efficiency [2]. This has been proposed as a substitute for liquid propellant rocket or ramjet engine [3]. In addition, it can replace the gas turbine engines for power generation also [4]. Due to its promising potential as a propulsive and power generation device, it has been researched worldwide based on both numerical and experimental investigations. It has been reported that the detonation wave propagates with high velocity deficit when compared to CJ detonation wave velocity [4]. In order to understand this RDE and to realize an engine to deliver adequate thrust, an experimental work has been initiated. An experimental engine has been designed based on the empirical correlations of [5]. In this study, it is analysed to evaluate the performance of the engine using simple one-dimensional modelling technique. Davidenko et al. [1], Shepherd and Kasahara [6] and Braun [7] have carried out simple modelling of the complex detonation wave phenomena. Various types of nozzles were tested by Fotia et al. [8] for propulsive purposes. One of the popular and compact nozzles for the RDE is the plug nozzle. The design of the plug nozzle is carried out based on the method suggested by Lee & Thompson [9]. The objective of this paper is to show how an engine analysis can be carried out on an RDE designed and realized based on empirical methods [10]. In addition, a plug nozzle has been designed for fitting it in to the annular combustor of RDE for getting incremental performance. This work establishes the conditions to be set for the proposed experiments and the performance expected from the engine tests with and without plug nozzle.

2 Rotating Detonation Engine Concept

In this engine, a combustible mixture is continuously injected inside the width of the coaxial cylindrical combustion chamber. After initiation of detonation by an ignition device, one or more transverse detonation waves rotate inside the annular width releasing large volume of product gases at high pressure. The expansion of these gases take a turn to create an axial flow at the exit of the combustion chamber and to produce thrust for the forward motion of the vehicle fitted to the engine. The rotating detonation wave engine is shown in Fig. 1. It consists of an annular cylindrical combustion chamber and a plug nozzle. The fuel (hydrogen) and oxidizer (air) are injected through several holes and meet at perpendicular to each other for better mixing. They get mixed as they move towards the nozzle end and get ignited using a

Fig. 1 Schematic of rotating detonation engine with a plug nozzle (not to scale)



pre-detonator fuelled by a mixture of hydrogen and oxygen. Transverse detonation waves rotate around the annulus and burn the mixture of fuel and oxidizer layer.

The detonation is assumed to be CJ detonation with a rotational frequency of the order of 3–15 kHz. The combustion products flow towards the open end and further expand through a plug nozzle. The flow in the annular width is supersonic throughout and does not need a sonic throat similar to the case of rocket engines using a convergent divergent nozzle.

3 Modelling of Injection Process

It is essential to obtain an injection model just upstream of the detonation for subsequent modelling based on axial flow model. For simplicity, one-dimensional steady flow equations (Eqs. 1–4) of continuity, momentum and energy are formulated and solved based on the control volume as shown in Fig. 2 to obtain the mixture properties of fuel and air prior to detonation in the annular combustor. State 1 is for the airflow; state 2 is for the fuel flow, and state 3 for the mixture conditions. In all the cases, the total pressure of the air is maintained at 4.5 bar (abs), and hence, the flow rate of air is constant at 3.852 kg/s. Depending upon the fuel-based equivalence ratio, the fuel flow rate is varied. As the number and diameter of the fuel injection holes are fixed, the fuel injection total pressure is varied to allow the required amount of fuel flow.

1. Continuity equation

$$\dot{m}_1 + \dot{m}_2 = \dot{m}_3 \quad (1)$$

$$\dot{m}_3 = \rho_3 A_3 V_3 \quad (2)$$

2. Energy equation

$$\frac{\dot{m}_1}{\dot{m}_3} \left(h_1 + \frac{V_1^2}{2} \right) + \frac{\dot{m}_2}{\dot{m}_3} \left(h_2 + \frac{V_2^2}{2} \right) = c_{p,3} T_3 + \frac{V_3^2}{2} \tag{3}$$

3. Axial momentum equation

$$\dot{m}_2 V_2 + p_2 A_2 + p_1 (A_3 - A_2) = \dot{m}_3 V_3 + p_3 A_3 \tag{4}$$

The axial momentum contribution of airflow is not considered as air is injected perpendicular to the axial direction. We have three equations and three unknowns (p_3, T_3, V_3). These equations can be solved using Newton–Raphson method. We can use isentropic equations to obtain the stagnation pressure, stagnation temperature and Mach number at the mixture state.

Figures 3, 4, 5 and 6 show the distribution of mass flow rate of fuel, Mach number, total and static pressures and total and static temperatures of the mixtures. As the mass flow rate of air is kept as constant for all the fuel-based equivalence ratios, the fuel flow rate continuously increases with increase in equivalence ratio as shown in Fig. 3.

Fig. 2 Control volume for the injection process

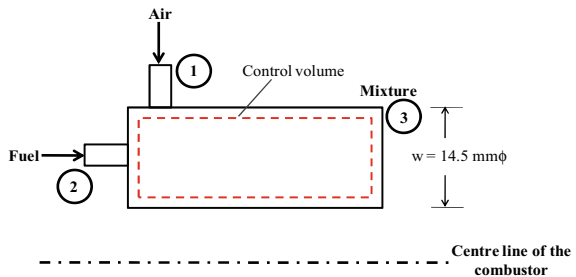


Fig. 3 Variation of fuel mass flow rate

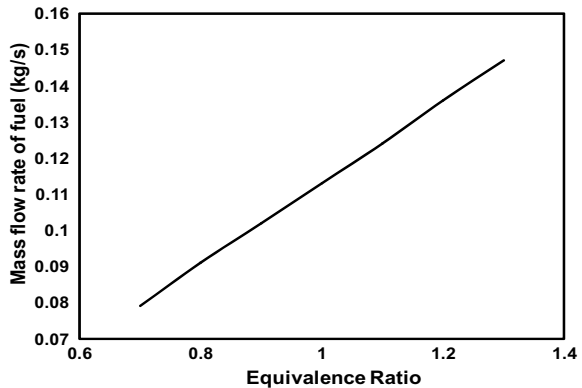


Fig. 4 Variation of Mixture Mach number

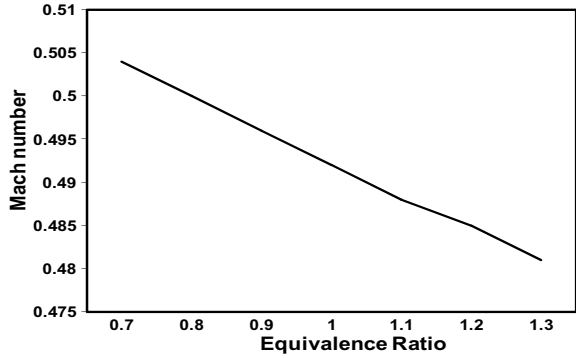


Fig. 5 Variation of total and static pressures

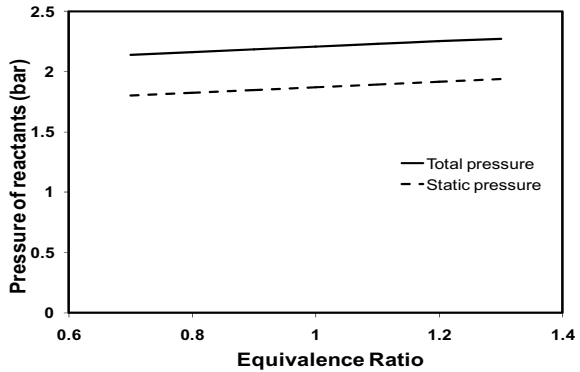
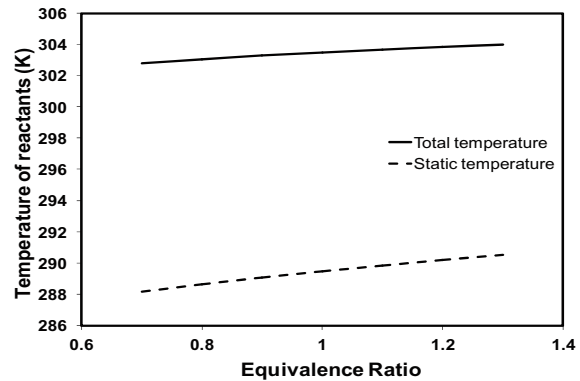


Fig. 6 Variation of total and static temperatures



The Mach number of the mixture over the range of equivalence ratios is shown in Fig. 4. A slight decrease in trend is noted. This may be due to the particular gas constant effect of the hydrogen–air mixture which in turn affects the sonic speed of the mixture. The sonic speed marginally increases in fuel-rich mixtures.

Figure 5 shows the distribution of static and stagnation pressures as a function of equivalence ratio. Both of them are almost constant over the equivalence ratios considered. The stagnation value is more compared to static quantity due to the finite Mach number of the flow. Similar trend is seen for the temperatures as shown in Fig. 6.

4 Computation of Detonation Properties

The CJ detonation computations are carried out using the wave fixed coordinate system. One-dimensional equations of mass, momentum and energy including energy of combustion are simultaneously solved to obtain the burned product state of the upper CJ point for a given fuel–air reactant mixture state. Here, the temperature of the burned products, as a result of heat release, is computed assuming chemical equilibrium. The flow equations are computed based on the shock and detonation toolbox [11]. Cantera software [12] is invoked for chemical equilibrium computations and is linked to the shock and detonation toolbox. The quantities of interest are heat release due to combustion of fuel–air mixture, CJ Mach number, velocity, pressure, temperature and density downstream of detonation wave. The CJ detonation phenomenon is not explained in detail as the focus of attention for this study is the plug nozzle design and analysis of RDE.

Figures 7, 8, 9 and 10 show the amount of heat release due to combustion, CJ Mach number, pressure and temperature as a function of fuel-based equivalence ratio. The heat release increases with increase in equivalence ratio. It levels off in the fuel-rich regime. The CJ Mach number is defined as the ratio between detonation wave velocity and sonic speed of the fuel–air mixture. It increases with increase in equivalence ratio. This is due to the increase in detonation wave velocity, as a result of increase in heat release.

Fig. 7 Variation of heat release due to detonation

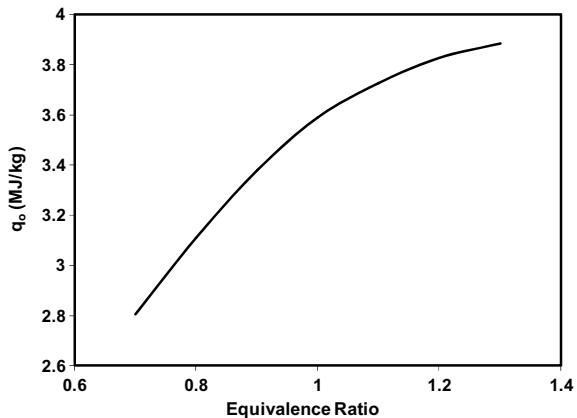


Fig. 8 Variation of CJ Mach number

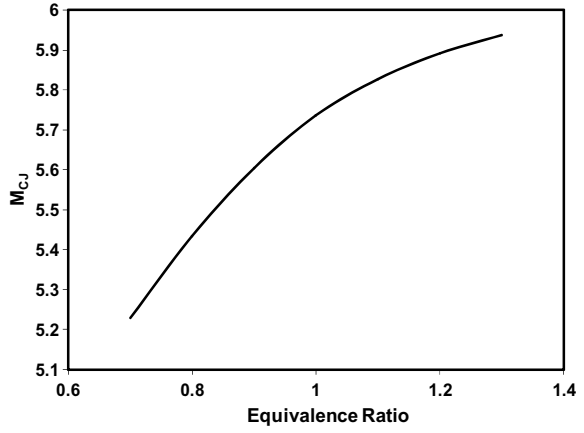


Fig. 9 Variation of CJ pressure

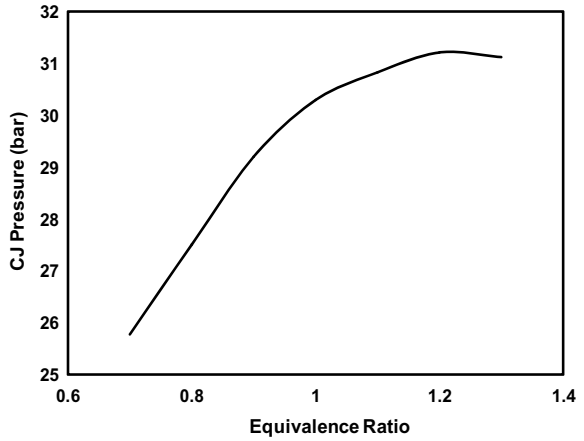
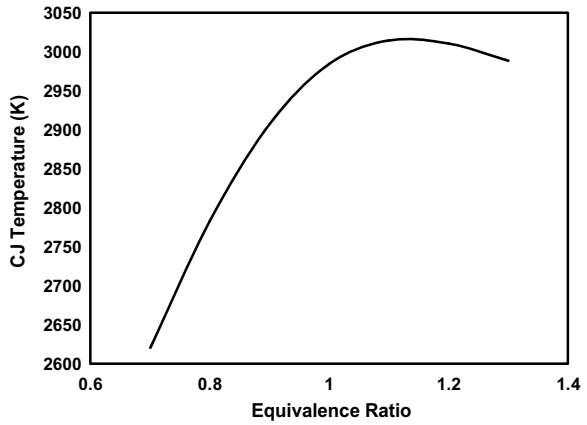


Fig. 10 Variation of CJ temperature



Though the sonic speed of the mixture increases with equivalence ratio, the increase in detonation wave velocity is appreciable and hence the increase in CJ Mach number. Heat release is appreciable as the stoichiometric condition is approached. This in turn increases the CJ pressure and temperature as shown in Figs. 9 and 10. The pressure value becomes almost constant in the fuel excess regime considered in this work. But, the CJ temperature decreases after attaining maximum at stoichiometry. This is due to the increase of the specific heat at constant pressure as the equivalence ratio increases. This increase in specific heat absorbs the heat release due to combustion and reduces the CJ temperature.

5 Axial Flow Model of Rotating Detonation Wave Engine

Schematic representation of the flow structure [1] of the axial flow model [6] is shown in Fig. 11. Fresh mixture is injected normal to the X-axis. The flow is considered in two reference frames, viz. fixed frame, FF and moving frame, MF attached to a detonation front. The flow velocities in MF are marked with an asterisk (*). In MF, the flow is considered to be in steady state. The “m” section refers to the mixture state just in front of the detonation wave. The “d” state is the flow state in the CJ plane.

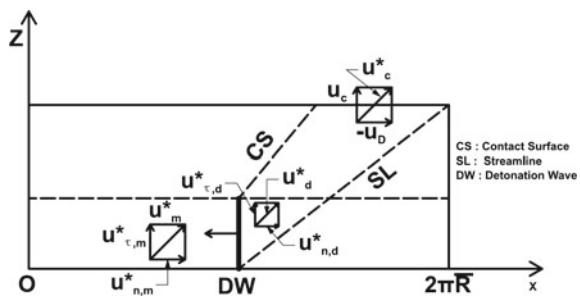
In FF, the flow conditions in the “m” section are determined from the total injection conditions and mixture Mach number. $u_{n,m} = 0$; $u_{\tau,m} = u_m$. Static state is same in FF and MF. The following expression for total enthalpy is used in MF state:

$$h_t^* = h + 0.5(u_n^{*2} + u_\tau^{*2}) \tag{5}$$

Chamber velocity is supposed to be axial in FF and must satisfy continuity equation. The expansion process is assumed to be isentropic between “d” state and “c” state (exit).

$$h_{tc}^* = h_c + 0.5(u_c^{*2} + u_{cJ}^{*2}) \tag{6}$$

Fig. 11 Flow structure postulated by Davidenko et al. for the axial flow model of RDE



Invoking the energy conservation principle in the sections “*m*”, “*d*” and “*c*”, we can write as follows:

$$h_m^* + u_{CJ}^2/2 = h_d^* + C_d^2/2 = h_c + u_c^2/2 + u_{CJ}^2/2 \tag{7}$$

Equating the stagnation enthalpies at “*m*” and “*c*” states, we get

$$h_m^* = h_c + u_c^2/2 \tag{8}$$

Here, $h_m = q_0 + c_{p3} t_3 + V_3^2/2 =$ enthalpy of the products and is equal to $h_c + u_c^2/2$, where q_0 is the heat released due to combustion per unit mass (Variation of this quantity with equivalence ratio is shown in Fig. 7). From this expression, we can get the axial velocity.

6 Propulsion Parameters Under Axial Flow Model (Without Nozzle)

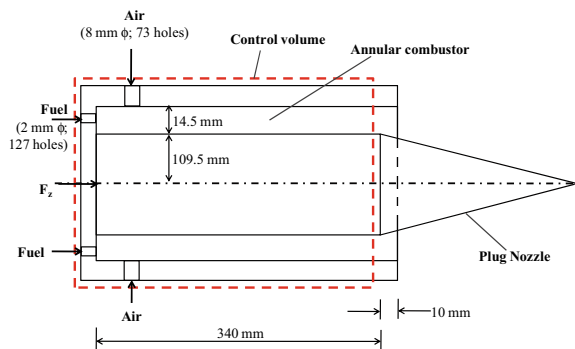
The control volume for the axial model is shown in Fig. 12. The combustion chamber is capable of producing thrust and related specific impulse due to flow expansion at the exit of the combustor. For an assumed static pressure at the exit of the combustion chamber, p_c , the static temperature can be evaluated assuming isentropic flow, i.e.

$$T = T_{CJ}(p_c/p_{CJ})^{(\gamma-1)/\gamma} \tag{9}$$

Axial velocity at the exit of combustion chamber is u_c and calculated by the expression as given below:

$$h_m = c_{pc}T + u_c^2/2 \tag{10}$$

Fig. 12 Control volume for axial flow model postulated by Shepherd and Kasahara



Exit Mach number is equal to the ratio of axial velocity to sonic velocity. Bycovskii et al. (2006) mentioned that the flow Mach number at the exit of the combustor is unity. Other researchers mentioned that the Mach number varies from 1 to 1.3. In the present study, the static pressure at the exit is varied in such a way that the Mach number comes close to unity, but still in supersonic regime.

Figure 13 shows the variation of total pressure ratio (chamber exit to mixture ahead of the detonation wave) as a function of equivalence ratio. It shows that the detonation produces strong additional total pressure in the event of flow expansion from downstream of detonation wave to the RDE combustor exit. This total pressure gain is the specialty of the detonation wave engine which is responsible for delivering high performance. The increase in total pressure is about three times more than the total pressure of the mixture supplied to the engine for detonation.

Figure 14 shows the static enthalpy of the products at the exit of the combustion chamber, h_c , as a function of static pressure at the exit of the combustion chamber

Fig. 13 Variation of total pressure ratio

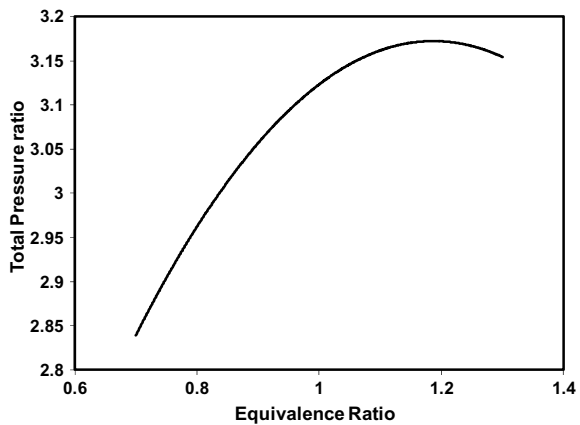
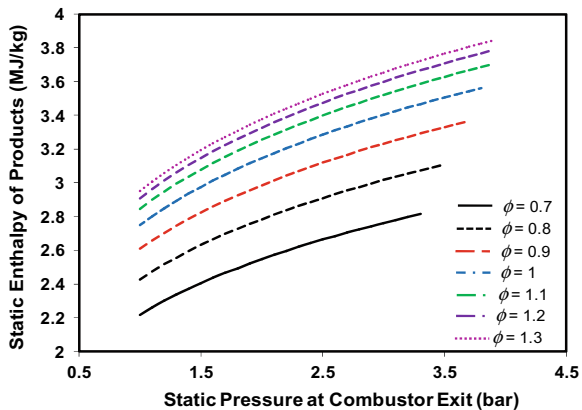


Fig. 14 Variation of static enthalpy of products



for various equivalence ratios. The static pressure is increased in small increments from the atmospheric pressure of 1 bar to get the condition of Mach number at the exit very close to unity and still the supersonic value in the range of 1.01 to 1.02.

Once the near unity Mach number is reached, the computations are stopped. Hence, the curves are terminating on the right-hand side at different static pressures. Greater than that pressure will produce subsonic speeds, which are practically not feasible and the supersonic flow would be expanded by a nozzle to produce propulsive performance. In addition, the velocity at the exit of the combustor would become an imaginary quantity when the static enthalpy of products exceed the total enthalpy of reactants. As the equivalence ratio increases from fuel lean to rich, the enthalpy of the products increases due to increase in static temperature as a result of increase in static pressure. This becomes an important input to the design of plug nozzle for further expansion of the flow.

$$F = \dot{m}_3 u_c + (p_c - p_a) A_{\text{annular}} - \dot{m}_2 V_2 - (p_2 - p_a) A_2 \tag{11}$$

$$\text{Specific thrust(N/kg/s)} = \text{Thrust/Total mass flow rate} \tag{12}$$

$$\text{Specific impulse(s)} = \text{Thrust}/(\text{Fuel flow rate} * g) \tag{13}$$

Figure 15 shows the variation of specific thrust as a function of equivalence ratio. The specific thrust increases with increase in equivalence ratio. Though there is a variation, it is nominal as the value of variation is from 1400 to 1600 Ns/kg over the variation of equivalence ratios from 0.7 to 1.3. It is mainly due to the nominal variation in the combustion chamber exit velocity from 860 to 980 m/s and the total flow rate from 3.93 to 4 kg/s. The heat release during the process of detonation heats up the products to increase the sensible enthalpy of the products. This energy at the combustor exit is converted to jet thrust and the pressure thrust

Fig. 15 Variation of specific thrust at combustor exit

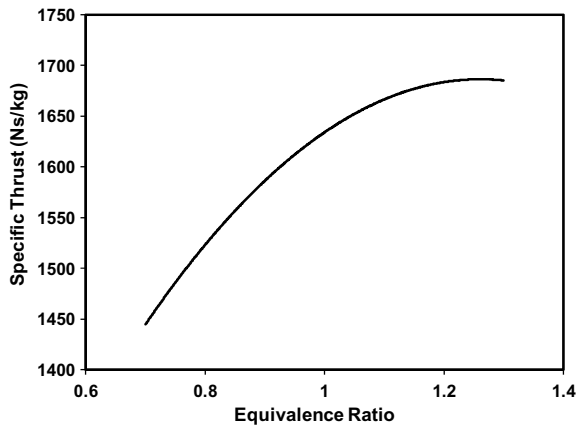
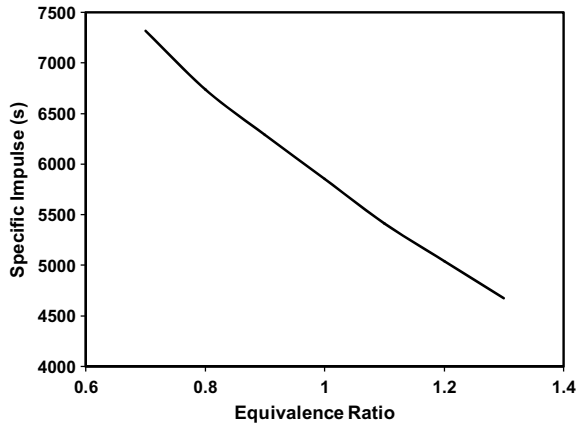


Fig. 16 Variation of specific impulse at combustor exit



as shown in Eq. (11). The heat release, product temperature and flow velocity are levelling off for fuel-rich conditions when the equivalence ratio is about 1.2. Figure 16 shows the variation of specific impulse with equivalence ratio. Though the specific thrust increases with increase in equivalence ratio, the specific impulse continuously decreases with increase in equivalence ratio. This is due to the variation of fuel flow rate corresponding to the variation of equivalence ratio. In this study, the airflow rate is kept constant and only the fuel flow rate is varied to change the equivalence ratio. It gives the indication that the effect of increase in fuel flow rate is appreciable compared to the increase in thrust. This is useful for further expanding the flow to obtain a large amount of thrust and related improvement in specific impulse using a plug nozzle.

7 Design of Plug Nozzle for RDE

Plug or spike nozzles are popular in RDE to improve the performance of the propulsion system. In the present case, a plug nozzle is designed using a very simple methodology based on Prandtl–Meyer expansion waves. As the combustor of the RDE is already designed and fabricated for the hydrogen–air system at stoichiometry, the nozzle design has been carried out at this condition. Analysis under different conditions of fuel-based equivalence ratios has been carried out for this known contour of the plug nozzle. The design methodology documented in Lee and Thompson is followed for the design with certain modifications. The design of the nozzle contour is carried out as follows:

As the engine with annular combustor is already available, the nozzle area ratio is known a priori. Based on the gas dynamic relationship, the Mach number at the nozzle exit is calculated by solving the equation given below:

$$\varepsilon = \frac{A}{A^*} = \frac{1}{M} \left[\left(\frac{2}{\gamma + 1} \right) \left(1 + \frac{\gamma - 1}{2} M^2 \right) \right]^{\frac{\gamma + 1}{2(\gamma - 1)}} \tag{14}$$

where ε is the expansion ratio. The above equation is solved in an iterative way using Newton–Raphson method. Using Prandtl–Meyer relation, a total flow-turning angle can be calculated using the following equation:

$$v_e = \left(\frac{\gamma + 1}{\gamma - 1} \right)^{\frac{1}{2}} \tan^{-1} \left[\frac{\gamma - 1}{\gamma + 1} (M_e^2 - 1) \right]^{\frac{1}{2}} - \tan^{-1} (M_e^2 - 1)^{\frac{1}{2}} \tag{15}$$

The optimum thrust coefficient, $C_{F, \text{opt}}$ can be calculated as:

$$C_{F, \text{opt}} = \gamma M_e \left(\frac{2}{\gamma + 1} \right)^{\frac{\gamma + 1}{2(\gamma - 1)}} \left(1 + \frac{\gamma - 1}{2} M_e^2 \right)^{-\frac{1}{2}} \tag{16}$$

The following procedure of calculation is for determining the external plug contour. The Mach number on the plug surface is increased from $M_x = M_{\text{cc, exit}}$ at the incident expansion wave to $M_x = M_e$ at the tip by regular increments, M_{in} . Here, $M_{\text{cc, exit}}$ is very close to unity based on the work of [5].

$$M_{\text{in}} = \frac{M_e - M_{\text{cc, exit}}}{N} \tag{17}$$

$$M_x = 1 + x M_{\text{in}} \tag{18}$$

The area of the revolved expansion wave is given below:

$$A_x = \pi (R_e - R_x) [x_x^2 + (R_e - R_x)^2]^{\frac{1}{2}} \tag{19}$$

From the geometry in Fig. 17

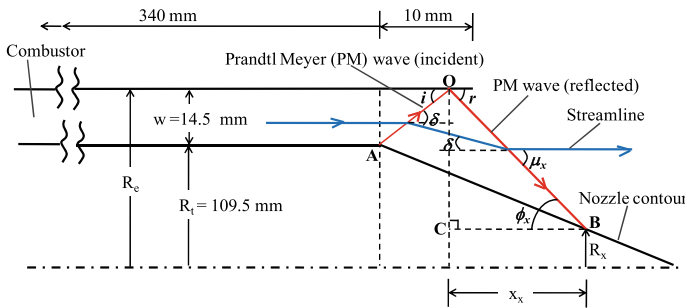


Fig. 17 Schematic of the interaction of Prandtl–Meyer wave with streamline and plug nozzle surface

$$\tan \Phi_x = \frac{R_e - R_x}{x_x} \quad (20)$$

Solving Eqs. (19) and (20),

$$A_x = \frac{\pi(R_e^2 - R_x^2)}{\sin \Phi_x} \quad (21)$$

The mass flow rate through the revolved expansion wave is:

$$\dot{m}_x = \rho_x A_x V_x \sin \mu_x \quad (22)$$

The mass flow rate through the throat is:

$$\dot{m}_t = \rho_t A_t V_t \quad (23)$$

The mass flow rate through these two sections should be equal; therefore, A_x can be determined as follows:

$$A_x = \frac{\left(\frac{\rho_t}{\rho_e}\right) A_t}{\left(\frac{\rho_x}{\rho_e}\right) \left(\frac{V_x}{V_t}\right) \sin \mu_x} \quad (24)$$

Equations (21) and (24) are solved for R_x :

$$\frac{R_x}{R_e} = \left\{ 1 - \frac{\left[\left(\frac{2}{\gamma+1} \right) \left(1 + \frac{\gamma-1}{2} M_x^2 \right) \right]^{\frac{\gamma+1}{2(\gamma-1)}} \sin(\mu_x)}{\varepsilon} \right\}^{\frac{1}{2}} \quad (25)$$

Once R_x is determined, x_x can be calculated using Eq. (20).

The pressure ratio at point “x” can be calculated using the following relationship:

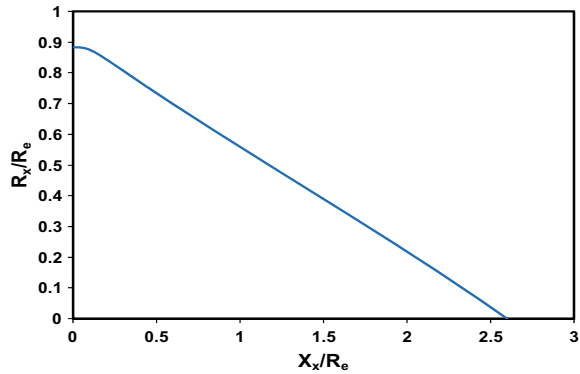
$$\frac{P_x}{P_e} = \left(1 + \frac{\gamma-1}{2} M_x^2 \right)^{\frac{-\gamma}{\gamma-1}} \quad (26)$$

The cumulative thrust is made up of the momentum flux and the pressure thrust at the throat surface plus the pressure integral down the plug to the point in question.

$$F_x = \dot{m}_t V_t + (P_t - P_a) A_t + \int (P_x - P_a) dA \quad (27)$$

$$I_{sp} = F_x / (\text{mass flow rate of fuel} * g) \quad (28)$$

Fig. 18 Plug nozzle contour plot



Based on the annular combustor geometry, the exit flow conditions and hydrogen–air stoichiometric conditions, plug nozzle has been designed by the procedure explained above. The contour above the symmetry axis is shown in Fig. 18. The same contour has been utilized in the computation of propulsion parameters, viz. thrust and specific impulse, at the conditions over the equivalence ratios 0.7–1.3.

Figure 19 shows the variation of axial thrust under different equivalence ratios on either side of the stoichiometry. The axial thrust increases with increase in equivalence ratio. Though the air mass flow rate is kept constant for all the conditions, the fuel flow rate increases with increase in equivalence ratio, thus making the total flow rate to increase. At a given equivalence ratio, there is appreciable increase in the value of thrust and specific impulse due to the pressure integral term (third term in Eq. 27) being predominant for about one length of the external radius (124 mm length of the nozzle). For the subsequent length of 198 mm (total length of the plug nozzle is 322 mm) the values are almost constant, indicating that the change in pressure integral term is negligible. This is attributed to the process of expansion in a diverging area with a constant total mass flow rate for a given equivalence ratio. Though it is nominal, variation of equivalence ratio varies with the total flow rate of the products

Fig. 19 Variation of thrust across plug nozzle

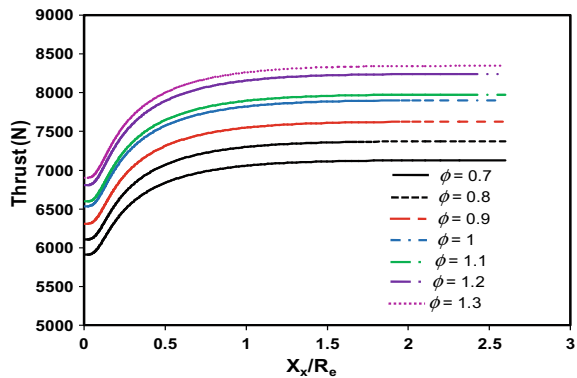
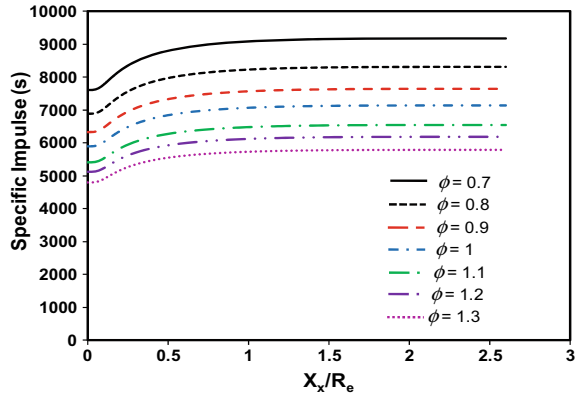


Fig. 20 Variation of specific impulse across plug nozzle

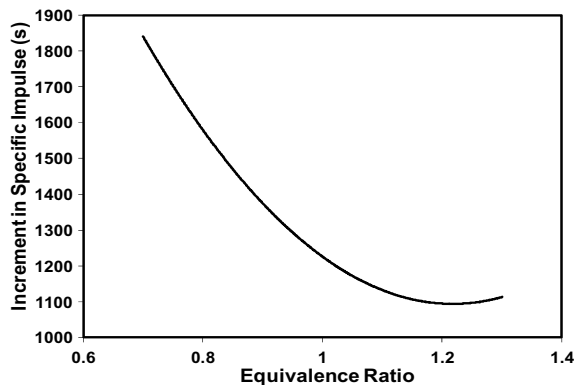


of combustion. In the range of equivalence ratios considered, the increment in thrust with and without nozzle is about 17–20%.

Figure 20 shows the variation of specific impulse with equivalence ratio. Specific impulse decreases with increase in fuel-based equivalence ratio. The decrease of specific impulse is due to the increase in fuel flow rate, in the event of increase in thrust. However, the increase in thrust is not appreciable as the fuel-rich regime commences. The fuel-based specific impulse resulted from the present analysis for our configuration using H_2 –air is 7129 s, an increment of 1277 s (about 18% increase) due to the addition of plug nozzle for the stoichiometric composition at a nozzle entry stagnation pressure of 6.9 bar. The fuel-based specific impulse based on the “axial flow model” [6] for the stoichiometric hydrogen–air mixture at the combustor exit static pressure of 1 bar without plug nozzle is 5383 s.

For the present combustor at the same condition, it is 5474 s which appears to be close while modelling the complex processes using simplified model equations. Figure 21 shows the increment in the value of specific impulse as a function of equivalence ratio. RDE is capable of producing thrust without the nozzle based on

Fig. 21 Variation of increment in specific impulse



the average force exerted on the porous injector surface or the momentum difference between the flow of products at the exit and the mixture entering the annular combustor as shown in Eq. (11). If higher performance is needed, further expansion of the products of combustion is possible by incorporating a nozzle, such as plug nozzle. The additional energy conversion process gives rise to additional thrust and the corresponding specific impulse, which is a figure of merit of the propulsion system. The incremental specific impulse varies from 1800 to 1100 s, which is substantial for the actual performance for a high-speed propulsion system.

8 Conclusions

The conclusions based on this study are given below:

1. The axial flow modelling of RDE along with the plug nozzle has been useful in obtaining the stagnation conditions to be set at the hydrogen and air plenum chambers for the equivalence ratios in the range of 0.7–1.3 to conduct the static tests.
2. The conditions ahead of the detonation wave are obtained through a simple mixing analysis of fuel and oxidiser as they enter the combustor perpendicular to each other.
3. The thrust and specific impulse are computed based on “axial flow model” of [6] and the flow structure of [1]. This model could yield the performance parameters, which are likely to emerge from the experiments proposed to be conducted at NCCRD, IIT Madras.
4. The fuel-based specific impulse based on the “axial flow model” [6] for the stoichiometric hydrogen–air mixture at the combustor exit static pressure of 1 bar without plug nozzle is 5383 s. For the present combustor at the same condition, it is 5474 s which appears to be close while modelling the complex processes using simplified model equations.
5. Computation of thrust with and without the plug nozzle indicated that the increase in thrust with nozzle is in the range of 17–20% for the range of equivalence ratios considered in this study.
6. The increase in fuel-based specific impulse resulted from the present analysis for our configuration using H₂–air is 18% due to the presence of plug nozzle for the stoichiometric composition at the nozzle entry stagnation pressure of 6.9 bar. This has clearly indicated the additional expansion process using plug nozzle. The plug nozzle design shall be incorporated in the existing test article to obtain additional propulsive performance of the RDE.
7. After obtaining the experimental data, the shortcomings and strength of these simple models can be assessed and corrective action can be taken using high fidelity models.

Acknowledgements The first author expresses his gratitude to CSIR, Government of India, for funding the project on RDE under the CSIR Bhatnagar Fellowship Scheme. The support extended by Prof. S R Chakravarthy, Coordinator, NCCRD, IIT Madras, for performing the research activities is sincerely acknowledged.

References

1. Davidenko DM, Eude Y, Gokalp I, Falempin F (2011) Theoretical and numerical studies on continuous detonation wave engines. In: AIAA pp 2011–2334
2. George AS, Driscoll R, Anand V, Gutmark E (2017) On the existence and multiplicity of rotating detonations. *Proc Combust Inst* 36:2691–2698
3. Yi TH, Lou J, Turangan C, Choi JY, Wolanski P (2011) Propulsive performance of a continuously rotating detonation engine. *J Propul Power* 27(1):171–181
4. Anand V, Gutmark E (2018) Rotating detonations and spinning detonations: similarities and differences. *AIAA J* 56(5):1717–1722
5. Bykovskii FA, Zhdan SA, Vedernikov EF (2006) Continuous spin detonations. *J Propul Power* 22(6):1204–1216
6. Shepherd JE, Kasahara J (2017) Analytical models for the thrust of a rotating detonation engine. In: GALCIT Report. CIT, CA, USA
7. Braun EM (2012) New detonation concepts for propulsion and power generation. PhD Thesis, University of Texas at Arlington, USA
8. Fotia ML, Schauer F, Kaemming T, Hoke J (2015) Experimental study of the performance of a rotating detonation engine with nozzle. In: AIAA 2015, 0631
9. Lec CC, Thompson DD (1964) FORTRAN program plug nozzle design. NASA TM X-53019
10. Roy RD, Amrutha P, Ramanujachari V (2019) Design of rotating detonation wave combustor based on detonation cell width correlations, In: Proceedings, 26th national conference on internal combustion engines and combustion, NIT Kurukshetra, India
11. Browne S, Ziegler J, Shepherd JE (2008) Numerical solution method for shock and detonation jump conditions. GALCIT Rep FM 2006 ; 006
12. Goodwin D (2010) Cantera: object oriented software for reactive flows. <https://code.google.com/p/cantera>

Feasibility Study of Hybrid Propulsion for Light Aircraft



G. Muthuselvan, B. R. Pai, M. Janaki Rami Reddy, Sadanand S. Kulkarni, M. E. Mohana Sundaram, Umesh Kumar Sinha, and S. Santhosh Kumar

Abstract Electric propulsion is rapidly entering the aviation sector. The main drivers are lower carbon footprint and lower noise emission. The present work examines the feasibility of hybrid propulsion for two-seater light aircraft, such as the Hansa 3 aircraft of CSIR-NAL. Both parallel and series arrangements of electric motors and internal combustion engines are considered. A general-purpose code is developed to determine the aircraft performance for different flight profiles and specific combination of power plant units. The state-of-the-art rotary (Wankel) engines are considered. Electrical hardware includes state-of-the-art motors and currently available lithium-ion batteries. A comparison is made between specific case of all-electric propulsion with various hybrid-electric propulsion system (HEPS). It is found that significant improvement in the performance of hybrid combinations with respect to all-electric case is observed. The work suggests that it is now an opportune time to enter the electric propulsion through the hybrid route.

Nomenclature

J	Advance ratio
V	Aircraft speed (m/s)
D	Propeller diameter (m)
C_P	Propeller power coefficient
P	Brake horse power from power plant (kW)
C_D	Drag coefficient
C_L	Lift coefficient
C_{D0}, K	Drag polar constants
ρ	Ambient density (kg/m^3)
n_s	Propeller speed (rps)

G. Muthuselvan (✉) · B. R. Pai · M. Janaki Rami Reddy · S. S. Kulkarni · M. E. Mohana Sundaram · U. K. Sinha · S. Santhosh Kumar
Propulsion Division, CSIR-NAL, Bangalore, Karnataka, India
e-mail: mechmuthul@nal.res.in

ϕ	Electrification factor (ratio of power from electrical system to total power from HEPS)
T_R	Thrust required (N)
P_T	Thrust power (kW)
m_f	Fuel flow rate (kg/h)
m	Mass of the aircraft (kg)
g	Acceleration due to gravity (m/s^2)
BSFC	Brake specific fuel consumption (g/kWh)
HEPS	Hybrid electric propulsion system

1 Introduction

With growing awareness of the need to reduce carbon footprint and pollution, and the trend toward use of renewable energy, electric propulsion has firmly entered ground transportation segment and is now also seriously entering the aviation sector. Rapid development in battery technology has been a major factor, but the energy density of batteries is still much lower than that of liquid fuels.

Also, lightweight high capacity electric motors have been developed. Though fully electric planes are entering the market in the microlight and sports aviation categories, an active field of research and development is for larger planes in the light aircraft and general aviation class. Here, the concept of hybrid propulsion is gaining grounds, with the prospect of better range and payloads.

Initial efforts are in the small aircraft segment and will gradually progress to larger aircraft. Rapid advancement in battery technology is permitting flight of microlight aircraft under 450 kg all up weight (AUW) while R&D efforts are ongoing for larger aircraft. An all-electric aircraft in the microlight and light sports aircraft (LSA) category (under 600 kg AUW) has recently come in the market, namely the Pipistrel Alpha Electro (2017). It has fairly good endurance of about 1 h and a cruise speed of 140 kmph. Larger aircraft (under 750 kg) and general aviation (GA) are being pursued in hybrid-electric configuration. Hybrid-electric propulsion was first demonstrated in 2011 by the Diamond Aircraft Co in their DA-36 Super Dimona, in collaboration with Siemens AG. The aircraft had a 70 kW electric motor and a 30 kW Wankel rotary engine in a series configuration. Since then a number of companies and institutions have joined the fray to develop hybrid powered aircraft. These include Siemens, Rolls Royce, GE, Safran, Airbus, VoltAero, NASA, and DLR.

With the Indian scenario in mind, the present investigation has been taken up to consider the feasibility of taking up R&D projects in this fast-developing field. The CSIR-NAL has developed a two-seater all-composite aircraft, the Hansa 3 for training and general use and is certified under the JAR-VLA category (under 750 kg AUW). An improved version, the Hansa NG is under development. CSIR-NAL has also developed Wankel rotary engines in the range of 30–65 hp, for UAV applications. In a collaborative project with DRDO, a 55 hp indigenous engine has been successfully

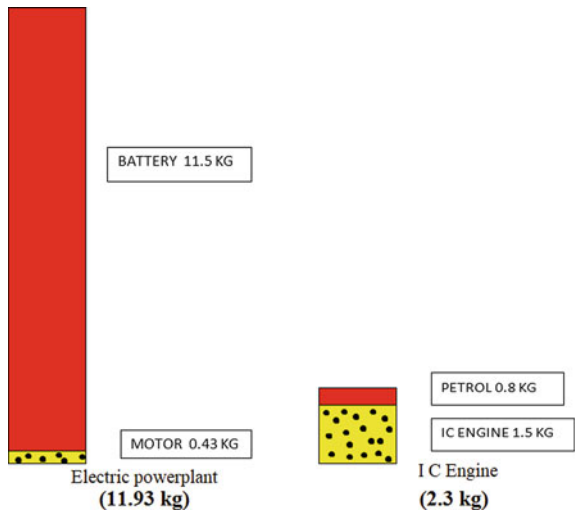
Fig. 1 CSIR-NAL Hansa aircraft



flown in a 350 kg class UAV. In this paper, the feasibility of developing a hybrid-electric power plant for a two-seater aircraft in the Hansa 3 class is considered (shown in Fig. 1), based on available electric components (i.e., batteries, motors, and accessories) and internal combustion engines. A procedure for rapidly evaluating the performance of a given combination of components is developed and used to arrive at a tentative scenario for further work in this field.

A basic feature of all-electric and hybrid propulsion plants which needs to be emphasized is their relative weight. A convenient way to grasp this is by evaluating the weight of a typical power plant to produce a unit thrust, say 1 kg force, from a propeller driving an aircraft at a typical speed of say 150 kmph. Figure 2 shows the comparison, based on typical values of governing parameters, namely motor weight and efficiency, battery weight (for typical Lithium-ion battery for aeronautical application), internal combustion engine weight and efficiency, propeller and transmission efficiency. It can be seen that electric plant will be about 5.5 times the weight of a pure IC engine-petrol combination. Moreover, a hybrid plant can be designed to get values in between and the electrification ratio (ϕ), namely the ratio of power from the electric-to total power of HEPS can be varied during various phases of flight to optimize the performance

Fig. 2 Relative weight of pure electric and I.C. engine system to provide thrust of 1 kg force at a velocity of 150 kmph



for a given application. This feature enables a unique and new feature for hybrid aircraft: its performance can be tailored for various application by simply varying the ratio of the battery and fuel carried for a particular sortie. For example, if the aircraft is to be mainly used for short training flights, it can carry more battery power and less fuel, thereby reducing the direct cost of operation (DOC) and pollution. For longer flights, it could carry a smaller battery pack and more fuel. These options are further discussed in the paper.

A good introduction to analysis of hybrid aircraft has been provided by Friedrich et. al [1]. The paper indicates that all-electrical propulsion is suited for slow flying and lightweight aircraft operating close to their $(L/D)_{\max}$ operating point. For hybrid aircraft, the ratio of maximum to minimum power requirement should be large. Junghsen et al. [2] discussed the power control strategies for the UAV propulsion system. Authors considered four different hybrid propulsion systems for small aerial vehicles applications. In the present study, four different power plant configurations are considered.

All-electric case is considered as reference case. Both in-house developed Wankel engine and engine of Wankel Supertec, Germany are considered in the present feasibility study. The range and endurance of aircraft is presented in the paper.

2 Description of Code

A general-purpose code is prepared to calculate the thrust power required at different stages of flight (takeoff, climb, cruise. and descent). The block diagram shown in Fig. 3 highlights the different stages of the calculations carried out in the code. The following parameters are specified as input conditions in the code.

1. Cruise altitude.
2. Ambient density.
3. Aircraft speed at climb, cruise, and descent.
4. Descent angle.
5. Variation of power available for climb with respect to altitude.
6. Aircraft geometric and weight details.
7. Drag polar and reference area
8. Electrification factor

The following equations are used to calculate the non-dimensional parameters of the propeller at different stages of flight.

$$\text{Advance ratio, } J = V/(n_s D)$$

$$\text{Propeller power coefficient, } C_P = P / (\rho n_s^3 D^5)$$

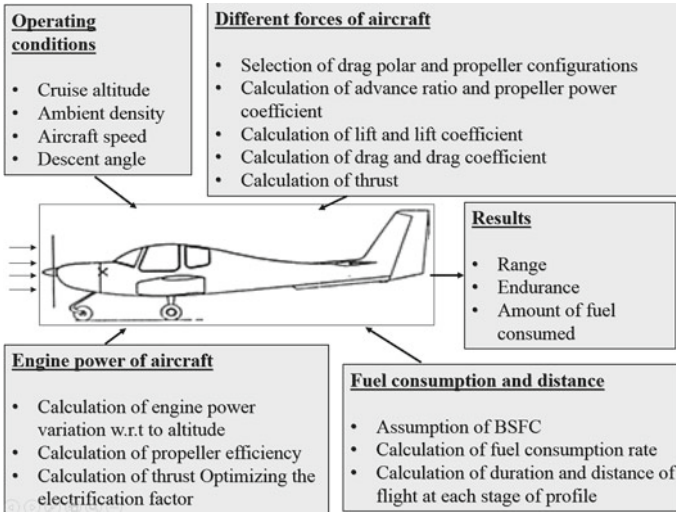


Fig. 3 Block diagram of different stages of the calculations carried out in the code

Using the characteristics plot of the propeller in terms of advance ratio and propeller power coefficient the propeller efficiency is calculated at different stages of the flight. The following equations are used to calculate the thrust power at different stages of the flight.

$$\text{Drag coefficient, } C_D = C_{D0} + K C_L^2$$

$$\text{Lift coefficient, } C_L = m g / (0.5 * \rho V^2 S)$$

$$\text{Thrust required, } T_R = 0.5 \rho V^2 S C_D$$

$$\text{Thrust power, } P_T = T_R * V$$

The thrust power required at different stages of flight viz., takeoff, climb, cruise, and descent are calculated using the solutions of above mentioned three equations. The Brake specific fuel consumption (BSFC) is defined by following formula.

$$\text{BSFC} = m_f / P_{\text{BHP}}$$

Using the measured values of BSFC of each engine the fuel flow consumption is calculated at each stage of the flight (takeoff, climb, cruise, and descent). Using aircraft speed at different stages of flight the total range and endurance is calculated. The electrification factor is defined as follows.

ϕ = Power from electrical unit / Total power supplied from hybrid power plant unit.

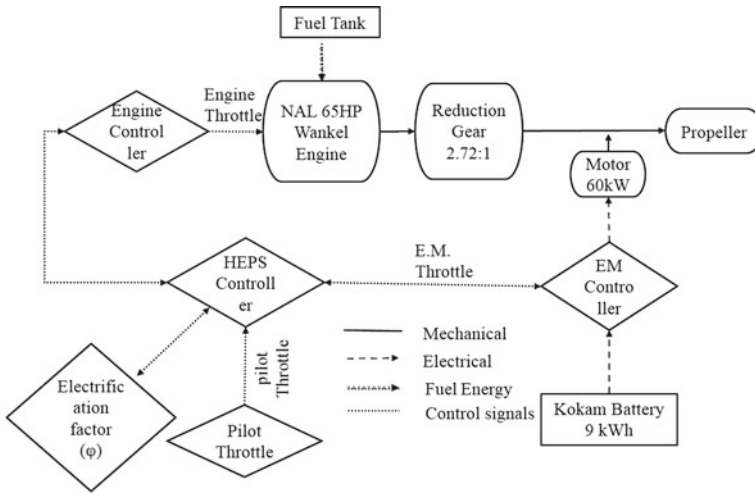
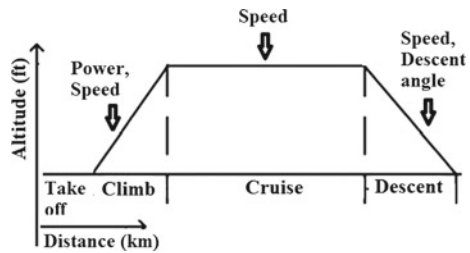


Fig. 4 Schematic layout of parallel configuration of HEPS

Fig. 5 Input conditions used in the HEPS code



The electrification factor is used in the code to quantify the distribution in energy between electric and mechanical power plant. At each stage of the flight, the electrification factor is appropriately varied to maximize the overall range of aircraft. The schematic layout of parallel configuration is shown in Fig. 4. The input conditions used in the code at different stages of flight mission is represented in Fig. 5.

3 Description of Battery Pack and Motor Details

The takeoff power requirement for the aircraft considered in the present study is around 75 kW. So the maximum power requirement for all-electric (AE1) case is fixed around 75 kW at propeller rpm of around 2200 rpm. To meet the requirement, a through survey was made and identified motors from M/s Rotex electric motor with power of 80 kW. Motor controller selected is BLDC motor controller from M/s MGM-Compro, Czechia operating with 400 V DC Bus. In the case of hybrid power plant

Table 1 Battery specifications

Sl No	Case id	Battery details			
		Energy density (kWh/kg)	Battery weight (kg)	Battery energy kWh	Max continuous C rate
I	AE 1	0.182	132	20	5
II	HbP1	0.169	67	9	5
III	HbP2	0.169	67	9	5
IV	HbP3	0.248	47	10	2

case, power from the engine is also used during takeoff and climb. So, the maximum power requirement for hybrid (Hb) case is fixed around 60 kW at propeller rpm around 2200 rpm. Similarly, REX90 BLDC motor is identified for hybrid-electric configuration (HbP1 and HbP2). Battery pack design depends on the number of cells/DC bus system voltage, current demand, and most critical was permissible weight availability to meet 1:1 fitment in existing aircraft configuration. Motor and controller selection decided the battery pack voltage and depending on electrification factor the suitable battery cells of lithium-ion batteries were identified from M/s Kokam Batteries. Dry cell weight fraction of 90% was considered tentatively for the design of battery pack for integration of battery cells, assembly, interconnection and battery management sensors integration and cooling requirements. Specifications of battery considered in the present study is shown in Table 1.

4 I.C. Engines for Hybrid Power Plant

High power-to-weight ratio and good fuel efficiency are the main factors in selecting I.C. engines for the hybrid configuration. Wankel Rotary Combustion Engine (WRCE) has gained considerable interest as viable power plants for small aircraft and unmanned aerial vehicles (UAVs) due to its inherent advantages. Only rotary Wankel engines are short listed for the present feasibility study. Four-stroke reciprocating engines were initially considered but are too bulky and heavy and two-stroke engines are not fuel efficient to meet the requirements. CSIR-NAL has established considerable expertise in analysis, materials, manufacture, and operation of Wankel engines over the past two decades. CSIR-NAL has developed a 55 hp engine jointly with DRDO for a tactical UAV applications. These engines have completed airworthiness qualification trials, and were successfully flight-tested. Further, a 65 hp engine was developed for a new UAV program. These are single rotor, liquid cooled engines. Both 55 and 65 hp Wankel engines are considered for the present study. It has been found that the 65 hp engine is a potential power plant for hybrid application to provide enough thrust during cruise (160 kmph) at cruise altitude of 6000 ft. The brief specifications of this engine are given in Table 2.

Table 2 Details of NAL 65 hp Wankel engine

Engine type	Wankel Rotary Combustion Engine
Thermodynamic cycle	Otto cycle
Maximum power (hp/kW)	65/48.5 at 8000 rpm @ sea level (without exhaust muffler)
Cylinder capacity (cc)	397
Number of rotors	1
Operating temperature	-40 °C to + 55 °C
Fuel supply system	Diaphragm type carburetor
Fuel	100 LL/93 Octane gasoline
Specific fuel consumption (g/kWh)	335–365
Engine lubrication system	Total loss lubrication
Engine aspiration	Naturally aspirated
Engine cooling	Liquid cooled
Ignition system	Capacitive discharge ignition
Propeller speed (rpm)	4000 @ maximum engine speed
Engine dry weight (kg)	30

The Wankel Supertec of Germany is producing Wankel engines with advanced features such as high pressure fuel injection, closed loop oil circulation and turbo-charging. Versions are available for stationary and mobile applications (up to 6000 rpm) and higher performance ones (up to 8000 rpm) are under development. The fuel efficiency and performance at higher altitudes is excellent. A major feature is that the engine can operate on ATF or diesel. This will be a useful factor for aircraft operating in most airports and also economically beneficial. Version with single rotor (351d) and dual rotor (352d) are available and have been considered in the present study. The brief specifications of this engine are given in Table 3.

5 Results and Discussion

Five cases of power plants are discussed in this section. The weight of each power plant is estimated such that the all up weight of the aircraft is within 750 kg for a cockpit payload of 140 kg. The weight of the fuel and battery is taken to be such as to match the permissible all up weight. The first case is that of an all-electrical power plant (Case AE1). The second case is that of a hybrid system (HbP1) comprising the NAL 65 hp Wankel Engine and a 60 kW electric motor in a parallel combination. The third case is that of a hybrid system (HbP2) comprising the Wankel SuperTec 351d and a 60 kW electric motor in a parallel combination. The fourth case is that of a hybrid system (HbP3) comprising the Wankel SuperTec 352d Wankel engine and a

Table 3 Details of Wankel Supertec diesel engines

Engine type	KKM351d	KKM352d
Engine displacement (cc)	350	350 × 2
Number of rotors	1	2
Max power (kW/Nm)	46/55 @ 8000 rpm	92/110 @ 8000 rpm
Charging	Turbo and Intercooler	Turbo and Intercooler
Fuel Injection	HP- Injection	HP-Injection
Weight (kg)	30	45
Engine performance at 6000 rpm (kW/Nm)	32/50	64/101
Power-to-weight ratio (kW/kg)	1.18	1.56
Fuel	ATF/Diesel	ATF/Diesel
Spec. fuel Cons (g/kWh)	290	285

60 kW electric motor in a parallel configuration. Further, details of these systems are given in Table 4. A CAD diagram of the hybrid plant for case 2 and case 4 are shown in Fig. 6a and 6b, respectively. The power plants are located within the nacelle space of the Hansa NG. The fifth case is series combination of mechanical and electric power plants and is discussed in Sect. 7 below.

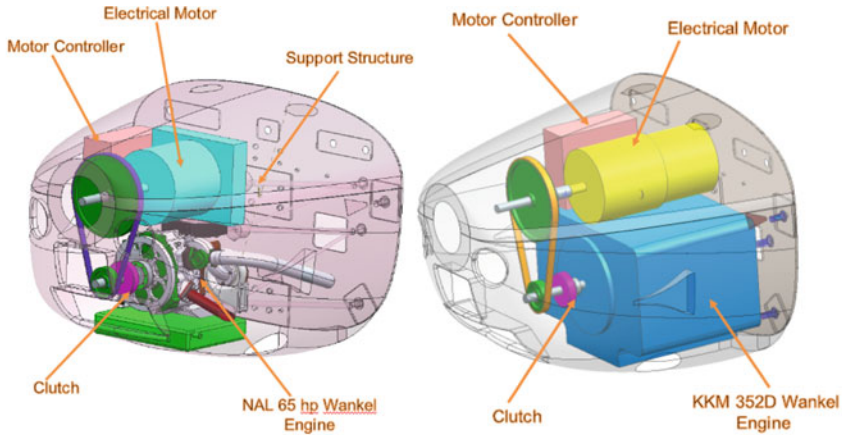
6 Parallel Configuration

Configurations of power plant are considered in the present study and are detailed in Table 4. All-electric power plant comprising electric motor, battery, and controller is considered as the reference case (case AE 1). The electrical motor with the maximum power of 80 kW is used with motor efficiency of 94%. Since, the total energy available for the overall flight profile is limited, the climbing altitude is restricted to 4000 ft only. The climb power maintained for all-electric case is similar with respect to Hansa NG aircraft. The aircraft speed of 130 and 160 kmph is maintained for climb and cruise condition of flight, respectively. The total range and endurance of all-electric case are calculated as 80 km and 0.58 h, respectively, as shown in Table 4.

In the first case of hybrid power plant configuration (HbP1), NAL 65 hp Wankel engine with electrical power plant constituted by 60 kW motor and battery with weight of 67 kg is considered. The total useful battery energy of 9 kWh with energy density of 0.169 kWh/kg is taken in the HbP1 configuration. Since, cruise power of NAL 65 hp Wankel engine is around 32 kW, the climbing altitude is restricted to 6000 ft. The cruise speed is set as 160 kmph. The thrust power required to overcome the drag force at 6000 ft altitude with aircraft speed of 160 kmph is 35.34 kW.

Table 4 Details of hybrid power plant and main results

Sl. No	Case id	Battery energy density (kWh/kg)	Motor power (kW)	Name of engine	Maximum power from engine (kW)	Cruise altitude (ft)	Cruise speed (Kmph)	Electrification factor during takeoff/climb	Electrification factor during cruise	Range (km)	Endurance (hr)
I	AE 1	0.182	80	-	-	4000	160	1/1	1	80	0.58
II	HbP1	0.169	60	NAL 65 hp	48.5	6000	160	0.35/0.34	0.12	247	1.65
III	HbP2	0.169	60	KKM 351	40	6000	160	0.47/0.43	0.15	179	1.16
IV	HbP3	0.248	60	KKM 352	75	8000	160	0.1/0.1	0.1	447	2.93



(a) Hybrid power plant using NAL -65 hp Wankel engine (b) Hybrid power plant using KKM 352 engine

Fig. 6 CAD diagram of hybrid power plant assembled in the engine cowl of Hansa NG aircraft

This power requirement is attained using the electrification factor (ϕ_{cr}) of 0.12. So, during the complete cruise operation 4.24 kW power is drawn from the electrical unit and balance power of 31.10 kW is produced from the NAL 65 hp Wankel engine. During the climbing stage of the flight constant climb power is maintained. The corresponding electrification factor (ϕ_{climb}) is 0.34. The total range and endurance of the HbP1 configuration are calculated as 247 km and 1.65 h, respectively. Compare to all-electric case the range and endurance significantly improved for the HbP1 configuration.

In the second case of hybrid power plant configuration (HbP2), KKM 351 Wankel engine with same electrical power plant used in the HbP1 configuration is considered. The KKM 351d engine is operated with ATF fuel. Since, cruise power of KKM 351 Wankel engine is around 30 kW, the climbing altitude is again restricted to 6000 ft in HbP2 case also. The cruise speed is set as 160 kmph. Since the cruise power of KKM 351 is less than the NAL 65 hp Wankel engine, higher electrification factor (ϕ_{cr}) of 0.15 is maintained during the cruise stage. During the complete cruise operation 5.30 kW power is drawn from the electrical unit and balance power of 30 kW is produced from the KKM 351d Wankel engine. During the climbing stage of the flight constant climb power is maintained. The corresponding electrification factor (ϕ_{climb}) is 0.43. The total range and endurance of the HbP2 configuration are calculated as 179 km and 1.16 h respectively. Since, more power is drawn from the electrical unit, the range and endurance of HbP2 are less than the HbP1 case.

In the third case of hybrid power plant configuration (HbP3), KKM 352d Wankel engine with electrical power plant comprising 60 kW motor and battery with weight of 47 kg is considered. The total useful battery energy of 10 kWh with energy density of 0.248 kWh/kg is taken in the HbP3 configuration. Since, cruise power of KKM 352d Wankel engine is around 58 kW, the climbing altitude is maintained to 8000. The cruise speed is set as 160 kmph. Since the engine power of KKM 352d is

marginally less than climb power of Hansa NG aircraft, the electrification factor of 0.1 is maintained so as to achieve total power of climb same as that as the Hansa NG at climb stage of flight. The cruise stage of flight using HbP3 is divided into two stages. In the first stage hybrid mode is operated with the electrification factor of 0.1. In the second stage of cruise, only IC engine power is used. The cruise power required at 8000 ft with cruise speed of 160 kmph is 35 kW. So, two stage of cruise is proposed for the HbP3 configuration. The total range and endurance of the HbP3 configuration are calculated as 447 km and 2.93 h, respectively.

Major benefit of hybridization is that the fuel consumption can be significantly reduced. In fact, fuel consumption can be optimized for each planned journey. A rough idea of this factor is indicated in Table 5, which compares the cost of fuel per seat-km for various configurations. The cost per unit of electricity or liter of fuel is indicated for each case. For all-electric case, the cost is about Rs 0.8 per seat-km and for the Wankel Supertec cases, it is closer to Rs 2.0 per seat-km. In addition to that, fuel consumed per seat-km and amount of CO₂ produced per seat-km is also mentioned in Table 5. It is of interest to note that the corresponding figures for Hansa3 with Rotax 914F3 engine are about 57.8 mL per seat-km, and CO₂ emission of 136 g per seat-km and fuel cost of Rs 6.65 per seat-km.

7 Series Configuration

In the series hybrid configuration, a generator is mechanically coupled to an IC Engine and the electrical output from the generator is coupled to the main electric motor driving the propeller under a suitable controller system. We need to distinguish two variants of this arrangement. In the first arrangement, there is provision for charging of the battery by the generator during certain phases of the flight. In the second arrangement, there is no provision for charging of the battery in flight. We are in the process of evaluating these arrangements, but the tentative position appears to be as follows: In the first arrangement, additional equipment required in addition to the generator is a rectifier and voltage converter and a complex control system. Moreover, the IC engine needs to supply power required for cruise and additionally to charge the battery. Our initial assessment is that the weight and bulk of such a system cannot be accommodated in the weight budget and space available in the present aircraft configuration. This arrangement, therefore, does not appear feasible.

In the second arrangement, where there is no battery charging, the position is as follows: In this arrangement, the main drive motor would be an 80 kW motor as for the all-electric case AE1. In addition, we need to accommodate a Wankel engine and a generator. This immediately rules out the two cases with the Wankel Supertec engines, 351d and 352 d, which are too large and heavy to be accommodated along with the 80 kW motor. This leaves the option with the NAL 65 hp Wankel engine. This could be accommodated along with a 30 kW generator. This power is not sufficient to provide for the cruise condition. So the total weight budget is also exceeded. So we come to the conclusion that a series configuration is not feasible for the selected

Table 5 Energy cost comparison for different cases of power plant

Sl. No	Case id	Battery energy (kWh)	Fuel consumed (Lit)	Cost of electricity consumed (Rs)	Cost of fuel consumed (Rs)	Total cost (Rs)	Range (km)	Cost/seat-km (Rs/km)	Fuel consumed per seat-km (mL/km)	CO ₂ produced per seat-km (g/km)
I	AE 1	20	0	122.2	0	122.2	80	0.76	0	0
II	HbP1	9	27	49.5	2295	2344.5	247	4.75	54.6	129
III	HbP2	9	14	49.5	350	399.5	179	1.82	39.1	92
IV	HbP3	10	36	55	900	955	447	1.79	40.3	95

* Unit cost for electricity: Rs 5 per kWh; Power petrol Rs 85 per lit; ATF Rs 43 per lit

application using readily available components. This conclusion can be revisited when lighter components become available.

8 Conclusions

The work suggests that it is now an opportune time to enter the electric propulsion sector through the hybrid propulsion route. It is found that the better power-to-weight ratio for rotary Wankel engines makes them a preferred choice. Areas are identified where improvements are needed to achieve competitive power plants for aviation. Moreover, the degree of electrification can be tailored to suit the intended application of the aircraft. The performance of hybrid aircraft can come close to that of comparable conventional aircraft in terms of rate of climb, propeller efficiency, fuel consumption of comparable aircraft weight. Hybridization of the power plant can significantly improve the range and endurance of all-electric aircraft. In the cases presented, this improvement can be as much as 450%. The variation of the electrification factor ϕ during flight can be a powerful tool to improve the economy of operations and also of course the emissions and pollution. The present analysis provides preliminary inputs for the design of a flight and power plant computer, which would be an essential element.

Acknowledgements The authors are thankful to the Director, CSIR-NAL for permitting to publish this work. The authors are thankful to the Head, Propulsion division for his encouragement to this work. The authors would like to acknowledge the help from the Center for Aircraft Design and Development (C-CADD) of CSIR-NAL for providing the data for the Hansa 3 and Hansa NG aircraft and for useful discussions. In particular, we would like to thank Shri. Abbani Rinku for his cooperation and advice. The authors would also like to acknowledge the support and guidance provided by Shri. K.M. Pillai, Senior Principal Scientist, CSIR-NAL.

References

1. Friedrich C, Robertson PA (2015) Hybrid-electric propulsion for aircraft. *J Aircraft* 52(1)
2. Junghsen L, Eric Spahr (2011) Design of hybrid propulsion systems for unmanned aerial vehicles. In: AIAA/ASME/SAE/ASEE Joint propulsion conferences & Exhibit 31 July–03 Aug 2011, San Diego, California

Combustion and Combustors

Combustion Synthesis of Functional Nanoparticles



Ajay V. Singh

Abstract Flame-synthesized carbon nanoparticles of varying sizes were produced in premixed stretch-stabilized stagnation ethylene-oxygen-nitrogen flames under various sooting conditions. The experimental setup consists of a burner with an aerodynamically-shaped nozzle, a stagnation surface/sampling probe assembly, and a scanning mobility particle sizer. The pseudo-one-dimensional formulation was invoked to simplify the stagnation flow field. A modified version of the OPPDIF code was used to compute the gas-phase species, temperature, and velocity profiles using USC Mech II as the reaction kinetics model, which consists of 111 species and 784 reactions. Thermophoretic velocities and particle residence times were calculated for each flame configuration. Soot volume fractions and particle size distribution functions were measured in a series of five atmospheric pressure ethylene-oxygen-nitrogen flames with maximum temperatures ranging from 1969 to 2132 K. The UV–Visible absorption spectral analysis was conducted in the 190–1400 nm range for the flame-synthesized nanoparticles to evaluate the optical bandgap from their resulting Tauc spectra. The results from the present study suggest a strong dependence of the optical bandgap on particle size. It is shown that quantum confinement effects, which arise due to the finite size of the particles, play an essential role in determining the final absolute value of the optical bandgap. In the present study, flame-synthesized carbon nanoparticles (CNPs) are found to exhibit quantum confinement behaviors.

Keywords Carbon quantum dots (CQDs) · Carbon nanoparticles (CNPs) · Flame-synthesis · Stagnation flames

1 Introduction

Flame-synthesized carbon quantum dots can bring about a transformative change in the field of quantum dot solar cells (QDSC). Carbon quantum dots (CQDs) have recently emerged as an exciting class of nanomaterials. They possess useful

A. V. Singh (✉)
Indian Institute of Technology Kanpur, Kanpur, U.P. 208016, India
e-mail: ajayvs@iitk.ac.in

© The Author(s), under exclusive license to Springer Nature Singapore Pte Ltd. 2023
G. Sivaramakrishna et al. (eds.), *Proceedings of the National Aerospace Propulsion Conference*, Lecture Notes in Mechanical Engineering,
https://doi.org/10.1007/978-981-19-2378-4_27

467

optoelectronic properties associated with their nanoscale structures and have the potential to replace the toxic metal-based quantum dots completely as they share traditional semiconductor-based properties. Flame-synthesized carbon nanoparticles (CNPs) are biocompatible and possess strong luminescence and can be easily dispersed in various solvents. Thus, flame-synthesized carbon quantum dots show bright promise for their integration into photovoltaic and light-emitting devices. Their fluorescent properties are attributed to the core and surface state emission. Carbon quantum dots (CQDs) are the youngest member of the family of functional carbon nanoparticles which have inspired extensive research because of their promising applications in energy conversion devices (solar cells), storage devices (batteries), photocatalysis, biosensors, drug delivery systems, transistors, and light-emitting diodes (LEDs). CQDs are specifically useful for applications in efficient photovoltaic devices. This research area is of prime importance for sustainable, affordable, environmentally friendly, and efficient renewable energy production. Carbon quantum dots (CQDs) combine several favorable attributes of traditional semiconductor-based QDs and do not incur the burden of intrinsic toxicity or elemental scarcity. Besides, CQDs can be manufactured in different nano-architectures and surface properties with highly scalable and accurate aerosol flame synthesis methods without the need for stringent, intricate, tedious, costly, or inefficient wet chemistry preparation steps.

Currently, CQDs are obtained from different methods including, laser ablation, candle or arc discharge soot, microwave pyrolysis, electro-oxidation of graphite, or thermal oxidation of biomass. None of these methods results in large quantities of CQDs that are uniform in size, internal nanostructure, and surface properties, which causes relatively low-quantum yields and requires several surface modification steps. This has also prevented fundamental studies on CQDs where their structure and surface chemistry need to be related to their physical and chemical properties for their applications in photovoltaic devices.

One of the main objectives of the present work is to generate flame-synthesized CQDs with different energy bandgaps. Stretch-stabilized stagnation flames can be used to produce carbon quantum dots with different sizes, internal nanostructure, and surface characteristics. Existing quantum confinement theory can be used to demonstrate the quantum dot behaviors of such flame-synthesized carbon nanoparticles (CNPs). The energetics of these flame-synthesized carbon quantum dots (CQDs) or carbon nanoparticles (CNPs) can be varied by controlling the particle size. Increased band energies of flame-synthesized carbon quantum dots can thus be utilized to promote, suppress, or rectify the electron transfer between two semiconductor nanostructures. The family of the premixed stretch-stabilized stagnation flames is an ideal candidate to obtain these carbon quantum dots. It is also feasible to use these benchmarked flames for the direct deposition of the carbon quantum dots on a substrate. However, synthesizing carbon nanoparticles with tunable opto-electronic properties requires the knowledge and understanding of flame synthesis and soot formation and oxidation mechanisms in flames.

1.1 Optical Bandgap

The bandgap in a crystal is defined as the minimum energy gap between the valence and conduction bands, which can either be direct or indirect depending on the type of transitions involved. In an amorphous semiconductor where there is no true gap, an arbitrary definition can be used for the optical bandgap. The optical band gap is commonly determined from the UV-Visible absorption spectrum using the Tauc model [1–4],

$$(\alpha h\nu)^{1/r} = B(h\nu - E_g^{\text{opt}}) \quad (1)$$

where α is the unitless extinction coefficient or absorbance, h is the Planck constant, ν is the light frequency, B is a constant independent of light frequency, and E_g^{opt} is the optical bandgap. The optical bandgap can be estimated by plotting $(\alpha h\nu)^{1/r}$ as a function of $h\nu$ and extrapolating the linear slope to zero absorption. Based on the type of transitions involved in a system, the power index r takes on different values for direct and indirect bandgap materials. It is shown that for indirect bandgap semiconductors such as silicon and germanium, the power index $r = 2$ predicts the absorption measurement quite well [1–4]. Davis and Mott [4] suggest $r = 2$ for indirect bandgap and $r = 1/2$ for direct bandgap material.

1.2 Effect of Hybridization

The optical bandgap is an essential indicator of the nature of flame-synthesized carbon nanoparticles. It serves as a useful parameter for both the physical and chemical characterization of the final soot particles [5–18]. The electronic orbitals of carbon atoms usually hybridize in three different forms, namely sp^3 , sp^2 , and sp . Based on the type of hybridization involved, either σ or π bonding states can exist in carbon structures [10]. Similarly, corresponding to each σ and π bonding state, a σ^* and π^* antibonding state exists with the energy gap (π - π^*) being lower than (σ - σ^*) [10]. In solid-state physics, the bandgap is defined as the energy difference between the highest occupied energy level of the valence band and the lowest unoccupied energy level of the conduction band. In soot particles, this energy gap mainly depends on the different hybridizations of the carbon atom wave functions, sp^2 or sp^3 , and the size of the π -bonded clusters of sp^2 carbon atoms [10, 19]. For carbon structures containing sp^2 sites, the filled π states form the valence band, and the empty π^* states form the conduction band. According to Robertson [20], the optical bandgap can be determined by the configuration of π states on the sp^2 sites. In a cluster model with planar clusters, Robertson et al. proposed that the optical bandgap of the given cluster can be represented as [19, 20],

$$E_g^{\text{opt}} = \frac{2\gamma}{M^{1/2}} \approx 2\gamma \left(\frac{a}{L_a} \right) \quad (2)$$

where M is the number of rings in the cluster, a is the lattice spacing, L_a is the conjugation length, and γ is a measure of π - π interaction. The above model, developed by Robertson, considers that the largest graphene layers only govern the (π - π^*) electronic transition feature, and therefore, fails to describe the internal structure of carbon nanomaterials containing graphene layers of various shapes and sizes [19, 20]. It is now well known that the above cluster model in Eq. (2) grossly over-estimates the size of the clusters as the bandgap is found to be affected by the distortions of the cluster [19]. It is, therefore, no longer possible to give a simple formula for the bandgap energy, as is pointed out by Eq. (2).

1.3 Effect of Molecular Size and Structure

Numerous studies were carried out in the past decades with a motivation to probe the size of nucleating and agglomerating aromatics [5–18, 21–24]. Minutolo and coworkers [10] showed that the extinction and absorption spectra in rich premixed flames could be used to correlate the optical, chemical, and physical properties of flame-synthesized nanoparticles. Following Minutolo's work, a sudden surge of optical bandgap studies took place over the past two decades [12–16]. Among the notable results are those of Allouis et al. [12], Ciajolo et al. [13], Tregrossi and Ciajolo [14], and Russo et al. [15–18]. More recently, the motivation for the studies of the optical bandgap for soot formed in flames comes from the fact that experimentally determined optical bandgaps can be easily correlated to the size of the PAHs in an aggregate [21–23, 25]. However, this is far from being accurate and will be addressed later in this manuscript. Russo et al. [15] and Tregrossi and Ciajolo [14] related the optical bandgap and maximum absorption peak in the UV–Visible absorption spectrum to the structural changes of carbon particles during the soot formation process in premixed flames. In more recent work, Russo and coworkers [17, 18] carried out a detailed UV–Visible spectral analysis to infer the structure of carbonaceous species and their evolution during the soot formation process. They concluded that heavier species graphitize during the soot formation process, thereby decreasing the optical bandgap. In the work of Russo et al. [18], the Tauc representation allowed the identification of different classes of absorbers having E_g^{opt} values ranging from 0.1 to 4 eV [18]. Three different classes of absorbers were identified where large aromatic structures (PAHs \gg 10 aromatic rings), PAHs $>$ 10 aromatic rings, and PAHs \sim 2–7 aromatic rings were associated with bandgaps of 0.1–1 eV, 2 eV, and 4 eV, respectively. Similar observations were made later by Tregrossi and coworkers [14].

1.4 Effect of Stacking, Clustering, and Agglomeration

In an attempt to address the size of the agglomerating aromatics in sooting flames, Miller and coworkers recently carried out extinction measurements to determine the optical bandgap (OBG) of soot particles and correlated it with the aromatic conjugation length (L_a) and the number of aromatic rings in the molecules (M) [21–24]. To validate the relationship reported by Ferrari and Robertson Eq. (2) [26], Miller and coworkers postulated that the clusters of moderately-sized PAHs dominate nascent soot particle morphology. They also advocated that the optical band gap of PAHs in these structures could be estimated by the energy difference between the highest occupied and the lowest unoccupied molecular orbitals (HOMO-LUMO) in isolated PAH monomers [17]. By fitting their computational results to the relationship proposed by Robertson and Ferrari [26], they observed the following relationship [21–24],

$$E_g^{\text{opt}} = \frac{5.8076}{M^{1/2}} + 0.5413 = \frac{1.4787}{L_a} + 0.5413. \quad (3)$$

They also hypothesized that PAH agglomeration occurred at a constant molecular size and the physical growth that followed determined the size and yield of the particulate matter. Tauc/Davis-Mott analysis of extinction measurements was conducted by Miller and coworkers in a variety of flame systems to determine the optical bandgap of soot particles [21–24]. The optical bandgap was then derived from the near edge absorption spectrum using Tauc analysis and was found to be equal to 2.1 eV for their laminar, non-premixed flames [22]. Interestingly, they measured nearly identical optical bandgap values under different sooting conditions. The measured optical bandgap was then compared with calculations of the electronic structure of a series of D_{2n} polynuclear aromatic hydrocarbons using time-dependent density functional theory (DFT). In a process to relate the optical bandgap to the size of PAH molecules, Miller and coworkers assumed that clusters of moderately-sized PAHs dominated nascent soot particles and that the electronic properties (OBG) in such systems were dominated by the molecular structure of the PAHs that comprise them [23]. They also correlated the HOMO–LUMO gaps for these PAHs with the number of aromatic rings in the molecules [21–24]. The HOMO–LUMO gap was found to decrease with increasing monomer size [23].

1.5 Shortcomings in the Optical Bandgap and HOMO–LUMO Gap Analysis

Though Miller and coworkers measured the optical bandgap for various sooting flame systems and were the first to show the molecular and agglomeration effects of PAHs on the optical bandgap, there is a source of uncertainty in their bandgap

analysis [21–24]. For instance, one source of uncertainty arises from the fact as to what type of transitions are involved in the bandgap, that is, whether they are direct or indirect. Miller and coworkers assumed the transitions to be direct [21–24]. In almost all previous experimental studies [5–17], indirect transitions were assumed for the calculation of the optical bandgap from their resulting Tauc spectra. Due to the consideration of direct transitions, the reported optical bandgap values by Miller and coworkers [21–23] were found to be substantially different from those reported by D’Alessio [5–8, 10] and other groups [11–17]. As opposed to earlier works [5–8, 11–17], Miller and coworkers also reported a single optical bandgap value for their various flame systems [21–24]. This seems to contradict earlier studies [5–8, 11–17, 27] and the present work. In a previous work [27], the optical bandgap was found to have a clear dependence on the particle size, suggesting a high sensitivity of the optical bandgap toward quantum confinement effects at the nanometer scale. In the present work, the optical bandgap for flame-synthesized carbon nanoparticles was found to vary under different sooting conditions. Previously, several research groups made similar observations, which indicated that the optical bandgap of soot varies with different sooting conditions [5–8, 11–17]. Thus, a single optical bandgap value of soot derived from flames under different conditions is not general or convincing.

Another source of uncertainty in Miller’s work arises from the fact that their interpolated optical bandgap value was found to be highly sensitive to the selected spectral range [19]. Assuming direct transitions that are quantum mechanically allowed, several regions in the Tauc spectra can be linearly extrapolated for calculation of the optical bandgap. For direct transitions, the selection of the spectral range in the Tauc/Davis-Mott analysis is essential since the extrapolated optical bandgap is highly dependent on this selection. For instance, Miller and coworkers chose the spectral range of 440–540 nm for their optical bandgap analysis [22]. The authors did not provide a clear justification for such a selection, and it appears to be arbitrary [22]. Uncertainties in the optical bandgap also arise from the fact that the effect of aliphatic linkages and functional groups on the electronic properties of PAH could be substantial. This particular fact was ignored by Miller and coworkers when they derived the size of PAHs from their optical bandgap measurements and quantum chemistry calculations. Previous studies suggest that nascent soot formed in premixed flat flames can contain a substantial amount of aliphatic and oxygenated compounds [28]. The type, orientation, and the number of functional groups in a PAH molecule can affect its electronic properties and, therefore, should not be neglected for the calculation of the HOMO–LUMO gap in such molecules. To understand the physical significance of optical bandgap for soot sampled through premixed flames, fundamental gaps in our current understanding of optical bandgap need to be bridged. The present paper is offered as a contribution toward this end.

Optical bandgaps measured through Tauc spectra for various flame-synthesized aerosols cannot be deduced entirely from the HOMO–LUMO gaps. Experimentally, the particle size distribution functions (PSDFs) probed by a scanning mobility particle sizer demonstrate a lognormal size distribution of flame-synthesized carbon nanoparticles. Contributions from all sized particles should, therefore, be considered for the interpretation of the measured optical bandgap. The Tauc model is only

rigorous and robust when it is applied to a sample with a uniform bandgap. Clearly, this is not the case here for flame-synthesized aerosols. The measured absorbance spectra for samples prepared by particle deposition onto substrates represent the contribution from particles of different sizes, which in turn possess variable band gaps due to quantum confinement effects. Quantum confinement due to a decrease of the particle size plays an important role in reducing the density of states for flame-synthesized nanoparticles and can widen the bandgap accordingly. The measured absorbance is thus an averaged property of the varying-sized particles present in the system. It should be calculated theoretically by considering the entire particle size distribution function of flame-synthesized aerosols. The present paper is also offered as a contribution toward this end.

Combustion synthesis has emerged as a promising method to produce nanostructured materials with well-defined physical and chemical properties. Flame design and particle collection method can help us in achieving a fine control of the particle size distribution, crystal phase, purity, and crystallinity. It is well known that pseudo-one-dimensional stretch-stabilized stagnation flames, although developed primarily for probing kinetics of nascent soot formation, also prove to be ideal for particle synthesis. Precise control over the flame synthesis of particles can be achieved in this configuration as particles experience similar growth histories due to the quasi-one-dimensional nature of the flame [27, 29–32]. The residence times in these flames can be precisely controlled to synthesize particles at reasonable production rates. Moreover, the setup can be scaled up to an industrial process. These flames offer great versatility in generating functional nanoparticles of interest with tunable properties.

This paper aims to measure the particle size distribution functions (PSDFs) and optical bandgap of flame-synthesized carbon nanoparticles in premixed stretch-stabilized stagnation flames and to address the current gaps in our understanding of the optical bandgap derived from UV–Visible absorption measurements. Flame-synthesized carbon nanoparticles of varying sizes were generated and measured in premixed stretch-stabilized stagnation ethylene-oxygen-nitrogen flames under various sooting conditions in a flame synthesis experimental setup developed at IITK. Previously, the UV–visible absorption spectral analysis was conducted in the 190–700 nm range to evaluate the optical bandgap for the flame-synthesized carbon nanoparticles [27, 30]. A strong dependence of the optical bandgap on the particle size both in terms of median mobility diameter and mean volume diameter is presented in this paper for premixed sooting flames, suggesting a critical role of the particle size. In the present work, theoretical results from Brus' theory are also calculated and compared against the experimental results. The current work also discusses the underlying assumptions in determining this optical bandgap from the UV–visible absorption measurements. Overall, the given paper aims to reproduce the experimental results of previous work [27, 30] and also addresses the current gaps in our understanding of the optical bandgap derived from UV–Visible absorption measurements. The given paper also outlines the underlying assumptions concerning the optical bandgap analysis and presents a complete theory to analyze the optical bandgap of flame-synthesized carbon nanoparticles. The numerical, theoretical, and experimental work presented in this paper was carried out exclusively at IITK. Using

(nozzle exit diameter = 1.43 cm). The plug flow at the exit of the burner produces a quasi-one-dimensional stagnation flow field leading to the stabilization of a flat, disk-shaped flame. In the given configuration, control over the flame-synthesized carbon nanoparticles can be achieved through uniformity of velocity and temperature profiles. Therefore, the carbon nanoparticles undergoing the growth process experience nearly identical temperature, concentration, and time histories. Typical conical characteristics associated with a Bunsen flame in which the fluid flow experiences varied time histories were thus eliminated in the present configuration. Therefore, a stretch-stabilized stagnation flame setup provides a uniform particle growth environment. To isolate the flame from the surrounding atmosphere and to protect it from external flow perturbations, a shroud of nitrogen gas was used. It also prevented the formation of a diffusion flame between the unburnt fuel and the surrounding air. The distance between the burner nozzle and the water-cooled stagnation surface, L , was kept at 1.0 cm for all the flames studied in this work. The flame standoff distance, typically measured from the stagnation surface, L_s , can be changed in this configuration by changing the flow rate of the unburned gas.

The aerosol sample in the post-flame region was drawn into a micro-orifice (127 μm diameter, 125 μm thickness), which was embedded in the sampling probe tube and was mounted flush to the stagnation surface. The flame-synthesized aerosol sample was immediately diluted with a cold nitrogen flow at 30 L/min (STP) to quench the chemical reactions and prevent particle–particle coagulation. The immediate dilution by cold nitrogen also eliminated the particle losses in the sampling line. A dilution ratio calibration (based on CO_2 concentration measurement) was used to correct the measured number density of flame-synthesized aerosols [33]. An optimum dilution ratio was carefully selected by following the established procedures in the literature [33–36]. A standard SMPS system (TSI 3082) was used to measure the particle size distribution functions of flame-synthesized aerosols. Corrections for diffusion losses within the system were accounted for as a function of particle diameter. Since mobility measurements can overestimate the particle size smaller than 10 nm in diameter, mobility diameter corrections were carried out in the present study using a well-established nanoparticle transport theory [36]. This overestimation of mobility diameter for particles smaller than 10 nm in diameter, stems from the inherent limitation of Cunningham slip correction. Cunningham slip correction cannot account for the transition from diffuse to specular scattering and does not consider the van der Waals gas–particle interactions. For particles smaller than 10 nm in diameter, both effects are expected to be crucial, and therefore, the correction of mobility diameters below 10 nm becomes necessary. The gas temperature at the nozzle exit (T_n) was measured with an uncoated fine-wire (125 μm in wire-diameter) K-type thermocouple. The thermocouple was placed carefully near the centerline of the flow. A type-K thermocouple was also used to measure the temperature at the stagnation surface (T_s). The thermocouple was 0.2 cm in wire diameter and was mounted flush with the stagnation surface such that its junction or bead was exposed to the sample gas at the surface. The boundary conditions for all the tested flames are tabulated in Table 1.

Table 1 Flame parameters^a and lognormal distribution parameters measured for the large particle-size mode

Flame No.	Velocity ^b , v_o (cm/s)	Global strain rate, a (s^{-1})	$L_s^{c,d}$ (mm)	$T_{f,max}^d$ (K)	$T_n \pm 10$ (K)	$T_s \pm 5$ (K)	$(D_{m,2})$ (mm)	$\sigma_{g,2}$	$N_2 \times 10^{-10}$ (cm^{-3})	$F_v \times 10^8$	t_p (ms)	E_g^{opt} (eV) [#]
A1 series: 16.5% C ₂ H ₄ /20.6% O ₂ /62.9% N ₂												
A	25	33.4	0.73	1973	397	324	12.9	1.50	5.9	14.00	11.2	0.74
B	30	38.6	0.59	1969	388	334	12.0	1.47	5.8	9.55	10.0	0.80
C	34	44.4	0.54	1971	392	328	11.3	1.42	6.5	8.61	9.1	0.85
A2 series: 17.3% C ₂ H ₄ /21.6% O ₂ /61% N ₂												
A	35	42.0	0.56	1998	355	311	13.4	1.46	1.2	4.16	8.6	0.65
B	43	57.1	0.51	2019	392	338	10.3	1.43	3.0	3.37	7.3	0.88
C	46	65.4	0.51	2039	424	361	8.7	1.42	3.5	2.00	6.9	0.94
A3 series: 17.4% C ₂ H ₄ /21.7% O ₂ /60.9% N ₂												
A	29	42.4	0.80	2011	440	358	13.6	1.40	2.1	5.02	10.3	0.72
B	43	59.0	0.54	2032	409	336	7.6	1.38	2.8	1.01	7.2	1.06
C	51	73.9	0.48	2046	431	354	7.3	1.39	3.0	0.96	6.2	1.07
A4 series: 17.6% C ₂ H ₄ /22% O ₂ /60.4% N ₂												
A	32	44.3	0.77	2052	417	350	11.2	1.44	2.7	3.67	8.6	0.77
B	44	62.9	0.57	2059	428	359	8.3	1.42	3.2	1.67	6.9	0.99
C	51	75.5	0.52	2068	443	369	7.0	1.37	3.0	0.79	6.2	1.10
A5 series: 19.4% C ₂ H ₄ /24.3% O ₂ /56.3% N ₂												
A	51	61.9	0.61	2122	364	345	4.7	1.22	7.5	0.38	5.9	1.35
B	61	78.8	0.54	2132	382	365	4.2	1.18	5.1	0.22	5.2	1.55

(continued)

Table 1 (continued)

Flame No.	Velocity ^b , v_o (cm/s)	Global strain rate, a (s^{-1})	$L_s^{c,d}$ (mm)	$T_{f,max}^d$ (K)	$T_n \pm 10$ (K)	$T_s \pm 5$ (K)	$\langle D_{m,2} \rangle$ (nm)	$\sigma_{g,2}$	$N_2 \times 10^{-10}$ (cm^{-3})	$F_v \times 10^8$	t_p (ms)	E_g^{opt} (eV) [#]
C	74	93.9	0.46	2131	380	371	3.6	1.16	1.8	0.05	4.6	1.67

[#]The errors associated with the determination of the optical bandgap (E_g^{opt}) were determined from the linear fitting in the Tauc spectrum and was found to be equal to ± 0.015 eV

^aAll unburned mixtures have the equivalence ratio = 2.4. Nozzle-to-stagnation surface separation (L) is 1 cm

^bUnburned gas velocity at 298 K and 1 atm. Sheath N_2 velocity for each flame is v_o

^cDistance from the stagnation surface to the position of maximum flame temperature

^dComputed using OPPDIF and USC Mech II

The evolution of the PSDF was determined for five series of ethylene-oxygen-nitrogen flames. The unburned gas composition and cold gas velocity (v_0) along with relevant boundary conditions are summarized in Table 1 for each series. The maximum flame temperatures ($T_{f,\max}$) computed using an OPPDIF code, and USC Mech II are also summarized in Table 1. As we move from the A1–A5 series, the maximum flame temperature increases and can be easily discerned from Table 1. For each series, lognormal distribution parameters measured for large-particle-size mode (number density, N_2 , and geometric standard deviation $\sigma_{g,2}$) along with particle residence time (t_p) and soot volume fraction (F_v) are also summarized in Table 1. In each series, the variation in unburned gas velocity changes the flame standoff distance (L_s) by altering the kinematic balance between the local flame speed and the normal flow velocity immediately upstream of the flame surface. Therefore, changes in the flame standoff distance result in different particle residence times for different flames in each series. Flame standoff distances were computed from OPPDIF computations using maximum flame temperature to be the flame zone marker. The nitrogen sheath flow velocity was kept the same as the cold flow gas velocity (v_0) as higher sheath flow rates resulted in perturbation of the flame edges. The effects of sheath nitrogen flow velocity on flame curvature for stretch-stabilized stagnation flames are discussed in the literature elsewhere [33]. For a specific series listed in Table 1, particle residence time decreases as we move from A to C. For each flame configuration, the evolution of PSDF was observed as a function of particle residence time. For a specific series, an increase in particle residence time resulted in increasing the median mobility diameter, $\langle D_{m,2} \rangle$, and soot volume fraction, F_v , of flame-synthesized carbon nanoparticles. A strong dependence of the median mobility size and soot volume fraction on experimentally determined optical bandgap (E_g^{opt}) is observed. As is evident from Table 1, the optical bandgap decreases as the median mobility size of flame-synthesized carbon nanoparticles increases. Similarly, for a specific series, an increase in the soot volume fraction due to higher residence times result in a corresponding decrease of the optical bandgap for flame-synthesized carbon nanoparticles.

The optical bandgap measurements for the five series of stretch-stabilized stagnation flames were taken from previous studies [27, 30], the procedure for which is outlined below. The combustion-generated carbon nanoparticles were sampled in atmospheric pressure, fuel-rich premixed $\text{C}_2\text{H}_4\text{--O}_2\text{--N}_2$ stretch-stabilized stagnation flames. The flame-synthesized carbon nanoparticles were deposited thermophoretically onto quartz slides (temperature equal to T_s) affixed to the stagnation plate at a distance of 1 cm from the nozzle exit. The UV–Visible absorption measurements were made using a Shimadzu UV-2401 PC spectrometer. The UV–Visible absorption spectroscopy allowed the spectroscopic analysis in the 190–700 nm range. The particles were deposited for a maximum duration of 60 s. To measure the optical bandgap of the collected particles, the UV–Visible absorption was carried out for flame-synthesized carbon nanoparticles against a reference quartz slide. Extreme care was taken first to match the absorbance spectra of the reference quartz slide and the one that was used for the thermophoretic sampling of the particles. For the optical bandgap calculation, indirect transitions (power index $r = 2$ in Eq. (1)) in a spectral range from 300 to 700 nm were chosen in the Tauc spectra to extrapolate the linear

slope to zero absorption. The optical bandgap for carbon nanoparticles synthesized under different flame conditions is summarized in Table 1. The maximum uncertainty in the optical bandgap calculation due to fitting errors was found to be less than 0.015 eV.

3 Results and Discussions

3.1 Computational Modeling

The gas-phase species concentration, temperature, and velocity profiles were measured using a modified version of the OPPDIF code. USC Mech II, consisting of 111 species and 784 reactions, was used as the reaction kinetics model [37]. For OPPDIF calculations, adaptive mesh refinement was used, where approximately 250 grid points were used to sufficiently resolve the flame. The pseudo-one-dimensional formulation was invoked to simplify the stagnation flow field. At the burner exit, the flow was designated as the uniform plug flow with a mass flux given by the experimental cold flow gas velocity and reactant composition. The boundary temperature at the burner exit, T_n , was equal to the measured burner or nozzle temperature. No-slip conditions were assumed at the stagnation surface boundary. The stagnation surface had a temperature T_s equal to the measured plate temperature. The net diffusive velocity at the stagnation surface was assumed to be zero due to a balance between thermal diffusion and Fickian processes [33]. Flow field perturbations due to the probe sampling effects at the orifice were not accounted for in the present study [33]. In all the flames studied, buoyancy and axial pressure gradient effects were assumed to be negligible since the flow velocities were small, and stagnation flames produced were not large, rendering buoyancy, and axial pressure gradient effects insignificant. The residence time of a Lagrangian particle traveling from the flame zone to the stagnation surface was calculated by considering the axial convective and thermophoretic velocities [33].

Global strain rates were measured according to the given formula, $a = v_0 (T_n)/L$, where $v_0 (T_n)$ is the unburned gas velocity at the nozzle exit corrected for the nozzle temperature. The changes in the unburned gas velocity also cause a variation in the flame standoff distance (L_s) and the particle residence time (t_p) within each series of the flame, and the same is tabulated in Table 1. For flame-synthesized particles, the finite residence time is calculated by determining the thermophoretic velocity (v_{th}), which is driven by the significant temperature gradient, $\partial T/\partial x$, at the stagnation surface. In this study, the thermophoretic velocity of the particle within the flame was calculated from Waldmann's theory in the free molecular regime [38],

$$v_{th} = \frac{\lambda(\partial T/\partial x)}{5\left(1 + \frac{\pi\psi}{8}\right)NkT}. \quad (4)$$

In the above equation, ψ is the momentum accommodation factor, N is the number density of the gas, and λ is the thermal conductivity of the gas-phase calculated from the transport properties of the mixture in the multi-component formulation. Traditionally, a value of 0.9 is chosen for ψ [39] based on Millikan's oil droplet experiments [40]. As is evident from Eq. (4) Boltzmann constant k and the local gas temperature, T , also contribute to the thermophoretic velocity of the given particle. The thermophoretic velocity was calculated numerically and added to the axial convective velocity to determine the particle velocity, v_p . The residence time of the flame-synthesized carbon nanoparticle was defined as the time interval for the particle to traverse from the calculated location of the peak flame temperature to the location of the stagnation probe. We assume that particle time zero starts at the peak flame temperature location, where particles start forming due to nucleation. Therefore, particle residence time (t_p) can be calculated by integrating the inverse of the particle velocity, v_p , from the peak flame temperature location, x_f to the location of the stagnation surface, L . Therefore, t_p is given as,

$$t_p = \int_{x_f}^L dx/v_p \quad (5)$$

where v_p is a sum of the axial convective velocity (v_c) and particle thermophoretic velocity (v_{th}) [33]. Particle residence times (t_p) for each tested flame are listed in Table 1. As is evident from the given table, for each series, the flames with the largest flame standoff distances correspond to the lowest velocity of the unburnt mixture, which in turn gives rise to larger particle residence times. Soot volume fraction increases as particle residence time increases since the particles have more time to grow following inception. Figure 2a shows the computed velocity profiles for flame A5b. The particle residence time for flame A5b is also shown in Fig. 2a. The axial convective velocity increases from the unburned gas velocity at the nozzle exit. It reaches a maximum at the flame zone due to a decrease in the gas density. It then subsequently falls with the gas-phase temperature to zero velocity at the stagnation surface. The thermophoretic particle velocity continuously increases from the location of the peak flame temperature and becomes a maximum at the stagnation surface. The concentration profiles of selected major and minor species along with the gas-phase temperature profile for flame A5b are plotted in Fig. 2b. It can be easily observed that the preheat zone of the given flame is not attached to the burner nozzle. The temperature rises from the nozzle temperature T_n to $T_{f,max}$ at the flame zone, and then subsequently falls to the stagnation plate temperature, T_s at the stagnation plate surface.

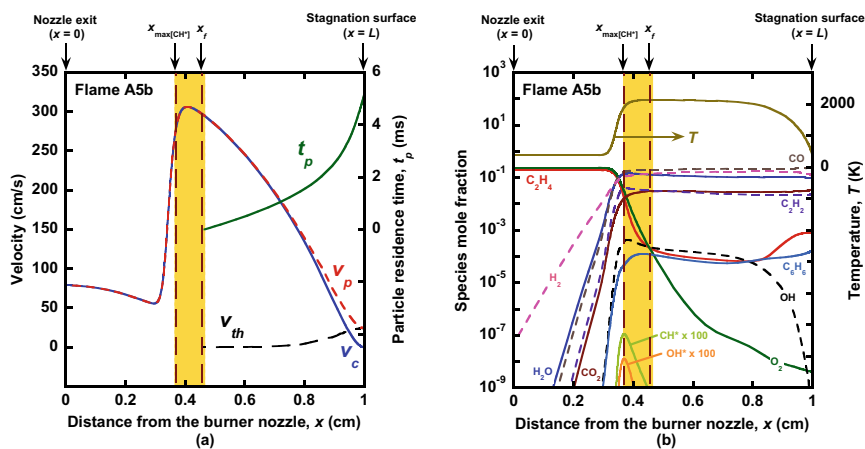


Fig. 2 **a** Profiles of velocity and particle residence time t_p computed for Flame A5b. **b** Species mole fraction profiles of selected major and minor species of flame A5b along with complete temperature profile. The orange band indicates the thickness of the blue flame zone with the vertical dotted lines representing the ignition point location corresponding to maximum CH^* concentration, $x_{\max}[\text{CH}^*]$, and peak flame temperature location, x_f . The orange band was measured experimentally using digital flame photographs

4 Experimental Results

4.1 Particle Size Distribution Functions

The evolution of particle size distribution functions (PSDFs) for the A1–A5 series flames is shown in Fig. 3. The PSDFs demonstrate a persistent bimodality for the lowest temperature flames studied (A1, $\sim 1971 \pm 2$ K, and A2, $\sim 2019 \pm 20$ K), as shown in Fig. 3. The observed bimodality is the result of competition between particle nucleation persisting in the post-flame region and particle size growth due to coagulation and particle aggregation. For low-temperature flames, the PAHs continue to grow beyond the flame, leading to continued particle nucleation in the post-flame region. The PSDF evolves to mostly an apparent unimodal distribution for A3 and A4 series flames (A3 $\sim 2028 \pm 18$ K and A4 $\sim 2059 \pm 9$ K). At high temperatures, the PAHs decompose thermally, thereby ending the nucleation process and removing the nucleation tail from the resulting PSDF. For the A5 series flames (A5, $\sim 2127 \pm 5$ K), unimodal distribution is observed, and the measured particle sizes are relatively small. A strong effect of flame temperature was observed on the measured PSDFs as nucleation and growth of soot were found to be suppressed at high temperatures. In all cases, the PSDF shape may be characterized by a bi-lognormal distribution function as follows:

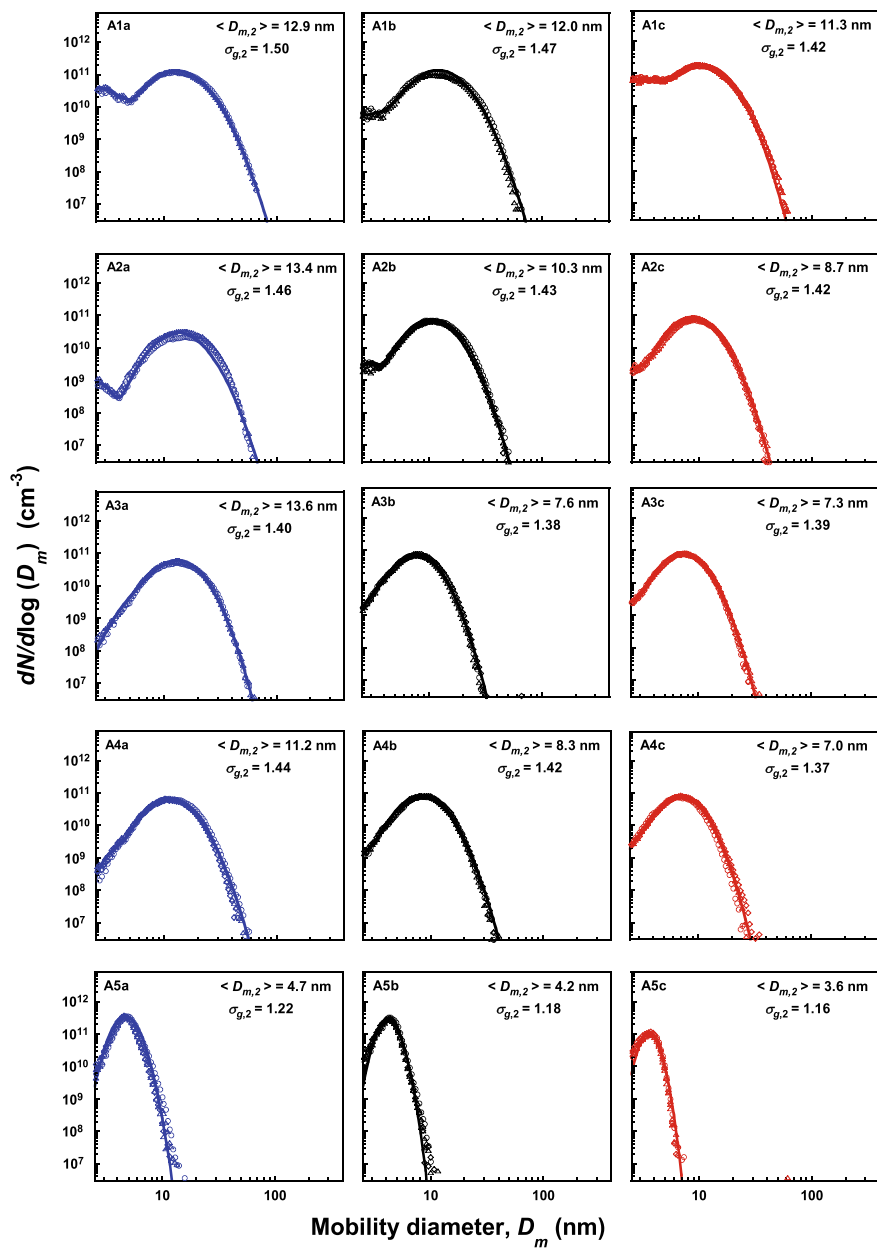


Fig. 3 Evolution of particle size distribution function for A1–A5 series flames. Symbols: experimental data (different symbols from repeated runs, showing data reproducibility); solid lines: fits using bi-lognormal/lognormal distribution function

$$\frac{dN}{d \log D_m} = \sum_{i=1}^2 \frac{N_i}{\sqrt{2\pi} \log \sigma_{g,i}} \exp \left[-\frac{[\log D_m - \log \langle D_{m,i} \rangle]^2}{2(\log \sigma_{g,i})^2} \right] \quad (6)$$

where N_i is the number density, $\sigma_{g,i}$ is the geometric standard deviation, and $\langle D_{m,i} \rangle$ is the median mobility diameter of the i th mode. We define $i = 1$ and 2 for the nucleation and coagulation mode, respectively. In all the cases shown in Fig. 3, the PSDF is characterized by either a bi-lognormal or lognormal distribution consisting of a geometric standard deviation σ_g and median mobility diameter $\langle D_m \rangle$ for each mode. A solid line represents fit to the entire distribution for each flame in each series. Since the data resolution in the small size range is limited, only the large-size mode ($i = 2$) parameters are listed in Table 1 and Fig. 3. As shown in Table 1, the median mobility size increases as particle residence time increases for each series of flames. The increase in the median mobility size is accompanied by an increase in the geometric standard deviation and soot volume fraction. The distribution number density (N_2) decreases as the particle residence time increases for low-temperature flames (A1–A3 series). However, it was found to increase slightly for high-temperature flames (A5 series). For A5 series flames, measured particle sizes are relatively small when compared to other series (<5 nm). The absolute particle number concentration can have relatively high uncertainties in the sub-5 nm range and could potentially be a reason for such behavior. The results from the present study show an excellent agreement with previous studies in terms of measured PSDFs and soot volume fraction [27, 30].

4.2 Direct Versus Indirect Optical Bandgap

Figure 4 shows the Tauc spectrum for flame A5b considering both the direct ($r = 0.5$ in Eq. (1)) and indirect transitions ($r = 2$ in Eq. (1)). In the case of a direct transition, a multi-bandgap fitting approach is applied as five straight lines of different slopes could be individuated on the Tauc diagram, starting from the visible going toward UV, indicating five different energy bandgaps related to different classes of absorbers. However, in the case of an indirect transition, a single straight line can be drawn on the Tauc diagram indicating a single optical band gap of 1.55 eV. It is to be noted that Miller and coworkers used a spectral range of 440–540 nm for their analysis of the optical bandgap from the Tauc spectrum [22]. In the case of a direct transition, the selection of the spectral range used in the Tauc analysis is important because the interpolated optical bandgap will be highly dependent on this selection. In a similar spectral range of 440–540 nm, as can be seen from Fig. 4, the interpolated optical bandgap for flame A5b was found to be 2.27 eV, which is quite similar to the one calculated by Miller and coworkers [22]. The indirect transition, on the other hand, suggests a single optical band gap value in the 300–700 nm spectral range. Thus, in this work, indirect transitions make more sense since they give us a unique solution, and the power index $r = 2$ in Eq. (1) is used to determine the optical bandgap for

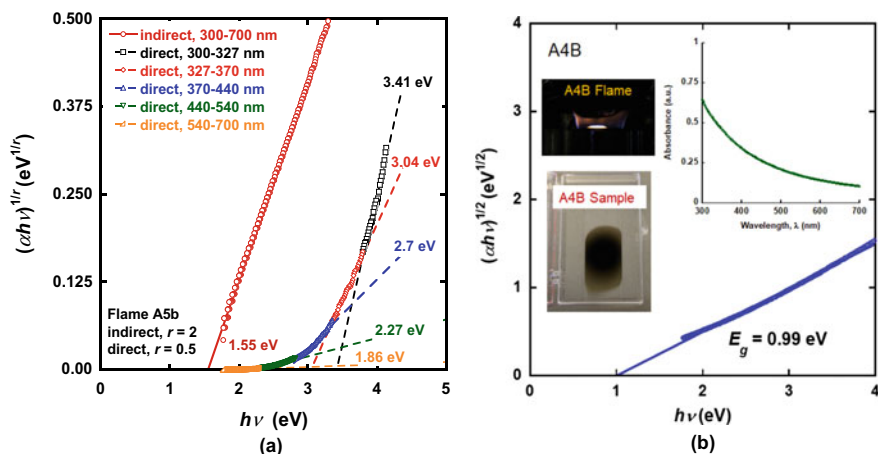


Fig. 4 **a** Comparison of the effect of direct and indirect transitions on interpolated optical bandgap. Five distinct linear regions could be identified in case of direct transition ($r = 0.5$ in Eq. (1)) corresponding to a given spectral range. **b** A typical Tauc and absorbance spectrum for carbon nanoparticles (CNPs) synthesized in flame A4b. The carbon nanoparticles collected on a quartz side are shown in inset along with a typical flame image of flame A4b

flame-synthesized carbon nanoparticles. The optical bandgap values listed in Table 1 are calculated considering indirect transitions (power index $r = 2$ in Eq. (1)). Figure 4b shows a typical Tauc and absorbance spectrum for carbon nanoparticles synthesized in flame A4b.

Tauc spectra were also measured for flame-synthesized carbon nanoparticles collected from flame A2b at different deposition times. Since all the particles were collected at the same location from the same flame, no difference in the optical bandgap was observed for different deposition times. The optical band gap was calculated to be 0.88 eV for all the cases, despite the difference in deposition times and hence film thickness. The absorbance was found to increase with the deposition time. However, no change in the calculated optical bandgap was observed. Thus, the optical bandgap was found to be independent of the film thickness. For optical bandgap calculations in indirect transitions, as depicted in Fig. 4, a spectral range of 300–700 nm was chosen in the Tauc spectra to extrapolate the linear slope to zero absorption. A similar spectral range (300–700 nm) was selected for the A1–A5 series flames for the calculation of the optical bandgap from their resulting Tauc spectra and is tabulated in Table 1. As seen in Table 1, each flame produces a distinct Tauc spectrum and the optical bandgap. A clear dependence of the optical bandgap on the median mobility size was observed. The optical bandgap was found to decrease as the median mobility diameter of the flame-synthesized particle increased. For instance, flames A5a, A5b, and A5c have distinct apparent optical bandgap values of 1.35, 1.55, and 1.67 eV, respectively. The corresponding median mobility diameters were 4.7, 4.2, and 3.6 nm, respectively. The optical bandgap decreases as the particles grow due to increased residence times. The size dependency of the optical bandgap can be

explained by the fact that the energy splitting between the occupied and the empty states increases as the median mobility diameter decreases due to the reduced density of the states via quantum confinement. Quantum confinement due to a decrease of the particle size plays an essential role in reducing the density of states for flame-synthesized nanoparticles and can widen the bandgap accordingly. At the nanoscale, as the size of the particle decreases, the decrease in the confining dimension makes the energy levels more discrete, which in turn widens the bandgap. Therefore, as the size is reduced, the electronic excitations shift to higher energies. This could cause a massive change in the optical properties of flame-synthesized carbon nanoparticles (CNPs) as a function of size. The results show that flame-synthesized carbon nanoparticles less than 15 nm in size exhibit substantial variation in optical properties with particle size and suggest a strong dependence of the optical bandgap on the particle size.

4.3 Size Dependency of the Optical Bandgap

The apparent optical band gap obtained using Eq. (1) should be understood as a particle ensemble-averaged value. The Tauc model is only rigorous when it is applied to a sample with a uniform bandgap. The absorbance measured for our flame-synthesized samples should be attributed to the absorbance of the carbon nanoparticles of different sizes, which in turn exhibit varying band gaps due to quantum confinement. The measured absorbance is, thus, an averaged effect of varying-sized nanoparticles and can be represented as,

$$A = \sum_i a(\nu, r_i) P_i, \quad (7)$$

where A is the measured unit less absorbance, $a(\nu, r_i)$ is the absorbance for a nanoparticle of the radius r_i at a specific photon frequency ν , P_i is the fraction of absorbance contributed by the particle of the radius r_i in the sample. P_i is proportional to $N_i V_i$, where N_i is the number density, and $V_i = (4/3)\pi r_i^3$ is the volume of the particle with radius r_i . If the optical bandgap as a function of the particle size is known, we can calculate the absorbance of the system by applying Eq. (1) in Eq. (7) and rearranging the terms. We can then express the absorbance as,

$$Ah\nu = B \sum_i [h\nu - E_g^{\text{opt}}(r_i)]^2 P_i \quad (8)$$

$$Ah\nu = B \left[(h\nu - \langle E_g^{\text{opt}} \rangle)^2 + \langle (E_g^{\text{opt}} - \langle E_g^{\text{opt}} \rangle)^2 \rangle \right] \quad (9)$$

where the brackets denote the volume-weighted mean values, as $\langle E_g^{\text{opt}} \rangle = \sum_i E_g^{\text{opt}}(r_i) P_i$ is the volume-weighted mean optical bandgap, and

$\left\langle \left(E_g^{\text{opt}} - \langle E_g^{\text{opt}} \rangle \right)^2 \right\rangle = \sum_i \left(E_g^{\text{opt}} - \langle E_g^{\text{opt}} \rangle \right)^2 P_i$ is the variance of the volume-weighted optical bandgap for given size distribution. Equation (9) shows that when the bandgap variance is small enough, Eq. (9) reduces to the same form as Eq. (1). Thus, the Tauc model can still be applied. In our experiment, the maximum variance is estimated to be 0.1 eV², which is much smaller than the first term in Eq. (9). This also explains the reasonably good linear relation in Fig. 4, despite the size distribution effect. However, we should understand that the experimentally-derived optical bandgap using the Tauc model is the volume-weighted mean bandgap $\langle E_g^{\text{opt}} \rangle$, as opposed to the bandgap of specific particle size. In this work, Brus' model is used to capture the size dependency of the optical bandgap [41]. Brus suggests that the bandgap of a semiconductor nanocrystal can be approximated as [41],

$$E_g \cong E_g^{\text{bulk}} + \frac{\hbar^2}{8r^2} \left(\frac{1}{m_e^*} + \frac{1}{m_h^*} \right) - \frac{1.8e^2}{4\pi\epsilon_0\epsilon_r r} \quad (10)$$

where E_g^{bulk} is the bulk semiconductor bandgap, e is the electron charge, ϵ_0 is the vacuum permittivity, ϵ_r is the particle relative permittivity, and m_e^* and m_h^* are the effective electron and hole masses, respectively. The second term of the above equation accounts for the quantum confinement effect, which leads to a larger bandgap for a smaller size; whereas, the third term is a correction for the electron-hole Coulomb interaction. Using Eqs. (9) and (10), the volume-weighted mean optical band gap can be expressed as,

$$\langle E_g^{\text{opt}} \rangle = \sum_i \left[E_g^{\text{bulk}} + \frac{\hbar^2}{8r^2} \left(\frac{1}{m_e^*} + \frac{1}{m_h^*} \right) - \frac{1.8e^2}{4\pi\epsilon_0\epsilon_r r} \right] P_i \quad (11)$$

$$\langle E_g^{\text{opt}} \rangle = E_g^{\text{bulk}} + \frac{\hbar^2}{8} \left(\frac{1}{m_e^*} + \frac{1}{m_h^*} \right) \left\langle \frac{1}{r^2} \right\rangle - \frac{1.8e^2}{4\pi\epsilon_0\epsilon_r} \left\langle \frac{1}{r} \right\rangle \quad (12)$$

The electronic properties of the material, the harmonic mean of electron and hole effective mass $2(1/m_e^* + 1/m_h^*)^{-1}$, the relative permittivity ϵ_r , and the bulk material bandgap E_g^{bulk} are fitted here against the experimental data. The expressions $\langle 1/r^2 \rangle$ and $\langle 1/r \rangle$ represent the volume-weighted mean values and are calculated by considering the particle size distribution function of a given flame. The above model can also be treated using the median mobility diameter. The results derived from Eq. (12) using the median mobility diameter and the volume-weighted $\langle 1/r^2 \rangle$ and $\langle 1/r \rangle$ are shown in Fig. 5a and b, respectively (open rectangles). It should be noted that the theoretical results presented in Fig. 5b are not a function of the mean volume diameter. However, theoretical results were plotted against the mean volume diameter in Fig. 5b for a better side-by-side comparison with the experimental results (open circles). Figure 5a and b also show the experimental results for the optical bandgap as a function of the median mobility diameter and the mean volume diameter, respectively. The fitted parameters for the harmonic mean of electron and

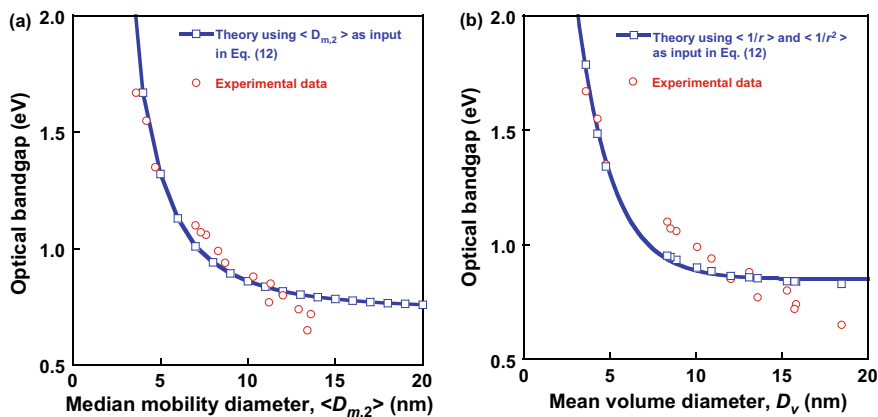


Fig. 5 The apparent optical bandgap measured using UV–Visible spectroscopy (open circles) and the bandgap calculated using Eq. (12) with fitted electronic properties (open rectangles). The apparent optical bandgap is plotted against **a** the median mobility diameter and **b** the mean volume diameter. The maximum uncertainty in apparent optical bandgap due to fitting errors was found to be less than 0.015 eV (not shown here). Symbols: experimental data (red circle) and theoretical data (blue square) using Eq. (12), solid lines: lines drawn to guide the eye

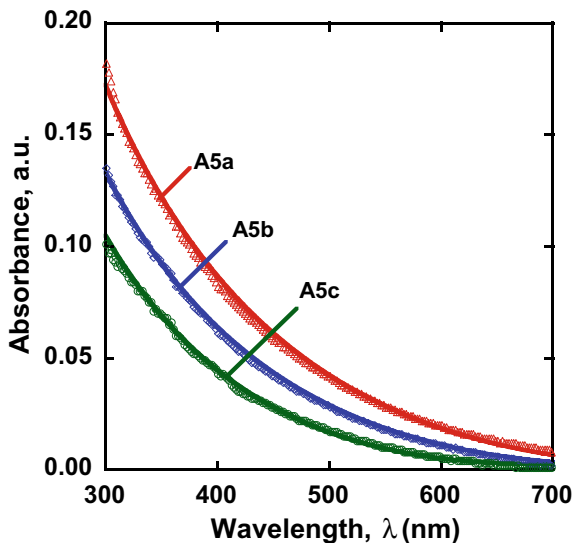
hole effective mass, relative permittivity, and bulk material bandgap are shown to be 0.2, 10, and 0.8163 eV, respectively, for the volume-weighted values of $\langle 1/r^2 \rangle$ and $\langle 1/r \rangle$.

However, using the median mobility diameter as an input in Eq. (12), fitted parameters are calculated as 0.178, 10, and 0.7431 eV, respectively, for the harmonic mean of electron and hole effective mass, relative permittivity, and bulk material bandgap. It should be noted that though both the median mobility diameter and the mean volume diameter can be used to report the particle size dependency of the apparent optical bandgap, representing the optical bandgap as a function of the mean volume diameter, D_v , makes more sense. Figure 5 shows the measured and fitted optical bandgap as a function of particle size using two separate treatments for the particle radius in Eq. (12). The left panel used the median mobility size as is for the $1/r$ and $1/r^2$ terms; whereas, the right panel used volume-weighted $\langle 1/r^2 \rangle$ and $\langle 1/r \rangle$ values along with the volume-weighted particle size.

For all series of flames studied, the optical bandgap measurements show that the particle size is the single most important parameter that impacts the optical bandgap. Figure 5 suggests a strong dependence of the optical bandgap on the particle size, which in turn depends on the flame conditions and particle residence times. This is seen in Fig. 5 and suggests the importance of various growth processes in the flame environment in altering the optical and electronic properties of these flame-synthesized carbon nanoparticles.

Similarly, to evaluate the non-linearity effect of the second term in Eq. (9), the electronic properties are also fitted directly against the absorbance measurement. The results are shown in Fig. 6 for the A5 series flame (A5a–A5c). The fitted electronic

Fig. 6 A5 series flames absorbance measurement using UV–Visible spectroscopy (symbols) and the absorbance calculated using Eq. (7) (solid lines). Symbols: experimental data, solid lines: theory using Eq. (7)



properties, considering the non-linearity effect, were evaluated to be 0.26, 10, and 1.0919 eV for the harmonic mean of electron and hole effective mass, relative permittivity, and bulk material bandgap, respectively. Using appropriate fitting parameters in Brus' expression, quantum confinement effects on the optical bandgap can be easily evaluated. The theoretical results shown here are in good agreement with the experimental results and indicate the importance of quantum confinement on the optical bandgap for flame-synthesized aerosols. The above results show that quantum confinement due to a decrease in particle size can widen the bandgap significantly. Quantum confinement effects render unique properties to these flame-synthesized aerosols in terms of tunable bandgaps that could be utilized further for photovoltaic applications.

5 Conclusions

The apparent optical bandgap for flame-synthesized aerosols can be deduced by considering the effects of the molecular size and structure, the particle size, and chemical composition. It is well known that PAHs are gaseous precursors to solid soot particles. These PAHs quickly grow in size due to chemical reactions and lead to particle inception. During the particle inception phase, the optical bandgap can be predicted by the HOMO–LUMO gap of a given PAH molecule. Following inception, primary particles undergo surface reactions and coagulate/agglomerate into larger fractal-like structures. Due to finite residence times associated with each flame configuration, flame-synthesized carbon nanoparticles can grow due to particle–particle coalescence/coagulation, agglomeration, and surface growth reactions. At this stage,

change in the density of states due to change in the particle size plays an important role and further affects the optical bandgap. Quantum confinement can alter the density of states and can widen or shorten the bandgap accordingly. An increase in the density of states due to an increase in the particle size can cause a further reduction of the optical bandgap. The present work suggests that the overall decrease in the optical bandgap due to quantum confinement could be as large as ~ 1 eV. However, beyond a certain mean volume diameter, the optical bandgap is found to approach an asymptote, and no further decrease in the optical bandgap is observed (see Fig. 5). The limit where this happens needs to be experimentally determined since a continuous reduction of the optical bandgap is observed as the particle size increases from 3.6 to 13.6 nm (see Table 1 and Fig. 5). Theoretical results predict the same be happening around a mean volume diameter larger than 20 nm (see Fig. 5). The optical bandgap measured through Tauc spectra for thermophoretically-sampled particles represents its final reduced value after they undergo stacking, surface growth, coagulation/agglomeration, functionalization, contamination, and quantum confinement. The final particle size is the single most crucial factor that impacts the apparent optical bandgap for these flame-synthesized aerosols.

The conclusions derived from the present study bring us to an important fact that flame-synthesized carbon nanoparticles can be tuned for desired optical bandgaps for applications in semiconductor devices and solar cells and exhibit promising capabilities to replace the traditional semiconductors like Silicon and CdTe. For instance, the semiconductors commonly used in commercial solar cells have bandgaps of 1.1 eV (Silicon) and 1.5 eV (CdTe). Our flames A4c and A5b can produce carbon nanoparticles having optical bandgaps of 1.1 eV and 1.55 eV, respectively. Such flame-synthesized carbon nanoparticles can be used to replace traditional semiconductors and can reduce the cost associated with such devices drastically. This can be a game-changer for both the industry and scientific community and can open new pathways for the development of cost-effective solar cells for masses, where currently the technology can be afforded by the elite few due to its exorbitantly high cost.

References

1. Tauc J (1968) Optical properties and electronic structure of amorphous Ge and Si. *Mater Res Bull* 3(1):37–46
2. Tauc J, Grigorovici R, Vancu A (1966) Optical properties and electronic structure of amorphous germanium. *Phys Status Solidi B* 15(2):627–637
3. Wood DL, Tauc JS (1972) Weak absorption tails in amorphous semiconductors. *Phys Rev B* 5(8):3144
4. Davis EA, Mott N (1970) Conduction in non-crystalline systems V. Conductivity, optical absorption and photoconductivity in amorphous semiconductors. *Phil Mag* 22(179):0903–0922
5. D'aleccio A, D'anna A, Gambi G, Minutolo P (1998) The spectroscopic characterization of UV absorbing nanoparticles in fuel rich soot-forming flames. *J Aerosol Sci* 29(4):397–409

6. Buchta C, D'Alessio A, D'Anna A, Gambi G, Minutolo P, Russo S (1995) The optical characterization of high molecular mass carbonaceous structures produced in premixed laminar flames across the soot threshold limit. *Planet Space Sci* 43(10):1227–1232
7. D'Anna A, D'Alessio A, Minutolo P (1994) Spectroscopic and chemical characterization of soot inception processes in premixed laminar flames at atmospheric pressure. In: *Soot formation in combustion*. Springer, Berlin, pp 83–103
8. D'alessio A, Gambi G, Minutolo P, Russo S, D'Anna A (1994) Optical characterization of rich premixed CH₄/O₂ flames across the soot formation threshold. *Proc Combust Inst* 25(1):645–651
9. Dischler B, Bubenzer A, Koidl P (1983) Hard carbon coatings with low optical absorption. *Appl Phys Lett* 42(8):636–638
10. Minutolo P, Gambi G, D'alessio A (1996) The optical band gap model in the interpretation of the UV-visible absorption spectra of rich premixed flames. *Proc Combust Inst* 26(1):951–957
11. Russo C, Alfè M, Rouzaud JN, Stanzione F, Tregrossi A, Ciajolo A (2013) Probing structures of soot formed in premixed flames of methane, ethylene and benzene. *Proc Combust Inst* 34(1):1885–1892
12. Allouis C, D'Alessio A, Beretta F, Borghese A (2000) Ultraviolet absorption and fluorescence measurements in turbulent spray flames. *Proc Combust Inst* 28(1):311–317
13. Ciajolo A, Apicella B, Barbella R, Tregrossi A (2000) Correlations of the spectroscopic properties with the chemical composition of flame-formed aromatic mixtures. *Combust Sci Technol* 153(1):19–32
14. Tregrossi A, Ciajolo A (2010) Spectral signatures of carbon particulate evolution in methane flames. *Combust Sci Technol* 182(4–6):683–691
15. Russo C, Stanzione F, Barbella R, Tregrossi A, Ciajolo A (2010) The characteristics of soot formed in premixed flames by different fuels. *Chem Eng Trans* 22:41–46
16. Russo C, Alfè M, Rouzaud JN, Stanzione F, Tregrossi A, Ciajolo A (2013) Probing structures of soot formed in premixed flames of methane, ethylene, and benzene. *Proc Combust Inst* 34(1):1885–1892
17. Russo C, Stanzione F, Ciajolo A, Tregrossi A (2013) Study on the contribution of different molecular weight species to the absorption UV–Visible spectra of flame-formed carbon species. *Proc Combust Inst* 34(2):3661–3668
18. Russo C, Stanzione F, Alfè M, Ciajolo A, Tregrossi A (2012) Spectral analysis in the UV-visible range for revealing the molecular form of combustion-generated carbonaceous species. *Combust Sci Technol* 184(7–8):1219–1231
19. Robertson J, O'reilly EP (1987) Electronic and atomic structure of amorphous carbon. *Phys Rev B* 35(6):2946
20. Robertson J (2002) Diamond-like amorphous carbon. *Mater Sci Eng R Rep* 37(4):129–281
21. Miller JH, Herdman JD, Green CD, Webster EM (2013) Experimental and computational determinations of optical band gaps for PAH and soot in a N₂-diluted, ethylene/air non-premixed flame. *Proc Combust Inst* 34(2):3669–3675
22. Adkins EM, Miller JH (2015) Extinction measurements for optical band gap determination of soot in a series of nitrogen-diluted ethylene/air non-premixed flames. *Phys Chem Chem Phys* 17(4):2686–2695
23. Adkins EM, Giaccai JA, Miller JH (2016) Computed electronic structure of polynuclear aromatic hydrocarbon agglomerates. *Proc Combust Inst* 36(1):957–964
24. Botero ML, Adkins EM, González-Calera S, Miller JH, Kraft M (2016) PAH structure analysis of soot in a non-premixed flame using high-resolution transmission electron microscopy and optical band gap analysis. *Combust Flame* 164:250–258
25. Alfè M, Apicella B, Barbella R, Rouzaud JN, Tregrossi A, Ciajolo A (2009) Structure–property relationship in nanostructures of young and mature soot in premixed flames. *Proc Combust Inst* 32(1):697–704
26. Ferrari AC, Robertson J (2000) Interpretation of Raman spectra of disordered and amorphous carbon. *Phys Rev B* 61(20):14095

27. Liu C, Singh AV, Saggese C, Tang Q, Chen D, Wan K, Vinciguerra M, Commodo M, De Falco G, Minutolo P, D'Anna A, Wang H (2019) Flame-formed carbon nanoparticles exhibit quantum dot behaviors. *Proc Natl Acad Sci* 116(26):12692–12697
28. Cain JP, Gassman PL, Wang H, Laskin A (2010) Micro-FTIR study of soot chemical composition—evidence of aliphatic hydrocarbons on nascent soot surfaces. *Phys Chem Chem Phys* 12(20):5206–5218
29. Sargasse C, Singh AV, Xue X, Chu C, Kholgy MR, Zhang T, Camacho J, Giaccai J, Miller JH, Thomson MJ, Sung CJ, Wang H (2019) The distillation curve and sooting propensity of a typical jet fuel. *Fuel* 235:350–362
30. Singh AV, Liu C, Wan K, Wang H (2017) Optical properties of flame-synthesized carbon nanoparticles. In: 10th U.S. National combustion meeting of the eastern states section of the combustion institute, 23–26 Apr, College Park, Maryland, USA
31. Liu C, Wan K, Singh AV, Wang H (2017) Ionization energy of flame-synthesized carbon nanoparticles. In: 10th U.S. National combustion meeting of the eastern states section of the combustion institute, 23–26 Apr, College Park, Maryland, USA
32. Sargasse C, Singh AV, Camacho J, Wang H (2017) Effect of distillate fraction of real jet fuel on sooting propensity—part 1: nascent soot formation in premixed stretch-stabilized flames. In: 10th U.S. National combustion meeting of the eastern states section of the combustion institute, 23–26 Apr, College Park, Maryland, USA
33. Camacho J, Singh AV, Wang W, Shan R, Yapp EK, Chen D, Kraft M, Wang H (2017) Soot particle size distributions in premixed stretch-stabilized flat ethylene–oxygen–argon flames. *Proc Combust Inst* 36(1):1001–1009
34. Camacho J, Liu C, Gu C, Lin H, Huang Z, Tang Q, You X, Saggese C, Li Y, Jung H, Deng L (2015) Mobility size and mass of nascent soot particles in a benchmark premixed ethylene flame. *Combust Flame* 162(10):3810–3822
35. Zhao B, Yang Z, Johnston MV, Wang H, Wexler AS, Balthasar M, Kraft M (2003) Measurement and numerical simulation of soot particle size distribution functions in a laminar premixed ethylene-oxygen-argon flame. *Combust Flame* 133(1):173–188
36. Abid AD, Camacho J, Sheen DA, Wang H (2009) Quantitative measurement of soot particle size distribution in premixed flames—the burner-stabilized stagnation flame approach. *Combust Flame* 156(10):1862–1870
37. Wang H, You X, Joshi AV, Davis SG, Laskin A, Egolfopoulos F, Law CK (2007) USC Mech Version II. High-temperature combustion reaction model of H₂/CO/C1–C4 compounds. http://ignis.usc.edu/USC_Mech_II.htm
38. Waldmann L (1959) Über die Kraft eines inhomogenen Gases auf kleine suspendierte Kugeln. *Z Naturforsch A* 14(7):589–599
39. Allen MD, Raabe OG (1982) Re-evaluation of Millikan's oil drop data for the motion of small particles in air. *J Aerosol Sci* 13(6):537–547
40. Millikan RA (1923) The general law of fall of a small spherical body through a gas, and its bearing upon the nature of molecular reflection from surfaces. *Phys Rev* 22(1):1
41. Brus L (1986) Electronic wave functions in semiconductor clusters: experiment and theory. *J Phys Chem* 90(12):2555–2560
42. Patil S, Singh AV (2022) The Effect of Flame Temperature on Nascent Soot Particles in a Series of Premixed Ethylene-Oxygen-Nitrogen Stagnation Flames, *Trans Indian Nat Acad Eng*. <https://doi.org/10.1007/s41403-022-00332-4>
43. Iyer MSK, Patil S, Singh AV (2022) Flame Synthesis of Functional Carbon Nanoparticles", *Trans Indian Nat Acad Eng*. <https://doi.org/10.1007/s41403-022-00329-z>

Using Ozone and Hydrogen Peroxide for Manipulating the Velocity Deficits, Detonability, and Flammability Limits of Gaseous Detonations



D. Santosh Kumar and Ajay V. Singh

Abstract Self-sustained propagation of detonation waves near limits is essential for the successful operation of detonation-based combustors since they suffer from high-velocity deficits near limits due to geometric constraints. This can potentially lead to its failure or attenuation near limits. The failure or attenuation of a detonation wave under such circumstances could lead to the failure of a detonation-based engine altogether. Existing models like Fay's model reasonably predict detonation velocity deficits for only stable mixtures. The present work focuses on estimating velocity deficits for both stable and unstable mixtures. The proposed model is similar to Fay's model with the modified reaction zone thickness calculated using $x = c(\Delta_i + \Delta_r)$. The value of c is found to be 33.2, 8.6, and 19.5 for H_2 -air, CH_4 - O_2 (unstable mixtures), and H_2 - O_2 -Ar mixtures (stable mixture) using existing experimental data. The proposed model predicts velocity deficits better than other existing models for both stable and unstable mixtures over a range of pressure ratios and tube diameters and also near the limits. The addition of O_3 and H_2O_2 at modest concentrations was shown to reduce the velocity deficits near propagation limits. The present work shows that the use of ignition promoters in trace amounts could help in the widening of detonation limits for detonation-based combustors.

Keywords Detonation cycle engines · Detonation limits · Ignition promoters · Induction length (Δ_i) · Induction time (τ_i) · Reaction length (Δ_r) · Stability parameter (χ) · Velocity deficit (ΔV)

1 Introduction

The widening of detonation propagation limits in gaseous detonations is one of the fundamental problems that needs to be addressed for the successful operation of detonation-based engines, such as the rotating detonation engine (RDE). These detonation-based engines are expected to operate in a variety of conditions using

D. Santosh Kumar · A. V. Singh (✉)
Indian Institute of Technology Kanpur, U.P, Kanpur 208016, India
e-mail: ajayvs@iitk.ac.in

© The Author(s), under exclusive license to Springer Nature Singapore Pte Ltd. 2023
G. Sivaramakrishna et al. (eds.), *Proceedings of the National Aerospace Propulsion Conference*, Lecture Notes in Mechanical Engineering,
https://doi.org/10.1007/978-981-19-2378-4_28

493

fuels that currently range from energy-dense liquid hydrocarbon fuels to gaseous fuels [1, 2]. One of the significant problems associated with RDEs is the stabilization and sustainment of detonation waves in the narrow channel of the combustor, where they can destabilize around tight curves. This, in particular, is important for the development of a small-scale detonation device for propulsion applications. Generally, detonations within limits will propagate with a stable velocity close to the Chapman-Jouguet velocity (V_{CJ}) with relatively small fluctuations. However, if the conditions approach the limits or are far from the limits, detonations propagate with significant velocity variations and deficits. The self-propagation of a detonation wave will depend on boundary conditions, particularly near the limits. The effect of the boundary condition is to reduce the propagation velocity below V_{CJ} , resulting in a velocity deficit and causing the detonation to attenuate and fail. This velocity deficit can be due to the heat and momentum losses and can be attributed to the boundary layer effects as proposed by Lee [3]. The finite thickness of the reaction zone is responsible for detonation vulnerability to boundary layer effects. The detonation wave velocity suffers from high-velocity deficits in smaller passages, and in general, $\Delta V/V_{CJ}$ is inversely proportional to the tube diameter as proposed by several researchers [4–10]. The higher the tube diameter ($1/d \rightarrow 0$), the closer the detonation wave would be to V_{CJ} . The detonation velocity is greatly influenced by the boundary layer when the diameter of the tube or channel is comparable with the boundary layer thickness.

Zeldovich [11] first investigated the effects of heat and momentum losses. Zeldovich [11] proposed that since the total momentum associated with a detonation wave is a function of volume, and because heat transfer and viscous drag are proportional to the wetted area of the tube, the velocity deficit in gaseous detonations should depend on the ratio of surface area to volume and thus on $1/d$. However, such a simplified treatment could not account for the two-dimensional effect of losses adequately. Manson and Guenoche [12] proposed an alternate mechanism for the velocity deficit. They considered a layer of reactive mixture adjacent to the wall quenches as a result of heat losses. In such scenarios, the reaction rate decreases significantly, leading to a decrease in the total chemical energy that goes to support the detonation. Again, this mechanism produced a dependence on the surface area-to-volume ratio. More definitive treatment of losses in 2-D was presented by Fay [13], in which the boundary layer was assumed to cause a divergence in the reaction zone, thereby resulting in a velocity deficit. In Fay's theory, the boundary layer causes the streamlines in the reaction zone to diverge and thus is responsible for a reduction in the detonation velocity. The flow divergence is due to the negative boundary layer thickness with respect to a reference coordinate system fixed to the shock wavefront. The boundary layer in the reaction zone responsible for the divergence of the streamlines will further result in a curved detonation front. Also, the detonation wave curvature is observed to be proportional to the rate of increase of the flow area away from the shock wavefront. For small curvatures, the detonation can be modeled as a quasi-1-D ZND model.

Using Fay's model, the velocity deficit for a given mixture and tube diameter can be calculated if the reaction zone thickness is known for estimating the boundary

layer thickness. The reaction zone thickness can be determined from the ideal ZND detonation model. However, researchers in the past found it to be unsatisfactory while predicting the velocity deficits as the theoretical reaction zone thickness was found to differ from the experimental value by at least two orders of magnitude. Some researchers used the detonation cell size, λ , rather than the ZND reaction zone length, for predicting the velocity deficits in real detonations. In real detonations, λ provides a more appropriate length scale to characterize the thickness of a cellular detonation. In a separate study [3], it was proposed to use cell length $L_c \approx 1.5\lambda$ in place of reaction zone thickness for unstable detonations. Moen et al. [14] later showed that critical tube diameter d_c could also be chosen as a length scale to characterize a real detonation front. The critical tube diameter can be related to the cell size using the following correlation of $d_c \approx 13\lambda$, which is valid for most explosive mixtures. One of the primary reasons for using critical tube diameter as the length scale for calculations of velocity deficit is because it can be determined less unambiguously. The critical tube diameter may be defined as the minimum diameter through which a planar detonation wave could emerge into an open space and continue to propagate as a spherical detonation. Using the correlation of $d_c \approx 13\lambda$ implies that $\lambda \approx d_c/13 \approx 0.077d_c$. Therefore, the cell length $L_c \approx 1.5\lambda \approx 0.11d_c$. Using the experimental values of detonation cell size or the critical tube diameter, since they are readily known for a variety of explosive mixtures, the cell length can be determined for a given fuel-oxidizer mixture. The calculated cell length can be used as the reaction zone thickness for a real detonation, where it can be used to calculate the area of divergence ξ from the displacement thickness δ^* . Therefore, the velocity deficit in various-diameter tubes can be obtained.

Laberge et al. [15] measured velocity deficits for stoichiometric acetylene-oxygen mixtures with high concentrations of argon dilution (stable mixtures), and the experimental results were found to agree with the Fay's model. Since the transverse waves in stable mixtures are relatively weak when compared to unstable mixtures, stable mixtures exhibit a regular cell pattern. Fay's model was found to predict the velocity deficits with reasonable accuracy in such mixtures. However, experimental results of unstable mixtures like C_2H_2 and C_2H_4 by Moen et al. [14] with low percentages of argon showed a considerable discrepancy in velocity deficit when compared with Fay's model. This indicates that boundary layer effects do not influence unstable detonations, since their propagation mechanism is dominated by instability in the detonation structure. In unstable detonations, transverse waves are strong, and cell patterns are irregular as opposed to stable detonations. For unstable detonations, as in the case of fuel-air mixtures, the velocity deficits were found to deviate from Fay's theory. Thus, it becomes essential to know whether the mixtures are stable or unstable for the application of Fay's model. Fay's model, in its present form, could only be applied for stable mixtures.

The initial studies on stability were made by Fickett et al. [16] using a one-step reaction model. The importance of transverse waves on the stability of mixtures for self-sustained detonation was carried out by Dupre et al. [17], Teodorczyk and Lee [18], and Radulescu and Lee [19]. Later, Ng et al. [20] defined the stability parameter based on the ratio of the induction to the reaction zone length. They also

included the temperature sensitivity of the induction reaction into the definition of the stability parameter. It is known that a long reaction time would tend to spread out the energy release and would reduce the effect of fluctuations in the induction time, which in turn could increase the stability of the mixtures. The numerical simulations by Radulescu et al. [21] with varying concentrations of argon in acetylene-air mixtures indicate that the shock pressure oscillations change from low-amplitude, high-frequency to low-frequency, and high-amplitude mode with a decrease in argon dilution from 90 to 70%. The effect of the addition of argon was found to increase the stability of mixtures. The same phenomenon was observed by Ng et al. [20], where they characterized the mixtures using the stability parameter, χ . The results by Ng et al. [20] indicate that the deviation of the stability parameter to higher values from the neutral stability boundary will increase the instability in mixtures. In contrast, the values below the neutral stability boundary would indicate stable mixtures. Various researchers mostly use the stability parameter, χ used by Ng et al. [20] for a quantitative description of the stability of detonation waves.

The velocity deficits are also greatly influenced by the type of boundary surfaces like smooth walls, rough walls, and porous walls. The maximum velocity deficits in smooth-walled tubes will be ~15% at detonation limits before it fails. However, a self-sustained detonation with rough walls can be observed with a velocity deficit of over 50%. The temperature behind the shock wave at very high-velocity deficits is very low for auto-ignition to occur, thus requiring new ignition and combustion mechanism for auto-ignition. Lee et al. [3] proposed that surface finish effects have to be taken into account for studying detonation phenomena, e.g., for smooth and rough-walled tubes. In smooth-walled tubes, it was observed that with an increase in the concentration of nitrogen for $C_3H_8-O_2$ mixtures, the detonation would transform from a multi-headed spin structure to a single-headed spin, as the limit is approached. The detonation in a smooth tube fails with the decoupling of the leading shock front from the reaction zone. However, the rough-walled tube can maintain the detonation wave with higher velocity deficits. Hence, rough-walled tubes have a positive effect on maintaining a self-sustained detonation wave with large velocity deficits of ~50%. These detonations with velocity deficits as high as 50% are known as low-velocity detonations.

Teodorczyk et al. [22] carried out experiments to study the detonation phenomenon on the effect of obstacles for rough-walled tubes to explain the ignition mechanism where temperatures behind the shock are well below auto-ignition temperature. It is observed that the diffraction of detonation waves around an obstacle is responsible for the failure of detonation by decoupling of reaction zone from the shock front. However, the reflected shocks from obstacles merge with the leading shock front to form detonation again. Therefore, obstacles or barriers in the flow path play an active role in the generation of strong transverse waves in rough walls. Thus, it can be understood that detonation in rough tubes can be more robust and can maintain steady propagation even with higher velocity deficits, where detonation fails in smooth walls. The roughness of tubes can also be increased by inserting a spiral coiled wire, in which the quasi-steady detonation wave speeds can be achieved with velocities as low as half of the CJ velocity. The role of boundary conditions, the nature of the

surface, the stability of mixtures, and obstacles or barriers in the path of detonation wave play a significant role in the determination of velocity deficits, which is essential in the design of detonation-based engines like RDE, as proposed by Randall et al. [23], Bykovskii and Vedernikov [24], Lu and Braun [25], and Kailasanath [26].

In real detonations, it is understood that detonation velocity will succumb to very high-velocity deficits of ~15% for stable mixtures and ~40% for unstable mixtures near their propagation limits before it fails. Since the velocity deficit is a function of reaction zone thickness, lower reaction zone thickness will lead to lower velocity deficits. Hence, reducing the length and time scales of a detonation wave without changing the gas dynamics and the thermodynamic properties of the resulting mixture can be a promising solution for the reduction of velocity deficits near the limits. Ignition promoters such as ozone and hydrogen peroxide offer the opportunity to resolve the problem of velocity deficit. We propose to use ozone and hydrogen peroxide as fuel-sensitizers for reducing the velocity deficits near the propagation limits. This methodology of sensitizing detonations with ignition promoters at low quantities can reduce the velocity deficits near the propagation limits. The effect of such doping is to reduce the velocity deficits by changing the ignition kinetics tremendously without changing the gas dynamics and relevant thermodynamic properties of both unburned and burned mixtures. Recent results by Magzumov [27], Crane et al. [28], and Kumar et al. [29] for gaseous detonations support this notion of fuel-sensitization, and results by Liang et al. [30], Kumar et al. [29], and Ivin et al. [31] show that ozone can be used in enhancing the detonability limits of detonating mixtures.

2 Objective

The objectives of the present work are:

- To formulate a modified theoretical model similar to Zhang and Liu [32], which can predict the velocity deficits in hydrogen and methane-oxygen detonations.
- To investigate the effects of ignition promoters on velocity deficits near the detonation limits.
- To examine the impact of ignition promoters on the stability parameter.

3 Methodology

3.1 *Fays Model*

In Fay's theory [13], the boundary layer causes the streamlines in the reaction zone to diverge and is responsible for the reduction in detonation velocity. If the divergence area is small, the flow in the reaction zone can be approximated as quasi-1D flow, and the conservation equation can be written as:

$$d(\rho u A) = 0 \tag{1}$$

$$\rho u A du + A dp = 0 \tag{2}$$

$$d\left(h' + \frac{u^2}{2}\right) = 0 \tag{3}$$

where h' includes the chemical energy Q . Integrating the above equations between the shock and the CJ plane gives Eqs. (4)–(6),

$$\rho_1 u_1 = \rho_2 u_2 (1 + \xi) \tag{4}$$

$$p_1 + \rho_1 u_1^2 = (p_2 + \rho_2 u_2^2)(1 + \xi) - \int_0^\xi p d\xi \tag{5}$$

$$h_1 + Q + \frac{u_1^2}{2} = h_2 + \frac{u_2^2}{2} \tag{6}$$

where ξ is the area divergence defined by, $\xi = \frac{A_2 - A_1}{A_1} = \frac{A_2}{A_1} - 1$.

Subscript 1 indicates the unburnt gaseous mixture upstream of the shock wave, and subscript 2 indicates the burned mixture downstream of the CJ plane, as shown in Fig. 1.

The velocity deficit can be expressed as

$$\frac{\Delta V}{V} = \left(\frac{V_{CJ} - V}{V_{CJ}}\right) \tag{7}$$

where V_{CJ} is the theoretical CJ detonation velocity, V is the actual detonation velocity, and ΔV is the detonation velocity deficit.

Solving the above Eqs. (4–6) and applying boundary conditions will result in a velocity deficit described as,

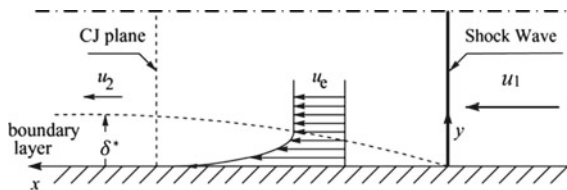


Fig. 1 Steady flow in the detonation wave near the tube wall (velocities are measured with respect to the coordinate system fixed to the shock front). The dotted lines indicate the outer edge of the boundary layer, which develops at the tube wall behind the shock front

$$\frac{\Delta V_1}{V_1} = 1 - \left[\frac{(1 - \nu)^2}{(1 - \nu)^2 + \gamma_2^2(2\nu - \nu^2)} \right]^{\frac{1}{2}} \quad (8)$$

where γ is the specific heat ratio, and ν is defined as

$$\nu = \frac{\varepsilon \xi}{(\gamma_2 + 1)(1 + \xi)}. \quad (9)$$

The area divergence ξ can be reduced in terms of boundary layer thickness δ^* for a round tube of radius R and diameter d , as

$$\xi = \frac{A_2}{A_1} - 1 = \frac{\pi(R + \delta^*)^2}{\pi R^2} - 1 \approx \frac{2\delta^*}{R} = \frac{4\delta^*}{d} \quad (10)$$

For smooth tubes, the boundary layer displacement thickness has been determined in shock tube experiments by Gooderum [33] as,

$$\delta^* = 0.22x^{0.8} \left(\frac{\mu_e}{\rho_1 u_1} \right)^{0.2} \quad (11)$$

where x is the distance from the shock front, μ_e is the viscosity of the gas in the reaction zone, and ρ_1 and u_1 are the density and the velocity in front of the shock (in the shock-fixed coordinate system).

Eqs. (7–11) can be solved for a given mixture with initial conditions by computing the value of reaction zone thickness x . According to Fay's model, the x is calculated by an empirical formula. Lee et al. used cell length, L_c , in place of reaction zone thickness, x , for the calculation of velocity deficit.

3.2 Modified Theoretical Model

In the present study, a new modified version of Fay's model was used for calculating the velocity deficits in gaseous detonations. The recent work by Crane et al. [28] suggested that detonation cell length can be modeled in terms of induction length, Δ_i and exothermic length, Δ_r . Zhang and Liu [32] carried out velocity deficit calculations using the Fay's model with modified reaction zone thickness as suggested by the work of Crane et al. [28] as, $x = c(\Delta_i + \alpha\Delta_r)$, where c is a constant and α is the proportionality factor between Δ_i and Δ_r , i.e., $\Delta_i / \Delta_r = \alpha$. The value of c is calculated by carrying out velocity deficit experiments and solving equations from (7) to (11). The equation used by Zhang and Liu [32], for calculating reaction zone thickness, x ultimately simplifies to a function of Δ_i , i.e., $x = c(2\Delta_i)$, after substituting ' α ' in $x = c(\Delta_i + \alpha\Delta_r)$. In the modified theoretical model proposed in this work, the reaction zone thickness (x) is modeled as $x = c(\Delta_i + \Delta_r)$, where Δ_i and

Δ_i represent the induction, and exothermic zone lengths, respectively, and can be calculated using a 1-D ZND model. The value of c in the above expression depends on the mixture composition. The value of ' c ' was evaluated from the velocity deficit experimental data reported in the literature elsewhere [32, 34, 35].

3.3 ZND Numerical Calculations

ZND computations were carried out using a modified version of the CalTech Shock and Detonation Toolbox (2018) [36]. Cantera (2018) [37], integrated with MATLAB and Python, was used for chemical kinetics simulation and to calculate the ZND length scales for $\text{H}_2\text{-O}_2$ and $\text{CH}_4\text{-O}_2$ detonations. The Foundation Fuel Chemistry Model Ver 1.0 (FFCM-1) by Smith et al. [38] is used in the present study. The Princeton ozone sub-model by Zhao et al. [39] was used to carry out calculations with ozone as a dopant. The uncertainties associated with the FFCM-1 model and the ozone sub-models can be found in the literature elsewhere [28]. The complete FFCM-1 model, including the ozone chemistry sub-model, comprises 39 species and 301 reactions. The governing equations for ZND model have been discussed in the literature elsewhere [40].

4 Results and Discussions

The present work focuses on studying velocity deficit experiments in three mixtures, $2\text{H}_2\text{-O}_2$ (unstable mixtures), $\text{CH}_4\text{-O}_2$ (unstable mixtures), and $2\text{H}_2\text{-O}_2\text{-3Ar}$ (stable mixtures). The reaction zone thickness (x) in the present study is modeled as $x = c(\Delta_i + \Delta_r)$, where Δ_i and Δ_r represent the induction and exothermic zone lengths, respectively. The velocity deficit experimental data of [32, 34, 35] for different tube diameters for the above three mixtures were used for the evaluation of c . The value of c is calculated by using velocity deficit values from experimental results and solving equations from (7) to (11) using a 1-D ZND model. If the velocity deficit is calculated from the experiment for a particular tube diameter, initial pressure, temperature, and equivalence ratio, the only unknown in Eqs. (7)–(11) is ' c ' value and the rest parameters can be calculated from 1-D ZND model. The nonlinear Eqs. (7)–(11) were solved simultaneously using MATLAB with velocity deficit experimental data of [32, 34, 35], where ' c ' values for different initial conditions were calculated for stable and unstable mixtures.

4.1 Unstable Mixtures

For unstable mixtures, the experimental data of [32, 34] for $2\text{H}_2 + \text{O}_2$ and $\text{CH}_4 + 2\text{O}_2$ mixtures at stoichiometric equivalence ratio are used to evaluate the value of c in $x = c(\Delta_i + \Delta_r)$, see Fig. 2a and b. It can be seen that the value of c varies over a wide range of pressure, and the average value was calculated based on statistical averaging. The value of c is found to be 33.2 and 8.6 for hydrogen and methane-oxygen mixtures, respectively, as shown in Fig. 2a and b. The reaction zone thickness was modeled as $x = 33.2(\Delta_i + \Delta_r)$ and $x = 8.6(\Delta_i + \Delta_r)$ for $2\text{H}_2 + \text{O}_2$ and $\text{CH}_4 + 2\text{O}_2$ mixtures, respectively. The modeled reaction zone thickness was then used in the Fay's model to calculate the velocity deficits in the respective mixtures. It can be seen from Fig. 3a and b that the proposed modified theoretical model predicts better when compared to Fay's model and the theoretical model proposed by Zhang and Liu [32]. Similar is the case for methane-oxygen detonations, where the modified reaction zone thickness given as $x = 8.6(\Delta_i + \Delta_r)$ reasonably predict the velocity deficits (see Fig. 3c). Fay's model does not predict velocity deficits for unstable mixtures when reaction zone thickness is modeled with cell length L_c . However, the same is not the case with the proposed theoretical model, which reasonably predicts the velocity deficit data for both $2\text{H}_2 + \text{O}_2$ and $\text{CH}_4 + 2\text{O}_2$ mixtures. Thus, the proposed modified model (designated as FFCM1 here) is more robust in predicting the velocity deficits in unstable mixtures when compared to earlier models. The same can be seen in Fig. 3, where the modified theoretical model (FFCM1) is observed to predict the experimental velocity deficit data trends quite accurately when compared to other models (Fays and Bo Zhang model).

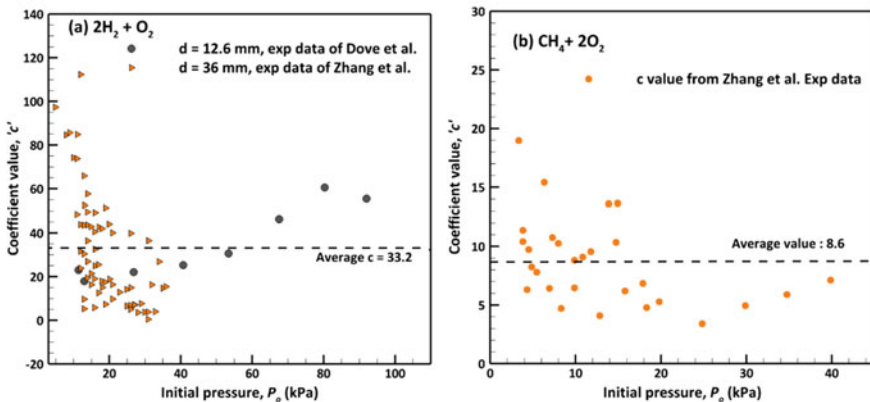


Fig. 2 Calculation of value of c in reaction zone thickness formula $x = c(\Delta_i + \Delta_r)$ for **a** $2\text{H}_2 + \text{O}_2$ mixtures and **b** $\text{CH}_4 + 2\text{O}_2$ mixtures. ZND calculations were carried out at a stoichiometric equivalence ratio and an initial temperature of 295 K

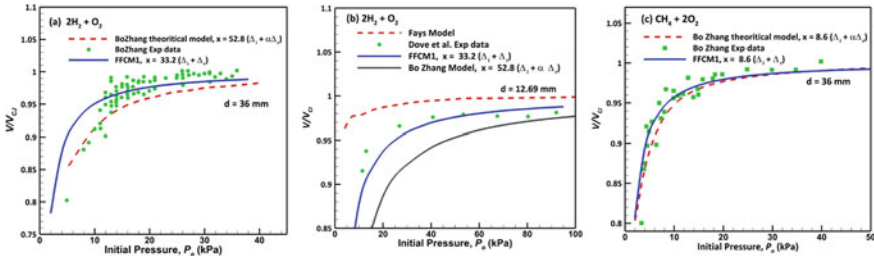


Fig. 3 Comparison of the proposed modified model (FFCM1) with other theoretical models for the prediction of velocity deficits in **a** and **b** hydrogen–oxygen detonations and **c** methane–oxygen detonations. Filled symbols represent the experimental data whereas dotted and solid lines represent the prediction by various theoretical models. ZND calculations were carried out for stoichiometric mixtures at an initial temperature of 295 K

4.2 Stable Mixtures

In the case of stable mixtures, the experimental data of $2H_2 + O_2 + 3Ar$ by Gao and Ng [38], as shown in Fig. 4a, are used to evaluate the value of c in $x = c(\Delta_i + \Delta_r)$. It can be seen that the value of “ c ” is reasonably constant over the range of initial pressures. The average c value for hydrogen–oxygen mixtures diluted with 50% Ar is found to be 19.5 (see Fig. 4a). In the case of stable mixtures, Fay’s model reasonably predicts the velocity deficits. The experimental velocity deficit results of Gao and Ng [38] for $2H_2 + O_2 + 3Ar$ mixtures agree well with Fay’s model, where

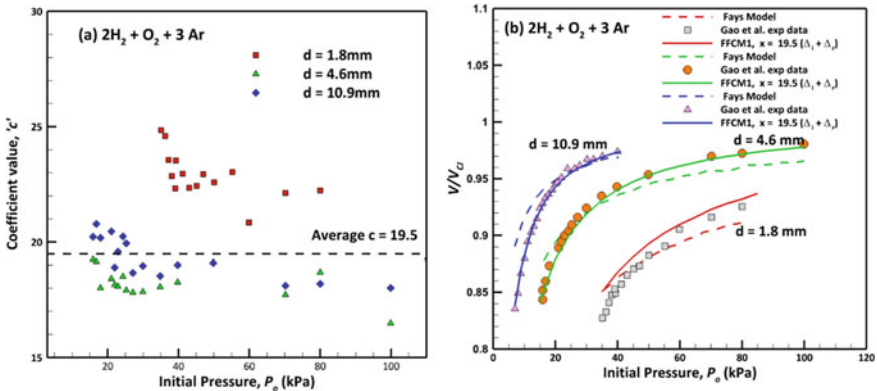


Fig. 4 **a** Calculation of c in the reaction zone thickness formula $x = c(\Delta_i + \Delta_r)$ for $2H_2 + O_2 + 3Ar$ mixtures diluted with 50% argon **b** comparison of velocity deficit results of the proposed modified model (FFCM1) with the experimental data of Gao et al. and Fay’s model for $2H_2 + O_2 + 3Ar$ mixtures diluted with 50% Argon. Filled symbols represent the experimental data. Dotted and solid lines represent the prediction by Fay’s and FFCM1 theoretical model, respectively. ZND calculations were carried out at a stoichiometric equivalence ratio and an initial temperature of 295 K

the reaction zone thickness is modeled as a cell length (see Fig. 4b). In the present study, the reaction zone thickness is also modeled as $x = 19.5(\Delta_i + \Delta_r)$, which is then used in Fay's model to predict the velocity deficit. It is observed that the proposed modified model (FFCM1) predicts the velocity deficit trends of Gao et al. more accurately when compared to Fay's model. It can be seen from Fig. 4b that near detonation limits, Fay's model, in its current form, performs poorly in predicting the velocity deficits for different tube diameters. However, using a modified theoretical model (FFCM1) proposed in the present work predicts the velocity deficits more accurately when compared to Fay's model for stable mixtures near the propagation limits. This is a remarkable result since, to date, no theoretical model can predict the velocity deficit trends in both stable and unstable mixtures. The proposed model of the present work is capable of predicting the velocity deficit trends in both the stable and unstable mixtures and holds a lot of promise for the detonation scientific community.

4.3 Effect of O_3 and H_2O_2 on Velocity Deficit

The effects of ignition promoters like ozone and hydrogen peroxide are studied for both stable and unstable mixtures. It can be seen from Fig. 5a–c that the addition of O_3 and H_2O_2 will reduce the velocity deficits significantly near the limits for H_2-O_2 , CH_4-O_2 , and H_2-O_2 mixtures diluted with 50% argon for various tube diameters. The results by Crane et al. and other researchers [28, 41] show that ignition promoters like ozone and hydrogen peroxide can effectively reduce the activation energy and the associated chemical length and time scales. They also increase the chain branching reactions, leading to an increase in the generation of free radicals like H, O, and OH, which result in faster ignition kinetics. Thus, the reaction zone thickness reduces with the addition of ignition promoters, thereby decreasing the velocity deficits. From Fig. 5 and Table 1, it can be seen that the velocity deficits are significantly reduced near the limits with the addition of ignition promoters from 0 to 20,000 PPM. It can be seen from Table 1 that velocity deficits can be improved by up to 20%

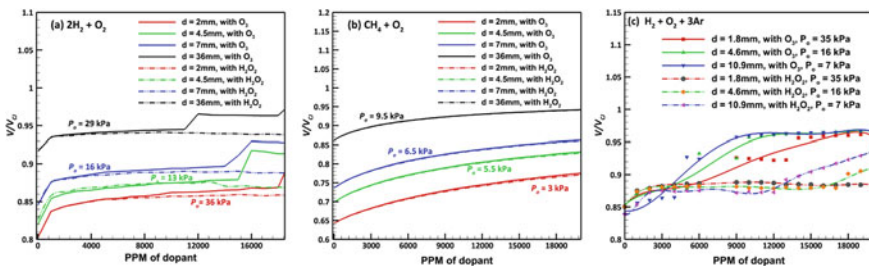


Fig. 5 Effect of O_3 and H_2O_2 on velocity deficits for **a** H_2-O_2 mixtures **b** CH_4-O_2 mixtures and **c** H_2-O_2 mixtures diluted with 50% argon. ZND calculations were carried out for stoichiometric mixtures at an initial temperature of 295 K

Table 1 Effect of O₃ and H₂O₂ on velocity deficits for stable and unstable mixtures

Composition	Dia (mm)	Critical pressure (kPa)	V/V_{CJ}	V/V_{CJ} @ O ₃ at 20,000 PPM	V/V_{CJ} @ H ₂ O ₂ at 20,000 PPM	% change @ O ₃	% change @ H ₂ O ₂
2H ₂ -O ₂	2.0	29	0.80	0.90	0.86	12.50	7.50
	4.5	16	0.82	0.91	0.87	10.98	6.10
	7.0	13	0.85	0.93	0.88	9.41	3.53
	36.0	6	0.91	0.98	0.94	7.69	3.30
CH ₄ -O ₂	2.0	9.5	0.64	0.78	0.77	21.88	20.31
	4.5	6.5	0.70	0.83	0.83	18.57	18.57
	7.0	5.5	0.74	0.86	0.86	16.22	16.22
	36.0	3	0.86	0.94	0.94	9.30	9.30
2H ₂ -O ₂ -3Ar	1.8	35	0.85	0.96	0.88	12.94	3.53
	4.6	16	0.85	0.97	0.90	14.12	5.88
	10.9	7	0.84	0.97	0.94	15.48	11.90

by using O₃ and H₂O₂ in trace amounts for methane-oxygen detonations, especially in narrow tubes. A similar improvement in the decrease of velocity deficit by ~13% can be seen for hydrogen-oxygen mixtures, with and without argon.

4.4 Effect of O₃ and H₂O₂ on Stability Parameter

The stability of mixtures can be better explained with the stability parameter. It is evident that stability of the detonation is a consequence of the temperature-sensitivity of the chemical reactions. Small fluctuations in the shock temperature result in large fluctuations in the induction delay time as well as the energy release rate of the recombination reactions. It should be noted that the induction time (or induction zone length) should be measured relative to the recombination time. A long reaction time will tend to spread out the energy release and thus reduce the effect of fluctuations in the induction time. Thus, a long reaction time has a stabilizing effect and this is taken into consideration explicitly in the stability parameter of Ng [20]. Large values of the stability parameter leads to gasdynamic instabilities in the reaction zone. The lower value of the stability parameter, χ , below the neutral stability boundary, represents more stable mixtures with regular cell pattern, and higher values of χ represent unstable mixtures with irregular cell pattern. It is desired to have stable mixtures with regular and uniform cell structures for lower velocity and pressure fluctuations. The addition of ignition promoters like ozone and hydrogen peroxide can have a significant impact on the stability parameter, where they reduce the activation energy and the ratio of the induction—to the reaction-zone length. The effects of the addition

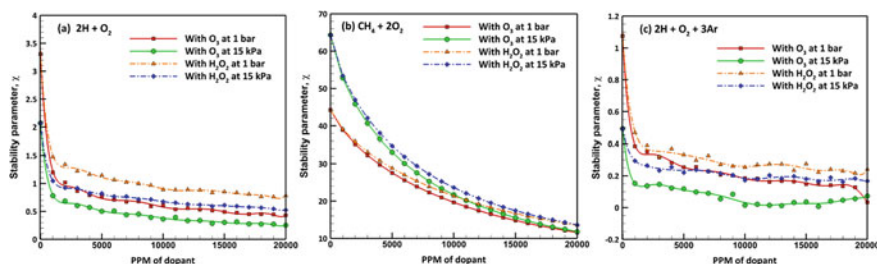


Fig. 6 Effect of O_3 and H_2O_2 ignition promoters on the stability parameter for **a** H_2 - O_2 mixtures **b** CH_4 - O_2 mixtures **c** H_2 - O_2 mixtures diluted with 50% argon. ZND calculations were carried out for stoichiometric mixtures at an initial temperature of 295 K and initial pressure of 15 kPa and 1 bar

of ignition promoters like O_3 and H_2O_2 on the stability of H_2 - O_2 , CH_4 - O_2 , and H_2 - O_2 mixtures diluted with 50% argon were estimated at initial pressures of 15 kPa and 1 bar. The results are presented in Figs. 6a–c. It can now be understood that the stability parameter reduces significantly with the addition of ignition promoters for both the stable and unstable mixtures.

Hence, it can be inferred that the addition of ignition promoters can steer the mixtures from unstable regimes toward stable regimes. Thus, the presence of ignition promoters not only reduces the velocity deficits but also seems to have a stabilizing effect on a detonating wave structure. The critical role of ignition promoters in detonating mixtures cannot be neglected, where they not only prevent the attenuation of a detonation wave but also stabilizes them, thus making it more robust near its propagation limits. This methodology can be successfully implemented in detonation-based engines to reduce the velocity deficits for varied flow conditions and engine geometries. Similarly, detonability and flammability limits can be extended for various fuel-oxidizer mixtures in the presence of ignition promoters at modest concentrations.

5 Conclusions

The proposed theoretical model for the prediction of velocity deficits in gaseous detonations in tubes was developed by modeling the reaction zone thickness as $x = c(\Delta_i + \Delta_r)$ and using it as a length scale in Fay's model. The reaction zone thickness x was calculated using ZND chemical length scales like induction length, Δ_i , and exothermic length, Δ_r . The value of c was estimated to be 33.2, 8.6, and 19.5 for the H_2 - O_2 (unstable mixtures), CH_4 - O_2 (unstable mixtures), and H_2 - O_2 mixtures diluted with 50% argon (stable mixtures), respectively, by using experimental velocity deficit data from earlier works. The proposed theoretical model reasonably predicts velocity deficits for both unstable and unstable mixtures over a wide range of pressures, tube diameters, and also near the detonation limits. The

addition of ignition promoters like O_3 and H_2O_2 in modest concentrations to fuel-oxidizer-diluent mixtures significantly impacts the detonation structure, where it reduces the chemical length and time scales significantly. The overall effect of such a doping would be to reduce the velocity deficits in gaseous detonations. This methodology of sensitizing a given fuel-oxidizer-diluent mixture with the help of ignition promoters like ozone and hydrogen peroxide can be used as a promising solution for reducing the velocity deficits in gaseous detonations, especially near the propagation limits. With this methodology, the detonation limits can be widened, and lower velocity deficits can be attained, which is essential for the sustenance of detonation waves for propulsion applications for a variety of engine geometries and varied flow conditions. This methodology could also prevent the failure of detonation waves near their propagation limits. The results from the present study show that the addition of O_3 and H_2O_2 at modest can significantly lower the stability parameter (χ), even for unstable mixtures. Ozone and H_2O_2 could have a stabilizing effect on irregular gaseous detonations and can be used to steer the unstable detonations toward a stable regime.

Acknowledgements The authors acknowledge the financial support for this work from the Aeronautics R&D Board, Ministry of Defence, Govt. of India vide Sanction Letter # ARDB/01/1042000M/I.

References

1. Dahake A, Singh AV (2021) Numerical study on NO_x emissions from a synthetic biofuel for applications in detonation-based combustors, AIAA 2021–3678, 2021 AIAA propulsion and energy forum, 9–11 August 2021, Virtual Event
2. Iyer MSK, Singh AV (2021) NO_x emissions from jet A-air detonations. AIAA 2021–3679, 2021 AIAA propulsion and energy forum, 9–11 August 2021, Virtual Event
3. Lee JHS (2008) The detonation phenomenon. Cambridge University Press, Cambridge
4. Camargo A, Ng HD, Chao J, Lee JHS (2010) Propagation of near-limit gaseous detonations in small diameter tubes. *Shock Waves* 20:499–508
5. Chao J, Ng HD (2009) Detonability limits in thin annular channels. *Proc Combust Inst* 32:2349–2354
6. Gao Y, Ng HD, Lee JHS (2015) Experimental characterization of galloping detonations in unstable mixtures. *Combust Flame* 162:2405–2413
7. Gao Y, Ng HD (2014) Minimum tube diameters for steady propagation of gaseous detonations. *Shock Waves* 24:447–454
8. Ishii K, Itoh K, Tsuboi T (2002) A study on velocity deficits of detonation waves in narrow gaps. *Proc Combust Inst* 29:2789–2794
9. Ishii K, Monwar M (2011) Detonation propagation with velocity deficits in narrow channels. *Proc Combust Inst* 33:2359–2366
10. Jackson S, Lee BJ, Shepherd JE (2016) Detonation mode and frequency analysis under high loss conditions for stoichiometric propane-oxygen. *Combust Flame* 167:24–38
11. Zeldovich YB (1950) *Zh Eksp Teor Fiz* 10:542 (1940). Translated in NACA Technical Memorandum 1261
12. Manson N, Guénoche H (1957) Effect of the charge diameter on the velocity of detonation waves in gas mixtures. *Sympos (Int) Combust* 6:631–639

13. Fay J (1959) Two-dimensional gaseous detonations: velocity deficit. *Phys Fluids* 2:283–290
14. Moen IO, Murray SB, Bjerketvedt D, Rinnan A, Knystautas R, Lee JHS (1982) Diffraction of detonation from tubes into a large fuel-air explosive cloud. In: 19th International symposium on combustion, pp 635–644
15. Laberge S, Knystautas R, Lee JHS (1993) Propagation and extinction of detonation waves in tubes bundles. *AIAA Prog Astronaut Aeronaut* 153:381–396
16. Fickett W, Jacobson J, Schott G (1972) Calculated pulsating one-dimensional detonations with induction-zone kinetics. *AIAA J* 10:514–516
17. Dupre G, Peraldi O, Lee JHS, Knystautas R (1988) Progress of detonation waves in acoustic absorbing walled tube. *Prog Astronaut Aeronaut* 114:248–263
18. Teodorczyk A, Lee JHS (1995) Detonation attenuation by foams and wire meshes lining the walls. *Shock Waves* 4:225–236
19. Radulescu M, Lee JHS (2002) The failure mechanism of gaseous detonations: Experiments in porous wall tubes. *Combust Flame* 131:29–46
20. Ng HD, Higgins AJ, Kiyana CB, Radulescu MI, Lee JHS, Bates KR, Nikiforakis N (2005) Non-linear dynamics and chaos analysis of one-dimensional pulsating detonations. *Combust Theor Model* 9:159–170
21. Radulescu M, Ng HD, Lee JHS, Varatharajan B (2002) The effect of argon dilution on the stability of acetylene-oxygen detonations. *Proc Combust Inst* 29:2825–2831
22. Teodorczyk A, Knystautas R (1989) Propagation mechanism of quasi-detonations. *Int Sympos Combust* 22:1723–1731
23. Randall S, Anand V, St. George AC, Gutmark EJ (2015) Numerical and Experimental study of heat transfer in a rotating detonation engine. 53rd AIAA Aerospace Sciences Meeting, Florida, USA
24. Bykovskii FA, Vedernikov EF (2009) Heat fluxes to combustor walls during continuous spin detonation of fuel-air mixtures. *Combustion, Explosion, and Shock Waves* 45:70–77
25. Lu FK, Braun EM (2014) Rotating detonation wave propulsion: experimental challenges, modeling, and engine concepts. *J Propul Power* 30:1125–1142
26. Kailasanath K (2000) Review of propulsion applications of detonation waves. *AIAA J* 38:1698–1708
27. Magzumov AE, Kirillov I, Rusanov V (1998) Effect of small additives of ozone and hydrogen peroxide on the induction-zone length of hydrogen-air mixtures in a one-dimensional model of a detonation wave. *Combust Explos Shock Waves* 34:338–341
28. Crane J, Shi X, Singh AV, Tao Y, Wang H (2019) Isolating the effect of induction length on detonation structure: hydrogen-oxygen detonation promoted by ozone. *Combust Flame* 200:44–52
29. Kumar DS, Ivin K, Singh AV (2021) Sensitizing gaseous detonations for hydrogen/ethylene-air mixtures using ozone and H_2O_2 as dopants for application in rotating detonation engines. *Proc Combust Inst* 38(3):3825–3834
30. Liang W, Wang Y, Law CK (2019) Role of ozone doping in the explosion limits of hydrogen-oxygen mixtures: multiplicity and catalyticity. *Combust Flame* 205:7–10
31. Ivin K, Singh AV (2019) Sensitizing ethylene-air and ethylene-oxygen mixtures for optimal performance of detonation cycle engines. In: 33rd national convention of aerospace engineers and national conference on emerging technologies in aerospace structures, materials and propulsion systems, November 16–17, pp 20–26
32. Zhang B, Liu H (2019) Theoretical prediction model and experimental investigation of detonation limits in the combustible gaseous mixture. *Fuel* 258:116132
33. Gooderum PB (1958) NACA Tech. Note 4243
34. Dove JE, Scroggie BJ, Semerjian H (1974) Velocity deficits and detonability limits of hydrogen-oxygen detonations. *Acta Astronaut* 1:345–359
35. Gao Y, Ng HD (2016) An experimental investigation of detonation limits in hydrogen-oxygen-argon mixtures. *Int J Hydrogen Energy* 41:6076–6083
36. Browne S, Ziegler J, Shepherd JE (2018) Numerical solution methods for shock and detonation jump conditions. GALCIT Report FM2006.006-R3, California Institute of Technology Revised September 2018.

37. Goodwin DG, Speth RL, Moffat HK, Weber BW (2018) Cantera: An object-oriented software toolkit for chemical kinetics, thermodynamics, and transport processes. <https://www.cantera.org>, 2018. Version 2.4.0. <https://doi.org/10.5281/zenodo.1174508>
38. Smith GP, Tao Y, Wang H (2016) Foundational fuel chemistry model version 1.0 (FFCM-1) <http://web.stanford.edu/group/haiwanglab/FFCM-1/index.html>
39. Zhao H, Yang Y, Ju Y (2016) Kinetic studies of ozone assisted low-temperature oxidation of dimethyl ether in a flow reactor using molecular beam mass spectrometry. *Combust Flame* 173:187–194
40. Kumar DS, Singh AV (2021) Inhibition of hydrogen-oxygen/air gaseous detonations using CF_3I , H_2O , and CO_2 . *Fire Saf J* 124:103405
41. Kumar DS, Singh AV (2019) Sensitizing gaseous mixtures for practical applications in rotating detonation engines. In: 33rd National convention of aerospace engineers and national conference on emerging technologies in aerospace structures, materials and propulsion systems, November 16–17, pp 14–19

Thermal Design of Cooling Configurations for an Afterburner V-Gutter of Advanced Aeroengine



Hanumanthu Gari Poornasree, Batchu Suresh, V. Kesavan,
and D. Kishore Prasad

Abstract Thrust augmentation of military aircraft engine is carried out during critical phases of flight with the help of an afterburner. In advanced aeroengines, afterburner entry temperatures are beyond material allowable temperature limits. Thus, it is vital to cool V-gutter even when afterburner is not in operation, to lower its metal temperatures and to achieve increased creep life. Present study is preliminary design of three cooling configurations for a given V-gutter geometry at design condition of operation of afterburner. 1D code is developed to arrive at geometry of each configuration after a parametric analysis. Effect of thermal barrier coating on the V-gutter metal temperature is studied. 3D conjugate heat transfer analysis (CHT) is carried out using FloEFD commercial software to study the local coolant flow field and its effect on metal temperatures.

Keywords V-gutter · Convective cooling · Impingement cooling · Heat transfer coefficient (HTC) · Conjugate heat transfer (CHT)

Nomenclature

C or y Spanwise pitch (mm)
CHT Conjugate heat transfer
 D_h Hydraulic diameter (mm)

H. G. Poornasree (✉) · B. Suresh · V. Kesavan · D. Kishore Prasad
GTRE, Bengaluru, Karnataka, India
e-mail: poornasreehg.gtre@gov.in

B. Suresh
e-mail: batchusuresh.gtre@gov.in

V. Kesavan
e-mail: kesavanv.gtre@gov.in

D. Kishore Prasad
e-mail: kishoreprasadd.gtre@gov.in

D_i	Curvature diameter (mm)
G_c	Cooling air cross flow rate (kg/s)
G_j	Jet mass flow rate (kg/s)
HTC	Heat transfer coefficient (W/m^2K)
K_L	Loss coefficient
K_b	Bend loss coefficient
K_{imp}	Impingement pressure loss coefficient
L	Length of the passage (mm)
LE	Leading edge
Nu	Nusselt number
Nu_1	Nusselt number without cross flow.
P1	Coolant passage near LE in Configuration-I,II
P2	Coolant passage near wake in Configuration-I, II
Pr	Prandtl number
Re	Reynolds number
SW	Sidewall
TBC	Thermal barrier coating
T_g	Gas temperature (K)
T_m	Metal temperature (K)
Tu	% Turbulence intensity
W	Width of passage P2 (mm)
b	Bend dimension in Configuration-II (mm)
d	Diameter of impingement hole in Configuration-III (mm)
e	Exit dimension in Configuration-II (mm)
v	Velocity (m/s)
x	Chordwise pitch (mm)
z	Impingement distance (mm)
ρ	Density (kg/m^3)
\emptyset	Diameter of exit hole in passage P1 of Configuration-I. (mm)

1 Introduction

Afterburner is used to augment the thrust of an aeroengine during critical phases of flight like take-off, landing, manoeuvres, etc. During operation of afterburner, the high-velocity gases coming out from the turbine are mixed with fuel from spray bars. This fuel–air mixture is burnt by anchoring the flame with help of V-gutter. V-gutter creates a recirculation zone of high-temperature combustible mixture at its wake region, providing the continuous source of combustion. In advanced aeroengines, wake gas temperatures are of the order of 2100 K, and afterburner entry gas temperatures are of the order of 1300 K. These temperatures are beyond the allowable temperature limit of the Nickel-based alloys used for the afterburner components. Thus, the components have to be cooled throughout operation of the engine to lower

metal temperatures and to achieve higher creep life. Bypass air originating from lower stages of compressor can be used for cooling. Different types of cooling techniques are employed in cooling different components. Wadia and James [1] have presented on the enhanced power through low-risk derivative technology of F110-GE-129 enhanced fighter engine. They have presented use of radial augmentor with cooled radial flame holder. They have stated that it provides reduced complexity and improved reliability. Over 50% improvement in life of augmentor parts is achieved due to advanced cooling. Lindblad et al. [2] outlined basic understanding of cooling, ignition, and combustion derived in the process of developing the cooled radial V-gutter for F404/RM12 engine. Main reason for developing a cooled V-gutter was to increase life compared to uncooled annular V-gutter. They designed a convective cooling system using the bypass air. They have concluded that the radial V-gutter meets its design goal and delivers thrust levels similar or slightly higher than that of the annular V-gutter. Schmidt et al. [3] have described the development programme, requirements, and design of V-gutter. They explained that main objective of cooling the V-gutter is to increase its creep life and thereby lower the afterburner life cycle cost. Suresh and Kumar [4] have presented the temperature prediction and validation of V-gutter for aeroengine afterburner. They have studied the influence of gas temperature and conductivity of TBC on metal temperature. Suresh and Kumar [5] have carried out the design of cooling configuration for V-gutter. They have discussed four different configurations. Smooth single channel, double channel configurations, and two ribbed configurations are studied. Broken rib configuration was considered best with lesser temperature compared to other three configurations. The present study is to design cooling configurations for V-gutter with impingement and convection cooling techniques.

2 Problem Definition

Aim of the present study is to design cooling configuration for a given radial V-gutter geometry at design condition for an afterburner. Two cooling configurations are designed with convective cooling technique, and third configuration is designed with impingement cooling technique. 1D code is developed to arrive at the geometry of each cooling configuration. 1D parametric study of each configuration is carried out to arrive at geometrical parameters. Cooling geometry with lesser coolant mass flow and metal temperatures within the allowable limits is selected. 3D metal temperature distributions are obtained from CHT analysis using FloEFD ver.19 software for the three configurations and are compared. One configuration is chosen based on the coolant flow requirement and metal temperatures.

3 V-Gutter Geometry

Radial V-gutter configuration with the bypass flow, core flow, and bypass casing is shown in Fig. 1. There are total of 13 radial V-gutters.

Cross section view of a radial V-gutter is given in Fig. 2. As shown in the Fig, the core gas flow region around V-gutter can be divided into three regions based on the type of flow, namely leading edge (LE), sidewall (SW), and wake regions.

During the operation of the afterburner, core gases are mixed with the fuel and are ignited. Flame gets anchored onto the V-gutter. Behind wake region, recirculation zones are created. Wake gets exposed to high-temperature combustible gases.

Pressure differential between the bypass air pressure (source pressure) and core gas pressure (sink pressure) acts as the driving force for the bypass air to flow as a coolant in the V-gutter. Temperatures and pressures of core gas, bypass air, and the hot gas temperature are considered as the aerodynamic inputs for the design. The order of hot gas temperature is 2100 K, and bypass temperature is 500 K. Pressure ratio between the bypass (total) and hot gases (static) is of order of 1.2.

Material of the V-gutter is a Nickel-based alloy, and material of thermal barrier coating (TBC) is a zirconium alloy. The material properties of the V-gutter and TBC are given in Table 1.

Fig. 1 Radial V-gutter configuration in afterburner

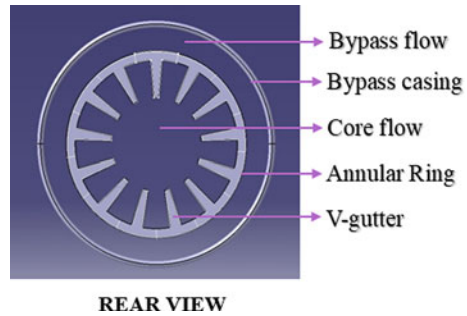


Fig. 2 Geometry details, core gas flow regions of V-gutter

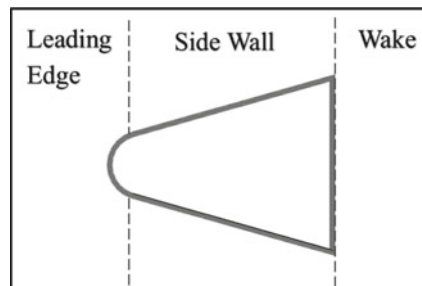


Table 1 Material properties of the V-gutter, TBC

Property, unit	Component	Value
k , (thermal conductivity), $\frac{W}{mK}$	V-gutter	20
	TBC	1.3
C_p (specific heat constant), $\frac{J}{kgK}$	V-gutter	540
	TBC	602
ρ (density), $\frac{kg}{m^3}$	V-gutter	8980
	TBC	5200

4 1D Analysis

1D flow networks are developed to predict the coolant pressure loss, coolant temperature rise, coolant heat transfer coefficients (HTC), and metal temperature, for given source pressure and sink pressure of radial V-gutter at design condition of afterburner.

External Gas Loads

Convective heat transfer to V-gutter from core gases is considered for LE, SW regions. Convective and radiative heat transfer are considered in the wake region.

External heat loads coming on to the V-gutter are estimated using the empirical correlations available in open literature.

Gas side HTC in LE is determined using the correlation by Lowery and Vachon [6] for flow past cylinder.

$$\frac{Nu}{\sqrt{Re}} = 1.01 + 2.624 \frac{Tu\sqrt{Re}}{100} - 3.07 \left[\frac{Tu\sqrt{Re}}{100} \right]^2 \tag{1}$$

Turbulence intensity of 5% is used.

Gas side HTC in SW is determined using correlation for turbulent flow over a flat plate

$$Nu = 0.037Re^{0.8}Pr^{0.333} \tag{2}$$

Gas side HTC in wake region is determined using the correlation by Andrew [7] and Hajime [8]

$$Nu = 0.172Re^{\frac{2}{3}} \tag{3}$$

Bulk gas temperature and pressures are used to estimate Nu.

Radiation in the wake region is by luminous radiation, and the relation by Lefebvre and Herbert [9] for the gas emissivity is used

$$\epsilon_g = 1 - \exp\left[-290P_gL(qL_b)^{0.5}T_g^{-1.5}\right] \tag{4}$$

where q —Fuel–Air ratio, L —Luminosity factor and L_b —Beam length, T_g —Gas temperature, P_g —Gas pressure.

Effective HTC is estimated for the wake region where the radiation effects are significant.

Core gas heat fluxes are estimated using the allowable metal temperatures. It is observed that heat flux is higher in the wake region. Thus, higher coolant heat transfer coefficients are required in the wake portion of the V-gutter. Three cooling configurations are designed.

4.1 Configuration-I

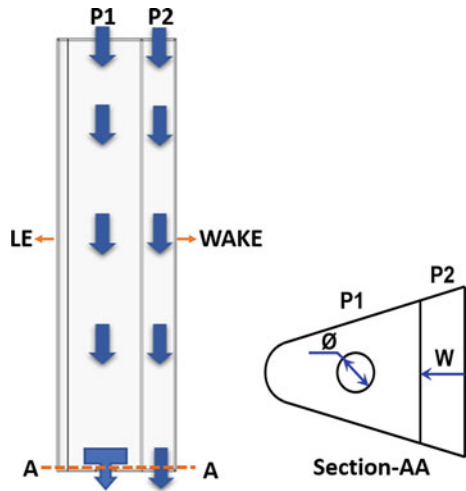
Simple convection cooling is employed for configuration-I. The cross section is divided into two passages P1 and P2 as shown in Fig. 3.

Bypass air enters passages P1 and P2 at the top. It exits into the core through the hole with diameter \varnothing at the end of the P1. In this configuration, the coolant flow exiting from the V-gutter can participate in the combustion since it is exited into the afterburner core. 1D flow network analysis is performed by developing a 1D code.

Following equations taken from Miller [10] and White [11] are used in the 1D flow network analysis of Configuration-I.

At the entry and exit of P1 and P2, there is a pressure drop due to area change which is estimated using

Fig. 3 Cooling configuration-I



$$\Delta P_{\text{area change}} = K_L \frac{\rho v^2}{2} \quad (5)$$

$$\text{Reynolds number, } Re = \frac{\rho v D_h}{\mu} \quad (6)$$

$$\text{Friction factor } f = 0.046 Re^{-0.2} \quad (7)$$

Pressure drop in the passages P1 and P2

$$\Delta P_{\text{passage}} = \frac{4fLv^2\rho}{2D_h} \quad (8)$$

$$Pr = 0.5424T^{0.042} \quad (9)$$

Dittus-Boelter correlation for Nusselt number,

$$Nu = 0.023Re^{0.8}Pr^{0.4} \quad (10)$$

V-gutter metal temperatures are estimated by heat balance of gas side loads and coolant side loads for LE, SW, and wake regions from 1D flow network. Gas side heat fluxes are estimated to obtain coolant temperature raise. 1D parametric study is carried out by varying exit hole diameter \emptyset of P1 and width W of P2 as shown in section-AA of Fig. 3.

4.2 Configuration-II

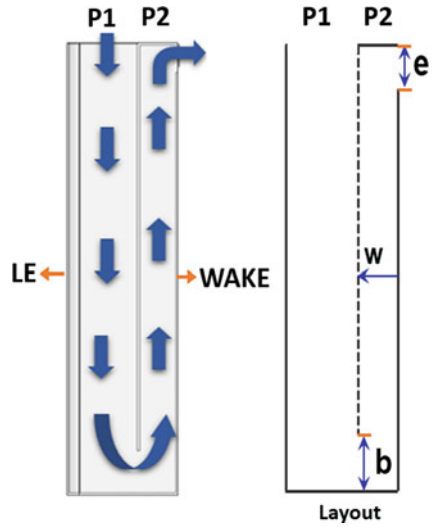
Convection cooling is adopted for second cooling configuration as shown in Fig. 4. Cross section is divided into two passages P1 and P2.

Bypass air enters through P1 at the top and is turned to flow through P2. The bypass air exits near the afterburner liner at the top of the P2. In this configuration, the coolant flow exiting from the V-gutter can act as coolant for the afterburner liner. 1D flow network analysis of Configuration-II is carried out using the Eqs. (5–10) and the following equation for pressure loss in the bend

$$\text{Pressure drop in bend [10], } \Delta P_{\text{bend}} = K_b \frac{\rho v^2}{2} \quad (11)$$

Coolant HTC in passages P1 and P2 is estimated. V-gutter metal temperatures and coolant temperature raise are estimated from 1D flow network. 1D parametric study is carried out by varying the width W of passage P2, exit dimension e, and 180° bend dimension b as shown in Fig. 4.

Fig. 4 Cooling configuration-II



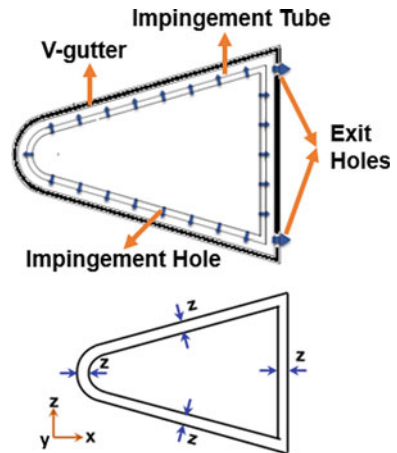
4.3 Configuration-III

Impingement cooling technique is adopted for third cooling configuration as shown in Fig. 5. An impingement tube with impingement holes is designed inside the V-gutter.

Bypass air enters the impingement tube, comes out through impingement holes and hits on the V-gutter surfaces, and then leaves through two rows of exit holes placed in the wake of the V-gutter.

1D analysis is carried out by assuming constant coolant pressure in the impingement tube. Cross flow effects in spanwise direction along the length of the tube are neglected.

Fig. 5 Cross section view of cooling configuration-III



Pressure loss across an impingement hole is estimated using the correlation by Dabagh et al. [12]

$$\Delta P_{\text{impingement hole}} = \frac{1}{2} K_{\text{imp}} \rho v^2 \quad (12)$$

where K_{imp} —impingement pressure loss coefficient,

$$K_{\text{imp}} = 0.97 + 0.465 M^2, \text{ M-Mach number} \quad (13)$$

Pressure loss across the exit hole is estimated using

$$\Delta P_{\text{hole}} = \frac{1}{2\rho} \left[\frac{m}{C_d A_{\text{hole}}} \right]^2 \quad (14)$$

C_d —coefficient of discharge, A_{hole} —area of hole, m^2 .

Impingement HTC in the LE region is estimated using correlation by Chupp et al. [13].

$$\text{Nu} = 0.44 \text{Re}^{0.7} \left(\frac{d}{C} \right)^{0.8} \exp \left(-0.85 \left(\frac{z}{d} \right) \left(\frac{d}{C} \right) \left(\frac{d}{D_i} \right)^{0.4} \right) \quad (15)$$

Impingement HTC on SW and wake region is estimated using correlation by Florschuetz et al. [14]. Effect of cross flow from the upstream impingement holes is considered whilst estimating HTC.

$$\frac{\text{Nu}}{\text{Nu}_1} = 1 - 0.596 \left(\frac{x}{d} \right)^{-0.103} \left(\frac{y}{d} \right)^{-0.38} \left(\frac{z}{d} \right)^{0.803} \left(\frac{G_c}{G_j} \right)^{0.561} \quad (16)$$

where Nu_1 is the Nusselt number without cross flow

$$\text{Nu}_1 = 0.363 \left(\frac{x}{d} \right)^{-0.554} \left(\frac{y}{d} \right)^{-0.422} \left(\frac{z}{d} \right)^{0.068} \text{Re}^{0.727} \text{Pr}^{\frac{1}{3}} \quad (17)$$

1D parametric study is carried out by varying spanwise pitch C and y , chordwise pitch x , impingement distance z , impingement hole diameter d , and exit hole diameter.

5 Results and Discussion of 1D Analysis

Configuration-I

1D parametric analysis is carried out by varying the \varnothing from 5 to 20 mm, W from 1 to 15 mm. Coolant mass flow through P1 increases with the \varnothing . Coolant mass flow through P2 increases with W.

The variation of coolant HTC in P1 with \varnothing and W is shown in Fig. 6.

In passage P1, as the \varnothing increases, coolant HTC increases due to increased coolant mass flow. This effect is higher at the higher values of \varnothing .

As W increases, the flow area of P1 decreases. Coolant HTC in P1 increases with increase in W because of the decreased P1 flow area and increased flow velocity. This effect is very less for $W \leq 2.5$ mm, and it is clearly observed at higher values of W. The coolant HTC with \varnothing of 10 mm is sufficient to cater the cooling in P1.

Variation in coolant HTC in P2 with W is shown in Fig. 7.

Initially as W increases, coolant HTC in P2 increases, reaches maximum at W of 2.5 mm, and then decreases with further increase in W. This is because, effect of increased mass flow rate on HTC is dominant up to W of 2.5 mm, and the effect of increase in the hydraulic diameter on HTC is dominant for the W values higher than 2.5 mm.

The dimension of W is finalised with 2.5 mm from Fig. 7.

Configuration-II

1D parametric analysis is carried out by varying W from 2.5 mm to 16 mm, e from 1 to 13 mm, and b from 3 to 25 mm. Exit area is maintained minimum and is the controlling area in this configuration. Upstream coolant flow area is maintained higher than that of the downstream flow area.

Fig. 6 Variation of coolant HTC in passage P1 with \varnothing and W in configuration-I

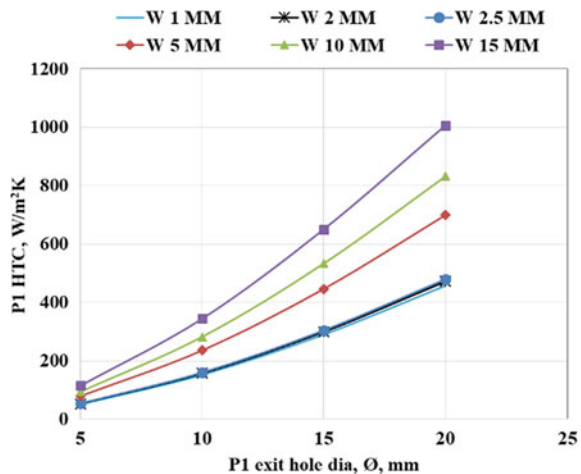
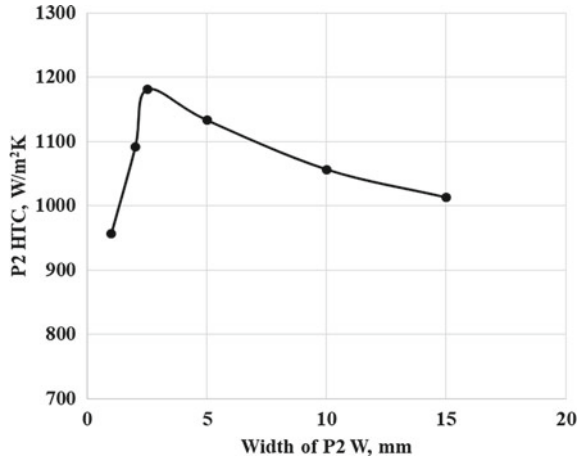


Fig. 7 Variation of coolant HTC in P2 with W in configuration-I



Variation of coolant HTC in P1 and P2 with W for $b = 20$ mm, $e = 5$ mm is plotted in Fig. 8.

With increase of W, the coolant flow area decreases and HTC increases in passage P1. Coolant side HTC in P2 decreases with increase of W due to increased flow area and decrease of flow velocity. For providing sufficient HTC in both P1 and P2, W of 15 mm is finalised.

Mass flow through passages P1 and P2 mainly depends on the e . As e increases, coolant mass flow increases.

Variation of coolant HTC in P1 and P2 with ‘ e ’ for $b = 20$ mm, $W = 15$ mm is plotted in Fig. 9.

As e increases, coolant HTC increases in both P1 and P2 due to the increase of coolant mass flow. At values of ‘ e ’ greater than 13 mm, exit area no longer remains

Fig. 8 Variation of coolant HTC in P1 and P2 with ‘W’ in configuration-II

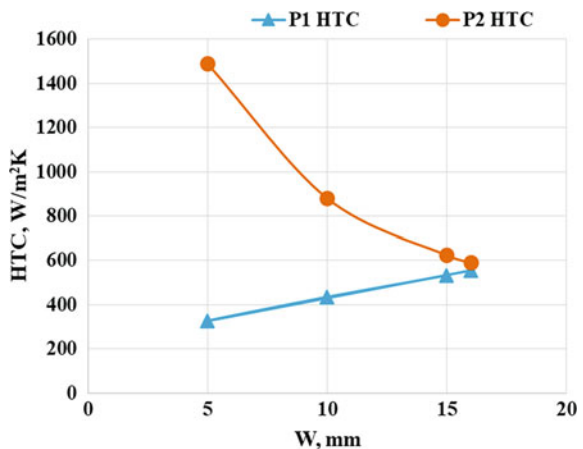
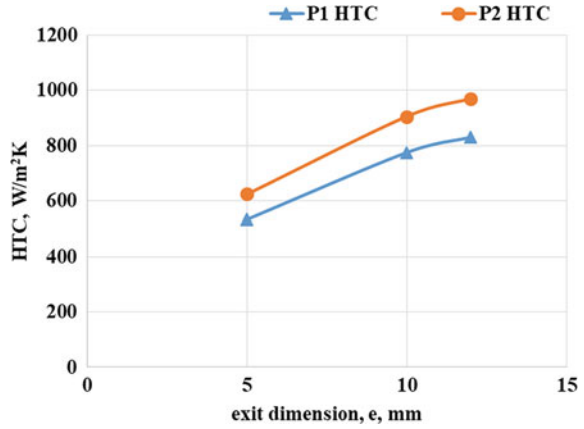


Fig. 9 Variation of coolant HTC in P1 and P2 with 'e' in configuration-II



the controlling area. The dimension of *e* is finalised as 13 mm, as it provides the sufficient coolant HTC in P1 and P2.

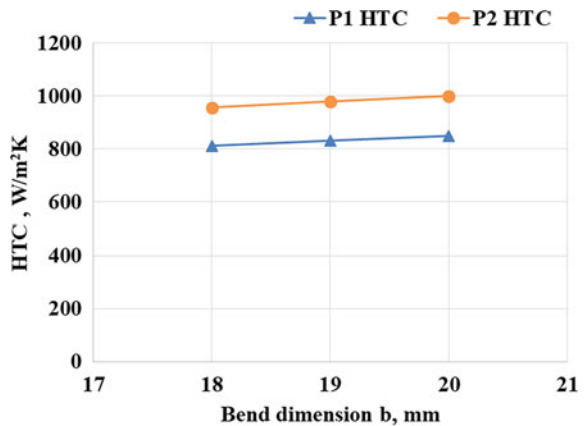
Variation of coolant HTC in P1 and P2 with *b* for *W* = 15 mm, *e* = 13 mm is plotted in Fig. 10.

Coolant HTC increases slightly with increase in *b* due to less pressure loss for higher bend dimension. Increasing the *b* further increases the bend area higher than that of P1 area which is not intended. The dimension of *b* is finalised with 20 mm for the configuration.

Configuration-III

1D parametric analysis is carried out for two impingement hole diameter *d* of 0.5 mm and 1 mm. *C/d* ratio is varied from 4 to 16 for the analysis of LE region. $\frac{x}{d}$ is varied from 5 to 10, and $\frac{y}{d}$ is varied from 4 to 8 for the analysis of SW and wake region. $\frac{z}{d}$

Fig. 10 Variation of coolant HTC in P1 and P2 with 'b' in configuration-II



is varied from 1 to 3 for LE, SW, and wake regions, exit hole diameter of 1 mm and 1.5 mm are analysed.

Geometrical parameters are chosen such that higher coolant HTC is achieved with lesser coolant mass flow. Finalised geometrical parameters from 1D parametric analysis for the configuration-III are $d = 0.5 \text{ mm}$, $\frac{x}{d} = 10$, $\frac{y}{d}$ or $\frac{C}{d} = 8$, $\frac{Z}{d} = 3$, and exit hole diameter = 1.5 mm.

Metal temperatures of the cooled V-gutter in all the three configurations were observed to be higher than the allowable limits. To reduce the heat flux coming onto the V-gutter and reduce the metal temperatures, TBC of 1 mm thickness is considered. 1D analysis is carried out, from the heat balance, it showed a reduction in metal temperature of 200 K in the wake region and of 100 K in the LE and SW regions with TBC. The geometries finalised from 1D analysis are taken to carry out CHT analysis.

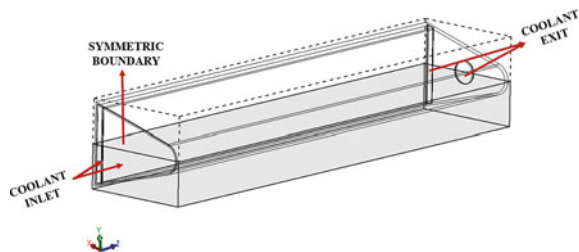
6 Numerical Method of Solution

3D CHT analysis is carried out using FloEFD Ver19, a commercial computational fluid dynamics software. 3D steady and compressible Navier–Stokes equations along with $k-\epsilon$ turbulence model are solved. FloEFD approximates spatial derivatives with implicit difference operators of second-order accuracy. The convergence criteria specified for goals of the analysis are $1 \times 10^{-3} \text{ kg/s}$ for mass flow rate, 1 Pa for fluid pressure, 1 K for averaged fluid temperatures, and 1 K for average wall temperatures. HP Z840 workstation with 44 quad core parallel processors and 128 GB RAM is used for carrying out the analysis.

7 Computational Domain

All the three configurations have geometrical symmetry and thermal symmetry (heat loads) about the centre plane of the V-gutter (parallel to XZ plane). Hence, symmetry boundary condition is applied as shown in Fig. 11 to reduce the mesh size.

Fig. 11 Computational domain of configuration-I with the symmetry boundary



The computational domain considered for the Configuration-1 is shown in as shaded portion as shown in Fig. 11. The accuracy of CHT results depends on the mesh near the boundary layer to capture the heat transfer effects. Finer mesh is generated near the solid–fluid interfaces where boundary layer is likely to be observed, and coarser mesh is generated in the fluid domain. FloEFD software is used to create geometric models (FloEFD has in-built SolidWorks interface) and generate mesh and for carrying out the analysis. FloEFD generates the Cartesian mesh (structured) and convergence of results is faster, so is found to be effective during the design phase of cooling configurations.

Basic mesh is generated with moderate mesh refinement. Mesh near the boundaries is refined by increasing the ‘level of basic mesh refinement’ in the ‘local mesh’ of solid–fluid interfaces. Refinement is a process of splitting a rectangular mesh cell into eight cells by three orthogonal planes that divide the cell’s edges in halves. An n -th level cell is 8^n times smaller in volume than the basic cell. TBC and V-gutter walls are also meshed to account for the conduction heat transfer.

Figure 12 shows the cross-sectional mesh of Configuration-I in computational domain refined to capture the boundary layers near the solid–fluid interfaces.

Boundary conditions applied for Configuration-I are shown in Fig. 13. CHT analysis is carried out with the total pressure and temperature specified at coolant inlet and static pressure and temperature at coolant exit.

Fig. 12 Mesh in the V-gutter cross section of configuration-I

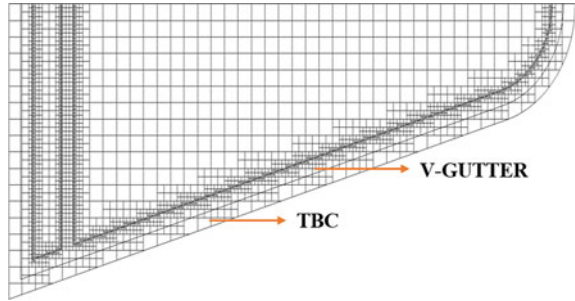


Fig. 13 Flow boundary conditions for CHT analysis—applied for configuration-I

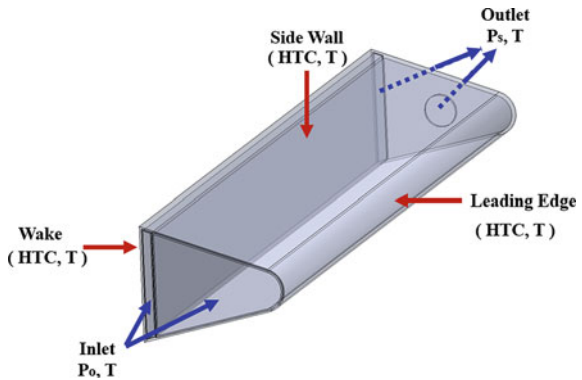
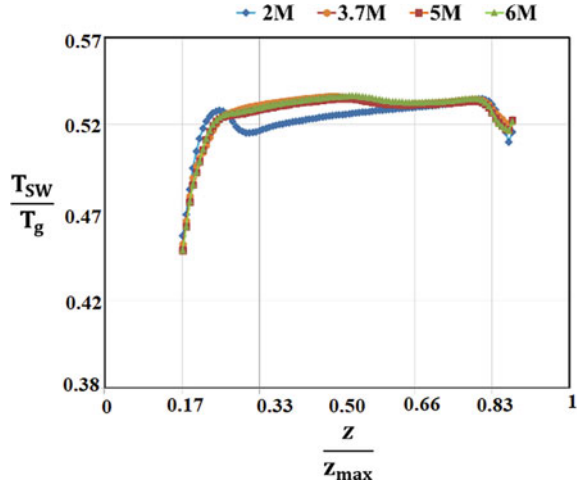


Fig. 14 Grid independence test for configuration-I



5% inlet turbulence intensity is considered for analysis. Outer wall boundary condition is applied for the gas side surfaces of LE, SW, and wake regions, with convective HTC and bulk gas temperature specified as shown in Fig. 13. CHT analysis is carried out until solution is converged for all the three configurations.

Grid independence test is carried out, and level of mesh refinement for solid–fluid interfaces is increased from 1st level to 4th level. Centre line temperature of the SW for the different meshes (M-million cells) of configuration-I is shown in Fig. 14. Metal temperatures in ratios of T_g are plotted with non-dimensionlised z values.

As the mesh size is increased beyond the 3.7 million for the Configuration-I, centre line SW temperature does not vary.

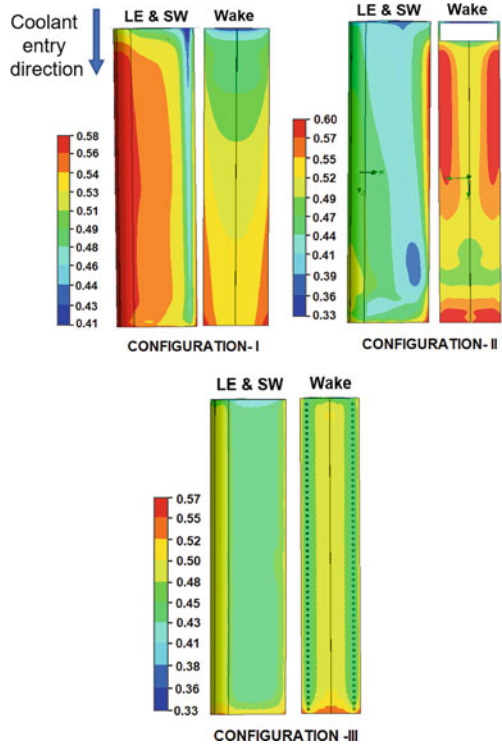
8 Results and Discussion of CHT Analysis

V-gutter metal temperature contours non-dimensionlised with core gas temperature T_g , for three configurations from CHT analysis are shown in Fig. 15.

Configuration-I has the maximum metal temperature of $0.58T_g$ at the LE region. The metal temperatures near the wake region are observed to increase gradually from inlet to the exit of the P2 due to coolant temperature rise. Locally, a low-temperature region is observed in the SW near the partition between P1 and P2 at the coolant entry. Coolant mass flow of 3.7% of bypass flow is utilised for Configuration-I.

Configuration-II has maximum metal temperature of $0.60T_g$ at wake region. There is a coolant temperature rise across P1 and P2 passage due to heat pickup. The coolant temperature at the end of P2 shows an increase of 100 K. This has resulted in showing maximum metal temperature at the wake region. Coolant mass flow requirement is 6.7% of bypass flow for Configuration-II.

Fig. 15 $\frac{T_m}{T_g}$ contours for three configurations



Configuration-III has maximum metal temperature of $0.57T_g$ at the wake region towards the bottom core side of V-gutter. Uniform metal temperature distribution is observed for this configuration. The coolant mass requirement is 3.1% of bypass flow.

Maximum metal temperatures in multiples of T_g and percentage coolant mass flow requirement for three configurations are in shown in Table 2.

Table 2 Coolant mass flow requirement and maximum metal temperature for three configurations

Configuration	% Coolant mass flow requirement	Max metal temperature
I	3.7	$0.58T_g$
II	6.2	$0.60T_g$
III	3.1	$0.57T_g$

9 Conclusions

1D flow network analysis is carried out to arrive at the geometries for all the three cooling configurations. CHT analysis shows the maximum metal temperature is lowest for Configuration-III with lowest coolant mass flow requirement with uniform temperature distribution compared to other two configurations. TBC has reduced the metal temperatures by a maximum value of 200 K.

Acknowledgements Thanks are due to the members of Heat Transfer Group for their help during this design work. Authors wish to thank to Shri M.Z. Siddique, DS&Director, GTRE for granting the permission to publish the work.

References

1. Wadia AR, James FD (2000) F110-GE-129 EFE—enhanced power through low risk derivative technology. In: Proceedings of ASME TURBOEXPO 2000 May 8–11, 2000, Munich, Germany
2. Lindblad K, Anderson L, Heligren A (2003) Development of cooled radial flame holder for F404/RM12 Afterburner, PartII, cooling, ignition and combustion ISABE 2003-1059
3. Schmidt H, Falk H, Backander P, Petterson B (2013) Development of a cooled radial flame holder for the F404/Rm12 Afterburner, Part-1 ISABE-2003-1058
4. Suresh B, Kishore Kumar S (2015) Temperature prediction and validation of v-gutter for an aero engine afterburner. *Int J Sci Eng Res* 6(11). ISSN 2229-5618
5. Suresh B, Kishore Kumar S (2017) Design of cooling configuration for V-gutter. *Int J Sci Technol Res*
6. Lowery GW, Vachon RI (1975) The effect of turbulence on heat transfer from heated cylinders. *Int J Heat Mass Transf* 18:1229–1242
7. Potter AE (1958) Effect of pressure and duct geometry on bluff-body flame stabilization. NACA TN 4381
8. Nakamura H, Igarashi T (2004) Variation of Nusselt No. with flow regimes behind a circular cylinder for Re from 7 to 30000. *Int J Heat Mass Transf* 47:5169–5173
9. Lefebvre AH, Herbert MV (1960) Heat-transfer processes in gas turbine combustion chambers. *Proc Inst Mech Eng* 174(12):463–473
10. Miller DS (2011) *Internal flow systems*, 2nd edn. Miller Innovations, UK
11. White FM (2001) *Fluid mechanics*, 4th edn. McGraw-Hill
12. Dabagh AA, Andrews G, Husain RA, Husain C, Nazari A, Wu J (1990) Impingement/effusion cooling: the influence of the number of impingement holes and pressure loss on the heat transfer coefficient. *J Turbomach* 112:467–476
13. Chupp RE, Helms HE, Mcfadden PW, Brown TR (1969) Evaluation of internal heat transfer coefficients for impingement cooled turbine airfoils. *J Aircraft* 6(3):203–208
14. Florschuetz LW, Truman CR, Metzger DE (1981) Streamwise flow and heat transfer distributions for jet array impingement with crossflow. *J Heat Transfer* 103:337–342

A Numerical Investigation on the Effect of Lip Geometry with Tangential Film Cooling on an Annular Combustor



Ananda Prasanna Revulagadda, Buchi Raju Adapa, Sangamesh C. Godi ,
Arvind Pattamatta, and C. Balaji 

Abstract The main objective of the present work is to study the effect of lip thickness and the lip cross section on the fluid flow behavior and effectiveness in tangential film cooling in a combustor liner. A three-dimensional jet exiting from a circular hole of diameter 2 mm is considered as coolant and the hot mainstream as a co-flow. The coolant and the mainstream are separated by a thick slab called the lip. A three-dimensional, steady-state numerical study is performed for different lip thicknesses (t) ranging from $0.25D$ to $2.5D$ and a blowing ratio of 0.5, 0.9, 1.5, and 2.5. Results are presented for a dimensionless stream-wise distance between 0 and 35. At all blowing ratios, a lip thickness of $0.25D$ (thin lip) performs better than the other lip thicknesses under consideration due to the attached flow. Additionally, it is observed that a change in the cross section (tapered) of the lip shows improvement in the film effectiveness, which may be attributed to the Coanda effect.

Keywords Film cooling · Gas turbine combustor · Coanda effect

Nomenclature

$$\text{BR} \quad \text{blowing ratio} = \frac{\text{mass flux of the coolant flow } (\rho_c U_c)}{\text{mass flux of the main flow } (\rho_h U_h)}$$
$$\text{DR} \quad \text{density ratio} = \frac{\rho_c}{\rho_h}$$

A. P. Revulagadda (✉) · B. R. Adapa · A. Pattamatta · C. Balaji
Department of Mechanical Engineering, Indian Institute of Technology Madras,
Chennai, 600036, India
e-mail: anand2chantiii@gmail.com

A. Pattamatta
e-mail: arvindp@iitm.ac.in

C. Balaji
e-mail: balaji@iitm.ac.in

S. C. Godi
Department of Mechanical Engineering, B.M.S. College of Engineering,
Bengaluru, Karnataka 560019, India
e-mail: sangameshcg.mech@bmsce.ac.in

© The Author(s), under exclusive license to Springer Nature Singapore Pte Ltd. 2023
G. Sivaramakrishna et al. (eds.), *Proceedings of the National Aerospace Propulsion
Conference*, Lecture Notes in Mechanical Engineering,
https://doi.org/10.1007/978-981-19-2378-4_30

D	diameter of the film cooling hole, m
S	slot height, m
t	time, s
T_C	coolant temperature, °C
T_h	mainstream temperature, °C
T_{aw}	adiabatic wall temperature, °C
u	stream-wise mean velocity, m/s
u'	fluctuating component of the jet velocity in the x direction, m/s
u_i	velocity tensor, m/s
U_c	mean velocity coolant at the hole exit, m/s
U_h	main stream velocity, m/s
U_{max}	local maximum velocity, m/s
VR	velocity ratio = $\frac{U_c}{U_h}$
X	distance along the stream-wise direction, m
X/S	dimensionless stream-wise distance
Y	normal distance from the wall surface, m
Y/S	dimensionless normal distance from the wall surface

Greek Alphabet

η	effectiveness
ρ	density

Subscripts

aw	adiabatic wall
b	base line geometry
c	coolant
h	main stream
i	initial
j	jet
m	modified geometry

1 Introduction

The combustion temperatures and pressures should be as high as possible to have higher thermal efficiency in the gas turbine. The heat convected from the combustion gases produces thermal stresses and creep, leading to lower life and failure of the combustor. A schematic of a typical annular combustor is shown in Fig. 1.

Combustion gases are typically at a temperature ranging from 1700–2400 K. The combustor liner metal cannot withstand such high temperatures for a prolonged period, and this reduces its life span. Additionally, even a small debris of the

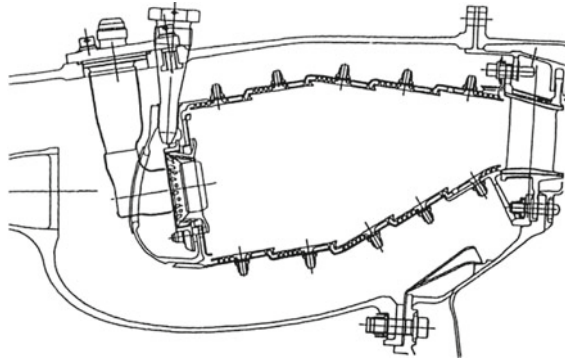


Fig. 1 Schematic of the cross section of an annular gas turbine combustor [4]

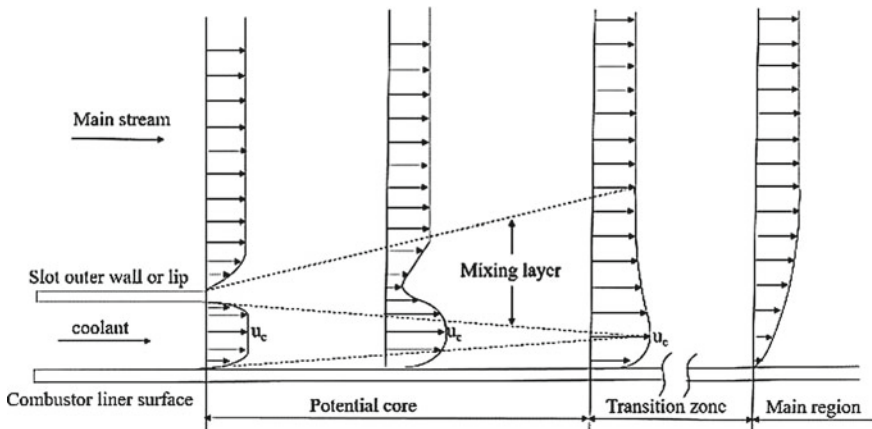


Fig. 2 Schematic of the film cooling

combustor can damage the whole turbine. Hence, cooling the metal surfaces is imperative. A few frequently used cooling techniques are ablation, transpiration, and film cooling. In ablation, a heat shield coating is coated on the surface. In char ablation, oxides such as carbon or silica are blazed to the combustor liner and are coated with char. This coating acts as a thermal barrier. In transpiration, the coolant air is fed into the surface, which is made up of porous material. Transpiration can provide efficient cooling. Even so, it is not widely used due to difficulties in manufacturing and also due to concerns involving the structural integrity of the combustor. In the last few decades; film cooling has played a significant role in cooling gas turbine components.

Figure 2 shows the schematic of the velocity distribution of the coolant and main-stream flow in film cooling. Here, a secondary fluid is introduced between the combustion gases and the combustor liner (i.e., introducing coolant into the boundary layer of the combustion gases). Since the secondary fluid is cooler and heavier than

the combustion gases, heat transfer to the liner from the hot gases will be reduced. The main objective of film cooling is to cool at the point of injection as well as in the region downstream of the injection. The injection of secondary air into the boundary layer increases the boundary layer thickness, which impedes the convection heat transfer.

Sturgess [14] considered film cooling optimization for minimum cooling airflow in aircraft gas-turbines. From experiments, it was identified that the potential core length would be maximum when the velocity ratio of the mainstream to the coolant is one. In the potential core of the film, the liner temperatures are under limiting conditions. Sivasegaram and Whitelaw [13] investigated the importance of slot lip thickness and injection angle. They identified that the effectiveness decreases if the slot thickness (t) to slot height (s) ratio increases beyond 0.25. With an increase in the injection angle, the effectiveness is reduced for a particular optimum blowing ratio. Nina and Whitelaw [7] studied the effectiveness of film cooling with three-dimensional slot geometries. They investigated the effect of open-area-ratio, slot lip thickness, and slot lip length for tangential holes configurations. The measurements demonstrated the requirement of the thin lip with long lip length and large open ratio. Practically, in regions with an insufficient supply of coolant through the tangential injection, augmentation can also be done by normal injection or splash cooling. They also investigated splash cooling and compared it with tangential film cooling. Experiments showed that tangential injection is better than splash cooling for the particular geometry considered. Rastogi and Whitelaw [10] investigated the effectiveness of three-dimensional film cooling slots. The coolant was injected tangentially through the slot, which is made up of discrete holes. They identified that the film cooling effectiveness is three-dimensional up to dimensionless stream-wise distance (X/S) of 30. The effects of blowing ratio and the density ratio were found to be similar to that of two-dimensional slots. Sturgess [15] analyzed the decay of film cooling effectiveness in the axial direction. This decay is because of the small and large-scale turbulent entrainment due to momentum exchange. Sturgess [15] concluded that practical geometry slots perform poorer than the ideal geometry with the same slot height and lip thickness. The performance degradation is due to the turbulence of the film generated at the metering ports of the slots, which have high-initial entrainments. The metering ports or injection holes cause non-uniformity of the film in the lateral direction. Sturgess [16] studied combustor cooling slots for high-film cooling effectiveness to design them for optimum performance. The prediction of film cooling effectiveness using developed phenomenological models for two-dimensional film cooling was not suitable for the actual combustor, as the flow is always three-dimensional. As in a three-dimensional flow, the average film cooling effectiveness depends on the circumferential uniformity of the film or lateral uniformity coming out of the slot. The geometrical mixing parameter for different slot designs was developed and examined with a view to differentiate good and poor film cooling slots. Mehendale and Han [6] conducted experiments to identify the effect of the mainstream Reynolds number on the film cooling effectiveness. Due to an increase in momentum with Reynolds number, the film cooling effectiveness was reduced. The effect of mainstream turbulence intensity was negligible at low-Reynolds numbers.

Li and Mongia [5] developed an improved method for the correlation of film cooling effectiveness of gas turbine combustor liners. They identified that the secondary air, which has low velocity, would be entrained into the mainstream at low-blowing ratios. A substantial portion of the lip edge is covered by secondary air (coolant). With an increase in the blowing ratio, the mainstream is entrained into secondary air at high velocity. Vortices at the lip edge were seen because of the sudden expansion. Silieti et al. [11] numerically investigated film cooling effectiveness for a single hole using conjugate and adiabatic wall boundary conditions. They observed significant differences between the adiabatic and the conjugate models. Further, they compared different turbulence models and concluded that the realizable $k-\epsilon$ model performs better. Pattamatta and Singh [8] investigated the applicability of various turbulence models in predicting heat transfer and flow characteristics of heated wall-jet flow and concluded that the realizable $k-\epsilon$ model with enhanced wall treatment shows the best agreement with experimental data as compared to other models. Singh et al. [12] explored the use of film heating as an analogy to film cooling. They concluded that, at a high-density ratio, film heating could not be considered an analogy to film cooling. Qu et al. [9] conducted investigations on film cooling effectiveness by a combined slot-effusion scheme. The drawbacks of film cooling far away from the slot and effusion cooling at its beginning stage are eliminated using this method. The combined cooling scheme was able to produce a better cooling effect with the same amount of coolant. Zhang et al. [18] conducted experimental investigations on the overall cooling effectiveness of t-type impinging film cooling. The effects of blowing ratio, jet to plate pitch, hole spacing, and hole diameter were investigated, and a better cooling performance was seen with an increase in the jet to the plate distance. At high-blowing ratios, a decrease of hole spacing leads to better cooling, and the hole diameter was observed to have little effect on the cooling performance. Kiyici et al. [3] investigated the effect of geometrical and the flow parameters on film cooling effectiveness and found that the effectiveness is high with a flat lip geometry compared to a lip with an angle.

From the above review of literature, it is seen that most of the previous studies on combustor liners are two-dimensional and are limited to impingement and crossflow situations. Therefore, in the present study, a detailed three-dimensional numerical investigation is conducted to investigate the effect of the lip thickness and a lip cross section (tapered) that creates a Coanda effect on the mainstream.

2 Problem Description

In combustor film cooling typically, the coolant is introduced into the mainstream boundary layer using a slot. The lip separates the mainstream and cold stream.

Figures 3a–c show a schematic of the combustor liner with tangential injection hole, the dimensions of the rectangular and the tapered lip configuration.

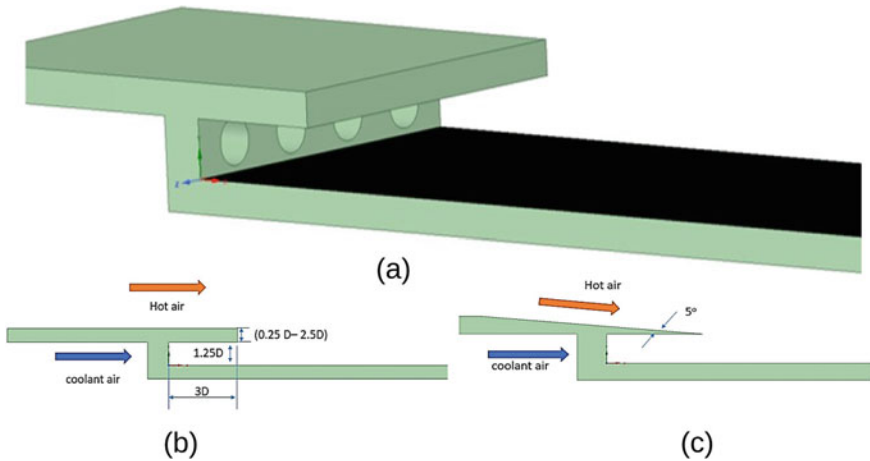


Fig. 3 Schematic of the **a** combustor liner under consideration, **b** rectangular lip, and **c** tapered lip

A parametric study is conducted to investigate the effect of lip thickness on film cooling effectiveness. The dimensionless lip thickness (t/D) values considered in this study are 0.25, 0.5, 1, 1.5, 2.5.

The tendency of the fluid to keep attached to the surface is called the Coanda effect. A Coanda effect is created to the mainstream by changing the cross section of the lip to a tapered arrangement. A numerical study is conducted to evaluate the Coanda effect with a tapered lip on the film cooling effectiveness by considering an taper angle of 5° . That is realizable engineering standpoint.

3 Numerical Methodology

Simulations are carried out to study the effect of lip thickness and lip cross section on the fluid flow and effectiveness in tangential film cooling in a combustor liner. The numerical studies help in a fuller exploration of the parameter space, which is otherwise difficult to accomplish through experiments that are expensive and time-consuming.

3.1 Mathematical Formulation

Finite volume-based ANSYS Fluent 19 [1] is used for solving the governing equations. The results obtained from the numerical investigations are compared with the results of Subbuswamy and Li [17] for the purpose of validation and are followed by detailed parametric studies.

3.2 Governing Equations

Three-dimensional steady, turbulent, incompressible flow, and heat transfer are considered. Air is the working fluid and is assumed to be incompressible. Thermo-physical properties of the air are constant, while viscous dissipation is considered. Body forces, natural convection, and radiation effects are all neglected.

The numerical study by Silieti et al. [11] reported that RKE-ewt can capture the flow and heat transfer characteristics compared to other available Reynolds averaged Navier Stokes (RANS) models. Hence, for the problem under consideration, the realizable $k-\epsilon$ model with enhanced wall treatment is used for modeling turbulence closure. The governing equations are expressed in the Cartesian coordinate system using an indicial form as follows.

Continuity equation:

$$\frac{\partial \bar{u}_i}{\partial x_i} = 0 \quad (1)$$

Momentum equation

$$\bar{u}_j \frac{\partial \bar{u}_i}{\partial x_j} = -\frac{1}{\rho} \frac{\partial \bar{P}}{\partial x_i} + \nu \frac{\partial^2 \bar{u}_i}{\partial x_j \partial x_j} + \frac{\partial (-\overline{u'_i u'_j})}{\partial x_j} \quad (2)$$

The energy equation

$$\bar{u}_i \frac{\partial \bar{T}}{\partial x_i} = \alpha \frac{\partial^2 \bar{T}}{\partial x_i \partial x_i} - \frac{\partial \overline{u'_i T'}}{\partial x_i} \quad (3)$$

The turbulent kinetic energy (k) and its dissipation rate (ϵ) are obtained by using transport equations as given in Pattamatta and Singh [8] and Godi et al. [2] when Reynolds stress ($-\overline{u'_i u'_j}$) is modeled by eddy viscosity two-equation model. More details of the values used for constants and equations in the turbulence model under consideration are given in ANSYS Fluent manual [1].

3.3 Computational Domain and Boundary Conditions

Figure 4 shows the computational domain for the combustor liner with a rectangular lip for a typical geometry. Details of numerical domain are $S = 1.25D$, $l = 3.5D$, $L = 60D$, $H = 20D$. The coolant stream and mainstream flows are given as uniform velocity inlet condition. The domain outlet is given as pressure outlet with zero-gage pressure. The two vertical surfaces are made to be periodic so as to simulate as a flow on a infinite flat plate in lateral direction and to capture jet to jet interactions. All the remaining walls are adiabatic with no slip condition. The main stream velocity is

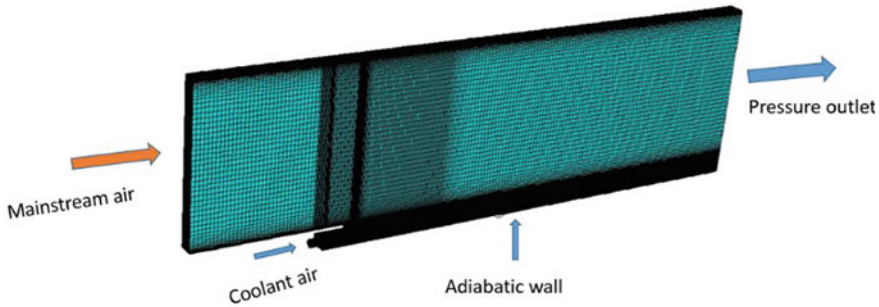


Fig. 4 Schematic of the computational domain employed in the current study

maintained at 25 m/s, and the turbulence intensity value of 2% is used for both main stream and the coolant. The temperature of the main stream is 60°C, and cold stream is 30°C, which gives a density ratio of 1.1.

3.4 Grid Generation and Grid Independence Study

Figure 5 shows a schematic of the grid mesh on the domain and at the inlet of two different configurations of the lip. The grids have been generated using the commercial software ANSYS ICEM CFD 19. 'O' type non-uniform grids are generated at the circular jet openings and non-uniform hexahedral grids on the other part of the computational domain [2]. The results of the grid independence studies are shown in Fig. 6. While discretizing, the number of nodes were increased from 0.5 million to 3.5 million. The effect of change in the centerline adiabatic effectiveness $\left(\eta_{aw} = \frac{T_h - T_{aw}}{T_h - T_c}\right)$ on the number of grids was examined in the axial direction by varying the grids in x , y , and z directions, and at the fluid inlet openings. It was observed that the solution became independent, or no significant change was seen in the centerline adiabatic effectiveness when the number of nodes changed from 1.5 million to 3.5 million. In view of the above, computational studies have been carried out for 1.5 million nodes. Further, in the case of turbulent flows with low-Reynolds number modeling to capture the near wall effect, the first cell height needs to be smaller than that of the thickness of the viscous sub-layer. For this, a non-dimensionalized near wall size called wall y -plus (y^+) is defined. For the simulations carried out in this study, $y^+ \approx 1$ has been maintained, which is highly desirable for near wall modeling [2].

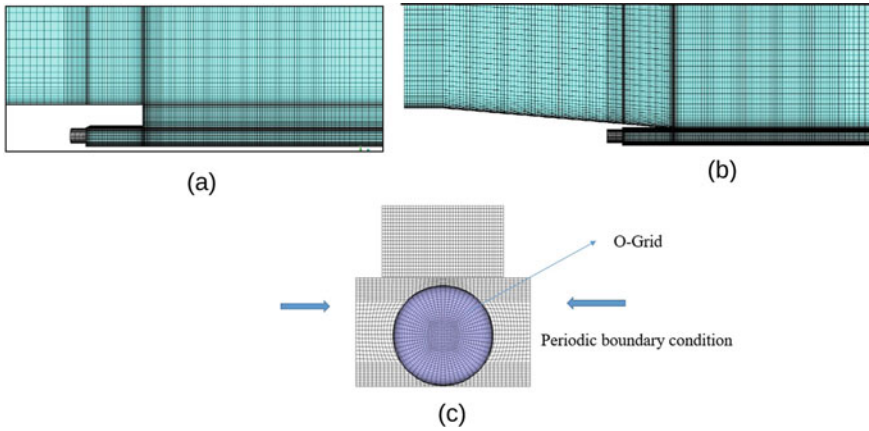
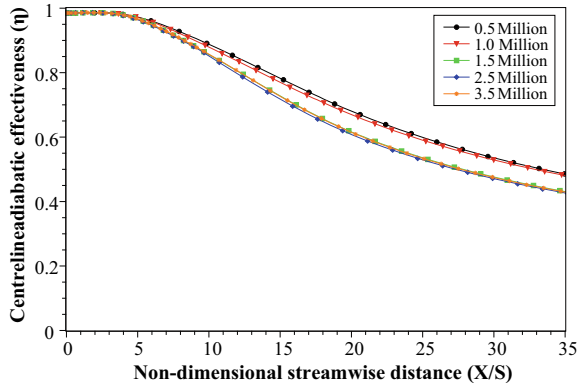


Fig. 5 Distribution of the grid for **a** rectangular lip configuration, **b** tapered lip configuration, and **c** at the cold jet inlet

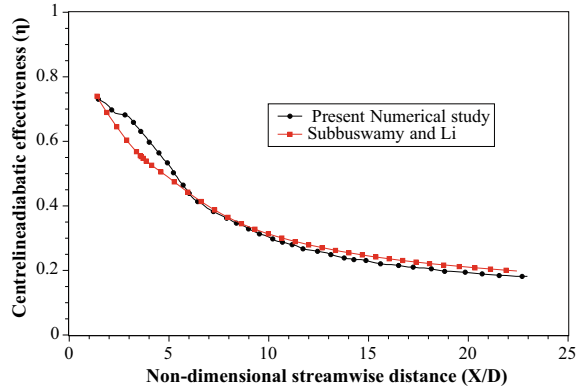
Fig. 6 Results of the grid independence study



3.5 Solution Procedure

The COUPLED scheme is used to handle the pressure-velocity coupling. The momentum and pressure-based continuity equations are solved together, making the convergence faster than other segregated solvers. This method is highly stable but at the same time, calls for massive computational resources. A second-order interpolation scheme is used for pressure. The second-order upwind scheme is used for the interpolation of velocity and temperature gradients and the turbulence equations. Further, absolute convergence criteria for the continuity equation are set to 10^{-5} , for momentum, energy, and turbulence quantities are set to 10^{-6} . Computations are carried out on the VIRGO cluster in high-performance computing Environment (HPCE) available at IIT Madras.

Fig. 7 Validation of the present study with Subbuswamy and Li [17]



3.6 Validation

The realizable $k-\epsilon$ with enhanced wall treatment model is used in this study to validate the numerical results of the present study against the results of Subbuswamy and Li [17]. The computational geometry has been suitably modified to facilitate the validation, and the results of this exercise the validation are presented in Fig. 7. Results are presented for a blowing ratio of 1.5 and a density ratio of 1.5. Both the mainstream and coolant flows are at a uniform velocity of 6 m/s resulting in a velocity ratio of 1. A very good agreement is observed between the results of Subbuswamy and Li [17] and the present numerical study and this seems as adequate validation of the numerical methodology along with the turbulence closure employed in the present study.

4 Results and Discussion

A parametric study is conducted to investigate the effect of lip thickness for $t/D = 0.25, 0.5, 1, 1.5, 2.5$ at blowing ratios (BR) = 0.5, 0.9, 1.5, 2.

4.1 Effect of Lip Thickness on the Effectiveness

Figures 8a–d show the stream lines and the velocity contours at different values of t/D and blowing ratios. For the problem under consideration in the present study, there is a systematic pattern of stream lines that can be seen for $t/D = 0.25, BR = 0.9$ (see Fig. 8a). However, a re-circulation zone 1 is created at the lip exit due to sudden expansion of mainstream (see Fig. 8b). An increase in re-circulation zone can also be seen with an increase in the lip thickness. Further, a re-circulation zone 2 is observed

in the stream-wise direction beyond $X/S = 5$. This second re-circulation zone can exist for higher lip thicknesses and for lower blowing ratios (see Fig. 8c). These re-circulation zones are the regions in the flow regime, where the pressure is low, due to which fluid from surroundings entertains into the flow and creates an unnecessary complex flow and enhancing mixing. Further, as the blowing ratio increases, the second re-circulation zones disappears due to high momentum of the coolant (see Fig. 8d). From the Fig. 8, it can be inferred that, because of re-circulation zone 1 and zone 2, the mixing of the hot and cold streams starts at the slot exit and beyond X/S

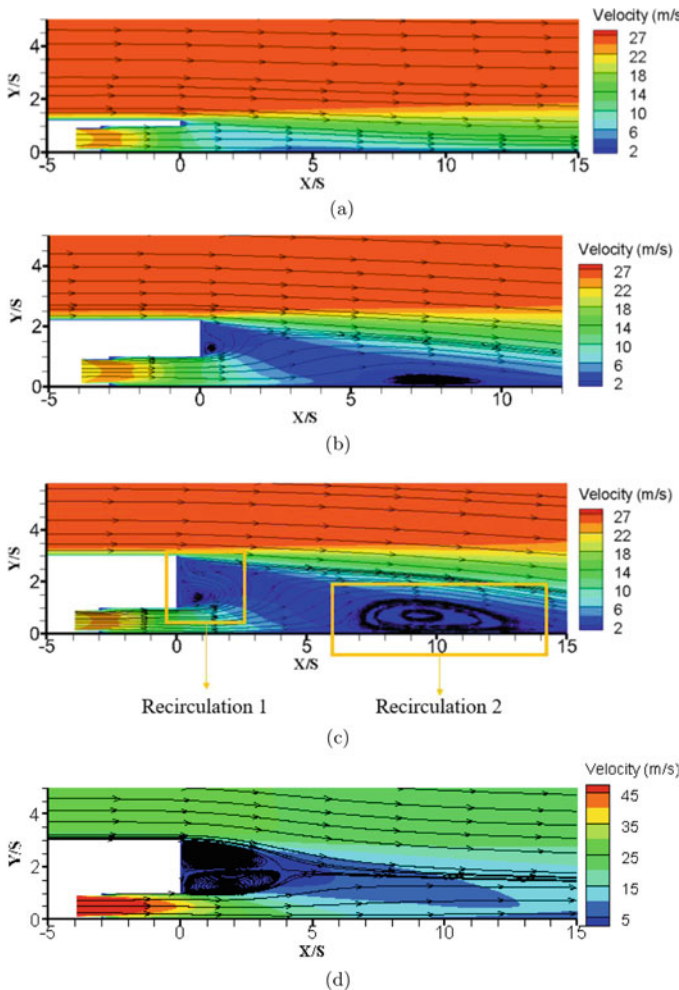


Fig. 8 Stream lines and velocity contours for **a** $t/D = 0.25$ **b** $t/D = 1.5$ **c** $t/D = 2.5$ at $BR = 0.9$ and at **d** $t/D = 2.5$ at $BR = 2$

= 5, respectively. Due to these re-circulation zones, there is an increase in the film temperature which results in lower film cooling effectiveness.

Figures 9a–d show the axial variation of effectiveness for various lip thickness at different values of blowing ratios. It can be observed that at low-blowing ratios of 0.5 and 0.9, the lip to diameter ratio (t/D) of 0.25 (thin lip) is performing better than the thick lip ($t/D > 0.25$) due to the elimination of separation of the flow. It is also observed that the effect of lip thickness on the effectiveness is more significant at the slot exit. Additionally, at high-blowing ratios, the thick lip performs better than that of the thin lip. This is attributed to the absence of intense mixing or no interactions between both the streams due to high momentum, which is due to shifting of the interaction between the coolant and the mainstream far from the slot exit in the mixing zone. In view of this, there is no second re-circulation zone is seen (see Fig. 8d).

4.2 Effect of Tapered Lip on the Effectiveness

To obtain a smooth interaction between coolant flow and the hot stream, the lip cross section has been changed from rectangular to trapezoidal, and this phenomenon is

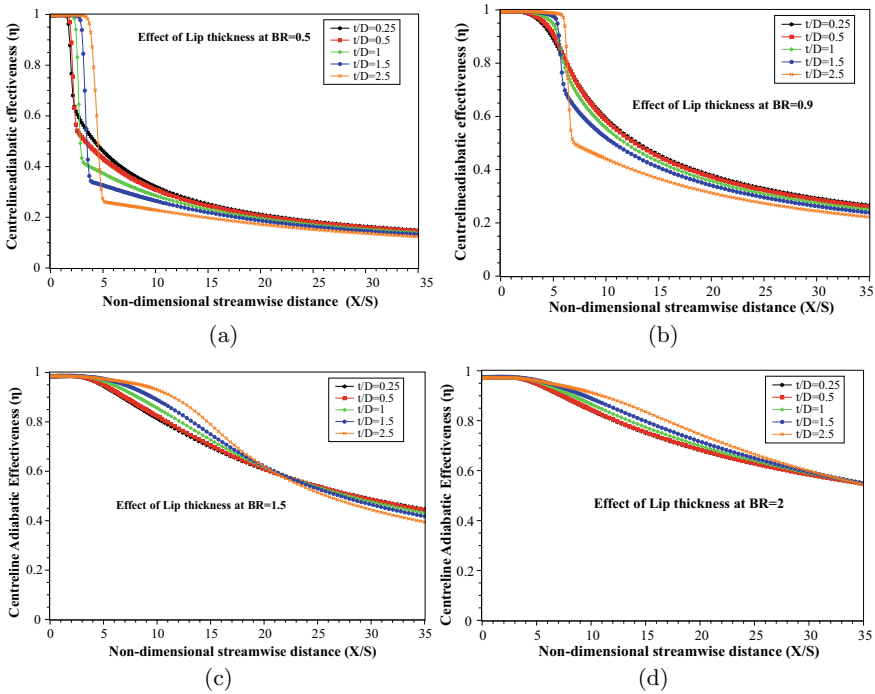
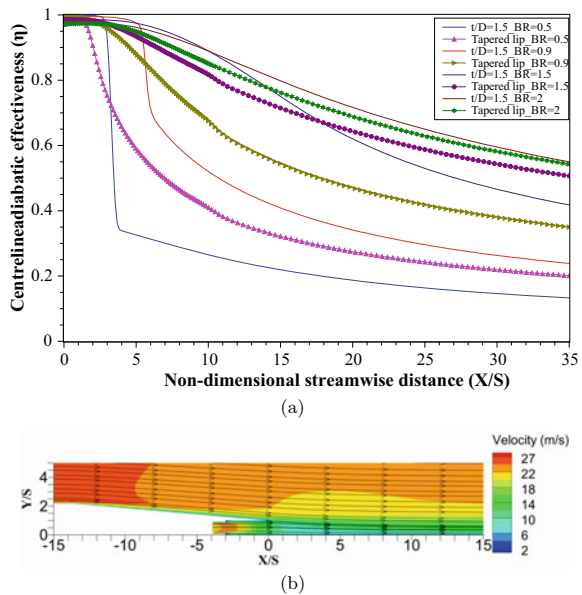


Fig. 9 Effect of lip thickness on the effectiveness at a BR = 0.5 b BR = 0.9 c BR = 1.5 d BR = 2

known as Coanda effect to the mainstream. A tapered or angled lip has been chosen, and its performance is compared with a rectangular lip having $t/D = 1.5$. From Fig. 10(a), it can be seen that angled lip shows better performance when compared with that of a rectangular lip at low-blowing ratios and it also observed that at a high-blowing ratio (BR) of 2, the tapered lip and rectangular lip show comparable performance. Figure 11 shows a comparison of the velocity profiles between flat and the tapered lips at $X/S = 15$ for a blowing ratio of 0.9. From the figure, it is observed that the velocity profiles of the tapered and flat lip are different due to the diverging of the mainstream stream lines in case of tapered lip (see Fig. 10b). This makes the coolant flow so as to attach to the surface without intense mixing. In view of this, with the tapered lip configuration, flow separation is eliminated, and the velocity difference between both the streams is reduced, thereby reducing the mixing of the coolant and the mainstream.

Figure 12 shows the relative effectiveness $\left(\frac{\eta_m}{\eta_b}\right)$ at different blowing ratios and by the location of the maximum enhancement. From this figure, it is seen that the effectiveness is improved to a maximum of 95, 45.5, and 21.5 % for blowing ratios (BR) of 0.5, 0.9, and 1.5, respectively. Further, a drop of 6.5 % in the relative effectiveness is seen at $X/S \sim 11$ and BR=2.

Fig. 10 Effect of taper lip on **a** effectiveness **b** streamlines and velocity contours



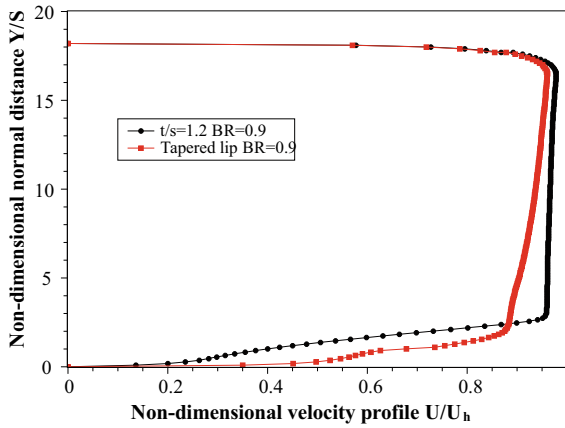


Fig. 11 Stream-wise component velocity profile of rectangular and tapered lip at $X/S = 15$ and $BR = 0.9$

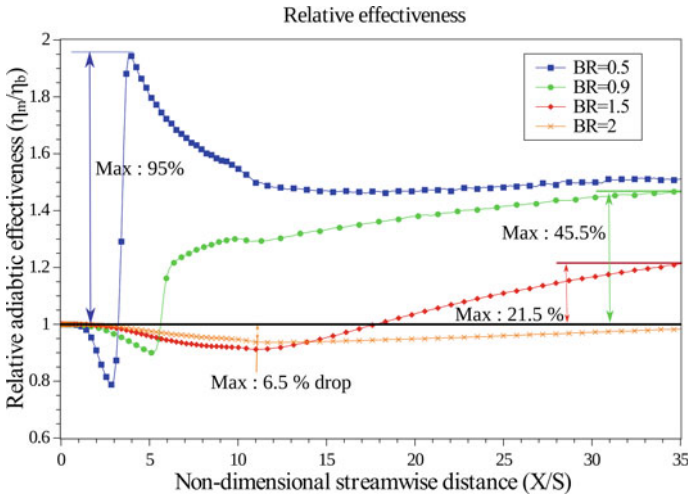


Fig. 12 Relative effectiveness at different blowing ratios

5 Conclusions

A three-dimensional numerical study based on RANS was conducted to investigate the effect of lip thickness and its cross section on the film effectiveness. The salient conclusions from this study are

1. Because of the reduced separation in the flow, at all blowing ratios, the overall performance of the thin lip is reasonably good.
2. At high-blowing ratios, a thick lip ($t/D = 2.5$) is having slight advantage over thin lip ($t/D = 0.25$) because of shifting the intense mixing away from the slot exit due to the high momentum of the streams.
3. The Coanda effect is introduced to mainstream by changing the cross section of the lip from rectangle to the taper. In view of this, there is an improvement of the effectiveness. At low-blowing ratios, there is a significant improvement in the film cooling effectiveness with the use of a tapered lip, and this effect reduces at higher blowing ratios.
4. The performance of the tapered lip is high at low-blowing ratios (between 0.5 and 1.5) and decreases with an increase in the blowing ratio.

Acknowledgements The support of high-performance computing center, IIT Madras is gratefully acknowledged. Financial assistance for this work was provided by the Gas Turbine Research Establishment (GTRE), Defense Research and Development Organization (DRDO), Government of India

References

1. ANSYS fluent: ANSYS fluent theory guide 15.0. ANSYS, Inc. Canonsburg, Pennsylvania, United States (2013)
2. Godi SC, Pattamatta A, Balaji C (2020) Heat transfer from a single and row of three dimensional wall jets—a combined experimental and numerical study. *Int J Heat Mass Transfer* 159:119801. <https://doi.org/10.1016/j.ijheatmasstransfer.2020.119801>
3. Kiyici F, Topal A, Hepkaya E, Inanli S (2018) Numerical investigation of gas turbine combustor liner film cooling slots. In: *Turbo expo: power for land, sea, and air*, vol 511104, p V05CT17A004. American Society of Mechanical Engineers
4. Lefebvre AH, Ballal DR (2010) *Gas turbine combustion: alternative fuels and emissions*. CRC Press
5. Li S, Mongia H (2001) An improved method for correlation of film-cooling effectiveness of gas turbine combustor liners. In: *37th joint propulsion conference and exhibit*, Salt Lake City, Utah, USA, p 3268. AIAA
6. Mehendale AB, Je-Chin H (1993) Reynolds number effect on leading edge film effectiveness and heat transfer coefficient. *Int J Heat Mass Transfer* 36(15):3723–3730
7. Nina M, Whitelaw JH (1971) The effectiveness of film cooling with three-dimensional slot geometries. *J Eng Gas Turbines Power* :425–430
8. Pattamatta A, Singh G (2012) Assessment of turbulence models in the prediction of flow field and thermal characteristics of wall jet. *Front Heat Mass Transfer (FHMT)* 3(2)
9. Qu L, Zhang J, Tan X (2017) Improvement on film cooling effectiveness by a combined slot-effusion scheme. *Appl Thermal Eng* 126:379–392
10. Rastogi A, Whitelaw J (1973) The effectiveness of three-dimensional film-cooling slots-i. measurements. *Int J Heat Mass Transfer* 16(9):1665–1672
11. Silieti M, Kassab AJ, Divo E (2009) Film cooling effectiveness: comparison of adiabatic and conjugate heat transfer CFD models. *Int J Thermal Sci* 48(12):2237–2248
12. Singh K, Premachandran B, Ravi M, Suresh B, Vasudev S (2016) Prediction of film cooling effectiveness over a flat plate from film heating studies. *Numerical Heat Transfer Part A: Appl* 69(5):529–544

13. Sivasegaram S, Whitelaw J (1969) Film cooling slots: the importance of lip thickness and injection angle. *J Mech Eng Sci* 11(1):22–27
14. Sturgess G (1968) Film cooling optimization for minimum cooling airflow in aircraft gas-turbines. In: *Combustion in advanced gas turbine systems*. Elsevier, pp 347–376
15. Sturgess G (1980) Account of film turbulence for predicting film cooling effectiveness in gas turbine combustors. *J Eng Gas Turbines Power* 102:524–534
16. Sturgess G (1986) Design of combustor cooling slots for high film effectiveness: Part i-film general development. *J Eng Gas Turbines Power* :354–360
17. Subbuswamy G, Li X (2008) Numerical study of film cooling enhancement in gas turbine combustor liner. In: *ASME international mechanical engineering congress and exposition*, Boston, Massachusetts, USA, vol 48715, pp 1237–1247
18. Zhang J, Yuan C, Ji P, Wei J, He X (2018) Experimental investigation on the overall cooling effectiveness of t-type impinging-film cooling. *Appl Thermal Eng* 128:595–603

Nanoboron Slurry Fuel Droplet Combustion for High-Particle Loading Ratio



Sunil Kumar Kumawat , Apurv Dilip Ghugare , Abhijeet Kumar ,
Srikrishna Sahu , and Ravikrishnan Vinu 

Abstract This paper investigates the influence of concentration of boron nano-particles on the combustion behavior of Jet A1-based slurry droplets especially for high-particle loadings. The nanofuel was prepared using commercially available boron nano-particles. The particle loading ratio (by weight) was varied from 2.5 to 50%. Shadowgraphic visualization of the burning droplet and direct flame imaging was carried out to examine the burning characteristics of horizontally suspended slurry droplet. While for particle loading up to 20%, the droplet combustion was dominated by vigorous oscillations and micro-explosions, beyond 20% loading, significant differences in the combustion behavior were observed which are discussed. The normalized surface area plot supported the observations and depicted clear departure from classical model for droplet burning.

Keywords Nano-particles · Combustion · Micro-explosion · Drop lifetime

1 Introduction

Since the last few decades, research on high-energy density fuels for various aerospace applications has led to the development of nanofuels that opens a promising future due to high reactivity, faster burning rate, high-calorific value, and reduction in ignition delay [1]. Nanofuels are liquid fuels with a stable suspension of nano-sized

S. K. Kumawat · A. Kumar (✉) · S. Sahu
Thermodynamics and Combustion Engineering Lab, Department of Mechanical Engineering,
I.I.T. Madras, Chennai 600036, India
e-mail: abhijeet.kr@alumni.iitm.ac.in

A. D. Ghugare · R. Vinu
Chemical Engineering Lab, Department of Chemical Engineering, I.I.T. Madras,
Chennai 600036, India

A. Kumar
Institut für Strömungstechnik und Thermodynamik (ISUT), Otto von Guericke Universität,
Magdeburg 39106, Germany

© The Author(s), under exclusive license to Springer Nature Singapore Pte Ltd. 2023
G. Sivaramakrishna et al. (eds.), *Proceedings of the National Aerospace Propulsion
Conference*, Lecture Notes in Mechanical Engineering,
https://doi.org/10.1007/978-981-19-2378-4_31

543

metallic or non-metallic particles (NP) such as Al, B, Fe, C, and CeO₂. Depending on the choice of NPs, the nanofuels exhibit different thermophysical properties such as thermal conductivity, mass diffusivity, surface tension, radiative property, and non-Newtonian viscosity, as compared to their respective base fuels. While higher loading of NPs in the base fuel is required to achieve the desired engine performance with the same capacity of the fuel tank, there are many challenges right from the synthesis of such slurry fuels, suspension stability, and transport, to issues related to the atomization of the slurry fuel, ignition, burning of the spray, emission, and presence of metallic oxides therein. Considering that combustion of the fuel droplets is one of the critical stages in the overall burning process, study of single nanofuel droplet combustion has attracted significant attention in the past as it provides a detail understanding of the fundamental process as well as a basis to develop models for spray combustion computation.

Tyagi et al. [2] observed that hot plate ignition probability of NP loaded diesel fuel was significantly higher than that of the base diesel fuel. Gan and Qiao [3] investigated the burning characteristics of fuel droplets containing micron- and nano-sized Al particles in suspension with ethanol and n-decane. The micro-explosion behavior of the micron-sized particle suspension occurred later than the nano-sized particle suspension with much stronger intensity for the same mass loading and surfactant concentration. Javed et al. [4] studied evaporation characteristic of n-heptane with varying concentrations of Al NPs at different ambient temperatures (100–600 °C) under atmospheric pressure and observed that nanofuel droplets vaporize in the same way as base fuel droplet and follow classical d^2 -law at all temperatures. They found that at lower temperature (100–300 °C), the evaporation rate of nanofuel, irrespective of the NP mass loading, is lower than that of pure heptane droplet. However, for higher ambient temperature (>400 °C), the evaporation rate of the nanofuel droplets is higher than that of the pure heptane droplet. Javed et al. [5] investigated the effects of high-ambient temperatures and various concentrations of Al NPs on the autoignition and combustion characteristics of heptane-based nano fluid droplets. It is observed that in contrast to the pure heptane droplets, the nanofuel droplets exhibited disruptive burning behavior at all temperatures (600–800 °C) and did not obey the classical d^2 -law. The NP was ejected from the droplets via micro-explosions that occurred early in droplet lifetime, was more intense at higher temperatures, and had larger NP concentrations. Because of these intense and frequent micro-explosions, almost no residue or agglomerated NPs remained on the fiber, and no distinct Al flame was observed. Ojha et al. [6] reported that the structure of the NP particle (whether amorphous or crystalline) has strong bearing on secondary droplet ejection and micro-explosions. Ojha et al. [7] studied slurry droplets of JP10 laden with sub-micron boron NP at 10% loading. Three different commercially available NP was tested, and considerable difference in burning characteristics was observed in spite of the same loading. Recently, Ojha and Karmakar [8] studied aluminum- and magnesium-decorated boron NP and Jet A1 slurry fuel. They found improved combustion characteristics for the above fuel in comparison with non-decorated boron and fuel slurry. Experiments were conducted up to 30% particle loading. Chandra et al. [9] conducted experimental study on burning on the burning characteristics of

Table 1 Particle loading ratios used in the earlier works in the literature and the current experiments

Authors	Base fuel	NP	Particle loading ratio
Gan and Qiao [3]	n-decane	Al	10%
Javed et al. [5]	n-heptane	Al	0.5, 2.5 and 5%
Ojha et al. [7]	JP10	B	10%
Chandra et al. [9]	JP10	B	2, 5, 7 and 10%
Ojha and Karmakar [8]	Jet A1	Al, Mg decorated B	10, 20 and 30%
Present study	Jet A1	B	2.5, 5, 10, 20, 30, 40 and 50%

JP10 fuel droplets for various particle mass loadings (2, 5, 7 and 10%). It was found that the burning of nanofuel shows oscillations and secondary droplet ejections due to bubble formation, growth, and merging. Table 1 summarizes the particle loading ratios used in various droplet burning experiments reported in the literature.

Several practical applications involving aero-propulsion systems necessitate very high-mass loading of NPs in order to meet the demand for the liberated thermal energy. Hence, more investigation is required for combustion of slurry fuels with high-mass loading ratio of the NP. Accordingly, the objective of the present paper is to study boron slurry droplet combustion for wide range of particle loading ratio from 2.5 up to 50%. The Jet A1 is used as the base fuel. All experiments are conducted under atmospheric conditions.

2 Experimental Methodology

Nanoboron and Its Characterization

Nanoboron used in droplet combustion studies was sourced commercially from Hongwu International, China. Based on high-resolution scanning electron microscopy equipped with energy dispersive spectroscopy (SEM-EDS), boron content in the sample was found to be ~88 wt.% with the rest being oxygen and magnesium. Figure 1 shows a typical SEM photograph. The nanoboron particles were irregular in shape and their particle size ranged between 50 and 400 nm. Based on powder X-ray diffraction analysis, nanoboron particles were predominantly amorphous in nature [10]. Few crystalline peaks could be attributed to the leftovers (NaCl, MgO, MgB₂) from the magnesiothermic reduction process. Ojha et al. [6] reported that amorphous boron powders exhibit better burning behavior, and crystallinity in the sample tends to dampen the combustion process. Amorphous nature of the sample is thus highly desirable. Pore size distribution analysis was also performed on the sample powders using the Barret-Joyner-Halenda (BJH) method, and the analysis revealed type-III curves accompanied by a H1-type hysteresis loop. Pore volume and specific surface area were found to be 0.07 cm³/g and 12 m²/g, respectively [10].

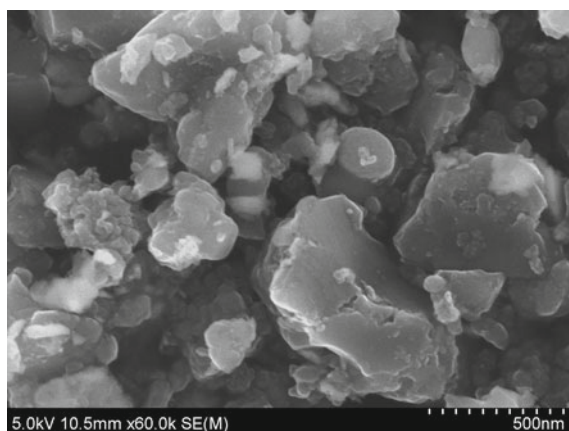


Fig. 1 SEM photograph of Boron NPs

2.1 Slurry Preparation and Its Stability

Slurry fuels of nanoboron in Jet A1 containing 2.5–50 wt.% of nanoboron were prepared. The general method of preparation of slurry fuels involves the addition of surfactants, viz., Span-80 and Tween-80, to Jet A1 fuel followed by complete homogenization. Boron nano-particles were then added, and the resulting slurry was ultrasonicated for 30 min in a bath type ultrasonicator. The temperature of the slurry was maintained at 25–30 °C. All the samples were periodically ultrasonicated, and also prior to droplet combustion experiments to prevent agglomeration of nanoboron particles. Further details regarding the preparation, characterization and stability of different nanoboron slurries are available in Ghugare et al. [10].

The surfactants imparted a certain degree of flowability to the nanoboron slurry as evident from Fig. 2. It was further observed that in the absence of surfactants the 50 wt.% nanoboron-Jet A1 sample behaved like a semi-solid lump, whereas with the addition of surfactants, the liquid like behavior of the slurry was pronounced.

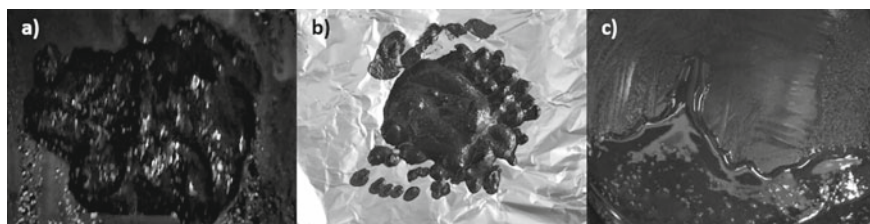


Fig. 2 Effect of addition of surfactants to 50 wt.% nanoboron in Jet A1 suspension. **a** No surfactant, **b** 0.5 wt.% each of Span-80 and Tween-80, **c** 1 wt.% each of Span-80 and Tween-80

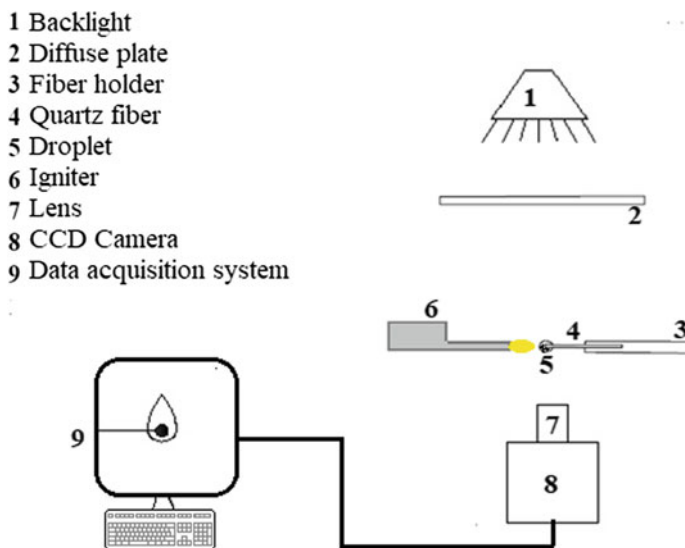


Fig. 3 Top view of experimental apparatus

2.2 Experimental Setup

The top view of the schematic diagram of the experimental apparatus is shown in Fig. 3. A quartz fiber of diameter 1 mm was chosen for depositing nanofuel droplet due to its low-thermal conductivity and inability to participate in combustion. A micro-pipette was used to suspend the nanofuel droplet (initial volume 8 μL) on a horizontal quartz fiber and was ignited using gas flame lighter under ambient conditions. The initial droplet size was about 2.4 mm. The droplet was back-illuminated with a strobe, and shadowgraphic visualization of the burning droplet was carried out using a CCD camera. In addition, direct flame photographs of the burning droplet were also captured using a digital camera.

2.3 Image Processing Procedure

The shadowgraph images were processed using in-house MATLAB-based image processing codes. As shown in Fig. 4, the grayscale images were first binarized using inbuilt function 'im2bw', which blackened the drop region. The area of the bright region outside the droplet in the image was identified using the inbuilt function 'regionprops', followed by subtraction of the obtained area of bright region in image from the total area captured by image. This provides the area of the dark region, which indicates the drop and fiber (as shown in Fig. 4b). In order to remove the projected area of fiber, the image consisting of fiber without drop was considered, followed by

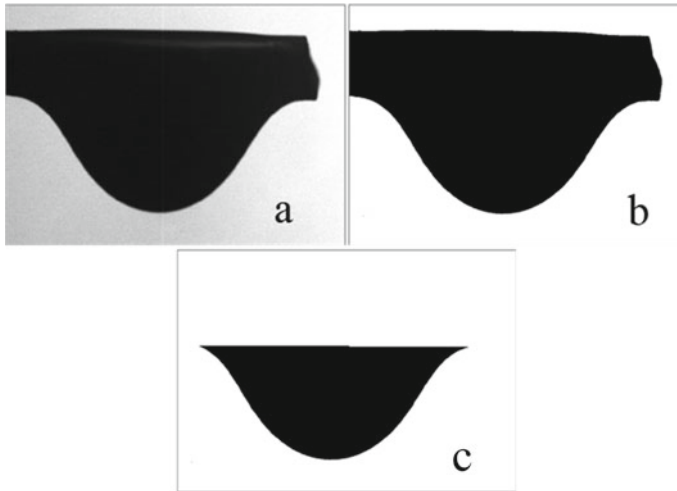


Fig. 4 a Raw image of the droplet, b binarized image, and c droplet image after filtering the fiber

identification of fiber area using the procedure mentioned above. Finally, the fiber area was subtracted from the drop+fiber area (as identified in Fig. 4b). This provides the projected area of the drop in the instantaneous image as shown in Fig. 4c. Then, a circle equivalent diameter of the droplet is calculated from the projected area of the droplet.

3 Results and Discussion

Figure 5a–g shows time sequence of the droplet flame photographs for the base fuel and the nanofuel for different mass loading ratios. In these images, the droplet itself is not always visible due to high-flame luminosity. The shadowgraph images shown in Fig. 6a–g overcome this issue as the liquid droplet and the residual of NP combustion are distinctly visible though the flame does not appear now. It is observed in Fig. 5a and 6a that the base fuel droplet burned steadily as evidenced by a consistent reduction in size of the droplet and the flame. For the nanofuel droplets with low to moderate mass loading of NPs (up to 20% loading), the combustion behavior can be divided into three stages. In the first stage, the nanofuel droplet burns similar to the base fuel. This is followed by the second stage, where the droplet undergoes volumetric expansion and contraction process due to vapor bubble formation as a result of liquid to vapor phase change in the vicinity of the preheated NPs. It is worthwhile to note that the thermal conductivity of boron is much higher than the base fuel due to which the particles are heated up much quickly than the liquid. This may be augmented by particle agglomeration, which increases with particle loading. As the bubbles swell, the droplet size appears to increase. The bubbles reach the droplet interface

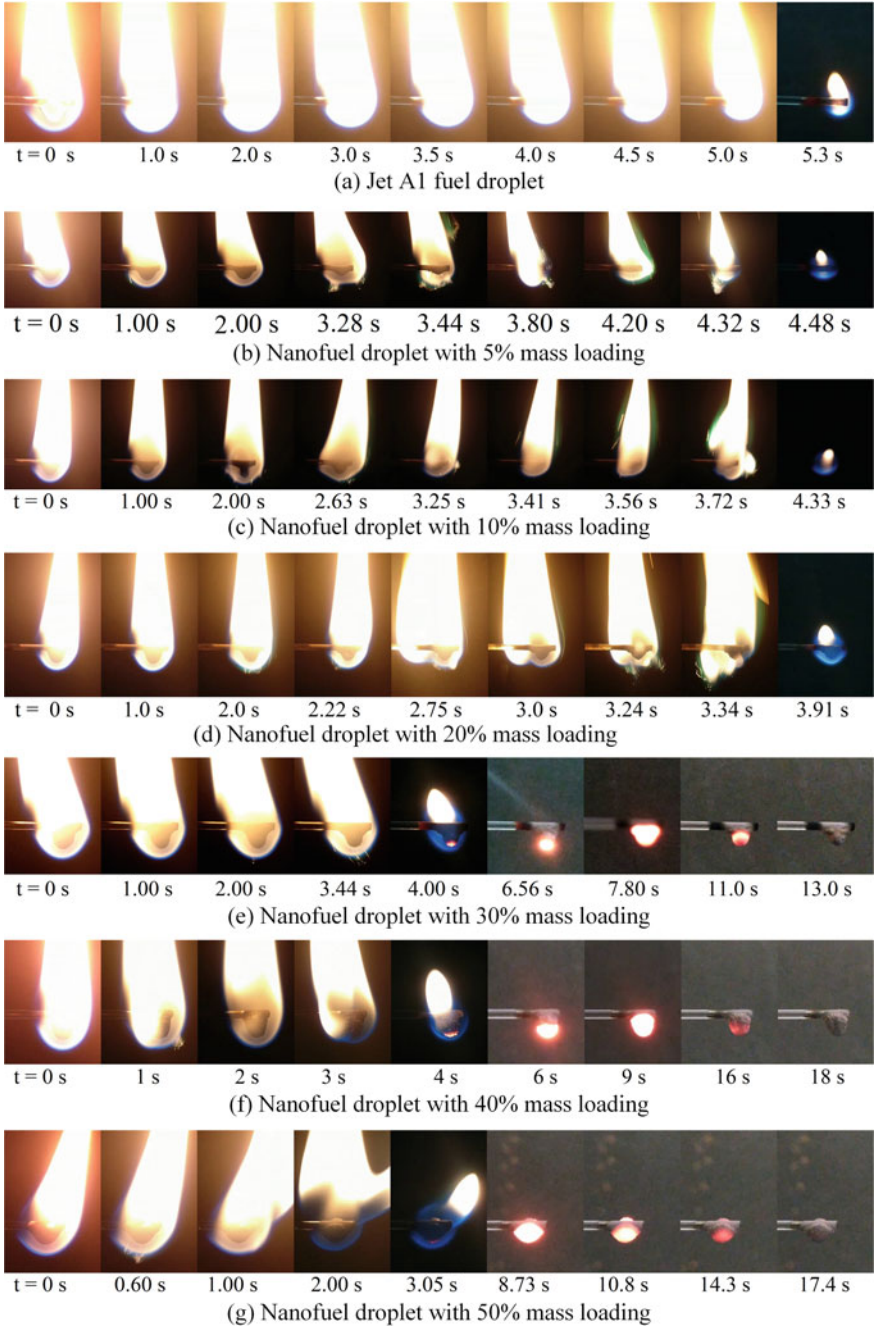


Fig. 5 Instantaneous images for burning of **a** pure Jet A1 droplet and nanofuel droplets with mass loading ratio of **b** 5%, **c** 10%, **d** 20%, **e** 30%, **f** 40% and **g** 50%

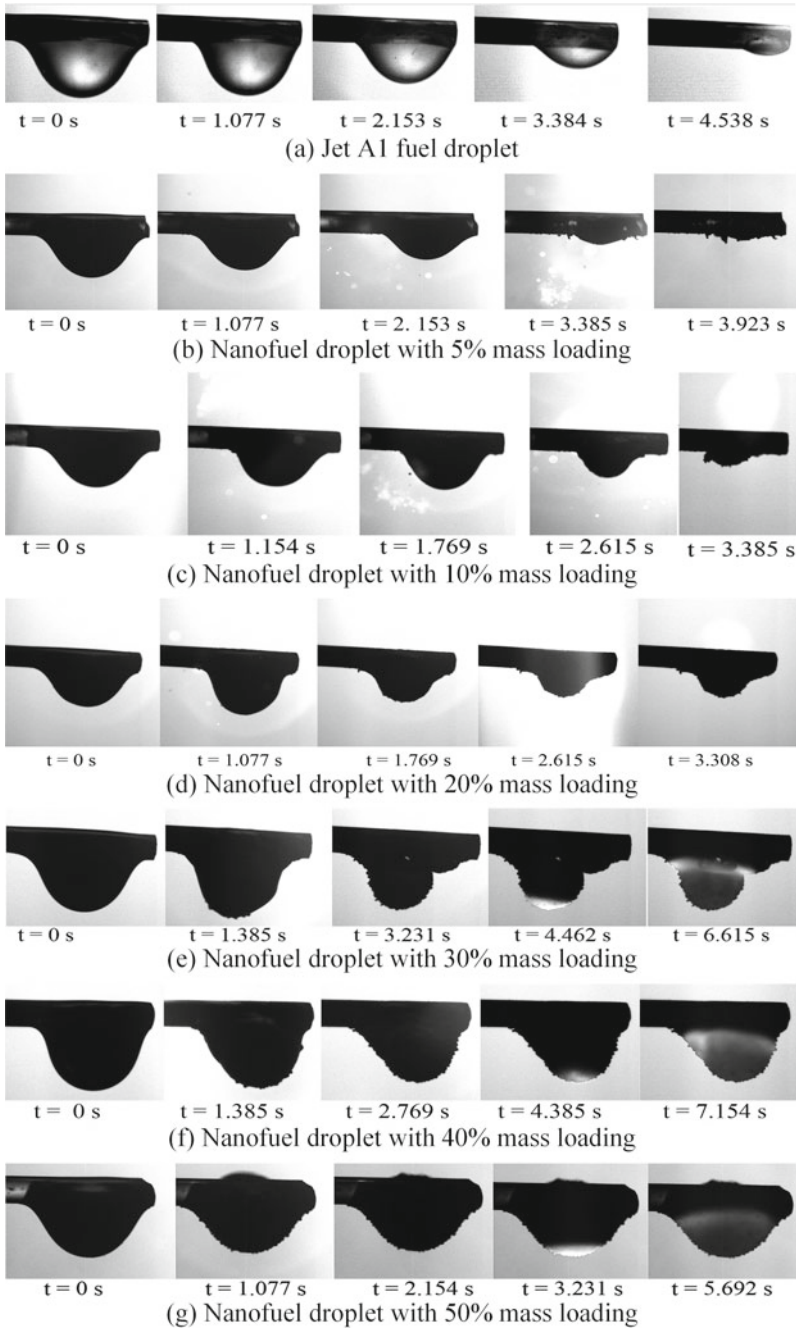


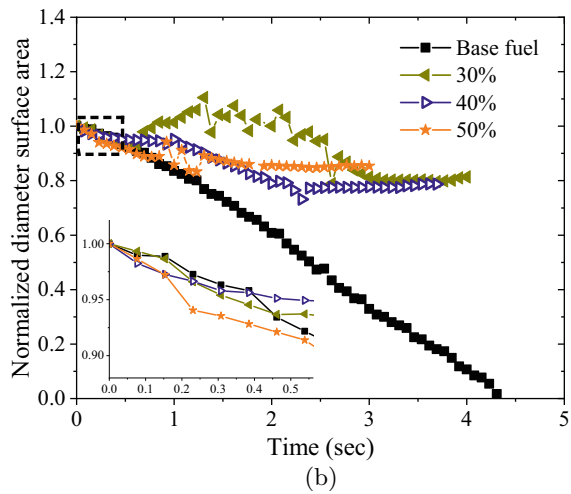
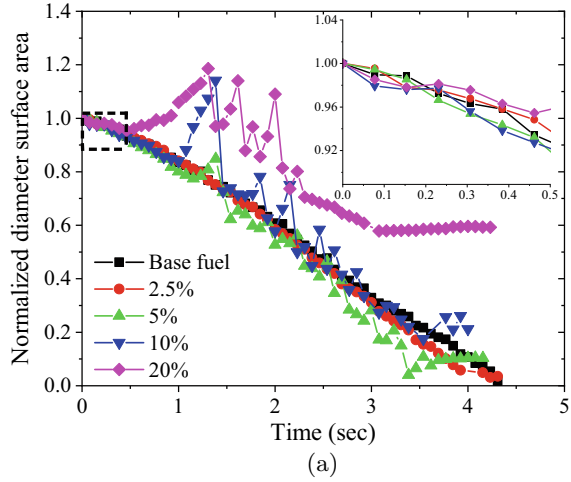
Fig. 6 Time sequence of instantaneous shadowgraph images of **a** pure Jet A1 droplet and nanofuel droplets with mass loading ratio of **b** 5%, **c** 10%, **d** 20%, **e** 30%, **f** 40%, and **g** 50%

and burst resulting in volume contraction and ejection of secondary droplets. This process continues for some duration leading to near harmonic variation of drop size. The ejected droplets may carry some NPs, and due to their small size and high temperature, burning time is small, while allows the boron NPs to oxidize to BO_2 . As shown in Fig. 5, a green envelope around the base diffusion flame is observed, which is attributed to the emission of BO_2 [9]. In spite of oscillations in droplet size, an overall size reduction continues to occur in the second stage. Although some NP burned simultaneously with the combusting liquid fuel, most particles agglomerate on the fiber when the loading is high. For loading below 20%, the agglomerated mass in the fiber is not significant. Hence, the flame appears till the droplet size is almost zero. However, for 20% loading, the size of the droplet does not appear to change after sometime. This refers to the third stage burning process, where no liquid is present. The liquid that remains within the particles, gasifies, and burns as it leaves the particle mass and mixes with the surrounding air. Hence, a premixed blue flame is observed in this stage. The flame extinguishes as soon as the liquid is exhausted.

Beyond particle loading of 20%, differences in the droplet burning behavior were observed as explained below. The initial smooth burning of droplet is observed similar to the above cases. However, interestingly, micro-explosions reduced significantly in the second stage. This is due to gasification of a significant fraction of the initial liquid in the initial steady burning phase. By the time, the NPs are heated up, the liquid content is reduced such that the probability of vapor entrapment is lower. For 30% loading, some bubble formation occurs resulting in expansion and contraction of the droplet. However, this effect reduces for 40 and 50% particle loading. For the above cases, the flame images show that the droplet flame continues to envelope the agglomerated particles (third stage), although, right after the flame extinguishes, a flame front appears to travel from the bottom side of the particle mass toward the fiber. Similarly, the shadow images indicate that during droplet burning, the particles begin to appear at the droplet interface near its bottom part, and then more particles are observed toward the upper part of the droplet. Then, only particles that stick to the fiber remain. As mentioned above, the flame then propagates through the agglomerated particle mass. The above observations are unique to higher particle mass loading cases and are not observed for loading below 30%. In these cases, no evidence of boron NP burning, i.e., presence of green flame could be identified. These observations highlight that as the particle loading ratio of nanofuels is increased, the residence time of the fuel droplets in the combustion zone should be longer to ensure particle reaction and heat release.

In order to compare nanofuel droplet burning with the classical d^2 -law model of droplet combustion, the temporal variation of normalized surface area of the burning nanofuel drop for different particle loading ratios is plotted in Fig. 7. It can be observed that the plot for pure Jet A1 shows a near linear trend in spite of that being a multi-component fuel. Thus, the burning characteristics of pure fuel closely agree with the d^2 -law [11]. However, as the NP mass loading ratio is increased, a clear departure from d^2 -law is evident. As discussed earlier, the plot highlights the three stage burning process as described earlier. The first stage is similar to the pure fuel droplet burning. In the second stage, volumetric oscillation of the nanofuel droplet

Fig. 7 Temporal variation of normalized surface area of a burning nanofuel droplet for different NP loading ratio



causes local fluctuations of surface area as shown in Fig. 7a. The overall reduction of droplet surface area is still similar to d^2 -law. Nevertheless, beyond certain time the surface area does not change with time indicating the flame extinction, which represents the third stage burning. In this stage, the surface area does not change as is clearly observed for 20% particle loading. With further increase in NPs mass loading ratio, deviation from the curve for the pure fuel begins at a much earlier stage. However, as demonstrated earlier in the visualization images, the surface area fluctuations are observed to reduce beyond 30% loading. The third stage burning, characterized by invariance of particle surface area, is dominant for these cases. The above discussion emphasizes the need for an advanced model for nanofuel droplet burning that must take into account the difference in combustion characteristics for low- and high-particle loading.

4 Conclusions

The present work aims to study the effect of boron nano-particle concentration on the combustion behavior of nanofuel slurry droplets with Jet A1 as base fuel. The focus is especially on the influence of higher range of particle loading ratio beyond 20%. The nanofuel preparation method and the stability of particle suspension were described in detail. The droplet burning experiments were conducted under atmospheric conditions. The results demonstrate different mechanism of nanofuel droplet combustion (three stage burning process) as compared to the base fuel and also a clear departure from the classic d^2 -law. For NP loading up to 20%, the slurry droplet burning is characterized by vigorous droplet expansion/contraction accompanied by micro-explosions that lead to particle combustion and appearance of a green flame. In contrast, beyond 20% loading, droplet oscillations and micro-explosions tend to reduce. A large agglomeration of NPs occurs on the fiber such that following the droplet flame extinction, a flame propagates through the remaining particles. The present experimental results not only demonstrate different mechanisms of nanofuel droplet combustion for high-particle loading but also highlights the need for an advanced model to describe such behavior and also for numerical simulation of spray combustion.

Acknowledgements The authors would like to acknowledge the financial support from the Center of Propulsion Technology (CoPT), Govt. of India.

References

1. Ojha PK, Karmakar S (2018) Boron for liquid fuel engines-a review on synthesis, dispersion stability in liquid fuel, and combustion aspects. *Prog Aerospace Sci* 100:18–45
2. Tyagi H, Phelan PE, Prasher R, Peck R, Lee T, Pacheco JR, Arentzen P (2008) Increased hot-plate ignition probability for nanoparticle-laden diesel fuel. *Nano letters* 8(5):1410–1416
3. Gan Y, Qiao L (2011) Combustion characteristics of fuel droplets with addition of nano and micron-sized aluminum particles. *Combust Flame* 158(2):354–368
4. Javed I, Baek SW, Waheed K (2013) Evaporation characteristics of heptane droplets with the addition of aluminum nanoparticles at elevated temperatures. *Combust Flame* 160(1):170–183
5. Javed I, Baek SW, Waheed K (2015) Autoignition and combustion characteristics of heptane droplets with the addition of aluminium nanoparticles at elevated temperatures. *Combust Flame* 162(1):191–206
6. Ojha PK, Maji R, Karmakar S (2018) Effect of crystallinity on droplet regression and disruptive burning characteristics of nanofuel droplets containing amorphous and crystalline boron nanoparticles. *Combust and Flame* 188:412–427
7. Ojha PK, Prabhudeva P, Karmakar S, Maurya D, Sivaramakrishna G (2019) Combustion characteristics of jp-10 droplet loaded with sub-micron boron particles. *Exp Thermal Fluid Sci* 109:109900
8. Ojha PK, Karmakar S (2020) Combustion characteristics of jet a-1 droplet loaded with aluminum/magnesium-decorated boron particles. *Int J Energet Mater Chem Propuls* 19(3):253–274

9. Chandra E, Patel U, Vinu R, Sahu S (2019) Burning characteristics of boron/jp10 nanofuel droplets. In: Gas Turbine India Conference, vol 83532. American Society of Mechanical Engineers, p V002T04A019
10. Ghugare AD, Dhanalakshmi R, Vinu R (2020) Preparation and characterization of nanoboron for slurry fuel applications. *Adv Powder Technol* 31(5):1851–1867
11. Spalding DB (1951) Combustion of fuel particles. *Fuel* 30(1):121–130

Effect of Surface Temperature on Fuel Drop Splashing on Solid Surfaces



Akshay Sreenivasan and Sivakumar Deivandren

Abstract Interaction of hydrocarbon fuel drops with high-temperature substrates is commonly encountered in combustion chambers, and such dynamics are relevant in design and optimization of fuel spray systems. Dynamics of fuel drops impacting on a heated solid surface in the splashing regime is investigated through high-speed imaging experiments. The effect of surface temperature in altering the impacting drop morphology and quantitative trends in splashing is studied in detail. The variation of splash behavior of drops impacting at three distinct drop Weber number (We) at different surface temperatures (T_S) is considered. For a fixed We , an increase in the surface temperature causes a shift in the impact dynamics from splashing to spreading, which indicates higher threshold We at higher T_S . The dynamics of the ejected liquid sheet and the spreading lamella post-impact are analyzed from the high-speed images to quantify the observed transitions.

Keywords Drop splashing · Heated surface · Fuels

Nomenclature

C_G	Speed of sound in gas (m/s)
D_0	Initial diameter of impacting drop (mm)
g	Acceleration due to gravity (m/s^2)
H	Impact height of drops (mm)
H_t	Initial height of lamella (mm)
k_B	Boltzmann's constant ($kg\ m^2\ K^{-1}\ s^{-2}$)
K_l	Constant multiplying lubrication force term
K_u	Constant multiplying suction force term
Oh	Ohnesorge number
P	Ambient gas pressure (Pa)

A. Sreenivasan (✉) · S. Deivandren
Department of Aerospace Engineering, Indian Institute of Science, Bengaluru 560012, India
e-mail: akshays@iisc.ac.in

Re	Reynold's number
T	Temperature of gas phase ($^{\circ}C$)
T_S	Surface temperature ($^{\circ}C$)
$T_{S,tr}$	Transition surface temperature ($^{\circ}C$)
t	Time elapsed from the instant of impact (s)
$t_{e,cr}$	Dimensionless critical sheet ejection time
V	Drop impact velocity (m/s)
V_e	Expansion velocity of liquid lamella (m/s)
V_t	Initial velocity of liquid lamella (m/s)
We	Weber number

Greek Symbols

α	Re-contact factor
β	Splash threshold parameter
γ	Ratio of specific heats
μ	Dynamic viscosity of drop liquid (Pa s)
μ_G	Dynamic viscosity of gas (Pa s)
ν_L	Kinematic viscosity of drop liquid (m^2/s)
ρ	Density of drop liquid (kg/m^3)
ρ_G	Density of gas (kg/m^3)
σ	Surface tension of drop liquid (N/m)
Σ_G	Destabilizing stress exerted by gas (Pa)
Σ_L	Stabilizing stress of surface tension (Pa)

1 Introduction

Impact of liquid drops on solid surfaces has fascinated many researchers, owing to the complex fluid dynamics it entails. Factors such as the drop size, impact velocity, liquid properties, and the surface topology are known to influence the impact dynamics of drops and are often expressed in terms of the following dimensionless terms,

$$Re = \frac{\rho V D_0}{\mu}, \quad We = \frac{\rho V^2 D_0}{\sigma}, \quad Oh = \frac{\mu}{\sqrt{\rho \sigma D_0}} \quad (1)$$

Of the various impact outcomes during the drop impact process [1], splashing has been an area of active research. In addition to the factors listed above, the gas phase that surrounds the spreading lamella in splashing has a key role in deciding the splash outcome as well as the threshold velocity of splashing. It is observed that the gas in the vicinity of the ejected liquid sheet exerts aerodynamic forces, which

leads to the disintegration of the liquid sheet into a spray of secondary droplets. Xu et al. [2] studied the effect of the surrounding gas pressure on splash threshold and observed that a reduction in the ambient gas pressure leads to suppression of corona splashing. Several studies have been proposed since the work by Xu et al. [2] that discuss the interplay of factors such as liquid properties and surface characteristics with the observed pressure effect [3–5].

The analytical model proposed by Xu et al. [2] based on the destabilizing stress from the gas phase and the stabilizing stress from the interfacial tension may be expressed using the following relation,

$$\frac{\Sigma_G}{\Sigma_L} \approx P \sqrt{\frac{D_0 V}{RT}} \frac{\sqrt{v_L}}{\sigma} \quad (2)$$

A more holistic model for the splash threshold considering the properties of both the liquid as well as the ambient gas phases was proposed by Riboux and Gordillo [6]. In this model, the lift force imparted by the gas beneath the expanding liquid sheet imparts a vertical velocity and acts to destabilize the sheet thus causing splashing, while the interfacial tension tends to stabilize the system. A splash threshold parameter (β) is defined based on this model, to estimate the splash threshold velocity of liquid drops impacting on solid surfaces, and is given by [6],

$$\beta = \left(\frac{K_1 \mu_G V_t + K_u \rho_G V_t^2 H_t}{2\sigma} \right)^{1/2} \quad (3)$$

Drop impact on heated solid surfaces has been investigated extensively in literature, as it provides the baseline scenario for applications such as spray cooling and fuel spray impingement [7, 8]. Investigation of the impact dynamics of fuel drops on surfaces at high-temperature conditions helps refine the guidelines for design of effective atomizers and spray impingement systems in combustion chambers. Studies on heated surface impact of liquid drops mainly focus on the impact morphologies and their classification with respect to the hydrodynamics as well as surface temperature parameter.

In the present work, we consider the splashing impact of millimetric liquid drops on a heated solid surface, to study the effects of surface temperature (T_S) in altering the splash outcome, which is not reported in literature in detail. Staat et al. [9] studied the impact of ethanol on heated sapphire surface and identified four different impact regimes such as deposition, contact-splash, bounce, and film-splash on We - T_S phase space. Although Staat et. al. [9] modeled the deposition to contact-splash transition with respect to the surface temperature, a detailed description of the transition regime and the underlying mechanism is still lacking in literature. In the present study, we address these issues through investigation of liquid drop splashing on heated surfaces. We study the variation of the splash threshold velocity with surface temperature and qualitatively explain the transition observed in the splash outcome with change in the surface temperature, for impact at constant We .

2 Experimental Setup

Figure 1 shows a schematic of the experimental setup used in the current work. Millimetric drops of identical size are dispensed using the micrometer-syringe arrangement and fall freely onto the target surface kept below. The drop dispenser assembly is mounted on a vertical traverse that is used to vary the impact height and thereby, the impact velocity. The drop impact dynamics are captured using a high-speed camera (Photron FASTCAM Mini UX100) and strobe lamp (PanaTech Asia), in backlighting mode.

The heating arrangement of the target surface consists of a flat plate heater (Heatcon Sensors), a temperature controller unit, and K-type thermocouple. The drop diameter (D_0) is estimated from the high-speed images captured just prior to impact. Owing to the reduced pixel resolution of the images at high frame rates of $50,000\text{ fps}$, the impact velocity is taken as the free fall velocity, $V = \sqrt{2gH}$, where H is the impact height measured from the tip of the hypodermic needle to the top face of the target surface.

Table 1 lists the physio-chemical properties of the test liquids evaluated at $25\text{ }^\circ\text{C}$, considered in the present study. Table 2 lists the impact conditions for the three test liquids considered in the present work.

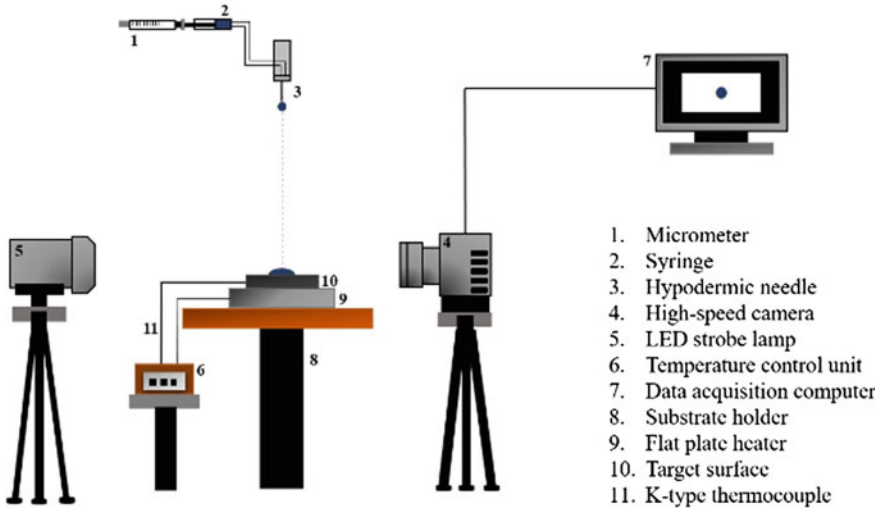


Fig. 1 Schematic of the experimental setup

Table 1 Liquid properties evaluated at ambient temperature of $25\text{ }^\circ\text{C}$

Fuel	Density (ρ) (kg/m^3)	Viscosity (μ) ($\text{mPa}\cdot\text{s}$)	Surface tension (σ) (N/m)
Ethanol	785	1.10	0.022
<i>n</i> -butanol	810	2.63	0.025
Diesel	818	3.46	0.027

Table 2 Impact conditions of the test liquids

Fuel	D_0 (mm)	We
Ethanol	2.32 ± 0.024	454, 542, 643
<i>n</i> -butanol	2.24 ± 0.032	346, 430, 505
Diesel	2.43 ± 0.014	471, 582, 700

3 Methodology

Two different types of experiments are conducted in the present work. In drop impact experiments at constant We , the liquid drops are impacted from a constant impact height onto the target surface at different surface temperatures, ranging from the ambient temperature to just below the Leidenfrost point of the respective liquid. Three trials are taken corresponding to each experimental setting, to ensure repeatability of the observed outcome. The threshold criterion of splashing is quantified by conducting the splash threshold experiments, wherein the splash-deposition limit of the impacting drops is experimentally determined corresponding to each surface temperature setting.

In the splash threshold experiments, drop impact is conducted from a particular height, and the impact dynamics are observed from the high-speed images. If the drop undergoes pure spreading and does not exhibit ejection of secondary droplets, the impact height is increased by a marginal amount. After this increment, if the impacting drop undergoes splashing, the corresponding height is taken as the threshold height corresponding to the surface temperature, and vice-versa.

4 Results and Discussion

4.1 Splash Morphology of Impacting Drops

The results and inferences from the drop impact experiments conducted at constant We are presented first. For each test fuel, liquid drops of nearly identical size are dispensed at constant We , as given in Table 2, and allowed to impinge on to the target surface, maintained at different surface temperature conditions. The drop impact dynamics captured using high-speed imaging, operating at a temporal resolution of 20 μ s, are used to explain the morphology of impacting drops and the resulting splash outcome. Figure 2 depicts the temporal evolution of a diesel drop impacting at $We = 471$, on the heated surface maintained at different temperatures.

In Fig. 2a, which denotes the impact of diesel drop on to the surface kept at ambient temperature ($T_s = 25^\circ\text{C}$), it can be observed that the impacting drop exhibits corona splashing, as endorsed by the ejection of thin liquid sheet and the subsequent ejection of secondary droplets. The liquid sheet is ejected after a certain time lapse from the instant of impact, and subsequently, the sheet grows radially. After $t =$

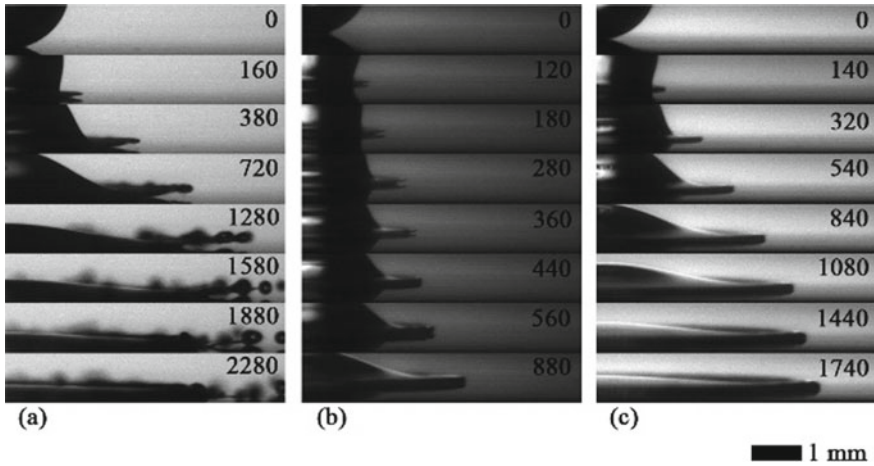


Fig. 2 Image sequence depicting temporal evolution of the dynamics of a diesel drop impacting at $We = 471$, on a heated solid surface kept at temperatures, **a** 25 °C, **b** 190 °C, and **c** 300 °C. The time elapsed from the instant of impact in (μs) is given in the top right corner of each image

1280 μs , perturbations in the liquid sheet grow and result in its disintegration, thereby generating a spray of secondary droplets that are ejected in all azimuthal directions. As the surface temperature is increased, it can be seen that splashing is no longer observed, and the ejected liquid sheet fails to disintegrate and instead re-contacts the spreading lamella. This particular impact morphology is termed as the ‘re-contacting regime’ in the current study and is not previously studied in literature. As seen in Fig. 2b, the liquid sheet grows radially for up to $t = 280 \mu\text{s}$ and then merged back with the base lamella that is spreading over the heated surface. Thereafter, splashing or secondary droplet ejection is not observed.

A further increase in the surface temperature shifts the impact outcome from the re-contacting regime to pure spreading regime, wherein the impacting drop simply spreads over the surface and exhibits no discernible signs of liquid sheet ejection and splashing, as depicted in Fig. 2c. Since the liquid properties and the impact conditions are held constant in these experiments, the observed variations in the impact morphologies may be attributed to only the surface temperature effects.

Figure 3 depicts the impact outcomes based on the characteristics of the liquid sheet in the form of $We-T_s$ matrix for impact of ethanol drops on the heated surface. The images of a given row correspond to the impact outcome for a particular surface temperature and for different impact We . Similarly, the images of a given column correspond to a particular We , for different surface temperatures. It can be observed that as the surface temperature is increased (moving up a column), the ejection of liquid sheet is no longer observed, and the impact outcome transitions from thin sheet splashing to the re-contacting regime to pure spreading. However, an increase in We (moving right in a row) enhances splashing, due to increased inertia of drop impact.

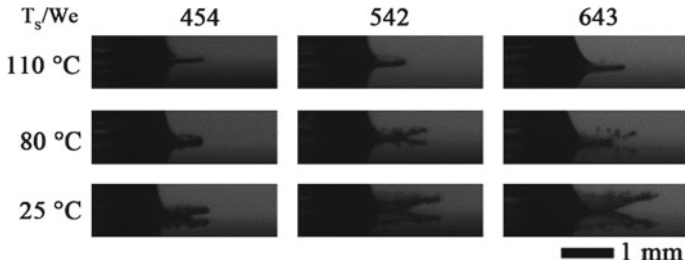


Fig. 3 We - T_s matrix depicting the liquid sheet evolution during impact of ethanol drop on a heated solid surface. All images are captured at $t = 300 \mu s$

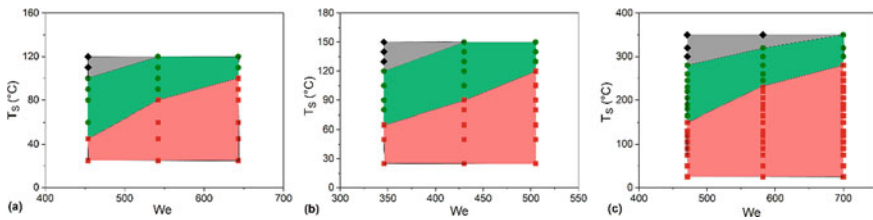


Fig. 4 Regime maps indicating the various impact outcomes observed during drop impact on a heated solid surface for **a** ethanol, **b** *n*-butanol, and **c** diesel

The impact morphologies observed during the impact of the test liquids on a heated solid surface are consolidated in the form of a We - T_s phase space/regime maps and are shown in Fig. 4. It can be seen from the regime maps that with an increase in the surface temperature, there is a discernible shift in the impact morphology from thin sheet splashing (red zone), to the re-contacting regime (green zone) to pure spreading (gray zone). It is speculated that with an increase in the surface temperature, the local gas density close to the expanding liquid sheet decreases and, hence, becomes incapacitated to sustain the liquid sheet up to the point of destabilization. This explains the experimental observation, wherein, splashing via thin sheet ejection is observed at low surface temperatures, while at higher temperatures, the thin liquid sheet fails to destabilize and instead re-contacts the spreading lamella.

4.2 Estimation of Splash Threshold

Following the procedure explained in the methodology section, the threshold We of splashing is determined for the three test liquids under consideration, corresponding to different surface temperatures ranging from the ambient temperature to below the Leidenfrost temperatures of the respective liquid. The splash threshold condition essentially represents the impact condition corresponding to which the drop is at the

incipiency of splashing and essentially represents the splash/deposition limit. Experimental image sequence corresponding to the splash threshold condition considered in the present work is illustrated in Fig. 5. Reported works in literature [10–13] investigated the splash threshold criterion only as a function of the liquid properties, impact velocity, and drop size.

The interesting discovery made by Xu et al. [2] stating that the ambient gas plays a role in controlling the splashing phenomenon, and that a reduction in the ambient gas pressure suppresses splashing, led more researchers to study the effect of ambient gas on the splash outcome. In this regard, the present work aims at understanding how the surface temperature, through localized reduction in the gas phase density, affects the splash threshold. Figure 6 depicts the variation of the splash threshold We with surface temperature (T_S) for the test liquids considered in the present work. The upper and lower limits of the threshold We obtained through experiments are also shown. From the variations depicted in Fig. 6, it can be clearly seen that there is an increase in the splash threshold We , with an increase in the surface temperature. As suggested previously, an increase in the surface temperature results in a reduction in the local gas density in the vicinity of the liquid sheet. As a result, the air film beneath the thin liquid sheet does not sustain the liquid sheet up to the point of its destabilization, and consequently, the impact regime transitions from splashing to spreading, via an intermediate transition regime.

The splash threshold parameter (β) reported by Riboux and Gordillo [6] is evaluated in the current study for drops impacting on the solid surface, at different surface temperatures. The splash threshold parameter (β) is defined as the ratio of the vertical velocity imparted to the liquid sheet by the aerodynamic forces from the gas film

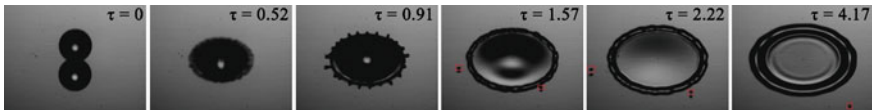


Fig. 5 Temporal evolution of a diesel drop impacting on heated surface at $T_S = 50\text{ }^\circ\text{C}$, at splash threshold/incipiency condition. The red squares represent the secondary droplets ejected during splashing. The impact We at which such a morphology is exhibited by the impacting drop is taken as We_{th} . Dimensionless time (τ) corresponding to each image is given in the top right corner

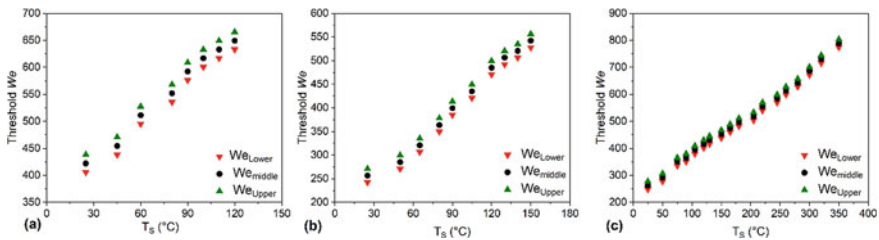


Fig. 6 Variation of splash threshold We with surface temperature (T_S) for **a** ethanol, **b** *n*-butanol, and **c** diesel

to the radial expansion velocity obtained from momentum balance. Following the procedure reported in Riboux and Gordillo [6], the expression for (β) is given as,

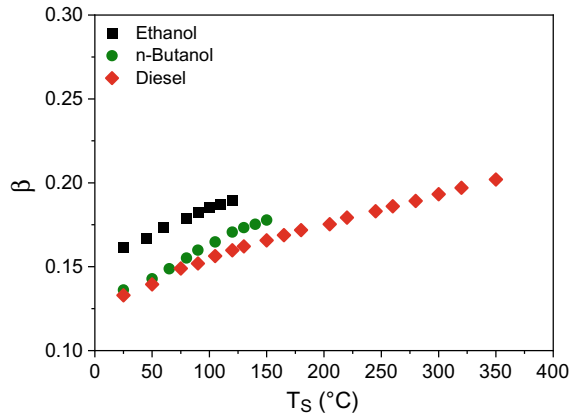
$$\beta = \sqrt{\frac{K_1}{2\sigma} \mu_G \frac{\sqrt{3}}{2} V t_{e,cr}^{-0.5}} \tag{4}$$

where V is the impact velocity, $t_{e,cr}$ is the critical time of sheet ejection, μ_G is the gas viscosity, σ is the surface tension, and the constant (K_1) is approximately constant and depends logarithmically on the physical parameters [6]. The critical time of sheet ejection $(t_{e,cr})$ is obtained corresponding to the experimentally obtained splash threshold We , using the procedure given in Riboux and Gordillo [6]. The variation of the gas viscosity with the surface temperature is accounted for using the two-coefficient Sutherland’s equation [14] given as,

$$\mu_G = \frac{C_1 T^{3/2}}{C_2 + T} \tag{5}$$

where T is the gas phase temperature in K, C_1 and C_2 are constants. The value of the splash threshold parameter (β) so calculated is plotted against the surface temperature (T_S) in Fig. 7. From Fig. 7, it is evident that there is an appreciable increase of β with T_S , which again validates the splash suppression effect of surface temperature. Further, the splash threshold parameter (β) is higher for lower viscosity liquid at constant surface temperature and thus validates the results reported in literature.

Fig. 7 Variation of splash threshold parameter (β) with surface temperature (T_S)



4.3 Characteristics of Re-Contacting Regime

The transition regime between thin sheet splashing and pure spreading is characterized by the tendency of the ejected liquid sheet to re-contact and merge with the spreading lamella. Thus, the liquid sheet does not disintegrate and produce secondary droplets. The temporal evolution of impact morphology of drops in this regime is shown in Fig. 8. In the current study, this transition regime is characterized using re-contact factor (α), defined as the time elapsed from the instant of impact to the instant the liquid sheet re-contacts the lamella, and is non-dimensionalized using the inertial time scale (D_0/V).

From the plots given in Fig. 9, the re-contact factor decreases with an increase in the temperature. This may be explained as follows: As the surface temperature increases, the gas phase in the vicinity of the heated surface beneath the expanding liquid sheet is heated up, and consequently, its density decreases. As a result, the liquid sheet fails to expand radially and instead merges back with the lamella.

More recently, Liu et al. [15] reported that Kelvin–Helmholtz (K-H)-type instability waves that are generated in the thin gas film beneath the expanding liquid sheet are responsible for destabilizing the liquid sheet and causing it to disintegrate and cause splashing. In the context of the findings by Liu et al. [15], the transition regime may be explained as follows. With an increase in the surface temperature, the gas

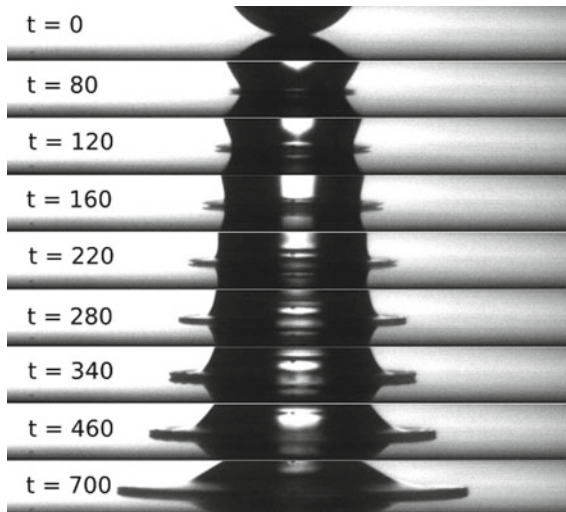


Fig. 8 Experimental image sequence of diesel drop impact at $We = 471$, and surface temperature (T_s) = 230 °C, indicating the transition regime where the thin liquid sheet lifts up post-impact ($t = 120$), grows spatially but fails to disintegrate to eject secondary droplets. The liquid sheet eventually merges back with the spreading lamella on the surface ($t = 340$) and thereafter spreads over the heated solid surface. All times indicated in the left are in μs

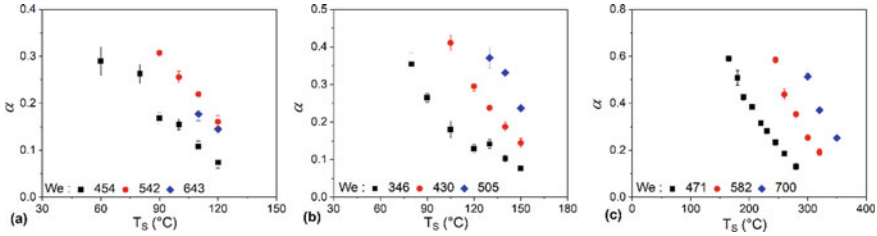
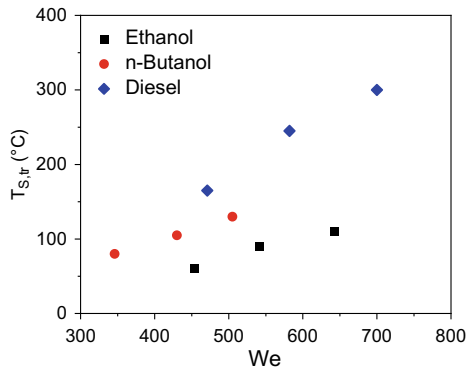


Fig. 9 Variation of re-contact factor (α) with surface temperature (T_s) for **a** ethanol, **b** *n*-butanol, and **c** diesel

Fig. 10 Variation of transition surface temperature with impact We for the three test liquids considered in the present work



phase density decreases, and the liquid sheet fails to expand up to the point, where the K-H instability waves propagate spatially and temporally, to destabilize the liquid sheet.

The transition or re-contacting regime is also quantified in terms of the transition surface temperature ($T_{s,tr}$), defined as the surface temperature above which splashing is no longer observed, and the impact morphology shifts to pure spreading, via the intermediate transition regime. The variation of $T_{s,tr}$ with We is described in Fig. 10. It is observed that the transition surface temperature increases with impact We , since higher impact velocities augment splashing and require higher surface temperatures for transition to pure spreading. For a given We , higher viscosity liquids exhibit higher transition surface temperatures.

5 Conclusions

Splashing of liquid drops impacting solid surfaces is commonly encountered in many fields and has been an area of active research interest. In the present work, we investigate the role of surface temperature in altering splash outcome when liquid drops impact on heated solid surfaces. High-speed imaging is employed to investigate

the morphological outcomes. It is observed that increase in the surface temperature suppresses splashing caused due to localized reduction in the gas phase density. Further, investigation of the impact dynamics at constant We reveals that with an increase in the surface temperature, the impact morphology of drops shifts from thin sheet splashing to pure spreading via an intermediate transition regime, which is characterized by the tendency of the liquid sheet to merge back to the spreading lamella before it can destabilize and disintegrate. The observed outcomes and transitions are modeled using the splash threshold models proposed by Xu et al. [2] as well as Riboux and Gordillo [6], and fair agreement is found in terms of the inferences made. The present work endorses the widely held speculation that the thin film of gas beneath the liquid sheet initiates the fluid dynamic instabilities responsible for splashing, and that the thermodynamic state of this gas phase is pivotal in determining the splash outcome. Further studies on rough surfaces may shed light on the possible interplay of surface temperature and surface roughness that enables us to accurately model fuel spray impingement processes.

Acknowledgements This work was carried out with the support of National Center for Combustion Research and Development (NCCRD), Indian Institute of Science, India.

References

1. Rioboo R, Marengo M, Tropea C (2001) Outcomes from a drop impact on solid surfaces. *Atom Sprays* 11:155
2. Xu L, Zhang WW, Nagel SR (2005) Drop splashing on a dry smooth surface. *Phys Rev Lett* 94:1
3. Xu L (2007) Liquid drop splashing on smooth, rough, and textured surfaces. *Phys Rev E* 75:1
4. Driscoll MM, Stevens CS, Nagel SR (2010) Thin film formation during splashing of viscous liquids. *Phys Rev E* 82:1
5. Stevens CS, Latka A, Nagel SR (2014) Comparison of splashing in high- and low-viscosity liquids. *Phys Rev E* 89:9
6. Riboux G, Gordillo JM (2014) Experiments of drops impacting a smooth solid surface: a model of the critical impact speed for drop splashing. *Phys Rev Lett* 113:1
7. Moreira ALN, Moita AS, Panão MR (2010) Advances and challenges in explaining fuel spray impingement: how much of single droplet impact research is useful? *Prog Energy Combust Sci* 36:554
8. Liang G, Mudawar I (2017) Review of drop impact on heated walls. *Int J Heat Mass Transf* 106:103
9. Staat HJJ, Tran T, Geerdink B, Riboux G, Sun C, Gordillo JM, Lohse D (2015) Phase diagram for droplet impact on superheated surfaces. *J Fluid Mech* 779:1
10. Mundo C, Sommerfeld M, Tropea C (1995) Droplet-wall collisions: experimental studies of the deformation and breakup process. *Int J Multiph Flow* 21:151
11. Yarin AL, Weiss DA (1995) Impact of drops on solid surfaces: self-similar capillary waves, and splashing as a new type of kinematic discontinuity. *J Fluid Mech* 283:141
12. Vander Wal RL, Berger GM, Mozes SD (2006) The splash/non-splash boundary upon a dry surface and thin fluid film. *Exp Fluids* 40:53
13. Palacios J, Hernández J, Gómez P, Zanzi C, López J (2012) On the impact of viscous drops onto dry smooth surfaces. *Exp Fluids* 52:1449

14. Sutherland W (1893) The viscosity of gases and molecular force. London Edinb Dublin Philos Mag J Sci 36:507
15. Liu Y, Tan P, Xu L (2015) Kelvin–Helmholtz instability in an ultrathin air film causes drop splashing on smooth surfaces. Proc Natl Acad Sci 112:3280

Transition Dynamics Between Luminous and Blue Whirling Flames



Sagar Singhal, Manish Sharma, Herambraj Nalawade,
and Pratikash P. Panda

Abstract This paper presents an experimental study to demonstrate transitions between luminous and blue whirling flames. We have designed a fixed-frame four-sided square aluminum test apparatus where liquid fuel is injected vertically upward from the center of the base plate, which reacts with self-entrained tangential air. Our experiments show evidence of the transition of a highly luminous non-premixed fire whirl into a blue whirling flame above the base surface. The formation of a blue whirling flame depends on the enhanced mixing and fuel spread above the metal surface. The smooth surface boundary leads to the formation of Ekman type boundary layer, which is shown to affect the flame. The transition from a fire whirl to a blue whirling flame is found to be dependent on the fuel spread over the metallic surface which depends on the fuel flow rate. This paper also shows the visual observation of flame patterns at different fuel flow rates, gap size (for air entrainment), and surface conditions (to identify the key parameters that are responsible for the formation of a blue whirling flame). The flame images show that a conical whirling flame with a laminar bluish base could be an essential (but not enough) condition to produce the transition to blue whirling flame.

Keywords Whirling flames · Air entrainment · Ekman layer

1 Introduction

There exist several strategies to control particulate emissions from combustion. The recently discovered blue whirl reported by Xiao et al. [1], a regime of the fire whirl, burns liquid hydrocarbon fuel with little visible soot. Whirling flames are different from swirl-stabilized flames. Whirling flames are defined as those produced by introducing air with a strong tangential component of velocity that generates a whirling flow. In case of swirl-stabilized flames, air is introduced into the combustor with

S. Singhal · M. Sharma · H. Nalawade · P. P. Panda (✉)

Department of Aerospace Engineering, Indian Institute of Science, Bangalore, CV Raman Road, Bangalore, Karnataka 560012, India

e-mail: pratikashp@iisc.ac.in

a combination of axial and tangential component of momentum. Most common example of a whirling flame is naturally occurring fire whirls. Fire whirls are vertical rotating column of fire that can go up to several kilometers in height. It is produced due to interaction of ambient vorticity and wildland fire. In this research, we present transitions dynamics between a luminous and blue whirling flames in a laboratory scale test set up.

In the past, wide research has been done on fire whirls to understand its structure and formation mechanism [2–4]. Xiao et al. [1] studied lab scale fire whirl above the surface of water to explore the feasibility to clear oil spills. Their experiments led to the discovery of a new type of flame, which looks small, stable, and blue which were called blue whirling flames. They also reported that the height of luminous conical whirling flame can vary from 20 to 70 cm while the height of blue whirling flame can vary between 4 and 8 cm. In a follow-up study, Hariharan et al. [5] have shown the formation of blue whirl for a range of heavy hydrocarbon liquid-fuels (*n*-heptane, iso-octane, and cyclohexane).

Temperature of blue whirling flame was found to be higher than the maximum flame temperature achieved in non-premixed combustion of liquid hydrocarbon fuel in pool fire [5]. Chung [6] performed numerical simulations to identify the flame and flow structure of the blue whirl, and Hu et al. [7] plotted circulation and heat release map for the blue whirling flame. They showed that formation of blue whirling flame occurs near extinction limit of fuel. Hariharan et al. [8] showed that blue whirling flame can be formed on surface of water, smooth metal surface, and porous surface. They showed that for formation of blue whirling flame, smooth surface boundary is required to form Ekman boundary layer. This layer forms near the base surface only when there is cyclostrophic disbalance between outward acting centrifugal force (due to rotating column of flame) and inward pressure gradient. Because on the base surface viscous effect tends to reduce the centrifugal effects. This cause inward radial entrainment of air near the base [9]. Thus, the simplistic concept of blue whirling flame could be harnessed toward the development of a low-emission, soot-free combustion technology.

The focus of this research is to demonstrate a new concept of blue whirling flame in a laboratory scale test apparatus. We show the transition dynamics of luminous fire whirl to blue whirling flame in fixed-frame four-sided square apparatus and discusses essential conditions for its formation. This paper also presents the visual observations of flame patterns for a range of key geometric and flow parameters.

2 Experimental Details

The experiments were performed in a fixed-frame four-sided square aluminum apparatus shown in Fig. 1a. Four slits in along the corners of the experimental test set up allowed tangential entrainment of air. The slit-gap size was varied from 15 to 45 mm as shown in Fig. 1b. The gap size of the slits was found to affect the formation and stability of the fire whirls and the blue whirling flame. A syringe pump (New Era

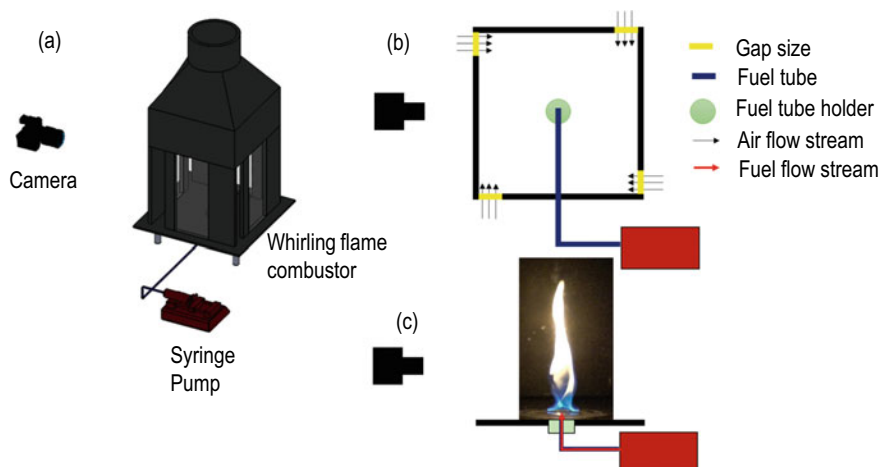


Fig. 1 a Experimental set up b Schematic diagram of top view of experimental set up c Schematic diagram of side view of experimental set up (flame image indicates the view captured by camera)

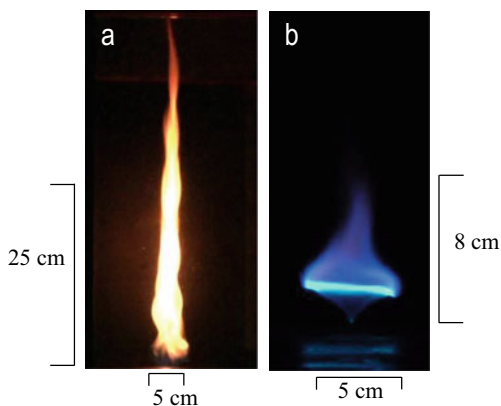
Pump Systems, Inc.) was used to deliver liquid *n*-heptane on to the center of the base plate using a copper tube of 4 mm ID. The copper tube was flushed with top of base plate as shown in Fig. 1c, and the liquid fuel was slowly squirted onto the surface. The flow rate of fuel was varied from 0.5 to 3 mL/min. The evolution of the fire whirl and its transition into a blue whirling flame was recorded using a Sony RX 10 MK IV camera. A mirror was used to image the top view of the whirling flame. The flame images were acquired at 250 frames per second and frames were extracted from videos and analyzed using ImageJ software.

Experiments were performed at ambient pressure and temperature. Initially, 2 mL of *n*-heptane fuel was squirted over base surface (near center) and ignited with the help of butane igniter. The flame first tends to lean toward slits. After 2 s, it starts to rotate in the combustor and stretch itself vertically upward, resulting in a luminous yellow whirling flame. Then, the fuel flow rate (controlled by syringe pump) was varied from 0.5 to 3 mL/min. For lower values of fuel flow rate (less than 1.5 mL/min), the yellow luminous whirling flame transitions first into a conical whirling flame with bright blue base and then eventually transitions into blue whirling flame in which bright blue ring lifts from the base surface and a faintly inverted blue cone was visible below bright blue ring.

3 Observations

Experiments were performed for different fuel flow rate, slit-gap size, and surface conditions. Figure 2 compares the height of a luminous conical whirling flame

Fig. 2 Image showing the scales of **a** luminous conical whirling flame and **b** blue whirling flame



and a blue whirling flame. The extracted images correspond to a fuel flow rate of 0.75 mL/min and gap size of 15 mm.

The measured height of luminous conical whirling flame and blue whirling flame is approximately 50 cm and 8 cm, respectively. The luminous conical whirling flame looks very slender, and the measured width for both the flames is approximately 5 cm. The luminous conical whirling flame evolves from a pool fire (height ~ 15 cm) through a series of flame patterns (flame tilting, flame rotating, and luminous cylindrical fire whirl). The height of luminous conical whirling flame increases because high circulation rate prohibits diffusion of air at whirl core, so flame stretches axially. In other words, turbulent mixing at fire whirl core reduces. The blue whirling flame looks very small, laminar, and completely soot-free as compared to luminous conical whirling flame. The transition to blue whirling flame was found to happen only from luminous conical whirling flame with blue ring at the base. In a recent computational study reported by Chung [6] shows that the blue whirling flame is a result of bubble mode of vortex breakdown. Bubble-mode vortex breakdown [10] consists of an axial stagnation point followed by recirculation zone. This recirculation zone increases the residence time so as complete combustion can occur. Soot recirculates and is consumed primarily in the recirculation zone.

The regions of blue whirling flame are shown in Fig. 3. Chung [6] have described that the purple haze, bright vortex rim, and faint inverted blue cone region represents the diffusion flame (enveloped by premixed lean flame), triple flame, and premixed rich flame, respectively. Triple flame was also discussed as the flame where lean premixed, rich premixed, and diffusion flame met.

The shape of inverted blue cone is due to presence of Ekman type boundary layer at the base surface. It produces premixed rich mixture of evaporated fuel and air. Hariharan et al. [11] have performed OH* chemiluminescence to analyze the reaction front in both luminous whirling flame and blue whirling flame, and it was reported that most of the reaction happens only in vortex rim region of blue whirling flame than in entire region of luminous whirling flame. Purple haze is the region where soot is being recirculated.

Fig. 3 Image indicating different regions of blue whirling flame (achieved for fuel flow rate of 0.75 mL/min and slit-gap size of 15 mm)

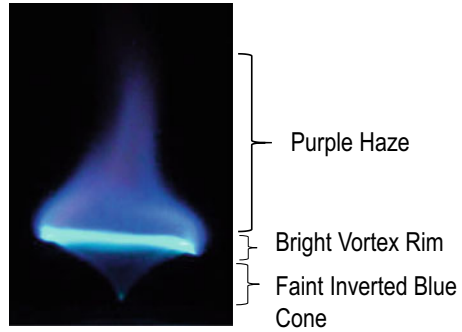


Figure 4 indicates the front view images of the transitions between blue whirling flame and luminous conical whirling flame for a fuel flow rate of 1.25 mL/min and slit-gap size of 15 mm. The back-and-forth transition shown, here is over a duration

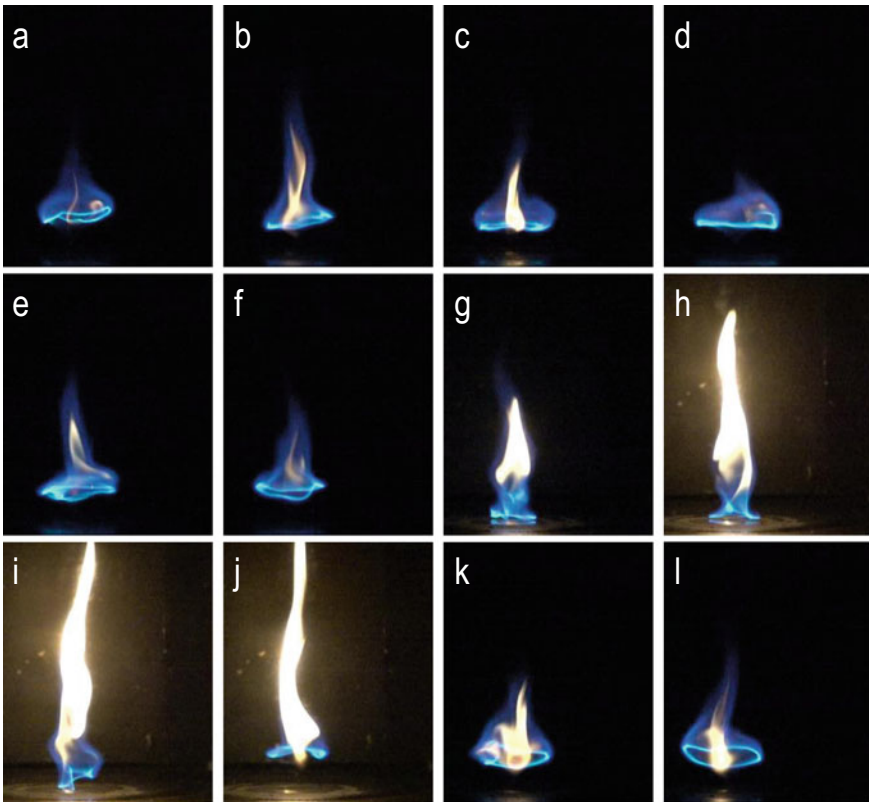


Fig. 4 Front view images of back-and-forth transitions between blue whirling flame and luminous conical whirling flame (fuel flow rate and slit-gap size were 1.25 mL/min and 15 mm, respectively)

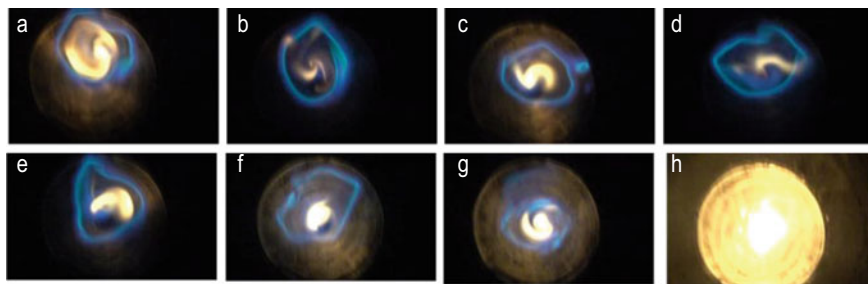


Fig. 5 Top view images of back-and-forth transitions between blue whirling flame and luminous conical whirling flame (fuel flow rate and slit-gap size were 1.25 mL/min and 15 mm, respectively)

of seconds. Blue whirling flame with a thin streak of soot in the center can be observed in Fig. 4a. The sooty region grows (Fig. 4b), diminishes (Fig. 4c), and then approximately vanishes (Fig. 4d). It grows again (Fig. 4e, f), and blue ring touches the surface (Fig. 4g). When the blue ring touches the surface, it forms luminous conical fire whirl (Fig. 4g, h). The blue ring again starts lifting from surface (Fig. 4i) and completely lifts (Fig. 4j), then it again transits into blue whirling flame with soot recirculation zone at the center. This back-and-forth transition between blue whirling flame and luminous conical whirling flame is due to intermittent fuel spread over the surface. Rate of fuel consumption lower than the rate of fuel injection results in intermittent fuel spread over the surface. When the fuel spreads over the surface, then blue ring reattaches to the base surface and after consuming fuel from the surface, it again lifts from the surface. Eventually, the sooty tip of the flame (as seen in Fig. 4j) moves downward and consumed at the vortex rim.

Figure 5 indicates the top view images of the transitions between blue whirling flame and luminous conical whirling flame for a fuel flow rate of 1.25 mL/min and gap size of 15 mm. In Fig. 5, the variation in flame luminosity at the center of the flame is observed. In the images from Fig. 5a–g, the yellow luminous zone was enveloped by a blue ring. The blue ring corresponds to the region of peak heat release rate, and the yellow luminous zone corresponds to the presence of soot. It can be seen that the recirculating soot layer gets consumed at the blue ring. But when the flame transitions into the luminous conical fire whirl (Fig. 5h), the blue ring cannot be observed. The back-and-forth transition shown here is over a duration of 2 s.

Figure 6 shows the effect of variation of fuel flow rate (0.5–2.75 mL/min) on most stable blue whirling flame structure at fixed slit-gap size of 15 mm. These images are the best possible case that resembles the blue whirling flame for the respective fuel flow rate. This figure indicates that the blue whirling flame (with all three regions) forms below fuel flow rate of 1.5 mL/min. Figure 6a indicates a blue whirling flame at a fuel flow rate of 0.5 mL/min that was stable for a duration of 2 s, and the frequency of transition to a blue whirling flames was 10 per min. The blue whirling flame quickly extinguishes within 40 s. As we increase the fuel flow rate there is an increase in the frequency of transition between conical whirling flame to blue whirling flame.

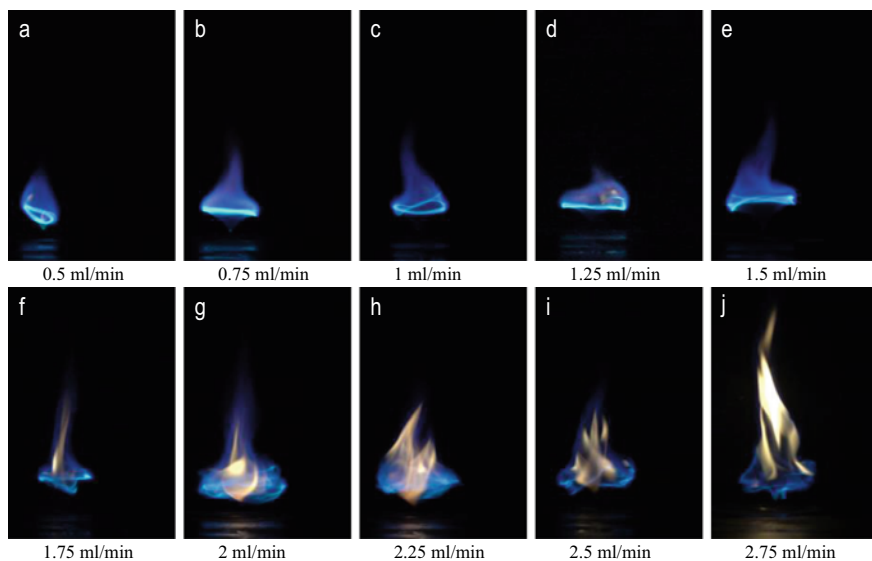


Fig. 6 Blue whirling flame images for different fuel flow rates at fixed slit-gap size of 15 mm

The increase in frequency of transition with increase in fuel flow rate may be due to increasing imbalance between rate of fuel injection and consumption. It can be observed that blue whirling flame was formed near extinction limit of fuel. Inverted blue cone was not observed in Fig. 6f–j. With an increase in fuel flow rate, there is an increase in the degree of richness of fuel near the base of the flame, as a result, there is an increase in the flame sootiness.

Figure 7 indicates the effect of variation of slit-gap size (15–45 mm) on the flame structure and stability at a fixed fuel flow rate of 1.25 mL/min. The flame structure is mostly luminous conical whirling flame for the slit-gap size of 45 mm (Fig. 7a). As

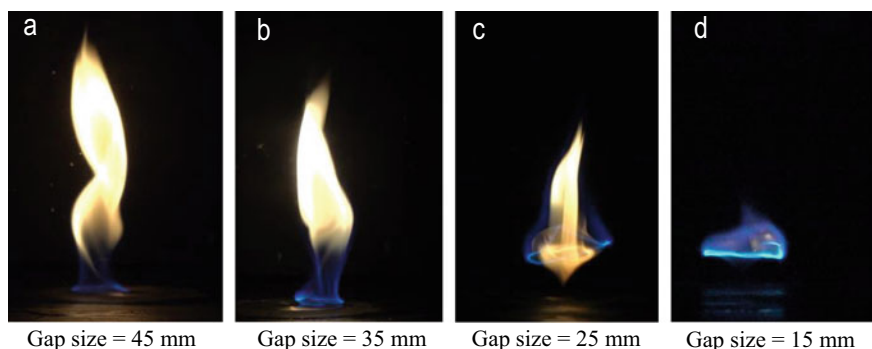


Fig. 7 Flame pattern for different gap size at fixed fuel flow rate of 1.25 mL/min

the gap size reduces to 35 mm the luminosity of the conical whirling flame reduces and the base of the flame shows the presence of bluish flame sheet (Fig. 7b). When the gap size was reduced to 25 mm the blue flame sheet lifts off from the surface and the flame structure transitions into a blue whirling cup holding a yellow luminous flame in the center (Fig. 7c). When the gap size was reduced to 15 mm there is a complete transition into blue whirling flame. Figure 7d shows all the three regions of blue whirling flame. For gap size of 35 and 45 mm, local circulation rate was not enough to produce bubble mode of vortex breakdown. The radial entrainment of air near the base surface was not enough to mix with evaporated fuel and to form the inverted cone for the slit-gap size of 35 and 45 mm. Hariharan et al. [11] compared the spontaneous OH* chemiluminescence between blue whirl and fire whirl and showed that in a blue whirl, a significant portion of combustion occurs in vortex rim while in the case of fire whirl, and there is distributed reaction zone in the whirling flame above. Table 1 summarizes the observations when gap size was varied from 15 to 45 mm.

Table 2 summaries the details of different surface condition used to show its effect on flame pattern. The role of surface boundary condition is also identified as an important parameter that influences the transition from a fire whirl to a blue whirl.

Table 1 Summarized observations of flame patterns for different gap size at fixed flow rate of 1.25 mL/min

S. No.	Gap size = 45 mm	Gap size = 35 mm	Gap size = 25 mm	Gap size = 15 mm
1	No bubble mode of vortex breakdown	No bubble mode of vortex breakdown	Bubble mode of vortex breakdown	Bubble mode of vortex breakdown
2	Heat release rate distributed over complete flame	Heat release rate distributed over complete flame	Less intense heat release rate at vortex rim	Intense heat release rate at vortex rim
3	Blue ring attached to base	Blue ring attached to base	Lifted blue ring from base	Lifted blue ring from base
4	No inverted blue cone	No inverted blue cone	No inverted blue cone	Inverted blue cone

Table 2 Different surface conditions

S. No.	Surface conditions	Fuel supply	Pan/tube diameter (mm)	Pan height (mm)
(i)	Fuel tube flushed with base surface	Continuous supply of fuel (0.75 mL/min)	4	
(ii)	Fuel pan kept above base surface	Fixed amount of fuel in the pan (10 mL)	50	30
(iii)	Fuel pan flushed with base surface	Fixed amount of fuel in the pan (10 mL)	50	30

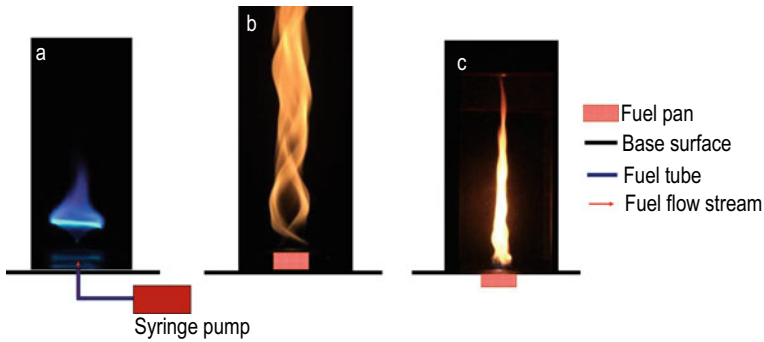


Fig. 8 Flame pattern for different surface conditions

We have investigated three different configurations, viz., (i) fuel tube flushed with the base surface, (ii) fuel pan kept above the base surface, and (iii) fuel pan flushed with the base surface. For case (ii) and (iii), where fuel pan was used, and pan was first filled with 3 mm diameter metal balls and then covered by a coarse wire mesh. 10 mL of fuel was poured in the pan, and fuel was flushed till the lip of pan.

Experiments were performed for all three cases to compare the flame structure. No transition was seen for case (ii). But when fuel pan was flushed with base surface, a conical whirling flame with blue flame was observed, but transition to blue whirling flame was not observed.

Figure 8 indicates the flame pattern for different surface conditions for the fixed gap size of 15 mm. Figure 8a shows a blue whirling flame when the fuel flow rate was 0.75 mL/min. For case ii (Fig. 8b), the luminous whirling flame was observed till all the fuel was consumed and the flame extinguished. A small luminous conical whirling flame can be observed for case iii (Fig. 8c), and there were rapid changes in the height of conical whirling flame. When fuel pan was kept over the base surface, then Ekman type boundary layer will not form due to presence of surface discontinuity at the lip of fuel pan.

4 Discussions

In the current experimental set up configuration, circulation rate is dependent on the heat release rate. So, if fuel consumption rate is high, then heat release rate will also be high. The high heat release rate will create a low-pressure region inside the combustor which leads to increase in air entrainment and circulation rate. Highly rotating free-vortex region imparts surface wave on fire whirl core. If core velocity is high than surface wave velocity, then it leads to disturbance at core and vortex breakdown occurs [2]. Ekman layer at the base results due to cyclostrophic disturbance between centrifugal force (acting outwards because flame rotates) and radial inward pressure

gradient. This disturbance is created due to the presence of viscous layer at base surface due to which radial inward velocity near the base surface produces [9].

Smooth surface boundary is essential condition but not enough to produce blue whirling flame. The smooth surface boundary helps in creating Ekman layer at the base surface due to which radial entrainment of air takes place near the base surface. The radial entrainment of air increases as local swirl (or rotation) increases. When the radial entrainment rate of air is high, then it can mix with vaporized fuel and forms an inverted blue cone. It also helps to prevent fuel slick over the surface. When the radial entrainment rate of air is low, then although air can mix with vaporized fuel and forms blue ring at the base, but it will not form an inverted blue cone.

The back-and-forth transition between luminous and blue whirling flame is due to intermittent fuel spread over the base surface. Intermittent fuel spread over the surface is due to lower depletion rate of fuel than injection rate of fuel. This imbalance between the two rates may be due to following reasons: (a) destabilization at base surface may inhibit the formation of Ekman type boundary layer, (b) flow disturbance at tangential slits, and (c) sporadic evaporation events at base surface due to hotspots on the surface of plate [8]. The imbalance between the two rates increases with increase in fuel flow rate. Therefore, frequency of back-and-forth transition increases with fuel flow rate.

5 Conclusions

In this paper, experiments were performed on a fixed-frame four-sided square aluminum apparatus. Air was naturally entrained through tangential slits. Hydrocarbon fuel, *n*-heptane of 99% purity was injected axially upward from base surface into the apparatus. Our experiments have shown the transition of sooty non-premixed whirling flame to blue whirling flame. Transition has been believed to happen due to disturbance that leads to formation of bubble mode of vortex breakdown. Blue whirling flame is small (8 cm in height when measured at 0.75 mL/min), laminar and soot-free. We have also presented the visual observation of flame patterns at different fuel flow rates, gap size, and surface conditions. Blue whirling flame was formed only near extinction limit of fuel. When the gap size was 15 mm, then blue whirling flame forms at fuel flow rate of 0.5–1.5 mL/min. The smooth base condition was found to be essential for fast mixing of evaporated fuel and radially entrained air. Intermittent fuel spread on the base surface and insufficient swirl led to back-and-forth transitions between luminous conical whirling flame (with blue flame at base) and blue whirling flame. Frequency of back-and-forth transition increases with increase in fuel flow rate because of insufficient swirl and increased frequency of intermittent fuel spread. At higher slit-gap size, circulation rate was not enough to produce blue whirling flame although smooth surface boundary condition was used. Blue whirling flame was not formed when fuel pan was kept above base surface due to discontinuity at the lip of fuel pan. Blue whirling flame was not stable for more than a minute because of intermittent fuel spread resulting from poor local swirl near

base. In current design of whirling flame test apparatus, circulation rate was dependent on heat release rate of fuel, so in the future, we are designing a new whirling flame apparatus to independently control heat release rate and circulation rate. Our goal would be to increase the range of operation as well identify conditions that could lead to blue whirling flame directly without any transition. In-situ laser diagnostics and computations will also be performed to visualize flow-flame interactions and blue whirling flame structure. A flow circulation versus heat release map will also be plotted to identify the regime of blue whirling flame.

Acknowledgements This work is supported by the Department of Science and Technology (DST) through the INSPIRE faculty award: DST/INSPIRE/04/2017/000585.

References

1. Xiao H, Gollner MJ, Oran ES (2016) From fire whirls to blue whirls and combustion with reduced pollution. *Proc Natl Acad Sci USA* 113:9457–9462
2. Emmons HW, Ying SJ (1967) The fire whirl. In: *Symposium (international) on combustion*, vol 11, pp 475–488
3. Lei J et al (2011) Experimental research on combustion dynamics of medium-scale fire whirl. *Proc Combust Inst* 33:2407–2415
4. Zhou K et al (2013) Effect of flow circulation on combustion dynamics of fire whirl. *Proc Combust Inst* 34:2617–2624
5. Hariharan SB et al (2017) The thermal structure of the blue whirl using different liquid fuels
6. Chung J et al (2020) The structure of the blue whirl revealed. *Sci Adv*
7. Hu Y, Hariharan SB, Gollner MJ, Oran ES (2018) Conditions for formation of the blue whirl
8. Hariharan SB et al (2019) The blue whirl: boundary layer effects, temperature and OH* measurements. *Combust Flame* 203:352–361
9. Dobashi R et al (2016) Experimental study on flame height and radiant heat of fire whirals. *Fire Technol* 52(4):1069–1080
10. Faler JH, Leibovich S (1978) An experimental map of the internal structure of a vortex breakdown. *J Fluid Mech* 313–335
11. Hariharan SB, Sluder ET, Gollner MJ, Oran ES (2019) Thermal structure of the blue whirl. *Proc Combust Inst* 37:4285–4293

Spray Injection and Atomization

Flow Dynamics in a Triple Swirl Burner



Neha Vishnoi, Agustin Valera-Medina, Aditya Saurabh, and Lipika Kabiraj

Abstract One of the most important milestones in gas turbine burner technology was the incorporation of swirling flows for flame stabilization. The objective of present work is the design and development of a generic fuel flexible multiple swirl burner with enhanced flashback resistance and low emissions. The burner design will allow operation in premixed and non-premixed modes with liquid and gaseous fuels. The investigated burner consists of 3 annular co-rotating swirlers: an outer radial swirler stage and two concentric axial swirler stages. Insights from the first isothermal and reactive numerical simulations for premixed methane–air combustion are being presented here. Results based on the characterization of the flow fields, temperature distribution, streamwise and azimuthal shear layer dynamics, and turbulence characteristics are presented. The velocity profiles obtained from isothermal numerical simulations are also validated by experimental results. Flame stabilization and flashback propensity are discussed with respect to the features of vortex breakdown, specifically the central recirculation zone (CRZ).

Keywords Central recirculation zone · Fuel flexibility · Flashback · Swirl flow

1 Introduction

Incorporation of swirling flows for flame stabilization in gas turbines is a crucial milestone in the industry that allows for efficient, and stable combustion with low NO_x emissions [17]. In such combustors, swirl is introduced to the incoming fuel–air mixture by stationary swirl vanes, which creates a vortex flow centered on the com-

N. Vishnoi (✉) · L. Kabiraj
Indian Institute of Technology Ropar, Rupnagar, Punjab, India
e-mail: 2018mez0019@iitrpr.ac.in

A. Valera-Medina
Cardiff University, Cardiff, Wales, UK

A. Saurabh
Indian Institute of Technology Kanpur, Kanpur, UP, India

© The Author(s), under exclusive license to Springer Nature Singapore Pte Ltd. 2023
G. Sivaramakrishna et al. (eds.), *Proceedings of the National Aerospace Propulsion Conference*, Lecture Notes in Mechanical Engineering,
https://doi.org/10.1007/978-981-19-2378-4_34

bustor's centerline. At significantly high swirl intensity, vortex breakdown occurs in the combustion chamber, thus forming recirculation zones. These recirculation zones mix hot products into reactants upstream of flame base. These recirculation zones are also responsible for increasing the flame speed [5]. At optimum swirl intensity, the flame is stabilized at the dump plane in the shear layers and is compact permitting the design of a shorter and lighter combustor. Additionally, swirl flows provide the control of the mixing pattern and temperature field for preventing autoignition, and flashback [10]. Vortex breakdown [6] is associated with formation of helical structures [23], and precessing vortex core (PVC) [1, 18] that acts as a source of unsteady flow and heat release, thus triggering thermoacoustic instabilities in the system. To address the stability issues associated with swirl flow, understanding the dynamics of vortex breakdown is crucial.

Most gas turbines are operated using natural gas because of its availability, low cost, and reliability. However, a combination of recent factors, including volatility in fuel supply and pricing, global and climatic concerns about carbon emissions, and excess risk from heavy dependence on a single energy source, have made the utilization of natural gas substitutes such as industrial, municipal, and agricultural opportunity fuel sources very attractive from environmental and economic standpoints. Nevertheless, a major barrier to the utilization of opportunity fuels remains in the inability of industrial gas turbines to operate effectively when powered by such fuels [26]. The lean premixed swirl stabilized combustors burning a wide variety of fuels are prone to flashback because they are highly tuned to operate on low-flame-speed fuels like natural gas. A solution to these hurdles is to develop state-of-the-art technologies for diluent-free ("dry") or wet, low NO_x and flashback-resistant combustion for fuel flexible gas turbines [2]. Lately, the leading gas turbine manufacturers like GE, Siemens, Hitachi, and dedicated research groups are focused on developing such state-of-the-art technologies [7]. The available fuels, being investigated, cover a wide range of Wobbe indices from those of high hydrogen content syngas produced in the IGCC with CO₂ capture and storage (CCS) systems to that of propane, and a wide range of flame speeds from that of natural gas to those of high hydrogen content fuels [2].

The long-term aim of the present work is the development of a novel fuel flexible multiple swirl burner with reduced detrimental thermoacoustic instabilities, low NO_x emissions, and stable combustion. The fuel blends to be specifically tested are methane-hydrogen or pure hydrogen. Toward this, a preliminary design for burner is proposed and comparative study of flow fields for isothermal and reactive flows has been investigated through numerical simulations. Reynolds Averaged Navier-Stokes (RANS) [4] simulation approach has been utilized here for flow description. This approach with simplistic combustion models [4] helps in simulating the mean flow field and effects of entire range of turbulent scales. Observations from the first set of simulations are presented as a function of axial velocity contours, turbulent kinetic energy contours, axial and tangential velocity profiles, and temperature fields. Experimental validation of RANS isothermal flow profiles has also been conducted. Streamwise and azimuthal shear layers are characterized by vorticity contours and profiles.

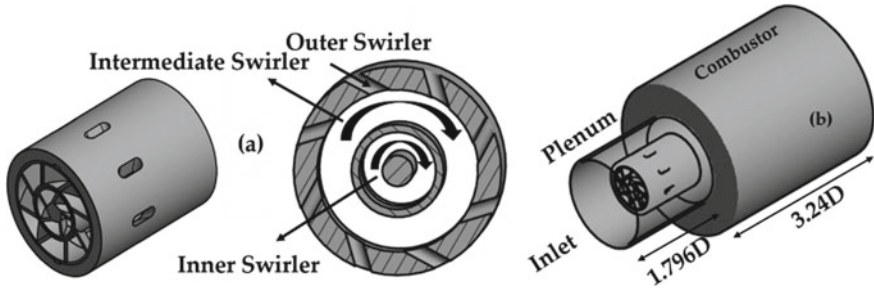


Fig. 1 **a** Triple swirl burner assembly and its perpendicular section; **b** computational domain

2 Test Case: Triple Swirl Burner

Triple Annular Research Swirler (TARS), a fuel injector, was developed by Goodrich Corporation in collaboration with General Electric Aircraft Engines (GEAE) for research purposes [21]. It has a complex geometry with design features analogous to an aero-engine application and has been investigated in numerous experimental and numerical studies [10, 16, 17]. A peculiar characteristic of TARS is the propagation of central recirculation zone (CRZ) upstream of the fuel injector exit, thereby stabilizing the flame inside the injector [8, 11]. The burner design investigated in the present work is derived from the TARS concept. The investigated burner is characterized by three co-axial air passages: outer radial swirlers and intermediate and inner axial swirlers (Fig. 1a). Different configurations of the burner can be realized by changing the swirl configuration (altering the vane angles of the three swirlers) or rotating direction (co-rotating or counter-rotating) to generate different swirling flow fields. In the present work, all the swirlers are co-rotating and the swirl configuration is $S504555$ corresponding outer, intermediate, and inner swirl vane angles of 50° , 45° , and 55° , respectively. The outer and intermediate swirlers comprise 8 vanes while the inner swirler has 5 vanes. The swirl numbers for the outer, intermediate, and inner swirlers are 0.79, 0.77, and 1.061, respectively. The overall length of the burner is 66 mm. The exit diameter of the burner is $D = 54$ mm and would be used as reference for normalizing coordinates.

3 Numerical Details: Computational Domain and Boundary Conditions

The dynamics of the flow within the triple swirl burner and in the combustor is simulated using RANS (Reynold’s Averaged Navier-Stokes) numerical model in STAR CCM+ at GTRC (Gas turbine research center), Cardiff University. Owing to the complex geometry of the burner, an unstructured polyhedral mesh with prism layer composed of 8.05 million cells was generated. SST $k - \omega$ turbulence model was

Table 1 Operating conditions for triple swirl burner

Condition	Case 1		Case 2		Φ
	\dot{m}_a (g/s)	\dot{m}_f (g/s)	\dot{m}_a (g/s)	\dot{m}_f (g/s)	
Isothermal	8.73	–	19.25	–	–
Reactive	8.73	0.379	19.25	0.835	0.75

used to predict the burner's exit flow field. The turbulent flame closure combustion model used for simulations is Zimont's TFC model [27]. This model involves the solution of a transport equation for the reaction progress variable. The closure of this equation is based on the definition of the turbulent flame speed. For the resolution of combustion, "Complex Chemistry" was employed, enabling the calculation of molar and mass fractions, chemical rates of production and heat release with up to 130 reactions and 27 species. Simultaneously, clustering methods were employed to reduce the computational expense of these Complex Chemistry calculations. The computational domain is presented in Fig. 1b. It consists of a plenum—upstream the burner, the burner itself, and a cylindrical confinement. The inlet is located at about $1.796D$ upstream of the dump plane. The cylindrical confinement is $3.24D$ long and $2.85D$ in diameter.

At inlet, for pressure, zero gradient condition is imposed. For temperature and species mass fractions, Dirichlet conditions are imposed. The inlet air temperature is 300K. At the outlet, pressure is atmospheric (101 kPa). No slip conditions are assumed at the walls with zero pressure gradient and species mass fractions. The walls are assumed to be adiabatic. The origin of the coordinates is placed near the center of the inlet of the plenum. The operating conditions for the present numerical study are tabulated in Table 1. Premixed air–fuel mixtures after passing through the triple swirl burner enter the dump combustor.

where \dot{m}_a and \dot{m}_f represent air and fuel (methane) flow rates, respectively. Φ represents equivalence ratio.

4 Laboratory Experiments

Isothermal experiments were performed using a vertical atmospheric test rig facility (Fig. 2) at Cardiff University. The test rig consists of a vertical air flow conditioning chamber, and a funnel extension for mounting of the burner. The experiments were performed for case 1 isothermal flow condition, and mean axial velocity data was obtained at different axial locations downstream the burner exit (Fig. 2) through LDA (Laser Doppler Anemometry) diagnostic technique.

A 3D Dantec traverse system, controlled by BSA software, was used to move the laser head stably in horizontal and vertical directions relative to the test rig. For experiments, the triple swirl burner with plenum was 3D printed using Polyamide

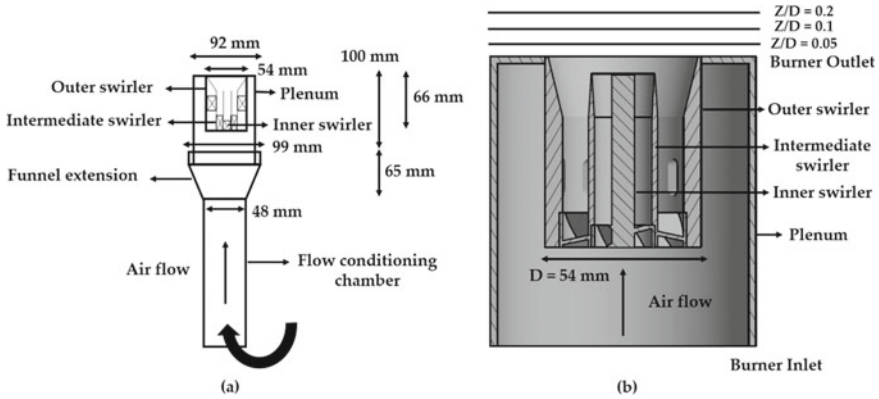


Fig. 2 Schematic of vertical atmospheric test rig and cross-section of burner with experimental measurement points

(Nylon (PA2200)) material. This material has good mechanical properties, dimensional stability, wear resistance, and high chemical resistance [14]. The air flow rate of 440 ltr/min was metered by Platon flow meter at a constant pressure of 2 bars. Aluminum dioxide powder was used as the seeding particles for flow visualization.

5 Results and Discussions

Formation of CRZ with reversed flow at burner’s axis because of vortex breakdown is the characteristic feature of swirling [3]. The shape and location of formation of CRZ is a function of swirl intensity and inlet Reynold’s number [17]. These flows are 3-dimensional whose dynamics are dependent on geometric considerations. In the present study, comparative flow fields from isothermal and premixed methane–air reactive simulations are presented and are characterized as a function of axial velocity streamwise and cross stream contours, turbulent kinetic energy contours, axial and tangential velocity profiles, and temperature fields. The information about the formation of inner and outer shear layers is provided through vorticity contours and profiles.

5.1 Velocity Field

Figures. 3 and 4 shows the streamwise axial velocity contours for flow field along the central axis of the burner for cases 1 and 2, respectively. A swirling motion is imparted to the air when passing through the three set of vanes which along with their shear layers merges near the burner exit. From the flow fields inside the burner

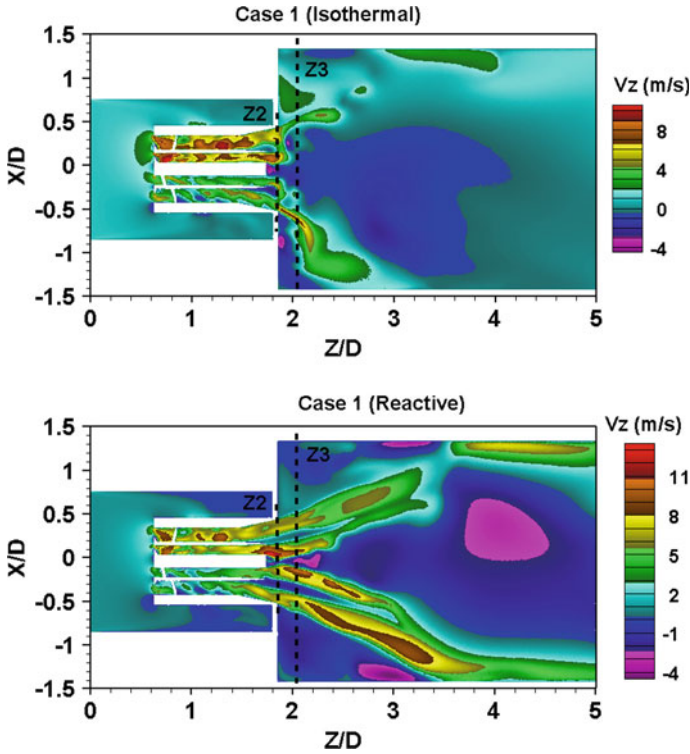


Fig. 3 Comparison of streamwise isothermal and reactive flow axial velocity contour for case 1. The coordinates are normalized by $D = 54$ mm

and plenum assembly, for all conditions, regions of reversed flow can be observed at the solid surface of outer swirler and plenum body (indicated by blue color for case 1 and blue and dark cyan colors for case 2). The highest velocities are observed throughout the flow passages in the burner.

Regions of reversed flow are observed at the tips of intermediate and inner swirlers which favors the merging of the jets. Unlike TARS, the inner swirler rod is extended up to the exit; therefore, no upstream propagation of CRZ through central route is possible. The reverse flow at the tips of inner swirler merges with the CRZ. Along the walls of the burner, boundary layer detachment is also observed. These observations are crucial for burner design in terms of two types of flashback [24]: boundary layer flashback when flame gets attached to burner rim and flashback due to upstream propagation of CRZ. In the present case, for the mass flow rates considered, flashback through inner and intermediate swirler tips is possible. This is the point of consideration for further modification in the burner design especially for incorporation of highly reactive fuels.

From the isothermal fields inside the combustor, the shape and size of CRZ can be comprehended. The shape of CRZ is spherical (approximately) as represented

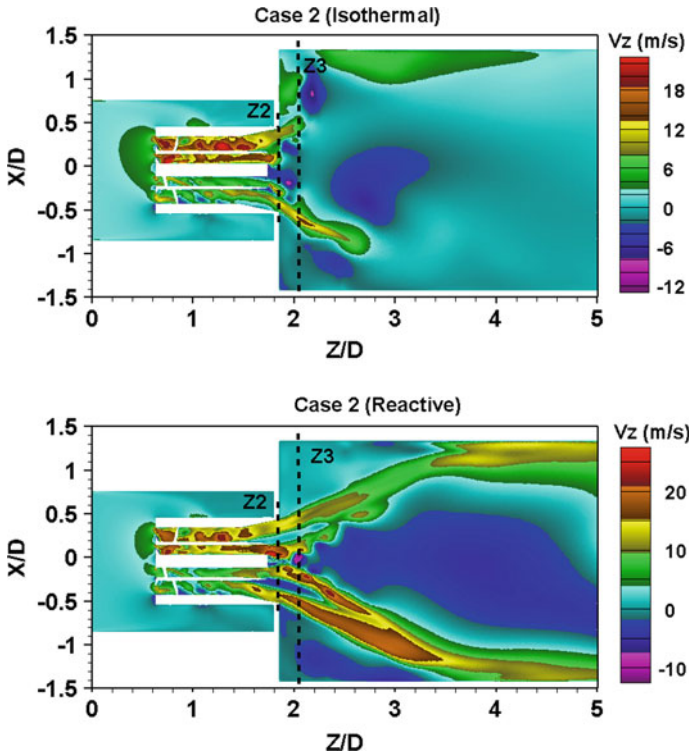


Fig. 4 Comparison of streamwise isothermal and reactive flow axial velocity contour for case 2. The coordinates are normalized by $D = 54\text{ mm}$

by blue color. The width of CRZ is $\pm 0.2D$ at the burner exit ($Z/D = 1.84$) which increases up to $\pm 0.75D$ at $Z/D = 3.5$. It is necessary to note these observations for size and strength of CRZ. Addition of highly reactive fuels like hydrogen to methane causes the upward shifting of the CRZ and also affects its size and strength which forms the basis for flashback [13]. Outside the CRZ, an annular jet emerges from the burner as indicated by green, yellow, and orange colors.

Changes in the temperature and density as a result of combustion heat release causes changes in the velocity flow fields when compared to isothermal conditions. For the reactive fields, the CRZs are strong for both the cases and differ in size and location relative to the burner exit when compared to isothermal cases. For the reactive cases, the CRZ is lifted and is narrowed near the burner exit. Its size becomes remarkably smaller, only $\pm 0.05D$ compared to $\pm 0.2D$ for the isothermal case at the exit. Further downstream, its size reduces. The CRZ is pushed downstream in the combustor with higher flow rates as can be seen for case 2. This reduces the chances of its upstream propagation through intermediate and inner swirler tips.

Figure 5 represents the velocity distribution at the exit plane of the burner (marked as Z2 in Figs. 3 and 4). The distribution shows the presence of CRZ with negative axial

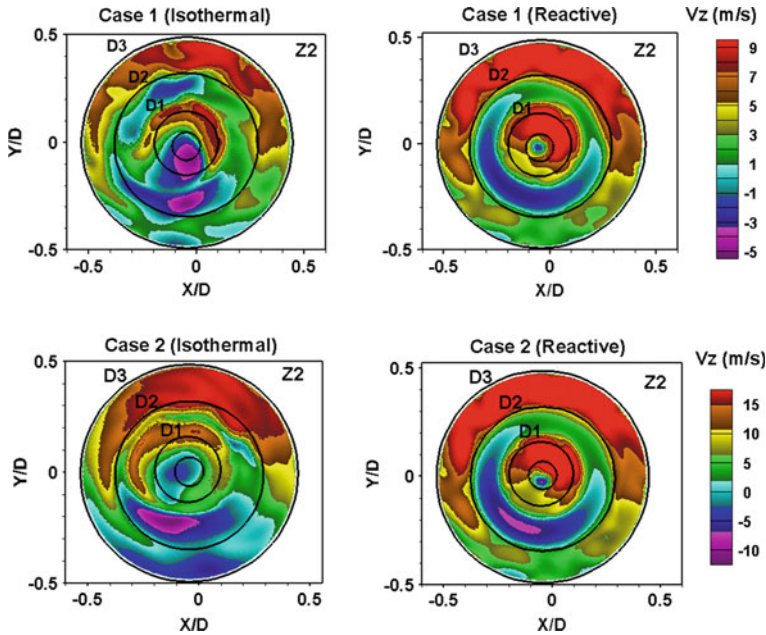


Fig. 5 Comparison of crosswise axial velocity contours at the exit of the burner (plane Z2) for isothermal and reactive flows. The coordinates are normalized by $D = 54$ mm

velocity around the axis of the burner. The strength of CRZ is low for reactive cases at burner exit confirming the lifting and constriction of CRZ in reactive flows. The non-uniformity of velocity distribution at the burner axis is captured by these contours. 2–4 velocity peaks can be observed at the burner exit. These peaks can be associated with the vane angles and number of vanes [8]. The flow generated by the swirlers was not completely mixed at the exit resulting in non-uniform flow with velocity values higher at certain regions. Such non-uniformities were also reported for TARS in various numerical and experimental studies [8, 10, 12]. For both isothermal and reactive flows, the reverse velocity regions at swirler tips (D1 and D2) are pronounced indicating the presence of a possible route to flashback and flame anchoring location. Improvements in the burner design need to be made for mitigating this flashback route.

The turbulent kinetic energy contours are representatives of the distribution of total turbulence from burner exit. Figure 6 represents the comparison of these contours for isothermal and reactive cases. From isothermal cases, it can be observed that the turbulence is robust at inner shear layer between annular jet and CRZ, whereas it is lowest inside CRZ. This intensity in the shear layer is nearly twice the level in CRZ for both the cases. This result agrees with the TARS configuration [17].

Combustion affects the distribution of turbulent kinetic energy by clearly defining the low- and high-turbulence velocity regions (Fig. 6) and disperses the turbulence

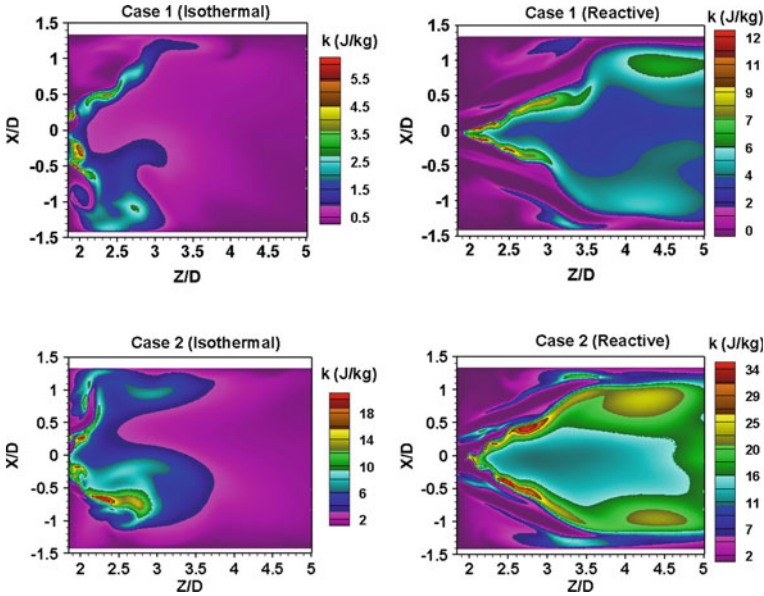


Fig. 6 Comparison of turbulent kinetic energy contours for isothermal and reactive flows inside the combustor

field into patches of turbulent regions. Like isothermal flows, the annular jet has higher turbulence compared to the inside of CRZ. Similar effect of combustion on turbulence is observed in TARS [17].

To quantify the observations from the velocity contours, spatially averaged axial and tangential velocity profiles are plotted for isothermal and reactive flows and are presented in Fig. 7. These profiles are obtained at Z2 and Z3 planes as marked in Figs. 3 and 4. Since, mass flow rates are not constant for the cases considered, all the velocity values have been normalized by $V_0 = 7.1\text{ m/s}$ (case 2) for comparison purposes.

As observed from crosswise contours, the velocity distribution has 4 peaks along the burner diameter and reversed flow at the swirler tips (D1 and D2 in isothermal and D2 in reactive flows, respectively) are also visible. These peaks are defined in Fig. 7. For reactive flows, positive velocity peaks are observed at the center of the burner unlike isothermal profiles even though the mass flow rates are constant for a particular case. The reason for this trend of velocity profiles can be explained by the temperature contours (Fig. 9). For reactive flows, the flame is found to flashback through the inner and intermediate swirler passages and is anchored inside the burner. Due to higher temperature regions at the tips of swirlers, the density reduces resulting in the increase in velocity and mass flow rates. The radial motion of the swirling flow is also observed to be enhanced remarkably by combustion (as observed from tangential profiles—red and green markers). Although the boundary conditions are

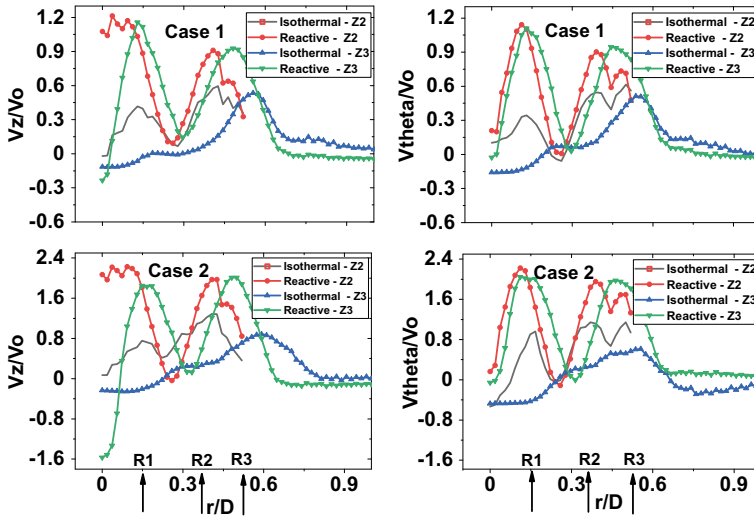


Fig. 7 Comparison of radial profiles of axial (left) and tangential velocities (right) for isothermal and reactive flows. Z2 and Z3 are the planes at burner exit and, in the combustor, respectively, as marked in Figs. 3 and 4. The velocity values are normalized by V_0

symmetric, yet flow fields are found to be non-uniform. These non-uniformities are typical for this design and are not observed in TARS.

5.2 Experimental Validation of Velocity Field

Figure 8 presents the comparison of mean axial velocity profiles obtained from RANS simulations and experiments at $Z/D = 0.05, 0.1,$ and 0.2 downstream the burner exit (consider the coordinates to be placed at the center of the burner exit). The plots characterize the non-uniform features of the flow field. The axial velocity mapping indicates a CRZ with reverse velocity. The width of CRZ increases on moving in downstream direction. Velocity profiles obtained from RANS simulations matches with the experimental profiles except for the location of peak velocity.

The velocity distribution from RANS simulations indicates the presence of separated flow at the boundaries of the swirlers (D1 and D2). This flow separation leads to the inward shifting of annular jet resulting in velocity displacement. However, no such flow separations are observed in experimental results (Fig. 8) indicating the attached flow. This disagreement between the RANS simulations and experimental results suggests the incapability of RANS to predict accurate behavior of turbulent swirling flow near a diverging region. Therefore, the next step would be to use the data obtained from experiments as inlet boundary conditions numerical model validation using LES.

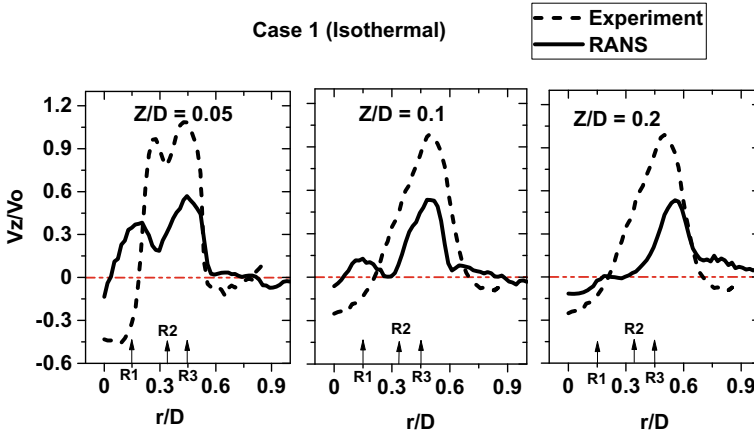


Fig. 8 Comparison between isothermal experiments and RANS simulation results for axial velocity profiles for Case 1 at different axial locations in the combustor. The coordinates are normalized by $D = 54\text{ mm}$ and velocity value by V_0

5.3 Temperature Distribution

Figure 9 shows the temperature distribution for reactive case 1 and 2 in the combustor. The temperature is uniformly distributed inside the combustor on both the sides of the burner axis and peak temperatures of around 2300 K and 1900 K are observed for the two cases, respectively. From the contours, it is observed that the flame is flashing back through the tips of inner and intermediate swirlers. The flame is stabilized at the inner shear layer between the swirling jet and CRZ, and at outer shear layer with the surrounding air and is anchored inside the burner. We are using adiabatic conditions for simulations therefore the difference in peak temperatures is possible. In practice, most burners would operate in the range of $\Phi = 0.6 - 0.65$ to bring down those temperatures, besides they would operate with an increase in pressure that would also reduce the flame size, thus controlling turbulence and mitigating large temperature spots. Therefore, we require some experiments for calibration of the model, including some temperature profiles of the casing/burner to determine heat transfer and more realistic values. This will be assessed through experimentations in further work. The temperature drops in the shear layers as can be visualized from radial profiles. Beyond the burner radii, the temperature field is constant and is toward the lower side. These observations from the contours suggest that the present configuration requires design modifications in terms of swirl number and Reynold's number. The higher flow rates may help in reducing the flashback issue but this may not help with higher reactive fuels.

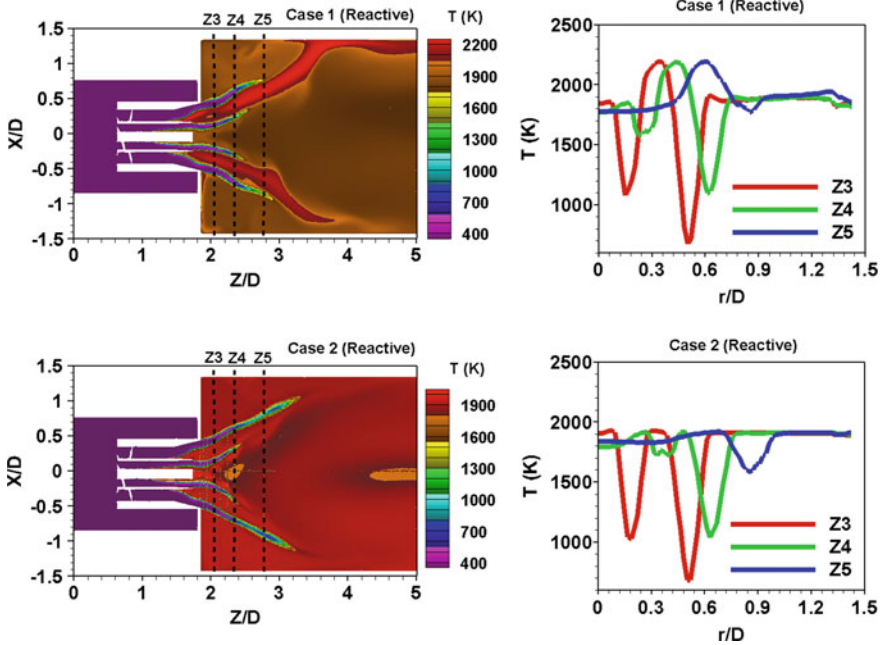


Fig. 9 Comparison of temperature distribution and its averaged radial profiles for reactive flow cases 1 and 2. The coordinates are normalized by $D = 54\text{ mm}$

5.4 NOx Emission Profiles

The methodology to determine NO_x (NO, NO₂, etc.) was through the resolution of the complex chemistry, thermodynamics, and transport properties of the complex mechanism. Figure 10 represents the radial profile of NO₂ emissions for the reactive flow case 2 at two axial locations farther downstream the burner exit. As the peak temperatures for case 2 lies within the range of 1800–1900 K, at an equivalence ratio of 0.75, the emission range is as expected, i.e., up to 4 ppm [20]. The emissions are higher near the burner center and reduce toward the walls of the combustor. NO₂ emissions increase exponentially with flame temperature. The contours for NO_x emission suggest that the emissions are within the reasonable range for lean premixed mixtures.

5.5 Shear Layer Dynamics

Figure 11 shows the characteristic features of a swirling jet. These features include an annular jet that emanates from the nozzle exit and passes between recirculation zones (inner (IRZ) and outer (ORZ)). The IRZ is associated with the interactions between

Fig. 10 Comparison of radial profiles of NO₂ emissions for reactive case 2 at two axial locations in the combustor: $Z/D = 2.78$ (Z_5) and $Z/D = 3.70$

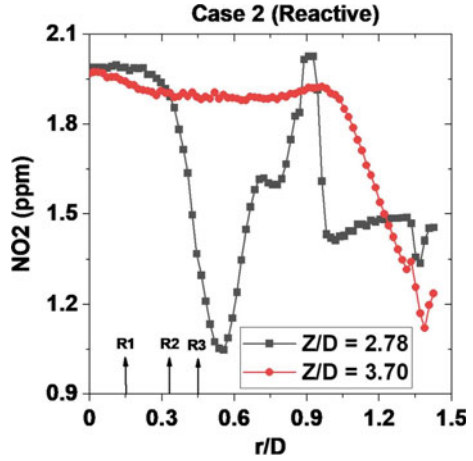
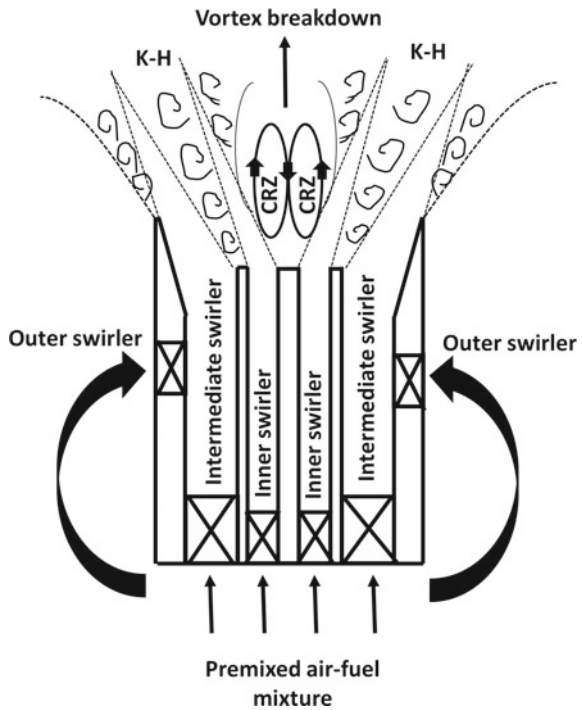


Fig. 11 Schematic representing features of a swirling jet. K-H indicate Kelvin–Helmholtz instability. This figure is reproduced from O’Conner et al. (2011) for triple swirl burner



vortex breakdown bubble (VBB) and center-body wake. This flow field forms the base flow in which the perturbations can grow or decay. Leibovich [15] and Rusak and Wang [22] presents an extensive study on VBB and instabilities. The size and location of VB is dependent on the swirl intensity, axial pressure gradient, geometrical features, and Reynold’s number [19]. Streamwise and spanwise shear layers separates

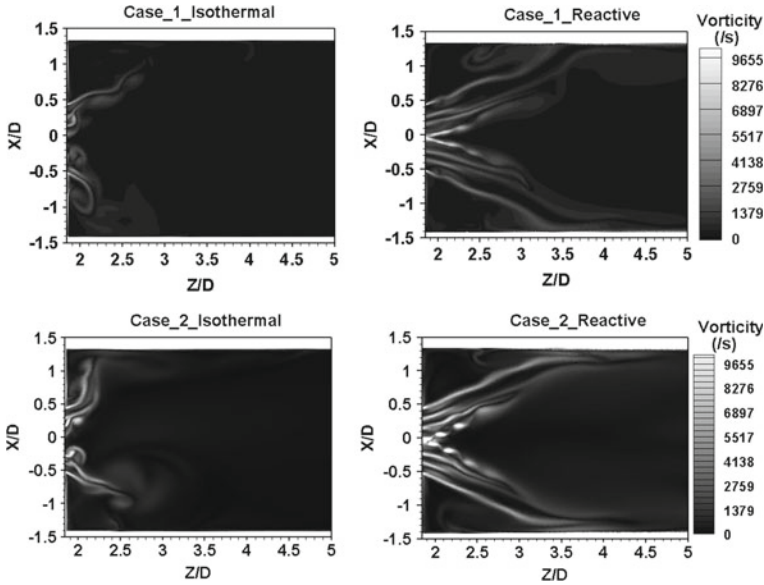


Fig. 12 Comparison of streamwise vorticity contours for shear layer visualization between isothermal and reactive flows. The coordinates are normalized by $D = 54$ mm

the annular jets and RZ. The shear layers are unstable and are associated with vortex rollup and forms concentrated regions of vorticity [9]. The flame is stabilized at inner shear layer between annular jet and CRZ and at the outer shear layer separating ORZ.

In the present study, the shear layer dynamics is presented by plotting the streamwise vorticity contours for isothermal and reactive flows. Figure 12 represents the comparison for the contours. The wrinkling of the shear layers is associated with vortex roll up that are convected in the downstream direction. Figure 12 clearly represents the vortex rollup phenomena. The beginning of the vortex rollup in inner shear layer (ISL-between CRZ and swirling jet) is clearly visible in the figure. These vortices grow as they convect downstream. These vortices are larger in size due to their interactions with CRZ. The presence of additional shear layers between inner and outer layers are indicative of multiple swirl passages in the burner.

Figure 13 shows the azimuthal shear layer through cross stream vorticity contours at two axial locations inside the combustor: $Z/D = 1.94$ and $Z/D = 2.04$ for reactive flows. The inner and outer shear layers along with two additional shear layers are clearly demarcated. These additional shear layers are generated due to multiple swirl passages and boundaries in the burner. The structures in these layers are larger in size and can be seen to roll up as the flow rotates. Due to the interaction of ISL with CRZ, the vortical structures in ISL are large and more diffuse. Figure 14 represents the vorticity profiles for the reactive cases along the line marked on Fig. 13. The presence of large vortical structures can be clearly seen in ISL with high magnitude of vorticity.

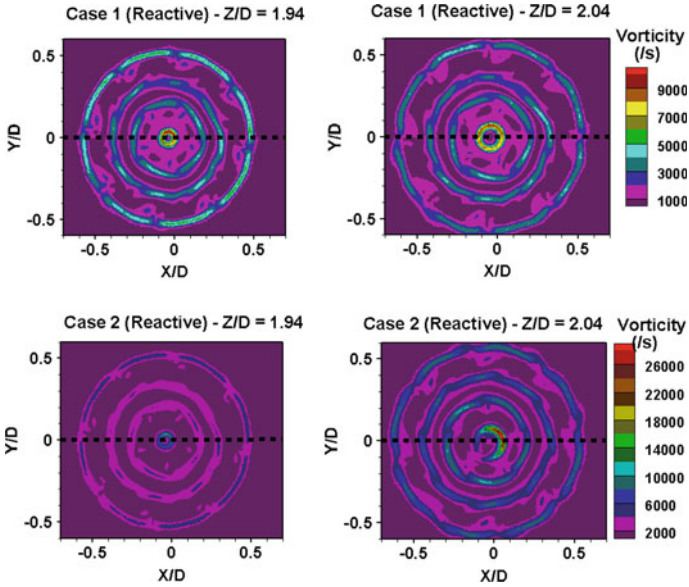


Fig. 13 Cross wise vorticity contours at two axial locations in the combustor: $Z/D = 1.94$ and $Z/D = 2.04$. The coordinates are normalized by $D = 54$ mm

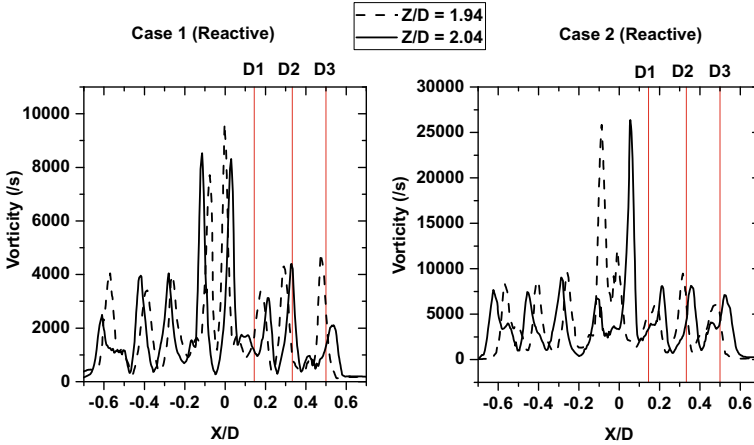


Fig. 14 Vorticity profiles for reactive flows at the locations marked in Fig. 13. The coordinates are normalized by $D = 54$ mm

Thumuluru and Lieuwen [25] have experimentally reported four flame topologies based on the position of VBB. The flame is anchored at the stagnation point behind the VBB, if it is detached from the center body. On the contrary, if the VBB is attached to the center body, the flame is stabilized in one or both the shear layers.

In the present configuration, VBB is attached to the inner swirler body, and flame is stabilized in the ISL. The flame has a tendency to stabilize on the intermediate swirler rim, thus creating an adverse effect on burner body. Higher flow rates and modifications in the burner are required to increase the Reynolds number.

6 Concluding Remarks

The abovementioned behavior of swirlers highlights the importance of parameters that govern these flows: swirl numbers, number of swirl vanes, the inlet boundary conditions, velocity profiles, and shear layer dynamics. Swirl of sufficient strength induces an adverse pressure gradient which causes vortex breakdown and flow reversal. This work aims at developing a generic fuel flexible swirl burner which can be operated in premixed or non-premixed modes and have stable combustion with minimum flashback. Toward this aim, a preliminary design of the burner employing three swirlers was proposed and corresponding mean flow fields were investigated with the help of RANS simulations. Compared to the top-hat velocity profiles, the triple swirl burner's profiles involve complex features. The isothermal and reactive flow fields indicate the upward propagation of recirculation zones causing the flame to stabilize inside the burner. This upstream propagation is not as severe as that of TARS but is a crucial consideration especially when dealing with higher reactive fuels. Higher temperature ranges are observed which may lead to higher NO_x emissions but as the present cases are simulated for adiabatic conditions, practical assessment of the burner will help in estimating the actual temperatures. The RANS simulation results are also validated using initial isothermal experiments, and the results were found to be well in agreement.

The ongoing work address appropriate methods to improve the flow fields. The issues to be explained relate to mitigating any chances of flashback, incorporating liquid and gaseous fuels injection locations, and using suitable laboratory data for LES simulations.

Acknowledgements This work is funded by SPARC project (No: SPARC/2018-2019/P243/SL) sponsored by MHRD. The simulations and experimental investigations were conducted at GTRC, Cardiff University.

References

1. Anacleto P, Fernandes E, Heitor M, Shtork S (2003) Swirl flow structure and flame characteristics in a model lean premixed combustor. *Combustion Sci Technol* 175(8):1369–1388
2. Asai T, Miura K, Akiyama Y, Karishuku M, Yunoki K, Dodo S, Horii N et al (2016) Development of fuel-flexible gas turbine combustor. In: *Proceedings of the 45th turbomachinery symposium, Turbomachinery Laboratories, Texas A&M Engineering Experiment Station*
3. Beér JM (1974) Combustion aerodynamics. In: *Combustion technology*. Elsevier, pp 61–89

4. Bray K (1996) The challenge of turbulent combustion. In: Symposium (international) on combustion, vol 26. Elsevier, pp 1–26
5. Driscoll J, Temme J (2011) Role of swirl in flame stabilization. In: 49th AIAA aerospace sciences meeting including the New Horizons forum and aerospace exposition, 108
6. Duwig C, Fuchs L, Lacarelle A, Beutke M, Paschereit CO (2007) Study of the vortex breakdown in a conical swirler using ldv, les and pod. *Turbo Expo: Power Land Sea Air* 47918:1–10
7. Global E (2020) Hydrogen gas turbines: the path towards a zero-carbon gas turbine. *ETN Global 2*
8. Grinstein FF, Young TR, Gutmark EJ, Li G, Hsiao G, Mongia HC (2002) Flow dynamics in a swirl combustor. *J Turbulence* 3(1):030
9. Ho CM, Huang LS (1982) Subharmonics and vortex merging in mixing layers. *J Fluid Mech* 119:443–473
10. Iudiciani P (2012) Swirl stabilized premixed flame analysis using of LES and POD. Lund University
11. Iudiciani P, Duwig C, Szász RZ, Fuchs L, Gutmark E (2011) Les of the interaction between a premixed flame and complex turbulent swirling flow. *J Phys: Conf Ser* 318:092007 (IOP Publishing)
12. Iudiciani P, Hosseini SM, Zoltan-Szasz R, Duwig C, Fuchs L, Collin R, Lantz A, Alde' n M, Gutmark E (2009) Characterization of a multi-swirler fuel injector using simultaneous laser based planar measurements of reaction zone, flow field, and fuel distribution. In: *Turbo expo: power for land, sea, and air*, vol 48838, pp 1041–1052
13. Kim HS, Arghode VK, Linck MB, Gupta AK (2009) Hydrogen addition effects in a confined swirl-stabilized methane-air flame. *Int J Hydrogen Energy* 34(2):1054–1062
14. Kundera C, Kozior T (2018) Mechanical properties of models prepared by sls technology. In: *AIP conference proceedings*, vol 2017. AIP Publishing LLC, 020012
15. Leibovich S (1978) The structure of vortex breakdown. *Ann Rev Fluid Mech* 10(1):221–246
16. Li G, Gutmark EJ (2005) Effect of exhaust nozzle geometry on combustor flow field and combustion characteristics. *Proc Combustion Inst* 30(2):2893–2901
17. Li G, Gutmark EJ (2006) Boundary conditions effects on nonreacting and reacting flows in a multiswirl combustor. *AIAA J* 44(3):444–456
18. Martinelli F, Olivani A, Coghe A (2007) Experimental analysis of the processing vortex core in a free swirling jet. *Exp Fluids* 42(6):827–839
19. OConnor J, Lieuwen T, Kolb M (2011) Visualization of shear layer dynamics in a transversely excited, annular premixing nozzle. In: 49th AIAA aerospace sciences meeting including the New Horizons forum and aerospace exposition, 237
20. Ouali S, Bentebbiche A, Belmraet T (2016) Numerical simulation of swirl and methane equivalence ratio effects on premixed turbulent flames and nox apparitions. *J Appl Fluid Mech* 9(2)
21. Pritchard Jr BA, Danis AM, Foust MJ, Durbin MD, Mongia HC (2002) Multiple annular combustion chamber swirler having atomizing pilot. US Patent 6,381,964
22. Rusak Z, Wang S (1996) Review of theoretical approaches to the vortex breakdown phenomenon. In: *Theoretical fluid mechanics conference*, 2126
23. Shtork S, Vieira N, Fernandes E (2008) On the identification of helical instabilities in a reacting swirling flow. *Fuel* 87(10–11):2314–2321
24. Syred N, Giles A, Lewis J, Abdulsada M, Medina AV, Marsh R, Bowen PJ, Griffiths AJ (2014) Effect of inlet and outlet configurations on blow-off and flashback with premixed combustion for methane and a high hydrogen content fuel in a generic swirl burner. *Appl Energy* 116:288–296
25. Thumuluru SK, Lieuwen T (2009) Characterization of acoustically forced swirl flame dynamics. *Proc Combustion Inst* 32(2):2893–2900
26. Venkatesan K (2011) Fuel flexible combustion systems for high-efficiency utilization of opportunity fuels in gas turbines. Technical report, General Electric Company, Boston, MA (United States)
27. Zimont VL (2000) Gas premixed combustion at high turbulence. turbulent flame closure combustion model. *Exp Thermal Fluid Sci* 21(1–3):179–186

Sheet Atomization of Gel Propellant Simulant



K. Vivek, Aditya Saurabh, Devendra Deshmukh, Deepak Agarwal,
and Lipika Kabiraj

Abstract Gelled propellants for rocket propulsion applications offer the advantage of safer storage and handling in comparison with liquid fuels. Sheet formation and break-up study of non-reactive gel simulant prepared with Carbopol 934 in de-ionized water was conducted for understanding atomization of gels by impinging jets configuration. Material properties of gels prepared and their flow behavior estimated. The simulant is injected through an orifice of 0.413 mm up to a range of 20 bar injection pressure is studied by analyzing high-speed shadow graph images of liquid jets impingement, sheet formation, and disintegration. The prominent effect of gelling agent concentration in sheet formation and break-up is revealed. Sheet break-up is occurring in two different modes for five different gel concentrations. Waves generated from impingement point caused break-up of sheets for low-concentration gels and high-velocity jets while tearing and hole formation in sheets led to their break-up for mostly high-concentration gels and particularly for low jet velocity modes. Droplet trajectories and their velocity at various locations in the periphery of sheets were measured for two different jet velocities for five gel concentrations.

Keywords Gel propellants · Atomization · Non-Newtonian

K. Vivek (✉) · L. Kabiraj
Indian Institute of Technology Ropar, Ropar, Punjab 140001, India
e-mail: 2018mez0025@iitrpr.ac.in

L. Kabiraj
e-mail: lipika.kabiraj@iitrpr.ac.in

A. Saurabh
Indian Institute of Technology Kanpur, Kanpur 208016, India
e-mail: asaurabh@iitk.ac.in

D. Deshmukh
Indian Institute of Technology Indore, Indore, Madhya Pradesh 453552, India
e-mail: dldeshmukh@iiti.ac.in

D. Agarwal
Indian Space Research Organization, Valiamala, Kerala 695547, India

© The Author(s), under exclusive license to Springer Nature Singapore Pte Ltd. 2023
G. Sivaramakrishna et al. (eds.), *Proceedings of the National Aerospace Propulsion Conference*, Lecture Notes in Mechanical Engineering,
https://doi.org/10.1007/978-981-19-2378-4_35

1 Introduction

In rocket propulsion, the requirement of energy dense and safe to operate fuel is of utmost importance. Gelled propellants offer these two essential qualities and qualify for further study of their atomization and combustion characteristics. The non-Newtonian nature of gelled propellants, along with yield stress, allows its storage like solid materials for which safety issues like leakage, sloshing, and spilling are non-existent. Having addressed these issues takes these gel propellants to the next level of requirement of a fuel which is the atomization capability. Fuel drop size and its distribution are a big concern for liquid fuels. High viscosity and shear thinning behaviors play advantage and disadvantage from the atomization angle. The impinging fluid jet configuration has better oxidizer fuel mixing and atomization capabilities. The liquid disintegration process depends on liquid injection pressure, injector design, and liquid properties. The studies include sheet dimensions like break-up length, sheet width, droplet formation sites, droplet velocity distribution, droplet size, and distributions. Liquid propellants are Newtonian, whereas, gelled propellants are non-Newtonian. Water is a simulant for propellant simulant as its physical properties are similar. Preparation of gelled propellant simulants involves a simulant for the propellant and a gelling agent which will dissolve in the propellant simulant.

Various reports about studies on the impinging jet of Newtonian liquids are fundamental steps for the non-Newtonian liquids. Reference [1] reported four different spray regimes for three different fluids with different physical properties. These regimes were closed rim pattern, periodic drop regime, sheet rim separation, and fully developed regime within a jet velocity range of 1.5–30.5 ms⁻¹. Sheet width and sheet length increase as jet velocity increased and reach a maximum value before fully developed flow. Hydrodynamic waves were observed above a critical liquid jet Weber number. Reference [2] study on impinging jet up to a jet velocity of 25 ms⁻¹ found that sheet break-up length increases with velocity and decrease of impingement angle. Theoretical study of two cylindrical impinging jets of fluid by [3] showed two break-up regimes. A low Weber number regime sheet dimensions were similar to experimentally measured values reported earlier, and the break-up is due to Taylor cardioidal waves, and a high Weber number break-up regime where break-up was due to Kelvin–Helmholtz instability. A study by [4] on Newtonian fluids with an impingement angle of 90° using 0.5 mm diameter injector showed ten different spray patterns, mostly subcategories found by [1]. For different surface tension and viscosity fluids, the sheet formed by impinging jets had a constant sheet length to width ratio for an increase in jet velocity, and this ratio increased with an increase in jet velocity.

Carbopol 941 in water described as power law fluid was used [5] to simulate RP-1 gelled fuel and water as RP-1 and reported low atomization quality because of high viscosity [6]. Carbopol 941 gel was also used as a simulant. A low break-up tendency of liquid was observed, which was attributed to higher intermolecular forces within the gel. Gelled kerosene loaded with Al particles and was atomized [7]

by impinging liquid jets from an injector of orifice 1.5 mm for a jet velocity range of $10\text{--}20\text{ ms}^{-1}$. High shear rates induced in the gel while flowing and impingement reduced the viscosity and mean droplet diameter. Ostwald and HB models were found suitable to describe the rheological behavior of Carbopol gels [8]. In [9], the HB model explained metalized gelled jet A1 fuel and observed a reduction in viscosity for increased shear rates. They identified three different spray patterns: ray shaped, ligament pattern, and a fully developed pattern for low, medium, and high generalized Reynolds number (Eq. 1). Various Newtonian liquids were studied [10] with an impinging jet configuration using 1 mm orifice injector. Regimes, namely ray shaped structure, rim and droplet separation, rimless separation, ligament structure, and fully developed patterns, are identified under a Reynolds Number and Weber number plot [11]. Study on Carbopol 941 was conducted with a triplet impinging set up with an orifice diameter of 1.1 mm.

They observed a delay in liquid break-up and atomization and explained that it was due to the gel's higher viscosity. Spray patterns with rims are also identified. Comparison [12] of sheet formation and disintegration of gelled and non-gelled water reported lesser disturbances in the sheet due to higher viscosity. For an increase in Reynolds number, break-up length was found to decrease. Carbopol 934 gel loaded with SUS302 nanoparticles was used [13] to study the rheological characteristics. Shear-thinning nature and presence of yield stress was reported, and the gel was described as HB fluid. The extended HB model was used to explain paraffin, jet A-1, and ethanol-based gelled fuels [14]. This extended model was mentioned to take consideration of whole range of shear rates occurring in propulsion application. Carbopol 934 gel atomization by impinging jets was compared with that of water [15]. The sheet length was found to increase with an increase in jet velocity. Four types of spray patterns were identified: open rim and no shedding drop; rimless sheet with ray shaped shedding; sheet with ligament separation; fully developed. Mean droplet diameter was also decreasing with an increase in jet velocity and converged to an asymptotic number. Carbopol gel was studied [16] and saw that the linear stability analysis method yield similar results to that of experimental for sheet break-up length and wavelength of power-law sheets. The break-up length and wavelength were found to decrease with an increase in Weber number. An impinging jet study [17] with Carbopol 934 solution using 0.6 mm orifice injectors and showed the existence of six types of spray pattern; open rim without shedding droplet, closed rim, open rim with shedding droplet, rimless sheet, bow-shaped ligament, and fully developed. The flow behavior under shear was described using power law. They also measured droplet velocities across various axes and observed higher velocities for larger droplets. The impact wave regime of impinging jets of gelled rocket propellant ISROsene loaded with alumina particles and had the wave propagation velocity to be slower than that of jets [18]. Break-up length increased with Weber number. An SMD of $200\text{--}400\text{ }\mu\text{m}$ was also observed [19]. In sheet formation of gel propellant, two new regimes were discovered, open rim with holes, and impact wave with longitudinal ligaments. Uneven distribution of mass or clustering of particles was seen as the reason for these regimes.

With this information, a detailed study on Carbopol 934 gel's atomization is conducted on a doublet like on like impinging jet configuration. Liquid sheet break-up, droplet velocity, and trajectory for different gelling agent concentrations under a range of injection pressures are studied.

2 Experiments and Setup

Carbopol 934 is an acrylic acid polymer soluble in water. Gel simulants are prepared using this gelling agent. A measured amount of gelling agent is mixed with de-ionized water (18.2 M Ω) by continuous stirring at 800 rpm using a magnetic stirrer. Stirring is continued up to twelve hours for proper dilution of the gelling agent. The pH of the solution is maintained neutral by the addition of Triethanolamine (TEA). The addition of TEA will produce a clear gel. After preparation of gel, it is stored in an airtight container. Gel samples with Carbopol concentration varying from 0.10 to 0.35 wt% by weight were prepared and stored. The surface tension of these samples was measured by pendant drop test in FTA1000 series contact angle instrument by First Ten Angstrom. This instrument uses the Laplace-Young equation to calculate surface tension. Variation of viscosity with the shear rate for each gel concentration is studied by rotational rheometer. Parallel plate geometry with 50 mm diameter flat plates and a gap of 1 mm between the plates is set for all measurements. A constant pre-shear of 10 s⁻¹ is given for 100 s to the sample to remove any shear history. An idle time of another 100 s will ensure the reversal of all stress. The sample is made to undergo a rotational shear rate test with shear rates increasing logarithmically from 0.001 to 1000 s⁻¹ in a duration of 3000 s.

A view of schematic diagram for spray characterization of two impinging jets in like on like configuration is shown in Fig. 1. Liquid fuel is stored in a 70 mm bore stainless steel cylinder. Pressurized nitrogen gas displaces an aluminum piston inside the cylinder for a maximum length of 300 mm. This piston drives out the liquid from the cylinder through two polyurethane tubes of 9 mm inner diameter whose other ends are connected to two nozzles of 0.41 mm. The impingement angle and pre-impingement length can be varied, and for the study, 2θ was kept at 90°, and the pre-impingement length was 10 mm. An ultrasonic sensor tracked the movement of piston. Pressure transducers mounted at reservoir exit. A valve connected at the end of the cylinder restricts the flow of fluid. The fluid coming out through the orifices is collected in a vessel which is kept below the impingement location, and one nozzle entrance shows corresponding pressure values.

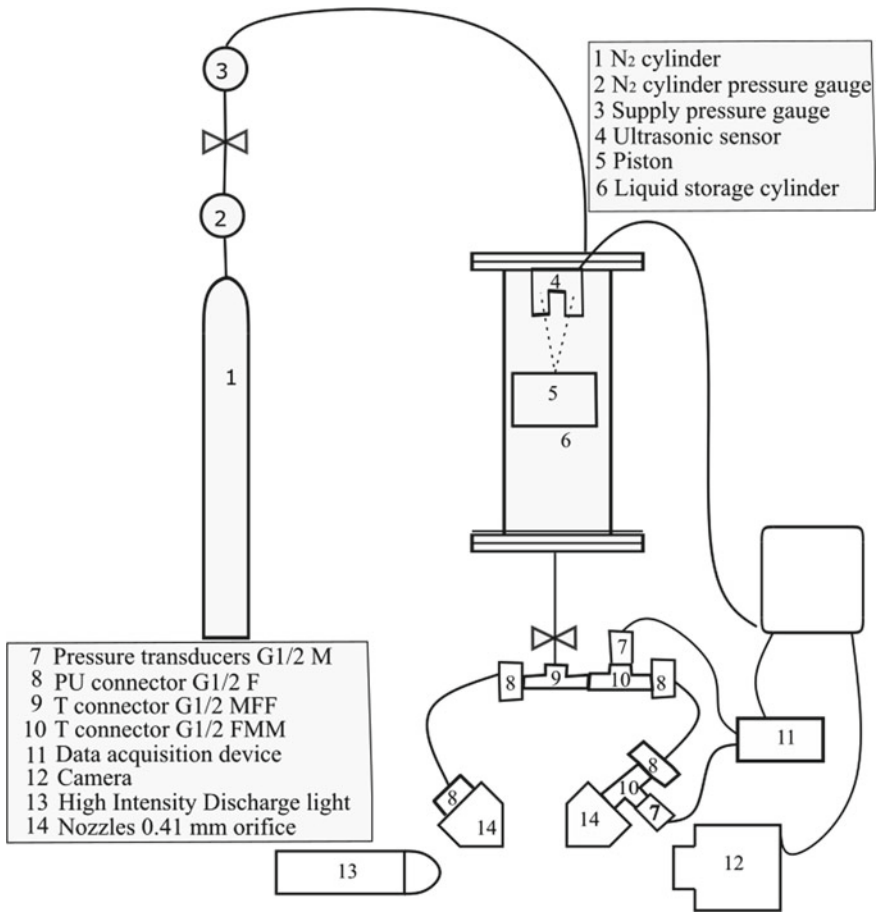


Fig. 1 Schematic diagram of atomization equipment and image acquisition

3 Experiments and Setup

3.1 Rheology Measurements

Results from rheology measurements of gel concentrations (0.10–0.35 wt%) confirmed the fluid’s shear-thinning nature. Test up to a shear rate of 1000 s⁻¹ showed that viscosity is continuously decreasing with an increase in shear rate. Figure 2 shows the viscosity-shear rate trends for gel concentrations on a log scale. As the concentration of the gelling agent increases, the viscosity is also found to be increasing. Kim et al. (2003) observed that more gelling agents increase the network structure inside the gel, thus requiring more shear stress to break the structures and

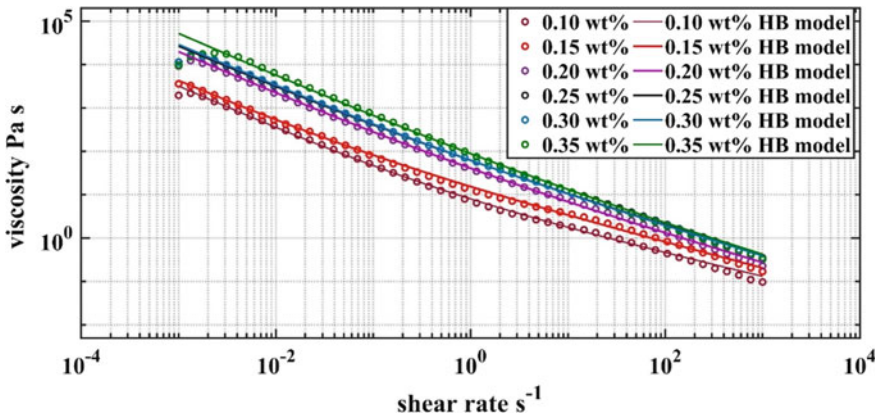


Fig. 2 Viscosity-shear rate trend and corresponding HB fluid model fit

flow. Herschel–Bulkley model is fitted to the experimental data point, and parameters describing the HB model are obtained. The model is given in Eq. 2.

$$\mu = \frac{\tau_0}{\dot{\gamma}} + K \dot{\gamma}^{n-1}. \quad (1)$$

The presence of yield stress was noted for all gel concentrations tested. The value of yield stress increased with an increase in gel concentration. For 0.10 wt% gel, the yield stress is 3 Pa, which is very low, and for 0.35 wt% the value for yield stress is found to be 48 Pa. This shows that as gel concentration increases, the gel behaves more like solid and more amount of initial stress is required to overcome the yield stress and make the gel start flowing. In Fig. 2, when the shear rate reached the maximum value, all the cases viscosity dropped below 1 Pa s. It is expected that a further increase in shear rate will take the viscosity value to a much lower level compared to that of water, which is the base fluid of the Carbopol gel. As gel travels through the nozzle and impinges, a high shear rate is expected to occur, which will reduce viscosity and thus atomization of the gel. As gel concentration increases, the exponent index, n , is decreasing. This shows that the liquid viscosity is getting more sensitive to change in shear rates. The HB model fit parameters are presented in Table 1. The density of the gel concentrations is taken to be 1000 kg m^{-3} and all measurements are carried out at a temperature of $25 \text{ }^\circ\text{C}$.

3.2 Jet Velocity

The graphical relation between injection pressure and jet velocity of fluids studied is shown in Fig. 3. It is clear from the figure that the initial injection pressure required to

Table 1 HB model parameters for gel concentrations

Carbopol (wt%)	Yield stress (Pa)	Consistency factor (Pa s ⁿ)	Exponent index
0.10	3.001	5.01	0.47
0.15	3.571	11.83	0.41
0.20	17.82	22.82	0.35
0.25	22.63	39.3	0.32
0.30	25.25	37.11	0.33
0.35	48	40.25	0.32

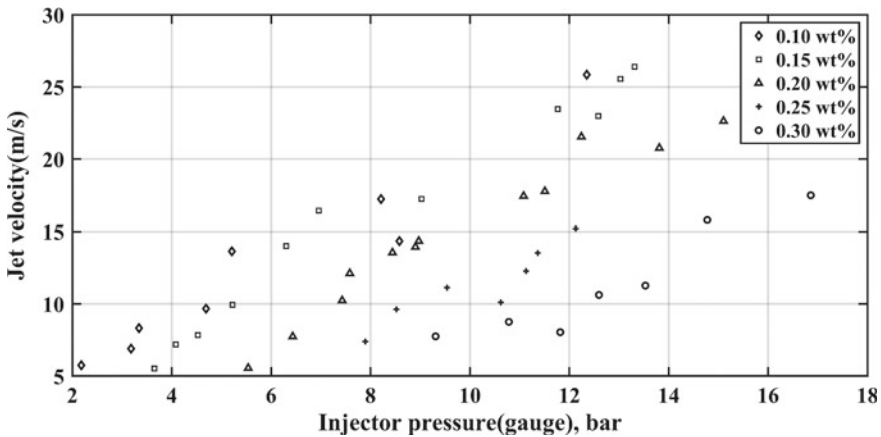


Fig. 3 Injection pressure versus jet velocity for five gel concentrations

make the liquid flow through the orifice increases for an increase in gallant concentration. For a concentration above 0.10 wt%, the existence of yield stress is shown. The shear-thinning nature of gels prepared and the existence of yield stress confirms the excellent selection of fluid model selected for this work. The increase in yield stress is due to the increased quantity of gelling agents which creates more network-like structures in the fluid. To break the firm structures, initial stress is required. After breaking the bonds, the liquid starts to flow. Measurements conducted were for low jet velocity range, 5–30 ms⁻¹.

$$\text{Regen} = \frac{\rho v^{2-n} d_0^n}{K \left(\frac{3n+1}{4n}\right)^n 8^{n-1}} \tag{2}$$

As the gels under study are non-Newtonian power-law fluids, a non-dimensional form of flow can be represented by generalized Reynolds number as shown in Eq. (2).

3.3 Sheet Break-up

Figure 4 shows representative images of spray formed by impinging jets of all gel concentrations at various injection pressures, with each row representing one gel concentration and five distinct injection pressure conditions starting from 0.10 wt% gel and ending with 0.30 wt% gel. The impinging jets form liquid sheets on a plane perpendicular to the axis of liquid jets.

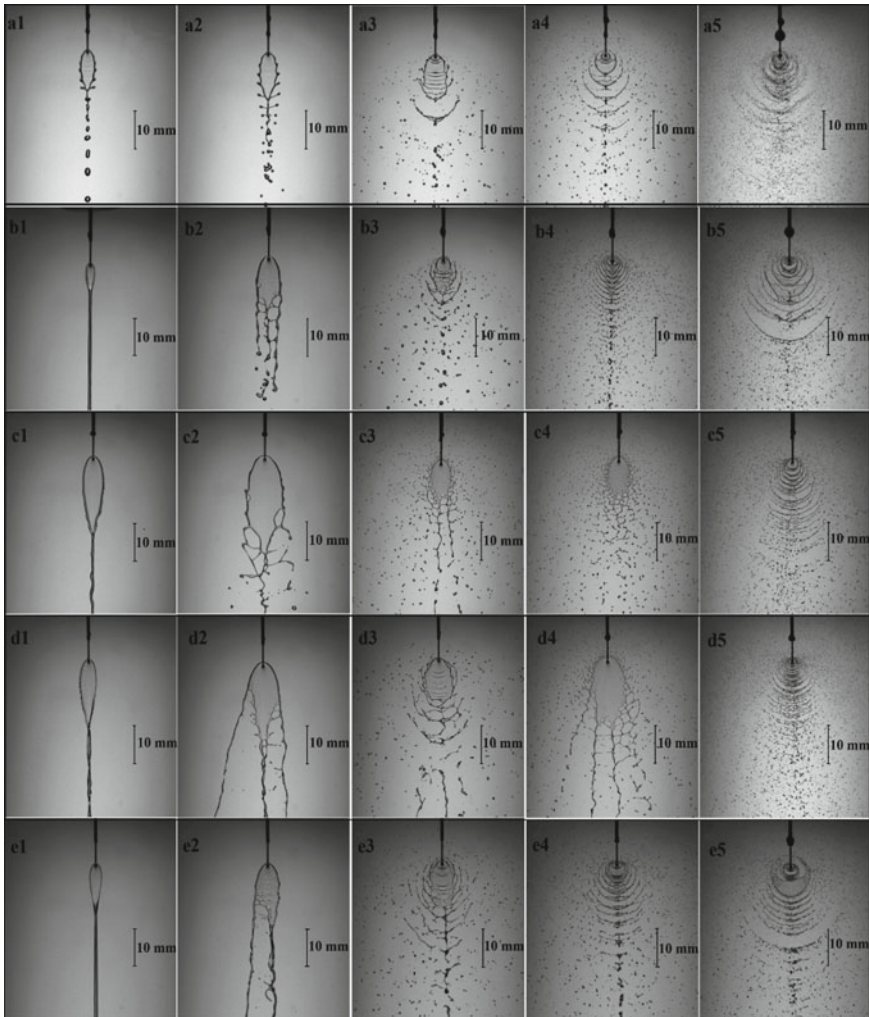


Fig. 4 Sheet break-up length and width representation for five gel concentrations. **a** 0.10 wt%, **b** 0.15 wt%, **c** 0.20 wt%, **d** 0.25 wt%, and **e** 0.30 wt%

The fluid elements are emerging from the impingement point spread in all directions for low jet velocities, as visible from Fig. 4. The vertical momentum of the liquid elements stretches the sheet a little above the impingement point. Note that sheet length is measured from the impingement point only (Fig. 4a1–a5). The liquid elements moving in the vertical direction above the impingement point in the sheet slowly lose their momentum and reach the rim of the sheet. These fluid elements then travel through the rim downwards and join other liquid elements that have lost momentum and continue to flow downward.

Any disruption in the jets is visible immediately on the rim. The horizontal component of velocity will slowly decay for fluid elements in the sheet. Only downward momentum persists, thus forming the sheet shape.

As jet velocity increases, the momentum of liquid elements also increases, resulting in the opening up of the bottom of the sheet. The fluid elements traveling in the rim have higher velocity, and this velocity helps them separate them from the hold of the liquid sheet. The sheet thickness near the rim must be less compared to other parts of the sheet. For higher concentration gels, the rim is seen to separate from the sheet without disintegration. Figure 4b2 shows the formation of perforations in the lower portion of the sheet. These perforations contain thin rims also.

Further increase in jet velocity is marked by a gain in momentum of fluid elements, which breaks out of the rim and spreads in the plane as droplets of various sizes. In Fig. 4, column three represents droplets emerging out from the sheet, but mostly below the impingement point. Images of higher viscosity gels look different from their lower concentration counterparts in the shape and size of liquid elements disintegrating from the sheet. While low-concentration gels form more droplets, the higher concentration ones mostly move out as ligaments.

For a higher concentration of gels shown, sheet break-up is mostly observed due to the sheet's tearing at the lower portion of the sheet. The multiple perforations formed in the sheet make it like a Web structure and are further stretched to form ligaments as they move away from the impingement point. This type of break-up is visible for cases b2–b3, c2–c4, d2–d4, and e2–e3. For 0.10 wt% gel, this mode is not visible under the ranges of jet velocities measured. One distinctive spray pattern for 0.10 wt% gel is that it behaves like water or a Newtonian fluid. It is because of low-viscosity value and high-surface tension similar to water.

Formation of waves originating from impingement point is visible for 0.10 wt% cases. These disturbances eventually cause the sheet to flap and disintegrate into droplets. As injection pressure increases, these disturbances are increasing, and it is seen that sheet dimensions are minimal and the bulk of fluid coming out of the orifices is moving away in waves after impingement. Frame a5 indicates a lot of atomization activity without any visible ligament formation. For gels of higher concentrations, especially from 0.20 wt% and above, wave-induced sheet break-ups are only visible at higher injection pressures (see Fig. 4c5, d5 and e5). The viscosity shear rate trend shows that the viscosity is attaining a value near to that of water at high shear rates. The shear rate achieved by the fluid is higher for higher injection pressures, and viscosity is reduced; this helps the formation of unstable wave generation at the impingement point.

Within each plot, break-up due to waves and perforations in the sheet are accommodated by giving red color boxes for wave-induced break-up and magenta for perforations induced break-up. For 0.10 wt%, gel wave-induced sheet break-up is prominent for a range of jet velocities studied. At low jet velocities (Fig. 4, column 1), sheet does not show break-up and continues to fall like a thread. As gel concentration increases, the lower portion of sheet has a higher tendency to form a single cylindrical (line) like flow structure. For low-viscosity gels like 0.10 wt%, the threads are visibly disintegrating into drops. In Fig. 5, a sheet break-up length and width are found to decrease initially and then increase. From frames, it was observed that due to increased occurrence of waves at higher jet velocity, the sheet got unstable, and as velocity further increased, more waves are created, and adjacent waves are found to overlap each other and a higher sheet dimension was observed.

For 0.15 wt% gel, wave-induced break-up cases show an initial increase in sheet dimension and then decreases for an increase in Reynolds number. For perforations induced break-up, the sheet length is found to decrease for an increase in Reynolds number. Sheet width for both break-up modes is approximately constant. For 0.20 wt% gel, perforations-induced break-up is found first to increase and then decrease for increasing Reynolds number.

For wave-induced break-up, the sheet dimensions decreased for an increase in Reynolds number. For 0.25 and 0.30 wt% gels, increase in Reynolds number causes reduction in sheet break-up length, but a slight increase in sheet width. Von Kampen et al. (2003) obtained a reduction sheet dimension for an increase in Reynolds number. This study conducted did not go to higher Reynolds number ranges to compare the results. For an increase in gel concentration, the drop velocity increase is observed for drops originating from the sheet's lower portion.

3.4 Droplet Profile and Velocity

From the edges of the sheet (see Fig. 4a2), small protrusions can be seen forming, trying to disrupt the sheet equilibrium. Depending on the jet velocity, the droplets attain velocities and follow particular trajectories. Figure 7 shows trajectories of a few liquid droplets for three gel concentrations for two different jet velocities. A set of 15–20 continuous frames is selected to trace three different droplets originating from the sheets of three different locations. Each droplet taken was considerably far from each other. Drop velocities are an average of all instances taken. Droplets originating from the top side of the sheet are having a higher horizontal velocity component. As jet velocity increases, the droplets are trying to move horizontally.

The velocity of droplets measured from these frames is presented in Fig. 7. As jet velocities increase, the droplet velocities also increase. It is observed that droplets originating from lower portion of the sheet have higher velocities than the droplets originating from the upper portion. For higher jet velocities, the increase in droplet velocity as we move down the sheet is also higher than the low jet velocity case. Waves starting to form from the impingement point are seen to slowly move in the

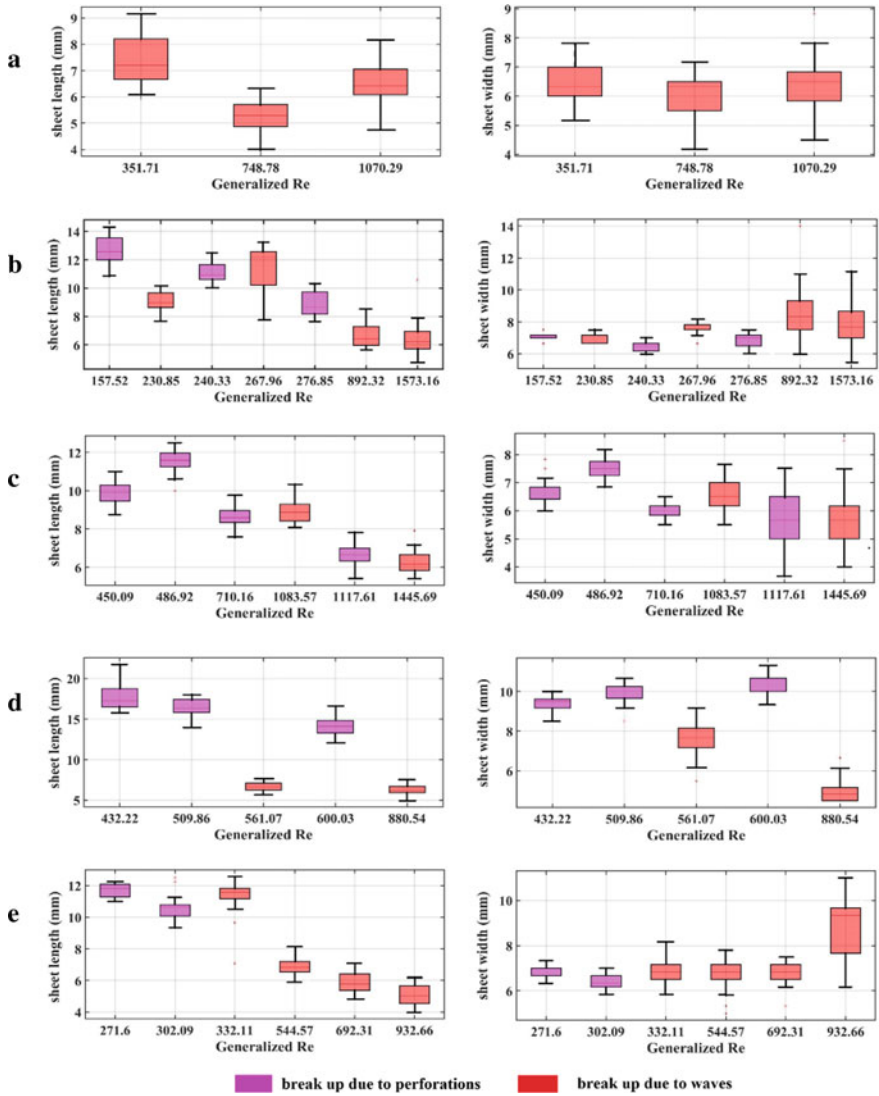


Fig. 5 Sheet break-up length versus generalized Reynolds number. Red color represents sheet break-up due to waves originating from impingement point and Magenta color represents sheet break-up due to perforations. X-axes and Y-axes represent sheet dimension in millimeter and generalized Reynolds number, respectively. **a** 0.10 wt%, **b** 0.15 wt%, **c** 0.20 wt%, **d** 0.25 wt%, and **e** 0.30 wt%

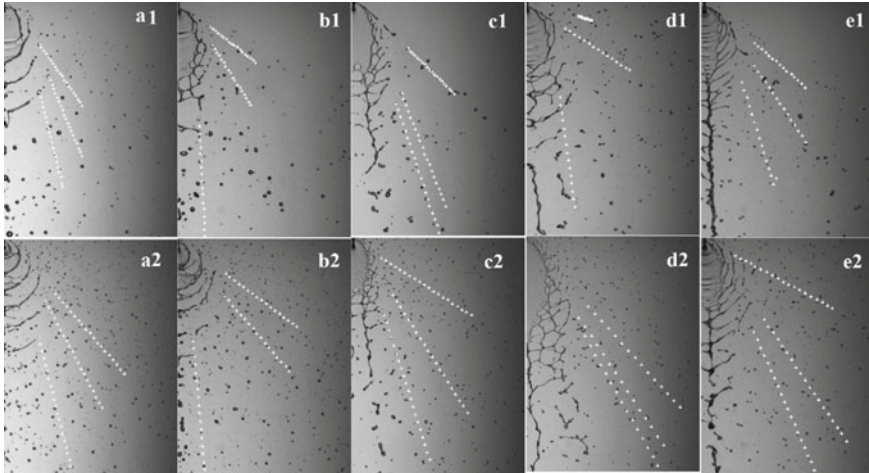


Fig. 6 Droplet trajectory followed for consecutive frames. **a1** and **a2** 0.10 wt%, and jet velocities 8.33 and 13.65 m/s. **b1** and **b2** 0.15 wt%, and jet velocities 7.02 and 9.94 m/s. **c1** and **c2** 0.30 wt%, and jet velocities 8.91 and 9.43 m/s. In each figure, trajectories of three different droplets are shown as white cross

form of an arc and the stretches to gain a horizontal shape and during this propagation, liquid droplets are thrown out from the ends. When these droplets are thrown before complete stretching, the velocity of droplets is found to be less. This occurs from waves near the impingement point. When waves stretch of in the middle of the sheet, the droplets emerging from its ends travel at a higher velocity. And liquid droplets found further downstream travel at an even higher velocity. The velocity of each droplet is observed to be constant for the displacement measured. For higher jet velocities, twenty number of instances were not obtained as the droplets move fast. In Fig. 6, one portion of the impinging jets is shown; the other is symmetric for most cases. As only three droplets are studied for each frame, a complete trajectory for droplets is not obtained and all locations in the sheet where droplet formation takes place are also not shown. For high concentration gels, the size of the droplets was not always spherical. An elliptical shape is more prominent.

4 Conclusions

Impinging jet atomization study of Carbopol gel is conducted experimentally. The focus was on sheet formation, disintegration mechanism for a range of Reynolds number and droplet velocity distribution for different jet velocities. As Reynolds number increases, sheet break-up lengths for perforations-induced break-up are

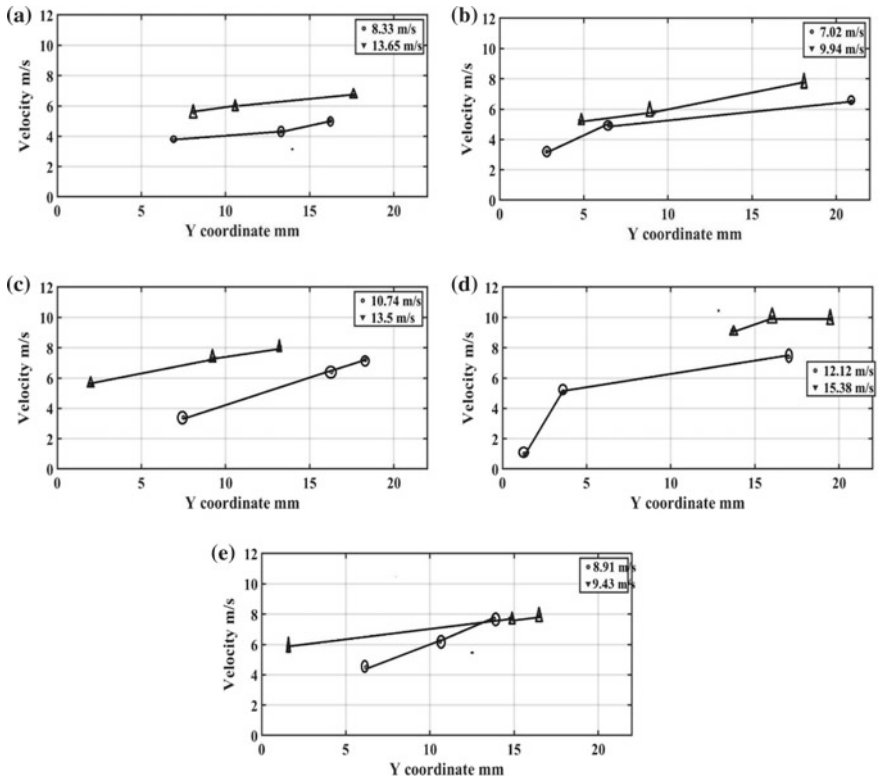


Fig. 7 Droplet velocity and drop origin location are represented for five gel concentrations. **a** 0.10 wt%, **b** 0.15 wt%, **c** 0.20 wt%, **d** 0.25 wt%, and **e** 0.30 wt%. For each case, drop velocity for two jet velocities is marked (the corresponding jet velocities are shown in legend)

found to decrease for 0.15–0.30 wt%. For higher Reynolds number, sheet break-up length for wave-induced break-up also reduced. Droplet velocity increases as we go down the sheet length. The droplet velocities are also found to be stable.

Acknowledgements We thank the Department of Mechanical Engineering, IIT Ropar for supporting this research with Rheometer facility. Sincere thanks to Spray and Combustion Laboratory, IIT Indore and its students and research scholars (Devashish Chorey and Vishal Jagadale) for the experiments’ instrumental support. Finally, we thank and acknowledge the financial support for the project by Liquid Propulsion Systems Center (LPSC), Indian Space Research Organization (ISRO), India.

References

1. Heidmann MF, Priem RJ, Humphrey JC (1957) A study of sprays formed by two impinging jets. NACA technical note 3835
2. Anderson WE, Ryan HM, Pal S, Santoro RJ (1963) Fundamental studies of impinging liquid jets. AIAA, 1992, pp 92–0458. Dombrowski N, Hooper PC (1963) A study of the sprays formed by impinging jets in laminar and turbulent flow. *J Fluid Mech* 18(3):392–400
3. Ibrahim E, Przekwas A (1991) Impinging jets atomization. *Phys Fluids A* 3(12):2981–2987
4. Lai W-H, Huang T-H, Jiang T-L, Huang W (2005) Effects of fluid properties on the characteristics of impinging-jet sprays. *Atom Sprays* 15(4)
5. Green J, Rapp D, Roncace J (1991) Flow visualization of a rocket injector spray using gelled propellant simulants. In: 27th joint propulsion conference, pp 2198
6. Chojnacki K, Feikema D (1994) Atomization studies of gelled liquids. In: 30th joint propulsion conference and exhibit, 1994, p 2773
7. Jayaprakash N, Chakravarthy SR (2003) Impingement atomization of gel fuels. AIAA 316:2003
8. Kim J-Y, Song J-Y, Lee E-J, Park S-K (2003) Rheological properties and microstructures of carbopol gel network system. *Colloid Polym Sci* 281(7):614–623
9. Von Kampen J, Alberio F, Ciezki HK (2007) Spray and combustion characteristics of aluminized gelled fuels with an impinging jet injector. *Aerosp Sci Technol* 11(1):77–83
10. Ciezki H, Tiedt T, Von Kampen J, Bartels N (2005) Atomization behavior of Newtonian fluids with an impinging jet injector in dependence upon Reynolds and weber numbers. In: 41st AIAA/ASME/SAE/ASEE joint propulsion conference & exhibit, 2005, p 4477
11. Lee I, Koo J (2010) Break-up characteristics of gelled propellant simulants with various gelling agent contents. *J Therm Sci* 19(6):545–552
12. Fakhri S, Lee JG, Yetter R (2009) Atomization and spray characteristics of gelled-propellant simulants formed by two impinging jets. In: 45th AIAA/ ASME/SAE/ASEE joint propulsion conference & exhibit, 2009, p 5241
13. Baek G, Kim C (2011) Rheological properties of carbopol containing nanoparticles. *J Rheol* 55(2):313–330
14. Madlener K, Ciezki HK (2012) Estimation of flow properties of gelled fuels with regard to propulsion systems. *J Propul Power* 28(1):113–121
15. Baek G, Kim S, Han J, Kim C (2011) Atomization characteristics of impinging jets of gel material containing nanoparticles. *J Nonnewton Fluid Mech* 166(21–22):1272–1285
16. Yang L-J, Fu Q-F, Qu Y-Y, Gu B, Zhang M-Z (2012) Break-up of a power-law liquid sheet formed by an impinging jet injector. *Int J Multiph Flow* 39:37–44
17. Ma Y-C, Bai F-Q, Chang Q, Yi J-M, Jiao K, Du Q (2015) An experimental study on the atomization characteristics of impinging jets of power law fluid. *J Nonnewton Fluid Mech* 217:49–57
18. Jejurkar SY, Yadav G, Mishra D (2018) Characterization of impinging jet sprays of gelled propellants loaded with nanoparticles in the impact wave regime. *Fuel* 228:10–22
19. Jejurkar SY, Yadav G, Mishra D (2018) Visualizations of sheet break-up of non-Newtonian gels loaded with nanoparticles. *Int J Multiph Flow* 100:57–76

A Parametric Study on Rotary Slinger Spray Characteristics Using Laser Diagnostics



Arnab Chakraborty , Mithun Das , Srikrishna Sahu, and Dalton Maurya

Abstract This paper reports an experimental study of spray characteristics in rotary slinger atomizers using different laser diagnostic tools. The main objective of the present study is to investigate the effect of size of the slinger orifices on liquid breakup dynamics and droplet size distribution over a wide range of rotational speed (5000–45,000 rpm) and liquid flow rates (0.2–2 lpm). Three different slinger discs having the same number of orifices but different sizes ($d_0 = 1, 1.5, \text{ and } 2 \text{ mm}$) are considered. The primary liquid breakup visualization is achieved using volumetric laser-induced fluorescence (VLIF) technique; whereas, the droplet size is measured by interferometric laser imaging for droplet sizing (ILIDS) technique. The results demonstrate critical role of orifice size on liquid breakup mode and droplet size up to rotational speed about 30,000 rpm, beyond which the aerodynamic force dominates the atomization process such that neither the orifice size nor rate of rotation has strong influence.

Keywords Slinger atomizer · Liquid breakup visualization · VLIF · ILIDS · Coriolis force

Nomenclature

AMD	Arithmetic Mean Diameter (μm)
Ro	Rossby Number
Q_l	Total liquid feed rate (lpm)
D	Droplet size (μm)

A. Chakraborty (✉) · M. Das · S. Sahu
Thermodynamics and Combustion Engineering Laboratory, Department of Mechanical Engineering & National Centre for Combustion Research and Development (NCCRD), IIT Madras, Chennai, Tamil Nadu, India
e-mail: junestar66@gmail.com

D. Maurya
Gas Turbine Research Establishment (GTRE), Bangalore, India

d_0	Diameter of slinger orifice (mm)
d_p	Diameter of the injection port on liquid delivery manifold (0.7 mm)
lpm	Litres per minute
N	Rotational speed of slinger (rpm)
VLIF	Volumetric Laser Induced Fluorescence
R_0	Radius of the slinger disc (45 mm)
ILIDS	Interferometric Laser Imaging for Droplet Sizing

1 Introduction

A rotary slinger atomizer in an annular combustor has been frequently used in small-size gas turbines, for instance, in Teledyne's J-69 and Turbomeca's Marbore engines. Simple design and low-cost are the advantages of such atomizer. In addition, importantly, it operates at lower injection pressure compared to pressure atomizer. For maximum power output of a turbine, slinger may be operated at higher rotational speed and it can exceed about 100,000 rpm. But at ideal or relight conditions, the rotational speed is typically in the range of 5000–20,000 rpm. The rotary atomizer is coupled to the turbine shaft and rotates at the shaft speed. The fuel from the pump is fed to discharge orifices on the periphery of the rotary disc. The orifice channels of the disc are drilled in radial or radial-axial direction with respect to the engine shaft. Due to the large centripetal acceleration, the liquid spreads along the inner walls of the atomizer cavity and form a liquid film that supplies the liquid into the orifice channels. Finally, the liquid is discharged from the orifices into the ambience, and it atomizes into droplets forming a spray around the slinger disc. As for any other atomizer, the size of liquid exit area (in the present case the diameter of slinger orifices) is an important design parameter that may strongly influence atomization behaviour, the study of which is the aim of the present paper.

Several studies have reported liquid breakup dynamics in the slinger atomizers. Dahm et al. [1] reported liquid breakup visualization in slinger atomizers for different sizes and shapes of orifices or holes over a wide range of rotational speeds. They stated film and stream modes of liquid injection through for each orifice. The injected film or stream undergoes various types of breakups depending on rotational speed of the disc and geometry of the orifice including subcritical and supercritical mode of breakup for film mode injection. The subcritical breakup refers to the collapse of the annular film, due to surface tension, to form a steam, while the supercritical breakup refers to direct disintegration of the liquid sheet at the orifice exit. The same group [2] conducted a theoretical analysis to predict liquid film thickness, jet diameter for circular as well as non-circular slinger orifice geometry based on film Reynolds number and aerodynamics Weber number, mass and momentum flux of the emerging liquid jet. The authors proposed a correlation for Sauter mean diameter (SMD) in terms of Weber number and Ohnesorge number. The droplet size data measured by Morishita [3] was used for this purpose. Choi et al. [4] performed

series of experiments using high-speed flow visualization and Phase Doppler Particle Analyser for droplet sizing. They considered three different orifice sizes and different arrangements of the orifices on the disc periphery. The experiments were performed in the speed range of 5000–40,000 rpm for a constant liquid mass flow rate. The subcritical mode of liquid breakup is observed up to 15,000 rpm while supercritical mode is observed to be predominant above 30,000 rpm. Droplet sizing measurements were done within 50 mm distance from the slinger disc surface. It is observed that liquid film thickness as well as the SMD decreases with increase in slinger rotational speed. SMD decreased with increase in orifice size. They proposed a linear correlation between SMD and liquid film thickness inside the injection orifice. Though atomization and spray characteristics in slinger atomizers have been studied by a number of other researchers in the past [5–9], they considered same size of orifices for all experiments.

The previous studies mostly used in direct photography for visualization of the liquid breakup process in slinger atomizers. However, the quality of the images degrades for high rotational speed and/or liquid flow rates. This can be overcome by the application of the volumetric laser induced fluorescence (VLIF) technique that allows objective way of visualization of the liquid core region, while the background and also products of atomization around the liquid core (especially for dense sprays) are filtered out. The present paper aims to investigate primary liquid breakup dynamics and spray characteristics in slinger atomizers having different orifice size, which has not gained much attention in the past. The experiments were performed in a high-speed slinger test rig designed to operate over a wide range of conditions. Different laser diagnostic tools were employed in the present work. The visualization of the liquid breakup is achieved by using the VLIF technique, which is advantageous over conventional method of direct imaging as explained above. The size of the spray droplets is measured by interferometric laser imaging for droplet sizing (ILIDS) technique. In the current work, the liquid breakup visualization experiments were performed for the slinger rotational speed in the range 5000–45,000 rpm and the liquid flow rate was varied in the range 0.2–2 lpm.

2 Experimental Set-up

A schematic of the slinger atomizer test rig is shown in Fig. 1. The unique slinger rig facility is housed at NCCRD, IIT Madras and comprises following key units.

(a) Slinger test rig

The slinger test bed consists of a heavy cast iron test bed with vibration absorber pads at its bottom. The high-speed drive is installed on a heavy test bed that dampens any vibrations during slinger operation. Moreover, a vibration sensor (range: 0–25 mm/s) was installed on the electric drive to monitor the performance of the slinger assembly especially for higher range of rotational speeds of the slinger disc. For all experimental conditions, the recorded vibration limit

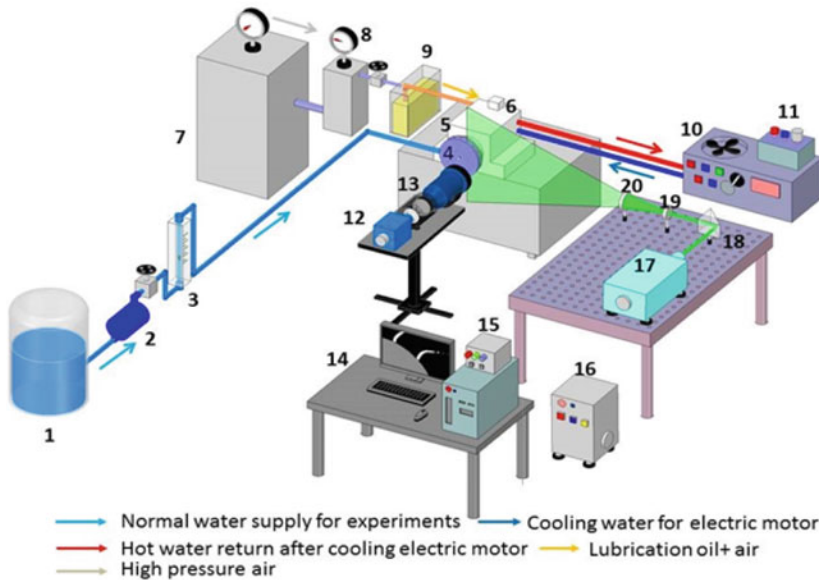


Fig. 1 Schematic of the slinger atomizer experimental set-up for VLIF experiment. 1. Water tank, 2. Pump, 3. Rotameter, 4. Slinger disc, 5. Liquid injection manifold, 6. Electric drive, 7. Air compressor, 8. Air strainer, 9. Lubrication oil chamber, 10. Cooling unit, 11. Frequency controller for electrical drive, 12. CCD camera, 13. Macro lens, 14. Data collection system, 15. Synchronizer, 16. Power box for laser, 17. Nd:YAG laser, 18. 90° beam deflection prism, 19. Cylindrical lens and 20. Spherical lens

was always less than 1 mm/s that ensured smoother and safer operation as per the standard for mechanical vibration. The motor shaft is connected to the shaft of the slinger atomizer, which is a circular titanium disc (radius, $R_0 = 45$ mm) containing 18 number of orifices on its outer periphery (Fig. 2). The liquid is delivered to the slinger disc via a liquid delivery manifold which contains 12 numbers of injection ports uniformly distributed over its periphery (Fig. 2 presents a schematic of the manifold). The diameter of each port is 0.7 mm. The purpose of the manifold is to evenly distribute the liquid to the inner side of the slinger. The liquid (water in the present case) is pumped to the liquid intake line of the manifold (as shown in the Fig. 1) via a rotameter connected to a regulating valve. The liquid goes into the manifold cavity and comes out through the injection ports as liquid jets that impinge on the inner surface of the slinger disc and create a liquid film that serves as a dynamic source of liquid supply. However, it is important to mention that the liquid impingement velocity at any higher liquid feed rate is 40–400 times smaller than the tangential velocity of the slinger disc. Thus, the possibility of liquid jet impingement causing splashing on the inner surface of the disc is minimal. In the present study, three slinger discs (A, B and C) with the same three slinger discs with the same number of orifices but different size of orifices, viz. 1, 1.5 and 2 mm,

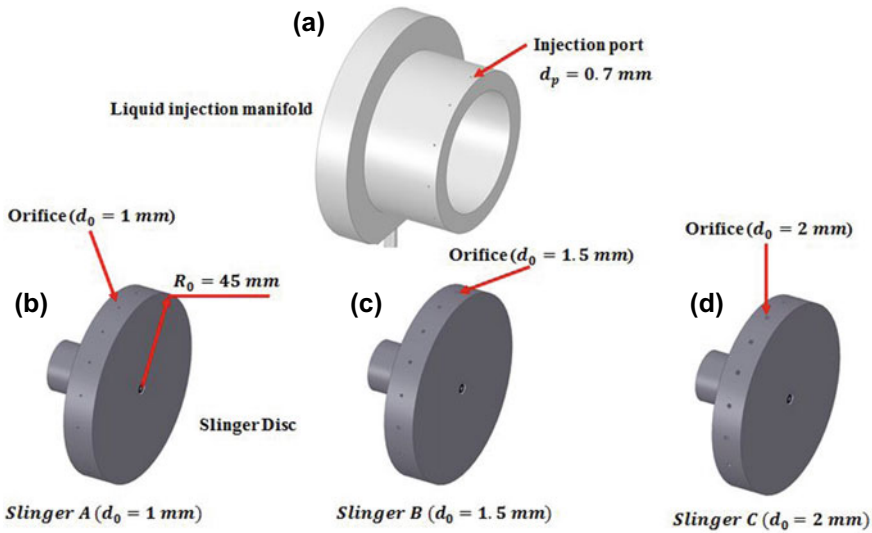


Fig. 2 (a) Liquid injection manifold, (b) Slinger A ($d_0 = 1\text{mm}$), (c) Slinger B ($d_0 = 1.5\text{mm}$) and (d) Slinger C ($d_0 = 2\text{mm}$)

Table 1 Details of the three slinger discs in present set-up

Parameters	Slinger A	Slinger B	Slinger C
Diameter of each orifice (d_0)	1 mm	1.5 mm	2 mm
Number of orifices (N_s)	18	18	18
Radius of the disc (R_0)	45 mm	45 mm	45 mm
Length of each orifice (l)	2 mm	2 mm	2 mm

are used (Fig. 2). The details of the slinger discs are summarized in Table 1. At any particular rotational speed of the disc, the liquid in the inner surface of the disc is ejected out of each of the slinger orifices and atomizes as it interacts with the surrounding air. However, as the liquid flows through each of the slinger orifice, it may not fill its inner surface of the orifice completely, and in such case, the liquid film is not uniformly distributed inside each orifice. The slinger rotational speed N was varied in the range 5000–45,000 rpm, and the liquid flow rate Q_l was in the range from 0.2 to 2 lpm.

(b) **Lubrication unit**

The lubrication unit ensures supply of oil from the lube oil chamber to the bearings of the high-speed drive for appropriate lubrication which is essential for smooth running of the slinger disc.

(c) **Cooling unit**

During the rotation of moving components such as shaft and bearing, heat generation due to friction raises the temperature of associated parts, which

needs to be lowered for hassle-free and safe operation. This is done by the cyclic circulation of the cool water through the heat exchanger.

Now we discuss the application of different laser-based techniques for the atomization and spray study in the current work. In the present work, the primary liquid breakup is visualized using volumetric laser-induced fluorescence (VLIF) technique (Fig. 1); whereas, the droplet size measurement is obtained using interferometric laser imaging for droplet sizing (ILIDS) technique as discussed below.

2.1 VLIF-Based Visualization of Liquid Breakup

In VLIF optical arrangement, a single pulse Nd: YAG laser (Quantel: Q-smart 850, 532 nm, 5 ns pulse width and 6.5 mm beam diameter) was used as the illuminating source. A cylindrical lens (focal length: -25 mm) and a spherical lens (focal length: $+250$ mm) were used to convert the laser beam to a sheet (height 5 cm and beam waist about 1–2 mm). The thickness of the laser sheet was adjusted while using slinger discs with different orifice sizes to ensure that the laser illuminates the whole orifice for all cases. The laser is synchronized with a CCD camera (PCO Pixelfly, 1040×1392 pixel², 14-bit and 13.5 Hz) using an Arduino board. In total, 400 images were captured using a 150 mm macro lens (Sigma, $f/2.8$). In this technique, adequate amount of Rhodamine 6G is uniformly mixed in water tank, then the water tagged with the dye is fed into the slinger during experiment. Upon illuminated by the green laser, the liquid absorbs the incident irradiation and fluoresces at the red-shifted light (with peak around 555 nm) which is captured by the camera equipped with a bandpass filter (550 ± 10 nm). Thus, the scattered light is rejected and only the fluorescent liquid core is imaged. This way the signal to noise ratio is high, and very good quality images with high background contrast is imaged. In order to highlight the advantage of the VLIF technique, we compare a VLIF image with front light illuminated image in Fig. 3 for the same operating condition of $Q_l = 2$ lpm and at $N = 30,000$ rpm for slinger disc B, as example. The above figure clearly demonstrates the potential of the VLIF technique, while the direct imaging suffers from poor contrast due to hindrance of light by the droplets around the liquid core so that imaging of the latter is very difficult. Nevertheless, for lower range of liquid flow rate and rotational speed, direct photography provides reasonably good images.

2.2 Droplet Sizing by ILIDS

The optical arrangement for application of ILIDS in the present experiments has been presented in Chakraborty and Sahu [10], Sahu et al. [9], and hence not repeated here. The same laser and sheet optics as mentioned earlier for VLIF technique were employed. The CCD camera was also same, although the optical setting for

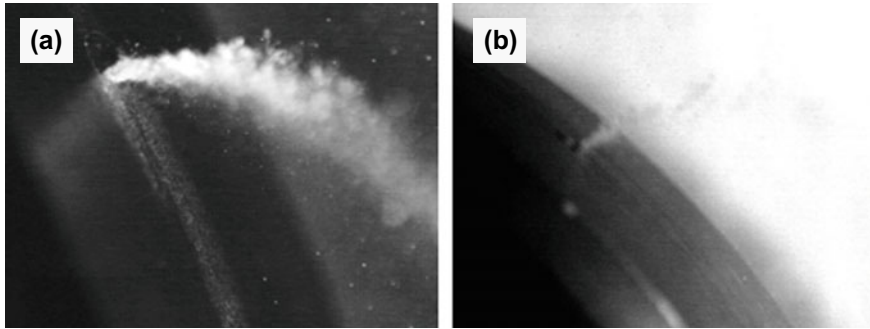


Fig. 3 (a) A sample VLIF image, (b) an image acquired by front light illumination using a stroboscope for $Q_l = 2$ lpm and at $N = 30,000$ rpm and Slinger B

ILIDS imaging system was different. The camera was oriented at the forward scattering angle, $\theta = 69^\circ$ (optimum angle for maximum interference while using water droplets). A 105 mm Nikon lens ($f/2.8$) was used to collect the scattered light. An optical compression unit (a pair of cylindrical lenses), positioned in between the CCD camera and the lens, compresses the circular fringe pattern from a droplet such that each droplet is finally imaged as a rectangular region with superposed fringes. A rectangular aperture (30×2 mm) was mounted on the lens to control the collecting angle, α , which was about 8° in the present case. The entire imaging system assembly was housed on a custom-made frame that also incorporates the Scheimpflug mount for the camera due to which the degree of defocusing remain almost same across the image (i.e. otherwise not possible due to non- 90° viewing in ILIDS). In the next step, the ILIDS images were processed to obtain droplet size, which is expressed as given below [11],

$$D = \frac{\lambda}{\alpha} \left(\cos\left(\frac{\theta}{2}\right) + \frac{m \sin\left(\frac{\theta}{2}\right)}{\sqrt{m^2 - 2m \cos\left(\frac{\theta}{2}\right) + 1}} \right)^{-1} n \tag{1}$$

where λ is the wavelength of the laser light and α is the collecting angle of the receiver. The above equation can be written as, $D = \kappa n$, where κ is an experimental constant that represents droplet diameter per fringe and is given by the bracketed term in Eq. 1. In the present experiments, κ was about $3 \mu\text{m}/\text{fringe}$. The details of the ILIDS image processing could be found out in Manish and Sahu [12], Boddapati et al. [13]. The application of the ILIDS technique for droplet size measurement in slinger atomizers has been demonstrated in our earlier study [10].

The ILIDS images were captured at the radial station at $R = 2R_0$ (R_0 is radius of slinger disc and equals to 45 mm) away from the slinger surface. The selection of the measurement plane is not arbitrary. Lee et al. [14] carried out combustion study in rotary atomizer of disc diameter of 40 mm, and they reported that the reaction zone

of combustion zone is within 50 mm distance away from the outer disc periphery. Accordingly, in the current study, the spray characteristics are decided to be measured at $2R_0$ location. For each experiment, 1000 ILIDS images were captured that ensured statistical convergence of the measured characteristic size of spray droplets. For $Q_l = 0.2$ lpm, the droplet sizing experiments were conducted up to $N = 45,000$ rpm. The characteristic droplet diameter is represented as arithmetic mean diameter (*AMD*) in the present study and defined as given by the expression;

$$\text{AMD} = \frac{\sum_1^n N_i D_i}{\sum_1^n N_i},$$

where N_i is the number of droplets in the size class represented by droplet size D_i and 'n' is the total number of images.

3 Result and Discussions

3.1 Liquid Breakup Morphology

The liquid breakup images close to the orifice exit are presented in Figs. 4 and 5 for $Q_l = 0.2$ and 2 lpm, respectively, for different rotational speeds. For each case, the images are shown for the three atomizers, i.e. slinger disc A, B and C (corresponding to orifice size, $d_o = 1$ mm, 1.5 mm and 2 mm, respectively). Before we discuss the influence of orifice size, some common observations are noted.

- (i) For each case, the primary breakup zone of the liquid, which is characterized by unbroken liquid length, is observed. The liquid, as it exists from the orifice, interacts with the surrounding air, which can be considered to approach the liquid (from the slinger reference frame) in cross-stream manner. Due to aerodynamic interaction with the air, the liquid breaks up when the disrupting forces dominate the surface tension forces.
- (ii) It is interesting to notice that for all rotational speeds and liquid feed rates, the liquid within an orifice channel is pushed to the side opposite to the direction of slinger rotation despite of having low aspect ratio of the orifice which is unique observation in the present study. This is attributed to the dominant role played by the Coriolis acceleration that tends to accumulate all liquid to one side of the channel as soon as the liquid enters the orifice. As a direct consequence of this, the liquid breakup mode is different in comparison with the case where the liquid exists all along the channel wall [1, 2]. Depending on the operating condition as well as slinger orifice size, broadly three different modes are observed, viz. stream-, transition- and film- modes depending on the structure of the liquid at the orifice exit.

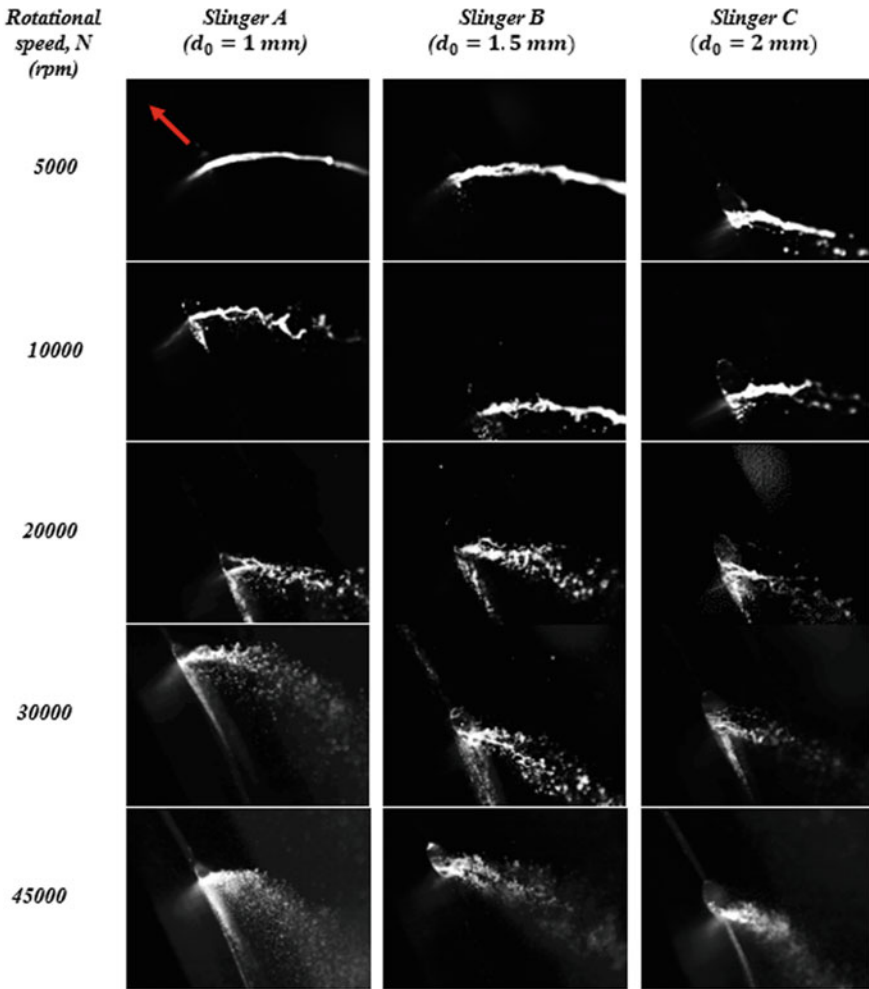


Fig. 4 Liquid breakup morphology for different size orifice in slinger atomizer over rotational speed of 5000–45,000 rpm at liquid feed rate, $Q_l = 0.2$ lpm. The arrow indicates the direction of rotation of the disc

(iii) As the slinger speed is made higher at the same liquid feed rate (compare images column-wise in Figs. 4 and 5), the breakup length appears to decrease, which is as expected, due to higher velocity of approach of the air flow. It is important to mention here that, due to oblique view, it is not possible to quantitatively indicate the breakup length and only qualitative comparison for different rotational speed and liquid feed rate can be made. Since the VLIF technique provides images with high background contrast, identifying the breakup point is less ambiguous. In addition, due to the same reason, for higher rotational speed (and the same Q_l) the liquid breakup structure in the

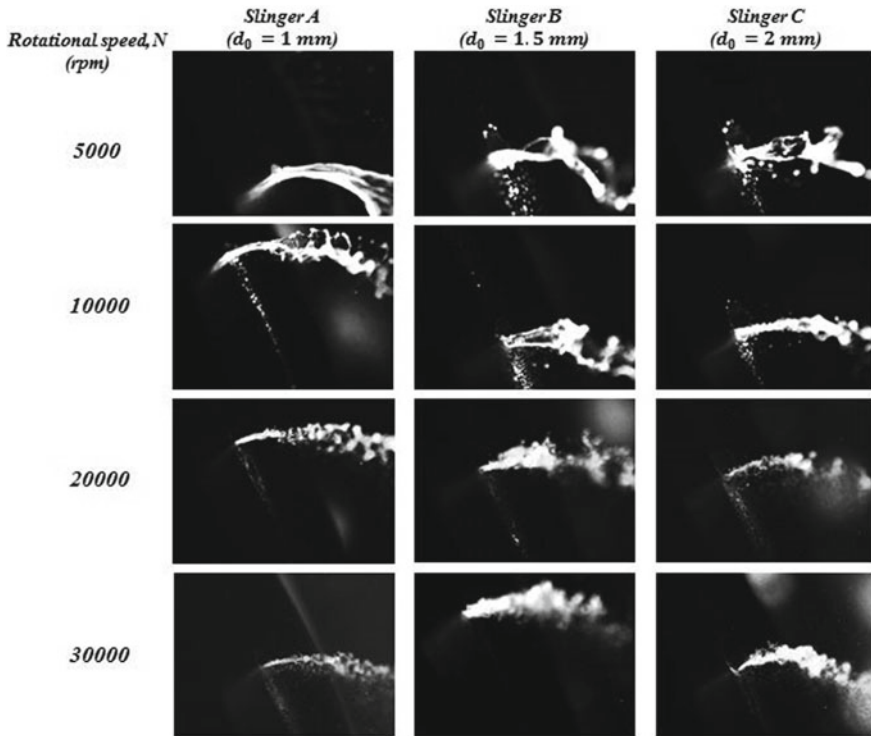


Fig. 5 Liquid breakup morphology for different size orifice in slinger atomizer over rotational speed of 5000–30,000 rpm at liquid feed rate, $Q_l = 2.0$ lpm

vicinity of an orifice changes from stream mode to sheet mode. Accordingly, the liquid breakup morphology away from the orifice changes from column breakup regime (at lower N) to sheet-, sheet-ligament multi-mode regime and sheer regime at higher N .

- (iv) As the liquid feed rate is made larger at the same speed (compare images for each case between Figs. 4 and 5), no general trend can be observed as the difference is dependent on the orifice size, as will be discussed later. In general, the liquid is wider at the orifice exit in Fig. 5 compared with Fig. 4. However, no significant difference in either breakup length or regime is evident.

In spite of the above common observations, which demonstrate the key roles of slinger speed and liquid feed rate, some striking influence of orifice size is also observed in the present experiments as explained below.

Even if the slinger speed and liquid feed rate are held constant, comparing the images row-wise either in Figs. 4 or 5, it can be noticed that the liquid breakup length is always larger for $d_o = 1$ mm, followed by $d_o = 1.5$ and 2 mm. In addition, interestingly, for lower range of N (up to about 20,000 rpm), the liquid mode changes from stream mode for $d_o = 1$ mm to film mode for $d_o = 2$ mm. This highlights the

role of curvature of the orifice channel such that smaller orifice leads to stronger effect of surface tension that tends to roll up the liquid resulting in the liquid to exit as a stream. It is worth to mention here that both Coriolis and surface tension forces influence the mode of liquid delivery within a slinger orifice. In fact, the balance between the above forces dictates the thickness and the width of the liquid. However, the curvature of the inner surface of the orifices aids to surface tension force even if the working liquid is the same. Hence, we attributed the observed difference to increased surface tension force. For larger orifice, the liquid is able to spread in the cross-stream direction due to which the liquid exits as a film. As a consequence, the breakup regime of the liquid varies with the diameter of the orifice for the same speed and liquid flow into the atomizer. For example, considering the case $N = 5000$ rpm and $Q_l = 0.2$ lpm in Fig. 4, column breakup corresponding to Rayleigh regime is evident for $d_o = 1$ mm, while a combined sheet-ligament regime occurs for $d_o = 1.5$ mm (ligaments of liquid appear on the boundary of the sheet), on the other hand, the sheet transforms into a bag structure that further breakups for $d_o = 2$ mm. For higher slinger speed ($N > 20,000$ rpm), the liquid breakup mode and regime are mostly governed by aerodynamic force, thus, the influence of orifice size is smaller. Overall, the current visualization images indicate that even if the slinger operating conditions are held same, and the liquid never fills up the orifice channel, smaller orifice size leads to poor atomization and vice versa. Though, no much difference in breakup morphology is observed between $d_o = 1.5$ and 2 mm.

Figure 6 presents the droplet size distribution measured at $R = 2R_o$ location for different slinger discs at $Q_l = 0.2$ lpm for the rotational speed range of 10,000–45,000 rpm. As the rotational speed of the disc is made higher for the same liquid feed rate, the size distribution is slightly shifted to left indicating production of smaller droplets. Thus, large numbers of smaller droplets are generated for higher rotational speed, as expected, due to improved atomization. However, an interesting trend is observed comparing the plots for different slinger discs in each subfigures in Fig. 6. For the same speed and liquid feed rate, the droplet size distribution is populated with smaller droplets as the orifice size increases from disc A to disc C. It can be observed that up to $N = 30,000$ rpm, as the orifice size is made larger, the probability of smaller droplets is higher and larger droplets is smaller. For very high rotational speed for instance, $N = 45,000$ rpm, the droplet size distribution for all slinger discs nearly overlaps. This is further highlighted in the AMD vs N plots shown in Fig. 7. For all discs, AMD reduces with rotational speed. Similar observations are reported by Rezayat and Farshchi [15], Choi and Jang [4] and Chakraborty and Sahu [10]. For a given rotational speed, the trend of AMD with orifice size appears non-monotonic. This is evident especially for $N < 35,000$ rpm and requires further investigation to relate droplet size with the observed liquid breakup mode. However, for high rotational speed ($N > 35,000$) no significant difference in droplet size for different discs are evident, which is attributed to rigorous liquid atomization which is nearly independent of boundary conditions at the orifices (see last row of images in Fig. 4). We note that we have verified the above for different liquid flow rates and speed up to 1 lpm and 10,000 rpm and found that the feed rate does not influence

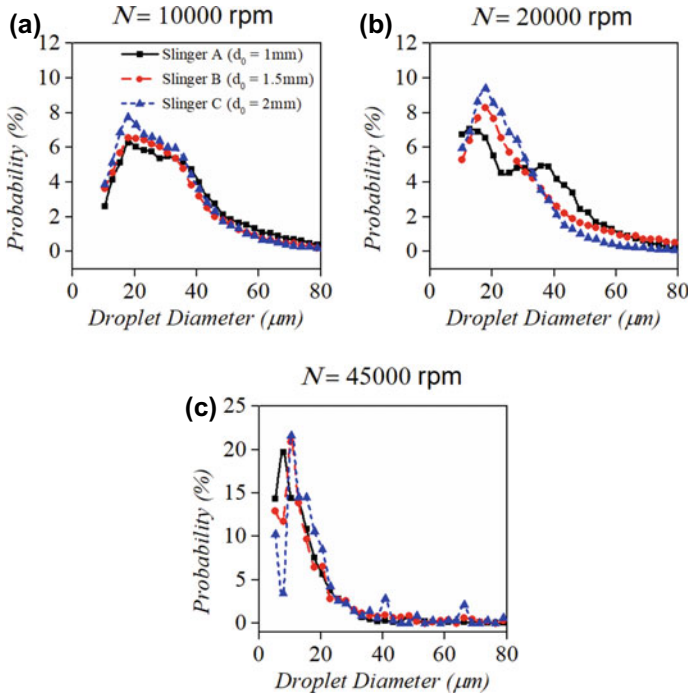
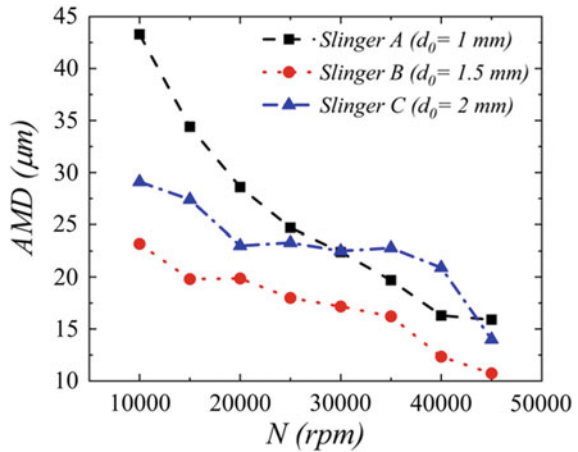


Fig. 6 Probability distribution of droplet size measured at $R = 2R_0$ location for different slinger discs at rotational speed of (a) 10,000 rpm, (b) 20,000 rpm, and (c) 45,000 rpm at liquid feed rate, $Q_l = 0.2$ lpm

Fig. 7 Droplet size (AMD) variation with rotational speed (N) at liquid feed rate $Q_l = 0.2$ lpm for different slingers



much the resulting droplet size. However, further experiments are being conducted currently for higher speed and feed rate.

The above trends for the droplet size and especially the role of orifice size can be explained considering the liquid breakup regimes discussed earlier for the current range of slinger operating conditions. For slinger disc A, Rayleigh type breakup occurs corresponding to the column breakup regime, as a result, the droplet size is of the order of the size of the columns. In contrast to the prevailing sheet and/or ligament breakup regime in disc B and C, the droplet size is smaller. However, at very high rotational speed such as $N = 45,000$ rpm, shear breakup is the dominating mode of breakup, and hence, mostly very small droplets are generated for all orifices with different size.

4 Conclusion

The motivation behind the present work is to investigate the effect of orifice size on liquid atomization and spray characteristics in slinger atomizers using different laser diagnostic tools. The present study demonstrates the potential application of VLIF technique for visualization of liquid breakup process near the slinger orifices, as high contrast images are obtained in comparison with direct photography. The ILIDS technique was used to measure droplet size. The visualization images demonstrated the dominant role of Coriolis-induced liquid breakup behaviour which means that the liquid in an orifice channel is pushed towards the side opposite to the direction of rotation. It was found that, up to about 30,000 rpm, for the same rotational speed and liquid feed rate, the mode of liquid flow (stream- or film- mode), breakup regime (column-, sheet- or ligament- breakup) and droplet size distribution vary with the size of the orifice channels. Smaller orifice size ($d_o = 1$ mm) promotes column mode liquid transport in the orifice that results in Rayleigh type breakup leading to generation of large-size droplets. Larger orifices ($d_o = 1.5$ and 2 mm) lead to film mode and sheet and/or ligament breakup regime which is responsible for small droplets in the spray size distribution. The results highlight that smaller the orifice size, larger is the *AMD*. At very high speed such as $N = 45,000$ rpm, shear breakup regime was observed for all slinger discs, and also *AMD* does not vary much with the diameter of the slinger orifices.

Acknowledgements The authors would like to acknowledge the financial support from the Centre for Propulsion Technology (CoPT), Govt. of India. The authors wish to thank Mr. Thileepan P for his assistance during the design and development of the slinger test rig.

References

1. Dahm WJA, Patel PR, Lerg BH (2006) Experimental visualizations of liquid breakup regimes in fuel slinger atomization. *Atom Sprays* 16(8):933–944
2. Dahm WJA, Patel PR, Lerg BH (2006) Analysis of liquid breakup regimes in fuel slinger atomization. *Atom Sprays* 16(8):945–962
3. Morishita T (1981) A development of the fuel atomizing device utilizing high rotational speed. In: *Aircraft engine; marine; turbomachinery; microturbines and small turbomachinery*, March 1981, vol 1. American Society of Mechanical Engineers, New York, pp 1–6
4. Choi SM, Jeong JH (2010) Spray behavior of the rotary atomizer with in-line injection orifices. *Atom Sprays* 20(10):863–875
5. Choi SM, Yun S, Jeong JH, Corber A (2012) Spray in cross flow of a rotary atomizer. *Atom Sprays* 22(2):143–161
6. Sescu C, Kucinschi BR, Afjeh AA, Masiulaniec KC (2011) Experimental test rig with results on liquid atomization by slinger injectors. *J Eng Gas Turbines Power* 133(11):210–213
7. Rezayat S, Farshchi M, Karimi H, Kebriaee A (2018) Spray characterization of a slinger injector using a high-speed imaging technique. *J Propul Power* 34(2):469–481
8. Rezayat S, Farshchi M, Ghorbanhoseini M (2019) Primary breakup dynamics and spray characteristics of a rotary atomizer with radial-axial discharge channels. *Int J Multiph Flow* 111:315–338
9. Sahu S, Chakraborty A, Maurya D (2020) Coriolis-induced liquid breakup and spray evolution in a rotary slinger atomizer: experiments and analysis. *Int J Multiph Flow* 135(2021):103532
10. Chakraborty A, Sahu S (2019) Liquid atomization in a high-speed slinger atomizer. In: *Volume 1: compressors, fans, and pumps; turbines; heat transfer; structures and dynamics*. American Society of Mechanical Engineers
11. Glover A, Skippon S, Boyle R (1995) Interferometric laser imaging for droplet sizing: a method for droplet-size measurement in sparse spray systems. *Appl Opt* 34:8409–8421
12. Manish M, Sahu S (2019) Droplet clustering and local spray unsteadiness in air-assisted sprays. *Exper Therm Fluid Sci* 100:89–103
13. Boddapati V, Manish M, Sahu S (2020) A novel approach for conditional measurement of droplet size distribution within droplet clusters in sprays. *Exp Fluids* 61:42
14. Lee DH, Kim HM, Park PM, You GW, Paeng KS (2009) Full rig test and high-altitude ignition test of micro turbojet engine combustor. In: *Proceedings of 2009 KSPE spring conference*. The Korean Society of Propulsion Engineers, Daejeon, pp 373–376
15. Rezayat S, Farshchi M (2019) Spray formation by a rotary atomizer operating in the coriolis-induced stream-mode injection. *Atom Sprays* 29(10):937–963

CFD Analysis of Primary Air Flow Field of a Swirl Injector Using Embedded LES-Based Hybrid Model



Rampada Rana, N. Muthuveerappan, and Saptarshi Basu

Abstract Injector plays a pivotal role in meeting requirements of combustion performance in terms of combustion efficiency, flame stability, ignition, lower emissions, etc. In a multi-swirler injector configuration, air flow field inside injector is mainly dictated by primary swirler. Present CFD studies have been attempted to characterize flow field of a conical nozzle fitted with a radial swirler. Embedded LES-based hybrid model has been used where computational domain is divided into three zones which are seamlessly connected by capturing the interface fluid dynamics. In LES zone, both time and spatial scales have been resolved based on the results of a precursor RANS analysis. Analysis is carried out with CFL no. around 2, time step of 1 μ s. The analysis is reasonably able to capture various unsteadiness (PVC, CTRZ, frequencies, TKE useful for the atomization of liquid fuel) which are not possible to be captured using URANS models.

Nomenclature

<i>CFD</i>	Computational Fluid Dynamics
<i>CFL</i>	Courant-Friedrichs-Lewy
<i>CTRZ</i>	Central Toroidal Recirculation Zone
<i>ELES</i>	Embedded LES
<i>FFT</i>	Fast Fourier Transform
<i>KH</i>	Kelvin-Helmoltz
<i>LDI</i>	Lean Direct Injection
<i>LPP</i>	Lean Premix Prevaporization
<i>LES</i>	Large Eddy Simulation
<i>MPI</i>	Message Passing Interface

R. Rana (✉) · N. Muthuveerappan
Gas Turbine Research Establishment, Bengaluru, Karnataka, India
e-mail: rana-rampada.gtre@gov.in

S. Basu
Department of Mechanical Engineering, Indian Institute of Science, Bengaluru, Karnataka, India

© The Author(s), under exclusive license to Springer Nature Singapore Pte Ltd. 2023
G. Sivaramakrishna et al. (eds.), *Proceedings of the National Aerospace Propulsion Conference*, Lecture Notes in Mechanical Engineering,
https://doi.org/10.1007/978-981-19-2378-4_37

<i>PIV</i>	Particle Image Velocimetry
<i>POD</i>	Proper Orthogonal Decomposition
<i>PVC</i>	Precessing Vortex Core
<i>RANS</i>	Reynolds Averaged Navier Stokes
<i>Re</i>	Reynolds Number
<i>RQL</i>	Rich burn Quick quench Lean burn
<i>SIMPLEC</i>	Semi-Implicit Pressure Linked-Consistent
<i>SGS</i>	SubGrid Scale
<i>TKE</i>	Turbulent Kinetic Energy
<i>URANS</i>	Unsteady RANS
<i>WMLES</i>	Wall Modeled LES
<i>ZLES</i>	Zonal LES

Small Letters

y^+	Non-Dimensional distance of centroid of cell from the wall
k	Turbulent Kinetic Energy
μ_t	Turbulent/Eddy Viscosity
Δx	Cell length in x -direction on wall surface
Δz	Cell length in z -direction on wall surface
c, v	Velocity of flow across a computational cell
Δt	Time step
μ_{sgs}	Subgrid-scale viscosity
$\mu_{laminar}$	Laminar Viscosity
r	Radial direction of flow

Capital Letters

C_μ	Constant
D	Diameter (Ref. geometrical dimension)
D_0	Diameter of nozzle exit
P_s	Static Pressure
P_{ref}	Reference Pressure
R_{ij}	Reynolds stress tensor
Re	Reynolds Number
U_a	Axial Velocity
U_r	Radial Velocity
U_t	Tangential Velocity
U_{ref}	Reference Velocity
X	X -co-ordinate
\mathbf{X}	Position Vector

Y	Y -co-ordinate
Z	Z -co-ordinate

Greek Symbols

Δ	Cell Size, Small Change
ϵ	Turbulent kinetic energy dissipation rate
ρ	Density of air
μ	Viscosity
θ	Circumferential direction of flow
ω	Vorticity Vector
Γ	Gamma Function

1 Introduction

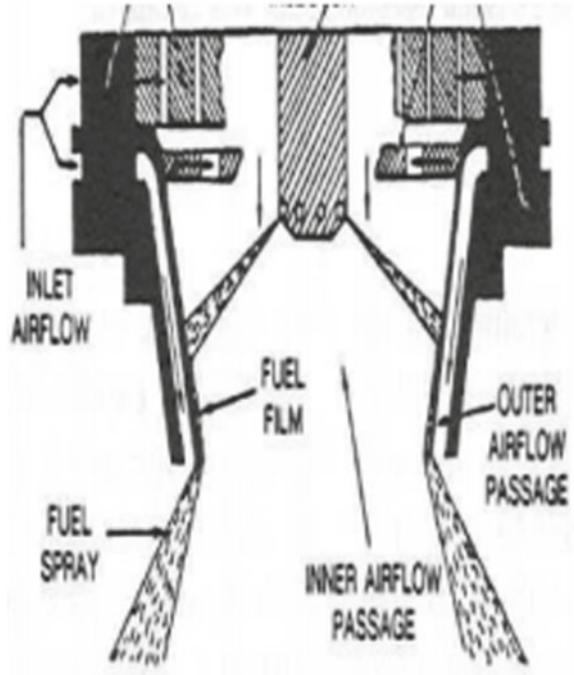
Improvement of specific fuel consumption through increase in thermal efficiency and that of specific thrust through burning of small air mass; both led to increment of pressure and temperature of gas turbine engines. According to Tacina [1], increases in pressure and temperature levels affect combustor in a way to the requirement of injector with large turn-down ratios meeting with parasitic requirements of uniform circumferential and radial temperature distributions and this is because of less amount of availability of dilution air for tailoring combustor exit temperature. With the injector in place and using different philosophies of combustor designs such as LPP, RQL, LDI, etc., NO_x emissions of the combustor can be controlled where uniform mixture of fuel vapor and air burnt at low temperature. Hence, the injector plays a pivotal role to meet better combustion performances requirements with respect to combustion efficiency, flame stability, better ignition characteristics, lower emissions, etc. In terms of achieving lower droplet sizes and better near flow field of injector, the requirements are achieved through better atomization of bulk fuel into droplets and distribution of same in terms of lower sizes and velocities. According to Cornea [2], tool with deeper understanding and predictive capabilities from first principle is required in this respect and especially to understand unsteady phenomena involving complex three-dimensional geometries of interest and complex phenomena; it may require approaches such as discrete vortex method or Large Eddy Simulation. Zhang et al. [3] performed numerical CFD calculations using URANS model for flow over flat plate under with and without adverse pressure gradient effects. They captured large-scale vortical structures of the flow when reattachment occurs after a separated region due to adverse pressure gradient and vortical structure remains in the field despite large effective eddy viscosity produced by the turbulence model and the model does not capture the small-scale vortical

structures requiring smallest grid cells as required in LES. Sankaran and Menon [4] performed LES studies to capture unsteady interaction between spray dispersion, vaporization, fuel–air mixing, and heat release in a realistic combustor. They found that presence of high swirl increases the droplet dispersion, activates CTRZ, and reveals large-scale organized structures which are then subjected to complex stretch effects due to a combination of stream-wise and azimuthal vortical motions leading to enhanced fuel–air mixing. They opined that compared to RANS calculations where full range of length scales are not modeled, LES could resolve the flow/geometry-dependent large-scale motions more accurately and their study was confined to a geometry of dumb combustor with conical nozzle entry; boundary conditions of the LES simulations were, however, based on non-dimensional stream-wise and tangential velocity profiles available at the swirler exit plane, MPI-based parallel computation systems for interacting among processors, are used to perform the simulations. Stone [5], in his Ph.D. studies, performed LES calculations in a simplified high Re gas turbine combustor flows to capture vortex flame interaction, vortex dynamics, vortex breakdown, and combustion dynamics. Wang et al. [6] carried out LES study of gas turbine injector consisting of radial swirlers oriented in both co- and counter- rotating directions, to predict the characteristics of flow field. Results of the numerical analysis were compared with experimental data. Boundary conditions for inlet domain were applied after swirler exit upon superimposing broadband noise with a Gaussian distribution on the mean velocity profile with its intensity extracted from RANS simulation, and the methodology is iterated to its sensitivity. Block-based structured hexahedral grid system with mean cell size inside the injector as 0.35 mm was used during grid preparation, and four steps Runge–Kutta scheme for time integration and second-order accurate center-differencing methodology for spatial discretization were used for numerical calculation. The ratio of resolve to total TKE exceeded 95% in the bulk flow field. The axial, radial and tangential velocities downstream of the injector vis-à-vis the experimental results were plotted and reduced order POD analysis were also carried out to dictate most energetic components in the flow field. Wang et al. opined from their studies that air flow field inside injector is mainly dictated by primary swirler and the impact of secondary swirler on the same is limited.

Current LES study on the flow field was performed to understand flow field evolution. Since, the flow evolution especially inside the injector using single swirler is fundamental and to avoid difficulties for experimentally evaluating the same, authors were motivated to carry out this LES study. And most literatures showed that swirler exit conditions were derived from separate analysis and were used as boundary conditions for the LES domain.

In this present study, embedded LES method, new computational method, is adopted where no separate analysis was performed to impose boundary conditions on inlets to LES domain, rather than analyses were performed on the full computational domain segmented into multiple zones and total grids were generated based on varied zonal requirements with reduced computational costs. The flow field performances were predicted and comparisons were made between radial variations of

Fig. 1 High shear swirl cup
[8]



normalized axial velocities of LES predicted results and experimental PIV data at different downstream locations of the injector.

2 Computational Methodology

2.1 Model Details

As fundamental components of high-shear injector schematically shown in Fig. 1, the injector model under study is consisting of radial swirler attached with a conical nozzle at the exit of swirler as shown in Fig. 2. The geometrical swirl number and swirler vane angle are 0.75° and 66.5° , respectively. For details, refer [7]. Fluid volume of the injector is shown in Fig. 3.

2.2 Grid Details

The computational domain extends from 500 mm in upstream direction in a cylindrical duct of diameter 100 mm as per the experimental setup, and the exit flow of

Fig. 2 Cut section of the mechanical model of the injector

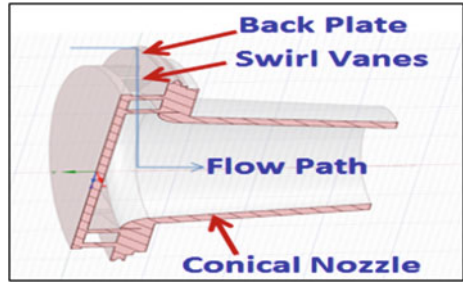
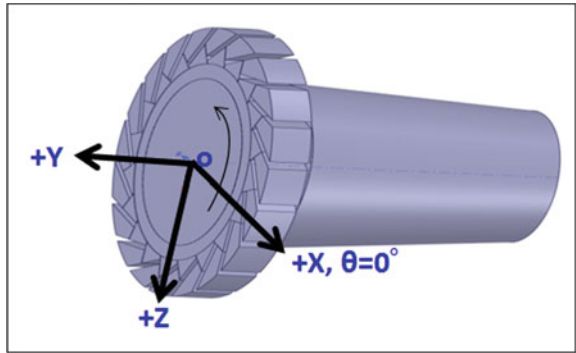


Fig. 3 Fluid volume disposition of the injector at decomposed condition



the nozzle is allowed to meet on to a domain of length more than 1600 mm in a rectangular duct with square cross-section of size 780 × 780 mm as shown in Fig. 4. Size of upstream domain is based on experimental duct size. The square shape of size 780 × 780 mm is based on the understanding of better accommodating tangential swirl flows exiting from the conical nozzle without downstream wall confinement effects on flow evolution as well as having better grid. For further details, refer [7].

The total domain is divided into three zones: First zone covers flows from upstream inlet through swirler vanes flows exiting into nozzle connected downstream analyzed

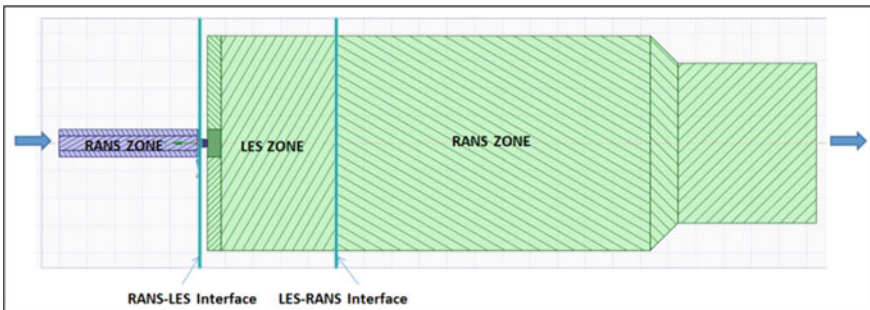


Fig. 4 Computational domain used for the analysis

by RANS model (realizable $k-\epsilon$ turbulence model with standard wall function); second zone covers RANS exit of first zone toward downstream of nozzle exit analyzed by LES model (wall-modeled LES); third zone includes toward the downstream of LES exit of second zone analyzed by same RANS model. Domains are seamlessly connected by capturing the interface fluid dynamics of the flow (discussed later).

Figure 5 shows grid details of the computational domain. The grid philosophies for the upstream and downstream RANS zones are kept same as in [7]. The densities of grids present in RANS zones are lesser because of non-resolving the scales there as shown in Fig. 5(a). Number of cells and size of grids required in the LES zone are based on the level of TKE to be resolved across the zone and accordingly the cell size Δx is arrived at. To make the turbulent model worked well, certain grid criteria is required to be met. As shown in Fig. 5(b), two layers of y^+ adaptations were carried out to resolve the extend of wall y^+ (150–200 were possible) keeping in view quality of grids such as skewness and minimum orthogonality requirement. The resulting aspect ratio of nozzle wall surface face sizes ($\Delta x / \Delta z$), i.e., along wall parallel plane, is found to reach ~ 13 which is more than the required value of maximum 2. However, aspect ratio based on cell-base length scale to cell wall distance is found to be 5.06 meeting the required acceptable limit of less than 10 [9]. Since, the phenomenon of interest is chosen to be away from wall, grid scheme of this order is considered to be acceptable. Time scale is worked out as $\frac{\Delta}{v}$, for which time step Δt is decided after ensuring that extend of smaller time step should lie in zone of interest. Cell size Δx

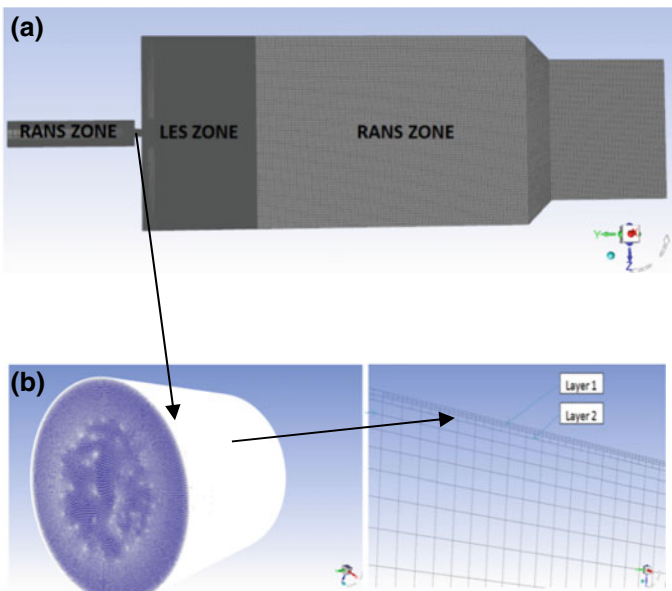


Fig. 5 a Computational grid used for the simulation. b Details of the grid LES zone (nozzle portion)

and time step Δt are connected to CFL number as $\frac{c\Delta t}{\Delta x}$. CFL number is to be as close to 1 to resolve the time scale. Typical value of Δx is 0.1 mm and Δt is kept at 1×10^{-06} s during the computation.

A grid of size of 9.7 million having maximum skewness of 0.91 generated using ANSYS Meshing has been arrived at after resolving both time and length scales.

2.3 Solver Details

ANSYS Fluent version 19.2 was used for the analysis. Analyses were carried out considering the flow as unsteady, incompressible, iso-thermal, and turbulent. Realizable $k-\varepsilon$ turbulence model is used in RANS zones. WMLES model was used in LES zone.

Time dependent RANS computations are performed as follows: The computations are performed after time averaging N-S equation resulting following set of equations which are required to be solved in CFD using finite volume methodology.

$$\rho \left(\frac{\partial \bar{u}_i}{\partial t} + \bar{u}_k \frac{\partial \bar{u}_i}{\partial x_k} \right) = -\frac{\partial \bar{p}}{\partial x_i} + \frac{\partial}{\partial x_j} \left(\mu \frac{\partial \bar{u}_i}{\partial x_j} \right) + \frac{\partial R_{ij}}{\partial x_j} \quad (1)$$

$$R_{ij} = -\rho \overline{u'_i u'_j} \quad (2)$$

$$R_{ij} = \mu_\tau \left(\frac{\partial \bar{u}_i}{\partial x_j} + \frac{\partial \bar{u}_j}{\partial x_i} \right) - \frac{2}{3} \mu_\tau \frac{\partial \bar{u}_i}{\partial x_j} \delta_{ij} - \frac{2}{3} \frac{\partial \bar{u}_i}{\partial x_j} \rho k \delta_{ij} \quad (3)$$

$$\mu_\tau = \rho C_\mu \frac{k^2}{\varepsilon} \quad (4)$$

k and ε values are solved separately by using two different independent equations thus called the model as two equations model.

The general equations for LES computations are shown below.

In LES computations, large-scale turbulent structures are directly solved using resolved scales and small-scale effects are modeled and solved through filtering the N-S equation as like RANS calculations, but with more details. The filtered equations are formed by space averaging or Favre (density weighed averaging) averaging (based on incompressible or compressible flows) of N-S equation. Followings are the conservation equations applicable for incompressible computations:

According to [10], the space averaged filtered continuity and momentum equations are as follows:

$$\frac{\partial \rho}{\partial t} + \frac{\partial}{\partial x_i} (\rho \bar{u}_i) = 0 \quad (5)$$

$$\frac{\partial}{\partial t}(\rho \overline{u_i}) + \frac{\partial}{\partial x_j}(\rho \overline{u_i u_j}) = \frac{\partial}{\partial x_j}(\sigma_{ij}) - \frac{\partial \overline{p}}{\partial x_i} - \frac{\partial \tau_{ij}}{\partial x_j} \quad (6)$$

The molecular viscosity σ_{ij} is defined as

$$\sigma_{ij} \equiv \left[\mu \left(\frac{\partial \overline{u_i}}{\partial x_j} + \frac{\partial \overline{u_j}}{\partial x_i} \right) \right] - \frac{2}{3} \mu \frac{\partial \overline{u_l}}{\partial x_l} \delta_{ij} \quad (7)$$

The subgrid-scale turbulent stress τ_{ij} is defined as

$$\tau_{ij} \equiv \rho \overline{u_i u_j} - \rho \overline{u_i} \overline{u_j} \quad (8)$$

The subgrid-scale turbulent stress τ_{ij} is computed from

$$\tau_{ij} - \frac{1}{3} \tau_{kk} \delta_{ij} = -2 \mu_t \overline{S_{ij}} \quad (9)$$

The isotropic part of the subgrid-scale stresses τ_{kk} is not modeled but combined with the filtered static pressure term. The rate-of-strain tensor $\overline{S_{ij}}$ for the resolved scale is defined by

$$\overline{S_{ij}} \equiv \frac{1}{2} \left(\frac{\partial \overline{u_i}}{\partial x_j} + \frac{\partial \overline{u_j}}{\partial x_i} \right) \quad (10)$$

where μ_t is modeled based on type of LES model requirement.

In current numerical simulation based on ELES or ZLES model, LES portion of the simulation is resolved using algebraic WMLES model, and μ_t has been defined accordingly. In WMLES, inner part of logarithmic turbulent layer is solved through zero-equation algebraic RANS, and outer part of turbulent boundary layer is solved through a modified LES formulation reducing LES grid requirement for high Re flows. The procedure could be useful when phenomena were considered away from wall, and wall boundary layers need not to be resolved.

In WMLES, eddy viscosity ν_t is calculated below with the use of a modified grid scale Δ to take care of grid anisotropies in wall-bounded flows:

$$\nu_t = \min \left[(\kappa d_w)^2, (C_{\text{Smag}} \Delta)^2 \right] \cdot S \cdot \left\{ 1 - \exp \left[- \left(y^+ / 25 \right)^3 \right] \right\} \quad (11)$$

where d_w : wall distance, S : strain rate, $\kappa = 0.41$ and $C_{\text{Smag}} = 0.2$ are constants, y^+ : normal to wall inner scaling, and modified grid scale Δ is given as:

$$\Delta = \min(\max(C_w \cdot d_w; C_w \cdot h_{\text{max}}, h_{\text{wn}}); h_{\text{max}}) \quad (12)$$

where h_{\max} : maximum edge length for a rectilinear hexahedral cell which is modified for other cell types and/or conditions based on an extension of this concept. h_{wn} : wall-normal grid spacing, and $C_w = 0.15$ is a constant.

Mass flow inlet and pressure outlet boundary conditions with air as computational fluid have been chosen for the analysis. All walls are considered to be at adiabatic conditions. At interior zone of the RANS–LES interface, vortex method is used to resolve turbulence from the modeled turbulence of upstream RANS calculations. According to [10], numbers of vortices are assessed through $N/4$, where N is number of cell faces and the vorticity transport is modeled and tracked as follows:

$$\omega(X, t) = \sum_{k=1}^N \Gamma_k(t) \eta(|X - X_k|, t) \quad (13)$$

Corresponding fluctuating velocity field computed using the Biot–Savart law as:

$$u(X, t) = -\frac{1}{2\pi} \iint \frac{(X - X') \times \omega(X') e_z}{|X - X'|^2} dX' \quad (14)$$

However, for the LES–RANS interface, “no perturbations” conditions were imposed so as to have a smooth transitions of flow from LES to RANS. Here, downstream RANS domain uses mean flow of LES, since perturbations are considered to be diminished at the interface.

For numerical computations, second-order upwind scheme for spatial resolutions for momentum, turbulent KE, etc., and second-order implicit scheme for time resolutions were used. SIMPLEC scheme was used for pressure velocity coupling. Residuals for convergence criteria were kept at 10^{-06} .

3 Results and Discussion

Results of CFD analysis are discussed in this section. It consists of time-dependent contour, vector, streamlines, and turbulent kinetic energy plots of the flow field. Data were captured after running simulations for much over five flow-through times through the computational domain (typical value for five flow-through times is ~ 0.013 s and data were recorded and time averaging was performed after ~ 0.03 s ensuring better stability in flow). SGS viscosity ratio $\left(\frac{\mu_{\text{sgs}}}{\mu_{\text{laminar}}}\right) \sim 500$, which is found to be lower than turbulent viscosity ratio calculated from RANS simulation as expected, thus ensuring dissipating nature of turbulence due to LES calculations (turbulent viscosity ratio from RANS calculation was 2200). Apart from this, it was also found from analysis that resolved spectrum in flow of interest (ratio of resolved TKE to the sum of resolved TKE and resolved TKE due to SGS averaging) is 97%, which

directly builds confidence of carrying out analysis using current model setup, length, and time scales resolved, etc.

3.1 Comparison of Normalized Velocities

Figure 6 shows comparison of normalized time averaged axial velocities between numerical prediction and experimental PIV results at different downstream locations of exit of the injector showing first-order dynamics of the system.

Results show there is a good agreement with the experimental data; the variations between them are lower.

Normalized time averaged radial and tangential velocities based on the numerical prediction are shown in Figs. 7 and 8, respectively.

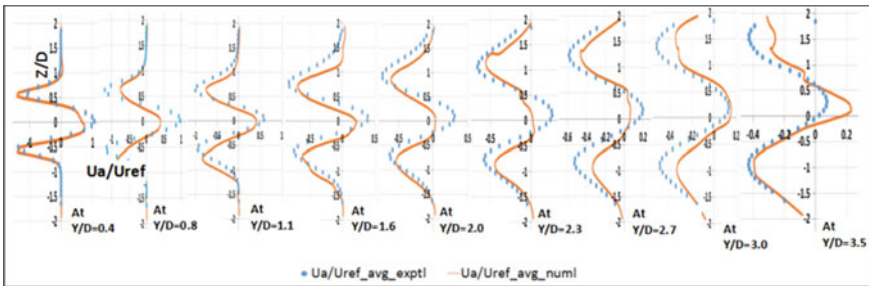


Fig. 6 Time averaged normalized axial velocity comparison

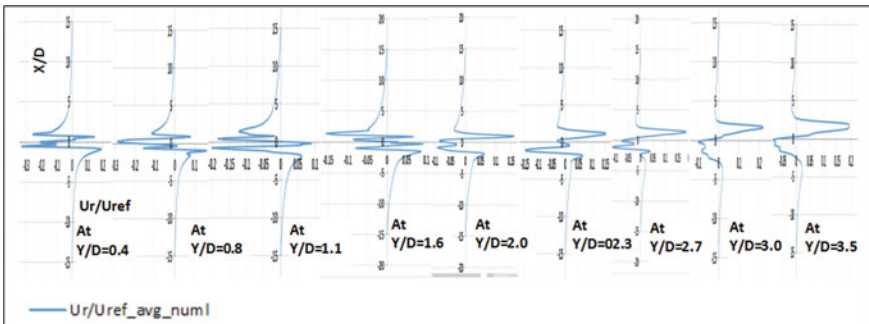


Fig. 7 Numerical prediction of time averaged normalized radial velocity variations along the injector axis

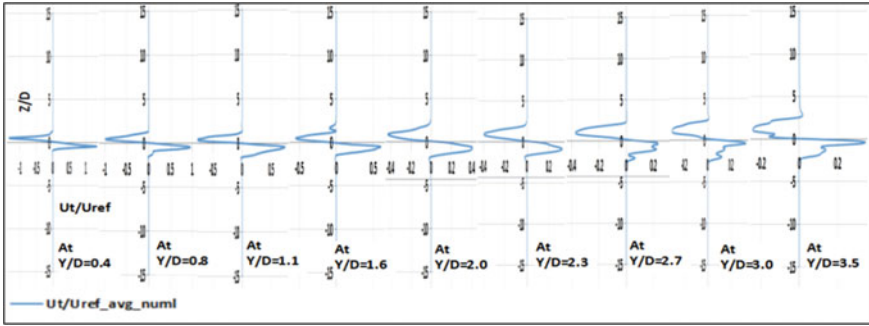


Fig. 8 Numerical prediction of time averaged normalized tangential velocity variations along the injector axis

3.2 Various Plots

3.2.1 Q-criteria

Figure 9 clearly shows presence of vortex inside and downstream of injector as it flows.

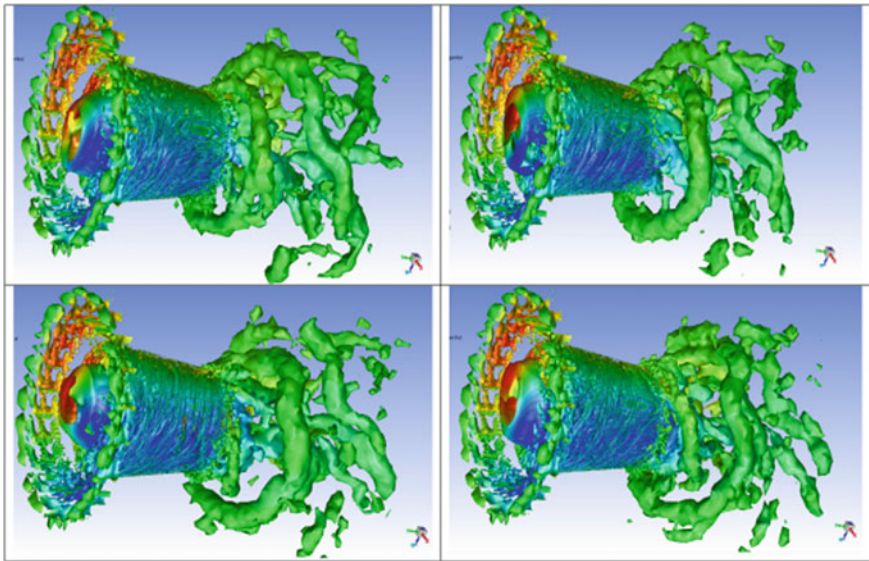


Fig. 9 Q-criteria iso-surface (based on 1% of maximum value at $Z = 0$ plane at location of interest) colored by tangential velocity: Data are plotted for every 0.1 ms time interval after mean flow fields were stabilized

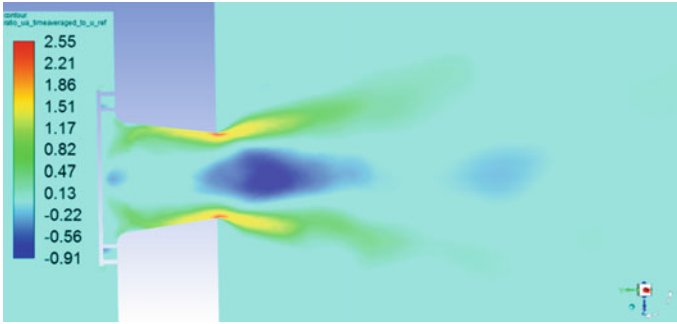


Fig. 10 Normalized time averaged axial velocity contour

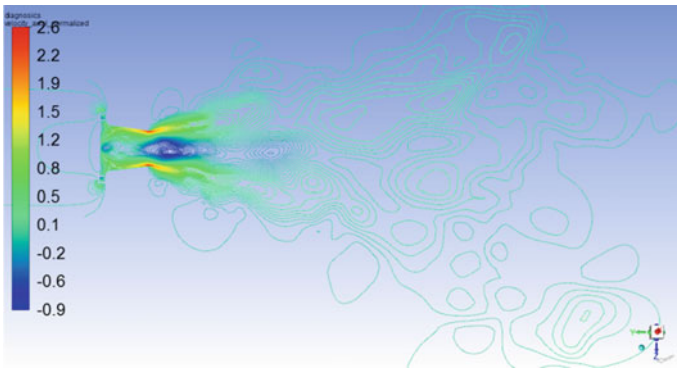


Fig. 11 Normalized time averaged axial velocity streamlines

3.2.2 Contour Plots of Axial Velocity

Figure 10 shows above contour plot of the normalized axial velocity showing recirculation zone near to exit of the injector.

3.2.3 Stream Line Plots

Figure 11 shows streamline plot of normalized axial velocity showing recirculation zone near to exit of the injector.

3.2.4 Vector Plots of Axial Velocity (r - y) and (r - θ) Directions

Figure 12 shows time averaged velocity vector plot colored by normalized axial velocity showing recirculation zone near to exit of the injector. There is also presence

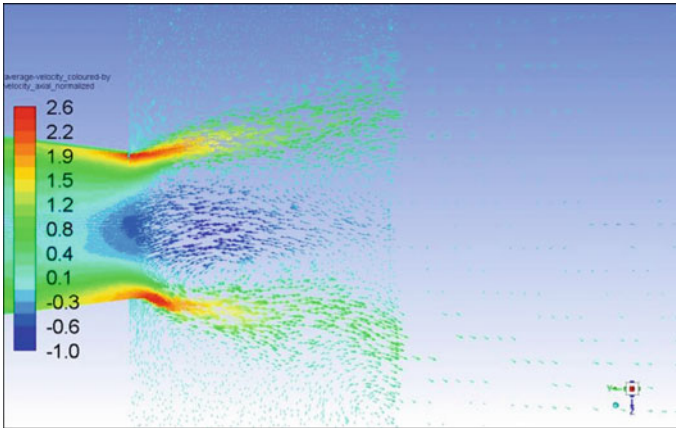


Fig. 12 Time averaged velocity vector colored by normalized axial velocity

of shear layer which fluctuates and vortices were also present due to K–H instability. This instability to atomize fuel film can be added up to that created by secondary swirler at the same location (Fig. 13).

Through above vector plots multiple phenomena are being tracked: In above plot (Fig. 13), normalized vorticity of flow is super-imposed on normalized axial velocity. It is seen high vortex started from swirler exit gradually reduces with flow with maximum vorticity occurring near injector wall when flow is inside the injector. Presence of vortex near the wall is due to presence of PVC (not shown here) at

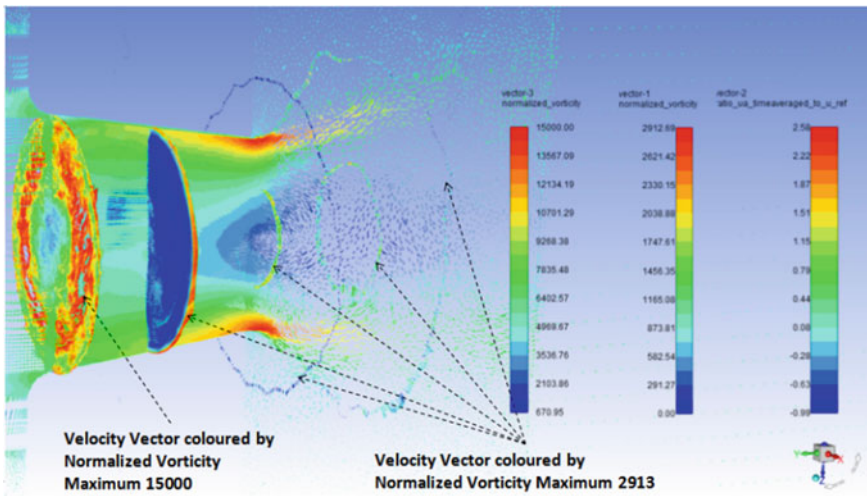


Fig. 13 Normalized vorticity-velocity fields

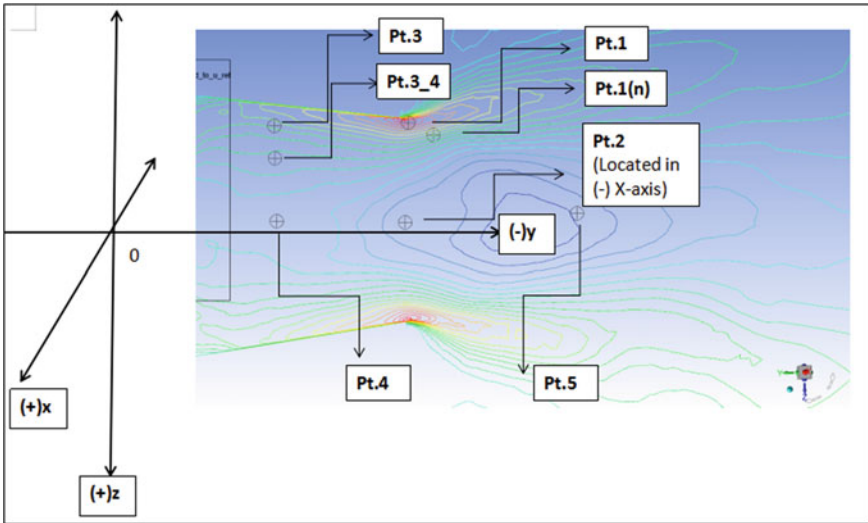


Fig. 14 Positions of various monitoring points for time-dependent tracking of various parameters

injector core, which continuously throws out air toward the wall. According to Shanmugadhas and Chakravarthy [9], PVC with primary spray continuously precessed due to primary air swirl which indirectly creates periodic droplet impingement on the wall and thereby forming non-uniform filming of fuel on the pre-filming wall. It is also seen that around the periphery of CTRZ magnitude of normalized vorticity is slightly higher than that near to the shear layer: This may also help to atomize and disperse the fuel droplets (Fig. 13).

3.2.5 Plots and Capturing Frequency Tracks

During the simulation run, time-based values of parameters such as U_a , U_t , U_r , and P_s are collected and stored at each of the locations mentioned above (refer Fig. 14) at each time step 1×10^{-06} s. These parameters are then plotted (refer Fig. 15) to reveal for any periodic phenomena.

Figure 15 shows the plotting of periodic signals captured w.r.t. time after removing initial transient data. FFT of the signals is shown in Fig. 16. Here, it may be mentioned that during the simulation run, it was observed that after flow-time of ~ 0.0524 s the time averaged values of parameters have been found to be varied within maximum $\pm 2\%$ of their mean values (results not shown here). And since this variation is small, hence, the solution was considered to be achieved statistically averaged value.

From Fig. 16, it is seen that at core of the injector near to axis and slightly away from injector tip, there are phenomena with 2.5 kHz frequency. This frequency can be considered for PVC and shear layer fluctuations.

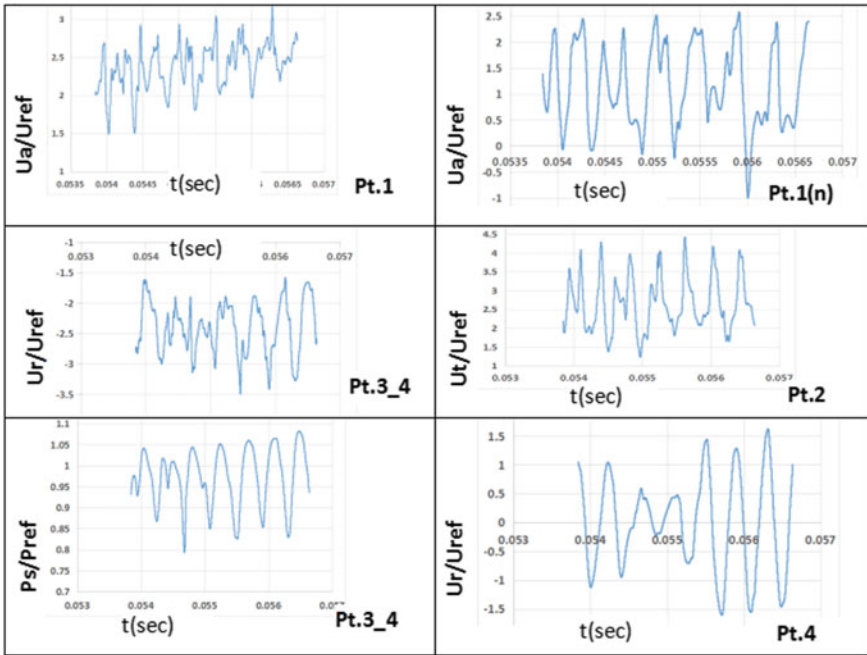


Fig. 15 Time-dependent signals of parameters at various monitoring points of the flow field collected over 2.8 ms

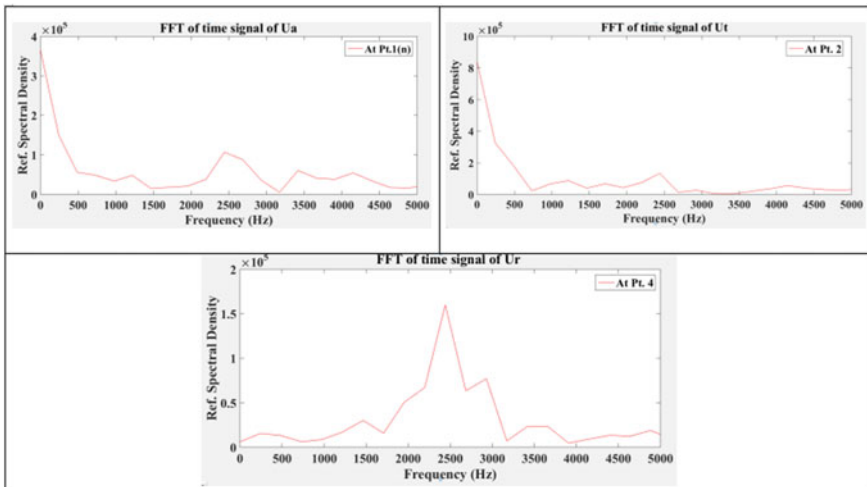


Fig. 16 FFT of respective time-dependent signals (second column of Fig. 15) showing various frequencies

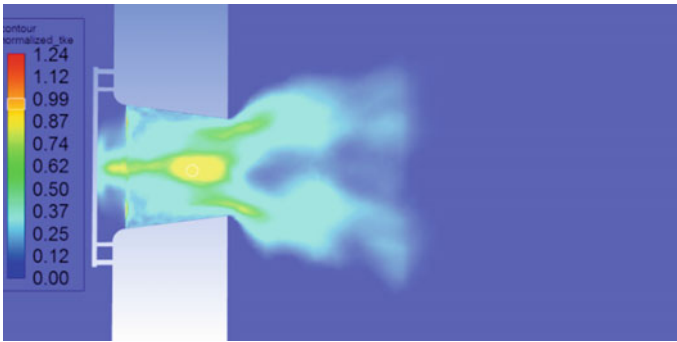


Fig. 17 Normalized TKE plot of the flow field

3.2.6 Turbulent KE Plots

Figure 17 clearly shows that most values of normalized TKE exist near the core and tip of the injector. Presence of TKE at starting of core is due to PVC, slightly at downstream TKE is due to presence of CTRZ; both these TKE would be useful for proper mixing of fuel–air droplets; where TKE presence near to injector lip would be helpful for fuel atomization and droplet dispersion. The spatial energetic modes could also be extracted using reduced order mathematical tool such as POD.

4 Conclusions

LES analysis is able to capture reasonably the flow field of a fuel injector fitted with single radial swirler, thus capturing important fundamental aspects of flow physics. WMLES model of ANSYS Fluent was used to capture turbulence in LES region. Closure trend behavior of numerical results and experimental data of the axial velocity shows that aspects of modeling for resolving the flow field are reasonable. Analysis could capture different vortices present in flow field useful for fuel atomization and droplet dispersion for proper mixing. It was found that vorticity present near to the injector wall surface and outer periphery of CTRZ (with which PVC fluctuates) could be useful for creating azimuthal instabilities on the fuel film and relevant frequency is 2.5 kHz. Positions of higher TKE fields have shown relevant phenomena in terms of fuel atomization and droplet dispersion. Modeling methodologies used here would be very useful for carrying out computational studies and database generation for the kind of complex geometry and physics. Since this preliminary study is aimed at considering a fixed location of the interfaces, studies can be further progressed by varying the placement of interface zones and their impacts on flow field so as to make the model more robust.

Acknowledgements Authors are very much grateful to Mr. M. Z. Siddique, DS & Director, Gas Turbine Research Establishment, Bangalore, for permitting to present this paper in the conference. The authors are also thankful to members of combustion group for their support and help extended during the course of the study.

References

1. Tacina R (1990) Combustor technology for future aircraft. NASA Technical Memorandum 103268 AIAA-90-2400
2. Correa SM (1998) Power generation and aero propulsion gas turbines: from combustion science to combustion technology. In: Twenty-seventh symposium (international) on combustion. The Combustion Institute, pp 1793–1807
3. Zhang HL, Bachman CR, Fasel HF (2000) Reynolds-averaged Navier-Stokes calculations of unsteady turbulent flow. AIAA-0143
4. Sankaran V, Menon S (2002) LES of spray combustion in swirling flow. *J Turbul* 3:N11. <https://doi.org/10.1088/1468-5248/3/1/011>
5. Stone C (2003) Large eddy simulation of combustion dynamics in swirling flows. PhD Thesis. Georgia Institute of Technology, School of Aerospace Engineering March 2003
6. Wang S, Yang V, Hsiao G, Hsieh SY, Mongia HC (2007) Large-eddy simulations of gas-turbine swirl injector flow dynamics. *J Fluid Mech* 583:9–122 (Cambridge University Press)
7. Rana R, Sonukumar, Muthuveerappan N (2019) RANS based iso-thermal CFD analysis of the flow field created by a radial swirler in a conical nozzle. GTINDIA2019-2726, <https://doi.org/10.1115/GTINDIA2019-2726GTIndia>
8. Cohen JM, Rosfjord TJ (1993) Influences on the sprays formed by high shear fuel nozzle/swirler assemblies. *J Propul Power* 9(1) Jan-Feb 1993
9. Shanmugasdas KP, Chakravarthy SR (2018) Wall filming and atomization inside a simplified prefilming coaxial swirl injector: role of unsteady aerodynamics. In: 2018 AIAA aerospace sciences meeting, 8–12 Jan 2018, Kissimmee, Florida
10. ANSYS (2016) ANSYS fluent theory guide